Molecules in the circumstellar envelope of the evolved carbon-rich star IRC+10216

Dissertation
zur
Erlangung des Doktorgrades (Dr. rer. nat.)
der
Mathematisch-Naturwissenschaftlichen Fakultät
der
Rheinischen Friedrich-Wilhelms-Universität Bonn

vorgelegt von
Denise Keller
aus
Birkenfeld (Nahe)

Bonn, 2016

Dieser Forschungsbericht wurde als Dissertation von der Mathematisch-Naturwissenschaftlichen Fakultät der Universität Bonn angenommen und ist auf dem Hochschulschriftenserver der ULB Bonn `http://hss.ulb.uni-bonn.de/diss_online` elektronisch publiziert.

1. Gutachter:	Prof. Dr. Karl M. Menten
2. Gutachter:	Prof. Dr. Norbert Langer
Tag der Promotion:	25.01.2017
Erscheinungsjahr:	2017

Abstract

Modern radio interferometers allow the imaging of spectral line emission over a wide range of frequencies with high angular resolution. We present a new spectral imaging survey of the carbon-rich asymptotic giant branch (AGB) star IRC+10216 between 18 and 40 GHz obtained with the Karl G. Jansky Very Large Array (VLA). This survey traces the distributions of different molecules in the circumstellar envelope (CSE) of this star in unprecedented detail at a resolution of 1 arcsec and strongly constrains the circumstellar chemistry. We identify 220 molecular transitions from 20 species, including several isotopologues, mostly from rotational energy levels and a few vibrationally excited states.

In this thesis, extensive work is put into the data calibration and imaging synthesis to ensure a high-quality data product. Most importantly, we thoroughly test different imaging parameters in the deconvolution of the interferometric data sets. We aim to extract as many molecular transitions with the most amount of physical flux as possible.

With a new automatized procedure, we perform a detailed spatio-kinematical study of the images of the molecular line transitions, probing mainly photochemical processes in the outer CSE. Most detected species are carbon-bearing molecules and are distributed in hollow spheres around the star. For the analysis we divide the image maps into four quarters and we extract radial emission profiles of the whole azimuthal sum and for each of the quarters. This work quantifies the three dimensional physical and chemical structure and substructure of IRC+10216 in unique detail.

We find a main molecular shell component at an angular distance of about 15 arcsec (corresponding to $\sim$ 500 stellar radii) and for the first time constrain a second shell component at $22 - 23$ arcsec from the star. Both components have a thickness of about $4 - 8$ arcsec, so they are mostly resolved. The morphology is clumpy and the shells are not centered on the stellar position and show asymmetries. For the molecules HC_3N, HC_5N, HC_7N, C_3N, C_4H, C_6H, and C_6H^- there are clear differences in the detailed substructure for the different quarters and the different species.

We qualitatively compare the VLA observations to state-of-the-art chemical models. Overall, we find a good correspondence between the azimuthally averaged data and the models. There are deviations in the substructure within the different image quarters, especially for the carbon chains C_4H and C_6H. The models do not completely reproduce the observations in a consistent way. Therefore, our VLA data provide excellent material to improve future chemical and radiative transfer models of the CSE of IRC+10216 and of AGB stars in general.

With the extracted information on the shell geometry from the VLA data, we are able to perform an approximate physical analysis of the CSE. We estimate molecular column densities and abundances of HC_3N and HC_5N. Especially for HC_5N the results compare well with previous studies. Furthermore, we discuss the effect of a more realistic density structure which includes density-enhanced shells in the circumstellar medium.

Several physical and chemical effects, and their feedback on each other, might shape the observed CSE morphology of IRC+10216. Local and global influences may create the clumpy shells in the CSE with non-concentric and non-regular substructures. We discuss possible explanations, such as directional mass loss, hydrodynamical impacts on the stellar wind, and internal and external non-isotropic UV-field sources.

The detailed empirical description of the morphology of the outer CSE of IRC+10216 in this thesis strongly contributes to the understanding of the carbon chemistry around AGB stars. The observational material shows that the active photochemistry is confined to a narrow density-enhanced region. Our analysis emphasizes the sensitivity of the probed molecules to UV radiation. It is mandatory for future chemical models to consider the complex substructure of the circumstellar medium, particularly the density-enhancements in form of shells, arcs, and clumps, and the subsequent UV shielding and penetration, to more thoroughly understand the physical and chemical structure around AGB stars. This will lead to a better knowledge on the production of complex carbon-bearing molecules in the Universe.

Contents

CHAPTER 1

Introduction

Stars are fundamental celestial objects studied by curious humans ever since. Stars are the major visible components and important sources of energy in the Universe. Not only do they yield significant physical feedback through, for example, stellar winds and radiation, they also have a crucial chemical effect on the interstellar medium by producing the heavy elements. Without stars the Universe consisted only of hydrogen and helium from the big bang. Stars are the unique origin of elements such as carbon, oxygen or iron (Bethe 1939; Burbidge et al. 1957). Through their evolution, particularly towards the end of their life cycle, stars distribute these heavy elements in the interstellar medium and enrich the environment of new generations of stars and planets. Stars therefore are paramount for the chemical evolution of the Universe, the galaxies and stellar systems like our solar system.

Only since the 20th century scientists started to understand the source of energy and light production from our Sun. From there, it has been possible to understand other stars and their evolution. The majority of stars are low-mass stars, as our Sun, that evolve into red giants and become white dwarfs in the end (Abell & Goldreich 1966; Iben & Renzini 1983). Red giants are very cool, extended, and luminous. Especially during the asymptotic giant branch (AGB) phase, they are important agents for the production of molecules and dust grains in the Universe (e.g. Busso et al. 1999; Habing & Olofsson 2003; Gail & Sedlmayr 2014) and are the focus of this work.

From the end of the 1960s onwards it became clear that molecules of various types abundantly exist in space and that in certain regions of the interstellar medium even almost all atoms are combined into molecules (Duley & Williams 1984). The expanding atmospheres of cool stars are suitable environments for forming molecules and larger compounds, i.e. dust grains. Also the cold, dense, and chemically enriched interstellar medium contains various types of molecules, especially complex organic molecules (e.g. Belloche et al. 2015), which are the building blocks of organic life. Many observed molecules in space were first detected in the circumstellar envelope around AGB stars, most of them in the nearby high mass-loss carbon-star IRC+10216 also known as CW Leo (Becklin et al. 1969; Kukarkin et al. 1971), which we target in this work.

By studying circumstellar environments we learn more about astrochemistry, the influence of temperature, density, shocks, radiation fields, and dust grains on the formation and destruction of molecules. Furthermore, the observational results can be linked to the internal physics and chemistry of these stars, i.e. nucleosynthesis, which yields an improved understanding of stellar evolution itself.

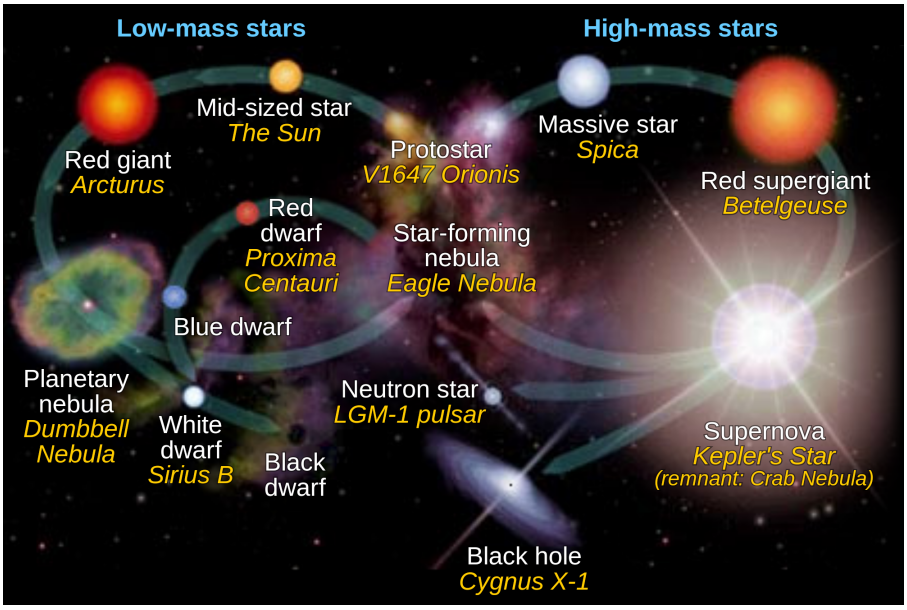

Figure 1.1: Sketch of the possible cycles of stellar evolution from a star-forming nebula to the respective end stage for low-mass stars ($0.8-8$ $M_\odot$) on the left and high-mass stars (from about 8 $M_\odot$) on the right. © NASA Goddard Space Flight Center

In this chapter, the astrophysical, chemical, and technical background required for this work is introduced. First, the context of stellar evolution is introduced that is important for AGB stars. We take a look at the theory about the formation of elements in stars – the nucleosynthesis. From the theoretical background, we aim to understand the emission of molecular compounds in the circumstellar medium of AGB stars, which are the focus of this work. Particularly, the carbon chemistry in the circumstellar envelope of IRC+10216, with the main focus on photochemistry, is discussed. We explain the molecules and their chemical network which are key to the analysis of this thesis. Finally, we describe the radio astronomical technology and interferometric methods with which the molecular emission is measured, processed and interpreted. The AGB star IRC+10216 is described in detail in Chapter 2.

The following text is largely based on Habing & Olofsson (2003), Langer (2009), Pols (2009), and references therein. Other references are mentioned explicitly throughout the text.

1.1 Stellar evolution and nucleosynthesis

The life cycle of stars, from molecular clouds to main-sequence stars to the final stages (white dwarf, neutron star, black hole or complete disappearance through explosion or merging in a binary system), is guided mainly by the initial stellar mass. The evolution also depends on the initial chemical composition and possible interactions with companion stars. This work focuses on a star that belongs to the group of low- to intermediate-mass stars with initial masses of about $0.8-8$ solar masses ($M_\odot$), the most common stars in the Universe. Most of these stars evolve into red giant stars and go through the asymptotic giant branch (AGB) phase, a phase that is characterized by atmospheric pulsations, strong stellar winds, and an extended circumstellar envelope (CSE). They end as white dwarfs, which are degenerate, very hot and luminous objects, that gradually cool down and become fainter (Figs. 1.1 and 1.2).

In this section we give an overview on stellar evolution and focus on the AGB phase.

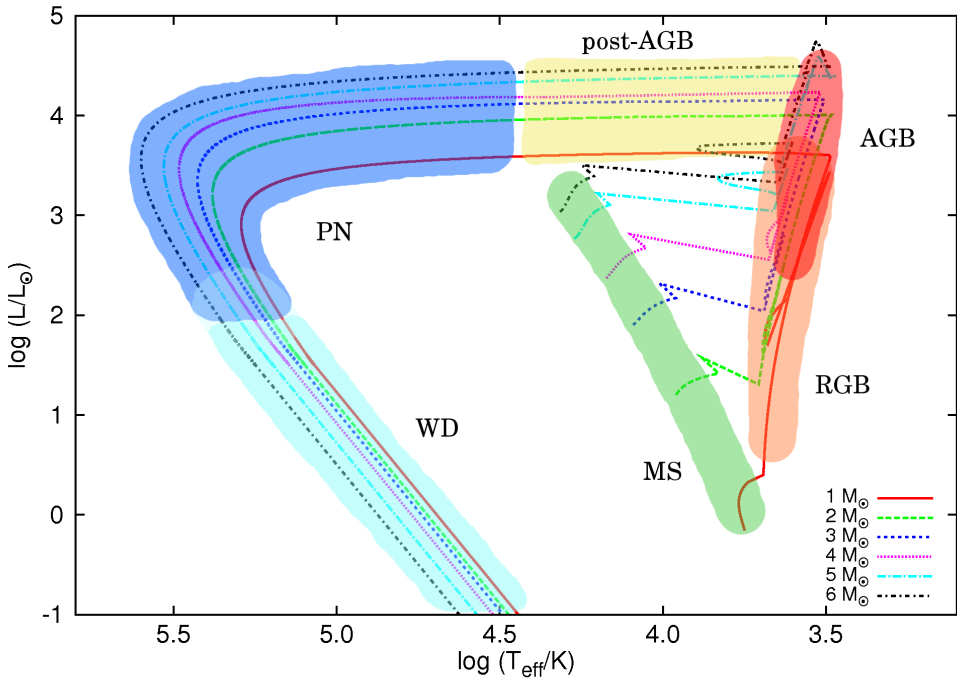

Figure 1.2: Hertzsprung-Russell Diagram of low- to intermediate-mass stars with evolutionary tracks modeled with the stellar evolution code *binary_c/nucsyn* (Izzard et al. 2004, 2006, 2009). The main sequence (MS, in green), red giant branch (RGB, in orange), asymptotic giant branch (AGB, in red), post-AGB (in yellow), planetary nebula (PN, in blue) and white dwarf (WD, in turquoise) phases are indicated. © Denise Keller

1.1.1 Stellar equilibrium, timescales, and equation of state

As a start, the states of equilibrium important for stellar evolution are described. A system is in equilibrium if the regarding parameters are in balance and no spatial and temporal changes occur. The equilibrium of stars is given by the balance of gravitational forces inwards and pressure gradient forces outwards, which is powered by the internal energy source of thermonuclear fusion and is radiated from the stellar surface. This *hydrostatical equilibrium* is associated with a global spherical shape. Changes of these force balances are directly interrelated with the physical and chemical evolution of stars.

The transfer of energy or matter in the form of heat and work between two systems through e.g. collision, scattering, absorption, etc. leads to *thermodynamic equilibrium*. If two systems are connected only through heat and encounter no net heat flow, they are in *thermal equilibrium*; if no transfer of matter is possible, the systems may not reach thermodynamic equilibrium. Systems in thermodynamic equilibrium are always in thermal equilibrium, however the converse is not always valid.

Because a star radiates and therefore is not isolated and looses energy to the surrounding medium, it is not in global thermodynamic equilibrium as a whole. However, the star can be divided into layers with constant temperature and pressure, which are much thinner than the radius of the star, but thicker than the interaction length between gas and photons, such that a balance is reached, called the *local thermodynamic equilibrium* (LTE). Also the composition of a medium can reach an equilibrium state. If forward and reverse reactions proceed with a very similar reaction rate, and therefore the amount of reactants and products does not change over time, the system is in *chemical equilibrium*.

A system in thermal equilibrium is characterized by a single uniform temperature. If this temperature

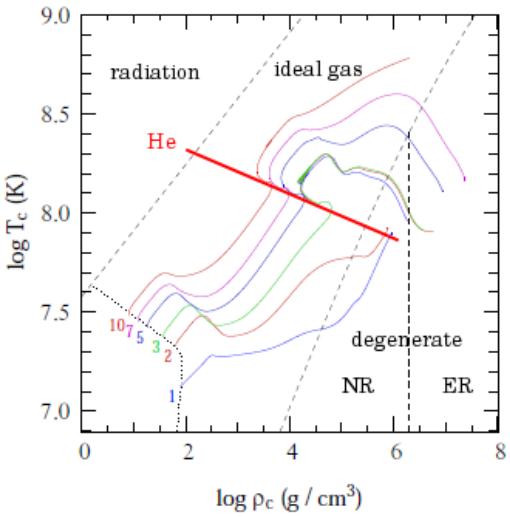

Figure 1.3: Evolution of 1 to 10 $M_\odot$-stars in terms of central temperature T_c and central density ρ_c. The dotted line shows the zero-age main sequence, the thick red line indicates the limit of helium ignition in the core and the dashed lines give the borderlines between the different equations of state describing the dominant pressure source: radiation, ideal gas, non-relativistic (NR) or extremely-relativistic (ER) degeneracy. AGB stars do not evolve to higher central temperatures, meaning that no further fusion cycles start. They evolve to white dwarfs with degenerate cores. Based on Pols (2009).

is given by an isotropic radiation field and the photon energy distribution follows the Planck function of a black body, the system is also in thermodynamic equilibrium. This determines the color and brightness of a star displayed in a Hertzsprung-Russell diagram (HRD, Hertzsprung 1913), which serves for the classification of groups of stars according to their observable properties and corresponding physical parameters, i.e. effective surface temperature and luminosity (Fig. 1.2).

These force and their changes also drive the nucleosynthesis evolution in the stellar interior. Stars may go through several nuclear fusion cycles during their evolution depending on their initial mass. The changes in dynamical, thermal and chemical structure are described by the intrinsic stellar timescales, which give the time the star needs to restore hydrostatic or thermal equilibrium after a disturbance and the duration of the nuclear burning phase, respectively. For the Sun, these timescales are of the order of 1000 s, 10^7 yr, and 10^{10} yr, respectively.

For high central temperatures (10^5 – 10^{10} K) and moderate central densities (10 – 10^4 g cm^{-3}), the star is dominated by radiation or ideal-gas pressure. For low temperatures and very high densities the material becomes degenerate and the pressure is dominated by the degenerate electron gas, hence becomes independent of the ambient temperature (Fig. 1.3). The state of the stellar material determines its reaction to disturbances and the energy transport outwards. For a certain temperature gradient between stellar layers, energy is transported from the interior outwards via radiation diffusion. For even higher temperature gradients, the energy is transported much faster, the gas becomes unstable and macroscopic movement of convection cells sets in. Convection occurs, for example, in very opaque layers with rather low temperatures, such as the extended envelopes of red giants.

1.1.2 Evolution towards the AGB phase

1.1.2.1 Main-sequence phase

The formation of a star is completed, once thermonuclear fusion of hydrogen to helium is efficiently ongoing in the stellar core. The star remains in this condition for about 90% of its life time. The so-called central hydrogen burning is the longest phase in the stellar life time and most stars are observed during this phase, hence form the most populated region in the HRD, the main sequence (MS, Fig. 1.2). The star's location on the MS is given by the initial mass of the star – the higher the mass the hotter and brighter. Also, the higher the mass the faster the evolution of the star. The duration of the main sequence is governed by the nuclear timescale of hydrogen burning and ranges from about 10^6 to 10^{10} yr for initial masses between 60 $M_\odot$ and 0.8 $M_\odot$, respectively. Stars with an initial mass below 0.8 $M_\odot$ have even longer nuclear timescales and have not yet evolved beyond the MS during the age of the Universe, which is about 10^{10} yr (Komatsu et al. 2011; Planck Collaboration et al. 2014). Given the initial mass function (e.g. Kroupa et al. 1993), low- to intermediate-mass stars with initial masses below 8 $M_\odot$ account for 99% of all stars. However, only 10% of these stars are considered to be evolved stars, i.e. post-MS. In addition, the post-MS evolution has several different evolutionary stages. Thus, there are few red giant stars. Moreover, only a few red giant stars are in our vicinity and therefore bright enough to be observed.

The thermonuclear fusion of hydrogen has two possible mechanisms depending on the temperature and density in the stellar core. Consequently, the fusion mechanism is coupled to the stellar mass and the metallicity – the content of elements heavier than helium. In low-mass stars (below 2 $M_\odot$) the proton-proton (pp)-chain dominates:

$$4\ {}^1\mathrm{H} \rightarrow {}^4\mathrm{He} + 2\nu_e + \gamma$$

(Bethe 1939). The amount of released energy is about 26 MeV per net reaction, or 4×10^{-12} J. For example, the Sun radiates about 3.8×10^{26} J s^{-1} from its surface due to this reaction chain. The energy production can also be translated into 6.4×10^{-6} Joule per gram of hydrogen. As a comparison, the energy budget of a chocolate bar is about 2×10^4 Joule per gram of chocolate.

In stars with masses greater than 2 $M_\odot$ the net production of helium nuclei, also called α-particles, is created through the so-called CNO-cycle where the catalysts for the reactions are carbon, nitrogen, and oxygen (Fig. 1.4). Especially the CNO-cycle has a very steep temperature dependence, and therefore the fusion happens only in regions of suitable conditions. As a notable by-product, this fusion cycle mainly converts carbon (^{12}C) into nitrogen (^{14}N).

The gradual increase of the helium abundance in the stellar core increases the molecular weight, which causes the central temperature to increase. As soon as the hydrogen fusion rate declines in the stellar core, due to decreasing abundance of hydrogen, the pressure forces outwards are not efficient anymore to balance the gravity forces inwards, such that gravity starts to dominate, which causes the core to compress and heat up. The hydrogen fusion shifts to layers further outwards with lower, thus suitable, temperature and pressure conditions. This means that there is no active nuclear fusion in the core anymore, which consists mostly only of the ashes of the former fusion cycle, namely helium. The hydrogen shell burning adds helium to the underlying core and increases the helium core mass gradually on a nuclear timescale.

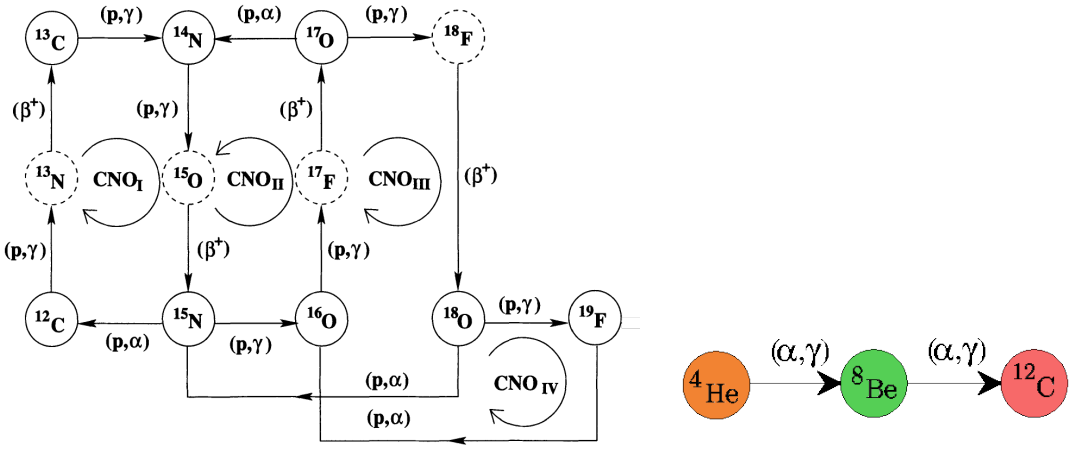

Figure 1.4: *Left*: Sketch of the CNO-cycles, with unstable isotopes in dashed circles (Lattanzio & Wood in Habing & Olofsson 2003). *Right*: The triple-α process: Fusion of helium (α-particle) to carbon via two α-particle captures.

1.1.2.2 Post main-sequence and red giant branch phase

As the stellar core is compressing, the envelope expands in response according to the viral theorem to maintain thermal equilibrium, also called the mirror principle. The H-burning shell stays in thermal equilibrium as long as the temperature is approximately constant. For this, as the core is compressing and heating, the overlying layers have to decrease in pressure and density which is only achieved by expanding outwards. Similarly, when the core expands the overlying burning shells contract in response (Pols 2009). During this hydrogen shell burning, the star changes its observable surface properties: It becomes cooler, therefore appears redder, and it becomes larger, therefore is more luminous than on the main-sequence, such that in the HRD the star moves towards and along the red giant branch (RGB, Fig. 1.2). Red giant stars are stable until the Hayashi limit. Stars with lower temperatures and/or greater radius cannot be in hydrostatic equilibrium (Hayashi 1961).

For stars with masses below about 2 $M_\odot$, the transition from hydrogen core- to shell-burning happens while maintaining thermal equilibrium, because of their degenerate core. For stars with higher masses thermal equilibrium is disturbed and the evolution towards the giant branch is very quick. The cores of these stars are dominated by convection and hydrogen shell burning happens in a thin shell, such that thermal equilibrium is easily disturbed. The stellar radius increases by a factor of at least 10 in just about 10^6 years on a thermal timescale. Almost no stars are observed in this phase because it is evolutionary so short. Thus, there is a gap in the HRD, the Hertzsprung gap.

For low-mass red giants ($M < 2\ M_\odot$), there is a tight relation between the stellar luminosity L and the core mass $M_{\rm core}$, due to their degenerate helium core, which does not depend on the thermal properties: $L \sim 2.3 \times 10^5\ M_{\rm core}^6$, where L and $M_{\rm core}$ are in units $L_\odot$ and $M_\odot$, respectively. The luminosity is given by the H-shell burning.

The loosely bound expanded envelope has no direct effect on the evolution of the stellar interior, however, it has an effect on the evolution of the star due to the amount of mass removed from the star. The exact mechanism for the mass loss on the RGB is under debate (e.g. Lattanzio & Karakas 2016). The first formula to derive an empirical relation between mass loss rate $\dot{M}$ and stellar parameters, such as luminosity L, radius R and surface gravity g was given by Reimers (1975): $\dot{M} = -4 \times 10^{-13}\ \eta\ L\ g^{-1}\ R^{-1}$,

where $\dot{M}$ is in units $M_\odot\ yr^{-1}$, L, R, g in solar units, and the scaling parameter η usually is $1/3 - 3$. With stellar parameters for theoretical evolutionary models, the relation is: $\dot{M} = -4 \times 10^{-13}\ \eta\ L\ R\ M^{-1}$, in solar units. The relation has been widely used and is good to explain the distribution of RGB stars in the HRD, but it does not describe AGB stars or metal poor stars well.

During the RGB phase, the stellar envelope is highly convective, like water in a boiling pot. Convective mixing is very fast and effective. If these convective cells reach into regions that are enriched by previous nuclear reactions, this material is mixed to the stellar surface, where a change in chemical composition becomes observable. During the RGB this occurrence is called first dredge-up (FDU), which particularly increases the helium and nitrogen abundance at the stellar surface (^{14}N by a factor of $3 - 4$, also ^{13}C by a factor of $2 - 3$). The isotopic ratios at this evolutionary phase are $^{12}C/^{13}C \approx 20$ and $^{16}O/^{18}O \approx 600$ (Lattanzio & Wood in Habing & Olofsson 2003).

1.1.2.3 Helium core burning

Once the temperature and density in the stellar core have reached a certain threshold (10^8 K, 10^4 g cm^{-3}, Fig. 1.3), helium fusion in the core begins. The whole star contracts again, in response to the core expansion, and reaches higher surface temperatures moving to the left in the HRD (on a thermal timescale), such that these stars form a helium-burning sequence in the HRD, also called horizontal branch (HB).

For low-mass stars ($M < 2\ M_\odot$) stable helium burning in the core is preceded by the so-called helium flash, which describes an explosive ignition of helium in the degenerate stellar core. In the degenerate state the pressure in the core is constant (given by the electron degeneracy pressure) and is independent of the temperature, such that a temperature increase is not balanced by a radius increase. The temperature rises until the degeneracy is lifted and the material behaves as an ideal gas again. The core then expands and becomes convective, the temperature drops and helium burning continues steadily (cf. Fig. 1.3). For stars with higher masses ($M > 2\ M_\odot$), the helium core burning starts non-degenerately. The main product of helium core burning is carbon (^{12}C) through the triple-α process:

$$^4He + {}^4He \rightarrow {}^8Be + \gamma\,,$$

$$^8Be + {}^4He \rightarrow {}^{12}C + \gamma\,.$$

The net energy production of the triple-α process is 7.27 MeV, which is much less than the energy production during hydrogen burning. Therefore the phase of He-core burning is much shorter than H-core burning. Furthermore, during this phase the H-burning shell dominates the stellar luminosity. The reaction chain can also be written as $^4He(\alpha,\gamma)^8Be(\alpha,\gamma)^{12}C$. A further α-capture creates oxygen: $^{12}C(\alpha,\gamma)^{16}O$ (Fig. 1.4).

When the helium core burning is not efficient anymore to counterbalance gravity, the core (now consisting mainly of C and O) contracts once again and becomes electron degenerate. Helium shell burning starts, which, together with the H-burning shell, provides the main stellar energy output. The stellar envelope expands even further than during the RGB and becomes convective again. The second red giant phase begins. In the HRD this group of stars is positioned asymptotically to the first red giant branch (Fig. 1.2), therefore the stars in this phase are called asymptotic giant branch (AGB) stars.

1.1.3 The AGB phase

In this section we focus on the internal structure and evolution of AGB stars. In Sect. 1.2 we describe the observable external properties in detail.

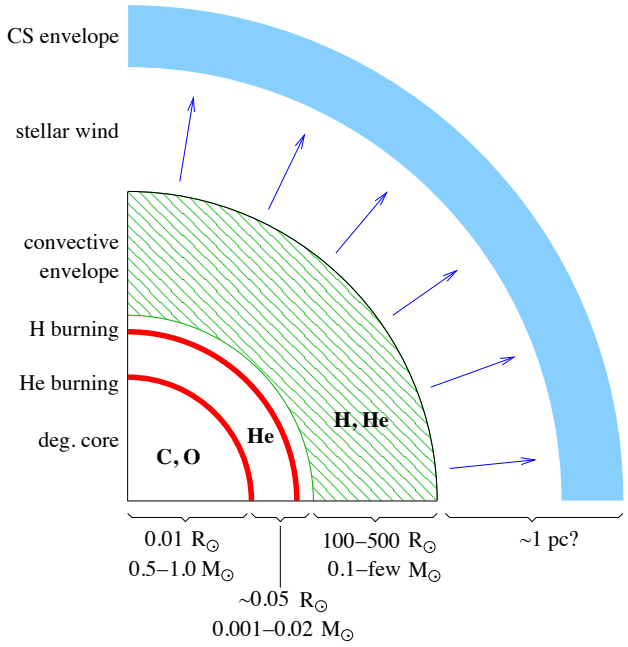

Figure 1.5: Schematic structure of an AGB star (Pols 2009).

The AGB phase is divided into two phases, the early-AGB (E-AGB) and the thermally-pulsing AGB (TP-AGB) phase. The AGB star consists of a degenerate C- and O- core, surrounded by a He- and a H-rich shell, and a huge convective envelope. Above lies the stellar atmosphere and a very extended circumstellar envelope (Fig. 1.5). No further fusion cycle in the core starts, due to the degeneracy and neutrino cooling. This determines the upper mass limit of about 8 $M_\odot$. AGB stars have surface temperatures of 1000 – 3000 K, luminosities up to the order of 10 000 $L_\odot$, and radii of 500 – 1000 $R_\odot$. Each AGB phase has a duration of the order of 10^6 years (depending on mass and metallicity) and especially the duration of the TP-AGB phase is mainly governed by the mass loss rate (Vassiliadis & Wood 1993). The E-AGB phase is a bit longer than the TP-AGB phase, but the changes during TP-AGB are more significant in terms of chemical and stellar evolution.

1.1.3.1 Early-AGB phase

At the beginning of the early-AGB, for stars with initial masses greater than about 4 $M_\odot$ (depending on composition), the stellar envelope expands so strongly, such that the temperature decreases significantly to extinguish the H-burning shell. As a consequence there is no thin radiative layer around the H-rich shell and the convective envelope expands deeper into regions enriched by products of the CNO-cycle. This ^{4}He- and ^{14}N-rich material is efficiently mixed throughout the convective envelope to the stellar surface, a process called the second dredge-up (SDU).

1.1.3.2 Thermally-pulsing AGB phase

There is an interplay between the He- and H-shell in the AGB star in which the burning turns on and off, due to the mirror principle described above. First of all, the H-shell burning adds helium and increases density and temperature to the underlying region, which starts the He-burning. Due to He-shell burning

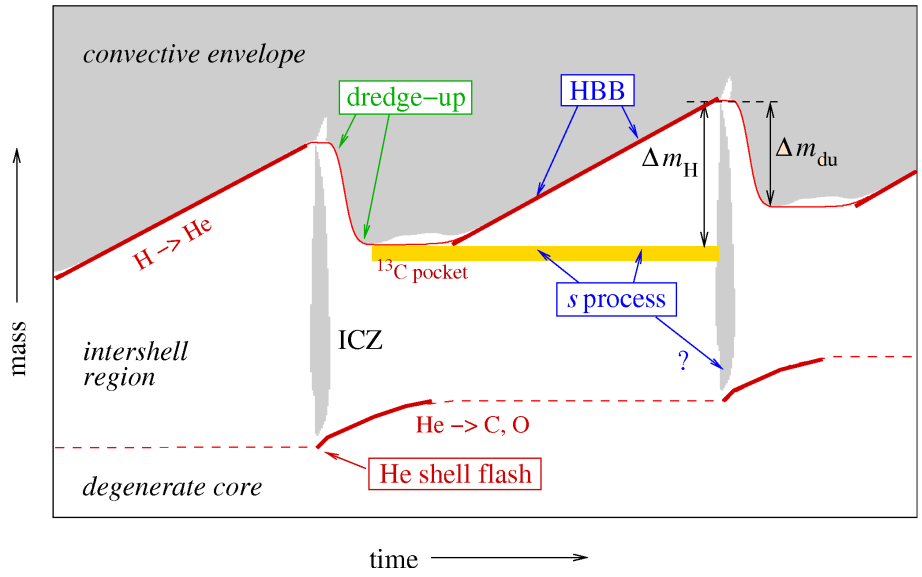

Figure 1.6: Evolution of an AGB star in the mass coordinate as a function of time. The mass coordinate has its origin at the stellar center and increases towards the stellar surface. Two thermal pulses (helium shell flashes) with the formation of an intershell convection zone (ICZ) are shown. The hydrogen burning shell expands into the convective envelope driving the third dredge-up, which mixes helium and carbon from the ICZ to the surface of the star. The amount of the dredged up material is given by $\Delta m_{\rm du}$, compared to the mass in the hydrogen layer $\Delta m_{\rm H}$. The time coordinate is highly non-linear (shell flash and dredge-up phases $\sim$ 100 years and interpulse phase $\sim 10^4$ years). The mixing causes a so-called ^{13}C pocket due to a high influx of protons. Through further α-captures in the helium-rich environment of ^{13}C and ^{22}Ne, there is a high number of neutrons. The conditions in TP-AGB stars are suitable to initiate a slow-neutron capture onto iron seeds, which produces elements heavier than iron (s-process). In massive AGB stars the base of the convective envelope is so hot that hydrogen burning via the CNO-cycle starts, called hot bottom burning (HBB, Pols 2009).

the mass and density of the C,O-core increases and becomes degenerate. However, the layer, in which He-fusion occurs, becomes thinner. The triple-α process is highly temperature sensitive. The thickness of the He-shell is much smaller than its radius, therefore the energy input by the nuclear fusion causes an increase in temperature at constant pressure and is not balanced by the energy loss. The He-burning layer becomes thermally unstable and ignites in helium shell flashes, called a thermal pulse (Schwarzschild & Härm 1965, Fig. 1.6) – the beginning of the thermally-pulsing AGB phase.

When helium ignites it is rapidly burned and the hydrostatic adjustments (expansion and cooling of the above layers) stop the fusion in the H-shell, such that the stellar radius and the He-luminosity increase by up to several orders of magnitude. The He-luminosity then dominates the surface luminosity (up to 10^6 $L_\odot$). The change of other stellar parameters over time during several thermal pulses is shown in Fig. 1.7. In this short phase ($\sim$ 100 years) the thin radiative layer between the convective envelope and the H-shell disappears and the convective envelope dips deep into the intershell zone and the products of helium burning, mainly carbon, are quickly mixed to the surface, called third dredge-up (TDU, Fig. 1.8).

In addition, a convective zone just above the He-shell, the intershell convection zone (ICZ), develops, because the energy from He-shell burning cannot be transported only by radiation (Fig. 1.6). This zone also mixes with the overlying convective envelope and mainly carbon (^{14}N), additionally ^{16}O,

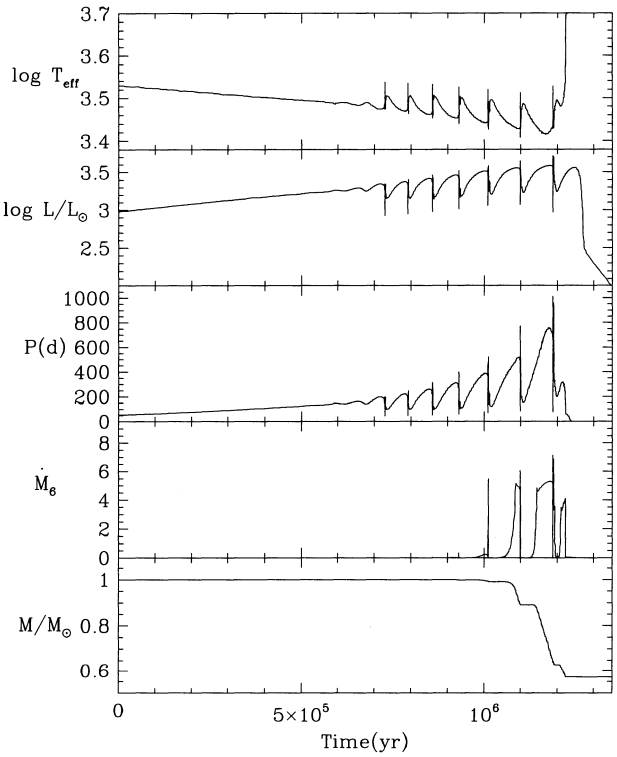

Figure 1.7: Evolution of an AGB star, with an initial mass of 1 $M_\odot$ and with solar metallicity, and its stellar parameters effective temperature, luminosity, pulsation period mass loss rate (in units of 10^{-6}) and the stellar mass (from top to bottom) as a function of time (Vassiliadis & Wood 1993).

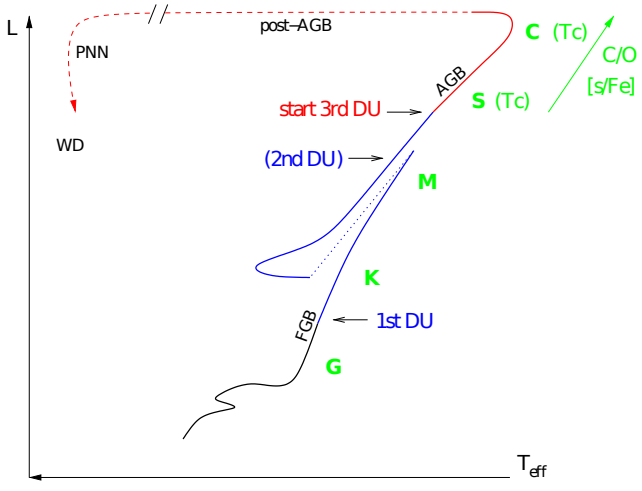

Figure 1.8: Evolutionary track of a low-mass star in the HRD, showing the various dredge-up events on the first giant branch (FGB) and the AGB. The letters G, K, M in green give the according spectral type and the letters S and C represent O-rich and C-rich stars, (Tc) indicates the enrichment of s-process elements. The C/O ratio and the abundance of elements heavier than iron increase during the evolution on the AGB (Pols 2009).

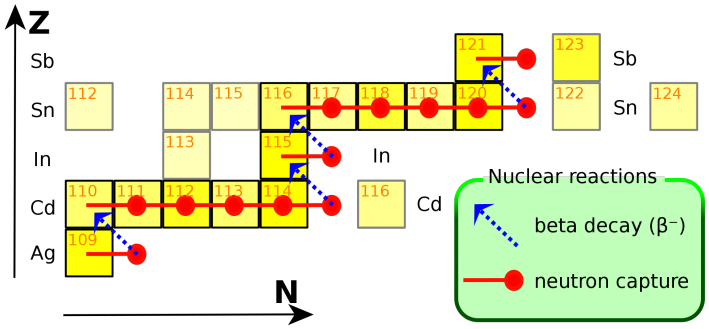

Figure 1.9: Path of the s-process neutron capture and beta-minus β^- decay in the nuclear chart, ranging from Ag (silver) to Sb (antimony). © Rursus, from `http://en.wikipedia.org/wiki/`

^{19}F, ^{22}Ne, ^{23}Na, ^{25}Mg, ^{26}Mg, ^{26}Al, and ^{27}Al are quickly mixed to the surface. The mixing within the convective envelope has further consequences. This material is rich in unprocessed hydrogen, which now mixes with the helium- and carbon-rich intershell region. Such that there is a fresh source of protons, which partly produces ^{13}C in a certain region via ^{12}C(p,γ)^{13}N($\beta^+\nu$)^{13}C, called the ^{13}C-pocket. In this pocket, ^{13}C reacts with the very abundant α-particles which produces ^{16}O and also many neutrons: ^{13}C(α,n)^{16}O (Busso et al. 1999). For more massive stars, with higher central temperatures, the reaction ^{22}Ne(α,n)^{25}Mg also occurs, most importantly producing a high neutron flux. The neutron density is between 7×10^7 cm^{-3} and 2×10^8 cm^{-3} (Langer 2009, and references therein). These neutrons are involved in a very significant process in AGB stars: the slow neutron capture, short the s-process. The neutrons are captured onto so-called iron seeds (elements heavier than iron) and via subsequent β^--decays form elements with higher mass numbers (Fig. 1.9), hence elements heavier than iron, e.g. strontium, technetium, or lead. The rate of neutron-captures is much slower than the rate of the β^--decay, therefore the name, such that an unstable isotope decays before it captures another neutron. If the rate of neutron-captures is much faster than the β^--decay, due to a very high neutron flux, the process is called to be rapid, short the r-process. The suitable astrophysical site for these conditions is a supernova explosion (Clayton 1968). In an AGB star, these heavy elements are brought to the stellar surface through reoccurring TDU events, where they become observable. The first evidence that these heavy elements originate from AGB stars and that they must have been produced within this evolutionary phase of the star was provided by the element technetium, specifically ^{99}Tc which has a half-life time of the order of 10^5 years (Langer 2009).

In the much longer interpulse phase ($\sim 10^4$ years), the He-flash extinguishes due to the expansion and the He- and H-burning continues steadily, where hydrogen dominates the surface luminosity again. The mass loss rate is coupled to the stellar luminosity and to the radial pulsations, therefore periodically increases due to the thermal pulses over time (Fig. 1.7). The highest amount of mass loss occurs during the last thermal pulses. The star develops the so-called superwind-phase where the mass loss rate can reach 10^{-4} M$_\odot$ yr^{-1} (Iben & Renzini 1983; Vassiliadis & Wood 1993).

The ejected mass forms a circumstellar envelope around the star. This envelope becomes unbound and expands away from the star, with possible several layers. This is observed for the target star of this work, IRC+10216. The star is at the end of the AGB phase with a high mass loss rate of 2×10^{-5} M$_\odot$ yr^{-1} (Winters et al. 1994; Menten et al. 2012, Sect. 2). Depending on the interaction between these circumstellar layers due to differing mass loss rate episodes and velocities, density enhancements and also a detached shell can form (e.g. Olofsson et al. 2000, and references therein).

The periodic ignition of the helium shell during the thermal pulses leads to an enormous expansion

of the surrounding medium, a medium with decreasing density and temperature for increasing mass coordinate. The change of properties has direct consequences on the energy and momentum transfer, because hot, dense, and fast layers collide with cooler, thinner, and slower layers, such that a shock front forms. Each thermal pulse might be slightly different with different resulting shock front properties (Gustafsson & Höfner in Habing & Olofsson 2003). The radial pulsation can be driven by opacity effects described in the so-called κ-mechanism, where opaque layers expand to larger radii due to the radiation pressure. At a region with smaller density and temperature the radiation escapes through the layers, hence this layer becomes transparent and contracts again. However, in a fully convective medium energy is not transported by radiation and therefore this mechanism cannot operate in this sense in the envelope of an AGB star. Thus, time-dependent convection has to be considered which is challenging to model (e.g. Aerts et al. 2010).

With every reoccurring thermal pulse and dredge-up the carbon abundance in the stellar envelope and atmosphere increases. As soon as the star has an abundance ratio of C/O > 1 in its atmosphere, the star becomes a carbon-rich object. Hence, there is an evolutionary sequence from oxygen- to carbon-rich stars. IRC+10216 is a carbon-rich star.

For stars with initial masses above 4 $M_\odot$, depending on composition, the radiative layer between the H-shell and the convective envelope is absent. The base of the convective envelope can start hydrogen-fusion via the CNO-cycle because the temperature is high enough ($\sim 5 \times 10^7$ K). This process is called hot bottom burning (HBB). The CNO-cycle converts ^{12}C predominantly into ^{14}N, which is directly mixed into the envelope via convection and opposes the evolution towards a carbon star through the mixed-up products of helium-burning from the ICZ, such that $^{12}C/^{13}C = 3 - 4$ after HBB compared to $^{12}C/^{13}C \approx 20$ before HBB (Karakas & Lattanzio 2007).

The further evolution depends predominantly on the core mass and the mass loss rate. The luminosity L of the star, therefore, can be parametrized by the core mass $M_{\rm core}$ (Paczyński 1971): $L = 5.2 \times 10^4 (M_{\rm core} - 0.5)$ where L and $M_{\rm core}$ are in units of $L_\odot$ and $M_\odot$, respectively. This relation is very reliable for low-mass AGB stars. For stars with deep convective envelopes, with no radiative buffer zone between the convective envelope and the H-layer, the luminosity can be much higher and the interpulse period shorter (Vassiliadis & Wood 1993). The mass loss during the AGB phase is underpredicted by the Reimers (1975) law, especially towards the end of the AGB phase during the superwind-phases. Detailed stellar evolution simulations with empirical mass loss relations are in good agreement with the observed properties of AGB stars, such as the amount and the multiple shell structure of the circumstellar material (e.g. Vassiliadis & Wood 1993; Mauron & Huggins 2000).

The AGB phase is terminated as soon as the stellar envelope is very thin ($10^{-2} - 10^{-3}$ $M_\odot$), a consequence of nuclear burning and strong mass loss (Vassiliadis & Wood 1994).

1.1.4 Evolution after the AGB phase

After the AGB phase, there is a remaining thin envelope surrounding the C- and O-core in which H-shell burning dominates the luminosity. The stellar radius decreases and the surface temperature increases at constant luminosity for the next $\sim 10^4$ years. At temperatures of about 30 000 K and higher, the energetic radiation might ionize the circumstellar material, if it is still dense enough, making the object visible as a planetary nebula. During this so-called post-AGB phase the star moves horizontally from right to left in the HRD (Fig. 1.2). When the burning layer becomes so thin (10^{-5} $M_\odot$) that the fusion is not efficient anymore, nuclear fusion stops and only the electron-degenerate carbon-oxygen core of the former AGB star is left. The star transformed into a white dwarf (in a fading time of about 10^5 years). Most of these objects have a mass of about 0.6 $M_\odot$ and a size similar to the Earth. The radius

stays constant while the white dwarf radiates the remaining thermal energy and therefore cools down with decreasing luminosity for at least $10^7 - 10^{10}$ years (Mestel & Ruderman 1967; Winget et al. 1987) until it becomes too faint to be observable ($L \lesssim 10^{-5}$ $L_\odot$). The low- to intermediate-mass stars do not go through further fusion cycles and end as degenerate white dwarfs.

Stars with initial masses between about 7 and 11 $M_\odot$ may become super-AGB stars, with possible violent fusion processes, becoming O-Ne(-Mg) white dwarfs or/and electron-capture supernova (e.g. Eldridge & Tout 2004; Izzard & Poelarends 2006; Siess 2006). Stars with initial masses above about $7 - 11$ $M_\odot$ become red supergiants and proceed reaching high enough temperatures and densities to start further fusion cycles in their core, e.g. carbon burning. The red supergiants, such as VY CMa, occupy similar regions in the HRD as AGB stars, however, they have a different internal structure. They may become Wolf-Rayet stars, stars that experienced very high mass loss rates and only their exposed cores are observed (e.g. Hamann et al. 2006; Crowther 2007). At the end of the nuclear fusion chain, possibly up to iron, the element with the highest binding energy per nucleus, the star (depending on its final mass) ends as a core-collapse supernova, turns into a neutron star or a black hole – the densest objects in the Universe.

Many of the low- to intermediate-mass stars become visible as planetary nebulae (PNe), with many different, often complex, shapes, morphologies, and different chemical compositions (e.g. Balick & Frank 2002). What fraction of stars create PNe is not well understood (Hall et al. 2013, Izzard & Keller 2015, Keller, Izzard & Stanghellini, in prep.). Many studies try to find the origin and reasons for the shaping of these objects (e.g. Stanghellini 2009). There are many unanswered questions, for instance, how is it possible to get from a spherical star, to an asymmetric and clumpy CSE, to a multilayered, bipolar planetary nebula? Current studies are not conclusive on which effects dominate the shaping – binary evolution and interaction, magnetic fields, disks and jets – and which stellar parameters are affected and could serve as a distinction tool (e.g. Soker 2006; De Marco 2009; Miszalski et al. 2009; Stanghellini 2009; Parker et al. 2015).

The properties of an object in a specific evolutionary stage, for instance, the morphology of CSEs around AGB stars, are connected with its specific evolutionary history. Especially binary evolution is one of the most debated topics in the past years as a possible solution to explain the observations of AGB stars and PNe. Due to a stellar or planetary companion, the spatial and chemical appearance of the circumstellar material is possibly influenced by gravitational interactions, directly via merging or common envelope phases, mass transfer, accretion, Roche-lobe overflow, and more. These physical effects may have consequences on the morphology of the circumstellar environment, such as spirals, asymmetries, jets, and also the chemical composition, which we target in this thesis.

1.2 Asymptotic giant branch stars and their circumstellar envelopes

Here we consider the observable properties of AGB stars, that are directly connected to the evolutionary history and internal properties of the star (Sect. 1.1). The stellar interior, atmosphere and circumstellar envelope (CSE) are all interconnected. The properties of the star, including the chemical composition of the stellar atmosphere and the mass loss morphology, are imprinted in the CSE (Olofsson in Habing & Olofsson 2003).

1.2.1 Atmosphere: Pulsations & variability

The observations of AGB stars show that there is a periodic change in its brightness, a sinusoidal light curve with periods of a few weeks up to thousands of years, such that they are characterized as long-period variables (LPV). The brightness variability is directly linked to the pulsation modes in the stellar envelope, driven by the thermal pulses. There are different pulsation type classifications. If the variability is regular with periods longer than 80 days and an amplitude larger than 2.5 mag in the visible (V-band), similar to the prototype star Mira, it is named Mira-type. The star IRC+10216 is such a Mira-type variable star. There are also semi-regular (SR) variabilities of type SRa (amplitude less than 2.5 mag in V) or SRb (amplitude less than for SRa and no clear periodicity), and with overlapping periods or irregular patterns (Aerts et al. 2010). The radius and the surface temperatures change by $10 - 20\%$ with luminosity changes of about 50% between minima and maxima of the period. From the observed lightcurves a luminosity-period relation is derived, which can be utilized to determine distances (Groenewegen & Whitelock 1996). Also similar types of pulsating stars exist, such as RR-Lyrae stars and Cepheid stars, which are all located on the so-called instability strip in the HRD. However, these stars have a different internal structure and are in different evolutionary stages than the Mira-type variables.

The atmosphere is the topmost part of the star, the loose connection between the very weakly bound "fluffy" layers of the stellar convective envelope, which could be referred to as the stellar surface, and the circumstellar environment in which molecules and dust begin to form. This region is strongly affected by time-dependent dynamical processes. The warm atmosphere has a temperature of about 3000 K (Gustafsson & Höfner in Habing & Olofsson 2003). Due to the pulsations and the expansion of the star, the topmost material is levitating and can become unbound from the star. This material then produces a density enhancement in cooler regions further away from the star (a few stellar radii away), which provides the conditions to the formation of molecules and dust ($T \sim 1500$ K, Tsuji 1964). In a hydrostatic atmosphere, like in our Sun, where the density drops exponentially with larger radii, without any density enhancements, the density is already much too low in the region where the temperature would be suitable for molecule and dust formation. On the surface of AGB stars large convection cells and hot spots exist, similar to our Sun, resulting in outbursts and asymmetries (Freytag & Höfner 2008), which are directly observable thanks to better and better infrared interferometry (e.g. Ohnaka et al. 2011).

1.2.2 Circumstellar envelope: Gas & dust

The ejected material surrounding the star forms the circumstellar envelope (CSE) consisting of molecular gas and solid-state dust particles. There are four main regions in the CSE (cf. Fig. 1.10):

1. *Inner wind*: In the outer atmosphere, molecules form under LTE conditions (for high densities and temperatures close to stellar photosphere, $3000 - 1500$ K). At larger radial distances (up to a few stellar radii) also pulsations, shocks, and non-LTE effects play a role. The temperature and density decrease exponentially with radius.
2. *Intermediate wind*: In this region dust condensation, grain growth, wind acceleration, and absorption of molecules onto dust grains occurs. The temperatures typically are $1500 - 500$ K at radial distance of a few ten stellar radii.
3. *Outer wind*: This region has a constant wind velocity, with temperatures of $500 - 10$ K and radial distance of a few thousand stellar radii. The region is dominated by photodissociation of molecules, neutral-neutral and ion-molecule reactions, and photochemistry. The density decreases with radius by r^2.

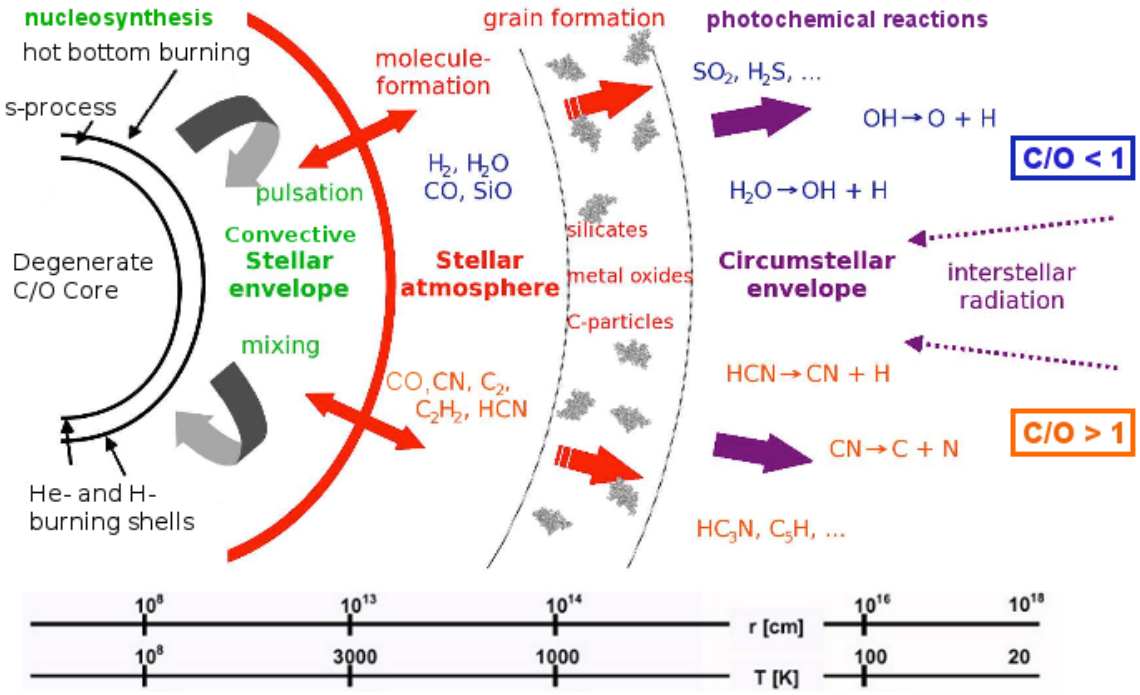

Figure 1.10: Schematic structure of the AGB star interior with nucleosynthesis, mixing and pulsations, its atmosphere with molecule formation and its circumstellar envelope with dust grain formation and photochemistry. The most abundant molecular and dust species are given depending on the chemical composition being oxygen-rich (C/O < 1) or carbon-rich (C/O > 1). Adapted from Habing & Olofsson (2003) and Maercker (2009).

4. *Bow shock*: This is the outer interaction bubble of the stellar proper motion with the interstellar medium.

1.2.2.1 Molecular gas

The molecules in the stellar atmosphere were first observed as broad absorption and emission bands in the infrared (e.g. Tsuji et al. 1997). There are three chemical types of AGB stars. For carbon-rich environments the molecules C_2H_2, CN, HCN, C_2, N_2 are most abundant compared to any other oxygen-bearing molecules, such that the abundance is C/O > 1, called C-type. For oxygen-rich environments H_2O, OH, SiO are most abundant, such that C/O < 1, called M-type (Fig. 1.10). If the ratio is C/O ~ 1 they are called S-type AGB stars. The simplest notion is that for C-rich stars almost all oxygen is bound in CO and vice versa for O-rich stars almost all carbon is bound in CO under thermodynamic equilibrium. This picture is shown to be an over-simplification and non-equilibrium and time-dependent effects have to be considered. Recently, warm water vapor has been found unexpectedly in the atmosphere of C-rich stars, e.g. IRC+10216 (Decin et al. 2010; Neufeld et al. 2011a,b).

The expected abundances of the elements at the stellar surface, also called yields, which then are available to form the molecules and dust grains observed in the CSE, are modeled by e.g. Karakas & Lattanzio (2007). However, there is a knowledge gap between the modeled yields at the stellar surface and the observed molecules in the CSE, in the stellar atmosphere and the dust formation zone. A lot of effort was recently put onto this region in terms of simulations and observations, also to further constrain

the distinction of the CSE regions (e.g. Fonfría et al. 2008; Cernicharo et al. 2011; Cherchneff 2012; Cernicharo et al. 2013).

1.2.2.2 Dust

For the formation of dust a cool and dense environment is necessary ($T \sim 1500$ K, $n \sim 10^8$ cm^{-3}), which is given in the (shock) compressed region a few stellar radii from the atmosphere of AGB stars (e.g. Gail & Sedlmayr 1999, 2014). The presence of dust in the CSE of AGB stars is seen in the infrared excess or broad infrared features in the spectral energy distribution and also in the spectra. AGB stars are the main source of dust in the Universe (Gail & Sedlmayr 2014).

The dust condensation is the transition of the material from gaseous to solid state, which is only possible when the temperature and pressure are low, given by this astrophysical environment. Then the growth from a small aggregation of molecules to large molecules and finally to complex macroscopic grains (sizes < 0.3 μm) occurs for low temperatures and high densities. The balance between dust condensation and destruction (through evaporation) has to be disturbed towards the creation of solids. This growth process is much easier to achieve in theoretical models with starting seed grains as reaction surfaces, on which then, for example, ice mantles form (e.g. Gail & Sedlmayr 1999). In this way, certain molecules can be locked in the dust grain or on its surface and disappear from the gas phase and are, thus, unobservable (depletion). When the dust heats up (evaporation) or is destroyed, the containing molecules can be ejected into the gas phase and become observable again. From this behavior the content of dust grains can be estimated (Gail & Sedlmayr 1999, 2014). At longer radial distances from the star the density decreases and no further dust growth is possible.

For oxygen-rich CSEs typical dust species are amorphous and crystalline silicates, aluminum oxides (corundum Al_2O_3) and titanium oxides (TiO_2), also olivines (e.g. Mg_2SiO_4) or pyroxenes (e.g. Mg_2SiO_3) for the low end of temperatures. It is yet not well constrained how the dust condensation and growth is proceeding exactly in oxygen-rich environments. For carbon-rich CSEs (like for IRC+10216) the most abundant dust species are amorphous carbon, silicon carbide (SiC) and titanium carbide (TiC). Furthermore, MgS, Fe-compounds, and more complex structures can be present (e.g. Lodders & Fegley 1999; Gail & Sedlmayr 2014).

Other studies investigate the dust formation through laboratory experiments or analysis of presolar grains from meteorites (e.g. Nittler 2008, and references therein). The components of material from before the formation of the solar system (presolar) can be extracted by their abnormal isotopic abundances compared to the solar composition. They mostly consist of SiC, TiC, Al_2O_3, and TiO_2 and therefore help to understand the (link of) dust formation in the CSEs of AGB stars.

The dust-to-gas ratio in CSEs is difficult to constrain, however an often-used value is 1/100, so there is a factor of 100 more gas than dust in the stellar wind.

1.2.2.3 Mass loss

To understand the mass loss of the star, the molecules and dust grains in the stellar atmosphere are crucial. A combination of the dynamical pulsation, which makes dust formation possible, and the radiation pressure on the dust grains cause the gas being dragged away from the star (via friction and momentum transfer). One can speak of thermal winds due to the gas pressure gradient and of radiation-driven winds via momentum transfer and radiation pressure, such that in summary a pulsation-enhanced dust-driven wind operates (Gustafsson & Höfner in Habing & Olofsson 2003).

The different propagating waves of material from the pulsations might interact with each other. One

wave might cool, fall back and is hit by the next shock wave, such that the material is compressed and accelerated outwards. The dust particles are accelerated outwards, with a faster velocity than the gas particles. This creates the so-called drift velocity, which is the difference between these two velocities. Further away from the stellar atmosphere the density and temperature drop. The dust formation stops and the outflow material expands with a constant velocity, which then is called the terminal velocity. Typical mass loss rates of AGB stars range from 10^{-4} to 10^{-9} $M_\odot$ yr^{-1} with terminal velocities of 10 – 30 km s^{-1}. As comparison, the solar wind is characterized by a mass loss rate of 10^{-14} $M_\odot$ yr^{-1} and a wind terminal velocity of 500 km s^{-1}.

The morphology of the CSE is caused by a combination of the gas- and dust-dynamics (e.g. a central binary system), the mass loss history of the star and the chemistry. The chemistry is influenced by small-scale structures and density-enhancements, such as clumps and shells, and the central and ambient UV radiation field (Sect. 1.3 and 1.3.5). These effects are analyzed in this thesis.

1.3 Molecules

Molecules are the main ingredient of this work, because they trace the physical and chemical properties of the circumstellar environment and are fundamental to understand the stellar evolution and galactic chemical evolution. There are various types and groups of molecules that behave differently in different physical and chemical environments, such as radiation or collisions, and therefore serve as indicators for densities or temperatures of certain regions. Through molecular spectroscopy and mapping, we learn about the current and past structure of the outflowing gas and dust and its interactions. From the spectral intensities and shapes, and the radial structure, we learn about chemical abundances, temperatures and densities. We can infer e.g. reaction rates, mass loss rates, etc., and therefore are able to link these observations to theoretical chemical networks and the internal nucleosynthesis and structure of the star. Furthermore, we improve the knowledge on the origin of the molecular species in the interstellar medium and on Earth.

Almost 200 molecules have been detected in the interstellar medium or circumstellar shells as of February 2016 (`https://www.astro.uni-koeln.de/cdms/molecules`). The identification of molecular emission from the interstellar medium is possible thanks to laboratory work that determines the rest-frequencies of the molecular transitions (Cologne Database for Molecular Spectroscopy, CDMS; and the Jet Propulsion Laboratory (JPL) catalog; Pickett et al. 1998; Müller et al. 2001, 2005). Molecules such as carbon-monoxide (CO), water (H_2O), hydrogen cyanide (HCN) or ammonia (NH_3) are found in space, which are also well-known on Earth. Most of these substances can be dangerous for a human, for example, inhaling CO or HCN is poisonous. However, studying them in space at a large distance (hundreds of parsecs or thousands of light years or 10^{18} meters) we can value them as carrying a lot of information on the properties of circumstellar shells and the origin of elements and molecules. A graphical representation of a few example molecules in three and two dimensions is shown in Fig. 1.11. The depicted molecule HC_3N belongs to the group of cyanopolyynes. This molecule and further chemically related species such as hydrocarbons are analyzed in detail in this thesis.

Many of these molecules are the basis of organic compounds that lead to important building blocks of biological compounds such as sugar, alcohol and amino acids which is of high importance to understand the formation of the DNA, the chemical-code carriers of life. Such molecules are mainly carbon compounds from carbon chains, fullerenes ("buckyballs"), to polycyclic aromatic hydrocarbons (PAHs). Carbon chains are abundantly observed in CSEs of AGB stars (such as IRC+10216, e.g. Cernicharo et al. 2000; Woods et al. 2003), however the heavier and more complex fullerenes and PAHs are not

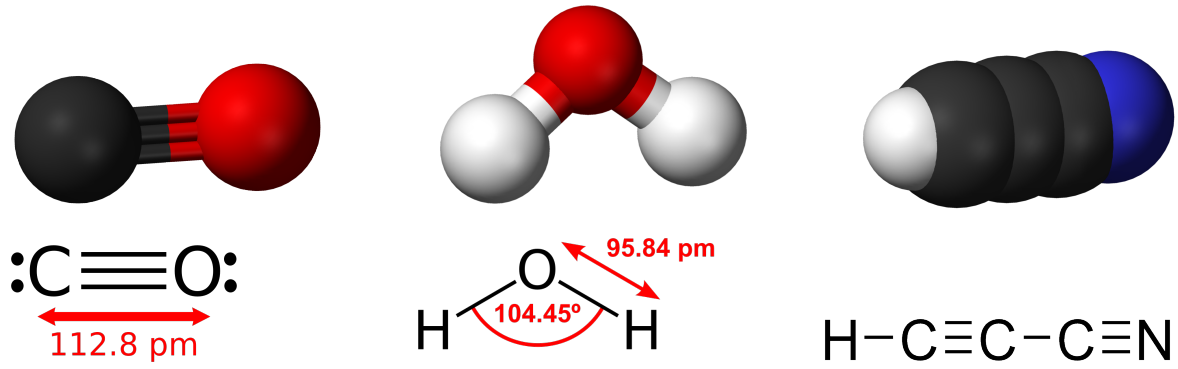

Figure 1.11: Three and two dimensional representation of carbon monoxide (CO), water (H_2O) and cyanoacetylene (HC_3N). © Ben Mills, from `https://en.wikipedia.org/wiki/`

seen around carbon-rich AGB stars (due to insufficient exciting UV radiation) but in more evolved post-AGB stars and PNe. So the link to their formation lies in this evolutionary stage, especially because PAHs have been observed in S-type AGB stars (Smolders et al. 2010). The heaviest molecules found to date are the cyanopolyyne $HC_{11}N$ in a cold dust cloud and the fullerenes C_{60} and C_{70} in a carbon-rich planetary nebula (Bell et al. 1997; Cami et al. 2010). Among the most-complex molecules is propyl cyanide C_3H_7CN observed in the star-forming region Sagittarius B2 (Sgr B2) near the center of our Galaxy (Belloche et al. 2014).

Most molecules were first detected in the carbon star IRC+10216, the cold dark cloud TMC-1, and the star-forming region Sgr B2, mainly because they are nearby and bright. Therefore many observational studies concentrate on these objects. More clues on the organic molecules from stardust come from the study of the presolar grains from meteorites as mentioned in Sect. 1.2.2.

1.3.1 Theoretical background on molecular emission

Molecules have different discrete electronic, rotational, or vibrational energy states according to quantum mechanics. The molecules can be excited via absorbing energy by radiation or collisions (mainly with H_2). If then the state changes from a higher to a lower energy level, the difference in energy is emitted in form of a photon with the energy equaling this difference. Every transition of each molecular species has a specific frequency by which it can be identified in observed spectra.

1.3.1.1 Molecular quantum states

With the tools of quantum chemistry and molecular physics, the Born-Oppenheimer approximation allows to treat the motion of the electrons and nucleus separately. In terms of the Schrödinger equation this means that the total wavefunction Ψ of a molecule can be separated into its electronic and nuclear (vibrational + rotational) components: $H\Psi = E_J\Psi$ with $\Psi = \psi_{\mathrm{electr}} + \psi_{\mathrm{nucl}}$.

The *electronic transitions* are associated with the emission and absorption of energy by the electrons, which is radiated with wavelengths in the visible and ultraviolet regime. For every electronic state there are several possible *vibrational states* of the molecule, which overlap with *rotational states*. There is a stretching and a bending mode, either by changing the length or the angle between the molecular bonds between the nuclei, which can be approximated with the harmonic oscillator (for the electronic ground state). For molecules with more than two nuclei, there are several more possible modes, such as asym-

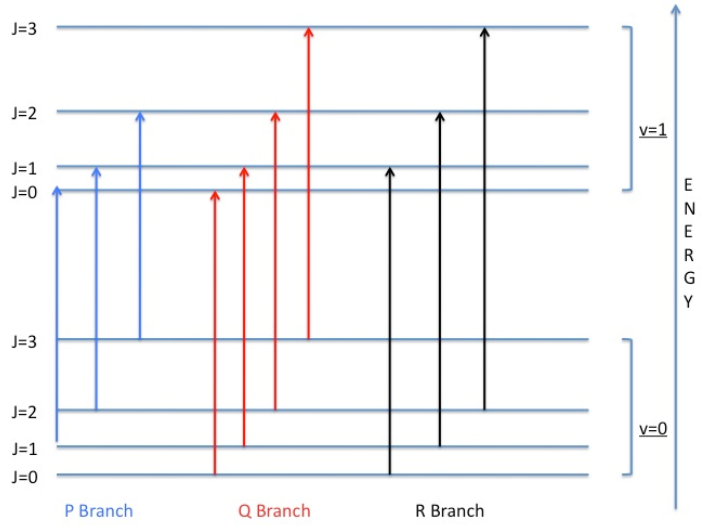

Figure 1.12: Schematic diagram of the P, Q, and R rotational transitions for two vibrational modes v. © Chun-Yi Lin, Zhou Lu (University of California, Davis).

metrical stretching of the bonds in the water molecule (cf. Fig. 1.11). The difference of these energy levels equals the energy of radio, sub-mm, and infrared photons. For every electronic and vibrational state there are also rotational states. There are quantized rotation axes depending on the moment of inertia of the molecule. The torque on the molecular dipole, which is the difference between the center of mass and the center of charge, can be increased by microwave irradiation (the effect also used in the microwave to heat up food) or collisions. If there is no permanent dipole moment, no (dipole) rotational transitions are excited, e.g. for H_2 or C_2H_2, the reason they cannot be observed directly through pure rotational transitions.

1.3.1.2 Molecular line transitions

For linear molecules, such as CO or HC_3N, the rotational energy levels are described by the Schrödinger equation for molecular rotation of a rigid rotor where every energy level has a rotational quantum number J with energy E_J:

$$E_J = \frac{\hbar^2}{2I} J\,(J+1)\,, \tag{1.1}$$

which is characterized by the moment of inertia of the molecule I:

$$I = \mu r^2 = \frac{m_1 m_2}{m_1 + m_2} r^2, \tag{1.2}$$

where μ is the reduced mass, with the masses m_1 and m_2 of the constituting atoms, and r the distance between the atoms, for the case of a diatomic linear molecule.

The quantum number follows the electric dipole moment selection rule $\Delta J = \pm 1$, because the total angular momentum has to be conserved. The transitions with $\Delta J = 1$ are defined as R-branch and those with $\Delta J = -1$ are defined as P-branch transitions. Transitions with $\Delta J = 0$ are called Q-branch and are allowed if the electronic or vibrational state change (Fig. 1.12). The observable molecular spectral lines are determined only by the rotational constant B which describes the characteristics of the

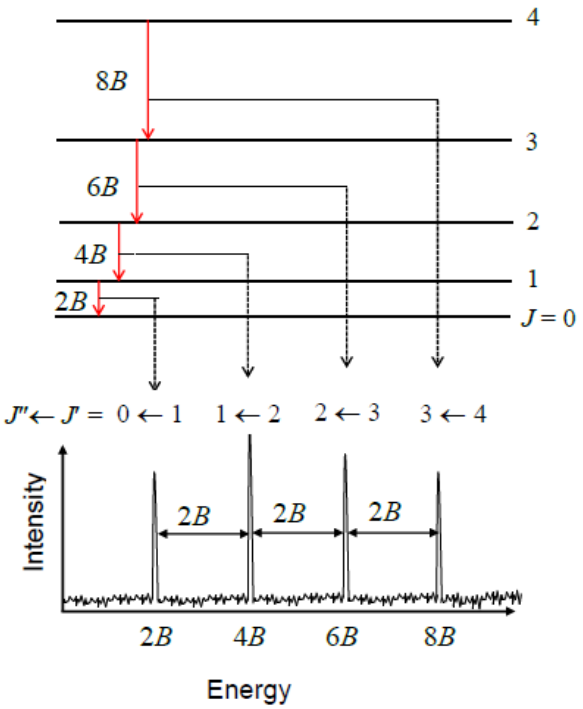

Figure 1.13: Illustration of the rotational energy levels of linear molecules with the rotational constant B and the according rotational spectrum observed during laboratory experiments. © Nnrw, from `https://commons.wikimedia.org/wiki/`

molecule (Fig. 1.13):

$$B = \frac{\hbar^2}{2I}. \tag{1.3}$$

The electronic states are described by the angular momentum quantum number Λ, the "good" quantum number Σ which consists of the spin quantum numbers S, and the molecular symmetry axis $\Omega = \Lambda + \Sigma$. The selection rules are $\Delta\Lambda = 0, \pm 1$, $\Delta S = 0$, $\Delta\Sigma = 0$, $\Delta\Omega = 0, \pm 1$. The vibrational energy

$$E_v = \omega \left(v + \frac{1}{2} \right) \tag{1.4}$$

is given by the harmonic oscillator with the vibrational frequency ω and the vibrational quantum number v which is also called vibrational mode. The normal modes are v_1 for symmetric stretching, v_2 for bending, and v_3 for asymmetric stretching. The more complex the molecules, the more bonds and the more vibrational modes there are. For N number of atoms, linear molecules have $3N - 5$ degrees of vibrational modes, whereas nonlinear molecules have $3N - 6$ degrees of vibrational modes. The selection rule is $\Delta v = \pm 1, \pm 2, ...$ and the intensity of the transition becomes weaker for increasing Δv. The transition between $v = 0$ and $v = 1$ is called fundamental vibration, and the transitions with v larger than 1 are called overtones.

Usually the vibrational and rotational transitions are combined because both states can change at the same time and one speaks of ro-vibrational spectroscopy (Tielens 2005). If a coupling of the electron spin and the orbital angular momentum (fine structure) or of the electron spin and the multipole moments of the nucleus (hyperfine structure) occurs, the emission line splits into several more possible energy

levels. Then the Born-Oppenheimer approximation is not valid anymore and more quantum numbers are necessary to describe the system. For the fine structure, the total rotational angular momentum J splits into the rotational angular momentum N and the electron momentum S:

$$J = N + S, \tag{1.5}$$

and for the hyperfine structure, the nuclear spin angular momentum F is the sum of the total rotational angular momentum J and the nuclear spin I:

$$F = J + I. \tag{1.6}$$

If the molecule is nonlinear, an additional quantum number K along the inertial axis is necessary to describe the rotational states. The molecules are divided into spherical top, symmetric top and asymmetric top depending on their dipole moment and rotation.

The behavior of observed transitions can be distorted by the coupling of the rotational and vibrational states and by centrifugal distortion which changes the bond lengths in the molecules and therefore the real molecule deviates from the assumption of the rigid rotor.

The molecular dipole moment is usually given in the cgs-unit Debye. Typical values for diatomic molecules are in the range of 0 to 11 D. The higher the dipole moment of a molecule, the more sensitive it is to the radiation field which exerts the torque on the molecular dipole.

Isomers are molecules with the same constituents but with a different shape, such as cyclic and linear molecules, e.g. l-C_3H. Their dipole moments are different, thus, their energetic and chemical properties differ.

1.3.2 Physical conditions in thermal equilibrium

In thermal equilibrium, the rotational and vibrational states are populated according to the Boltzmann distribution. In other words, the number density of molecules in an excited state n_u, relative to the number density of molecules in the lower state n_l, are described by a single Planck temperature:

$$\frac{n_u}{n_l} = \frac{g_u}{g_l} \exp\left(-\frac{\Delta E}{kT_{\rm ex}}\right), \tag{1.7}$$

where $g_{u,l}$ are the statistical weights or degeneracy factors of the transitions which equal to $2J + 1$, $\Delta E = h\nu$ is the energy difference between the two levels with h the Planck constant and ν the transition frequency, k is the Boltzmann constant and $T_{\rm ex}$ is the excitation temperature. In some cases, the excitation temperature is not a real temperature, it is the Planck temperature that measures the ratio of the energy levels, populated according to the Boltzmann distribution. In a two-level system, the excitation temperature is determined by a balance between radiative and collisional excitations and de-excitations. If collisional excitation dominates, the temperature equals the kinetic temperature of the gas and it is called "thermalized". This is determined by the so-called critical density. The critical density is defined as

$$n_{\rm crit} = \frac{A_{ul}}{C_{ul}}, \tag{1.8}$$

where A_{ul} is the Einstein coefficient of spontaneous emission (cf. Eq. 1.9), and C_{ul} is the collisional rate coefficient of two levels. When the gas density is much larger than the critical density, collisions (mainly with H_2) dominate the excitation processes and level populations are given by the Boltzmann distribution

with the kinetic temperature of the gas. When the gas density is smaller than the critical density the excitation temperature of transitions is much smaller than the ambient temperature. For example, for the transition $HC_3N(J = 3 - 2)$ the critical density is about 1.2×10^4 cm^{-3} and the H_2 density in the CSE of IRC+10216 is about 3×10^4 cm^{-3} at a radius of 3×10^{16} cm , so the transition is thermalized. The transition probability and strength is described by the Einstein coefficient of spontaneous emission

$$A_{ul} = \frac{8\pi h\nu^3}{c^3} B_{ul} \, , \tag{1.9}$$

where B_{ul} is the Einstein coefficient of stimulated emission. The Einstein coefficient A_{ul} is inversely proportional to the life time of the energy level. For dipole emission, it can be expressed as

$$A_{ul} = \frac{64\pi^4\nu^3}{3hc^3} \frac{|\mu_{ul}|^2}{g_u} \, , \tag{1.10}$$

where $|\mu_{ul}|^2$ is the dipole matrix element of the transition (e.g. Mangum & Shirley 2015).

If the stimulated absorption coefficient B_{lu} dominates and the upper level is overpopulated by pumping mechanisms, maser emission occurs (microwave amplification by stimulated emission of radiation). This emission is characterized by very high brightness and small spatial extent (associated with dense gas clumps). Most typical maser sources in CSEs are OH, H_2O, SiO, and HCN. Certain rotational or vibrational energy levels are pumped by radiation, most probably from the stellar photosphere, such that a population inversion occurs. Collisional pumping (mainly collisions with H_2) is also important. The observed intensity of this transition then implies kinetic temperatures far beyond physical values for these environments (>> 10000 K).

1.3.2.1 Radiative transfer

In local thermal equilibrium (LTE), the specific intensity of the observed object is given by the blackbody radiation in a certain solid angle:

$$I_\nu = B_\nu(T_B) = \frac{2h\nu^3}{c^2} \left(\exp\left(\frac{h\nu}{kT_B} \right) - 1 \right)^{-1} \, , \tag{1.11}$$

where T_B is called the brightness temperature, which can describe the actual thermodynamic temperature of the medium, especially in the Rayleigh-Jeans approximation ($h\nu/kT \ll 1$). The propagation of a beam of radiation with specific intensity I_ν through a medium with length ds is described by the radiative transfer equation:

$$\frac{dI_\nu}{ds} = \epsilon_\nu - \kappa_\nu I_\nu, \tag{1.12}$$

where ϵ is the emitted energy by spontaneous emission at frequency ν in units of power per unit volume, per unit frequency, per unit solid angle, and κ is the attenuation coefficient at frequency ν due to absorption or stimulated emission in units of length^{-1}. This equation does not include scattering from electrons or dust grains. Equation 1.12 can be rewritten in terms of the optical depth $d\tau_\nu$. The optical depth is a concept which describes the transparency of the emitting material along the line of sight for a certain transition. If $\tau_\nu \ll 1$, the material is fully transparent and is called optically thin. If $\tau_\nu > 1$, the material is rather opaque and is called optically thick. Such that, with

$$d\tau_\nu = \kappa_\nu ds, \tag{1.13}$$

the specific intensity is

$$\frac{dI_\nu}{d\tau_\nu} = S_\nu - I_\nu, \tag{1.14}$$

with the source function $S_\nu = \frac{\epsilon_\nu}{\kappa_\nu}$. The solution of the radiative transfer equation assuming LTE results in

$$I_\nu = I_\nu(0)\, e^{-\tau_\nu} + B_\nu(T_{\rm ex})\,(1 - e^{-\tau_\nu}) \ . \tag{1.15}$$

The observed intensity I_ν is given by the background intensity $I_\nu(0)$ attenuated by the interstellar medium $e^{-\tau_\nu}$ plus the integrated intensity attenuated by the medium along the line of sight.

1.3.2.2 Column density

The column density is a measure of the number of particles in a column of gas (per unit area) along the line of sight. The radiative transfer properties of the molecular emission are related to the molecular column density, as it describes what part of the emission is observable. The opacity is related to the column density in the upper transition state N_u as

$$\tau = \frac{c^2 \phi_\nu}{8\pi\nu^2}\, A_{ul} \left(\exp\left(\frac{h\nu}{kT_{\rm ex}}\right) - 1\right) N_u \ . \tag{1.16}$$

The column density is also related to the integrated intensity W of the observed transition. For an optically thin and extended uniformly emitting source:

$$N_u = \frac{8\pi k}{hc^3} \frac{\nu^2}{A_{ul}}\, W \ , \tag{1.17}$$

with $W = \sum T_{\rm mb} \Delta v$, where $T_{\rm mb}$ is the brightness temperature measured by the main beam of the telescope and Δv is the velocity resolution or channel width of the observation (Sect. 1.4.2). The column density for a particular energy level and for the total population of all energy levels relate as

$$N_u = \frac{g_u\, N_{\rm tot}}{Q(T)} \exp\left(-\frac{E_u}{kT}\right), \tag{1.18}$$

where g_u is degeneracy factor (statistical weight) of the upper level, E_u is the energy of the upper level, k is the Boltzmann constant, T is the (constant) equilibrium or excitation temperature, $N_{\rm tot}$ is the total number of molecules per cm^{-2}, $Q(T)$ is the partition function:

$$Q(T) = \sum g_u \exp\left(-\frac{E_u}{kT}\right). \tag{1.19}$$

1.3.2.3 Rotation-temperature diagram

A widely-used method in radio and (sub)mm astronomy to determine column densities and fractional abundances from observations of molecular emission lines is using the rotation-temperature diagram. With this diagram, the rotation or excitation temperature and the total column density of the molecule is estimated directly. The relation in Eq. 1.18 can be rewritten:

$$\ln\left(\frac{N_u}{g_u}\right) = \ln\ N_{\rm tot} - \ln\ Q(T) - \frac{E_u}{kT} \ , \tag{1.20}$$

such that this equation depends only on the observed integrated intensity W (cf. Eq. 1.17) as a linear function of the upper energy level E_u. The slope m of this function is the negative inverse of the excitation temperature ($m = -T^{-1}$). Based on the partition function from a molecular spectroscopy catalogs (e.g. CDMS), the total column density can be computed from the y-axis intercept.

The number density of a molecule A in units cm^{-3} is the column density N_{tot} within a path ds along the line of sight:

$$n_A = \frac{N_{\mathrm{tot}}}{ds} \,. \tag{1.21}$$

The fractional abundance then is

$$f_A = \frac{n_A}{n_{H_2}} \,. \tag{1.22}$$

For CSEs of AGB stars, the number density of the H_2 gas is described by the mass-continuity equation:

$$n_{\mathrm{H_2}} = \frac{\dot{M}_{\mathrm{gas}}}{4\pi r^2 \mu m_{\mathrm{H_2}} v_{\mathrm{exp}}} \,, \tag{1.23}$$

where $\dot{M}_{\mathrm{gas}}$ is the gas mass loss rate, r is the radial distance from the star, $\mu = 1.4$ is the mean molecular weight of the gas including He and CO, $m_{\mathrm{H_2}}$ is the weight of an hydrogen molecule, and v_{exp} is the expansion velocity of the gas, for the case of an spherically symmetric smooth outflow.

1.3.3 Molecular spectroscopy and velocity definitions

Observational molecular spectroscopy is the major tool to investigate the spatial, kinematical and energetic structure of an object.

1.3.3.1 Spectral line properties

The observed spectral line width is mostly caused by the Doppler effect. The line is broadened by the velocity distribution of the molecules mainly due to the temperature. Those that move away from the observer emit at lower frequencies (red-shifted), than those moving towards the observer, which emit at higher frequencies (blue-shifted), compared to the rest frame. The velocity away from the observer is defined to be positive, while the velocity towards the observed is negative, relative to the rest frame with velocity zero.

The width of the line indicates the temperature of the gas and the global velocity field (e.g. the expansion velocity) of the molecular gas. Asymmetrical shapes infer asymmetrical velocity fields due to turbulences or outflows.

The spectral line shape also includes information on the response of the telescope (e.g. resolution) and the transparency of the emitting material. If the material is optically thick ($\tau_\nu > 1$), only emission from the surface of the material reaches us, the rest is opaque. If it is optically thin ($\tau_\nu \ll 1$), the material is transparent and the emission from every layer is visible. This effect is frequency dependent (Eq. 1.16) and gives hints on the density and composition of the material. The optical depth of a certain transition can already be coarsely identified by the spectral line shape of the transition (Fig. 1.14).

Another velocity that is read off the spectral line is the proper motion of the object itself, in the studied case here, of the star. The frequency position of the molecular emission line is shifted with respect to the expected restfrequency by the motion of the star in space, due to the Doppler effect. For radio

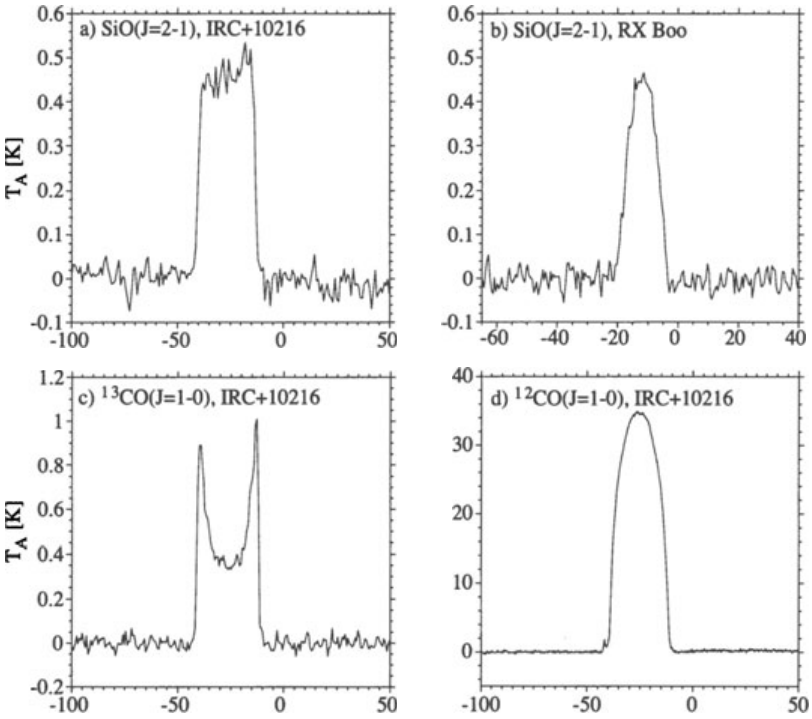

Figure 1.14: Observed spectral line shapes of molecules in the circumstellar shell: a) optically thin, spatially unresolved, b) optically thick, spatially unresolved, c) optically thin, spatially resolved, where the peaks originate from the front- and rear side of the shell, d) optically thick, spatially resolved (Olofsson in Habing & Olofsson 2003).

frequencies the following relation is used to relate radial velocity and frequency:

$$v_{\text{radio}} = c\,\frac{f_0 - f_{\text{sky}}}{f_0}, \tag{1.24}$$

where v_{radio} is the velocity of the star with respect to the Local Standard of Rest (LSR) [1], c is the speed of light, f_0 is the rest frequency of the transition, and f_{sky} is the measured frequency of the transition in the sky.

1.3.3.2 Velocity fields of CSEs

For the outer circumstellar envelope of AGB stars, a constant velocity field is usually measured. The half-width of the spectral line equals the expansion velocity of the gas. The line shapes indicate emission from a shell-like structure (Fig. 1.14). If the shell is a hollow sphere (Fig. 1.15) and the material is optically thin, the spectral line appears as a double peaked line (Fig. 1.14, c), where the peaks originate from the edges of the shell. If there are several nested shells, several peak components are expected in the spectral line, depending on the intensity of the emitting region and the resolving power of the observatory. Every observed velocity component (limited by the spectral resolution of the receiver) represents the projection of the three dimensional radial velocity field within the molecular shell onto

[1] The LSR is a frame of reference with the Sun as the origin. It follows the mean motion of the stars in the Galactic disc near the Sun on a circular orbit around the Galactic center.

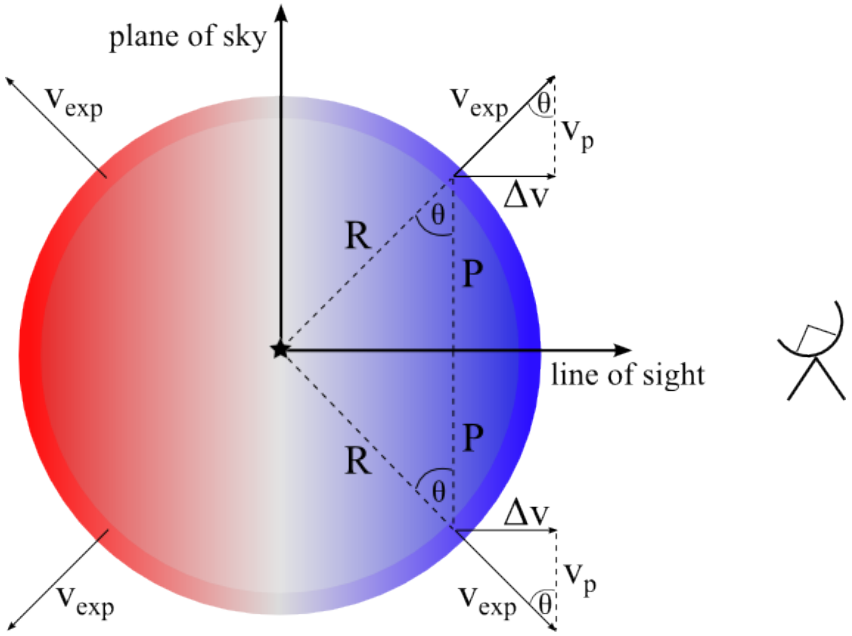

Figure 1.15: Geometry of an expanding circumstellar hollow sphere, with a certain width, with radius R, projected radius P, projection angle θ, constant expansion velocity v_{exp}, velocity along the line of sight Δv relative to the stellar velocity with respect to the Local Standard of Rest (LSR), and projected velocity v_{p} in the plane of the sky. The part of the shell that expands towards the observer is blue-shifted, with $\Delta v < 0$, and the part that moves away from the observer is red-shifted, with $\Delta v > 0$. © Denise Keller

the line of sight. Therefore we are able to reconstruct a three dimensional picture of the different physical components of the shell; from the furthest red-shifted side away from the observer, through the plane in the sky which contains the star, to the closest blue-shifted side towards the observer (Fig. 1.15).

1.3.4 Chemical reactions of molecules in CSEs

There are several possibilities to form and destroy molecules through various reaction types in the circumstellar medium. In order for chemical processes to take place, the reaction timescale has to be shorter than the expansion timescale of the circumstellar material. The expansion is the overall dominating motion which is always present. Furthermore, shocks and UV radiation alter the conditions in the gas, such as compression, heating or injection of additional energy to activate reactions. The relevant reaction types important in CSEs are (Glassgold 1996):

$$\text{Neutral-neutral: } A + B \rightarrow C + D \tag{1.25}$$

$$\text{Ion-molecule: } A^+ + B \rightarrow C^+ + D \tag{1.26}$$

$$\text{Radiative association: } A^+ + B \rightarrow AB^+ + h\nu \tag{1.27}$$

$$\text{Dissociative recombination: } A^+ + e \rightarrow B + C \tag{1.28}$$

$$\text{Photodissociation: } A + h\nu \rightarrow B + C. \tag{1.29}$$

The CSE of an AGB star is divided into four regions of distinct dominating chemistry (Fig. 1.16), which are described in the following.

Close to the star in the photosphere molecules are formed under LTE conditions. The most abundant

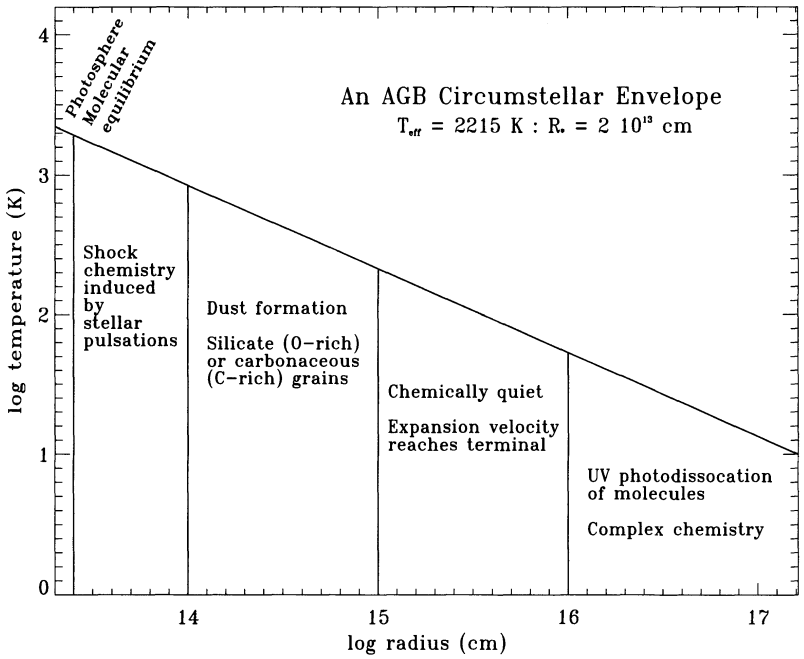

Figure 1.16: Schematic structure of the circumstellar envelope of AGB stars showing the dominating chemistry in each region described by the ambient temperature as a function of radial distance from the central star (Millar in Habing & Olofsson 2003).

molecules besides H_2 and CO in a C-rich environment in LTE are C_2H_2, N_2, HCN, CS, and SiS (Fonfría et al. 2008). There is a competition between LTE chemistry and shock induced chemistry in the outer atmosphere. Fast shocks might destroy molecules by collisional dissociation, which free up atomic oxygen and form new oxygen-bearing molecules, as OH or H_2O, and through further reactions e.g. SiO, even in a carbon-rich environment. The molecular abundances can therefore be different by several orders of magnitude than expected from equilibrium chemistry (Millar in Habing & Olofsson 2003).

In the dust formation zone (radius $\lesssim 10^{15}$ cm), molecules and dust grains interact mainly through collisions, as long as the collision timescale is shorter than the expansion timescale. Also molecules might react on the surface of dust grains, or might be accreted onto or evaporated from the dust surface depending on the temperature, mass loss rate, expansion velocity and radiation field strength.

When the density and temperatures become so low, that the dust formation declines, the wind acceleration stops, reaches its terminal velocity and the chemistry becomes rather "quiet". The abundances "freeze-out" and the material expands further away from the star (Fig. 1.16). In the outer CSE there is a competition between reactive collision that increases the complexity and photodissociation that decreases the complexity of the molecules. For radii $\gtrsim 10^{16}$ cm the photodissociation by energetic UV photons from the ambient interstellar medium dominates and eventually for larger radii splits up most of the molecules depending on their individual binding energy. The stronger the molecular binding the larger the radii where it is found, for example, CO has a very high dissociation energy and is found at radii of the order of 10^{17} cm in IRC+10216 (Cernicharo et al. 2015). This region is also called photochemical shell, because certain complex and heavy molecules, e.g. HC_3N, are formed and are present in this confined shell around the star due to UV-photon induced chemistry (Sect. 1.3.5). Such a photochemical shell around IRC+10216 is studied in this work.

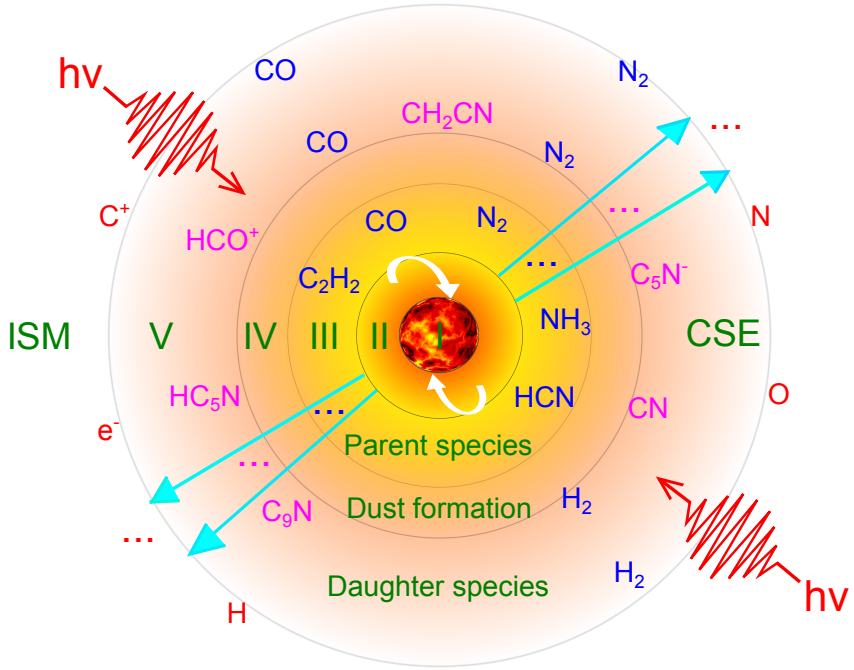

Figure 1.17: Schematic structure of the circumstellar chemistry in carbon-rich stars like IRC+10216 (Li et al. 2014).

Furthermore, penetration of cosmic rays into the CSE, gamma ray emission due to radioactive decay of unstable elements (e.g. ^{26}Al) in the CSE, and radiation from the internal photo- and chromosphere might ionize the molecules in the CSE. Ionization creates free electrons and positively charged molecules. The ionized molecules recombine with free electrons and are dissociated into smaller molecules, usually by splitting off a hydrogen atom. The dissociative recombination is only found in CSEs and the ISM and cannot be reproduced in laboratories on Earth yet. Molecular hydrogen H_2 is an important reactant in ion-molecule reactions which adds complexity. In atomic form H is unreactive. For the case of negatively charged molecules, anions, the reactions with H, however, are important in adding chemical complexity and building large hydrocarbons. Anions exist out to large radii because the ionization fraction increases with radius, e.g. C_4H^- and C_6H^- have been observed in IRC+10216 (Kawaguchi et al. 1995; Cernicharo et al. 2007). Ion-molecule and neutral-neutral reactions produce, for example, cyanopolyynes (Sect. 1.3.5, Millar et al. 2000, 2007), which we explore in this thesis. If a molecule has unpaired valence electrons, it is highly reactive to close its valence shell and to be in a energetically preferred state. Such molecules are called radicals, e.g. OH or C_2H.

1.3.5 Circumstellar photochemistry

The circumstellar photochemistry involves the photodissociation of molecules followed by chemical reactions by reactive radical molecules (Glassgold 1996). The molecules formed in the inner CSE are called parent species. For carbon-rich CSEs these are C_2H_2 and HCN. Those molecules that react with UV photons in the outer CSE and form new molecules are daughter species, such as HC_5N, CN, C_5N^- (Fig 1.17). *The following text is largely based on Millar in Habing & Olofsson (2003). Other references are mentioned explicitly throughout the text.*

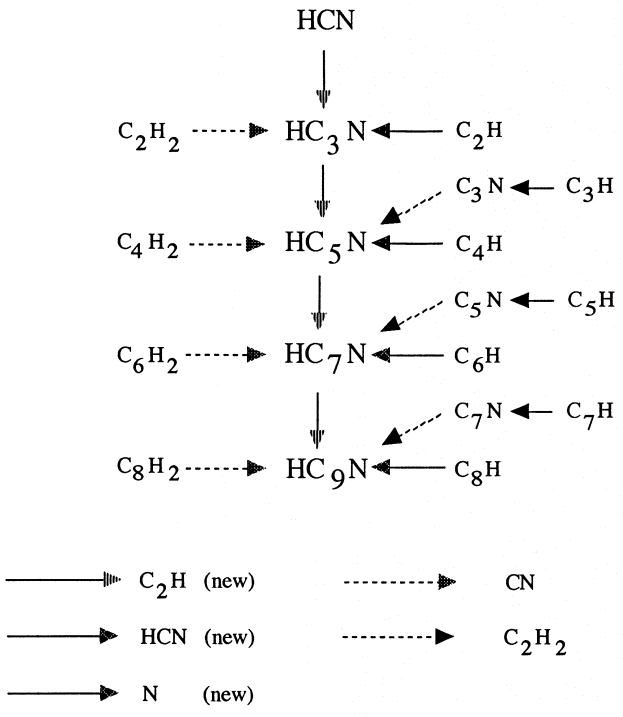

Figure 1.18: Chemical pathways that lead to formation of cyanopolyynes (Millar & Herbst 1994).

To quantify these processes, chemical models are developed, which aim to reproduce observed abundances and spatial distributions. For the models it is important to consider molecular photodissociation cross sections, shielding by dust and absorbent molecules, e.g. H_2, and the stellar and interstellar radiation field. However, the photodissociation by stellar UV photons is not yet included in the chemical or radiative transfer models. Also the photodissociation of N_2 and CO is important to include in chemical models (Li et al. 2014). Furthermore, the adopted initial stellar and CSE parameters are crucial for the results of the photochemical models, such as molecular abundances, mass loss rate, expansion velocity, dust extinction, and temperature distribution. The group of molecules which are interesting for carbon-rich and high mass-loss rate environments, as observed for IRC+10216 and presented in this thesis, are discussed in the following.

Hydrocarbons are molecules that only consist of hydrogen and carbon. In general the carbon molecules such as C_2H_2, C_2H, C_2, and also C, C^+, are very reactant with each other. Reactions with H_2 are not favored because it consumes energy (endothermic), therefore the hydrocarbons consist of only a few H atoms. Acetylene C_2H_2 is the parent molecule of this group. Photodissociation of C_2H_2 and ion-molecule chemistry of its photo-products is important for the formation of carbon-chains C_nH consisting of up to ten carbon atoms. Important example reactions are

$$C_2H_2 + h\nu \rightarrow C_2H + H, \tag{1.30}$$
$$C_2H + C_2H \rightarrow C_4H + H, \tag{1.31}$$
$$C_2H + C_2H_2 \rightarrow C_4H_2 + H, \tag{1.32}$$
$$C_4H_2 + h\nu \rightarrow C_4H + H. \tag{1.33}$$

Reactions with e.g. C_3H^+ lead to the formation of carbon chains with odd carbon numbers, e.g. C_3H.

Negative ions are important for the formation of polyacetylenes C_nH_2 and large carbon chains (Cherchneff & Glassgold 1993).

Cyanopolyynes are molecules that consist of a cyano group CN and a group of polyynes, which are compounds of carbon single- and triple-bonds ($HC_{2n+1}N$). The parent molecule relevant for this group is hydrogen cyanide HCN. The most efficient reactions to form cyanopolyynes, as HC_3N, are neutral-neutral reactions involving parent and daughter species (Howe & Millar 1990) as

$$CN + C_2H_2 \rightarrow HC_3N + H, \tag{1.34}$$

$$C_2H + HCN \rightarrow HC_3N + H, \tag{1.35}$$

$$C_3N + C_2H_2 \rightarrow HC_5N + H, \tag{1.36}$$

$$C_5N + C_2H_2 \rightarrow HC_7N + H, \tag{1.37}$$

see also Fig. 1.18 (Cherchneff et al. 1993; Millar & Herbst 1994).

Silicon- and sulphur-bearing molecules are also involved in the photochemistry with the parent species acetylene and hydrogen cyanide. Additional parent molecules are SiS, SiO, SiC_2, and CS, which are part of several reactions mentioned in Sect. 1.3.4. A few examples related to IRC+10216 are given in the following. There are reactions involving only parent molecules:

$$SiC_2 + C_2H_2 \rightarrow SiC_4 + H_2, \tag{1.38}$$

but also radical-molecule reactions:

$$SiC_2 + C_2H \rightarrow SiC_4 + H. \tag{1.39}$$

Photodissociation of SiC_2 forms SiC, and photodissociation of SiC_4 forms SiC_3. However, the abundance of SiC_2, which is an order of magnitude greater in the outer CSE than in the inner CSE, suggests that there are additional producing reactions. The photodissociation of CS, SiS, and SiH_2 leads to very reactive S, S^+, and Si, Si^+, which participate in reactions with C_2H_2, HCN, and C_2H and form e.g. C_2S and SiC_2 through dissociative recombination:

$$Si^+ + C_2H_2 \rightarrow SiC_2H^+ + H, \tag{1.40}$$

$$SiC_2H^+ + e^- \rightarrow SiC_2 + H. \tag{1.41}$$

The centrally peaked radial distribution of SiS and CS suggests that a large portion of these molecules depletes onto dust grains.

The radial distribution of carbon chain molecules and cyanopolyynes derived from photochemical models for IRC+10216 yield molecular shells with a distinct radius and extent where the abundance peaks for each molecule (Fig. 1.19, Millar & Herbst 1994; Millar et al. 2000). The interferometric observations of presumed parent and daughter species confirm the expected shell-like spatial distribution of the photochemically active species (cf. Sect. 2) and that daughter species are at larger radii than their parent species. For example, the CN shell surrounds the emission of HCN, similarly C_3N has been observed to have its peak emission at larger radii than HC_3N (e.g. Bieging & Tafalla 1993). The radial overlap of parent species and its photo-products make it possible that daughter species are created in abundance.

The carbon chains with an odd number of carbon atoms are less abundant than those with an even number of carbon atoms – for the cyanopolyynes it is vice versa – given by the number of carbon atoms

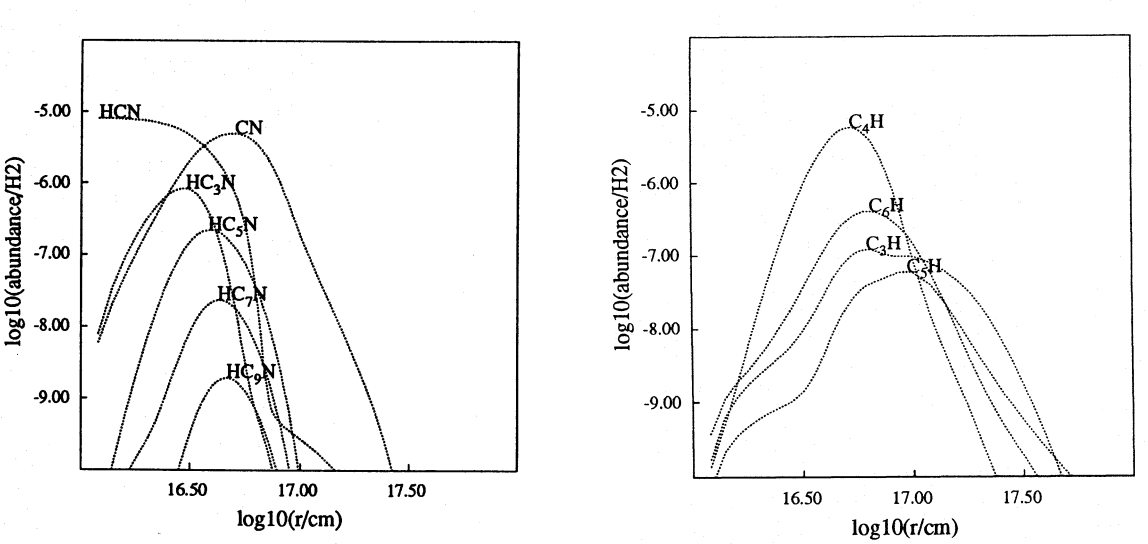

Figure 1.19: The radial distribution of cyanopolyynes (left) and carbon chain molecules (right) from chemical models for IRC+10216 (Millar & Herbst 1994).

of their parent species. $HC_{2n+1}N$ with triple and single bonds are found to be much more abundant than $HC_{2n}N$ with double bonds (e.g. Cernicharo et al. 2004, and references therein). It is similar for C_nN with an even number of carbon atoms (Anderson & Ziurys 2014). The formation of these carbon molecules with odd and even carbon atoms are decoupled from each other, because usually two triply-bond carbon atoms are added in the process, such that the very abundant parent molecules C_2H_2 and HCN grow in carbon atoms by 2. Similarly, these reactions might form e.g. HC_4N (Cernicharo et al. 2004):

$$C_3H + HCN \rightarrow HC_4N + H, \tag{1.42}$$

$$C_3N + CH_2 \rightarrow HC_4N + H. \tag{1.43}$$

The less abundant species of the groups C_nH, $HC_{2n}N$, and C_nN are located in the same photochemical shell of the CSE at similar temperatures and radial positions as the ones with even and odd n, respectively.

However, the early photochemical models, e.g. by Cherchneff et al. (1993); Cherchneff & Glassgold (1993); Millar & Herbst (1994), could not fully reproduce the observed spatial distributions of hydrocarbons, cyanopolyynes and related silicon- and sulphur-bearing molecules. This means that the conditions in the CSE are not completely accounted for in these models. For example, the lack of accurate photodissociation rate coefficients is a drawback of photochemical models (e.g. Cherchneff & Glassgold 1993). From the models it is expected that the longer the carbon chain the longer the radius at which it is most abundant. However, several observed intensity maps of IRC+10216 show that e.g. C_2H, C_4H, C_6H coexist in a shell at the same radius within about 2 arcsec width (Guélin et al. 1999; Dinh-V-Trung & Lim 2008). Given by the distribution and the CSE dynamics, this indicates that these molecules must have been formed quasi-simultaneously within about 200 yr. Considering only neutral-neutral reactions in the gas-phase, without dust grains or shocks, this is not fast enough (> 1000 yr, Guélin et al. 1999).

Furthermore, there are shell-like density enhancements observed in the CSE of IRC+10216 consisting of dust and molecular gas (Leão et al. 2006; Dinh-V-Trung & Lim 2008; Mauron et al. 2013; Cernicharo et al. 2015, Ch. 2). The structure is different than in a smooth CSE, which has a large influence on the

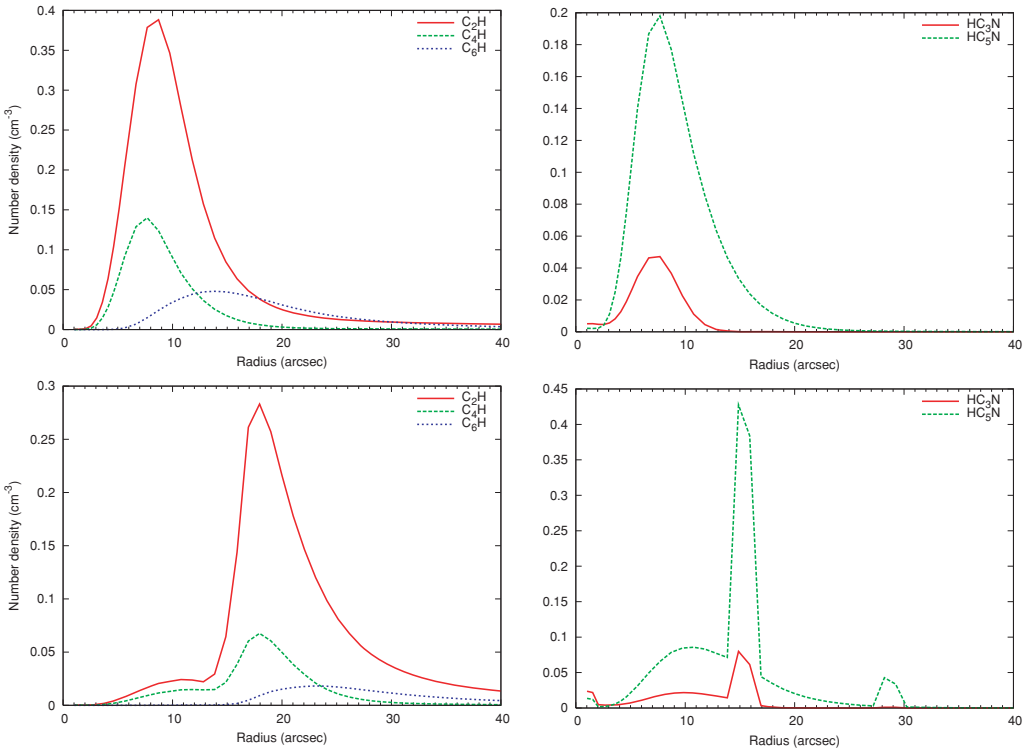

Figure 1.20: Circumstellar radial profiles of C_2H, C_4H, C_6H, HC_3N, and HC_5N for IRC+10216 from chemical models (Cordiner & Millar 2009). The top panel shows the radial distribution for a smooth CSE. The bottom panel shows the radial distribution for a CSE with density-enhanced shells, which better compares to the observed CSE structure and the observed radial distribution of these molecules (Guélin et al. 1999; Dinh-V-Trung & Lim 2008).

chemistry. Most importantly, the shielding of UV radiation in these density-enhanced dust shells of the CSE causes the molecules that are sensitive to this radiation to exist at larger radii with thinner widths than expected from the chemical modeling of a smooth CSE without dust shells (Fig. 1.20). The more recent models that adapt such density enhancements in the CSE match the observed radial emission profiles of IRC+10216 much better (Brown & Millar 2003; Cordiner & Millar 2009). The presented chemical models are compared to the results of this thesis (Chapters 4 and 6).

1.4 Radio astronomy and interferometry

In the last decades, many different telescopes have been developed and used to cover more and more parts of the electromagnetic spectrum in order to observe the properties of various astronomical objects in further detail.

Radio astronomy, covering wavelengths of 1 mm $\lesssim \lambda \lesssim$ 10 m and frequencies of 300 GHz $\lesssim \nu \lesssim$ 30 MHz, is rather young. However, it has vastly broadened our understanding of the cold and dusty parts and of the energetically most extreme objects in the Universe. Many discoveries of objects or regions which are opaque or undetectable in the optical have only been possible with radio astronomy, e.g. molecules in the dusty Galactic plane or synchrotron emission from pulsars. Radio astronomy opens a new window to the Universe and can be performed with ground-based observatories, because a broad

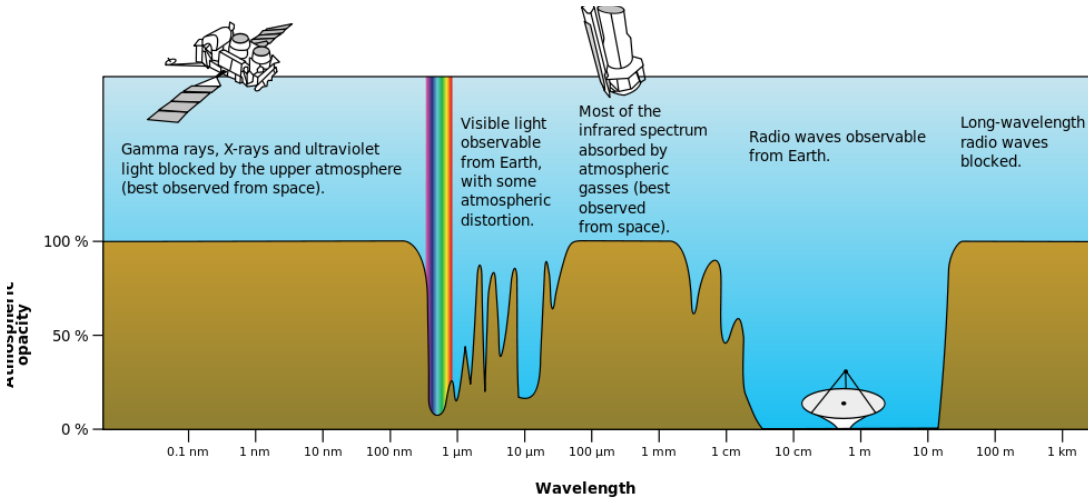

Figure 1.21: The Earth's atmospheric opacity as a function of wavelength. The radio window allows observations in the radio regime with ground-based telescopes. © Mysid, from `https://commons.wikimedia.org/wiki/`, adapted from NASA.

part of radio radiation is not absorbed by the Earth's atmosphere, given by the so-called atmospheric windows (Fig. 1.21).

For sub-mm emission there are narrower confined wavelength windows, for which the radiation is not absorbed by mainly water vapor and oxygen molecules in the atmosphere. The strongest absorption bands are around 22.3 GHz and 60 GHz, respectively. The weather conditions are mainly governed by the water content quantified by the precipitable water vapor (pwv) of the atmosphere measured by several radiometers and with atmospheric models on the observatory site. To extend the limits of the atmospheric windows and improve the observation conditions, modern radio and sub-mm observatories go high and dry – to deserts at high altitudes (> 3000 m) with pwv < 4 mm or even above the Earth's atmosphere with airborne observatories or satellites.

1.4.1 History

It all started with the engineer Karl Guthe Jansky in the 1930's. He investigated interferences and radio disturbances at the very long wavelengths (14.6 m, 20.5 MHz) of transatlantic communication for the Bell Telephone Laboratories. With his directional antenna he noticed a strong reoccurring signal peaking every 24 hours. At first he suspected the Sun as the source, but further observations indicated that the signal origins a fixed direction in the sky with a period of 23 hours and 56 minutes, which does not match the Sun's position. This period rather hints an astronomical object (over the course of a sidereal day), which Jansky then identified as to be the Galactic center. He concluded that the emission comes from interstellar gas and dust in the Galaxy. The position of the peak emission was later assigned with Sagittarius A. Jansky was the first to detect radio signals from an extraterrestrial source. Shortly later, Grote Reber repeated Jansky's work and observed along the visible Galactic band with his parabolic antenna and detected radio emission at 162 MHz from further known sources, such as Cassiopeia, Canis Major, and also the Sun (Reber 1940, 1944). This was the first sky survey in the radio range.

The pioneering work of Jansky and Reber marked the start of radio astronomy. In honor of Jansky, the unit of flux density, the major measure of radio emission, was named after him: 1 Jy $= 10^{-26}$ W m^{-2} Hz^{-1}. Also the recently extended Very Large Array was renamed Karl G. Jansky Very

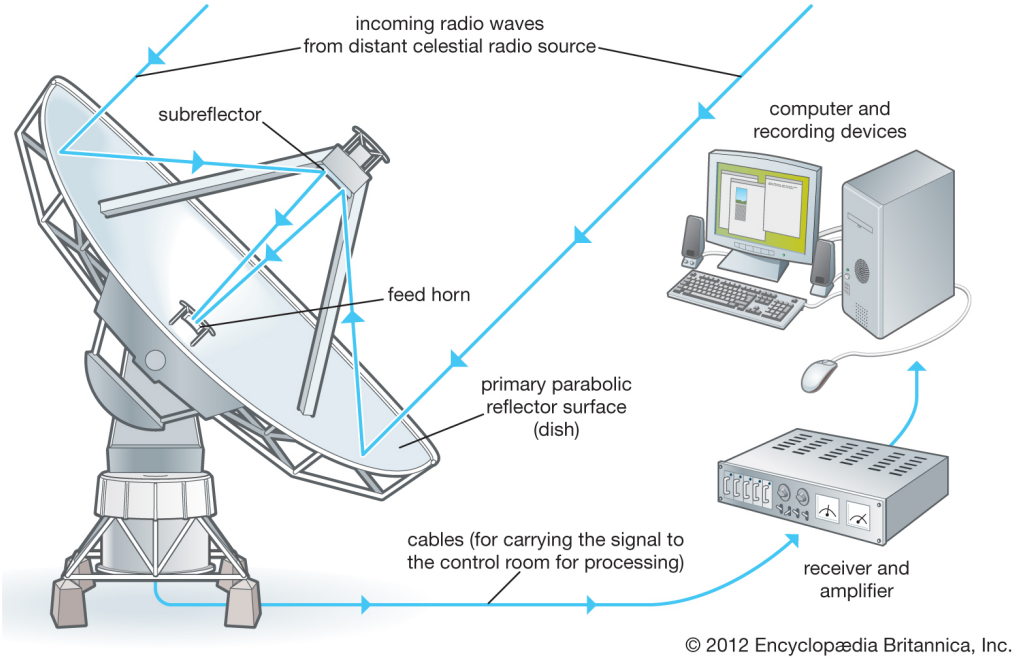

Figure 1.22: Sketch of a radio telescope (with the ray path) consisting of the primary parabolic mirror, the subreflector (secondary mirror), the feed horn collecting the radio signals, the receiver system (with amplifiers), and recording devices. © Encyclopaedia Britannica, Inc.

Large Array by the National Radio Astronomy Observatory (NRAO) in 2012 to remember Jansky's contribution to radio astronomy.

The first spectral line that was detected in the radio was the 21-cm (1.4 GHz) line of neutral hydrogen (Ewen & Purcell 1951), predicted by Hendrik van de Hulst. This transition is very important for radio astronomy as it opens the possibility to map, for example, the structure of our Galaxy.

The radio emission, that we study in this work, mostly traces low energy transitions from low temperature regions, which are well described by the Rayleigh-Jeans approximation of Planck's law ($h\nu/kT \ll 1$). The sources of this emission mostly are neutral hydrogen, recombination lines, other molecules, and the cosmic microwave background (CMB). The first molecule discovered in the radio regime was OH (Weinreb et al. 1963), after which many discoveries of molecular species followed (Sect. 1.3).

1.4.2 Single-dish radio telescopes

In the following, important concepts of radio astronomy, such as the radio telescope receiver system and flux density, are introduced. *The text is largely based on Klein (2006) and Condon & Ransom (2016)* .

Typically, a radio telescope consists of a parabolic reflecting dish, with a secondary mirror, a feed horn, and a receiver system (Fig. 1.22). The incoming radiation is focussed in the primary focus and reflected into the secondary focus by the subreflector. The parabolic shape of the single-dish telescope is necessary to focus the incoming radiation into a single wavelength-independent focal point. Thereby the far-field plane waves are converted into spherical ones. Most of the time, the feed horn is placed in the secondary focus because there the focal plane (the plane over which the radiation is focussed) is much larger than at the primary focus and the feed horn is better protected from unwanted radiation, that

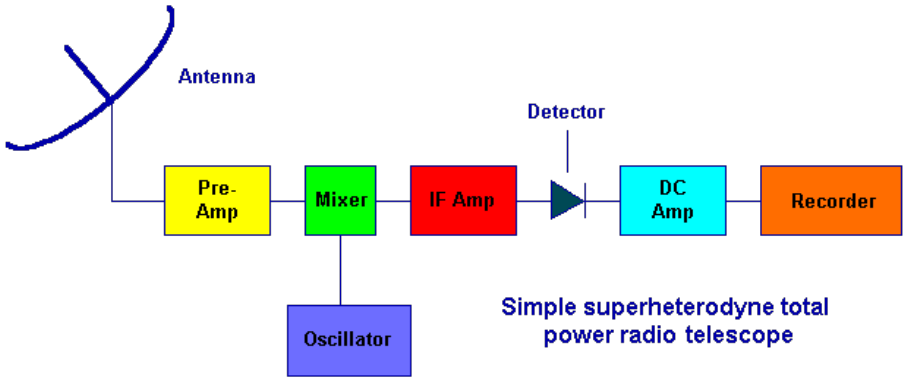

Figure 1.23: Signal path in the receiver system of a radio telescope with the heterodyne principle, consisting of a cooled pre-amplifier, a frequency down-converter also called mixer (with a local oscillator), a bandpass filter, an intermediate frequency (IF) amplifier, a detector which converts voltage to total power, an analog-to-digital converter, and a digital recorder. © Jim Sky

is reflected ground radiation from the Earth ($T \sim 300$ K) and artificial radio emission interferences. The feed horn is a horn-shaped antenna which converts the incoming radio waves through the aperture into a beam, with the advantage of minimum signal loss through a gradual impedance transition rather than a sudden end to the waveguide. The horn also acts as a filter to feed only a single mode into the waveguide and the electronics. To achieve this, the horn size is chosen according to the aimed wavelength of the signals, the larger the wavelength the larger the size. The waveguide (a metal tube or a cable) transfers the signal into the receiver system.

1.4.2.1 Receiver system

The receiver system, also called radiometer, consists of a cooled pre-amplifier, a frequency down-converter also called mixer (with a local oscillator), a bandpass filter, an intermediate frequency (IF) amplifier and a signal converter (Fig. 1.23). A radiometer basically measures broadband noise and the receiver system of a radio telescope is designed to extract the weak noise signal coming from an astronomical source from a sum of several other strong noise sources. The receiver measures a noise power P_ν per bandwidth $\Delta\nu$ which is proportional to the noise temperature of the whole system $T_{\rm sys}$ if the Rayleigh-Jeans approximation is valid (Nyquist's law):

$$P_\nu = kT_{\rm sys} \,, \tag{1.44}$$

where k is the Boltzmann constant. Integrating over the bandwidth gives $P = kT_{\rm sys}\Delta\nu$. The overall system temperature consists of the sum of all (mostly independent) noise contributors:

$$T_{\rm sys} = T_R + T_A \tag{1.45}$$

$$= T_R + T_{\rm sky} + T_{\rm atm} + T_g + \ldots \,, \tag{1.46}$$

where T_R is the receiver temperature, T_A is the antenna temperature which consists of $T_{\rm sky}$ the brightness temperature from the sky and the astronomical source, $T_{\rm atm}$ the atmospheric temperature and T_g the ground temperature. As mentioned, the receiver noise temperature dominates the system noise tem-

perature, so it should be minimized as much as possible. The system consists of several components, each with a temperature T_i and gain factor G_i ($i = 1, ..., N-1$), where $G > 1$ for amplification and $G < 1$ for loss. The total temperature of a receiver with N elements then is

$$T_R = T_1 + \frac{T_2}{G_1} + \frac{T_3}{G_1 G_2} + \ ... \ + \frac{T_N}{G_1 G_2 ... G_{N-1}} \ , \tag{1.47}$$

such that the first component is the main contributor to the overall noise temperature of the receiver. Therefore especially the first pre-amplifier needs to be cooled to minimize the thermal noise. A good typical receiver temperature is below 100 K.

The antenna temperature contains the desired, very weak, astronomical signal. In order to detect the signal, a strong amplification is necessary. Furthermore, we make use of the fact that the source signal is correlated whereas the noise background signal is not. Ideally, the noise is randomly distributed, therefore behaves as Gaussian noise. The average of several observations j with a standard deviation of σ_j each for a given time interval has a total standard deviation of

$$\sigma_{\rm tot} = \frac{\sigma_j}{\sqrt{N}} \ , \text{with } \sigma_j = \sigma \ , \tag{1.48}$$

where N is the sample size. The total uncertainty of astronomical observations ΔT, also called sensitivity or root-mean square deviation $\sigma_{\rm rms}$, is given by the system noise temperature ($\sigma = T_{\rm sys}$). The sampling is given by the bandwidth $\Delta\nu$ and the integration time τ ($N = \Delta\nu\,\tau$), such that

$$\sigma_{\rm rms} = \Delta T \approx \frac{T_{\rm sys}}{\sqrt{\Delta\nu\,\tau}} \ , \tag{1.49}$$

which is called the radiometer formula. The formula shows that to improve the sensitivity or the signal-to-noise ratio by a factor of 2, the observation time has to be increased by a factor of 4.

The pre-amplified high-frequency (HF) signal would cause strong feedback effects in the system and is much more difficult to handle in terms of electronics. To avoid this, the heterodyne detection principle is employed. The HF signal is converted to an intermediate frequency (IF) by mixing it with a local oscillator (LO) signal at similar frequency. The output of the mixer are the IF frequency $\nu_{\rm IF} = |\nu_{\rm LO} - \nu_{\rm s}|$ and the beating components, which lead to two HF components centered at the signal (s) and image (i) frequency:

$$\nu_s = \nu_{\rm LO} + \nu_{\rm IF} \qquad \nu_i = \nu_{\rm LO} - \nu_{\rm IF} \ , \tag{1.50}$$

called the lower and upper sideband, or signal and image band. The further receiver components work only with the IF, which is much easier to process for the electronics. Through the data processing the signals from these sidebands are interpreted. The receiver can be tuned to a specified desired signal frequency, which is crucial for spectroscopy, by changing the LO frequency. The rest of the electronics does not need to be changed and works at fixed frequency ranges.

After the mixing, a bandpass filters the unwanted frequency bands (which defines the bandwidth of the receiver system), and the IF signal is amplified (Fig. 1.23). Then this signal is processed by the detector, which is a square-law diode transforming the input voltage to its squared value, which is proportional to the noise power, our desired quantity. So the detector converts the noise voltage, which has a mean of zero, to squared voltage which has a mean proportional to the input noise power, which is proportional to the antenna temperature. The input voltages vary on very short timescales, so the signal

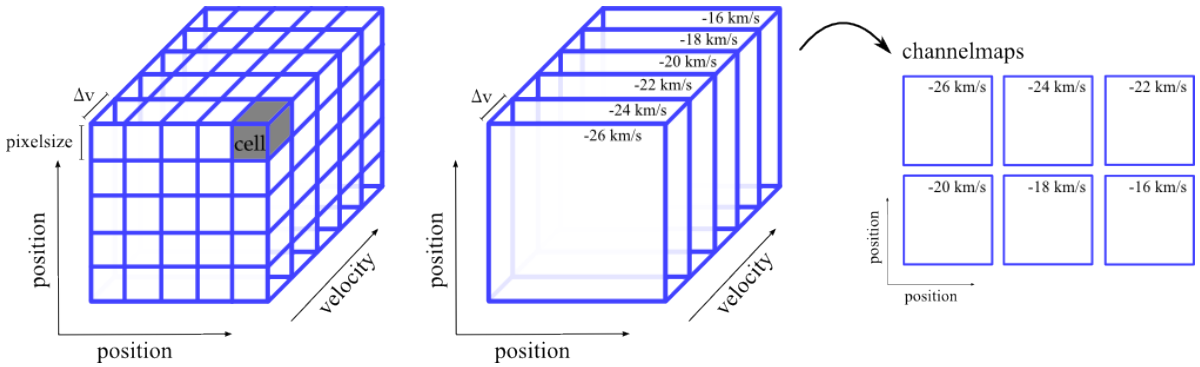

Figure 1.24: The data is stored in a three-dimensional cube consisting of layers of position-position maps (RA and Dec) for a number of velocity channels. The maps have a chosen extent divided into a number of pixel cells with a chosen width (pixelsize), according to the angular resolution of the observation. Each velocity channel contains the measured flux density distribution of the source per bandwidth. When splitting up the data cube into each velocity channel we create channel maps, when adding up along the velocity axis we create a moment-0 map of velocity-integrated intensity or a column density map. © Denise Keller

fluctuations are summed over a certain integration time by an integrator. The output of the integrator is the smoothed voltage as a function of time. With a large enough sample size N, this amplitude distribution is of Gaussian shape with an uncertainty σ_{rms} (Eq. 1.49). Finally, the output is converted in an analog-to-digital converter (ADC) for further digital processing.

The signal then is processed in a so-called backend, e.g. a Fast Fourier transform spectrometer. This spectrometer converts the measured voltage per time $U(t)$ into power per frequency $P(\nu) \sim |U(\nu)|^2$, to obtain a power spectrum which is essential to analyze spectral line emission. The measured power is split into equally-spaced channels (Fig. 1.24). The data is stored in data cubes, which consist of position-position maps of the source for a number of channels. Each channel contains the measured power or flux density distribution of the source per frequency interval (bandwidth) or per velocity interval (Eq. 1.24).

1.4.2.2 Antenna beam

The angular response or directivity of the antenna is described by Fourier optics. The incoming radiation from the far-field shows a Fraunhofer diffraction pattern as it passes the aperture (given by the feed horn). The measured power pattern of the telescope, also called antenna diagram, is the squared Fourier transform of the electric field distribution across the aperture. The pattern has a main lobe or main beam with a half power beam width (HPBW) or full-width half-maximum (FWHM) width and further weaker maxima called the sidelobes (Fig. 1.25). The HPBW determines the angular resolution of the telescope. However, this is a two dimensional geometry, such that we consider solid angles. The beam solid angle

$$\Omega_A = \iint_{4\pi} P(\theta, \phi)\, d\Omega \tag{1.51}$$

is the integration over the whole sphere 4π, which is the sum of the directivity of the main beam and the sidelobes. The main beam solid angle Ω_{mb} is integrated over the main lobe, for a symmetrical Gaussian shape it is $\Omega_{\mathrm{mb}} = \frac{\pi}{4 \ln 2}\, \theta^2_{\mathrm{HPBW}}$. The main-beam efficiency expresses the ratio of the main-beam and the

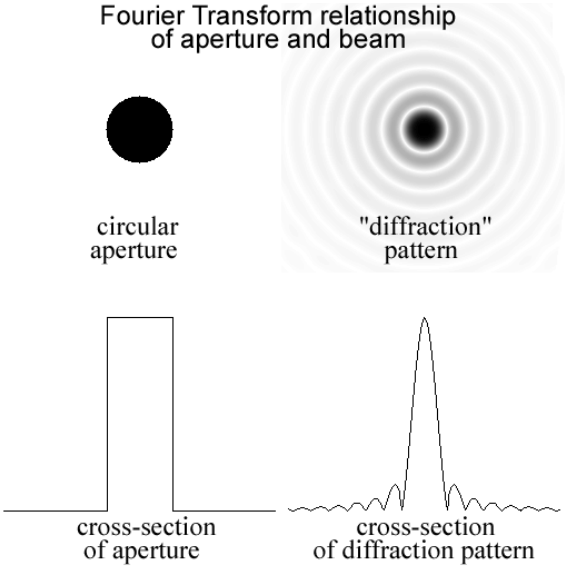

Figure 1.25: Relationship between the aperture and power pattern of a radio telescope. The diffraction pattern is the squared Fourier transform of the aperture illumination and consists of a main beam with a half power beam width (HPBW) and several higher-order sidelobes. © Dale E. Gary

total solid angle:

$$\eta_{\mathrm{mb}} = \frac{\Omega_{\mathrm{mb}}}{\Omega_A} \,, \tag{1.52}$$

and describes the amount of incoming power that is measured by the main beam, also called the beam filling factor. Due to blocking by the secondary mirror, the support structure of the telescope, and other effects, this efficiency is less than 1, rather $\eta_{\mathrm{mb}} \lesssim 70\%$. For a Gaussian beam and source size the beam filling factor is $\frac{\theta^2_{\mathrm{source}}}{\theta^2_{\mathrm{beam}}+\theta^2_{\mathrm{source}}}$. Another important efficiency is the aperture efficiency which describes the effective collecting area as a fraction of the geometrical area of the telescope:

$$\eta_A = \frac{A_{\mathrm{eff}}}{A_{\mathrm{geo}}} \,, \quad A_{\mathrm{eff}} = \frac{\lambda^2}{\Omega_A} \,. \tag{1.53}$$

1.4.2.3 Flux density

The flux density of the source is the power density received by the telescope per bandwidth and per effective area of the telescope:

$$S_\nu = \frac{2P_\nu}{A_{\mathrm{eff}}}. \tag{1.54}$$

The power over the whole bandpass $\Delta\nu$ is $P = \frac{1}{2}A_{\mathrm{eff}}S_\nu\Delta\nu$, where the factor of $\frac{1}{2}$ comes from the fact that there are two polarizations.

The brightness temperature T_B of a source is given by the Rayleigh-Jeans approximation of Planck's

law:

$$B_\nu = \frac{2\nu^2 k}{c^2} T_B = \frac{2k}{\lambda^2} T_B \,, \tag{1.55}$$

where B_ν is the surface brightness in units of W m^{-2} Hz^{-1} per solid angle.

1.4.2.4 Calibration

The final receiver output, which is the total power of the observed radio source, has to be further processed to extract the flux density of the astronomical source. First, the receiver noise temperature T_R is determined and subtracted from the total system temperature T_{sys} or total power. The usual method is the so-called hot-cold measurement, where a hot and cold component with known temperatures T_h and T_c are observed. The measured total power each then is

$$P_h = (T_R + T_h) \times G \tag{1.56}$$

$$P_c = (T_R + T_c) \times G \,, \tag{1.57}$$

where G is an unknown gain. The receiver temperature then is expressed by the ratio of the two measurements, which also eliminates the gain:

$$\frac{P_h}{P_c} = \frac{T_R + T_h}{T_R + T_c} = y \tag{1.58}$$

$$\Leftrightarrow T_R = \frac{T_h - yT_c}{y - 1} \,. \tag{1.59}$$

Second, the measured antenna temperature needs to be corrected for the atmospheric temperature and further background sources. Therefore, observations are scheduled to measure the target source (on) followed by regular measurements of a blank part of the sky near to the source with similar atmospheric conditions (off, by wobbler-, position- or frequency-switching), which then is subtracted from the on-observations. Furthermore, the attenuation through the atmosphere is considered:

$$T_b = T_{\mathrm{atm}} \, (1 - e^{-\tau}) \tag{1.60}$$

$$T_A = T'_A \, e^{-\tau} \,, \tag{1.61}$$

where τ is the atmospheric opacity and T'_A the antenna temperature corrected for atmospheric losses. With the forward efficiency F_{eff} of the telescope we describe the sky temperature as

$$T_{\mathrm{sky}} = F_{\mathrm{eff}} \, T_{\mathrm{atm}} \, (1 - e^{-\tau}) \,, \tag{1.62}$$

and the ground temperature

$$T_g = (1 - F_{\mathrm{eff}}) \, T_{\mathrm{amb}} \,, \tag{1.63}$$

where T_{amb} is the ambient temperature, which is measured with the so-called chopper wheel method on a wheel installed in the optical path of the telescope. The measurement of the ambient temperature is subtracted from the output measurement of the sky temperature. The temperature of the atmosphere is assumed to be very similar to the ambient temperature ($T_{\mathrm{amb}} \approx T_{\mathrm{atm}}$). Now we calculate the ratio of

these two calibration measurements to determine the corrected antenna temperature:

$$\frac{P_{\rm on} - P_{\rm off}}{P_{\rm amb} - P_{\rm sky}} = \frac{T'_A e^{-\tau}}{T_{\rm atm} F_{\rm eff} e^{-\tau}} \tag{1.64}$$

$$\Leftrightarrow T^*_A = \frac{P_{\rm on} - P_{\rm off}}{P_{\rm amb} - P_{\rm sky}} T_{\rm atm} = \frac{T'_A}{F_{\rm eff}} \, . \tag{1.65}$$

We then have a quantity called the corrected antenna temperature T^*_A, which ideally only contains the amplitude from the target source, corrected for the atmospheric and instrumental losses.

1.4.2.5 Main beam temperature

We measure a main beam temperature $T_{\rm mb}$ which is related to the antenna temperature as

$$T_{\rm mb} = \frac{T'_A}{\eta_{\rm mb}} = \frac{F_{\rm eff}}{\eta_{\rm mb}} \, T^*_A \, . \tag{1.66}$$

The flux density (Eq 1.54) is related to the antenna temperature as

$$S_\nu = \frac{2k}{A_{\rm eff}} T_A \, , \quad [S_\nu] = \mathrm{W\ m^{-2}\ Hz^{-1}}. \tag{1.67}$$

The relation between the flux density of the source and the received antenna temperature depends only on the telescope properties, which means effective collecting area and the forward efficiency when considering the corrected antenna temperature.

The relation between flux density and main beam temperature is

$$S_\nu = \frac{2k}{\lambda^2} \Omega_s \, T_{\rm mb} \, , \tag{1.68}$$

for a source with a solid angle of Ω_s. The equation is valid for unresolved sources, if the source is smaller than the telescope beam with a uniform brightness temperature. If an observed object is resolved its angular extent is larger than the beam solid angle of the antenna and $T_A \approx T_B$.

1.4.3 Radio interferometry

In this thesis, radio interferometric data of the Very Large Array (VLA) is used. In the following the basics of the technology and observing method of radio interferometry are introduced. *The following text is largely based on Klein (2006), Wilson et al. (2013), and Condon & Ransom (2016) .*

Single-dish telescopes are limited in terms of angular resolution and sensitivity given by their finite size and collecting area. They cannot be built much larger than the currently largest fully steerable single dishes, i.e. the Effelsberg 100-m telescope (MPIfR) and the 102-m Green Bank Telescope (NRAO). For larger diameters the primary dish has to be fixed and supported by the surrounding landscape. Examples for such telescopes are the 305-m Arecibo observatory in Puerto Rico and the Five-hundred-meter Aperture Spherical Telescope in China.

To increase the observation capabilities (angular resolution and sensitivity) several telescopes are combined to interferometers and aperture synthesis and signal correlation is performed. The future of astronomy lies in interferometry. There are more and more interferometers used and being developed

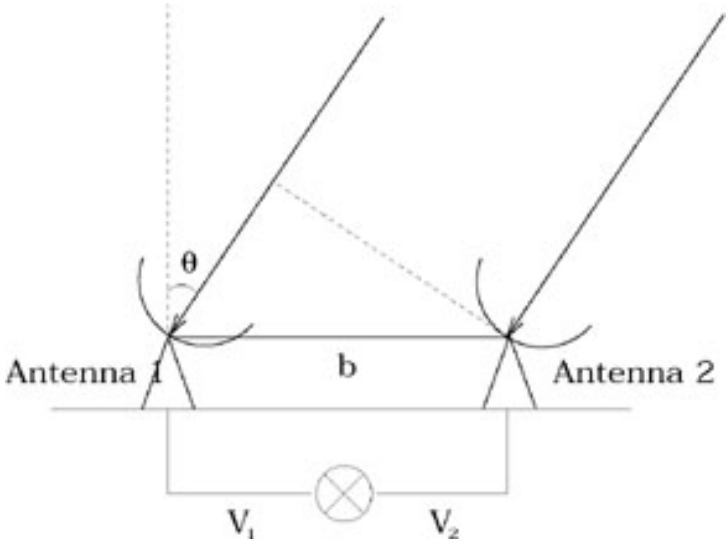

Figure 1.26: A simple sketch of a two-element interferometer. The radiation from a source arrives at antenna 1 with a geometric delay of $\sin\theta$ compared to antenna 2. The distance between the antennas is called baseline b. The received signals (time-varying voltages V_1 and V_2) are multiplied and integrated in the correlator. © Birkinshaw & Lancaster, University of Bristol

in different frequency regimes, for example the Very Large Telescope Interferometer (VLTI) in the optical, the Submillimeter Array (SMA), the NOrthern Extended Millimeter Array (NOEMA), and the Atacama Large Millimeter/submillimeter Array (ALMA) in the submm, and the Very Large Array (VLA), the Australia Telescope Compact Array (ATCA), and the Square Kilometer Array (SKA) in the radio regime.

1.4.3.1 Interferometer principles

In principle, an interferometer consists of at least two (identical) telescopes and receives signals which are brought to interference (Fig. 1.26). The combination of the signals is performed in the correlator consisting of a multiplier and subsequent integrator. The interference patterns are called fringes.

Through the correlation of the signals, the array approximates a telescope with the diameter of the longest distance between the antennas in the array. The field of view of the array is given by the diameter of the single telescopes in the array, also called the primary beam. The angular resolution of the array is given by the length of the longest distance between the telescopes, called maximum baseline. The longer the baseline the smaller the angles which are resolved by the array. For example, the VLA has four possible configurations with maximum baselines between 1 km and 36 km, respectively, which can be chosen depending on the science case. The angular resolution then is between 3 arcsec and 0.09 arcsec for observations around a frequency of 22 GHz in the K-band.

We assume that the source is much further away than the distances between the telescopes, the telescopes are all in the same plane, the bandwidth is much smaller than the observed frequency, and the angular size of the source is much smaller than the angular distance between two interference maxima (fringe width), which is valid most of the time. The signal from the source arrives as a planar wavefront at the telescopes with a certain angle to the zenith axis (Fig. 1.26). Each telescope has a different distance to the source and the wavefront arrives at slightly different times at each telescope – the geometrical delay. For the observation a phase reference position is chosen and the delay and phase at each

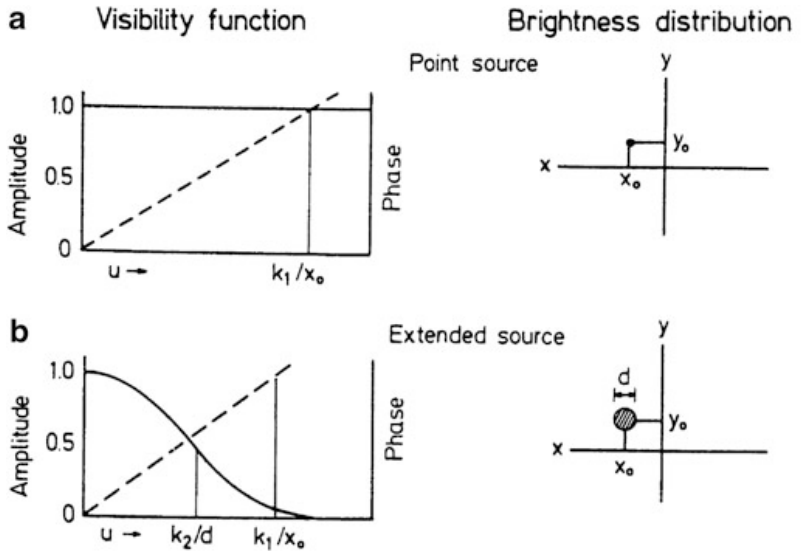

Figure 1.27: Transformation from the visibility function to the brightness distribution of a point source (a) and a Gaussian shaped extended source (b) both displaced from the origin. In the left panel, the solid line is amplitude and the dashed line is phase (Wilson et al. 2013).

telescope are measured relative to this position. The phase therefore gives the spatial information of the source.

With the spatial information and the information on the intensity distribution, an image map of the source structure is recovered. When performing spectroscopy, we also gain information on the structure along the line of sight from the different velocity components, as described in Sect. 1.3.3 and Fig. 1.24 in Sect. 1.4.2.1.

1.4.3.2 Visibility function

The received signals are called visibilities, which consist of an amplitude (unit of flux density W m^{-2} Hz^{-1} or Jy) and phase (unit of degrees). The visibility is the convolution of the brightness distribution and the fringe pattern for a given baseline. To obtain the brightness distribution $B(l, m)$ of the source the inverse Fourier transform of the visibility function $V(u, v)$ is calculated (Fig. 1.27):

$$B(l, m) = \int \int V(u, v)\, e^{2\pi i(ul+vm)}\, du\, dv\ . \tag{1.69}$$

The visibility is measured in the coordinate system (u, v, w). The orthogonal vectors u (east direction) and v (north direction) span the plane of the telescope baselines, also called aperture plane. The w-vector is perpendicular to this plane and points to the science target and defines the phase reference position. The coordinates are measured in units of wavelengths at the center frequency of the observation. Through the inverse Fourier transform we change from the uv-plane to the coordinate system (l, m) in the plane of the sky, also called image plane. The positions are measured relative to the phase reference center, which is also the origin of the brightness distribution in the lm-plane. In other words, we transform from the aperture distribution of the antennas in the uv-plane to the far-field radiation pattern in the plane of the sky (Fig. 1.28, cf. Fig. 1.25).

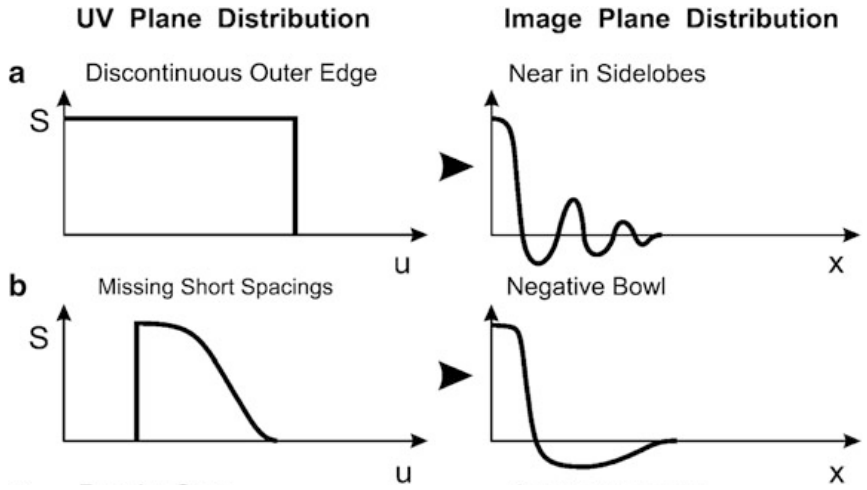

Figure 1.28: Transformation of an one-dimensional aperture pattern in the *uv*-plane to the antenna diagram (the resulting beam) in the image plane for a constant aperture with a discontinuous edge (a) and a Gaussian shaped aperture with missing short spacings (b) (Wilson et al. 2013).

1.4.3.3 Aperture synthesis

Every baseline of the interferometric array measures a range of Fourier components of the brightness distribution. To obtain a realistic approximation of the brightness distribution the visibility function has to be determined as good as possible, which is called aperture synthesis. Many different baselines should be covered in the *uv*-plane. This is achieved by placing many antennas in the *uv*-plane and by the rotation of the Earth which changes the positions of the antennas relative to the source over time. Circles and ellipses are then sampled in the *uv*-plane, depending on the elevation of the source. The *uv*-coverage depends on the observing duration, the elevation of the source, the number of antennas, and the shape of the array. For observing with a high angular resolution for a wide range of declinations, a two-dimensional array with at least a northsouth and eastwest extent is a good choice. An example is the "Y"-shaped configuration of the VLA (Fig. 1.29). The array is rotated by 5° with respect to the northsouth coordinate axis to ensure good angular resolution also for sources near a declination of zero.

Since the baselines cannot be smaller than the diameter of the telescopes without overlapping, the interferometer cannot cover scales smaller than that. These short spacings in the *uv*-plane are sensitive to extended radiation in the plane of the sky. These are then missing in the solution of the brightness distribution, because the interferometer basically filters out these scales. This effect is known as missing short- or zero-spacing problem. In the aperture distribution in the *uv*-plane there then is a central hole. In the image domain, there then is a "negative bowl" underneath the brightness distribution which causes negative flux values (Figs. 1.28, b and 1.30). This means that with an interferometer alone the total flux of an extended source cannot be measured. The larger the scales of the source brightness distribution the more severe the effect. This problem is centrally important for the VLA data of the rather extended circumstellar material of IRC+10216 used in this thesis. Only observations with single-dish telescopes can fill this gap in the *uv*-coverage. Therefore, single-dish telescopes are still very necessary and desired.

Figure 1.29: Aerial photo of the Very Large Array (VLA) in the high plains of San Augustin in New Mexico, USA, depicting its "Y"-shape in the most compact configuration. © NRAO, Associated Universities, Inc.

1.4.3.4 Calibration

The measured data cannot be used directly. First, corrections have to be applied regarding the antenna positions, atmospheric opacity, and antenna response. Second, the phases and amplitudes, and subsequently the flux values, have to be calibrated using the delay and bandpass measurements, phase and amplitude calibrator and flux calibrator sources. A detailed description of the calibration procedure for the VLA data is given in Sect. 3.3.

1.4.3.5 Imaging synthesis

There are always parts of the visibility function which are not covered and therefore the "true" image of the source cannot be fully recovered. The procedure of deconvolution and "cleaning" interpolates between these missing information in the *uv* and/or image plane to reconstruct an image that closely reflects the brightness distribution. An interferometric image map does not have one unique solution, it often is called to be the "best guess" of the real source structure.

For a first estimate of the sky surface brightness in the image domain (diffraction pattern), the visibility function and the sampling function (aperture distribution) are Fourier transformed, similar to the aperture and illumination pattern of single-dish telescopes (cf. Fig. 1.25, Sect. 1.4.2.2, p. 38). The resulting image is called the "dirty image", which is the brightness distribution convolved with the "dirty beam". The dirty beam is given by the response of the interferometer to a point source, the point spread function.

The subsequent goal is to deconvolve the dirty image to achieve a so called "clean image" which consists only of the "true" brightness distribution convolved with a (usually) Gaussian beam, the "clean beam". The sky surface brightness has the unit of flux density per solid angle (W m^{-2} Hz^{-1} $ster^{-1}$ or Jy $beam^{-1}$).

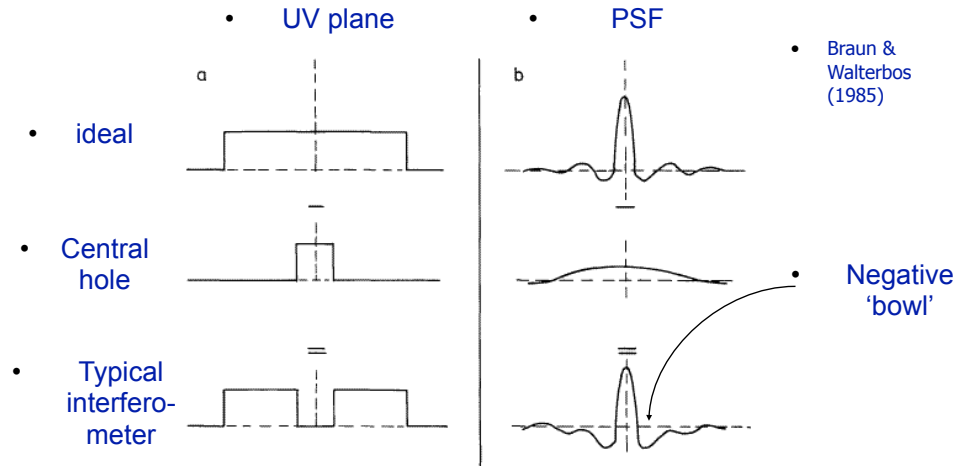

Figure 1.30: Negative bowl effect of interferometric observations caused by missing zero-spacings in the *uv*-plane. The point spread function (PSF) lies in the image domain. © Brian S. Mason, NRAO (after Braun & Walterbos 1985)

During the imaging synthesis, the visibility and/or intensity distribution is regridded to transfer the data from the array geometry to the rectangular matrix of the image map. The distributions can be weighted in several possible manners, depending on which scales should be emphasized.

The procedure of deconvolution with the CLEAN algorithm and the available weighting schemes used for this thesis are described in detail in Sect. 3.4.1. The image recovery depends on subjective parameter choices during the calibration and the imaging synthesis, such that it can be very time consuming to find the best fitting solution for individual objects. An in-depth discussion on testing the parameters involved during the imaging synthesis is presented in Sect. 3.4.2.

1.5 Aim

The aim of this thesis is to analyze the unbiased and unprecedented spectral line and imaging survey data of the carbon-rich AGB-star IRC+10216 obtained with the Karl G. Jansky Very Large Array to constrain the physical and chemical structure of circumstellar envelopes of AGB stars. This work focusses on the photochemistry of carbon-bearing molecules in the outer CSE through an empirical study of the CSE emission structure, three dimensional geometry, and clumpiness. We aim to uniquely constrain the location of the brightest molecules in the survey and their chemical feedback on each other.

The structure of this thesis is as the following:

- Chapter 1: Introduction
- Chapter 2: The star of the stars: The carbon-rich AGB star IRC+10216
- Chapter 3: The VLA spectral line and imaging survey
- Chapter 4: Radial emission profiles of molecular lines
- Chapter 5: Physical analysis
- Chapter 6: Physical and chemical interpretation
- Chapter 7: Prospects (Effelsberg, ALMA)
- Chapter 8: Conclusions and outlook

In the following chapters, we first introduce the target source of this work IRC+10216 and its observations with the VLA in detail (Chapters 2 and 3). The VLA data and its calibration and processing are explained in Sections 3.2 and 3.3. We present the extensive testing of the aperture synthesis imaging (Sect. 3.4), as this part of the data reduction contains many rather subjective parameter choices, which rely on human judgement and experience. This makes it very time-consuming to produce a reliable data product which is comprehensible. In Sect. 3.5 we show the observational results, i.e. the full composite spectrum of IRC+10216, the imaged spectral lines and the image maps. Furthermore, we estimate the amount of missing flux in the VLA data by comparing with observations of identical molecular transitions with the Effelsberg 100-m telescope (Sect. 3.6). In Chapter 4, we introduce the data analysis method and present the radial emission profiles of the molecular lines of HC_3N, HC_5N, HC_7N, C_3N, C_4H, C_6H, and C_6H^- (Sect. 4.1). We compare these radial profiles qualitatively to two different chemical models of IRC+10216 of these chemically connected species (Sect. 4.2). For a quantitative analysis of the radii, widths, and peak fluxes of the molecular shells, we approximate the radial profiles by Gaussian distributions. The method and results are presented in Sections 4.3 and 4.4. With these results we quantitatively compare to previous observations and chemical models of IRC+10216 and draw first conclusions (Sect. 4.5). With the determined parameters of the molecular shells, we perform an approximative physical analysis to estimate the column densities and abundances of HC_3N and HC_5N from the VLA data (Chapter 5). Possible effects on the excitation of the molecular lines for different assumptions on the density structures of the CSE are discussed. In Chapter 6, we take a deeper look into the results from the analysis, fitting, and comparisons and put them into the context of the molecular shell geometry and chemistry. Explanations and implications for the observed CSE morphology and its inherent chemistry are considered from intrinsic or external effects, namely the mass loss mechanism and history, hydrodynamics, magnetic fields, convection cells, a central binary system, UV irradiation and photodissociation, and its connected chemical network. We close with the prospects and conclusions of this thesis (Chapters 7 and 8).

CHAPTER 2

The star of the stars: IRC+10216

2.1 The carbon-rich star IRC+10216

The center of this work is the evolved red giant star IRC+10216. The star is located in the constellation Leo at the coordinates $(\alpha_{J2000}, \delta_{J2000}) = (09^h47^m57.4^s, 13°16'43.6'')$, $(l, b) = (221°.45, +45°.06)$, beneath the well-known constellations the Little and Big Dipper in the sky on the northern hemisphere (Fig. 2.1). The star was cataloged during the Two Micron Survey (which later became the 2 Micron All Sky Survey 2MASS, Skrutskie et al. 2006) or Infrared catalog (IRC) conducted by Neugebauer & Leighton (1969), where it received the name IRC+10216. Later it was also cataloged in the General Catalogue of Variable Stars (GCVS, Kukarkin et al. 1971), where it received the designation CW, therefore it is often called CW Leonis. Other catalog names are IRAS 09452+1330, Peanut nebula (Le Bertre et al. 1989), RAFGL 1381, and more.

The star was then observed between 1.25 and 19.5 μm by Becklin et al. (1969). From the spectral energy distribution and the spectral properties they already concluded that this galactic source has an optically thick dust shell. Subsequently, the star is very faint in optical wavelengths (visible magnitude between around 1 and 11). However, it is very bright in the mid-infrared, it even is the brightest object at $5 - 10$ μm outside of the solar system and the third brightest object at 12 μm after the Galactic Center and η Carinae. Thus, IRC+10216 is one of the most studied stars. Its brightness has a regular long-period variability of the order of 600 days and several orders of magnitude brightness difference (2 mag at 2.2 μm, Becklin et al. 1969, total luminosity by a factor of 2.5, Le Bertre 1988). The monitoring of the variability of IRC+10216 in the infrared and optical by Le Bertre (1988, 1992), and references therein, led to the characterization as a Mira-like variable star with a period of 649 days. Later the determination of the period from radio and infrared photometry (in a longer time interval) resulted in $P = 630 \pm 2.9$ days (Menten et al. 2012). Many spectral features originate from carbon molecular compounds, which are much more abundant than oxygen bearing compounds (C/O > 1), such that the star is named carbon-rich (Herbig & Zappala 1970).

The first molecular line emission observed around IRC+10216 was that of CO (J = 1 − 0) (Solomon et al. 1971). The parabolic spectral line shape and line width of about 30 km s^{-1} indicates that the emission originates from an expanding sphere with a terminal velocity of about 15 km s^{-1}. This velocity is the escape velocity from the surface of the red giant star. Shortly afterwards, more and more molecular species were detected around IRC+10216, more on this in the next section. From the molecular line

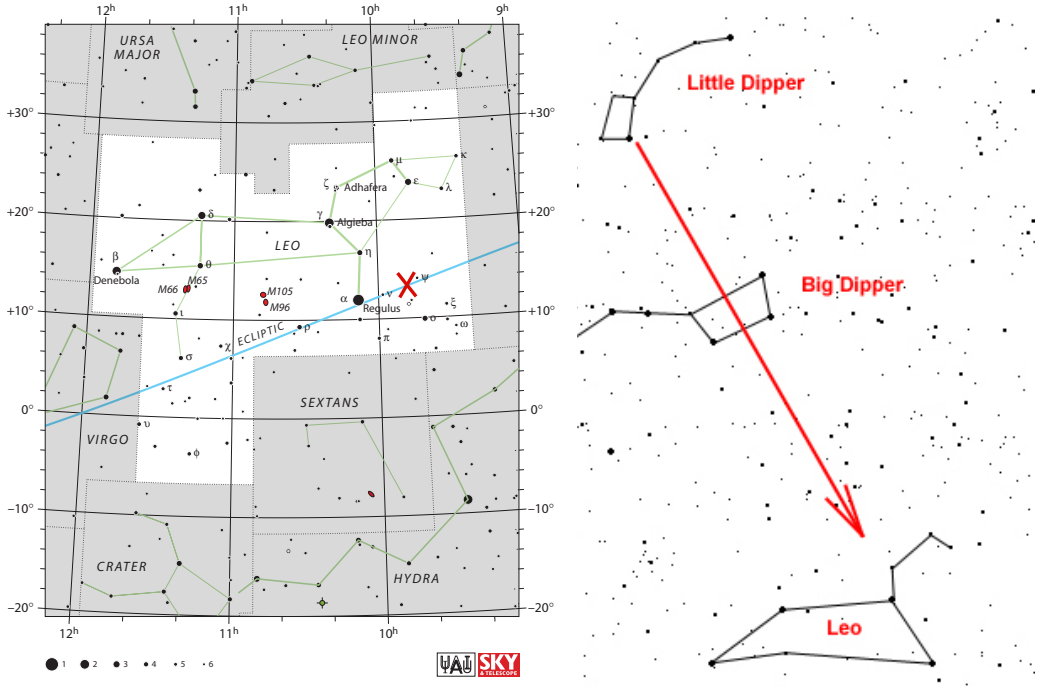

Figure 2.1: *Left*: IRC+10216 in the constellation Leo, the Lion, marked by the red cross © IAU. *Right*: Location of the constellation Leo in the sky on the northern hemisphere relative to the well-known constellations Little and Big Dipper © Frank De Caire

intensities together with line profiles and envelope modeling (of optically thin lines), the mass of the molecular material is estimated to be of the order of $10^{-3} - 10^{-2}$ $M_\odot$ (Solomon et al. 1971; Morris 1975) and the mass loss rate from the star is determined to be of the order of 10^{-5} $M_\odot$ yr^{-1}. More recent studies find 2×10^{-5} $M_\odot$ yr^{-1} (Crosas & Menten 1997). From the mean velocity of the various molecular lines, the systemic velocity (relative to the Local Standard of Rest, LSR) of the star of -26 km s^{-1} is determined. The spectral type is C9.5 (Cohen 1979). The carbon-to-oxygen ratio is about 1.4 (Winters et al. 1994).

This particular object is so important for astrophysicists due to its proximity of about 120 – 150 pc (Crosas & Menten 1997; Groenewegen et al. 2012), calculated from modeling the CO emission. The size in the sky is comparably large and so features of its photosphere and structures in the circumstellar envelope can be resolved and studied in detail. For a distance of 130 pc, the stellar luminosity varies from 13000 to 5200 $L_\odot$, the effective temperature between 2800 and 2500 K, and the stellar radius between 500 to 390 $R_\odot$, between the maximum and minimum brightness of IRC+10216 (Men'shchikov et al. 2001).

From stellar evolutionary models and the C, N, O isotopic ratios of IRC+10216 an initial stellar mass of 3 – 5 $M_\odot$ is estimated. This also agrees with the estimate of the envelope mass, thus the entire amount of mass lost until now, of about 1 – 3 $M_\odot$ and the current mass estimate of about 0.6 – 0.8 $M_\odot$ (e.g. Guelin et al. 1995). More recently, Kahane et al. (2000) conclude from observed isotopic ratios, s-process elements and comparison to AGB model predictions that the progenitor mass of IRC+10216 is below 2 $M_\odot$. Furthermore, Villaver et al. (2002) find a good agreement with their evolutionary models for an initial mass of IRC+10216 for 1 – 1.5 $M_\odot$. These findings indicate that this star is a carbon star at the end of the AGB phase towards the evolution into a planetary nebula (in conjunction with stellar

Table 2.1: Summary of the properties of IRC+10216 (Menten et al. 2012, and references therein).

Distance	130 pc	Gas mass loss rate	2×10^{-5} $M_\odot$ yr^{-1}
Stellar luminosity	5200 – 13 000 $L_\odot$	CSE radius	1 – 180″
Effective temperature	2500 – 2800 K	CSE dust formation zone	< 0.3″
Stellar radius	390 – 500 $R_\odot$	Stellar radius	0.03″
Stellar mass	0.6 – 0.8 $M_\odot$	CSE expansion velocity	14.5 km s^{-1}
Stellar period	630 d	LSR velocity	−26.0 km s^{-1}

1 pc = 3.09×10^{16} m or 3.26 lyr, 1 $L_\odot$ = 3.83×10^{26} W or 3.83×10^{33} erg s^{-1}, 1 $R_\odot$ = 6.96×10^{10} cm, 1 $M_\odot$ = 1.99×10^{30} kg

Table 2.2: Observed isotopic ratios and molecular abundances of IRC+10216 for a few examples (Kahane et al. 2000; Agúndez et al. 2012, and ref. therein).

Ratio	Value	Molecule	Abundance relative to H_2
$^{12}C/^{13}C$	45 ± 3.5	CO	6×10^{-4}
$^{14}N/^{15}N$	> 4400	C_2H_2	8×10^{-5}
$^{16}O/^{17}O$	840 ± 200	HCN	2×10^{-5}
$^{16}O/^{18}O$	1260 ± 280	NH_3	2×10^{-6}
$^{29}Si/^{30}Si$	1.45 ± 0.13	SiS	1.3×10^{-6}
$^{28}Si/^{29}Si$	> 15.4	CS	7×10^{-7}
$^{34}S/^{33}S$	5.55 ± 0.31	SiO	1.8×10^{-7}
$^{32}S/^{34}S$	21.8 ± 2.6	H_2O	1×10^{-7}

evolutionary models), which has important implications for the expected nucleosynthesis products from the stellar interior observed in the star's circumstellar envelope (Winters et al. 1994; Men'shchikov et al. 2001; De Beck et al. 2012; Menten et al. 2012). Table 2.1 shows the current determination of parameters of IRC+10216. The abundances and isotopic ratios of a few example species observed for IRC+10216 are listed in Table 2.2.

2.2 The circumstellar envelope of IRC+10216

The very high mass loss rate of IRC+10216 creates a dense and extended circumstellar envelope (CSE), which is bright and chemically rich. The star's CSE is mainly well observable due to its large apparent size in the sky due to its small distance compared to other stars. Since the 1970's more and more molecular emission lines were detected (CN, CS, HCN, SiS, SiO, HC_3N, C_2H, etc.; Wilson et al. 1971; Morris et al. 1971, 1975; Wilson et al. 1973; Tucker et al. 1974). To this date more than 80 molecules have been detected in the CSE of IRC+10216 so far (e.g. Agúndez et al. 2012), making this object one of the most important chemical laboratories in astronomy, still with many enigmas (Keller et al. 2015).

For the temperature and density radial profiles of IRC+10216's CSE, usually a power law is assumed $T_{\rm kin}(r) \propto r^\alpha, \alpha < 0$, constrained from CO emission (e.g. Crosas & Menten 1997; De Beck et al. 2012, and references therein). The dust mainly consists of amorphous carbon, silicon carbide and magnesium sulfide.

The overall morphology of the CSE seen in various maps of different wavelengths is spherical, with

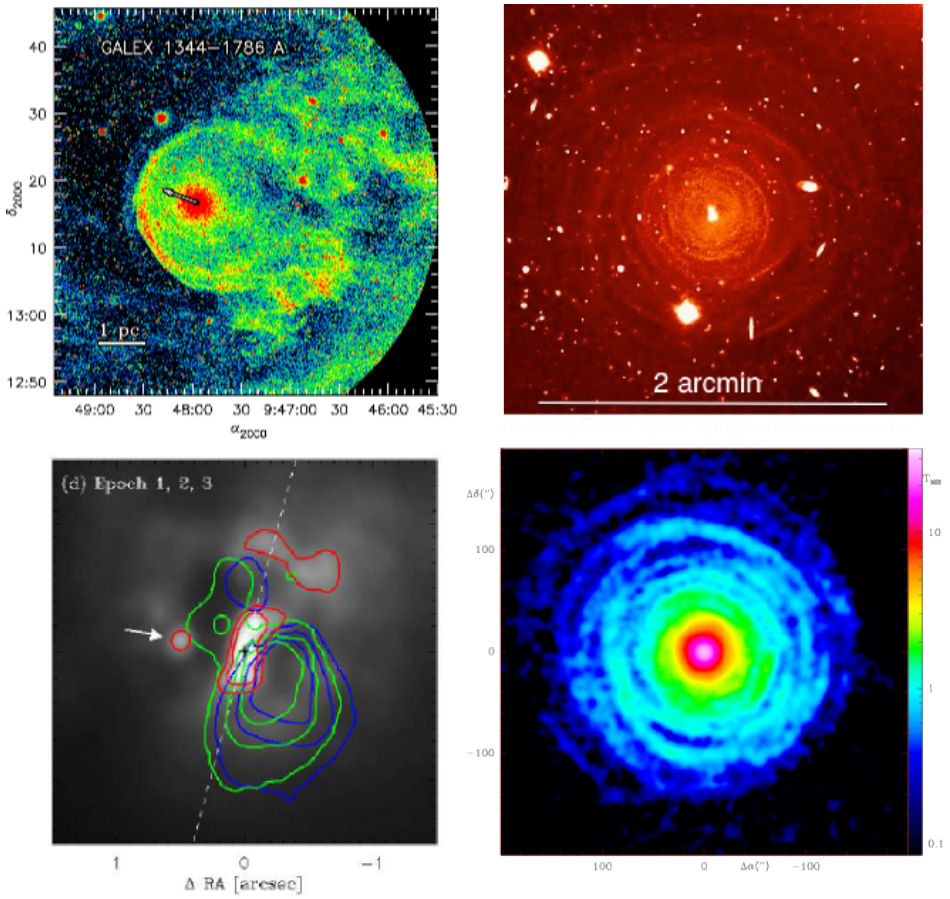

Figure 2.2: Various observation maps of IRC+10216's CSE. *Top row*: UV observations with the Galaxy Evolution Explorer (GALEX), which illustrates the bow shock due to the movement of the star (indicated by the arrow) through the ISM (Sahai & Chronopoulos 2010; Menten et al. 2012, left). Optical observations of dust-scattered light with the Very Large Telescope (VLT, Leão et al. 2006) show the density enhancements in the CSE (right). *Bottom row*: Optical observations with the Hubble Space Telescope (HST) focus on the innermost region around the central star within 2″ and may hint clumps or a faint companion (indicated by the arrow) very close to the star (Kim et al. 2015a, left). Molecular emission map of CO(2-1) obtained with the Institut de Radioastronomie Millimétrique (IRAM) 30m telescope extends up to a radius of 180″ (Cernicharo et al. 2015, right).

a substructure of multiple thin shells, arcs and clumps (e.g. Lucas & Guélin 1999, Fig. 2.2). The extent of the CO emission is observed up to a radius of 180 – 240 arcsec (for the distance of 130 pc this equals $3.6 - 4.8 \times 10^{17}$ cm, which is of the order of 10 000 stellar radii). With the radial expansion velocity, the age of the expanding shell results in $7 - 10 \times 10^3$ years (Cernicharo et al. 2015). Observations of the bow shock region with the Galaxy Evolution Explorer (GALEX) in the UV suggest ages even longer than 3×10^4 years (Sahai & Chronopoulos 2010, Fig. 2.2).

The separations between the shells observed in light scattered by the dust in the CSE are between 5 – 20 arcsec, which translates to 200 – 800 years (Mauron & Huggins 1999). The exact cause of the interval of these density enhancements remains unclear. The time scale does not fit to known internal mechanisms, e.g. the time scale between pulsations is about 10^4 years and the time scale of the variability of IRC+10216 is 630 days. Possible explanations are an intrinsically modulated mass loss rate or a dynamical modulation of the mass loss due to a binary companion.

The distribution of carbon-bearing molecules as clumpy shells coincides with the quasi-spherical structures seen in dust-scattered light (Dinh-V-Trung & Lim 2008; Decin et al. 2011; Cernicharo et al. 2015, Fig. 2.3). This strongly implies a physical and chemical link between these species in the CSE. It is not well understood to what extent these density-enhanced shells influence the chemistry of carbon molecules in carbon-rich CSEs in general. Comparing chemical models with observations still shows many inconsistencies. However, the fitting results are better when including density-enhanced shells (Guélin et al. 1999; Cordiner & Millar 2009, Sect. 1.3.5).

The observed morphology of IRC+10216's CSE is probably caused by a combination of dynamics and chemistry, in the outer CSE mainly by photochemistry which creates hollow molecular shells (Fig. 2.4). In this work we focus on the morphology of the outer CSE to constrain the inherent dynamics and chemistry. The substructure might be formed due to variable mass loss processes by stellar pulsations, cyclic magnetic activity or a central binary system. Several observational hints are e.g. from infrared and optical observations of the central region of IRC+10216's CSE which reveal a bipolar clumpy nebula (e.g. Kim et al. 2015a, and references therein). Observations from the Atacama Large Millimeter/submillimeter Array (ALMA) and the Institut de Radioastronomie Millimétrique (IRAM) of CO imply a companion-induced spiral structure when compared with detailed geometrical radiative transfer models. The spiral arm spacing is determined to be $\sim$ 1.12 arcsec for the inner wind which translates to an orbital period of about 55 years with a position angle of $\sim$ 20 deg (Fig. 2.5, Decin et al. 2015). However, Cernicharo et al. (2015) conclude an orbital period of 800 years from their fits to CO observations in the outer wind. The binary hypothesis is currently the most favored explanation, but the studies are not conclusive yet.

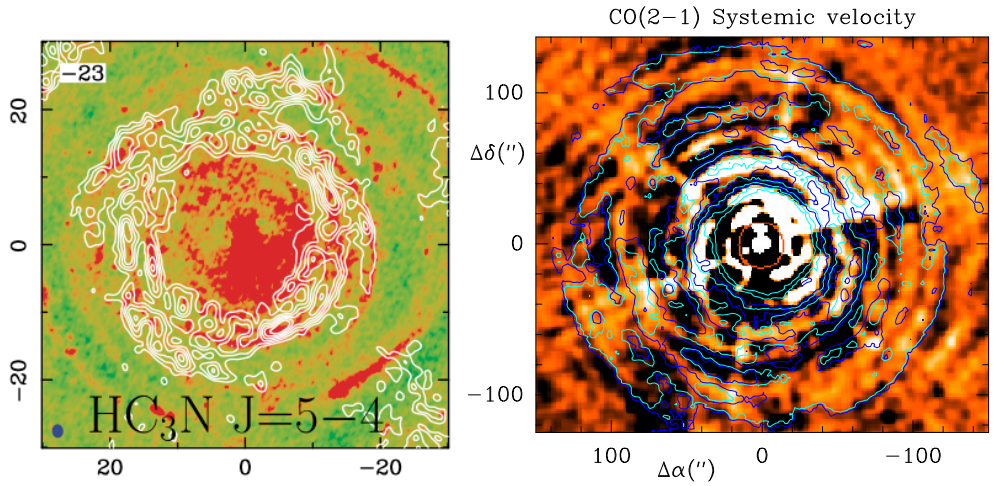

Figure 2.3: Overplotted observations of IRC+10216's CSE of optical observations from the VLT and the molecular emission of HC_3N(5-4) from the VLA (Dinh-V-Trung & Lim 2008, left) and a superposition of CO(2-1) emission from the IRAM 30m telescope and from the Herschel satellite (Decin et al. 2011; Cernicharo et al. 2015, right).

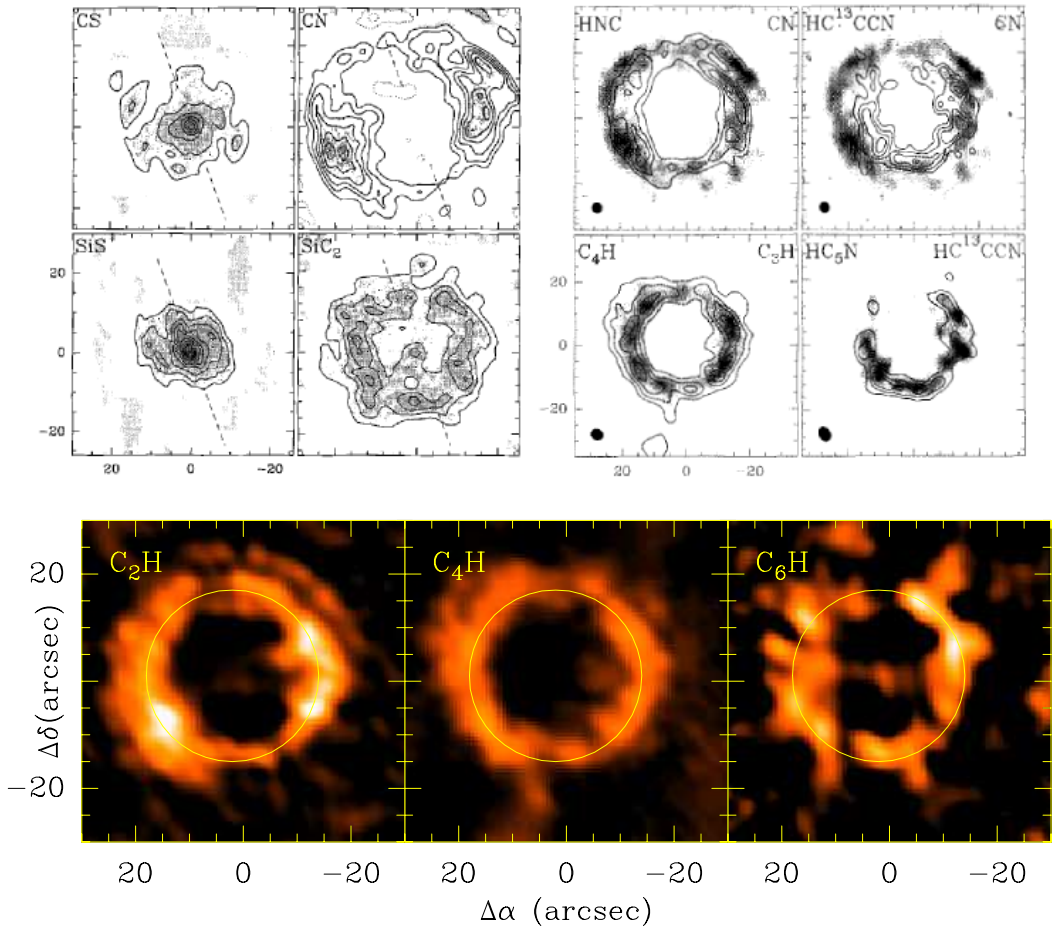

Figure 2.4: Molecular distribution maps of IRC+10216's CSE obtained with the Plateau de Bure Interferometer (PdBI Lucas et al. 1995; Lucas & Guélin 1999; Guélin et al. 1999).

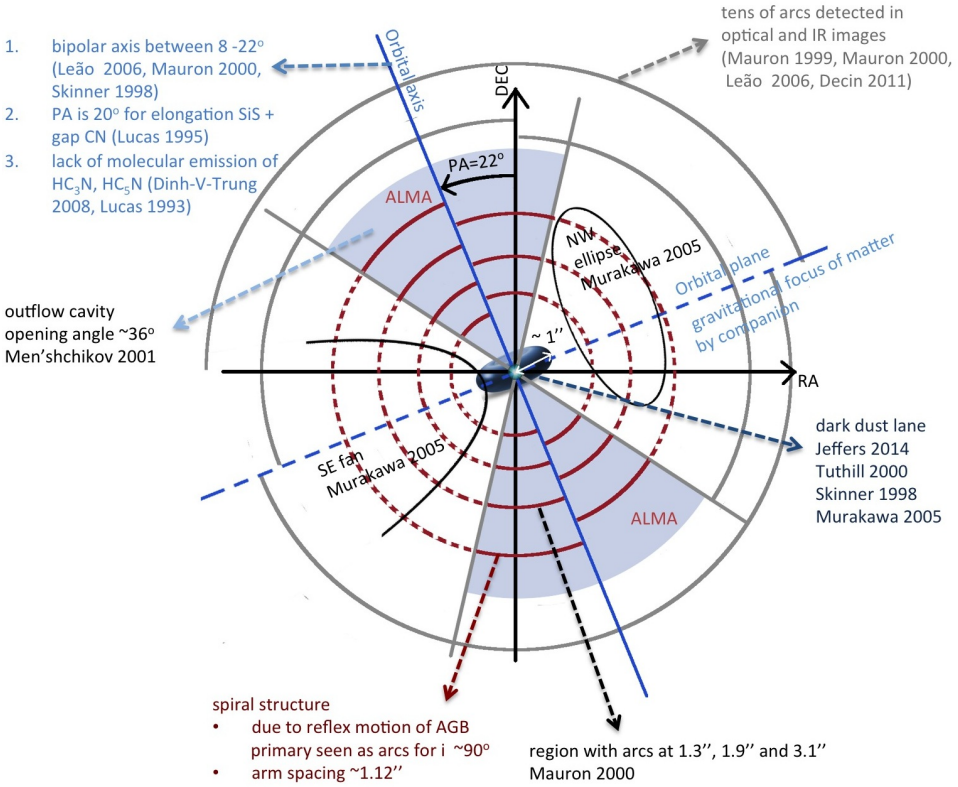

Figure 2.5: Sketch of the inner wind region of IRC+10216 indicating the different observational results which signal the presence of a binary companion (Decin et al. 2015, and references therein).

CHAPTER 3

The VLA spectral line and imaging survey

Surveys are essential observing programs to get an unbiased view on the object of interest for a large frequency or spatial range. In this work, we aim to have a detailed view on the CSE of IRC+10216, independent on the pulsation period and subsequent possible line strength changes. Surveys are a good technique to detect and confirm newly found molecular species by observing many transitions simultaneously. With better and better receiver technology larger and larger parts of a spectrum (bandwidth) can be observed with higher and higher accuracy (resolution, channel width). To also achieve a very good spatial and angular resolution of the CSE, the observatory of choice is an interferometer, like the Very Large Array (VLA).

Parts of the observational material used for this thesis have been published in the conference series "Why Galaxies care about AGB stars III: A closer look in space and time" (Keller et al. 2015).

3.1 Previous surveys

Before we introduce our new VLA survey, we briefly review previous spectral surveys of IRC+10216. The previous spectral surveys are indispensable in advancing major steps in the understanding of the circumstellar environment of carbon stars.

Kawaguchi et al. 1995 This survey was conducted with the Nobeyama 45m single-dish radio telescope between 1991 and 1994 and is the first spectral survey for 28 – 50 GHz (6 – 10 mm). The sensitivity in antenna temperature units is $T_{\rm A}^{*} < 10$ mK, the spectral resolution is 500 – 625 kHz, where 2 GHz are covered simultaneously. The beam sizes are $\theta = -0.21287 + 5.597\lambda_{\rm mm} = 35$ to 60 arcsec for this telescope, and the on-source integration time is more than one hour. Several molecular species were newly identified, such as C_6H, C_2S, C_3S, C_4Si, MgNC, and C_6H^-. In their work the rotational temperatures and column densities of the observed molecules are determined.

Cernicharo et al. 2000 This very deep spectral survey was observed with the IRAM 30m single-dish telescope for 129.0 – 172.5 GHz (2 mm) between 1986 and 1997. The spectral resolution is 1.25 – 1.0 MHz, with some channels with 100 kHz. The beam sizes are around 15 arcsec. The survey contains various newly detected carbon-chain and radical molecular species and many unidentified spectral lines.

He et al. 2008 With the Kitt Peak-12m telescope and the Submillimeter telescope (SMT) of the Arizona Radio Observatory (ARO) this spectral survey at 130 – 160 and 219 – 268 GHz (1.3 mm and 2 mm) has been performed. The spectral resolution or channel width is 0.195 MHz and 1 MHz for the 2 mm and 1 mm part respectively. The sensitivity is 10 – 20 mK for an integration time of 1 hour. The beam sizes are around 43 and 31 arcsec (for 145 and 240 GHz, resp.). The signal-to-noise in this spectral survey is better than that of Cernicharo et al. 2000. For the first time, ^{13}CCH and HN^{13}C have been detected.

Patel et al. 2011 With the Submillimeter Array (SMA) the first extended interferometric survey in the frequency range of 294 – 355 GHz has been conducted in January and February 2007, and February 2009. The resolution is 0.812 MHz per channel. The observations were performed with baselines of 9.5 to 69.1 m, beam sizes of about 3 arcsec×2 arcsec, and for integration times of 7 – 9 hours. The measured continuum flux density is 0.65 and 1.0 Jy at 300 GHz and 350 GHz, resp., with an uncertainty of the absolute flux calibration of about 15%. The survey contains many narrow emission lines, which probe the dust formation zone of the CSE for the first time. From the distribution of the molecular emission in the image maps the authors infer the radial location of the molecules around star and link this to their excitation temperatures.

Gong et al. 2015 A spectral survey at 18 – 26 GHz (∼ 1.3 cm) was performed with the Effelsberg 100-m single-dish radio telescope in 2012 and 2013. The spectral resolution is 61 kHz per channel. The beam sizes are between 35 and 50 arcsec. The noise level in the survey is about 1 mJy per 0.7 km s^{-1}. One highlight from this survey is the observation and non-LTE analysis of NH_3.

Further important surveys were done with the Infrared Space Observatory (ISO), the Plateau de Bure Interferometer (PdBI), the Berkeley Illinois Maryland Association (BIMA) interferometer, the Submillimeter Telescope (SMT), and the Herschel satellite (Guélin 1994; Cernicharo et al. 1996, 2010; Tenenbaum et al. 2010).

Despite the surveys at mm and sub-mm range and observations of IRC+10216 in the radio range with single-dish telescopes, an interferometric survey in the radio range has been missing so far. The VLA spectral line and imaging survey, presented and analyzed in this thesis, closes this gap.

3.2 Observations

The Karl G. Jansky Very Large Array (VLA[1]) is an interferometer with 27 antennas (25 m diameter each) equipped with new sensitive, wide band receivers and a powerful new correlator. In comparison to the former VLA, the improvement of the sensitivity, maximum bandwidth, spectral frequency resolution, etc. is at least by a factor of 10. Using these new capabilities, a spectral line and imaging survey of IRC+10216 covering a large frequency range of 18 – 50 GHz (K, Ka, Q-band) was conducted (PI: M. Claussen). The survey traces the molecular distribution, especially in the outer CSE, in unprecedented detail, with a sensitivity of the order of 1 mJy and resolution of 1 arcsec corresponding to brightness temperatures of 0.5 – 5 K. This is the first interferometric survey of this kind in this frequency range with this sensitivity and resolution.

[1] The VLA is a facility of the National Radio Astronomy Observatory, which is a facility of the National Science Foundation operated under cooperative agreement by Associated Universities, Inc.

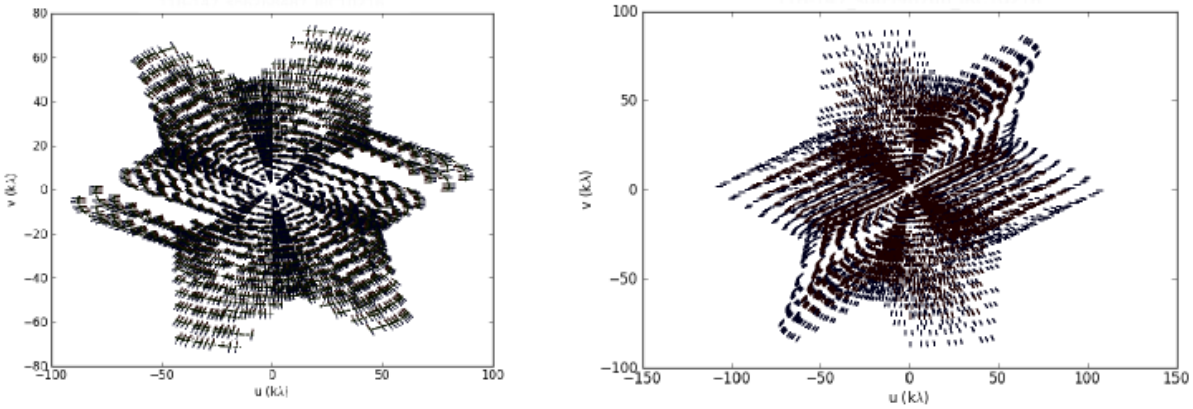

Figure 3.1: *uv*-coverage in units of wavelengths (kλ) of the VLA survey of IRC+10216 of the K-band (left) and the Ka-band (right) depicting the typical pattern of observations with a small declination with the VLA.

We present the work on the observations of IRC+10216 with the K- and Ka-band receivers, which were performed between 8 and 22 December 2011 with the array in its most compact D configuration with 27 antennas. For each observation set the science target IRC+10216 was observed with single pointings for 21×300 s, hence 1.75 hours. The total observing time on target were 21 hours for a total of 12 data sets (each raw data set is about 200 GB). The star was observed at a medium phase of $\phi = 0.51 - 0.63$ during its pulsation period, which varies between 1 and -1 at maximum and minimum brightness, respectively.

In this work we analyze the observations of the frequency range $18 - 38.2$ GHz, with beam sizes of 1.5 to 4.5 arcsec. Each spectral window has 512 channels, each channel has a width of 125 kHz, hence a bandwidth of 64 MHz. Each data set has 32 spectral windows, such that each data set covers about 2 GHz in the spectral frequency range. It was observed in double polarization RR and LL. The phase center was set to $(\alpha_{\mathrm{J2000}}, \delta_{\mathrm{J2000}}) = (09^h47^m57.38^s, 13°16'40.66'')$, which is offset in declination by about $3''$ compared to the position of the radio continuum emission from the central star. This setup was chosen to avoid possible artifacts at the phase center from the (at that time) rather new correlator. This causes the center of the continuum and the center of the point spread function to be shifted against each other. This has no effect on the imaging process for our analysis for which we consistently use the center of the radio continuum at $(\alpha_{\mathrm{J2000}}, \delta_{\mathrm{J2000}}) = (09^h47^m57.437^s, 13°16'43.850'')$. The *uv*-coverage is shown in Fig. 3.1 and depicts the typical shape for VLA observations at low declinations with good coverage. The slight differences between the two patterns arise from slightly different source elevations (Sect. 1.4.3). The minimal and maximal baselines are 35 m to 1.03 km. This translates into a resolution of $2 - 4$ arcsec and a largest angular scale (that the interferometer is sensitive to) between 44 and 66 arcsec. The theoretical primary beam is $45/f(\mathrm{GHz}) = 150$ to 72 arcsec. For the imaging we chose the pixel sizes, such that $3 - 4$ pixels cover one synthesized beam (satisfying the Nyquist sampling). For calibration the following calibrator sources were used:

- Pointing: J1008+0730, J1331+3030, J1229+0203
- Phase and amplitude: J0954+1743
- Flux: J1331+3030
- Bandpass: J1229+0203

In the following we discuss the data reduction in detail.

3.3 Calibration and data reduction

The data reduction, calibration and imaging is performed with the program Common Astronomy Software Application (CASA), developed as the successor for Astronomical Image Processing System (AIPS) for data processing of the most modern astrophysical interferometric facilities, mainly VLA and ALMA. Either with the help of the CASA pipeline or with manual interactive CASA scripts (CASA versions 4.1 – 4.4) following the instructions from the NRAO CASA guides (which is preferred for spectral line observations), we proceed with these steps:

1. Data inspection & flagging:
   - Check observational setup, antenna configuration (select possible reference antennas in center of array), elevation of observed sources
   - Identify channels or antennas with zero amplitude or other technical problems
   - Exclude (flag) anomalous antennas or certain time- or channel ranges with technical problems
2. Corrections:
   - Antenna positions in the array (from monthly 3D position measurements, for correct baseline lengths and correct phases between the antennas)
   - Atmosphere opacities (from atmospheric model considering seasonal weather conditions, opacities at zenith and as a function of elevation)
   - Antenna efficiencies and gain curves (from antenna response as a function of elevation)
3. Model flux calibrator:
   - Use NRAO models for well-known resolved flux calibrator sources (image model of source)
   - Scale the total flux from model to data according to observed frequency, per spectral window (for which the task setjy was used)
4. Delay:
   - Correct phase variations as a function of time and channel (“delay”)
   - Apply phase-time and phase-channel, and amplitude-channel solutions (bandpass)
5. Gain calibration:
   - Use corrected phases to calculate correlated amplitude per antenna
   - Derive flux densities for other calibrator sources from flux calibrator model (see step 3.)
6. Continuum subtraction of science target in *uv*-plane
   - Determine channels with no spectral line emission
   - Create model of continuum emission from line-free channels (fitorder=1)

The calibration uncertainty, given by the absolute fluxes of the flux calibrator (3.0 – 1.7 Jy for 18 – 38 GHz) and its standard deviation (0.38 Jy), is about 20%.

The data suffers from several technical problems. A well known problem caused in the intermediate frequency passband is the so-called subband 0 problem (EVLA Memo #154, Morris & Momjian 2012). It describes the loss of sensitivity at the edges of the subbands (each 1 GHz bandwidth) of the WIDAR correlator, which is caused by the bandpass shape and mostly affects the 0-th subband (more than 10%). For our data this means an increased noise level at the edges of the subbands or at every spectral window 0, 15, 16, and 31. For this reason the frequency setup was chosen to have an overlap for these frequency ranges, to achieve a similar signal-to-noise ratio as for the other spectral windows. Another problem often faced in radio astronomy is the radio frequency interference (RFI). This is the interference of strong radio signals from artificial, man-made, sources such as satellites, radar or radio devices with the very sensitive receivers of radio telescopes. Mainly the short baselines in the array pick up the artificial

signals from close by (compared to the astronomical sources). In our data the strongest RFI is around 18.3 GHz and the affected data has to be flagged severely. These problems cause gaps or parts with increased noise levels in the spectral coverage.

3.4 Imaging synthesis and CLEAN algorithm tests

A major step in the data reduction of interferometric data is translating the visibilities in the *uv*-plane to a source-intensity distribution in the image-plane – the deconvolution (e.g. Taylor et al. 1999). Furthermore, we transform from the dirty to the clean image with the CLEAN algorithm.

3.4.1 CLEAN algorithm

The CLEAN algorithm finds an iterative solution to the convolution equation to find the position and strength of the emission. There are several variations of the algorithm, the original one is of Högbom (1974):

- find position of brightest emission peak in dirty image, assume point source, record position and magnitude
- subtract this peak from the dirty image (peak intensity $\times$ dirty beam, damping factor)
- repeat until no peak above a flux limit is found
- dirty image minus peak positions is the residual image
- convolve CLEAN model components (record of point sources) with CLEAN beam
- combine image of CLEAN components convolved with CLEAN beam with image of residual flux (for noise estimate)

A progression of the CLEAN algorithm was made by Clark (1980) by introducing minor and major cycles. In the minor cycle only points with peak intensities from the dirty image are taken into account if a fraction of these peak fluxes is higher than the flux of the highest sidelobe. In the major cycle the point source model from the minor cycle is Fourier transformed, multiplied with a weighting function, transformed back and subtracted from the dirty image. The Cotton-Schwab (CS) algorithm is like the Clark procedure, but works with ungridded visibility data (Schwab 1984). This algorithm is faster because in the major cycle the subtraction is performed on all fields simultaneously. Another advance of the CLEAN algorithm is to use a scale-sensitive deconvolution with additional Gaussian CLEAN components to the delta point functions, which is called Multi-Scale (MS) CLEAN (Cornwell 2008). This version is important for imaging extended objects, as in our survey. The scales are chosen between 0, one beamsize and half of the largest spatial axis in unit of pixels. Furthermore, a small scale bias between 0 and 1 can be set, where with 1 the smallest scales are weighted the highest.

During CLEANing, the visibilities are regridded in velocity space according to the chosen rest frequency of the aimed transition, the result is given as sky frequency. There is the possibility to restrict the algorithm to a certain area of the image to search for CLEAN components by setting a mask.

The visibilities can be weighted with different schemes, to alter the instrumental response function, depending on the observed structures and depending on the interest for the analysis. The possible weighting schemes are uniform, natural or Briggs. Uniform weighting equally weights each spatial structure, such that the side lobes are well suppressed, but the overall signal-to-noise ratio is lowered. Natural weighting equally weights each visibility, such that the natural peak sensitivity of the instrument is preserved, which yields stronger signal (main lobe and side lobe) than for uniform weighting. There is also a compromise possible between these two, called the Briggs weighting (Briggs 1995). With the

robust parameter between −2.0 and 2.0 one can choose between options close to uniform or natural weighting, respectively. After experimenting with a robust parameter of 0.5 − 0.7, we decided to use natural weighting for all of our images to make use of the option with the highest possible sensitivity especially for the extended spatial scales in our observations.

3.4.2 Parameter testing

To ensure a reliable imaging synthesis and reduce the effect of subjective parameter choices, we performed extensive testing of several parameters important in the procedure: "psfmode", "imagermode", "multiscale" and "mask". Those parameters were optimized in close collaboration with Ka Tat Wong.

(a) psfmode : 'clark' or 'hogbom'
(b) imagermode : 'csclean' or ' '
(c) multiscale : [0,5,10] or []
(d) mask : (whole image) or (the inner quarter)
(e) imsize : number of pixels

(a) In minor cycles, Clark CLEAN convolves the CLEAN component models (CCs) with a gridded point-spread function (dirty beam), while Högbom CLEAN convolves with the true ungridded PSF. Clark CLEAN is problematic when having non-Gaussian dirty beams and low S/N.

(b) In major cycles, CS CLEAN subtracts the models from the uv domain (not in the image domain), while imagermode=' ' subtracts from the image domain, which is prone to aliasing of the sidelobes because of the gridding.

(c) When multiscale is set, the Högbom algorithm is used regardless of the input of "psfmode".

(d) CASA has two different default arguments for the CLEAN mask (i.e. region within which CCs are searched), depending on the argument of "imagermode". If imagermode='csclean' and mask=[ ], then it will clean the full image. If imagermode=' ' and mask=[ ], then it will clean the inner quarter of the image.

After comparing the images from different combinations of arguments, we have the following conclusions:

(a) psfmode : 'hogbom' (uses true PSF) is better than 'clark' (uses gridded PSF)
(b) imagermode : 'csclean' (subtracts from uv domain) is better than the default (subtracts from image domain)
(c) multiscale : less affected than point model
(d) mask : (the inner quarter) is much better than (the whole image)
(e) imsize : the larger the better

1. Clark CLEAN does not produce reliable results for our data. The resultant images still look very "dirty".

2. In all cases in which the whole image was CLEANed, the results have strong stripes and/or divergence problems (esp. for low S/N).

3. Using imagermode='csclean' or ' ' (both with psfmode='hogbom') gives slightly different results (it is not completely clear how MS CLEAN, CS CLEAN and Högbom influence each other).

4. When forcing the usage of the full image in imagermode=' ' by setting mask=box[...], the results are worse than in imagermode='csclean' and default mask (i.e. the full image), especially for point-model CLEAN. In both cases, we used psfmode='hogbom' and the identical region for CLEANing.

5. imagermode='csclean' with a mask around the inner quarter gives better results than imagermode='' and the default mask (i.e. inner quarter). In both cases, we used psfmode='hogbom' and the identical

region for CLEANing.

6. A larger mask region for the CLEANing of e.g. 256×256 pixel for an image size of 512×512 pixel gives better results than a region of 128×128 pixel for an image size of 256×256 pixel.

7. The improvement is larger for point-model CLEAN compared to MS CLEAN. MS CLEAN is not as sensitive to deviations/ differences as the point-model, because in MS CLEAN due to the usage of Gaussian components the information is smeared out – more than with only point-models.

8. MS CLEAN usage gives greater flux by a factor of 1.5 compared to the point-model CLEAN with the same parameters, the rms error is similar.

When using the Cotton-Schwab algorithm with a threshold, there may be strange behavior when hitting the threshold with a major cycle. In particular, it may be above the threshold again at the start of the next major cycle. This is particularly noticeable when CLEANing a data cube, where different channels will hit the threshold at different times.

We conclude that the best options are either Multiscale CLEAN or Cotton-Schwab CLEAN with using an image as large as possible (compromise with computational capabilities) and restrict the CLEAN mask to the inner quarter (or similar) of this image. If there is an intended image size, it is best to double this value for choosing the image size for CLEANing and to set the mask at the inner quarter, such that this mask size includes the intended region.

3.4.3 Final imaging synthesis

For the first deconvolution (dirty image) we use the following settings:

imagermode =	csclean
mode =	channel
restfreq =	' '
outframe =	LSRK
weighting =	natural
interactive =	false
threshold =	1.0 mJy
imsize =	320
cell =	$\sim 1/3\times$ beam
niter =	0

Then we measure the rms noise level $\sigma_{\rm rms}$ of the dirty image from channels without emission.

A major problem or shortcoming of the VLA survey and any other interferometric data that covers extended emission is the missing spacing problem. The emission of scales larger than the array-characteristic largest angular scale is simply filtered out and causes a lack of the full flux information. In the images maps of strong emission this is seen as the negative bowl effect (Fig. 1.30, Sect. 1.4.3, p. 45). An estimate of the amount of missing flux for the VLA data in comparison to observations of the same transitions with the Effelsberg 100-m telescope are presented in Sect. 3.6. Due to the missing flux in the data, depending on the extent and the rest frequency of the emission, the physical analysis is not fully reliable. Because single-dish telescopes have less sensitivity, the full extent of the faint extended part of the emission is not known and can only be estimated. However, the position of the shells and clumps with peak emission in our images are reliable, because they originate from a confined small area. The determined ring width and the peak flux, on the other hand, are lower limits.

For the final imaging synthesis (CLEAN image) we use the following settings:

imagermode =	csclean
mode =	velocity
restfreq =	<frequency of transition>
outframe =	LSRK
weighting =	natural
interactive =	false
threshold =	$1.5 - 2.5\sigma_{\rm rms}$
imsize =	1024
cell =	$\sim 1/3\times$ beam
niter =	100 000
psfmode =	hogbom
multiscale =	[0,5,10], smallscalebias=0.6, gain=0.3
mask =	<circle of 40 arcsec radius around central star>

3.5 Final data product

In this section we present the imaged spectral line VLA survey data, which are the extracted full composite spectra from the continuum subtracted dirty images from the interferometric data cubes, and the CLEAN images and spectral lines of the brightest transitions. Furthermore, we compare the spatial distributions of certain chemically connected species within our survey, and to the optical observations of dust-scattered light.

Parts of the presented observational results have been published in the conference proceedings of "Why Galaxies care about AGB stars III: A closer look in space and time" (Keller et al. 2015).

3.5.1 Spectrum of IRC+10216

The emission lines in the extracted spectra of IRC+10216 are identified with the help of the molecular line catalogues CDMS and from JPL. We only consider spectral lines with intensities greater than 3 times the rms noise level and with more than one transition of its species. The brightest molecules identified in our survey are: SiS, HC_3N, and HC_5N. In total we detected 220 transitions in this survey, including tentative detections with low intensities, from 20 molecular species. Further interesting line emission is from e.g. HC_7N ν_{15}=1 and several isotopologues of cyanopolyynes and silicon monosulfide, which are however mostly very weak (Figs. 3.2, 3.3, and A.1 - A.11 and Tab. A.1). The detected species are grouped into the following molecular families:

Cyanopolyynes	HC_3N, HC_5N, HC_7N, $(HC_9N,)^*$
Carbon chains	C_3H, C_4H, $(C_5H,)^*$ C_6H, $(C_8H,)^*$ C_3N,
Negative ions	$(C_5N^-,)^*$ C_6H^-,
Metal-bearing molecules	MgNC,
Silicon and sulfur-bearing molecules	C_2S, C_3S, C_2Si, C_4Si, SiS.

* tentative detection

The composite spectrum consists of emission from 18.0 to 38.2 GHz with small gaps between 18.0 and 26.5 GHz due to difficult calibration, because of RFI, or missing frequency coverage (Fig. 3.2). The root mean square (rms) noise level is 0.02 – 0.07 mJy or 0.6 – 1.4 mJy beam^{-1}.

Table 3.1: List of radio continuum flux density and its root mean square (rms) error of IRC+10216 averaged over a region of 12 arcsec diameter around the center. The radio continuum has been estimated from channels with no spectral line emission and imaged for frequency intervals of 1 GHz.

Frequency (GHz)	Flux density (mJy)	rms error (mJy)	Frequency (GHz)	Flux density (mJy)	rms error (mJy)
18.0	3.540	1.098	29.0	10.282	0.702
19.0	4.196	1.158	30.0	9.280	1.816
21.0	5.251	1.346	31.0	8.642	1.918
22.0	5.674	1.419	32.0	11.388	2.453
23.0	6.207	1.428	33.0	11.388	1.926
24.0	6.777	1.491	34.0	12.076	1.902
25.0	7.536	0.667	35.0	11.954	1.760
26.0	8.556	0.731	36.0	12.290	2.035
27.0	8.561	0.747	37.0	11.417	1.803
28.0	9.759	0.723	38.0	15.259	2.648

The radio continuum has been estimated from channels with no spectral line emission for frequency intervals of 1 GHz. The flux densities and its rms error have been determined from a region of 12 arcsec diameter around the center in the CLEANed images of the radio continuum estimates (3.5 – 15.2 mJy beam^{-1} for 18 – 38 GHz, Tab. 3.1). Fitting a power law as $S_\nu \propto \nu^\alpha$ to the VLA data results in a factor of $\alpha \approx 1.69$, which compares well to the findings of e.g. Menten et al. (2006) and approximates an optically-thick black-body radiation with a spectral index of about 2.

A closer look at the spectrum in pieces of 500 MHz for a circular region around the peak continuum position of the star is shown in Figures A.1 - A.11.

3.5.2 Image maps of IRC+10216

We produce CLEAN images, as described in Sect. 3.4, and channel maps of the brightest transitions (Figs. 3.4, 3.5, and B.1 - B.56). For the further analysis we focus on the cyanopolyynes HC_3N, HC_5N, and HC_7N, and chemically related carbon-bearing molecules C_3N, C_4H, C_6H, and C_6H^-.

The spectral lines of e.g. HC_5N(14-13) and HC_7N(30-29), extracted from the CLEANed images (Fig. 3.3), nicely illustrate optically thin emission from a shell structure (cf. Fig. 1.14, c). For HC_5N(14-13), there is the effect of blue wing absorption, due to a slight optical thickness of the shell, such that the observer does not completely see through the blue part which then appears less intense than the red part, which causes the red peak of the spectrum ($v > -26$ kms^{-1}) to be slightly stronger than the blue part ($v < -26$ kms^{-1}, Fig. 3.3). This spectral shape is observed for most of the covered transitions (Figs. A.13 - A.15).

The images of these molecular species show that the overall structure is the expected ring-like molecular distribution for the emission at the systemic velocity (Fig. 3.4). These transitions probe the photochemical shells we aim to study (Sect. 1.3.5). The three-dimensional geometry becomes clear when considering the full data cube with several velocity components, which then depicts the molecular emission of a hollow sphere (Fig. 3.5). The substructure is clumpy and with broken arcs.

The location of most clumps of HC_3N, HC_5N, HC_7N, and C_3N coincide (Figs. 3.4 and 3.6). The heavier molecule HC_7N is much more clumpy compared to HC_3N and HC_5N. Also the effect of sensitivity has to be considered, because the emission from HC_7N is much weaker than that from HC_3N,

which also contributes to the observed appearance of the emission maps. When comparing the molecular emission to the observations of dust-scattered light (cf. Fig. 2.2, top right, p. 50), their spatial distribution corresponds very well (Fig. 3.6, left). Especially the broken arcs or second shell components coincide with the density enhanced dust shells. The molecular gas and the dust shells are clearly linked.

The clumps have angular sizes from a beamsize of about $2.0'' \times 3.0''$ up to about $3.0'' \times 7.7''$, which corresponds to physical sizes of 3.9×10^{15} cm up to 15.6×10^{15} cm for a distance to IRC+10216 of 130 pc. The intensity contrast between the clumps of HC_3N, HC_5N, and HC_7N to the surrounding medium is a factor of 1.5 up to 7.6.

Most carbon-bearing molecular transitions observed in this survey originate from the hollow photochemical shell of IRC+10216. The silicon-bearing species, e.g. the parent molecule SiS, probe centrally-peaked molecular gas, as expected from chemistry considerations (Sect. 1.3.5). When comparing the spatial distribution of bright transitions, e.g. of SiS, HC_3N, and C_3N, with each other, we see that they are roughly distributed as expected (Fig. 3.6, right). The centrally-peaked SiS emission is surrounded by shells of HC_3N and C_3N emission. The spatial distribution of the molecules in the photochemical shells is analyzed, quantified and discussed in detail in Chapters 4 and 6.

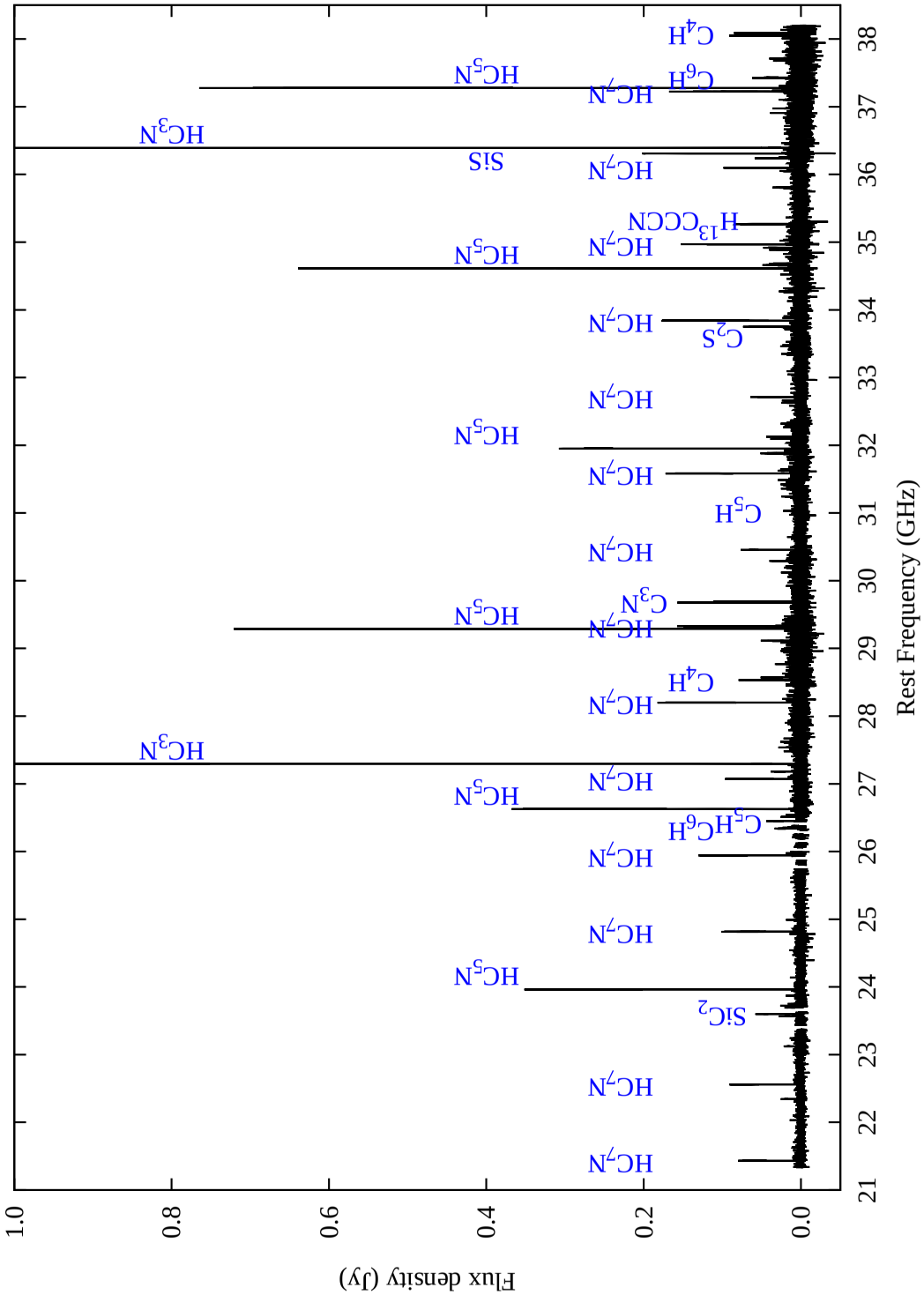

Figure 3.2: Composite spectrum of the molecular emission around IRC+10216 from our VLA survey at 18.0 - 38.2 GHz. There are small gaps between 18.0 and 26.5 GHz due to difficult calibration (RFI) or missing frequency coverage. The frequency range 26.5 – 38.2 GHz is published in Keller et al. 2015.

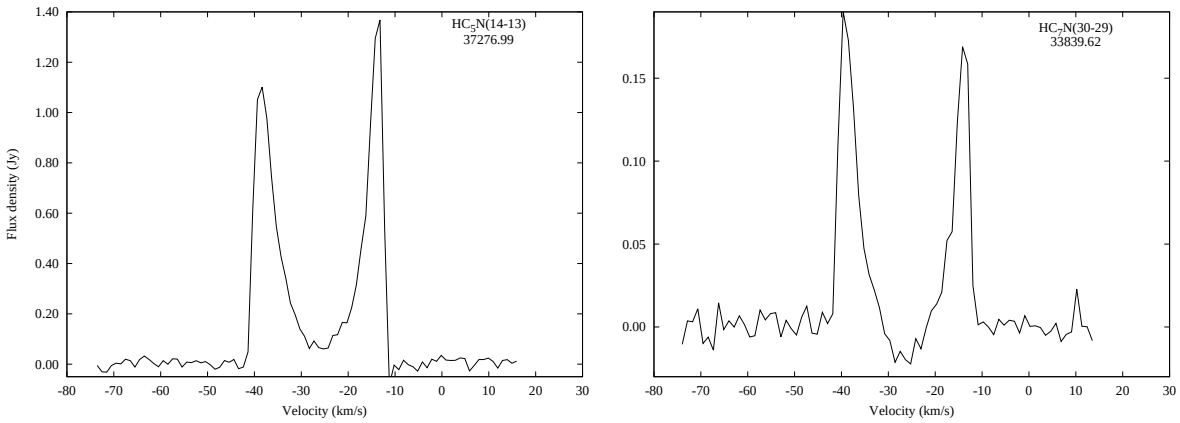

Figure 3.3: Spectral line emission of HC_5N(14-13) and HC_7N(30-29) of IRC+10216 from the CLEANed images averaged for an aperture region of 30 arcsec radius. The rest frequency of the transition in MHz is given on the top right. The spectral lines probe the optically thin photochemical hollow shell of IRC+10216.

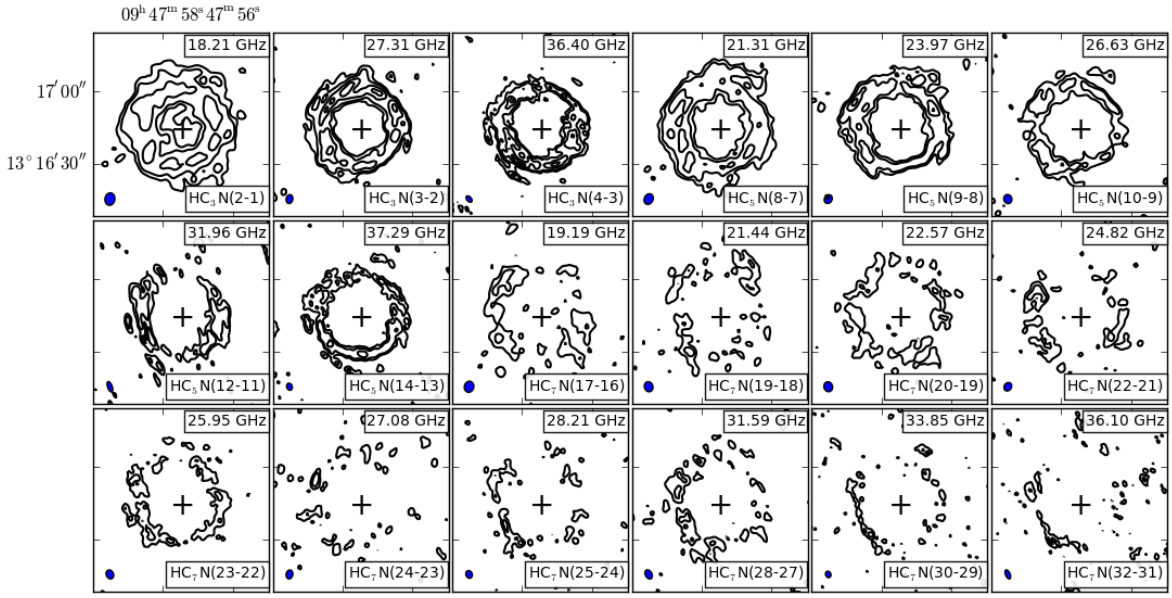

Figure 3.4: Contours of molecular emission of HC_3N, HC_5N, and HC_7N around IRC+10216 at the systemic velocity of -26 km s^{-1}. The contour levels are 2, 4, 8, 12 $\times\sigma$. The position of the radio continuum from the central star at $09^h47^m57.437^s$, $13°16'43.850''$ is marked with the +. The blue ellipse shows the synthesized beam of each data cube respectively. These maps allow comparisons of the molecular shells of chemically related species, showing that the position of most clumps coincide and the heavier the cyanopolyyne the clumpier the structure.

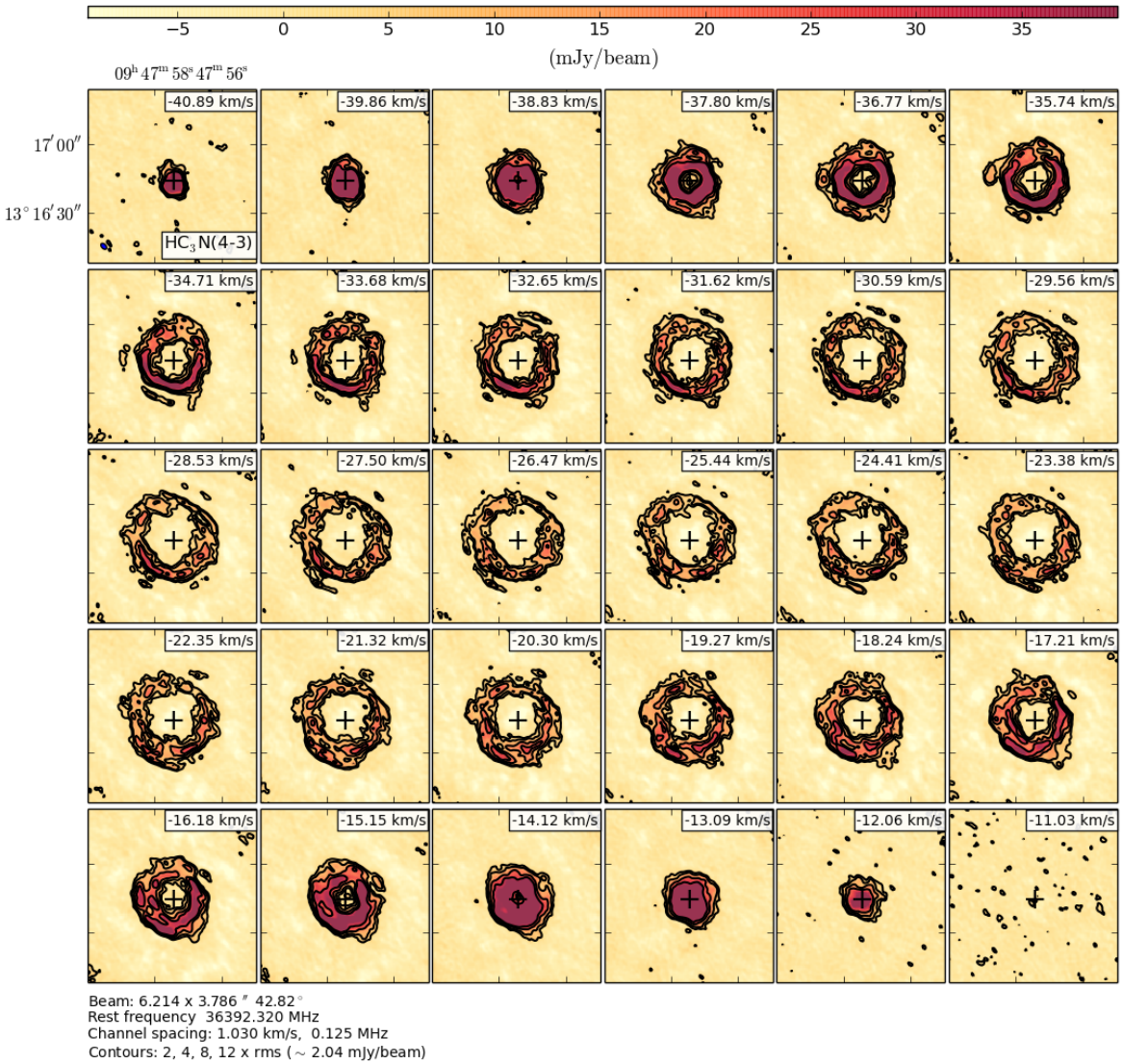

Figure 3.5: Contours of molecular emission of HC_3N(4-3) around IRC+10216 for all velocity components in the data cube. The contour levels are 2, 4, 8, 12 $\times \sigma$(= 2.04 mJy beam^{-1}). The position of the radio continuum from the central star at $09^h47^m57.437^s$, 13°16′43.850″ is marked with the +. The blue ellipse in the top left panel shows the synthesized beam of the data cube (6.2 × 3.8″, 42.8°). These channel maps illustrate the three dimensional structure and substructure of IRC+10216's photochemical shell.

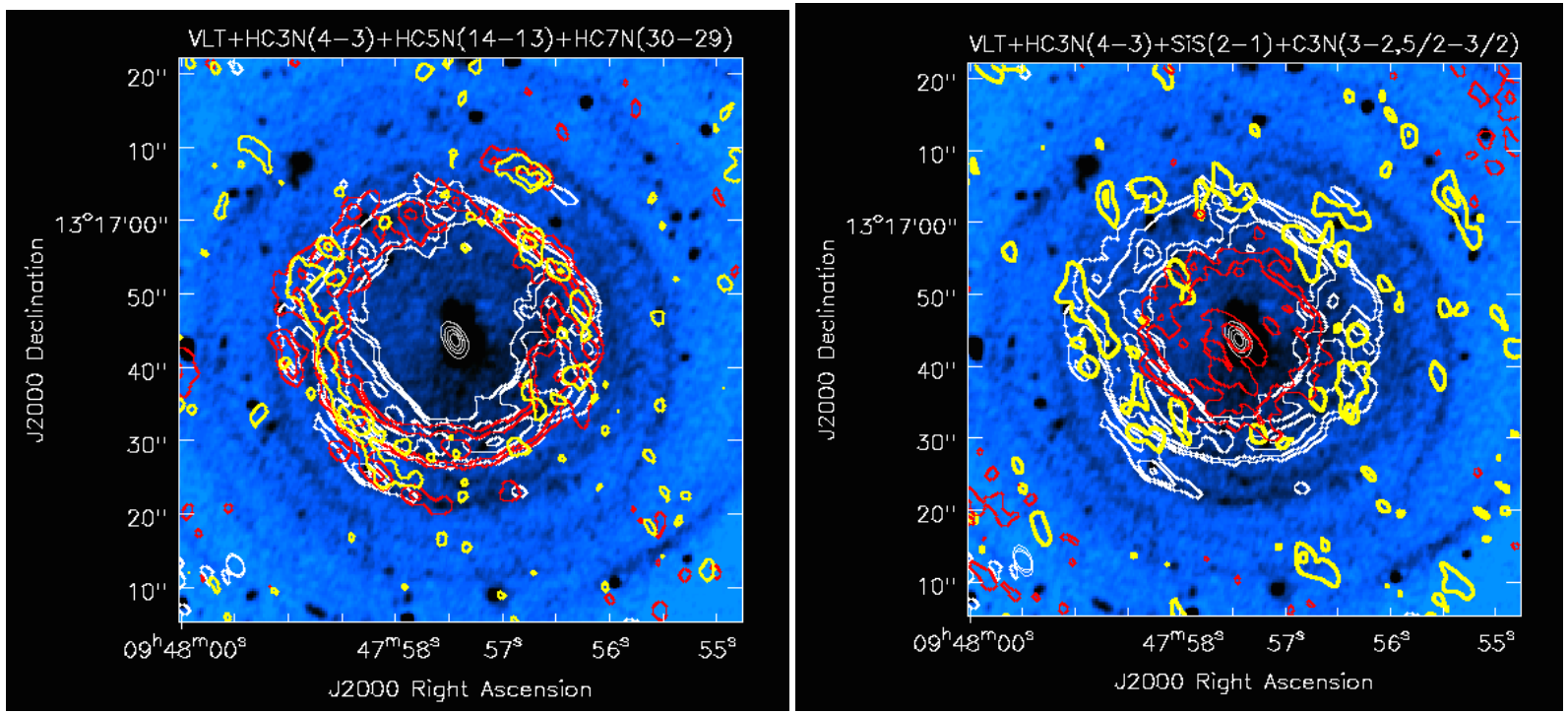

Figure 3.6: Overlay of the contours of molecular emission around IRC+10216 from our VLA survey at the systemic velocity of −26 km s^{-1} of HC_3N, HC_5N, and HC_7N (left) and of HC_3N, C_3N, and SiS (right) and the optical image of dust-scattered light from the VLT observations of Leão et al. 2006. The central ellipsoid is the continuum emission at 36 GHz. *Left*: The transition HC_3N(4-3) is shown in white, HC_5N(14-13) in red and HC_7N(30-29) in yellow contours. The contour levels are 2, 4, 8, 12 $\times\sigma$ respectively, where σ is 2.04 mJy beam^{-1} for HC_3N(4-3) and HC_5N(14-13), and 0.89 mJy beam^{-1} for HC_7N(30-29). The spatial distribution of the dust shells (VLT image) and the molecular emission (VLA contours) corresponds very well. The VLA images show that the emission structures of HC_3N, HC_5N, and HC_7N are very similar. The location of most clumps of these species coincide. *Right*: The transition HC_3N(4-3) is shown in white, SiS(2-1) in red, and C_3N(3-2,5/2-3/2) in yellow contours. The contour levels are 2, 4, 8, 12 $\times\sigma$. For HC_3N σ = 2.04 mJy beam^{-1}, for C_3N σ = 0.94 mJy beam^{-1}, and for SiS σ = 1.62 mJy beam^{-1}. The spatial distribution of these molecules is as expected from chemical models. The emission of SiS mostly originates from the central region, whereas HC_3N and C_3N have a larger extent and are mostly distributed in a shell surrounding SiS.

Table 3.2: Comparison of measured flux density S_ν (peak and integrated) of IRC+10216 with the VLA (this work) and the Effelsberg 100-m telescope (Gong et al. 2015) for transitions of HC_3N and HC_5N for the same beam sizes.

Transition	VLA		Effelsberg		Fraction of missing flux in VLA data	
	S_ν (mJy)	$\int S_\nu d\nu$ (mJy km s^{-1})	S_ν (mJy)	$\int S_\nu d\nu$ (mJy km s^{-1})	from S_ν	from $\int S_\nu d\nu$
HC_3N(2-1)	253.7	5049.6	275.0	5759.1	0.08	0.12
HC_5N(8-7)	176.5	2961.8	228.4	4963.3	0.23	0.40
HC_5N(9-8)	237.8	3386.8	366.8	7494.0	0.35	0.55

3.6 Comparison to single-dish observations

As an estimate for the amount of missing flux in the VLA survey, we compare three transitions in the frequency range of 18 – 26 GHz observed with the VLA and with the Effelsberg 100-m telescope (Gong et al. 2015) regarding their peak flux, integrated intensity, and spectral line shape.

The VLA data is convolved with a beam of the size equal to the beam size of the Effelsberg telescope (”smoothed“) for the according observing frequency. We make sure that the total flux density in the maps of the original and smoothed VLA data sets is conserved. We then compare the brightest transitions which have an extended structure in the emission maps: HC_3N(2-1), HC_5N(8-7), and HC_5N(9-8) at 18.196, 21.301, and 23.964 GHz, respectively. The according beam sizes are given by $750/f$(GHz), and are 41.7, 35.7, and 31.3 arcsec, respectively. The single-pointing observations with the Effelsberg 100-m telescope with these beam sizes therefore should receive the total amount of flux which is enclosed roughly in that region.

From the smoothed VLA data, we extract the peak average flux density within the beam around the stellar position $(\alpha_{J2000}, \delta_{J2000}) = (09^h47^m57.437^s, 13°16'43.850'')$ and the flux density integrated over the whole line profile for each transition and compare it to the same parameters from the Effelsberg data (Tab. 3.2). The amount of missing flux in the VLA data is less than about 50% of the assumed total flux from the Effelsberg data. The fraction of missing flux increases with increasing observing frequency. However, it also has to be taken into account that the beam size of the Effelsberg telescope decreases with increasing frequency, such that possibly not the total amount of flux is measured for higher frequencies. The minimum baseline length from the VLA survey is 35 m, which means that emission with an angular extent larger than 57 – 38 arcsec is filtered out by the interferometer for 18 – 26 GHz and therefore missing. The effect is strongest for the velocity components closest to the stellar velocity (Fig. 3.7). For the peaks of the spectral lines, furthest from the stellar velocity, more of the flux is conserved, because this emission is concentrated in a small area in the image maps (cf. e.g. Fig. 3.5).

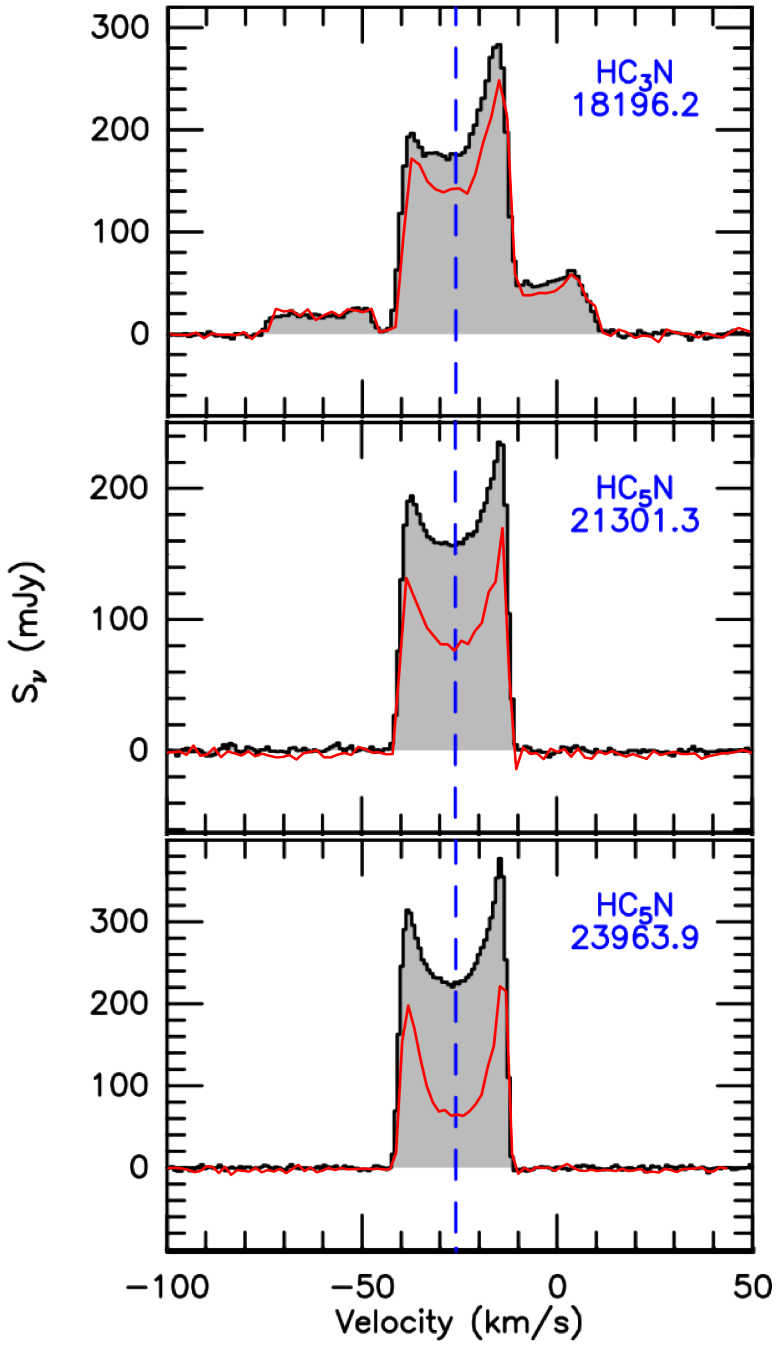

Figure 3.7: Spectral lines of HC_3N(2-1), HC_5N(8-7), and HC_5N(9-8) as observed with the VLA (red line, this work) and the Effelsberg telescope (black line, Gong et al. 2015) illustrating the missing flux problem in the VLA data. The y- and x-axes of each overplotted spectral line are the same.

CHAPTER 4

Radial emission profiles of molecular lines

To quantify how our observations compare to the predictions of chemical models with focus on the photochemistry in the outer CSE, we have developed an automatized procedure with *Python* to extract radial intensity profiles of the molecular emission from the image maps of our survey in a reproducible and reliable manner. We aim to empirically answer the following questions:

- At what radial distance from the central star is the molecular emission located and where does the emission intensity peak for each channel?
- How many molecular shell components are there?
- What is the thickness of the emitting molecular shells?
- What are the relative peak intensities for different parts of the molecular shells?
- What is the three dimensional structure (as a function of velocity)? What correlations are there regarding physical structure (e.g. velocity, density) and regarding chemistry (expected radial abundance)?

This work performs a detailed analysis of the morphology of the outer CSE for 7 molecules (HC_3N, HC_5N, HC_7N, C_3N, C_4H, C_6H, C_6H^-) and 44 transitions, to obtain an unprecedented understanding of the three dimensional physical and chemical structure of IRC+10216.

4.1 Method

For the determination of the radial emission profiles, we have a few assumptions on the CSE:

- the center of the emission is at the position of the central star
- the velocity field is spherically symmetric with a constant expansion velocity
- the emission intensity distribution is approximated by a Gaussian function

These assumptions approximate the molecular shell well to the first order. Deviations from this simple model indicate the substructure, which we aim to analyze as well. It has to be considered that we are working with interferometric data which suffers from the missing spacing problem, especially for the extended source structures. As noted before, the position of the shells and clumps in our images are determined reliably, because the area they originate from is similar to the beam size. The determined ring width and peak flux are only lower limits.

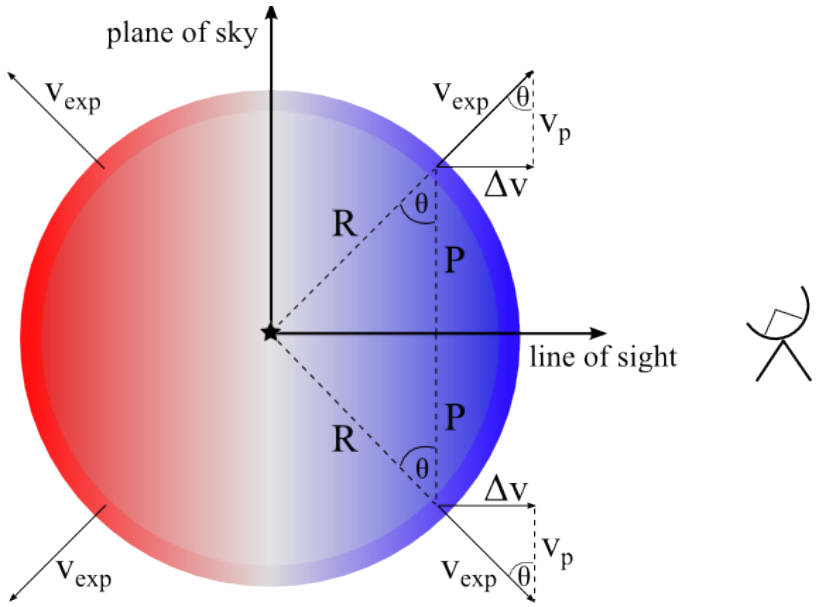

Figure 4.1: Geometry of an expanding circumstellar hollow sphere (as shown in Fig. 1.15), with a certain width, with radius R, projected radius P, projection angle θ, constant expansion velocity $v_{\rm exp}$, velocity along the line of sight $\Delta v = v_{\rm ch} - v_*$, with the measured velocity in each channel $v_{\rm ch}$ and the stellar velocity v_* with respect to the Local Standard of Rest (LSR), and projected velocity $v_{\rm p}$ in the plane of the sky (cf. Eqs. 4.2, 4.3). The part of the shell that expands towards the observer is blue-shifted, with $\Delta v < 0$, and the part that moves away from the observer is red-shifted, with $\Delta v > 0$. © Denise Keller

4.1.1 Molecular shell geometry

The data cubes consist of information on the two dimensional position and intensity of the molecular emission for several velocity components in every channel (Fig. 1.24, p. 37). So we analyze a three dimensional object. Here we assume a spherical expanding shell, which is projected into two dimensional planes. We do not make assumptions on the actual physical density structure, just the velocity field. Each velocity component or interval Δv is the projection of velocity cones of this three dimensional sphere. Along each velocity cone the material is Doppler-shifted with respect to the stellar velocity, given by the expansion velocity $v_{\rm exp}$. The geometry is described as

$$v_{\rm exp}^2 = v_p^2 + \Delta v^2 \,, \tag{4.1}$$

$$\cos\theta = v_p / v_{\rm exp} = \sqrt{1 - \frac{\Delta v^2}{v_{\rm exp}^2}} \,, \tag{4.2}$$

where $v_{\rm exp}$ lies along the radial expansion axis, v_p is the projected or tangential velocity component and lies in the plane of the sky, and $\Delta v = v_{\rm ch} - v_*$ is the difference between the measured velocity in each channel $v_{\rm ch}$ and the stellar velocity v_* with respect to the Local Standard of Rest (LSR) and lies along the line of sight, and θ is the projection angle which lies between v_p and $v_{\rm exp}$ (Fig. 4.1).

For each slice of the data cube we see a projected sum of emission along such velocity cones, which, for optically thin emission from an expanding hollow sphere, appear as rings (cf. Fig. 3.5, p. 67). For the velocity components furthest from the stellar velocity we observe the smallest extent, because the expansion axis lies parallel to the line of sight and the emission from these components are furthest blue-

and red-shifted, respectively, and probe the poles of the sphere closest to or furthest from the observer. At the stellar velocity the expansion axis lies perpendicular to the line of sight and in the plane of the sky, so we directly measure the extent of the emission without projection.

4.1.2 Deprojection

Assuming that the molecular emission has a spherical shape, then the measured distances between the emission and the central star in each image map for a certain velocity interval are also projected into the plane of the sky with the projection angle θ. With the described assumptions on the three dimensional geometry, we calculate intrinsic distances, such that the deprojected distances for several velocity components all yield one radius. So we aim to determine the intrinsic shell radius of the molecular emission not only from the extent at the systemic velocity but from all velocity channels:

$$R = \frac{P(v_{\rm ch})}{\cos\theta} = P(v_{\rm ch}) \left(\sqrt{1 - \left(\frac{v_{\rm ch} - v_*}{v_{\rm exp}} \right)^2} \right)^{-1} \quad , \tag{4.3}$$

where $P(v_{\rm ch})$ is the projected distance in the image map which is a function of the center velocity $v_{\rm ch}$ in each channel, $v_* = -26$ km s^{-1} is the LSR or systemic velocity of IRC+10216, and $v_{\rm exp} = 14.5$ km s^{-1} is the expansion velocity of the circumstellar material of IRC+10216. The expansion velocity is approximately constant (measured from the spectral lines) and we assume that it describes a spherical velocity field (Fig. 4.1). The uncertainty is given by the Gaussian error propagation as

$$\begin{aligned} \Delta R &= \sqrt{\left(\frac{\partial R}{\partial P} \delta P \right)^2 + \left(\frac{\partial R}{\partial \cos\theta} \delta\cos\theta \right)^2} \\ &= \sqrt{\left(\frac{\delta P}{\cos\theta} \right)^2 + \left(-\frac{P}{\cos^2\theta} \delta\cos\theta \right)^2} \, , \end{aligned} \tag{4.4}$$

where δP is the uncertainty of the projected distance which is given by the chosen bin width and $\delta\cos\theta$ is the uncertainty of the projection angle which depends on the velocity resolution $\delta v_{\rm ch}$ of the data:

$$\begin{aligned} \delta\cos\theta &= \sqrt{\left(\frac{\partial\cos\theta}{\partial v_{\rm ch}} \, \delta v_{\rm ch} \right)^2} \\ &= \frac{\partial}{\partial v_{\rm ch}} \left(\sqrt{1 - \left(\frac{v_{\rm ch} - v_*}{v_{\rm exp}} \right)^2} \right) \delta v_{\rm ch} \\ &= -\left(v_{\rm ch} - v_*\right) \left(v_{\rm exp}^2 \sqrt{1 - \left(\frac{v_{\rm ch} - v_*}{v_{\rm exp}} \right)^2} \right)^{-1} \delta v_{\rm ch} \, . \end{aligned} \tag{4.5}$$

We also get three dimensional information or indications on the deviations from the assumed symmetrical sphere, hence the molecular wind velocity. If the referred distances for example vary for the red- and blue-shifted part, then the molecular shell might have asymmetries regarding the velocity field (not a constant outflow velocity at all angles) or regarding the density and chemical structure.

4.1.3 Azimuthal sum and quadrants

From the data cubes we extract the emission maps of each channel or velocity component and determine the flux of every pixel in the image. For each of these pixels with the coordinates (x, y) the radial distance D to the central pixel at the position of the star $(x_0, y_0) = (09^h47^m57.347^s, 13°16'43.850'')$ is calculated:

$$D = \sqrt{(x - x_0)^2 + (y - y_0)^2} \tag{4.6}$$

To determine more information on the substructure and asymmetries of the molecular shell, we divide the image into four quarters (Fig. 4.2) and in the following investigate the spatial information of these quarters individually:

$$\text{Quarter 1: } (x > x_0), (y \geq y_0) \tag{4.7}$$
$$\text{Quarter 2: } (x \leq x_0), (y > y_0) \tag{4.8}$$
$$\text{Quarter 3: } (x < x_0), (y \leq y_0) \tag{4.9}$$
$$\text{Quarter 4: } (x \geq x_0), (y < y_0) \tag{4.10}$$

We divide the calculated distances into intervals with the according flux values. Every distance interval (with increasing radius) consists of a sum of flux values for a different number of pixels. To be able to compare the fluxes of the different intervals with each other, we calculate average flux values. The sums of flux values are normalized by the number of pixels:

$$I_{\mathrm{norm}} = I_{\mathrm{sum}}/N_{\mathrm{pixel}}, \tag{4.11}$$

where $I_{\mathrm{sum}} = \sum_j^{N_{\mathrm{pixel}}} I_{\mathrm{j}}$ is the sum of flux values in each given distance interval (or bin) and N_{pixel} is the number of pixels in each bin. So we basically determine the average flux in each annulus around the center (radial intensity profiles). The uncertainty is

$$\begin{aligned}
\Delta I_{\mathrm{norm}} &= \sqrt{\left(\frac{\partial I_{\mathrm{norm}}}{\partial I_{\mathrm{sum}}}\delta I_{\mathrm{sum}}\right)^2 + \sigma_{\mathrm{spread}}}\,, \\
\text{with } \delta I_{\mathrm{sum}} &= \sqrt{\left(\frac{\partial I_{\mathrm{sum}}}{\partial I_{\mathrm{j}}}\delta I_{\mathrm{j}}\right)^2} \\
&= \sqrt{\sum_j^{N_{\mathrm{pixel}}} \left(\delta I_{\mathrm{j}}\right)^2} = \sqrt{\sum_j^{N_{\mathrm{pixel}}} (\sigma_{\mathrm{rms}})^2} \\
&= \sqrt{N_{\mathrm{pixel}} \times \sigma_{\mathrm{rms}}^2}\,,
\end{aligned} \tag{4.12}$$

where the uncertainty of each pixel ΔI_{j} is given by σ_{rms} which is the standard deviation of the whole image map and therefore the same value for each pixel. The normalized flux additionally has an uncertainty given by its spread, described by the standard deviation:

$$\sigma_{\mathrm{spread}} = \frac{1}{\sqrt{N_{\mathrm{bin}}}} \sum_k^{N_{\mathrm{bin}}} \left(I_{\mathrm{norm,\,k}} - \langle I_{\mathrm{norm}} \rangle\right)^2 . \tag{4.13}$$

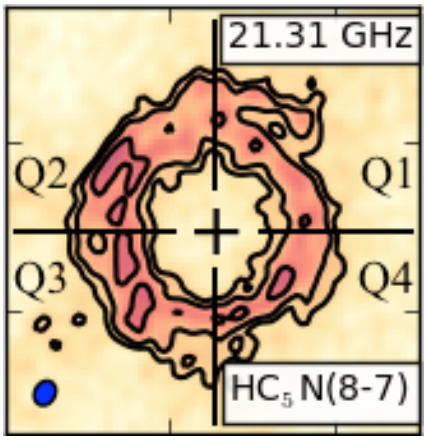

Figure 4.2: Devision of every emission maps into quarters Q1, Q2, Q3, Q4.

So that finally

$$\Delta I_{\rm norm} = \sqrt{\sigma^2_{\rm rms}/N_{\rm pixel} + \sigma^2_{\rm spread}}\,. \tag{4.14}$$

For the most extreme velocity components (at maximal radial shift from the stellar velocity) we encounter several problems for the further analysis. First, the projection angle is largest so there is a geometrical degeneracy of shell radius and shell width (Fig. 4.1). Therefore the deprojection suffers from much larger uncertainties (given by the width of the ring, which is expected to be several arc seconds) than for the components close to the stellar velocity. Second, these images with very different scales are differently "seen" by the interferometer. Each channel has a different amount of flux missing by scales that are filtered out. The channels with the largest velocity difference to the stellar velocity with compact emission from the poles of the emission shell suffer from less missing flux than those channels close to the stellar velocity with extended ring emission, which might be filtered out. For those channels where the projected scales are similar, the flux difference is less than about 30%, which we have estimated by the shape of the observed spectral lines and by simulated interferometric observations of a simple symmetric sphere (in collaboration with Ward Homan, KU Leuven) .

We choose to only use the channels with $|\Delta v| = |v_{\rm ch} - v_*| < 7.5$ km s^{-1} for the further analysis. By excluding those channels with the extreme velocities we avoid these effects that just increase the uncertainties and still have enough channels at hand to deduce the three dimensional information. The deprojected radii are re-binned with a bin width of 2 arcsec, because it is approximately similar to the smallest beam size and the expected half width of the shell. A smaller binning is not physical and a larger binning looses information.

Additionally, we add the deprojected channels along the velocity axis to increase the signal-to-noise ratio. For every deprojected distance bin with normalized flux $I_{\rm norm}$ we calculate the sum along the velocity components v for $|\Delta v| < 7.5$ km s^{-1} (with total number $N_{\rm v}$), which yields

$$I_{\rm velsum} = \frac{1}{N_v}\sum_{v}^{N_v} I_{{\rm norm},v}\,, \tag{4.15}$$

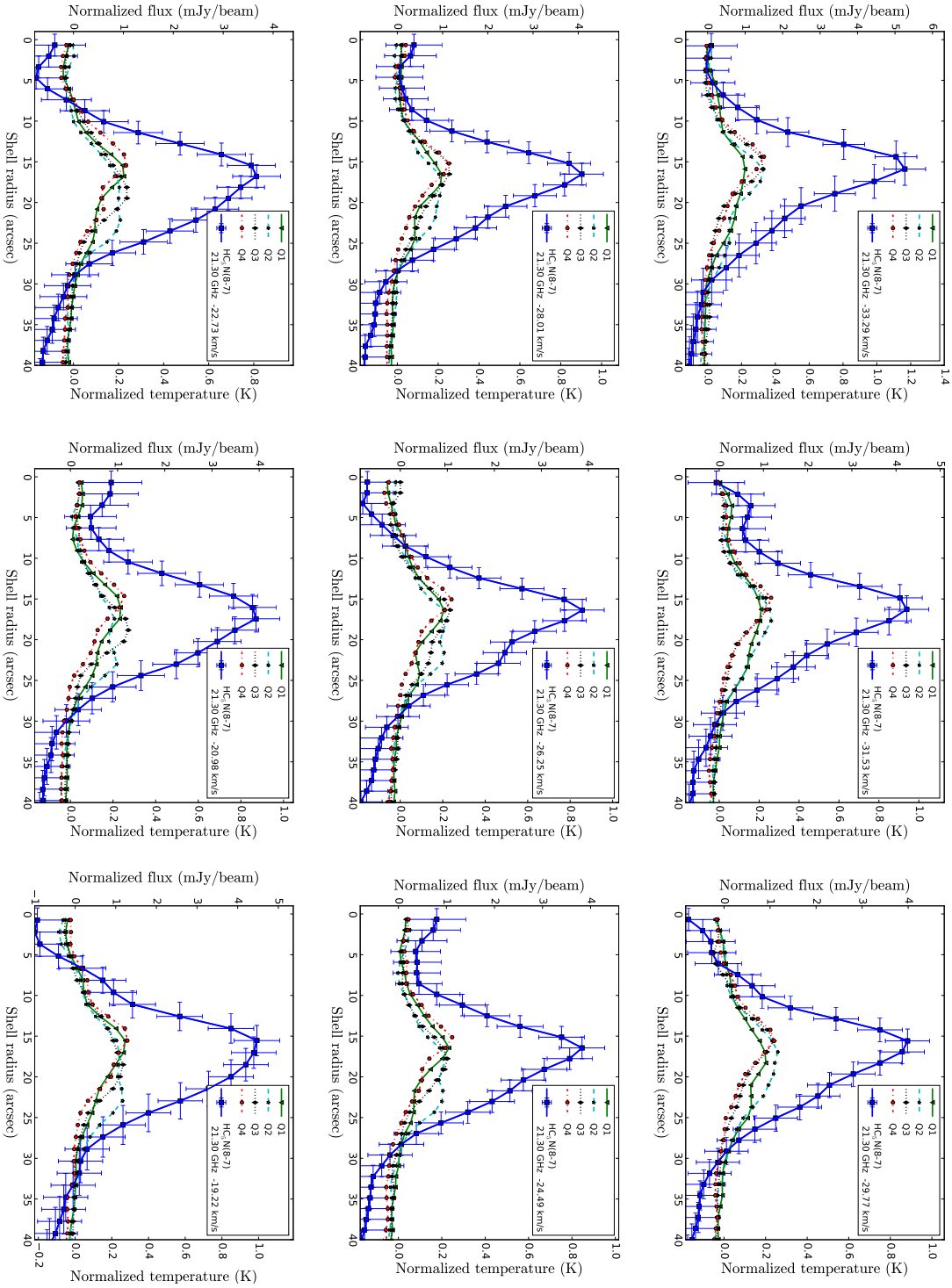

Figure 4.3: Radial emission profiles of $HC_3N(8\text{-}7)$ for each channel with $|\Delta v| < 7.5$ km s^{-1} for the four quarters (Q1, Q2, Q3, Q4) and their azimuthal sum (blue) from the VLA data. The left y-axis shows the average or normalized flux and the right y-axis shows the corresponding brightness temperature. The error bars in x- and y-direction are determined by Eqs. 4.4 and 4.12.

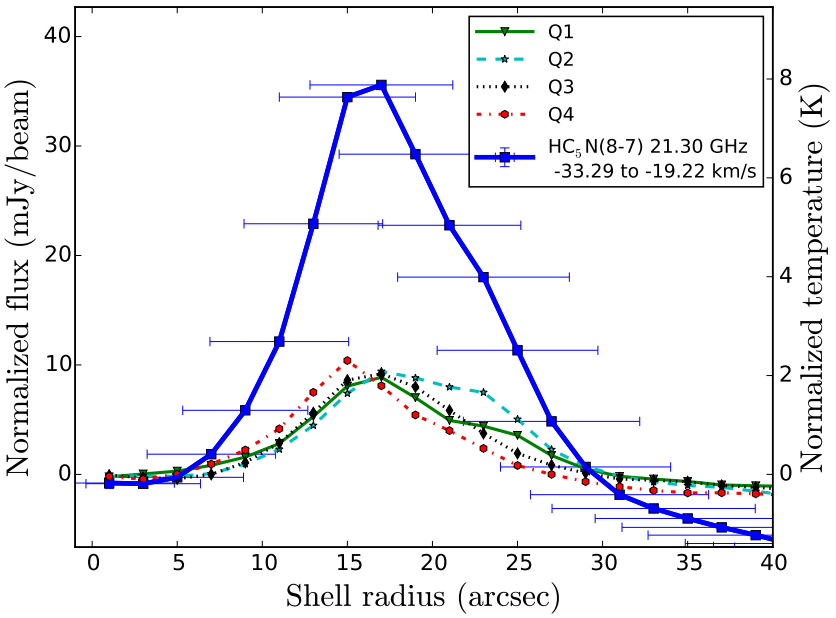

Figure 4.4: Radial emission profiles of HC_5N(8-7) for velocity integrated flux of $|\Delta v| < 7.5$ km s^{-1} for the four quarters (Q1, Q2, Q3, Q4) and their azimuthal sum (blue) from the VLA data. The left y-axis shows the average or normalized flux and the right y-axis shows the corresponding brightness temperature. The error bars in y- and x-direction are determined by Eqs. 4.16 and 4.17. The uncertainty on the average flux is smaller than the plotted symbols.

$$\Delta I_{\mathrm{velsum}} = \frac{1}{N_v} \sqrt{\sum_{v}^{N_v} (\Delta I_{\mathrm{norm},v})^2} \quad \text{, and} \tag{4.16}$$

$$\Delta R_{\mathrm{velsum}} = \frac{1}{N_v} \sqrt{\sum_{v}^{N_v} (\Delta R_v)^2} \, . \tag{4.17}$$

4.1.4 Radial emission profiles

We produce radial emission profiles of normalized flux versus deprojected shell radius (angular distance to the star) for the azimuthal sum and the four image quarters individually for every channel and for the velocity sum ($|\Delta v| < 7.5$ km s^{-1}) of every transition of every molecule with a ring-like emission distribution and high enough signal-to-noise: HC_3N, HC_5N, HC_7N, C_3N. For the weak transitions of C_4H, C_6H, and C_6H^-, we create only radial emission profiles from velocity integrated flux for $|\Delta v| <$ 7.5 km s^{-1}. As an example, the radial intensity profiles for HC_5N(8-7) for each channel and for the velocity sum are shown in Figures 4.3 and 4.4, respectively.

First, we qualitatively compare the radial profiles of velocity integrated flux from the VLA data to the results of the chemical and radiative transfer modeling of IRC+10216 from Cordiner & Millar (2009) in Sect. 4.2.1 and to radial abundance profiles from the chemical models of Millar & Herbst (1994) in Sect. 4.2.2. Second, we perform a quantitative analysis using Gaussian fits that are explained in Sect.

4.3. The corresponding results are described in Sect. 4.4 and compared to previous observational and chemical modeling studies in Sect. 4.5.

4.2 Qualitative comparison of radial intensity profiles to chemical models

4.2.1 Comparison to Cordiner & Millar (2009)

The chemical model of Cordiner & Millar (2009) (cf. Sect. 1.3.5, Fig. 1.20, p. 32) is the most sophisticated and most realistic model of IRC+10216 available at the moment. The unique part of their model is adding thin density-enhanced shells of H_2 gas to the spherically symmetric density structure of the CSE (based on Brown & Millar 2003). Their study explores the effects of enhanced UV shielding in these dense shells, which aim to resemble the observed shells of dust and molecular gas around IRC+10216 (cf. Fig. 2.2).

This model is calibrated by the previous observations of the molecular shells by Guélin et al. (1999) and Dinh-V-Trung & Lim (2008) and of the dust shells by Mauron & Huggins (2000). Based on this, the density structure is chosen to have density-enhancements of 2 arcsec width with a distance of 12 arcsec to each other. In these density-enhanced shells, the number density of H_2 is enhanced by about one order of magnitude compared to the underlying radial density profile which falls as r^{-2}. The studies on the molecular shells were performed with the Plateau de Bure interferometer (PdBI) and the VLA with its former receivers and correlator. The angular resolution of these observations are very similar to our data. The observational studies conclude that the analyzed molecules all coincide in a ring of the same radius of 15 – 16 arcsec and a width of about 2 – 3 arcsec. Therefore, in the calculations the radial positions of the density-enhanced shell at 15 arcsec has been fixed for every molecule to best reproduce the observations. The temperature profile is based on Crosas & Menten (1997). The initial abundances of the parent species in the chemical network, e.g. for C_2H_2 8×10^{-5} (relative to H_2), are taken from Millar et al. (2000) and Fonfría et al. (2008).

Additionally, Cordiner & Millar (2009) calculate the molecular excitation by performing radiative transfer modeling of the molecular transitions of HC_3N, at about 45.5 GHz, of C_4H, C_6H, and C_6H^- in the frequency range 80 – 90 GHz (mmline code, Justtanont et al. 1994). For the molecules HC_5N, HC_7N, and C_3N the radiative transfer modeling has not been performed, because the collisional rates are not (well) determined at the moment (Schöier et al. 2005). The authors have provided us with the radial intensity profiles.

We compare these chemical and radiative transfer modeling results to the radial intensity profiles extracted from the VLA data for the velocity-integrated flux of the inner line profile ($|\Delta v| < 7.5$ km s^{-1}) for the azimuthal sum over the emission region of HC_3N, C_4H, C_6H, and C_6H^- (Fig. 4.5). This comparison gives insights on the overall structure of the CSE of IRC+10216. To consider the substructure, we also compare the model to the profiles for each quarter of the image maps from the VLA data for transitions around 29 GHz (Fig. 4.6).

For the comparison we choose the profiles of velocity-integrated flux to have a better signal-to-noise ratio compared to, for example, considering just the single velocity channel closest to the stellar velocity. Especially for the quarters of the weak transitions of C_4H, C_6H, and C_6H^- the signal-to-noise ratio is low. Of course, in that way information on parts of the substructure of the molecular shell is averaged out, however, we analyze the substructure in a quantitative manner in the following chapters in more detail.

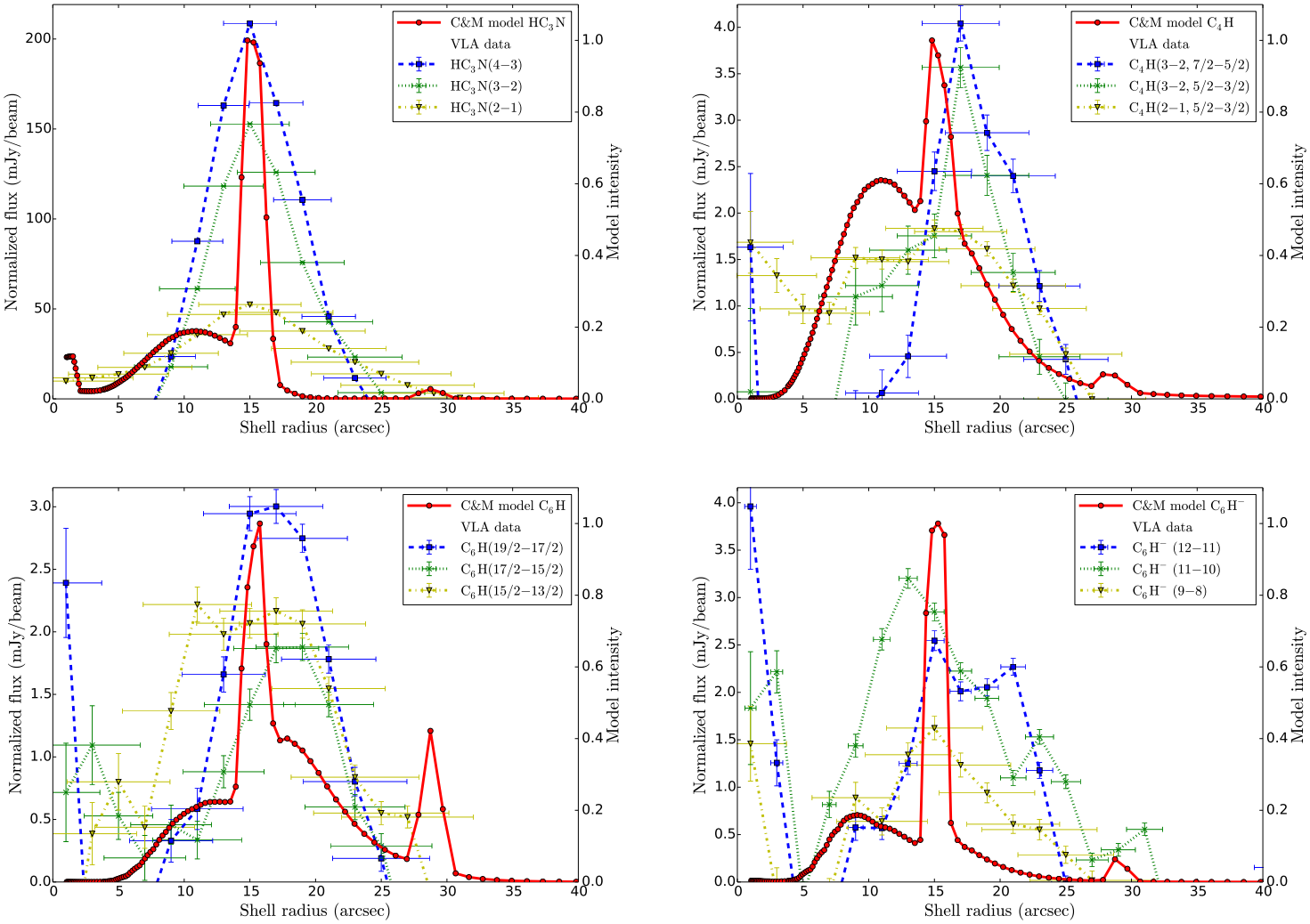

Figure 4.5: Comparison of the radial intensity profiles from the VLA data for the velocity-integrated flux ($|\Delta v| < 7.5$ km s^{-1}) for the azimuthal sum over the emission region of HC_3N, C_4H, C_6H, and C_6H^- and the chemical and radiative transfer models of Cordiner & Millar (2009, C&M, solid red line). The average beam size for HC_3N(4-3) is 2.5″, for HC_3N(3-2) is 3.2″, and for HC_3N(2-1) is 4.7″. For C_4H the average beam sizes are 3.0″, 3.1″, and 4.4″, respectively. For C_6H the beam sizes are 3.32″, 3.5″, and 4.3″, respectively. For C_6H^- the beam sizes are 2.6″, 3.18″, and 3.4″, respectively. The transitions from the VLA data are for frequencies 18 – 38 GHz, whereas the modeled transitions are HC_3N(5-4) at 45.5 GHz and those of C_4H, C_6H, and C_6H^- are for frequencies 80 – 90 GHz. The model intensities have an arbitrary scale and are given relative to its maximum value on the right y-axis. The error bars of the VLA data in x- and y-direction are determined by Eqs. 4.17 and 4.16.

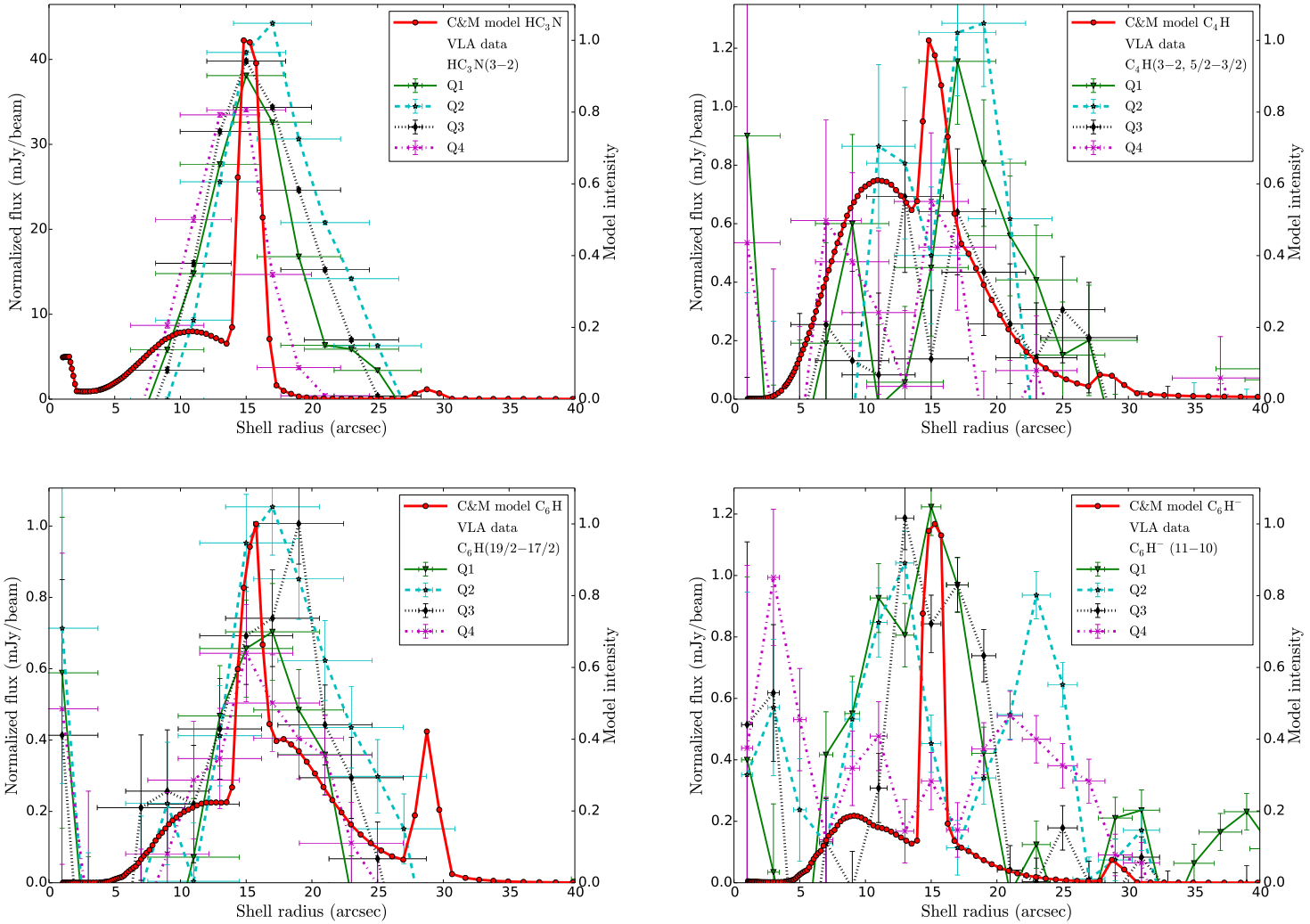

Figure 4.6: Comparison of the radial intensity profiles from the VLA data for the velocity-integrated flux ($|\Delta v| < 7.5$ km s^{-1}) for each quarter Q1, Q2, Q3, Q4 of the emission region of HC_3N, C_4H, C_6H, and C_6H^- and the chemical and radiative transfer models of Cordiner & Millar (2009, C&M, solid red line). The transitions from the VLA data are for frequencies around 29 GHz, whereas the modeled transitions are HC_3N(5-4) at 45.5 GHz and those of C_4H, C_6H, and C_6H^- are for frequencies 80 – 90 GHz. The model intensities have an arbitrary scale and are given relative to its maximum value on the right y-axis. The error bars of the VLA data in x- and y-direction are determined by Eqs. 4.17 and 4.16.

First of all, it has to be emphasized that the comparison is qualitative. The radial intensity profiles from the model and from the VLA data cannot be compared on a one-to-one basis for the following reasons. The profiles from Cordiner & Millar (2009) have an arbitrary intensity scale given by the product of the level population and the molecular number density at each radial position. They are not directly comparable with each other for the different molecules. The model intensity is not convolved with any beam function. In our comparison we focus on the shapes and radial positions of the profiles. The model and the data probe different energy levels of the molecules, as the modeled transitions were in the range 80 − 90 GHz and the data covers transitions for 18 − 38 GHz. The difference of the energy levels is between 20 and up to 60 K between the modeled and observed transitions. The different ranges might trace slightly different temperature regions in the CSE and therefore the higher energy levels result in slightly smaller radial positions for the modeled molecules compared to the lower energy levels from the VLA data. However, the excitation temperature of e.g. HC_3N is estimated to be about 13 K (e.g. Jewell & Snyder 1984), the region we are considering has a gas temperature of the order of 100 K, so the observed transitions should all be rotationally excited in that region.

HC_3N For the radial intensity profiles of the azimuthal sum from the VLA data of HC_3N, the correspondence to the model of Cordiner & Millar (2009) is good (Fig. 4.5, top left). The radial positions at maximum intensity of HC_3N from the VLA data and from the model are in good agreement. The observed shells are thicker than the modeled ones due to beam smearing. The average beam sizes for the HC_3N transitions are 4.65 arcsec, 3.23 arcsec, 2.50 arcsec, respectively, for increasing frequency. For HC_3N, in the VLA data there is no prominent inner shell component around 10 arcsec observed contrary to the broad inner component in the chemical model. Furthermore, there is no observed shell component around 29 arcsec as seen in the chemical model.

When considering the quarters (Fig. 4.6, top left), quarter Q1 and Q3 compare well with the model for HC_3N, whereas quarters Q2 and Q4 deviate slightly within the uncertainties. Quarter Q2 spans out to larger radii and has its maximum intensity at a radius larger than the chemical model. Quarter Q4 is thinner and exists at radii smaller than the other quarters and than the thin main shell of HC_3N in the chemical model.

C_4H The overall shape of the radial intensity profiles of the azimuthal sum from the VLA data of C_4H roughly agrees with that from the model of Cordiner & Millar (2009) (Fig. 4.5, top right), especially for the transition C_4H(3-2,5/2-3/2). However, the observations show a large portion of the molecular emission originates from a region at much larger radii than expected from the chemical model. Also, the peak emission of C_4H is at a slightly larger radius than in the chemical model. There is no observed shell component at a radius of about 27 arcsec as seen in the chemical model. The average beam sizes for these transitions are 4.42 arcsec, 3.05 arcsec, and 3.04 arcsec for increasing frequency.

For the individual quarters of the C_4H emission from the VLA data the uncertainties are high, especially for the quarters Q3 and Q4 (Fig. 4.6, top right). The emission is mainly originating from the quarters Q1 and Q2. Quarter Q2 has a prominent inner component at about 10 arcsec radius within the uncertainties, which is also present in the intensity profile from the chemical model of C_4H.

C_6H The radial intensity profiles of the VLA data and the model of C_6H agree well with each other (Fig. 4.5, bottom left). As mentioned before, the width of the profiles from the VLA data are wider than those from the model due to the beam convolution. The average beam sizes for these transitions are between 4.25 arcsec and 3.32 arcsec. From the radial profiles of the VLA data with their uncertainties,

we conclude that the emission of C_6H is found at slightly larger radii than modeled by Cordiner & Millar (2009). The modeled radial profile has a second shell component directly following the main thin shell component at about 16 – 18 arcsec, which is also observed in the VLA data. However, the VLA data does not show a bright shell component of C_6H at about 29 arcsec.

The radial behavior and peak position of the C_6H emission from quarters Q1 and Q4 agree very well with the chemical model (Fig. 4.6, bottom left). The shell components in quarters Q2 and Q3 are brighter than in the other quarters and extent to larger radii than in the chemical model, as seen for HC_3N and C_4H.

C_6H^- The anion of C_6H also has a good correspondence of the radial intensity profiles from the VLA data and the model (Fig. 4.5, bottom right). The molecular emission is also observed to be wider than in the chemical model. The average beam sizes are between 3.36 arcsec and 2.63 arcsec. The transition C_6H^-(11-10) shows a shell component at a radius of about 30 arcsec, which is predicted by the chemical models for all the analyzed molecules (between 27 and 29 arcsec), but only clearly observed for this transition.

This outer shell component observed in the VLA data mostly originates from quarter Q1 (Fig. 4.6, bottom right). This quarter also has an inner component at about 12 arcsec, which the chemical model predicts at about 8 arcsec. Quarters Q1 and Q3 agree very well with the chemical model in terms of the radial position of the intensity peak of the C_6H^- emission. Quarter Q2 has two prominent shell components, at about 13 and 23 arcsec, similar to quarter Q4 which, however, is much weaker than Q2. The radial intensity profile from the chemical model does not have such an outer shell component at 23 arcsec.

The chemical and radiative transfer model by Cordiner & Millar (2009) is designed to match the observational results of Guélin et al. (1999) and Dinh-V-Trung & Lim (2008). This is the reason, that the modeled molecules have their maximum intensity at the same radius of 15 arcsec and a small shell thickness of about 2 arcsec.

The VLA observations overall roughly compare well with the previous observations and the chemical model, especially when considering the azimuthal sum of the VLA data. The distributions from the VLA data are broadened by the beam of the observation contrary to the model which does not include a beam function. Most observed transitions and most emission quarters of C_4H, C_6H, and C_6H^- have an inner component at radii between 8 and 12 arcsec, but no bright component at about 29 arcsec, which both are predicted by the model of Cordiner & Millar (2009). For the analyzed transitions, the data of quarter Q1 agrees very well with the model, whereas for quarter Q2 the molecular emission is observed at larger radii than in the model. For quarters Q3 and Q4 there is no conclusive behavior.

In the VLA data there is a signal at radii smaller than 2 arcsec for C_4H, C_6H, and C_6H^-. This emission is not expected from the chemical model and might also not be physical. These scales are smaller than the beam sizes in the VLA survey, therefore are not resolved, and should be interpreted with caution.

The qualitative comparison of the VLA observations to the model already reveals deviations to the model, especially for the carbon chain molecules C_4H and C_6H. Our VLA data therefore provide excellent material to be used to improve future models of the chemical and physical structure of IRC+10216's envelope.

4.2.2 Comparison to Millar & Herbst (1994)

We compare the radial intensity profiles from the VLA data (as in Sect. 4.2.1) qualitatively to the radial abundance profiles of Millar & Herbst (1994) (cf. Sect. 1.3.5, Fig. 1.19, p. 31) for every covered molecule. This chemical model includes the most current calculations on reaction rates of neutral-neutral reactions and the pathways of cyanopolyyne and carbon-chain formation. Time-dependent modeling of the chemistry in the CSE of IRC+10216 has been performed. The model is based on previous works by Howe & Millar (1990), Cherchneff et al. (1993), and Cherchneff & Glassgold (1993). For the calculations a smooth spherically symmetric CSE expanding with a constant outflow velocity has been assumed (r^{-2} distribution). The effect of varying the external radiation field strength G and the initial abundance of the parent species C_2H_2 on the abundances of hydrocarbons and cyanopolyynes is explored in this study. The calculations of Cordiner & Millar (2009) are comparable in terms of their chemical network as they are mostly based on Millar & Herbst (1994) and subsequent studies (e.g. Brown & Millar 2003).

We create diagrams of the observed radial distribution of HC_3N together with HC_5N, HC_7N, C_3N (with nitrogen compound) and HC_3N together with C_4H, C_6H, C_6H^- (without nitrogen compound) for transitions of a similar energy range around about 29 GHz for absolute radius units in cm. We assume a distance to IRC+10216 of 200 pc, as it has been utilized in Millar & Herbst (1994). These radial intensity profiles are then overplotted with the radial abundance profiles of Millar & Herbst (1994) (Fig. 4.7). The original data were not available. We choose the radial profiles which have been modeled with the lowest external UV radiation field strength of $G = 1/3$ and the highest initial abundance of the parent species C_2H_2 of 5×10^{-5} (relative to H_2), because the authors conclude that these are the settings which reproduce the observations best. The radial profiles from the VLA data only represent a certain region in terms of energy levels and a subset in terms of molecular abundance in comparison to the chemical model which includes a much larger sample of energy levels. The comparison of the relative behavior between the molecules from the observations and from the abundance model still is qualitatively good.

The observed molecular shells from the VLA data are confined to smaller regions than in the model of Millar & Herbst (1994), because this model does not account for density-enhanced shells. In the VLA observations, the molecules HC_5N, HC_7N, and C_3N are found at larger radii than HC_3N. This is also expected from the chemical model, however, with a larger distance between the molecules than observed. C_3N is expected at larger radii than HC_3N, because C_3N is formed by reactions with the photodissociation product of HCN, namely CN, which is expected to exist at much further distances from the central star than HC_3N. The VLA observations of C_3N(3-2,5/2-3/2) support this notion.

The chemical model of Millar & Herbst (1994) predicts the emission of C_4H and C_6H to peak at much larger radii than it is observed and at radii larger than those of HC_5N and HC_7N. The emission peak of the longer carbon chain C_6H is expected at a larger radius than the one of C_4H. The intensities of C_4H and C_6H observed with the VLA have their maxima at the same radius (cf. Figs. 4.5 and 4.6) and very similar to the radial maxima positions of HC_5N and HC_7N (Fig. 4.7).

The comparison of the radial profiles from the VLA data to the two chemical models (Millar & Herbst 1994; Cordiner & Millar 2009), which have comparable chemical networks but have different assumptions on the density structure of the CSE, shows that there are very good agreements but also deviations between the VLA data and both chemical models. This suggests that the circumstellar medium of IRC+10216 is more complex than one of the chemical models alone can reproduce; it rather is a combination of them. Furthermore, the modeled CSEs are only an one-dimensional approximation of the intrinsic shell structure which is not completely smooth or spherically symmetric. More of the substructure, such as the clumpiness, has to be taken into account in future models.

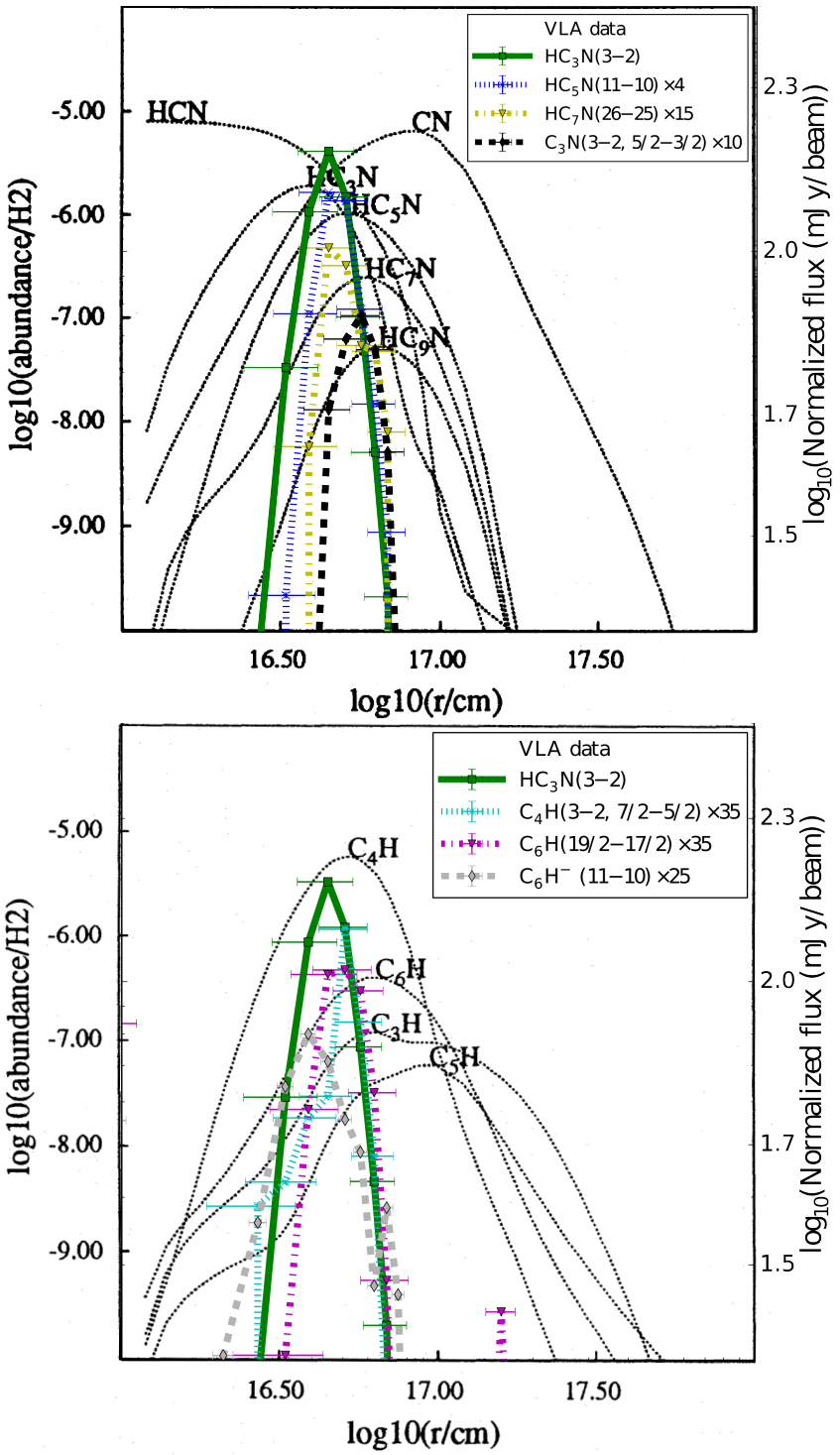

Figure 4.7: Comparison of the radial intensity profiles from the VLA data for the velocity-integrated flux ($|\Delta v| <$ 7.5 km s^{-1}) for the azimuthal sum over the emission region of the cyanopolyynes HC_3N, HC_5N, HC_7N and C_3N (*top*) and of the carbon chains C_4H, C_6H, and C_6H^- (*bottom*) and the radial abundance profiles from the chemical models of Millar & Herbst (1994, solid black lines). The observed transitions probe a similar energy range at a frequency of around 29 GHz. The intensities are scaled relative to HC_3N, as given in the legend on the top right, to be comparable to HC_3N. The external UV radiation field strength in the model is $G = 1/3$ and the initial abundance of C_2H_2 is 5×10^{-5} (relative to H_2). The x-axes of both diagrams are the same. For converting the angular distances from the VLA data to absolute distances as in Millar & Herbst (1994), we assume a distance of 200 pc to IRC+10216.

To quantify the spatial distribution of the molecular shell of IRC+10216 in more detail, in the following, we determine the radial positions of the shell components by Gaussian fits to the radial intensity profiles from the molecular transitions observed with the VLA.

4.3 Gaussian fits

To each radial profile from the VLA data (Sect. 4.1.4) we fit a Gaussian distribution

$$g(r) = F_{\rm max} \exp\left(-(r - R_{\rm max})^2 / 2W_{1/2}^2\right) . \tag{4.18}$$

where $F_{\rm max}$ is the amplitude or the peak flux, $R_{\rm max}$ is the shell radius at peak flux, and $2W_{1/2}$ is the shell width. These are our fit parameters. For most radial profiles two Gaussian components are necessary to describe the measured distribution:

$$G(r) = F_{\rm max\,1} \exp\left(-(r - R_{\rm max\,1})^2 / 2W_{1/2\,1}^2\right) + F_{\rm max\,2} \exp\left(-(r - R_{\rm max\,2})^2 / 2W_{1/2\,2}^2\right) . \tag{4.19}$$

As the fitting procedure (fitting the function $G(r)$ to the data points) we use the algorithm *curve_fit* of the *Python* package *Scipy* which performs a non-linear least square fit routine. The algorithm minimizes the sum of squared residuals (difference between data and fit model) and returns the optimal parameter values and errors. For the calculations we use a (absolute sigma) weight given by the error of the flux in the data cube to get physical meaningful uncertainties for the fit parameters.

According to the observed properties of the emission, we define meaningful restrictions for the fitting routine to improve the fit results. We restrict the fit to data points with radii between 5 and 35 arcsec and with positive flux, to avoid flux from scales smaller than one beamsize and from the sidelobes which both do probably not represent real emission, and the negative bowl effect which appears as negative flux values. The second Gaussian component is defined to be centered at distances larger than those of the first component and to have a smaller width than the first component. As the initial guesses $[F_{\rm max\,1}, R_{\rm max\,1}, W_{1/2\,1}, F_{\rm max\,2}, R_{\rm max\,2}, W_{1/2\,2}]$ for the fitting routine we use

$$F_{\rm max\,1} = max(I_{\rm norm}) \tag{4.20}$$

$$R_{\rm max\,1} = r(I_{\rm norm} == F_{\rm max\,1}) \text{ , if } r(I_{\rm norm} == F_{\rm max\,1}) \leq 19'' \text{ or} \tag{4.21}$$

$$15'', \text{ if } r(I_{\rm norm} == F_{\rm max\,1}) > 19'' \tag{4.22}$$

$$W_{1/2\,1} = (r(n-1) - r(0))\,/8 \approx 3.75'' \tag{4.23}$$

$$F_{\rm max\,2} = max(I_{\rm norm}) \times 0.6 \tag{4.24}$$

$$R_{\rm max\,2} = 23'' \tag{4.25}$$

$$W_{1/2\,2} = (r(n-1) - r(0))\,/16 \approx 1.875'' , \tag{4.26}$$

where n is the number of used data points. If the fitting procedure of $G(r)$ is not successful (results have infinitely high uncertainties), two Gaussian components do not approximate the data points well. Then, we fit a single Gaussian function $g(r)$. If still no solution is found, then there is no value shown in the later analysis of the results.

Examples of the resulting Gaussian fits for HC_5N(8-7) are shown in Fig. 4.8 (at the stellar velocity and for the velocity sum). Further fit results are in Figs. C.1 - C.13 (stellar velocity), Figs. C.14 - C.25 (velocity sum) and summarized in Tabs. C.1 (each channel) and C.6 (velocity sum) for the azimuthal sum, and in Tabs. C.2 - C.5 (each channel) and Tabs. C.7 - C.10 (velocity sum) for each quarter.

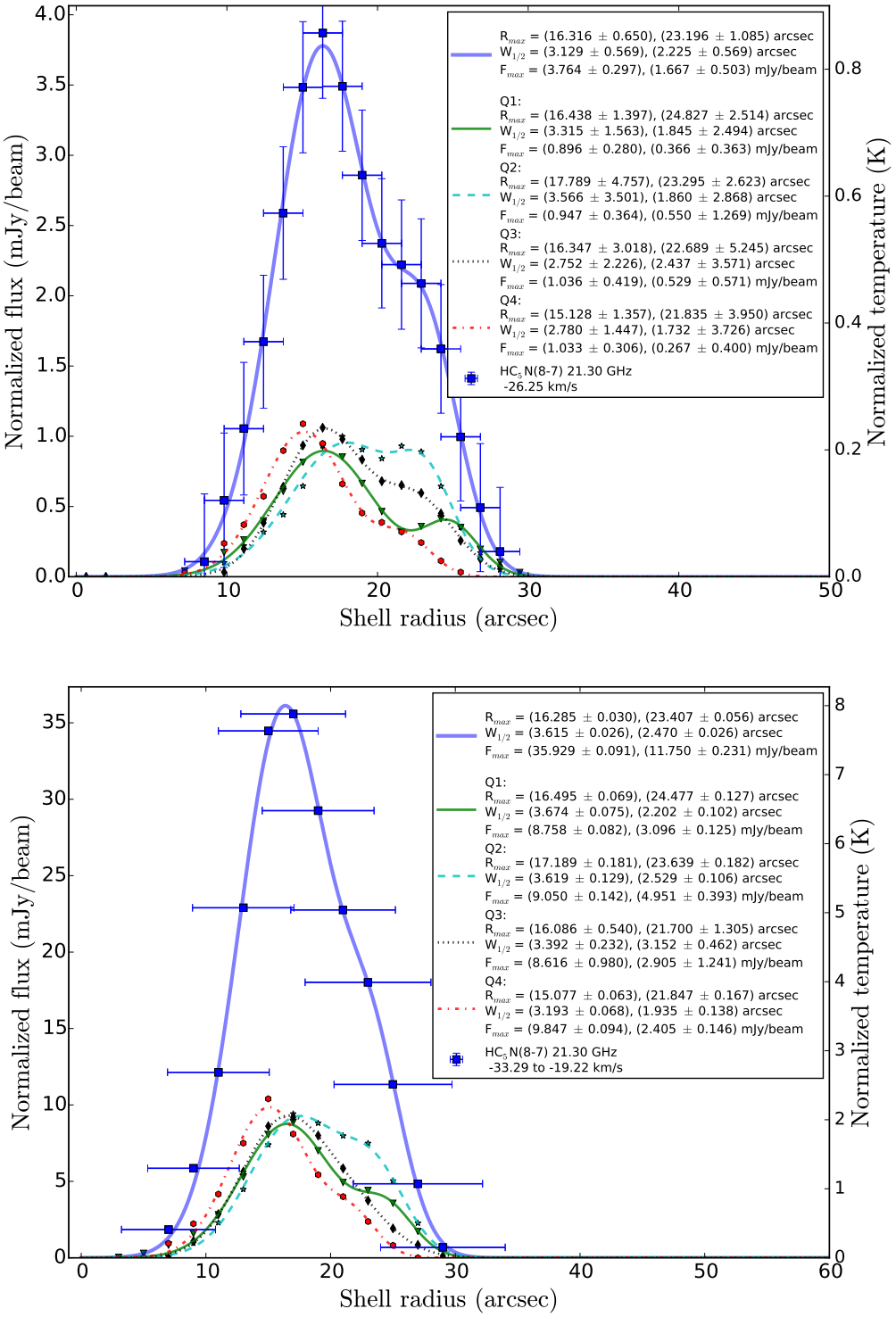

Figure 4.8: Radial emission profiles of HC_5N(8-7) at $v_{ch} = -26.25$ km s^{-1} (*top*) and for velocity integrated flux of $|\Delta v| < 7.5$ km s^{-1} (*bottom*) from the VLA data (data points) and the according Gaussian fit results (lines) for the four quarters (Q1 - straight green, Q2 - dashed turquoise, Q3 - dotted black, Q4 - dashdotted red) and their azimuthal sum (thick blue). The error bars of the data points in x- and y-direction are determined by Eqs. 4.4 and 4.12 (*top*) and Eqs. 4.17 and 4.16 (*bottom*). The Gaussian fit parameters are shell radius at maximum flux R_{max}, half shell width $W_{1/2}$, and maximum flux F_{max} for two components each. The determined best-fit values are given in the legend on the top right.

4.4 Results of Gaussian fits

From the resulting fit parameters of the radial emission profiles we explore the circumstellar geometry and chemistry of IRC+10216. On the one hand, we get three dimensional information on the emitting sphere, e.g. shell radius and width, and on the other hand, we get chemical information on the correlation between the analyzed molecules.

Overall, we find that most molecular lines originate from a shell radius of around 15 − 16 arcsec, which agrees well with the expectation from previous observations and chemical models (Tab. 4.1), and a shell width of 4 − 6 arcsec (Tab. 4.2), which is broader than earlier observed and modeled (e.g. Guélin et al. 1999; Cordiner & Millar 2009). For the first time, we constrain a radius of a second shell component which lies around 22 − 23 arcsec for most transitions of these cyanopolyynes and carbon chains (Fig. 4.9, Tabs. C.1 - C.10).

For most transitions, the shell widths are the same in both shell components (Fig. 4.9). There are a few transitions for which no second shell component has been found, e.g. C_3N(2-1,3/2-1/2), C_4H(2-1,5/2-3/2), C_6H^-(11-10). The first shell component of these transitions have a larger shell width compared to other transitions of the same species. They were observed with the largest beam sizes of the VLA survey of 4 − 6 arcsec, so these shells are not fully resolved. There is no significant difference in fitted radial position and shell width between the different transitions of one molecule. Even though transitions from higher energy levels might be expected at smaller radii than those from lower energy levels.

From the fitted shell parameters for each channel we are able to identify differences between the velocity components along the line of sight. We plot the resulting fit parameters of the molecular line emission profiles of HC_3N, HC_5N, HC_7N, and C_3N as a function of relative velocity Δv for each channel for the azimuthal sum and for each quarter (Figs. 4.10 - 4.14). We visualize how significantly the molecules are separated from each other among each other and among the shell components. We also explore differences between the quarters. For each molecule we calculate an weighted average of the fitted shell radius

$$R_{\mathrm{aver}} = \sum_v w_v R_{\mathrm{max,v}} \Big/ \sum_v w_v \,, \tag{4.27}$$

with the weight of each point for each velocity component v

$$w_v = 1/\Delta R^2_{\mathrm{max,v}} \,, \tag{4.28}$$

given by the uncertainty of the Gaussian fit result. The uncertainty of the weighted average is

$$\Delta R_{\mathrm{aver}} = \sqrt{\sum_v w_v \left(R_{\mathrm{max,v}} - R_{\mathrm{aver}}\right)^2 \Big/ \sum_v w_v} \,. \tag{4.29}$$

The weighted averages of the fitted radii for the molecules are shown in the bottom legend of Figs. 4.10 - 4.14. Similarly, we determine the weighted averages of the fitted shell width (Figs. C.26 - C.30). Additionally, from the radial profiles of the velocity integrated flux, we calculate the weighted averages of the fitted shell radii and the shell widths for the quantitative comparison to previous chemical models and observations (Tables 4.1 and 4.2).

First of all, we note that the difference in radial position between the molecular species in each shell component is rather small within the uncertainties (Figs. 4.10 - 4.14). However, there are trends visible.

The relative behavior between the molecules HC_3N, HC_5N, and HC_7N in the first shell component is

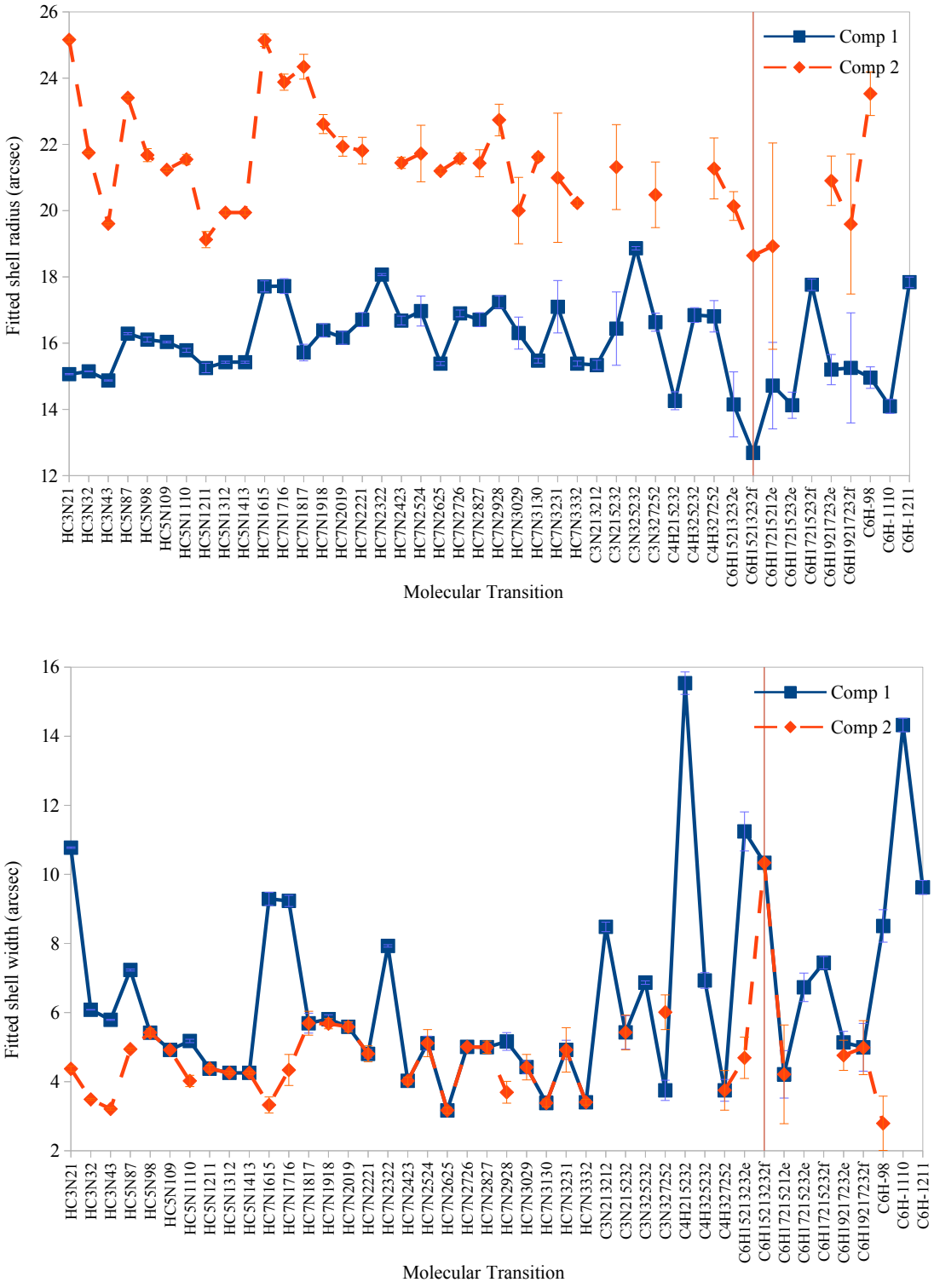

Figure 4.9: Resulting shell radius (top) and shell width (bottom) from the Gaussian fits to the radial profiles of all analyzed molecular transitions for velocity integrated flux for the azimuthal sum from the VLA data for two shell components (blue and red).

as expected from chemical models (Sect. 1.3.5 and 4.2). The peak intensity of each molecule is found at increasing radius following the sequence $HC_3N \rightarrow HC_5N \rightarrow HC_7N$. The intensity of C_3N is expected to peak at larger radii than for HC_3N, but from the Gaussian fitting and the weighted averages we find C_3N at similar or even smaller radii than of HC_3N. However, note that only four transitions of C_3N were analyzed, two of them with large uncertainties due to a low signal-to-noise ratio, such that the uncertainty on the weighted average is high. Furthermore, the transition C_3N(3-2,5/2-3/2) is observed at larger radii than HC_3N (Fig. 4.7, Sect. 4.2.2). The molecules C_4H, C_6H, and C_6H^- are expected at larger radii than HC_7N (Fig. 1.19, p. 31), but we find the peak intensities of these molecules at similar or smaller radii than of HC_7N (Tab. 4.1, cf. Fig. 4.7, Sect. 4.2.2). Also for these species the low signal-to-noise ratios have to be considered when interpreting these findings. For the second shell component the uncertainties are higher than for the first component. There might be the tendency of the sequence $HC_3N \rightarrow HC_7N \rightarrow HC_5N$ with increasing fitted shell radius (Figs. 4.10 - 4.14).

The molecular emission in the quarters for the first shell component, for most transitions, are at increasing radii following the sequence Q4 → Q1 → Q3 → Q2, with largest differences between Q2 and Q4 of about 2−4 arcsec, which is partially slightly larger than the beam sizes in the data cube, hence not fully resolved (Figs. 4.10 - 4.14). For the second component, within the large uncertainties, there is the indication of the sequence Q4 → Q3 → Q2 → Q1 with increasing fitted shell radii. The largest differences are about 3 arcsec, which is not fully resolved depending on the transition. The behavior between the molecules and between the quarters in the second shell component deviates from that of the first component.

The simple assumption of one average shell radius for all velocity components for each molecule does not fully describe the measured distribution. Especially when not considering the azimuthal average, which averages out information on the substructure, and rather considering certain regions individually the deviations become evident. There are differences for the blue- and red-shifted part (Figs. 4.10 - 4.14). The deviations from this average shell radius indicate an offset of the molecular emission center to the central position of the star and an asymmetric outflow velocity field on large and also small scales. This suggests that the shell is not fully symmetric along the line of sight. Furthermore, the medium is clumpy. The major clumps and arcs are in quarters Q1 and Q3 (cf. e.g. Fig. 3.4, p. 66).

For many transitions there is no second shell component found for quarter Q4. This may be an effect by external UV radiation which is stronger for the southwest region in quarter Q4 and therefore has increased photodissociation rates compared to the northeast region in quarter Q2. The shell width is thickest in quarter Q2 and thinnest in quarter Q4. This difference in molecular shell width and number of dust shells has been noted in previous observations with various telescopes (Mauron & Huggins 1999; Leão et al. 2006; Dinh-V-Trung & Lim 2008; Decin et al. 2011; Cernicharo et al. 2015).

In quarter Q3 there is a strong difference between the fitted shell radii for the blue- and red-shifted parts (Fig. 4.13). The fitted radius for the first component in the red-shifted part is larger by up to a few arcsec compared to the blue-shifted part. For the second shell component it is the other way around. Furthermore, there is the indication (in correspondence with the channel maps) that for the red-shifted part of quarter Q3 there is no distinct second shell component, as seen for whole quarter Q4.

The fitted peak fluxes, as mentioned above, are only lower limits to the intrinsic total flux of the molecular emission due to the missing flux problem. The relative flux values for the same transition and similar spatial scales are not affected and henceforth are those that we consider in the following. The fitted peak intensity of the first shell component relative to the second component is between a factor of 1.5 and 10.5 when considering the azimuthal average of the emission.

For quarter Q2, we find the largest deviation from this average. For several transitions, mostly of

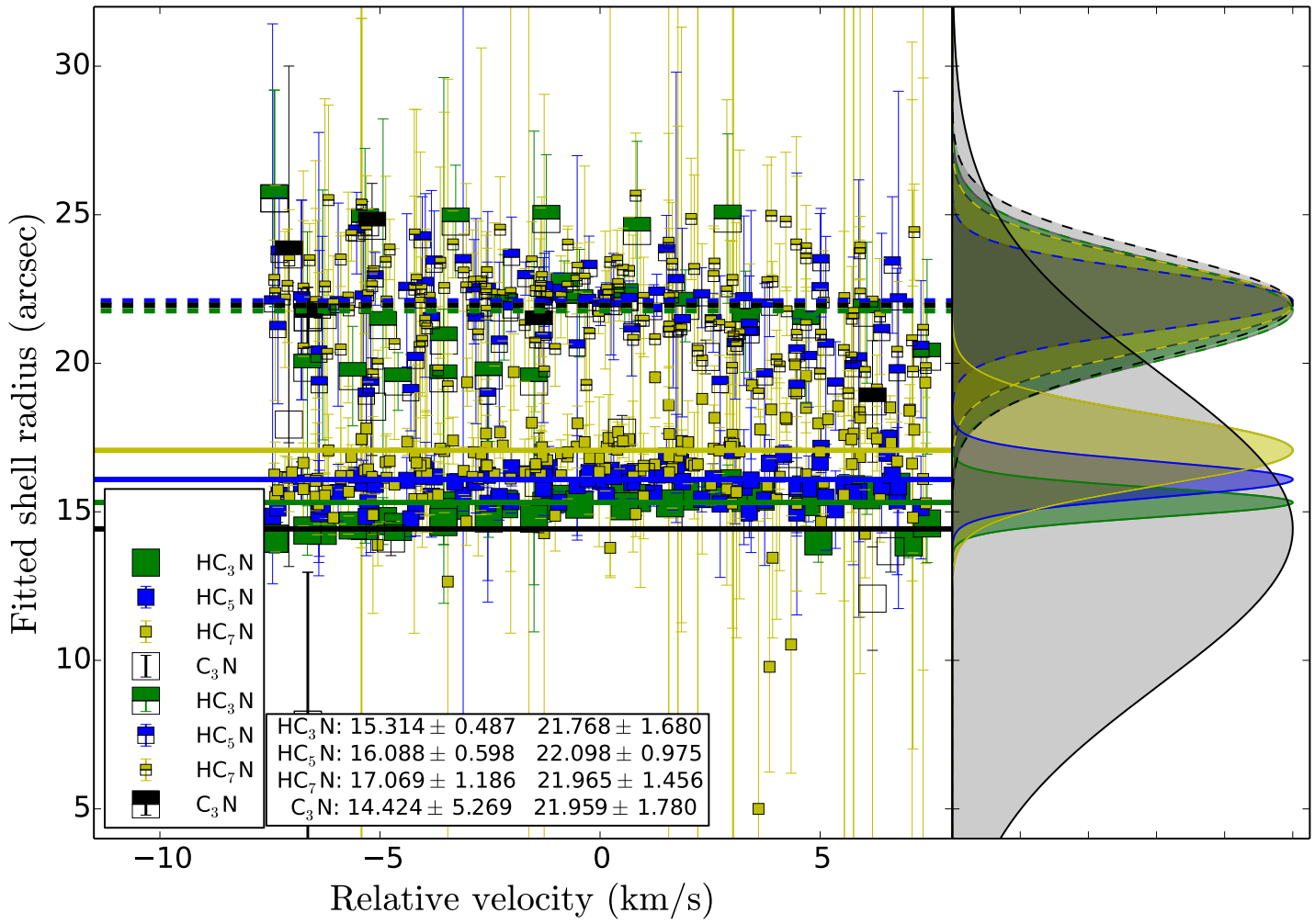

Figure 4.10: Resulting shell radius from the Gaussian fits to the radial profiles of each molecular transition of HC_3N (green), HC_5N (blue), HC_7N (yellow), and C_3N (black) for each channel, hence as a function of velocity (zero means the position of the star), for the azimuthal sum for two shell components. The error bars are the uncertainties from the fitting routine resulting from the flux uncertainties in the original data cube. The lines and the values in the text box are the weighted averages of each molecule for two shell components (Eq. 4.27). These averages are visualized in the histograms on the side. The peak amplitude is arbitrarily set to the same value for each molecule, the width gives the uncertainty of the weighted average (Eq. 4.29).

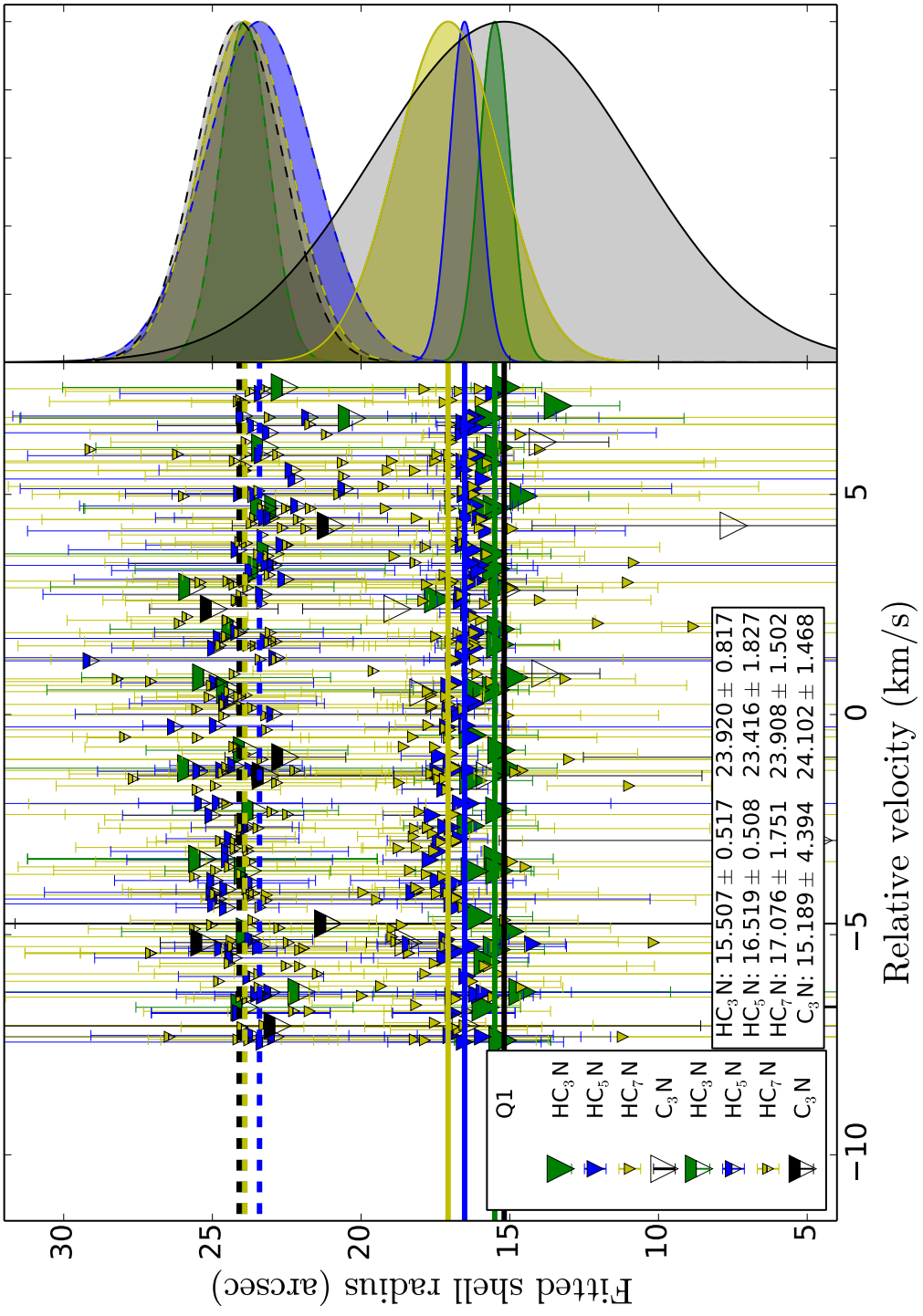

Figure 4.11: As Fig. 4.10 for quarter Q1.

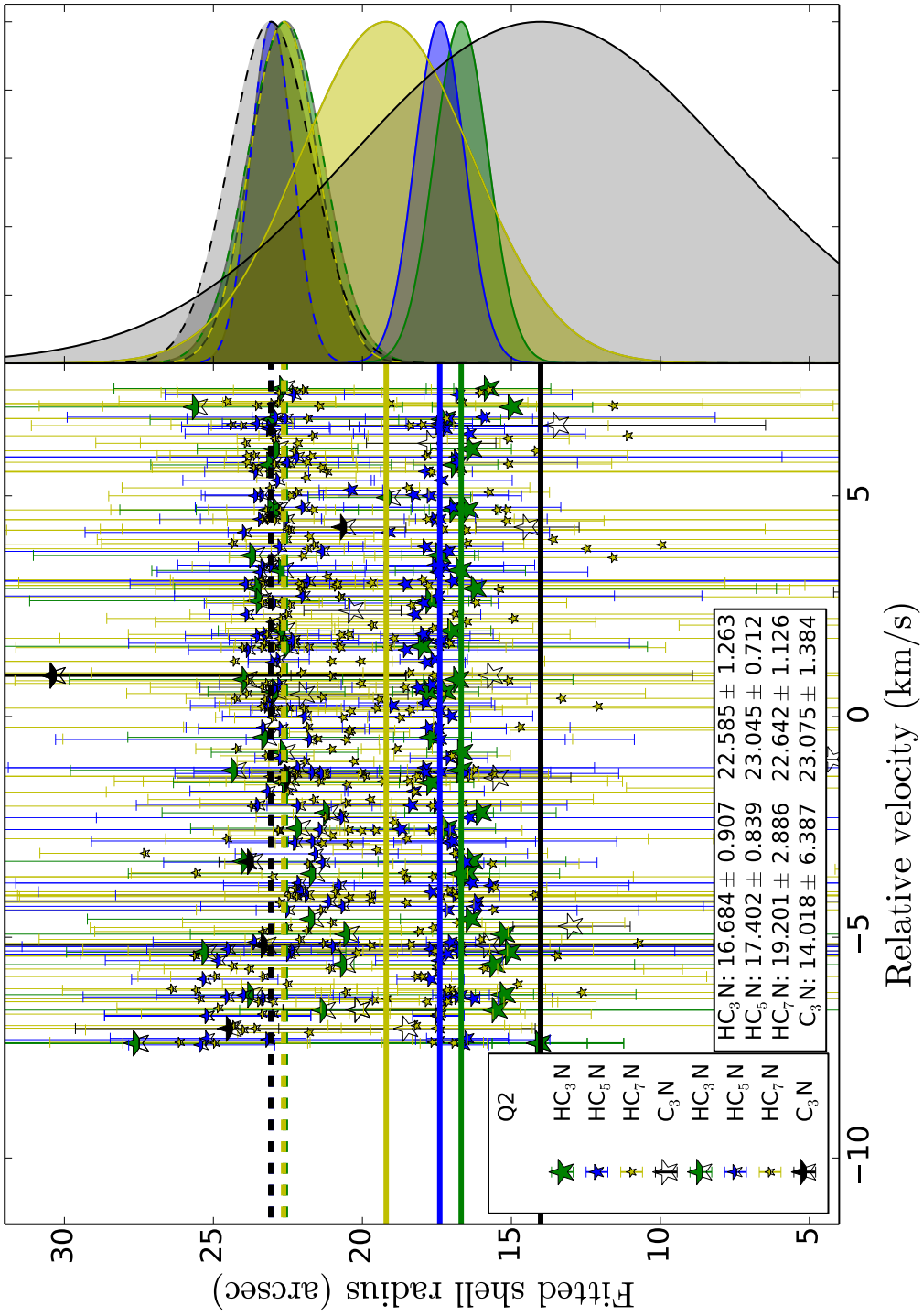

Figure 4.12: As Fig. 4.10 for quarter Q2.

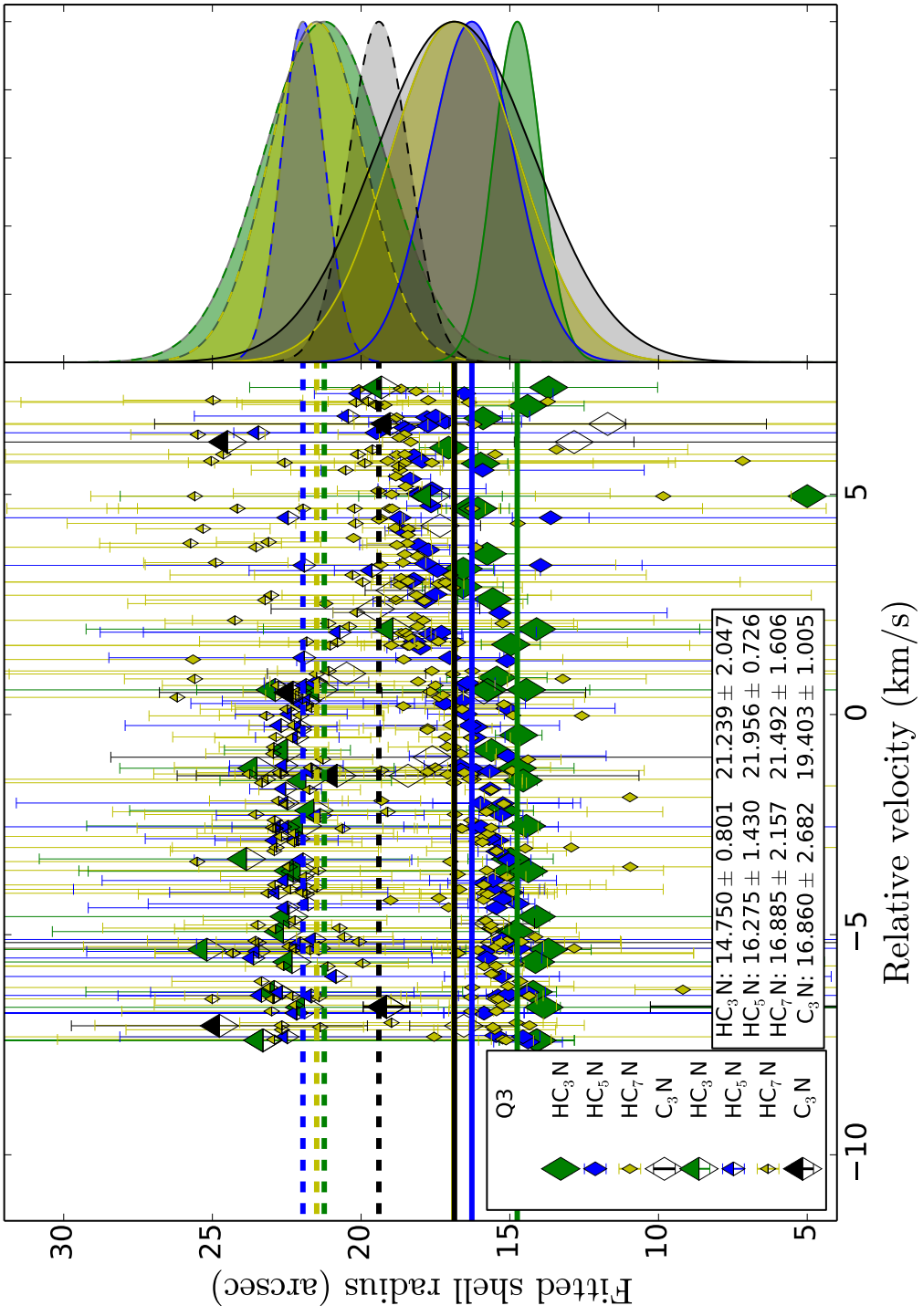

Figure 4.13: As Fig. 4.10 for quarter Q3.

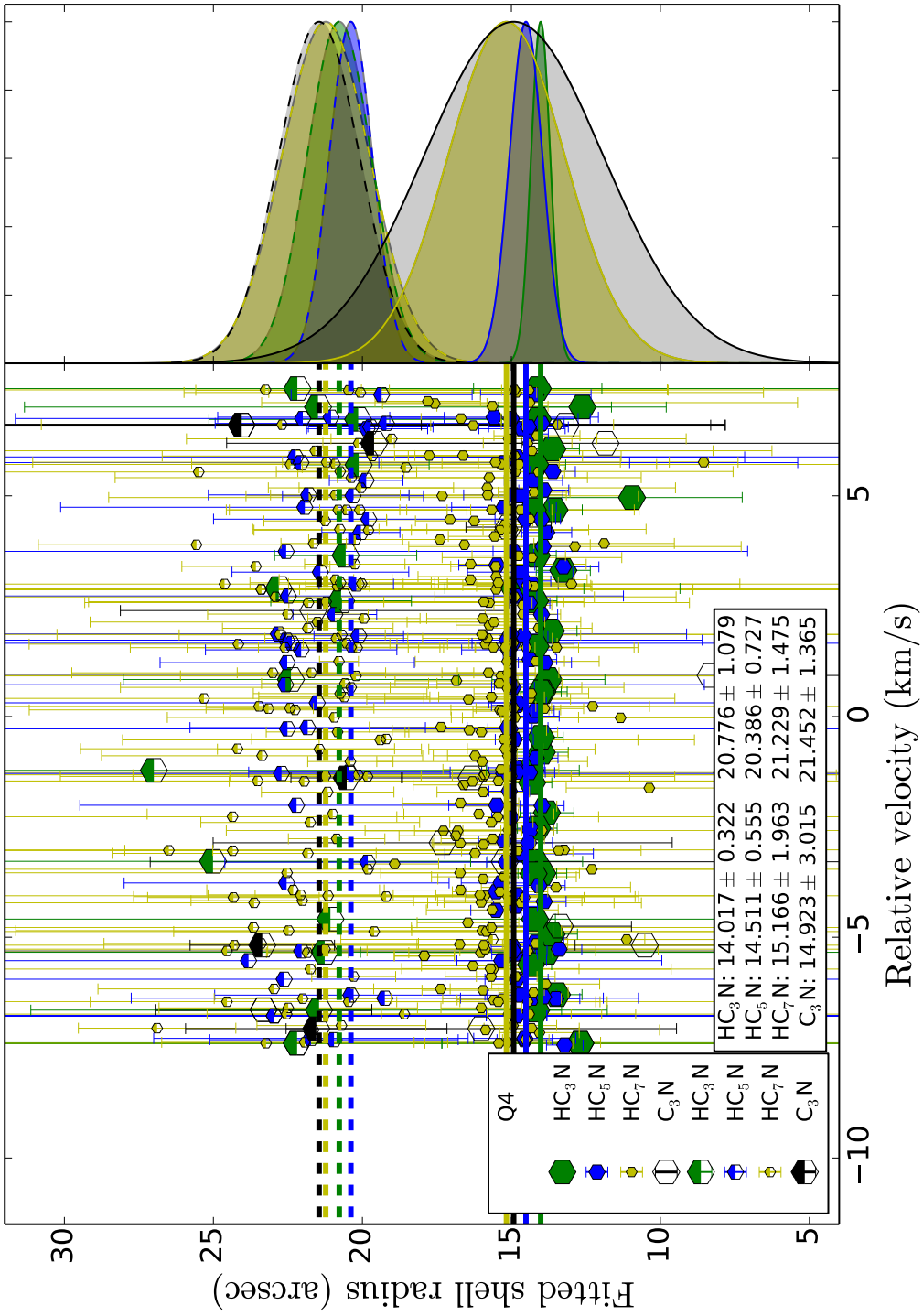

Figure 4.14: As Fig. 4.10 for quarter Q4.

HC_7N, the intensity of the second shell component is brighter than of the first component. Overall, the two shell components in Q2 are closer together and similar in brightness especially compared to those of quarter Q4. For Q4, if there is a second component its brightness is weak compared to the first shell component (cf. e.g. Fig. C.15 and C.17).

The clump in quarter Q1 is the largest clump and it is the main contribution to the flux of the second shell component in this quarter. The distance between the first and second shell component is largest for quarter Q1 compared to the other quarters.

The described behaviors hint that the radial positions and widths of the shell components are affected due to altered UV shielding and penetration in those regions. The complex column density structure of the molecular shells influences the photochemistry. There are several possible reasons and explanations to interpret this, which we consider in the following sections.

4.5 Quantitative comparison of fit results to previous studies

For the quantitative comparison of the findings from the VLA data and previous work on the emission structure of the cyanopolyynes and carbon chains around IRC+10216, we summarize the determined values of the radial positions and widths in angular and absolute units (Tables 4.1 and 4.2). We assume a distance to IRC+10216 of 130 pc.

4.5.1 Shell radii and widths

We focus on the morphology of the molecules in the outer shell that is dominated by photochemistry, analyzed in this thesis. For HC_3N, HC_5N, C_3N, C_4H, and C_6H earlier observational data are available. The results of the Gaussian fits of the azimuthal sum and velocity integrated flux for the radii and shell widths of the first shell component of these species observed with the VLA have good agreement with the previous observational findings within the uncertainties (Tables 4.1 and 4.2). Our study confirms and constrains a second shell component, for the first time, for many transitions of various species.

Particularly, the results of the analysis of HC_3N and HC_5N from (pre-upgrade) VLA data by Dinh-V-Trung & Lim (2008) are in very good correspondence to ours. Furthermore, their study also finds shell components at a radius of about 25 arcsec. Another previous study (Fong et al. 2003) quantitatively constrains several shell components between 20 and 25 arcsec for CO(1-0).

As discussed in detail in Sect. 4.2, the overall qualitative correspondence to the chemical models is very good, with interesting deviations when considering the details. From quantitative results of our analysis and of the chemical models these details become clearer (Tables 4.1 and 4.2).

The expected radial sequence of the cyanopolyynes and carbon chains from the chemical models (e.g. Millar & Herbst 1994) match the described trends in our observational results. However, the radial separation between the molecules is smaller. The exact values of the radial positions is not consistently reproduced by the chemical models for all considered molecules.

The shell widths in the models with a smooth density structure are larger than observed. For the models which implement the shell structure, particularly Cordiner & Millar (2009), the shell widths (fixed to 2 arcsec) are underestimated, when comparing to our fitting results. For the model by Brown & Millar (2003), the width for HC_3N and HC_5N is reproduced within a factor of 2, however, for C_4H and C_6H the modeled width deviates by a factor of $5-6$ from the fitting results of our study. The fitted shell widths for the cyanopolyynes and carbon chains from the VLA data are of similar size within the uncertainties.

When considering the results of the quarters, the substructure becomes more apparent (cf. Figs. 4.11 - 4.14). There are different properties for each quarter. As found in Sect. 4.2.1 and 4.4, the fitted shell radii and widths of quarters Q2 and Q4 deviate the most from the previous observational findings and the azimuthal average of this work (Tables 4.1 and 4.2).

Previous studies also describe the non-regular distribution of the shells (e.g. Mauron & Huggins 2000; Fong et al. 2003; Dinh-V-Trung & Lim 2008), which supports our findings for the different quarters. When calculating the azimuthal averages, the information on the substructural properties are weakened or lost. Therefore it is very valuable and important to perform such a detailed analysis as presented in this thesis.

4.5.2 Shell separation

The spatial separation between the shell components can be translated into a kinematic timescale. For a distance of 130 pc and an expansion velocity of 14.5 km s^{-1}, the separation between the shell components at a radial distance of about 16 and 23 arcsec, hence 7 arcsec, equals a timescale of about 300 years, from our analysis.

Previous detailed studies of the dust shells surrounding IRC+10216 in the optical/infrared regime with the VLT (Mauron & Huggins 2000; Leão et al. 2006) and with the Herschel satellite (Decin et al. 2011) find several shells with different radial distances from the star depending on the position angle, for distances of about 90 up to 320 arcsec. For the spatial separation a wide range of 5 – 20 arcsec (Mauron & Huggins 2000; Leão et al. 2006) and 10 – 35 arcsec (Decin et al. 2011), is found which corresponds to ages of about 200 – 800 and 400 – 1500 years, respectively. It has to be noted that the VLT observations have angular resolutions of the order of 1 arcsec and measure the light scattered from the dust shells, whereas the Herschel observations measure the dust emission directly with angular resolutions of 5.5 to 11 arcsec. Mauron & Huggins (2000) and Leão et al. (2006) observe very thin shells of about 1 to 2 arcsec width, which is much smaller than found in the Herschel observations owing to the angular resolution. The observed dust shells are non-concentric. Several of these thin shells seem to merge with each other, such that no clear regular timescale pattern can be deduced for the whole envelope (Leão et al. 2006). Decin et al. (2011) measure a shell thickness of 5 – 8 arcsec, which compares well to the findings in this work.

Observations in the radio regime, for example, by Fong et al. (2003) of CO(1-0) with an angular resolution of 12 arcsec estimate an intershell spacing timescale of about 1300 up to 2900 years for regions of radial distances to the central star of 26 up to 120 arcsec. They conclude that the width and separation of the shells increase with increasing radial distance. However, for the dust observations this has been examined and could not be confirmed (Leão et al. 2006; Decin et al. 2011).

The VLA observations by Dinh-V-Trung & Lim (2008) find a shell separation between 3 and 9 arcsec, which translates into about 130 to 380 years. Their observations have similar resolution to our VLA observations (2 – 3 arcsec) and match our results well.

Observations of CO(2-1) with the IRAM 30-m telescope (Cernicharo et al. 2015) reveal that this molecule extends to radial distances of up to at least 180 arcsec. The observed morphology of CO is very similar to the shell structure of the dust. This study finds a shell separation which equals a timescale of about 800 years (assuming the same distance and expansion velocity as above) for a beam size of 11 arcsec. They also note that the shell separation might increase with increasing radial distance.

Recent observations of ^{13}CO in the inner CSE of IRC+10216 (inner 6 arcsec) with ALMA hint that the molecular morphology has a spiral structure (Decin et al. 2015). The angular resolution is about

0.2 arcsec. From their observational material a spiral arm spacing of 1.12 arcsec is estimated, which equals a timescale of about 50 years (for a distance to IRC+10216 of 130 pc), which is much smaller than observed in the outer CSE of IRC+10216.

Our study only covers a small spatial range of the outer CSE. From observations of other molecular species and the dust it becomes apparent that there are many more shells at larger radii in the CSE than traced with our study. Furthermore, the morphology might change when the CSE reaches larger radii, maybe with a stronger effect for molecules than for dust. Observations with different angular resolutions might lead to different interpretations of the morphology and its evolution. Molecular shells that appear as broad, mostly regular spherical shells in observations with low resolution, might in fact consist of several thin shells which are very close to each other and might have widened and interacted or merged during the radial expansion, and which can only be resolved in high resolution observations. Therefore it is important to consider a wide range of spatial scales, including the region considered for this work, to draw conclusions on the global morphology, kinematics, and mass loss history of the CSE of IRC+10216 and AGB stars in general, to which this work contributes to.

4.5.3 Density contrast

The density contrast between the molecular shells and the intershell region can be estimated by the observed intensity contrast of the molecular emission (e.g. Brown & Millar 2003). This work finds a contrast of a factor of about 2 up to 8, which corresponds very well to previous observational results (e.g. Mauron & Huggins 2000; Fong et al. 2003; Leão et al. 2006; Dinh-V-Trung & Lim 2008; Cernicharo et al. 2015; Decin et al. 2015). The intensity ratio of the two shell components found by our analysis is between a factor of 2 and 10.

The problem of missing flux has to be considered. The emission from the extended low density components in the intershell region are affected more than the compact thin shells (cf. Sect. 3.6). The shell-intershell contrast therefore might be slightly smaller than measured with the VLA.

4.5.4 Shell asymmetries

Previous observations noticed the shift of the stellar position against the center of the molecular emission by $2-3$ arcsec to the southwest (e.g. Fong et al. 2003; Cernicharo et al. 2015), as found in this work. The southwest part of the molecular shell is in quarter Q4 in our analysis. Therefore, this shift is the main reason that the fitted radii of the molecular emission are largest for quarter Q2 and smallest for quarter Q4.

Also the large scale asymmetry of the shell has been observed and analyzed. In their VLT data Leão et al. (2006) remarked that the southwest part has less shells and arcs than the northeast part of the shell. This has been supported by the observations of the dust emission (Decin et al. 2011). The same has been reported for the molecular emission of CO(2-1) (Cernicharo et al. 2015) and the emission of HC_3N and HC_5N (Dinh-V-Trung & Lim 2008). The emission maps and the fitting analysis discussed in this thesis confirm the earlier observations.

Furthermore, there has been a decrease in molecular emission observed on an axis along a position angle of about 20 degrees (counterclockwise from north) (cf. Figs. 2.3 and 2.4, e.g. Lucas et al. 1995; Mauron & Huggins 2000; Leão et al. 2006; Dinh-V-Trung & Lim 2008). This is supported by several transitions in our VLA data. The innermost emission around the central star has a bipolar shape with a position angle of about 22 degrees. The southern part is brighter by 40% than the northern part (Leão et al. 2006). Models of the inner CSE of IRC+10216 taking mostly the optical, near-infrared and ALMA

observations into account (Men'shchikov et al. 2001; Decin et al. 2015) suggest that these regions are outflow cavities due to a central binary system, which has its orbital plane perpendicular to this angle. External effects might additionally influence the molecular shell geometry.

It becomes evident that neither the models assuming a simple smooth density structure nor the more current models including density enhancements with a regular shell separation and width represent the observed molecular shell geometry completely.

Possible explanations for the observed and described CSE morphology are related to non-isotropic external UV irradiation and photodissociation, hydrodynamical effects due to a central binary system, a variable mass loss history maybe due to a magnetic cycle at the surface of the star, and more, which are further discussed in Chapter 6.

Regarding the chemistry, the current models do not yet include the influence by dust grains directly (e.g. grain-surface reactions) and the porosity or clumpiness of the medium which leads to a stronger UV penetration at radii smaller than previously assumed. Furthermore, the possibility of UV radiation by an internal source (e.g. white dwarf companion) has not been computed yet, but is starting to being considered (Millar 2016). The external UV field is assumed to be isotropic in the models, which might not be accurate.

Accounting for the deviations from symmetry and better resembling the intrinsic molecular shell geometry together with an increased understanding of the dominating chemical reactions will lead to an improvement of future models of the chemical and physical structure of IRC+10216's envelope.

Table 4.1: Radial positions of cyanopolyynes and carbon chains around IRC+10216 found in chemical models, observational studies, and this work. From the VLA data the weighted molecular averages from the radial profiles of the azimuthal sum and of the quarters of the velocity integrated flux of the first shell component are shown. All values are in angular (arcsec) and absolute (cm) units assuming a distance to IRC+10216 of 130 pc. Those values preceded by "∼" have been read off from the radial profiles in the according reference.

Molecule	Radius from chemical models						Radius from observations		This work					
	(10^{16} cm)			(arcsec)			(10^{16} cm)	(arcsec)	(10^{16} cm)	(arcsec)	Q1	Q2	Q3	Q4
HC_3N	3.9[a]	3.5[b]	2.9[c]	20.0[a]	18.0[b]	15.0[c]	2.9[d,f]	15.0[d,f]	2.9± 0.1	15.1 ± 0.1	15.5 ± 0.3	16.7 ± 0.5	14.6 ± 0.3	14.1 ± 0.2
HC_5N	5.1[a]	4.0[b]	2.9[c]	26.2[a]	20.6[b]	15.0[c]	3.1[f]	16.0[f]	3.1± 0.1	15.9 ± 0.3	16.5 ± 0.1	17.2 ± 0.2	16.8 ± 0.5	14.8 ± 0.4
HC_7N	5.7[a]	...	...	29.2[a]	...	...	...	...	3.3± 0.2	17.0 ± 1.2	17.2 ± 0.4	20.0 ± 1.8	16.8 ± 0.9	15.1 ± 0.7
C_3N	8.7[a]	...	...	44.6[a]	...	...	3.5[d]	18.0[d]	3.6± 0.2	18.4 ± 1.1	17.6 ± 1.2	21.4 ± 0.7	18.4 ± 0.4	16.7 ± 0.5
C_4H	5.4[a]	∼6.6[b]	2.9[c]	27.7[a]	∼33.9[b]	15.0[c]	3.1[e]	16.0[e]	3.1± 0.2	15.9 ± 1.2	15.5 ± 1.2	18.6 ± 1.1	13.1 ± 4.2	16.3 ± 0.5
C_6H	∼6.3[a]	∼7.9[b]	2.9[c]	∼32.4[a]	∼40.6[b]	15.0[c]	3.1[e]	16.0[e]	3.3± 0.3	16.9 ± 1.5	16.4 ± 1.4	18.1 ± 1.7	16.1 ± 2.1	14.3 ± 0.9
C_6H^-	...	...	2.9[c]	...	...	15.0[c]	...	...	3.2± 0.4	16.3 ± 1.8	14.3 ± 1.1	13.0 ± 1.8	16.4 ± 1.6	15.8 ± 0.3

References: [a] Millar & Herbst (1994), [b] Brown & Millar (2003), [c] Cordiner & Millar (2009), [d] Bieging & Tafalla (1993), [e] Guélin et al. (1999), [f] Dinh-V-Trung & Lim (2008)

Table 4.2: Shell widths of cyanopolyynes and carbon chains around IRC+10216 found in chemical models, observational studies, and this work. From the VLA data the weighted molecular averages from the radial profiles of the azimuthal sum and of the quarters of the velocity integrated flux of the first shell component are shown. All values are in angular (arcsec) and absolute (cm) units assuming a distance to IRC+10216 of 130 pc. Those values preceded by "∼" have been read off from the radial profiles in the according reference.

Molecule	Width from chemical models						Width from observations		This work					
	(10^{16} cm)			(arcsec)			(10^{16} cm)	(arcsec)	(10^{16} cm)	(arcsec)	Q1	Q2	Q3	Q4
HC_3N	3.0[a]	2.5[b]	0.4[c]	15.4[a]	12.9[b]	2.0[c]	1.9[d]	10.0[d]	1.3 ± 0.3	6.5 ± 1.4	6.0 ± 1.0	6.4 ± 1.1	6.6 ± 2.3	5.6 ± 0.5
HC_5N	5.4[a]	2.5[b]	0.4[c]	27.7[a]	12.9[b]	2.0[c]	1.8[f]	9.0[f]	1.0 ± 0.2	5.1 ± 1.0	5.4 ± 0.7	5.0 ± 0.7	5.7 ± 1.3	4.7 ± 0.9
HC_7N	6.0[a]	...	...	30.8[a]	...	...	...	...	1.1 ± 0.4	5.9 ± 2.0	5.0 ± 1.1	6.7 ± 1.5	5.3 ± 1.4	4.4 ± 1.4
C_3N	7.2[a]	...	...	36.9[a]	...	...	1.9[d]	10.0[d]	1.4 ± 0.2	7.0 ± 0.8	5.6 ± 2.2	7.3 ± 0.8	6.2 ± 0.8	5.9 ± 1.0
C_4H	3.6[a]	∼9.4[b]	0.4[c]	18.5[a]	∼48.5[b]	2.0[c]	0.5[e]	3.0[e]	1.6 ± 0.9	8.2 ± 4.4	6.5 ± 3.7	7.3 ± 1.7	8.2 ± 4.6	4.6 ± 1.6
C_6H	∼10.0[a]	∼6.8[b]	0.4[c]	∼51.4[a]	∼35.2[b]	2.0[c]	0.5[e]	3.0[e]	1.4 ± 0.3	7.0 ± 1.5	8.0 ± 2.7	6.8 ± 1.1	7.1 ± 2.0	6.6 ± 2.1
C_6H^-	...	...	0.4[c]	...	...	2.0[c]	...	...	2.3 ± 0.5	11.8 ± 2.5	7.9 ± 1.6	5.8 ± 2.2	6.8 ± 0.6	6.5 ± 2.1

References: [a] Millar & Herbst (1994), [b] Brown & Millar (2003), [c] Cordiner & Millar (2009), [d] Bieging & Tafalla (1993), [e] Guélin et al. (1999), [f] Dinh-V-Trung & Lim (2008)

CHAPTER 5

Physical analysis

With the determined values on the shell geometry and together with further assumptions on the molecular emission, we are able to perform a physical analysis of the CSE of IRC+10216. We compute the column densities and fractional abundances of the brightest transitions in our survey of HC_3N and HC_5N assuming local thermal equilibrium in the CSE. These calculations are only approximative estimates in comparison to a complete shell model including radiative transfer modeling.

5.1 Molecular column densities

The column density of a molecular transition gives the number of molecules per unit area (cm^{-2}) along the line of sight. With knowledge on the observed molecule, in the following we deduce the excitation temperature and the total number of molecules in the considered region with the method of the rotation-temperature diagram (Sect. 1.3.2.2 and 1.3.2.3).

For such calculations the emission is usually assumed to be optically thin, uniform and extended (filling the beam, such that the beam filling factor is 1). We assume that all of the emission originating from a certain velocity component is located in the same plane in the sky. The column density of the upper energy level for a certain transition then is

$$N_u = \frac{8\pi k \nu^2}{hc^3 A_{ul}} W \,, \tag{5.1}$$

where k is the Boltzmann constant, ν is the rest frequency of the transition, h is the Planck constant, c is the speed of light, A_{ul} is the Einstein coefficient of the transition, and W is the measured integrated intensity of the transition:

$$W = \int T_{\rm mb}\, dv = \sum_i T_{{\rm mb},i}\, \Delta v \,, \tag{5.2}$$

where $T_{{\rm mb},i}$ is the main-beam temperature in each velocity channel i with the channel width Δv. The considered emission lines of HC_3N and HC_5N are optically thin. This is indicated by the shape of the spectral lines and because the intensity ratio of the main molecule and its isotopologues roughly equals the abundance ratio of $^{12}C/\,^{13}C$ of 45 (Agúndez et al. 2012).

The observed emission is resolved by the VLA beam and depicts the geometry of a hollow sphere. To

fulfill the other assumptions, we only use the emission which is concentrated in a small area, due to the projection effect, and which should be uniform over this extent: the emission from the shell poles. This part of the molecular emission is the most blue- and red-shifted part in the peaks of the spectral line. For the emission from the rest of the shell, the simple assumptions are not valid because of the spherical shell geometry which is not parallel to the plane of sky. The emission of one radial velocity component might spread over several channels of the data cube.

Furthermore, the problem of missing flux is most severe for the channels close to the stellar velocity, because it is very extended compared to the beam. The emission furthest from the stellar velocity almost no flux is missing (Sect. 3.6). Most of the measured flux is concentrated in these parts, has the highest signal-to-noise ratio, and approximates the total amount of the integrated intensity of the transition.

We assume that the molecular shell is spherically symmetric, and therefore the flux from both poles originates from the same radial distance. For this calculation we ignore all the deviations from symmetry in the substructure, which have been noted earlier. To calculate more accurate abundances, a detailed radiative transfer modeling of the molecular shell would be necessary.

We use the emission within one beam from the velocity components in the data cubes with $-44 < v_{\mathrm{ch}} < -35\,\mathrm{km\,s^{-1}}$ and $-17 < v_{\mathrm{ch}} < -8\,\mathrm{km\,s^{-1}}$, so a linewidth of $9\,\mathrm{km\,s^{-1}}$ each. We calculate the mean of the integrated intensity from both peaks of the spectral line, assuming that the intensity in both parts is roughly the same. The uncertainty of the column density then is

$$\Delta N_u = \frac{8\pi k \nu^2}{hc^3 A_{ul}} \Delta W_{\mathrm{mean}} \text{ , with} \tag{5.3}$$

$$\Delta W_{\mathrm{mean}} = \sqrt{\left(\frac{1}{2}\,\sqrt{N_{\mathrm{ch},1}}\,\sigma_{\mathrm{rms},1}\,\Delta v\right)^2 + \left(\frac{1}{2}\,\sqrt{N_{\mathrm{ch},2}}\,\sigma_{\mathrm{rms},2}\,\Delta v\right)^2} + \sigma_{\mathrm{calibration}}\,, \tag{5.4}$$

where N_{ch} is the number of channels in each shell pole, σ_{rms} is the root-mean square-root error estimated from the emission line free channels of the CLEANed image of the transition, and $\sigma_{\mathrm{calibration}}$ is the uncertainty from the flux calibration, which is about 20% (Sect. 3.3). The resulting column densities for each covered transition of HC_3N and HC_5N are shown in Table 5.1.

In the following we determine the total column density of HC_3N and HC_5N with the rotation-temperature diagram method (Sect. 1.3.2.3). We utilize the following equation

$$\ln\left(\frac{N_u}{g_u}\right) = \ln\ N_{\mathrm{tot}} - \ln\ Q(T) - \frac{E_u}{kT} \text{ , with} \tag{5.5}$$

$$\Delta \ln\left(\frac{N_u}{g_u}\right) = \frac{\Delta W_{\mathrm{mean}}}{W_{\mathrm{mean}}} \tag{5.6}$$

and fit a linear function of the shape $y = b + mx$ to it, where b is the y-intercept and the m is the slope, such that

$$T_{\mathrm{rot}} = -m^{-1} \text{ , with} \tag{5.7}$$

$$\Delta T_{\mathrm{rot}} = \Delta m\, m^{-2} \text{ , and} \tag{5.8}$$

Table 5.1: The column densities of the upper energy level u for each transition of HC_3N and HC_5N determined from the mean integrated intensity W_{mean} from the from the VLA data determined with the approximations mentioned in the text.

Transition	W_{mean} (K km s^{-1})	ΔW_{mean} (K km s^{-1})	N_u (10^{14} cm^{-2})	ΔN_u (10^{14} cm^{-2})
HC_3N(2-1)	12.985	2.949	21.390	4.858
HC_3N(3-2)	34.326	7.246	35.183	7.427
HC_3N(4-3)	27.544	5.963	20.417	4.420
HC_5N(8-7)	6.794	1.575	6.036	1.399
HC_5N(9-8)	8.182	1.919	6.420	1.505
HC_5N(10-9)	7.974	1.946	5.600	1.367
HC_5N(11-10)	8.626	2.148	5.485	1.365
HC_5N(12-11)	11.811	2.835	6.859	1.646
HC_5N(13-12)	7.587	1.989	4.054	1.063
HC_5N(14-13)	13.462	3.160	6.662	1.564

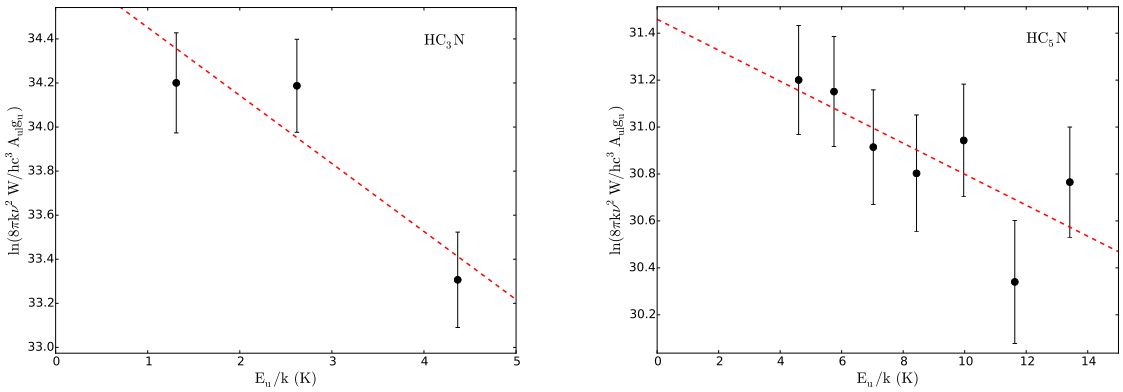

Figure 5.1: The rotational-temperature diagram of HC_3N and HC_5N for the VLA data to determine the rotational temperature and the total column density of these molecules. The dashed red line shows the linear fitting function. The results of the fit are given in the text and in Table 5.2.

$$N_{tot} = \exp(b + \ln Q) \text{ , with} \tag{5.9}$$

$$\Delta N_{tot} = \exp(b + \ln Q)\ \Delta b\ . \tag{5.10}$$

We use the *Python* fitting routine *curve_fit* (cf. Sect. 4.3) taking into account the uncertainties of the determined column densities ΔN_u. The values for Δm and Δb result from the fitting routine. The resulting rotation-temperature diagrams of HC_3N and HC_5N are shown in Figure 5.1.

For HC_3N there are only three transitions covered, where one is from a dataset with difficult calibration. Therefore, the fitting results of T_{rot} and N_{tot} have to be taken with caution. The determined rotational temperature of 3.2 ± 1.1 K is much lower than what previous studies have found, e.g. 24.7 ± 18.5 K (very high uncertainty, Gong et al. 2015) and 26 K (no value on uncertainty given, Kawaguchi et al. 1995).

For HC_5N we cover seven transitions, however, the range of energy levels we cover is still very small. The transition HC_5N(13-12) has much lower intensity than expected, probably due to a calibration

Table 5.2: The total molecular column densities of HC_3N and HC_5N determined with the rotational-temperature diagram from the VLA data, with the rotational temperature from a previous study (a) in comparison with the results from previous observational studies (a, b) and from chemical models (c, d, e). References: a) Kawaguchi et al. (1995), b) Gong et al. (2015), c) Millar & Herbst (1994), d) Brown & Millar (2003), e) Cordiner & Millar (2009).

Molecule	N_{tot} (10^{14} cm^{-2})		N_{tot} (10^{14} cm^{-2})				
	This work (Fig. 5.1)	with T_{rot} from a)	a)	b)	c)	d)	e)
HC_3N	86.48 ± 27.05	40.50	17.0	14.0	26.0	14.0	6.7
HC_5N	5.43 ± 1.51	2.43	2.3	4.6	9.8	4.5	35.0

problem. Our analysis results in a rotational temperature of 15.1 ± 7.0 K, which compares reasonably to previous determinations of 18.8 ± 1.3 K (Gong et al. 2015) and 29 ± 6 K (Kawaguchi et al. 1995).

For the calculation of the total column density the fitting results of the rotational temperature from our VLA data have several uncertainties. Therefore we also consider the excitation temperatures from Kawaguchi et al. (1995) to deduce the molecular column density from our VLA data and compare the results (Tab. 5.2). These excitation temperatures for HC_3N and HC_5N are very similar and close to the ambient kinetic temperature of about 20 K (cf. Sect. 5.3). The emission of these two molecules originates from a very similar region in the CSE.

The column densities of HC_3N from the VLA data differ by at least a factor of two to the values from the literature. As mentioned above, the determination is rather uncertain because the VLA data only covers three data points in a very narrow energy range. The results for HC_5N are corresponding well to the previous studies, except for e) Cordiner & Millar (2009). This probably is due to a higher initial abundance of the parent species C_2H_2 and HCN in the model, which results in a lower column density for HC_3N and a higher one for HC_5N compared to the other models.

5.2 Molecular abundances

The molecular abundance is the number of molecules per unit volume (cm^{-3}) relative to H_2. Its determination requires knowledge on the density and velocity structure of the gas, the location of the molecule, etc., in the CSE of IRC+10216. From the continuity equation, assuming a smooth outflow from the star which has decreasing density with increasing radius, the number density of the H_2 gas is

$$n_{H_2} = \frac{\dot{M}_{gas}}{4\pi r^2 \mu m_{H_2} v_{exp}} \text{ , with} \tag{5.11}$$

$$\Delta n_{H_2} = \frac{\dot{M}_{gas}}{4\pi \mu m_{H_2} v_{exp}} \frac{2\Delta r}{r^3} \text{ ,} \tag{5.12}$$

where $\dot{M}_{gas} = 2 \times 10^{-5}\,M_\odot\,yr^{-1}$ is the gas mass loss rate of IRC+10216, r is the radial location of the considered molecules HC_3N and HC_5N, respectively, $\mu = \sum_i x_i m_i / m_{H_2} = 1.4$ is the mean molecular weight taking the whole gas content (H_2, He, CO) into account, $m_{H_2} = 2 \times m_H = 2 \times 1.007825$ u $= 3.347 \times 10^{-27}$ kg is the molecular weight of the H_2 molecule, and $v_{exp} = 14.5$ km s^{-1} is the constant expansion velocity of the gas.

For the radial location of HC_3N and HC_5N we take the results of the Gaussian fits to the VLA data from the first shell component of the azimuthal sum of the velocity integrated flux (Tab. 4.1). The intensity from the first shell component is the dominating part for most transitions.

The number density of the considered molecule (A) is

$$n_A = \frac{N_{\mathrm{tot}}}{s} \text{ , with} \tag{5.13}$$

$$\Delta n_A = \sqrt{\left(\frac{\Delta N_{\mathrm{tot,\,A}}}{s}\right)^2 + \left(-\frac{N_{\mathrm{tot,\,A}}}{s^2}\Delta s\right)^2} \text{ ,} \tag{5.14}$$

where s is the path length of the molecular emission along the line of sight, hence the molecular shell width. For the shell width and its uncertainty we also take the values determined from the Gaussian fits to the VLA data.

For these calculations, we assume spherical symmetry for the hollow sphere and a constant shell width. We knowingly neglect any substructure and asymmetries. We assume that the values from the Gaussian fits, which take only emission close to the stellar velocity into account, also apply for the emission components furthest from the stellar velocity. Furthermore, as a first approximation we assume that the first shell component dominates in terms of density (as it does in terms of intensity by at least a factor of 2 up to 10) and therefore we only consider the width of the first shell component and ignore the second shell component for the calculation of the molecular abundance.

The fractional molecular abundance then is

$$f_A = \frac{n_A}{n_{\mathrm{H_2}}} \text{ , with} \tag{5.15}$$

$$\Delta f_A = \sqrt{\left(\frac{\Delta n_A}{n_{H_2}}\right)^2 + \left(\frac{n_A}{n_{\mathrm{H_2}}^2}\Delta n_{\mathrm{H_2}}\right)^2} \text{ .} \tag{5.16}$$

Assuming a smooth outflow, the number density of H_2 at a radius of about 3×10^{16} cm is about 2×10^4 cm^{-3} (Eq. 5.11), which is the same as for the smooth density profile of e.g. the chemical model of Cordiner & Millar (2009). For the maximum number density of HC_3N and HC_5N they find about 0.04 and 0.2 cm^{-3}, respectively, from the modeled radial profiles with a smooth density structure. These results are very different from our findings, which might be because the assumption of a smooth outflow is not approximating the intrinsic density structure of the CSE well enough.

Comparing our results for the abundances to previous determinations from observational studies and chemical models, we find that for HC_3N the difference is about one order of magnitude even for the calculations with the better constrained rotational temperature (Tab. 5.3). For HC_5N the determined abundances from our VLA data and previous studies correspond better. As mentioned above, the column density is better constrained for HC_5N than for HC_3N.

The chemical models we compare to (Millar & Herbst 1994; Brown & Millar 2003) use very similar chemical networks but different assumptions on the density structure of the CSE. The latter one is including density-enhanced shells in the model. However, for HC_5N this does not have a large effect on the modeled abundance. Our value for the HC_5N abundance compares quite well with the findings from these chemical models, given that our estimate has several approximative assumptions and only covers a small range of energy levels. The value of the observational study from Gong et al. (2015) deviates by an order of magnitude from our result, which might be due to different assumptions on the molecular

Table 5.3: The number densities and fractional abundances of HC_3N and HC_5N determined from the VLA data (Tab. 5.2) in comparison with the results from previous observational studies (b) and from chemical models (c, d). The number density of H_2 is determined from Eq. 5.11 at the radial locations r of the molecules from the Gaussian fit results. The abundance from the VLA data when including a density-enhancement with a density of 10×10^4 cm^{-3} is also shown (Sect. 5.4). For the number densities the shell widths s from the Gaussian fit results is assumed (cf. Tables 4.1 and 4.2). References: a) Kawaguchi et al. (1995), b) Gong et al. (2015), c) Millar & Herbst (1994), d) Brown & Millar (2003).

Molecule	r ($''$)	s ($''$)	n_{H_2} (10^4 cm^{-3})	n_A (10^{-2} cm^{-3})		f_A ($\times 10^{-6}$)				
				This work	T_{rot} from a)	This work	T_{rot} from a)	b)	c)	d)
HC_3N	15.1	6.5	2.64±0.18	66.53±25.86	31.15	25.19±9.95	11.80	0.67	1.58	2.30
			10.00	66.53±25.86	31.15	6.65±2.59	3.12			
HC_5N	15.9	5.1	2.31±0.15	5.43±1.86	2.43	2.35±0.82	1.05	0.22	1.00	1.10
			10.00	5.43±1.86	2.43	0.54±0.19	0.24			

extent (up to 30 arcsec as the radius).

5.3 Excitation analysis

For a crude excitation analysis, we consider the critical densities of the covered transitions of HC_3N and HC_5N and examine the conditions of their excitation.

The critical density is described by the ratio of the Einstein coefficient A_{ul} and the collisional excitation rate C_{ul} of the transition at a certain kinetic temperature of the gas:

$$n_{\rm crit} = \frac{A_{ul}}{C_{ul}} \,, \tag{5.17}$$

assuming that the molecular transitions are only collisionally excited.

The collisional rate coefficients are determined by extensive theoretical calculations for collisions of the molecule with He atoms and H_2 molecules. For HC_3N these values are tabulated on the Leiden Atomic and Molecular Database (LAMDA, Green & Chapman 1978; Schöier et al. 2005). For HC_5N the collisional rate coefficients are not available yet. To estimate these coefficients one can extrapolate from HC_3N by taking into account the larger mass and size of HC_5N, and therefore larger cross section, compared to HC_3N. So those rotational transitions with the same J-level at the same kinetic temperature have to be scaled by a factor of 1.5 to get the coefficients for HC_5N from HC_3N (Chapman et al. 2009).

Considering previous studies on the radial kinetic temperature structure of IRC+10216 (e.g. Crosas & Menten 1997), we assume a kinetic temperature of about 15 − 20 K at a radius of 3×10^{16} cm (Fig. 5.2, left). This kinetic temperature and our determination of the rotational temperature from HC_5N from the VLA data of 15.1 ± 7.0 K compare well. The fact that these two temperatures are approximately equal supports that our assumption of LTE conditions is valid for this region in the CSE. The density structure used for the models are either smoothly decreasing with r^{-2} or with additional enhancements at certain radii of a density greater by a factor of 5 than the smooth function (Fig. 5.2, right).

A further check for LTE is how the H_2 density and the critical density of the molecular transitions compare to each other. If $n_{H_2} > n_{\rm crit}$ the molecular transitions in the CSE are excited under LTE

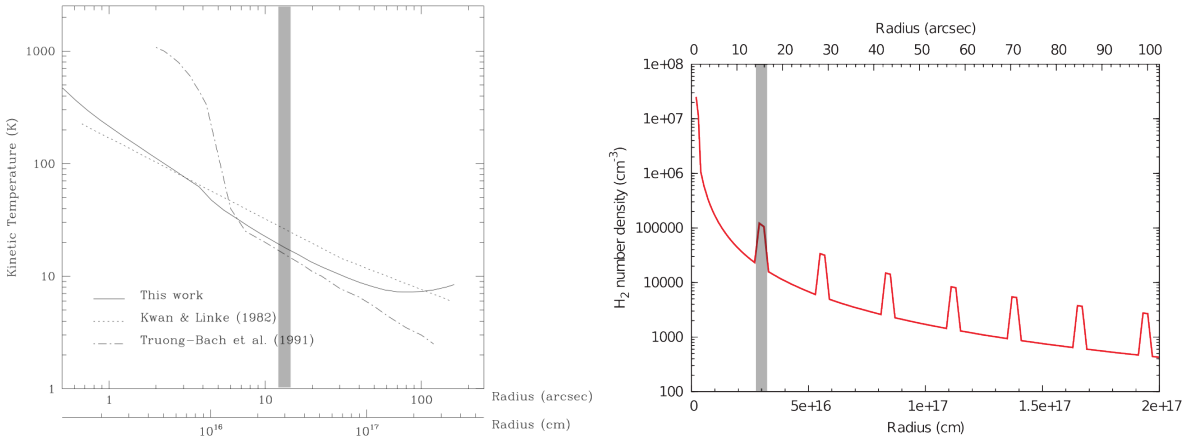

Figure 5.2: The kinematic temperature (left) and H_2 density structure (right) of IRC+10216 as a function of radial distance to the star from the models Crosas & Menten (1997, left) and Cordiner & Millar (2009, right), respectively. The grey shaded area around a radius of 3×10^{16} cm is the region we consider in our calculations.

Table 5.4: The critical densities of HC_3N and HC_5N for a kinetic temperature of T_{kin} = 20 K (Fig. 5.2). The radial locations r of the molecules are determined from the Gaussian fit results for the azimuthal sum of the velocity integrated flux.

Transition	r (10^{16} cm)	A_{ul} (10^{-6} s $^{-1}$)	C_{ul} (10^{-10} cm^{-3} s $^{-1}$)	n_{crit} (10^3 cm^{-3})	n_{H_2} (10^3 cm^{-3})
HC_3N(2-1)	2.93	0.39	0.97	4.03	25.88
HC_3N(3-2)	2.95	1.41	1.20	11.77	25.59
HC_3N(4-3)	2.89	3.47	1.20	28.94	26.54
HC_5N(8-7)	3.17	0.99	1.65	6.02	22.14
HC_5N(9-8)	3.13	1.42	1.80	7.90	22.64
HC_5N(10-9)	3.12	1.96	1.65	11.89	22.84
HC_5N(11-10)	3.07	2.62	1.65	15.89	23.57
HC_5N(12-11)	2.97	3.42	1.65	20.71	25.25
HC_5N(13-12)	2.95	4.36	1.50	29.05	25.44
HC_5N(14-13)	3.00	5.46	1.95	27.99	24.68

conditions. The critical densities of the transitions of HC_3N and HC_5N covered by our VLA data are shown in Table 5.4. The radial positions of these transitions are determined by the Gaussian fits of the azimuthal sum of the velocity integrated flux. For most transitions the assumption of LTE is certainly valid. Only for transitions from the highest J-levels, HC_3N(4-3), HC_5N(13-12), and HC_5N(14-13), LTE cannot be directly assumed because these have slightly larger critical densities than the corresponding H_2 density. The values for the densities are very similar and the comparison can be influenced by a slight change of the radial locations of the molecule or of the gas density.

5.4 Density-enhanced shell structure

For the above calculations of the molecular abundances of HC_3N and HC_5N we assume a smooth density structure, which does not fully describe the observed density structure of IRC+10216.

When we increase the H_2 number density from 2×10^4 cm^{-3} to 1×10^5 cm^{-3} at a radius of 3×10^{16} cm (Fig. 5.2) to approximate a density-enhanced shell, as done by Cordiner & Millar (2009), the fractional abundances of HC_3N and HC_5N decrease by about a factor of 5 accordingly: $(6.65 \pm 2.59)\times10^{-6}$ cm^{-3} and $(5.43 \pm 1.86)\times10^{-7}$ cm^{-3}, respectively (Tab. 5.3). The value of the observed molecular column density from the VLA data remains the same. The density enhancement in the shell is estimated by the observed density contrast between shell and intershell medium, which is about $3-10$ (also found in this work).

In the model by Cordiner & Millar (2009), the column density of HC_3N changes from 4.8×10^{14} cm^{-2} to 6.7×10^{14} cm^{-2} when including density-enhanced shells on top of the smooth outflow. For HC_5N the column density is 2.7×10^{15} cm^{-2} for a smooth density structure and 3.5×10^{15} cm^{-2} for a shell structure. So the column densities of HC_3N and HC_5N are larger when considering the density-enhanced shells. This means that the molecular column density or the number density as well as the gas number density in such shells are increased in the model. Therefore, the resulting fractional abundance in the model is not altered strongly by the different assumptions on the structure, unless other parts in the modeling are influenced by the increased density, i.e. the reaction rates. The determination of the abundance and density structure independent of each other is very difficult.

Similarly, for our examination of the LTE conditions, we find that when assuming an increased H_2 density of 1×10^5 cm^{-3}, LTE is much easier maintained in the considered region.

We consider the excitation conditions within the second shell component, regarding the lower density, from the intensity ratio of the first and second shell which is about $2-10$. For an order of magnitude lower H_2 density for the smooth CSE model (cf. Tab. 5.4), the critical densities would be larger than the H_2 densities and the molecular transitions would not be excited under LTE conditions. However, for the density-enhanced model (Fig. 5.2, right) the H_2 densities are still high enough to maintain LTE conditions in the second shell. Therefore, our excitation analysis based on the LTE assumption (Sect. 5.1) is expected to deliver reliable results.

While a more accurate complete shell modeling including radiative transfer is out of the scope of this thesis, these calculations enable useful approximate estimates of the physical conditions in the CSE.

CHAPTER 6

Physical and chemical interpretation

In this chapter we bring the results of our analyses and comparisons into the context of the physical and chemical interpretation of the circumstellar envelope (CSE) of IRC+10216.

The CSE of IRC+10216 is approximated by a sphere of molecular gas and dust, which is composed of density-enhanced shells, arcs and clumps. The shell and clump distribution of gas and dust coincides and is mostly non-concentric and non-regular in its substructure. The chemically connected species and their reactions are confined to the regions of increased density.

In the outer CSE, on which we focus in this thesis, the cyanopolyynes and carbon chains are most abundant in spheres around the central star that are brightest at radial distances of $15 - 16$ and $22 - 23$ arcsec, with a thickness of about $4 - 8$ arcsec for each shell component. The results of this work fit in the framework of results from numerous previous observational studies of IRC+10216. Our new morphological results for several chemically connected molecular species are valuable additions to construct a global view on the intrinsic molecular shell geometry and its chemistry. This will lead to an improvement of future models of the chemical and physical structure of the envelope of IRC+10216 and of AGB stars in general.

For the interpretation of the observed molecular shell morphology, the mass loss mechanism, mass loss history, hydrodynamic effects of and on gas and dust, and the UV-induced photochemistry have to be considered.

6.1 Molecular shell morphology

Possible explanations for the observed CSE morphology are due to intrinsic and extrinsic effects. Intrinsic effects might be caused by a globally or locally variable mass loss rate of the star, short-term local changes in the stellar atmosphere connected to a magnetic cycle or convection cells. Extrinsic effects are the hydrodynamical effects on the CSE by a binary companion and a possible directional UV irradiation and hence photodissociation from the Galactic plane or from a hot companion.

6.1.1 Enhanced mass loss episodes

The thin dense shells in the CSE may be created by short episodes of enhanced mass ejections. The timescales between such variations of the mass loss rate would have to match the observed shell sepa-

rations of 200 to 1500 years, assuming a constant expansion velocity (cf. Sect. 4.5.2). These timescales are not represented by any known internal periodic mechanism of AGB stars. The pulsation period, which is 630 days for IRC+10216, is much shorter, and the interpulse period between helium flashes, which is of the order of 10^4 years, is much longer.

6.1.1.1 Link to thermal pulses

From the observations of carbon stars with a bright confined detached shell of CO and dust, a connection to the latest thermal pulse is favored (e.g. Olofsson et al. 2000; Steffen & Schönberner 2000, and references therein). During a short period with an increased mass loss rate due to the helium shell flash a fast dust-driven outflow develops, which interacts with the slower denser shock-driven wind and creates a thin compressed shell in the CSE. Because of the long timespan between thermal pulses, the expansion timescale of the shell, and the photodissociation radius of CO ($\sim 10^{17}$ cm), there is only one such shell visible around these carbon stars.

The width of such a detached shell (e.g. of TT Cyg, Olofsson et al. 2000) is very similar to the widths of the shells in IRC+10216 (about 2×10^{16} cm) and constrains the period of enhanced mass loss to about 500 years. The radial position of about 3×10^{17} cm is comparable to the largest radial extent of CO and dust emission found around IRC+10216 (Leão et al. 2006; Decin et al. 2011; Cernicharo et al. 2015). At larger radii the intensity of CO strongly decreases because photodissociation dominates. However, for IRC+10216, the brightness of the CO shells across the envelope out to the photodissociation radius indicates a constant mass loss rate within a factor of 2 for the corresponding look-back time of about 8000 years (Cernicharo et al. 2015). Recent observations of R Scl with ALMA reveal that its shell is in fact not detached, and the CSE is filled with dimmer CO gas, which even has a spiral structure, probably tracing the mass loss history since the last thermal pulse and the interaction of the wind with a binary companion (Maercker et al. 2016).

There are only a few stars known with a detached shell which are possibly linked to thermal pulses. For example, in the Mass-loss of Evolved StarS (MESS) survey in the far-infrared with the Herschel satellite, in which the large scale structure of evolved stars has been imaged, 15 out of 78 AGB stars and supergiants have a ring-like detached shell (Cox et al. 2012). All of these objects are carbon-rich, and there has been no detection of an oxygen-rich AGB star with a ring-like structure. There might be a connection of the stellar and chemical evolution of the star (from oxygen- to carbon-rich), the occurrence of the thermal pulse, the dust content, and the morphology of the CSE. In summary, it is unlikely that thermal pulses are a main reason for the shaping of IRC+10216's CSE.

6.1.1.2 Wind-wind interactions

In principle, the concentration of gas and dust in thin shells at certain radial distances from IRC+10216 could be explained by the interaction of a fast inner wind and an outer slower wind (close to the star) as described in Sect. 6.1.1.1 (Steffen & Schönberner 2000). However, the physical connection to the observed timescales of the shell separation would remain unclear in this scenario.

Most stars of the MESS survey show signs of wind-ISM and/or wind-wind interactions. The interaction of the stellar wind with the ISM in the bow shock region does not influence the circumstellar structure (Decin et al. 2011; Cox et al. 2012). The mass loss history of IRC+10216 can be traced up to a radius of about 390 arcsec. Beyond this radius turbulence and instabilities dominate the medium due to the termination shock by the wind-ISM interaction while the star is moving through the ISM.

Furthermore, the observed timescales in the outer CSE might not represent the intrinsic period of time

between the creation of the shells at the events of mass ejection from the stellar surface, for example, if the distance and width of the shells increases with radius (Fong et al. 2003). It is possible that the thin shells are intrinsically even thinner and closer to each other than currently observed (at least for the dust, Leão et al. 2006), since available data are limited by their angular resolution. Thus, the timescales might be even smaller than currently estimated. Also, the thin shells seem to interact and merge, which smears out the original dynamical information. The wind interaction therefore also occurs in the outer CSE. Correspondingly, from the VLA data we find a second molecular shell component at about 23 arcsec which is at a smaller radius than predicted by the chemical model by Cordiner & Millar (2009) that uses a density structure with enhancements at 15 and 29 arcsec and peak emission accordingly at these radial positions.

Hydrodynamical models of a two-fluid outflow, which include the effect of a drift between gas and dust in the stellar wind, find a quasi-periodic mass loss with periods similar to the observed timescales of a few hundred years for IRC+10216 (Simis et al. 2001). If this mechanism applies, it would suggest that gas and dust are not spatially coupled.

6.1.1.3 Magnetic fields

The physical origin of an enhanced mass loss rate, other than possibly due to the thermonuclear thermal pulse and subsequent third dredge up every 10^4 years, is unclear. The mechanism should occur every few hundred years, assuming that the inferred timescales from the circumstellar shells are accurate. In general, for a dust-driven wind (radiation pressure on dust grains), the mass loss rate can increase due to enhanced dust formation close to the star. Observations of the innermost region of IRC+10216 in the infrared show various dust clumps with sizes of about 0.1 arcsec (e.g. Leão et al. 2006). The dust and gas shells at larger scales are also clumpy, which might be an imprint from the ejection.

A proposed scenario is cyclic strong magnetic activity which causes magnetic cool spots on the atmosphere of AGB stars (as observed for our Sun, Soker & Clayton 1999; Soker 2000). The gas in these spots has a lower temperature and density than their surroundings which faciliates dust formation close to the spots and leads to an enhanced mass loss rate. The spots might occur mostly around the equator region, and therefore the mass loss rate might be the highest around the equator. The AGB star therefore would appear asymmetrical and eject incomplete shells and arcs into the CSE, as it is observed for IRC+10216. Other spots might enhance dust formation and mass loss in a specific direction, which may explain the observed dust clumps close to the star and the clumpiness of the CSE.

The source of the solar-like magnetic field (dynamo model) which would predict the length of the magnetic cycle for AGB stars is under debate (e.g. Soker & Clayton 1999; Blackman et al. 2001). The magnetic activity (with a periodicity of $200-1000$ years) necessary to explain the observed shell features infers that the AGB star experiences tidal interaction with a planetary or stellar companion. The rotation angular speed of the AGB star presumably is slow, up to about 0.3 of the Kepler velocity (Soker 2000), such that the magnetic field is not globally important, the structure of the star is not altered significantly and that no jets form. The companion then is constrained to be a low-mass main-sequence star with a mass of up to 0.5 $M_\odot$ and in an orbit with a period of about $50 - 150$ years (Soker 2000). These values match well with the results on the central binary system of IRC+10216 inferred by Decin et al. (2015).

During the subsequent evolution of the star towards the post-AGB and PN phase, its rotation speed may increase which favors the formation of jets in the system, which may explain the more dramatic morphologies of many PNe in comparison to most AGB stars (e.g. Soker 2006).

The magnetic activity can be semiperiodic, as known in main-sequence stars, which may explain the non-regular shell separation in the CSE of IRC+10216. However, the appearance of the CSE is probably

dominated by the hydrodynamic effects on the circumstellar material by the companion, which may diminish the influence and the possibility for validation of the magnetic spots (e.g. Soker 2006). On the other hand, the observed non-concentric and non-regular morphology of the gas and dust shells might indicate a combination of various periodic effects, which may be given by the magnetic cycle and the orbital binary period (Soker 2002b,a).

Another scenario proposes that the solar-like magnetic cycle in single AGB stars causes a periodic compression of the magnetized wind by the periodic variation of the field strength, without any variations of the mass loss rate, and forms the observed shells in the circumstellar medium (García-Segura et al. 2001). In this case, the shell spacing would be strictly periodic, which is not observed. Due to the assumed steady mass loss rate, in these magnetohydrodynamical simulations the density structure in the shells would fall as r^{-2}. From observations, also the radial intensity profiles presented in this work, the radial density structure is much steeper. The scenario only examines one aspect of the observed CSE morphology, so assuming that this mechanism is valid, to explain the complete morphology, a combination with further mechanisms has to be considered.

There are observations of oxygen-rich red giants which constrain the magnetic field strength by polarimetric observations of Zeeman splitting in the maser emission of e.g. SiO and H_2O. For a few stars such measurements result in magnetic field strengths of several Gauss close to the star (e.g. Vlemmings et al. 2005; Aurière et al. 2010, and references therein). These measurements are yet uncertain. Also for IRC+10216 there are spectro-polarimetric measurements which yield a tentative conclusion of a global radial magnetic field pattern with possible complex morphology (Girart et al. 2012).

6.1.1.4 Stellar atmospheric models and observations

Another aspect is the hydrodynamical morphology of the stellar atmosphere and the stellar wind acceleration, which possibly also has a connection to the magnetic fields (Sect. 6.1.1.3). Two and three dimensional models of the atmospheres of AGB stars predict large convection cells in the photosphere, instabilities in the outflow, and hence inhomogeneous dust formation (Woitke 2006; Freytag & Höfner 2008). With these models the formation of incomplete shells, arcs and small-scale dust clumps, which might interact with each other, is possible.

In support of the notion of inhomogeneous dust formation are near-infrared imaging observations of bright spots (probably of dust) with changing brightness and location over a long range of epochs in the most inner region of IRC+10216 (Stewart et al. 2016) and of a sample of other AGB stars (Wittkowski et al. 2016; Ohnaka et al. 2016). Furthermore, there are recent observations of convective spots and inhomogeneities on the atmosphere of red supergiants, such as Betelgeuse and Antares, with the VLT interferometer (e.g. Ohnaka et al. 2013; Kervella et al. 2016; Montargès et al. 2016).

6.1.2 Binary hypothesis

The evidence for a binary system in the center of the CSEs of many AGB stars is growing. There are several indications by observations, which are in good correspondence with models, that the main shaping agents of the material around AGB stars are binary companions directly or indirectly (cf. Sect. 6.1.1.1 and 6.1.1.3). For IRC+10216, a binary system is suspected as well, but not clearly confirmed.

The indications for a central binary system in IRC+10216 are the offset stellar position, the bipolar inner shape, the regions of less dense molecular gas at a position angle of about 20 degrees, and the approximated spiral structure in the inner wind. Similar structures have been observed for other AGB stars, with clearer indications of a binary companion. For example, the spiral structure in the CSEs of R

Scl (Maercker et al. 2016) and LL Peg (Morris et al. 2006; Mauron & Huggins 2006) or the indication of a main sequence companion star by a blue excess in the optical spectrum of CIT 6 (Schmidt et al. 2002).

The spiral structure is probably created by the reflex motion of the AGB star, due to its companion, around the center of mass of the binary system and the subsequent hydrodynamical effect on the material in the CSE (e.g. Mastrodemos & Morris 1999). The wind from the mass losing star might also be gravitationally focussed towards the orbital plane (e.g. Huggins et al. 2009). The observed shell separation or spiral arm separation then equals the orbital period of the binary system. The current constrains for IRC+10216 are very different depending on the type of observations. Cernicharo et al. (2015) suggest an orbital period of 800 years from their medium resolution imaging of the CO shells in the outer CSE. Decin et al. (2015) estimate an orbital period of about 55 years from the spiral structure observed in ^{13}CO in the inner CSE with high resolution. There are also recent ALMA observations at sub-arcsec scales of NaCl which suggest to have a spiral structure as well (Quintana-Lacaci et al. 2016).

The ejected shells and formed spiral arms might interact and compress in the inner CSE (e.g. Mohamed & Podsiadlowski 2012). Towards larger radii, the spiral arms might widen, through which the spiral arms or shells in the CSE interact or merge and would become unrecognizable as spiral arms in the outer CSE (Homan et al. 2015). From our VLA data we cannot draw conclusions if this indeed is the reason for the observed morphology. The covered spatial range of the photochemical region of the CSE is rather narrow and there are no obvious hints in the data.

The orbital motion of the star might explain the offset between the stellar position and the center of the molecular emission, which is also observed in the VLA data of this work. Subsequently, material is ejected from the star from different orbital positions and might cause the not fully regular pattern of the shell morphology in the CSE of IRC+10216. Depending on how eccentric the orbit is, the mass loss rate could be periodically enhanced near periastron. This could also create a large scale asymmetry of the gas distribution in the CSE, causing the thicker or more numerous shells in the northeast region of IRC+10216 (Cernicharo et al. 2015), which has been noted for the VLA observations of this work as well. Through shocks the material might become clumpy and diminish the molecular material along the orbital axis, which is estimated for IRC+10216 at the position angle of around 20 degrees (cf. Fig. 2.5, p. 53, Decin et al. 2015, and references therein).

There are no direct detections of a companion of IRC+10216. From the model attempts and together with the observations, the possible companion is constrained to be a low-mass main-sequence star (Decin et al. 2015, cf. Sect. 6.1.1.3). If IRC+10216 indeed is part of a binary system, the companion will dominate the hydrodynamical shaping of the CSE and the effects discussed above (Sect. 6.1.1) are secondary.

6.1.3 Galactic UV irradiation and photodissociation

The global shape of the CSE of IRC+10216 and other AGB stars may be influenced by non-isotropic (directional) UV irradiation and subsequent photodissociation of the molecules and dust.

A possible explanation is a stronger external UV field from a certain direction from young bright stars in the Galactic disk. For AGB stars which are located above the Galactic plane there might be a noticeable effect. The region towards the Galactic plane might appear slightly different compared to the remote side.

For IRC+10216, it has been observed that the northeast part of the CSE has a larger extent and a more pronounced shell- and arc-like structure than the southwestern part (Sect. 4.5), which is also confirmed

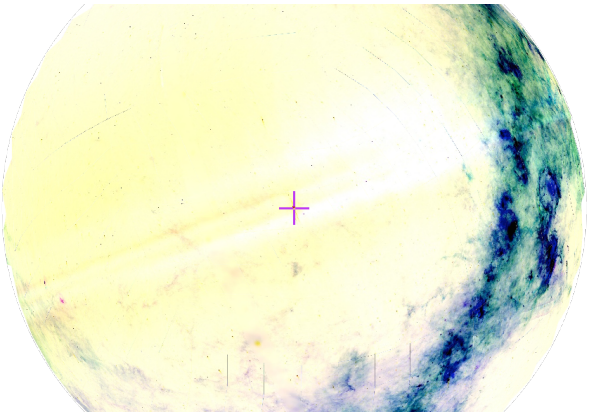

Figure 6.1: The position of IRC+10216 in equatorial coordinates (J2000) relative to the Galactic disk imaged with the Infrared Astronomical Satellite (IRAS) and the Improved Reprocessing of the IRAS Survey (IRIS) catalog (12 − 100 μm). The position of IRC+10216 is marked with the magenta +. The orientation of this figure is equal to the images obtained with the VLA and presented in this work. North is up, east is to the left. © Aladin Lite

in this thesis. The effect probably is stronger for molecules particularly sensitive to UV radiation, such as HC_3N and HC_5N, compared to the dust grains. The Galactic plane indeed is located in the southwest to the star (Fig. 6.1). IRC+10216 has an angular distance to the Galactic plane of 40 degrees, assuming that the Galactic disc has an extent of ±5 degrees in Galactic coordinates (l = 221°, b = 45°).

There are observations of other carbon-rich AGB stars with CSEs that suggest a connection between their large scale structure and the direction of the Galactic plane.

For AFGL 3068, also known as LL Peg, there is a clear spiral structure observed in optical light scattered from the dust (Morris et al. 2006; Mauron & Huggins 2006). The carbon star is located in the southern sky and has a distance to the Galactic plane of 35 degrees (l = 93°, b = −40°). In the direction of the Galactic plane the dust spirals are brighter (Fig. 6.2 and 6.3, left), which is interpreted as illumination of the dust by the Galactic plane. There seems to be no effect on the large scale morphology of the dust, such as less shells towards the Galactic disk. There are no image maps of molecular species available. The shaping of the spiral structure is best explained by a central binary system (Morris et al. 2006; Kim & Taam 2012; Homan et al. 2015).

For CIT 6, also known as RW LMi, there are several observations of the molecular and dust shells and arcs. This star is very similar to IRC+10216 regarding its chemical content, mass loss rate, and evolutionary stage. The star is located in a similar Galactic region as IRC+10216 and is about 50 degrees above the Galactic plane (l = 198°, b = 56°). The shell structure has been observed for various species, such as CN, HCN (Lindqvist et al. 2000), HC_3N (Dinh-V.-Trung & Lim 2009; Claussen et al. 2011), CO (Kim et al. 2013, 2015b), and the dust (Schmidt et al. 2002). It is proposed that the CSE of CIT 6 might have a spiral structure as well (Kim et al. 2013, 2015b). The inner region might be bipolar and shows signs of an excess in blue light, which hints at a main-sequence star companion of spectral type A-F (Schmidt et al. 2002). The distribution of HC_3N and the dust coincide (Schmidt et al. 2002), as for IRC+10216. All these observations note that the CSE is not fully symmetric. Especially in the observations of HC_3N it becomes apparent that the emission structure is very faint in the western part, which is in the direction of the Galactic plane (Fig. 6.2 and 6.3, right). This effect is indicated also in the CO observations, but less pronounced, because CO has a higher bond energy than HC_3N. The dust shells are most prominent in the south-southwest direction, similar to the dust illumination observations for AFGL 3068.

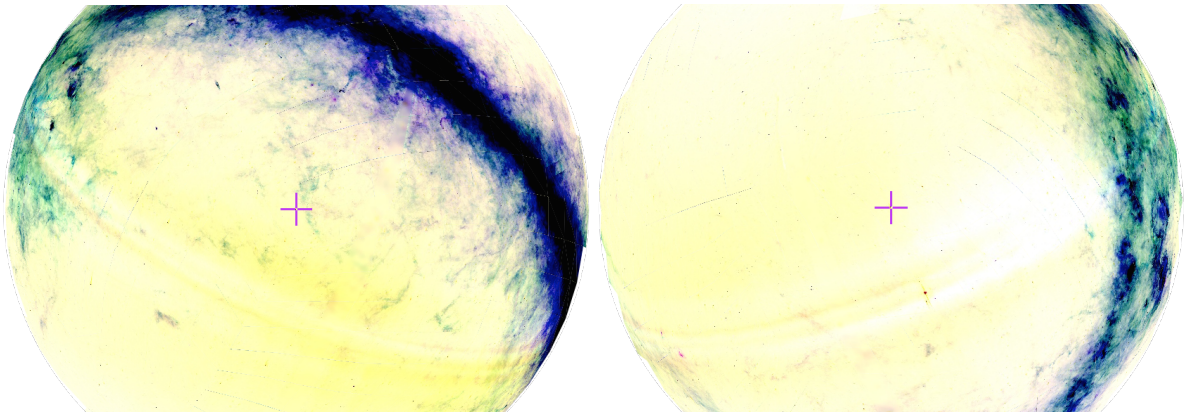

Figure 6.2: The position of AFGL 3068 (LL Peg, left) and CIT 6 (RW LMi, right) in equatorial coordinates (J2000) relative to the Galactic disk imaged with the Infrared Astronomical Satellite (IRAS) and the Improved Reprocessing of the IRAS Survey (IRIS) catalog (12 − 100 μm). The position of each star is marked with the magenta +. North is up, east is to the left. © Aladin Lite

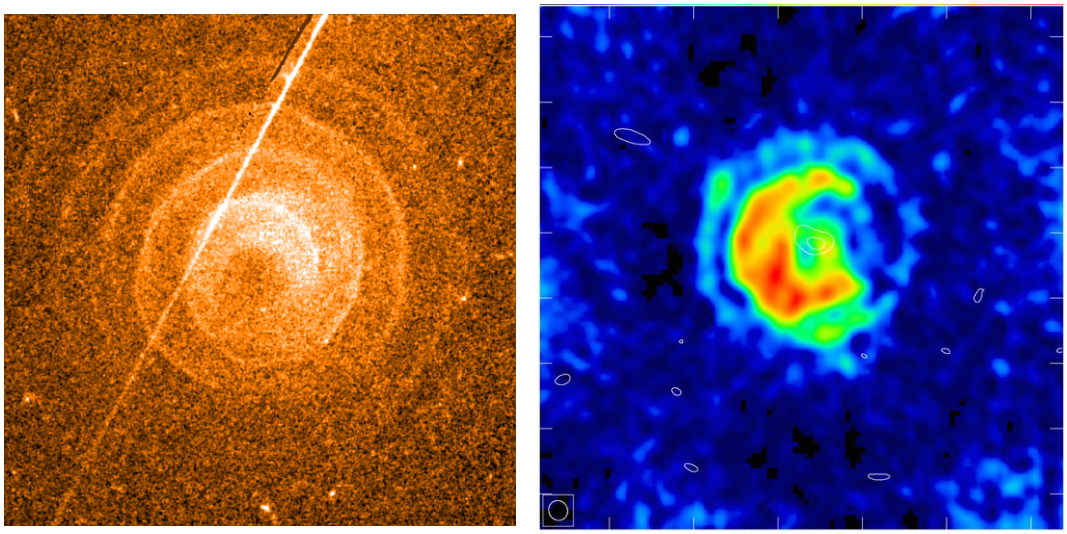

Figure 6.3: The CSE of AFGL 3068 (LL Peg, left) and CIT 6 (RW LMi, right) in equatorial coordinates (J2000). North is up, east is to the left. AFGL 3068 is shown in optical light scattered off the dust shells (Mauron & Huggins 2006). The image has an extent of 26.6 arcsec on each side. For CIT 6 the HC_3N emission is shown (Dinh-V.-Trung & Lim 2009). The extent of the image is about 40 arcsec. In the direction of the Galactic plane (cf. Fig. 6.2) the dust around AFGL 3068 is illuminated stronger and the molecular emission of HC_3N is fainter.

From the observations of a sample of other AGB stars in the dust-scattered light (e.g. Mauron & Huggins 2006) it becomes apparent that most of them are asymmetric, but there is no obvious correlation with the direction of the Galactic plane for the dust. The favored scenario of the dominant shaping is due to a central binary system.

Further observations of the distribution of UV-sensitive molecules, e.g. HC_3N, in the CSE of other AGB stars are necessary to draw conclusions. With a large sample we are able to examine if the Galactic UV irradiation has a significant impact in shaping the structure of CSEs via photodissociation.

6.2 Molecular shell chemistry

The carbon chemistry in the photochemical shell of IRC+10216, studied in this thesis, is given by the physical conditions in the CSE (temperature, density, UV field distribution) and is influenced by the dynamics imprinted in the molecular and dust shell geometry. The observed distribution of the molecular gas is partially shaped also by the dominating chemical reactions. There is an interplay between (magneto-)hydrodynamical and chemical effects, which should be both studied to approach a full understanding of the CSE.

6.2.1 Chemical network

From various observational studies and the efforts of chemical models together with successful laboratory work, the knowledge on the chemical network of the molecules in the gas-phase in the outer envelopes of carbon-rich AGB stars, particularly IRC+10216, is advanced. The dominant reaction rates of most of the involved species are well constrained (e.g. Millar 2016).

The molecular species we focus on are the hydrocarbons and cyanopolyynes in the outer CSE. Their formation is mostly based on ion-molecule and neutral-neutral reactions, respectively, and both are affected by photodissociation. The initial abundance of the involved parent species C_2H_2 and HCN is crucial for the determination of the dominating (production and destruction) reactions and their rates.

Furthermore, the photodissociation rates given by the UV field strength have a large effect on the resulting abundances of these molecules, however, these rates are not accurately known.

The amount of free electrons due to ionization (by cosmic rays or UV photons) and dissociative recombination in the photochemical shell is also substantial, for example for the anion C_6H^- and its neutral equivalent (e.g. Millar & Herbst 1994; Cordiner & Millar 2009; Millar 2016, and references therein, Sect. 1.3.5).

Therefore, particularly carbon chains and their anions such as C_6H and C_6H^- might be more directly affected by photodissociation and photoionization due to their chemical pathways in comparison to cyanopolyynes, such as HC_3N or HC_5N. For the comparison of chemical models and the results from the VLA data in this thesis (Sect. 4.2 and 4.5), we find the largest deviations for C_4H and C_6H.

There are also chemical reactions which have not been taken into account yet, which might have a considerable influence of the resulting column densities and peak abundances. For example, the photodissociation and self-shielding by N_2 and CO has been included for the first time in the chemical model of IRC+10216 by Li et al. (2014), and shows an effect mainly on the nitrogen chemistry in the photochemical regions in the CSE. The column densities of e.g. C_3N are increased by a factor of 10 and the radii of peak abundances change and compare better with observational results in comparison to previous models. The modeled position of peak abundance for C_3N of 18 arcsec corresponds well with the results in this thesis. However, the determined positions of the other molecules do not compare well to the model. The uncertainties of the Gaussian fits from our observations for C_3N are rather high. Furthermore, this model assumes a smooth outflow in the CSE. Favorably, this new understanding of the nitrogen chemistry is combined with models which include a density-enhanced shell density structure.

The chemical conditions and rates might be changed by density enhancements, clumpiness, and asymmetries of the medium, discussed in Sect. 6.1.

6.2.2 Density-enhanced shells

Active photochemistry is confined to a narrow region in the dust and gas shells, which has an extent of about 4 to 8 arcsec as found in this thesis and previous observational studies (Sect. 4.5). The fact that the distributions of dust and gas correspond very well indicates that the morphology of the thin shells indeed is governed by dynamics rather than molecular chemistry. The consequence is that the reactions to create more complex, heavier molecules (e.g. longer carbon chains) happen on a faster timescale due to the increased density and, hence, occur simultaneously rather than sequential (e.g. Millar 2016, cf. Sect. 1.3.5 and 4.2). This probably is the reason for the small difference in the radial positions of the abundance and intensity peaks of these molecules. The photochemical region, however, still is wide enough to develop the expected radial sequence (larger molecules at larger radii), as found in this thesis. This is contrary to the assumptions in the chemical model of Cordiner & Millar (2009), where the cyanopolyynes and carbon chains are all at the same radial positions of 15 and 29 arcsec in very thin shells (2 arcsec) following the used density structure (Sect. 4.2.1). In our analysis we find a second component at about 23 arcsec and no bright component at 29 arcsec given by the physical conditions.

Another reason for the discrepancy between the predictions from chemical models and the observed molecular distribution of the outer CSE of IRC+10216 might be the influence of grain surface reactions, which have not been considered yet. Grains might contribute to the production or destruction/absorption of molecules in the gas phase (Millar 2016). However, the exact mechanisms in the low temperature environment of the outer CSE are not clear.

6.2.3 UV irradiation and photodissociation

The impinging UV radiation varies across the CSE for different position angles and for different radii depending on the extinction by dust, due to the shells and clumps in the medium. Furthermore, the asymmetry of the dust and molecular shell distribution probably causes a non-isotropic penetration by the external UV photons (e.g. Millar 2016). Also the gas temperature and column density of the molecular shells play an important role (e.g. Li et al. 2014). At the dense shells and clumps the UV radiation is shielded efficiently and in the region of lower density it is able to pass. Due to the clump-interclump and shell-intershell density contrast, this can have a significant effect on the local reaction rates and abundances. A small fraction of the interstellar UV field might penetrate into the inner CSE and change the radial molecular distribution as expected from standard CSE models (Agúndez et al. 2010; Millar 2016).

The motivation for including the clumpiness of the medium into models has been the detection of warm water vapor in the inner envelope of IRC+10216 and other carbon-rich AGB stars unexpected from equilibrium chemistry (Decin et al. 2010; Lombaert et al. 2016). Subsequently, there are models of UV penetration in the inner CSE (a few percent of the interstellar UV field for radii $< 10^{15}$ cm, Agúndez et al. 2010) and a scenario involving detailed models of non-equilibrium shock-induced chemistry (Cherchneff 2012). However, both only partly reproduce the observed water abundance and correlations with the stellar properties (Lombaert et al. 2016).

The recent detection of CH_3CN in the inner envelope of IRC+10216 with ALMA supports the scenario of a small fraction of UV photons reaching into the inner CSE, maybe even to the photosphere (Agúndez et al. 2015). However, the model predicts a centrally peaked distribution whereas the observations show a hollow sphere within the inner 2 arcsec. From standard CSE models (e.g. Agúndez et al. 2008) this molecule is expected to be most abundant around 15 arcsec with a weak component within the inner 1 arcsec, similar to the chemically related cyanopolyynes, such as HC_3N (cf. e.g. Cordiner

& Millar 2009). The model with UV penetration shows an increased HC_3N abundance in the inner CSE (Agúndez et al. 2010; Decin et al. 2010). This might be an aspect to the discrepancy between the abundances from observations and models, as in our estimate for HC_3N and HC_5N in Ch. 5.

In this thesis, we find evidence for an inner component at radii of $8 - 12$ arcsec for C_4H, C_6H, and C_6H^- (Sect. 4.2.1), which are probably more affected by UV irradiation and subsequent photoionization and photodissociation reactions. But there is no clear emission of HC_3N, HC_5N, and HC_7N at radii smaller than 12 arcsec (2.3×10^{16} cm, for a distance to IRC+10216 of 130 pc) in the VLA data.

The recent calculations by Millar (2016), that are based on the model by Agúndez et al. (2010) but with different radiative transfer for the FUV photons, are in line with our results. The calculations show a distinct effect on the radial abundance distribution of hydrocarbon anions, such as C_6H^-. For radii smaller than 3×10^{16} cm the abundance of these anions is increased by two orders of magnitude compared to the model with a spherically symmetric outflow.

So the penetration of a fraction of external UV photons into the CSE down to the star plays an important role for the understanding of the photochemistry in the clumpy CSE of IRC+10216. However, other mechanisms, such as the shock-induced chemistry, probably have a contribution as well. Future observations with higher angular resolution of the inner envelope will help to further constrain this.

Another aspect could be an internal irradiation from stellar photons, either by the AGB star itself or a possible companion.

For IRC+10216, the amount of emitted energetic photons is probably very small as the star is cool ($\sim$ 2500 K). However, considering that the star is at the end of the AGB phase, its stellar surface hydrogen envelope becomes thinner and the exposure of the hot C,O-core gradually increases which releases UV photons. The pulsation-driven shock waves might also reach high enough temperatures. For these, however, there is currently no observational evidence.

The possible companion of IRC+10216 most likely would be a low-mass main-sequence star and also would not emit a large amount of UV photons. A white dwarf companion is unlikely because no UV signature or clear hints in the optical spectra have been measured (Decin et al. 2015). However, it is possible that an accretion disk in the orbital plane with an extent of a few AGB-stellar radii is present around a low-mass companion. This disk might be hot enough to emit UV photons (Saladino et al., priv. comm.). These scenarios have to be investigated further in detail.

Since the AGB star is enshrouded in dust, most of the UV radiation would be absorbed and would not reach the outer CSE. However, considering the clumpy structure of the inner CSE, a certain amount of UV photons might reach the outer layers and molecules with weak bonds might be photodissociated even by photons of relatively low energy (Millar 2016). This might have considerable effects on the chemistry and hence the molecular shell morphology.

For future work it will be very interesting to examine how strongly an internal UV field may be attenuated and still have an effect on the CSE. Or in other words, what is the minimum amount of internal UV photons to have an effect on the CSE morphology and chemistry?

CHAPTER 7

Prospects

In this chapter, two future projects that were developed during the thesis are presented. The projects involve additional complementary observations with the 100-m Effelsberg telescope and the Atacama Large Millimeter/Submillimeter Array (ALMA). These observations will constrain the global molecular properties of IRC+10216 and will indicate how representative IRC+10216 is among other carbon stars.

7.1 Global molecular properties: Zero spacings observations of IRC+10216 with the Effelsberg 100-m telescope

The rich dataset presented in this thesis is incomplete without observations with a single-dish telescope providing the zero-spacing correction to recover flux missing from the interferometer maps. Knowing the correct flux densities is vital when performing radiative modeling to extract physical information on the star's envelope. The short-spacing corrections are needed for the highest possible frequency range of the VLA survey, because the density of the observed spectral features is high and the flux information from different energy levels for each of the molecules is needed.

The 100-m Effelsberg radio telescope with the new wide-band receiver is the ideal facility to complement to the VLA observations between 18 and 26 GHz, because it provides the necessary overlap in baseline lengths and large bandwidth, to obtain the complete picture of IRC+10216.

To this date, the new wide-band (8 GHz) K-band receiver has not been fully developed. The successfully granted observations with the 100-m Effelsberg telescope (*Proposal 87-14, October 2014, PI: D. Keller*) were performed with the current K-band receiver (2.5 GHz) for frequencies 23.5 – 26.0 GHz in January and March 2016. The data currently is being calibrated by Effelsberg staff and will be combined with the VLA observations soon for further analysis and physical interpretation to constrain the global molecular properties of IRC+10216.

7.2 How unique is IRC+10216? Carbon-bearing molecules around carbon-rich AGB stars with ALMA

Most observations of circumstellar chemistry have so far focussed on one single object, IRC+10216, especially for interferometric observations, as in this thesis. The Atacama Large Millimeter/Submillimeter

Array (ALMA) provides great improvement in sensitivity and angular resolution. With ALMA it is now possible to significantly enlarge the sample of carbon stars, which are further away than IRC+10216, allowing a detailed comparison of their circumstellar structure and chemistry.

Linking the ALMA observations to our VLA survey of IRC+10216, we consider that the VLA survey lacks high excitation-lines which limits the study of the physical conditions in the CSE. The ALMA observations will provide complimentary data of the same molecules at higher excitation.

The observing proposal (*ALMA-Proposal 2015.1.01271.S, PI: D. Keller*) has received the ranking C, which means it is a filler project. Observations of IRC+10216, CQ Pyx, U Hya, V Hya, RW LMi, II Lup, and V358 Lup were performed between March and September 2016 and the calibrated data of most of the objects have been delivered to this date.

We will use a radiative transfer code for the analysis of all the spectral lines, to derive the molecular abundances, analyze the molecular excitation and thermal balance in the envelope. We expect to detect a large number of new lines due to the high sensitivity. We will perform LTE/RADEX modeling and the radial profile analysis developed for this thesis will be utilized.

CHAPTER 8

Conclusions and outlook

In this thesis we present a detailed empirical examination and description of the molecules in the circumstellar envelope (CSE) of the evolved carbon-rich star IRC+10216. Our data has been measured with the Very Large Array (VLA) covering the molecular line emission at high angular resolution and great sensitivity. The interferometric mapping of the molecular emission in the radio regime has been fairly unexplored for this star. Therefore, the spectral line and imaging survey of this work is an important addition to the studies of IRC+10216. The various molecules covered by our observational data are involved in UV-photon induced chemistry. By constraining their spatial distribution, the understanding of the chemical reactions and related physical influences is greatly improved in the cool ($10 - 500$ K) outer CSE of IRC+10216 at radial distances of 500 to a few 1000 stellar radii or $10^{16} - 10^{17}$ cm. The knowledge can be applied to similar regions, e.g. molecular clouds, to better understand the production of complex carbon-bearing molecules in the Universe.

The molecular emission is covered unbiased and simultaneously, which minimizes systematic uncertainties. We perform a careful data calibration and aperture synthesis imaging, for which we extensively test the imaging algorithm to ensure a high quality data product. The procedure is not trivial and requires a large time investment to optimize many different parameter choices, which depend on the data set, on the astronomical object and on experience.

From the calibrated survey data we identify 220 molecular transitions from 20 species. The detected transitions originate from carbon-bearing molecules, except for SiS, and are cyanopolyynes, carbon chains and their anions, metal-, silicon-, and sulfur-bearing molecules. Most of these species are distributed in hollow spheres around the star, surrounding the centrally-peaked emission from SiS. We focus on the cyanopolyynes and carbon chains that are the brightest transitions and trace the photochemical region of the CSE of IRC+10216. The substructure of these hollow spheres are shells, arcs, and clumps and their exploration is essential to understand the formation and shaping of the observed CSE morphology and the inherent chemistry.

In this thesis we develop automatized procedure with Python to extract radial emission profiles and their properties, namely peak flux, radial position, and width, with physically meaningful error calculations from the observational data. For the identified components we estimate physical properties and analyze the chemistry. These results are compared to models of circumstellar chemistry.

8.1 Conclusions

From the VLA survey data we find that the molecular emission of HC_3N, HC_5N, HC_7N, C_3N, C_4H, C_6H, and C_6H^- is concentrated in two main shell components. These are located at radial distances of about 15 and 23 arcsec from the star with a thickness of 4 – 8 arcsec each. The molecular shells coincide with the dust shells observed in the optical and near-infrared regime. The emission from all covered energy levels of one species is found at the same radii within these shells. The emission from HC_5N, HC_7N, C_3N is found at larger radii than HC_3N with the sequence $HC_3N \rightarrow HC_5N \rightarrow HC_7N \rightarrow C_3N$ with increasing radius. The carbon chains C_4H, C_6H, and C_6H^- are observed at the same radii and very similar to the radial positions of HC_5N and HC_7N. Furthermore, C_4H, C_6H, and C_6H^- have a weak inner component at radii between 8 – 12 arcsec, predicted by chemical models but that have not been observed before. Our results are limited by the angular resolution and sensitivity (including the missing flux) from the observational data and the uncertainties from the determination of the radial profile properties.

The structure of the shells is complex and not spherically symmetric. The center of the molecular emission is shifted with respect to the stellar position. There are differences in the emission structure along the position angle, or in the different image quarters in the plane of the sky, and along the line of sight as a function of velocity. The blue- and red-shifted shell parts show deviations from each other and from spherical symmetry, particularly for the southeast region, which give important clues on the three dimensional geometry. The southwest region is thinner than the other parts of the shell, has mostly only one main component, and is closest to the star. For several transitions there is less molecular emission around a position angle of 20 degrees counterclockwise from north.

Our observations clearly show the clumpiness of the medium. These are small scale over-densities within the shell structure which are brighter than the surrounding medium by a factor of 2 to 8. The physical sizes of the clumps are between about 3 and 7 arcsec ($4 - 16 \times 10^{15}$ cm), which are mostly resolved by the VLA data. The properties of the first and second shell component differ, with higher uncertainties for the second shell due to a lower signal-to-noise ratio. The second shell component at larger radii consists of more arcs and clumps rather than a complete shell and has a lower intensity by a factor of 2 to 10 than the first shell. There is evidence that the radial sequence of the molecules in the second component is slightly different than in the first component. With a constant expansion velocity, the separation between the shells can be translated to a dynamical timescale which is about 300 years from our VLA data.

In comparison to previous observational and modeling studies, our results from the VLA data compare well, especially the azimuthal averages of the molecular emission from the main shell component. Our study refines the quantitative description of the CSE properties. The chemical models include an advanced understanding of the ion-molecule and neutral-neutral reactions in the outer CSE of IRC+10216, which are most important for the production and destruction of cyanopolyynes and carbon chains. For the models a realistic representation of the physical and dynamical conditions in the CSE of IRC+10216, namely an expanding density-enhanced structure composed of shells and clumps, is very important to reproduce the observations. So far, a smoothly outflowing stellar wind (decreasing density with radius as r^{-2}) and an approximate density-enhanced shell structure have been used in models. The observed radial positions, sequence, and abundances of these molecules from our VLA data are partially well reproduced by the models using these two types of density structures. However, none of the models alone reproduces the observed features completely in a consistent way. The detailed description and comparison of our VLA data provides an unprecedented view into the outer CSE of IRC+10216. Hence, this data contributes greatly to constructing of a global view of the CSE of IRC+10216 and leads to the

improvement of future chemical and radiative transfer models, not only for this particular AGB star.

From our observational material we cannot clearly exclude or favor certain effects which are the sources of the clumps and shells and their distribution. Our study empirically constrains the CSE morphology traced by the molecular gas. It is very probable that a combination of physical mechanisms are responsible for the observed structures within the CSE. Directional mass ejections by magnetic spots and/or convection cells in the stellar atmosphere might cause the clumps. Subsequent wind-wind interactions might compress the ejected mass into thin shells with a non-regular and non-concentric pattern. At the same time non-isotropic external or even internal UV radiation might shape the asymmetric shell distribution by photodissociation. However, if there is a binary companion present in the inner wind of IRC+10216, it will dominate the hydrodynamical shaping of the CSE by the movement of the AGB star around the center of mass and/or the gravitational focussing of the CSE material. A binary system could also explain the described asymmetries of the molecular emission.

The (magneto-)hydrodynamical geometry influences the inherent chemistry. The photochemical reactions are confined to the thin shells in the CSE consisting of gas and dust, which are formed dynamically. A crucial but yet uncertain influence is the photodissociation and photoionization rate given by the ambient UV field strength. The clumpy shell structure of gas and dust leads to a non-isotropic UV irradiation with subsequent complex UV shielding and penetration conditions. This mainly influences the distribution of the carbon chains and their anions, which also show the largest deviations between models and observations in this work. Furthermore, additional shielding by molecular species, such as N_2 and CO, is considerable. Because the dust and molecular gas are co-spatial, an additional influence is expected from grain surface reactions, which have not been considered in models yet.

In summary, the morphology of the observed molecular emission around IRC+10216 is very complex with non-regular, non-concentric, and porous shells. For a global understanding of the dynamics and chemistry in the CSE, a joint effort is needed from both observations and chemical modeling. The observations have to cover the full wavelength regime at different spatial resolutions for different regions of the CSE. The chemical models need to include more details of the physical and chemical properties of the CSE, including full radiative transfer. This work is a major observational contribution to a detailed description of the outer CSE of IRC+10216 from high angular resolution imaging with the VLA.

8.2 Outlook

For the future, interferometric observations in the radio, submm, optical, and near-infrared regime are very important tools to further constrain the circumstellar environment in terms of molecular gas and dust. Because the overall average radial distribution is already approximated well by models, the future model and observational studies improve by focussing on the substructure of the CSE. For a certain radial range there is already good knowledge of the physical and chemical conditions of the CSE from various molecular species. Continuos follow-up observations with improved telescope and receiver technology and subsequent improved spatial resolution and sensitivity, e.g. with NOEMA and ALMA, will help to further refine the empirical knowledge on the CSE.

Furthermore, very high angular resolution observations of the most inner region, e.g. with ALMA, reveal new insights of the CSE of IRC+10216. New molecular species are (already) detected and unexpected molecular distributions in the inner CSE challenge current chemical models. Newly observed high energy transitions, i.e. high-J and from vibrationally excited states, of various molecules together with complimentary lower energy transitions from other studies can be combined for a thorough and consistent picture of the CSE. Furthermore, the future efforts of polarimetric observations will help to

further constrain the magnetic field strength and distribution around IRC+10216 and other AGB stars. Optical and near-infrared interferometry with high angular resolution and detailed modeling will obtain more information on the atmospheric features, which may be very important to explain the observed small scale structures of the CSE. Additionally, these observations might find direct hints of a companion for a exclusion or conclusion of the binary hypothesis.

A major challenge for the future interferometry are the amounts of collected data and its processing. There are already data reduction pipelines, e.g. for VLA or ALMA data, which are very useful helpers for the astronomers. This will gain more and more necessary improvements, especially for spectral line data, over time. For this thesis, however, these tools have only been partially usable.

The combination of the VLA data of IRC+10216 with single dish observations, e.g. with the Effelsberg 100-m telescope, is mandatory for the zero spacings correction due to the missing flux problem. Subsequent calculations including radiative transfer and the spherical three dimensional structure will lead to improved determinations of the physical conditions in the CSE of IRC+10216.

There will be interesting new findings of the circumstellar chemistry, regarding abundance distributions and reactions rates, when considering the complex non-isotropic UV irradiation through a porous and clumpy medium together with the detailed CSE morphology, partly provided by this thesis.

The procedures developed and utilized in this thesis are applicable to other similar objects. Future studies of a sample of carbon stars will reveal how representative the physical and chemical conditions of IRC+10216, described in this thesis, are among other AGB stars.

In sum, the progress of advanced telescope technology and image processing of molecular and dust emission will enable an improved knowledge of the physics and chemistry in the circumstellar environment of evolved stars and in the interstellar medium in general.

APPENDIX A

Spectral line emission

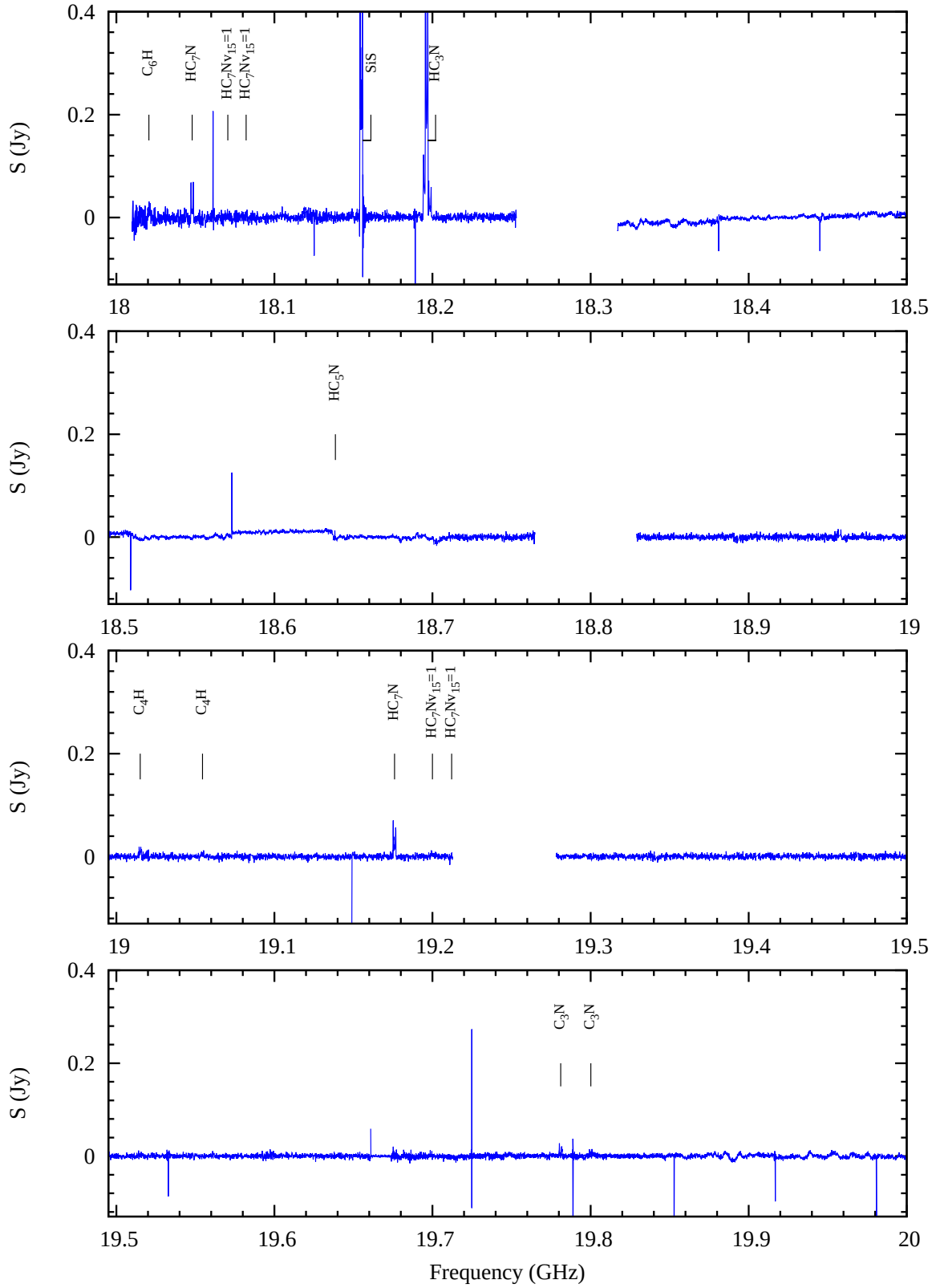

Figure A.1: Spectra of IRC+10216 for a circular region with radius 30 arcsec around the continuum peak position of the star.

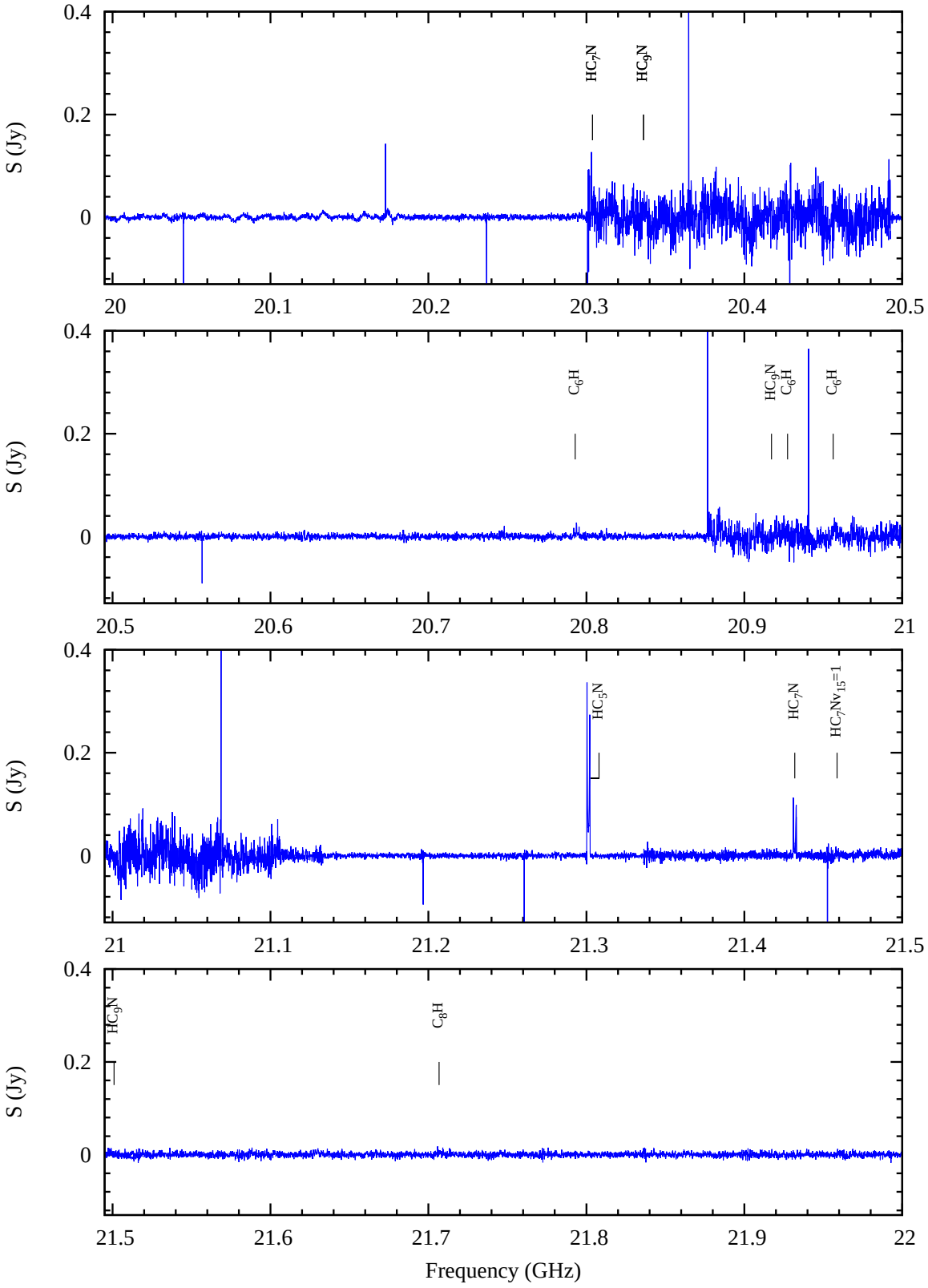

Figure A.2: Fig. A.1 cont'd.

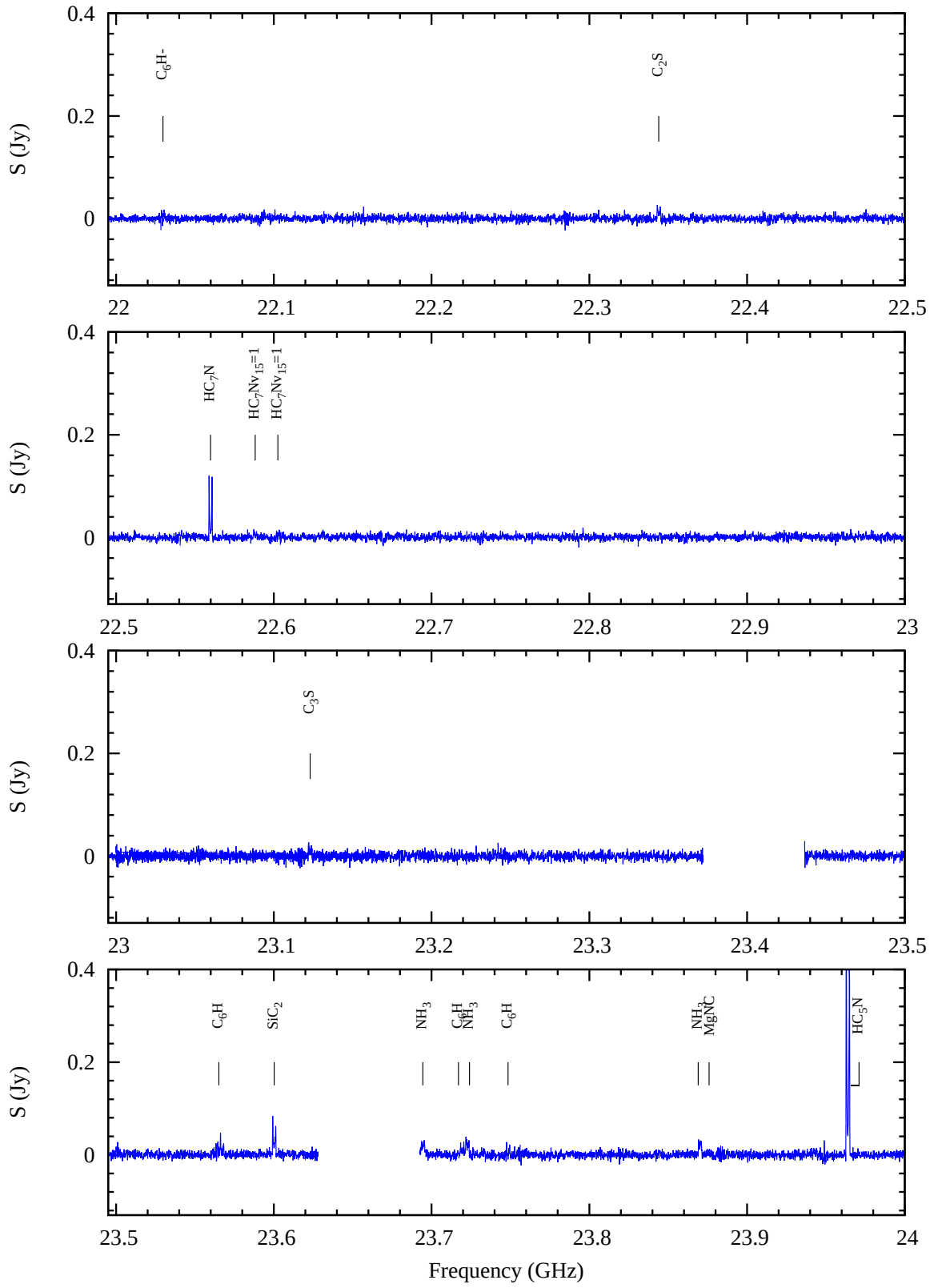

Figure A.3: Fig. A.1 cont'd.

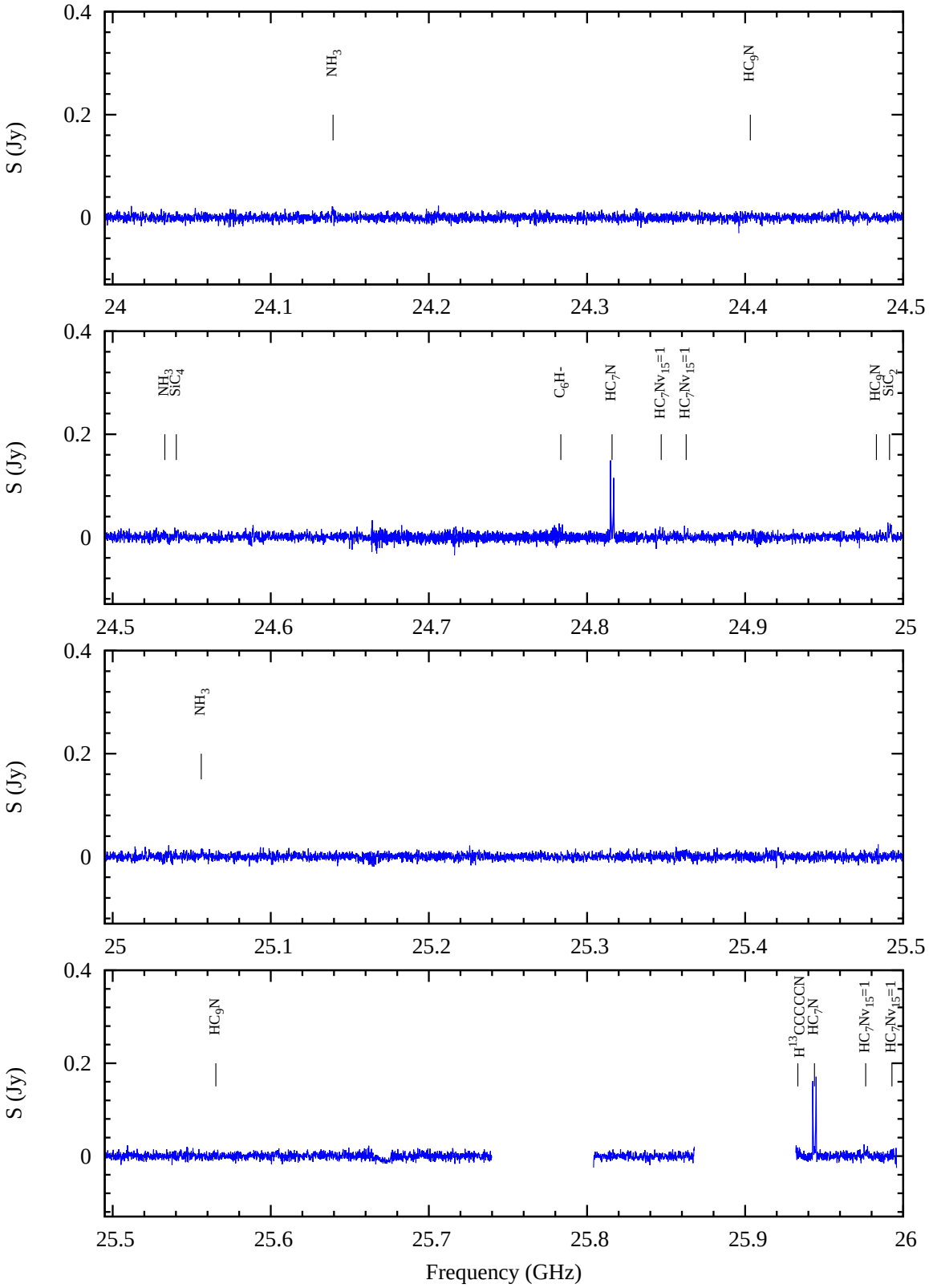

Figure A.4: Fig. A.1 cont'd.

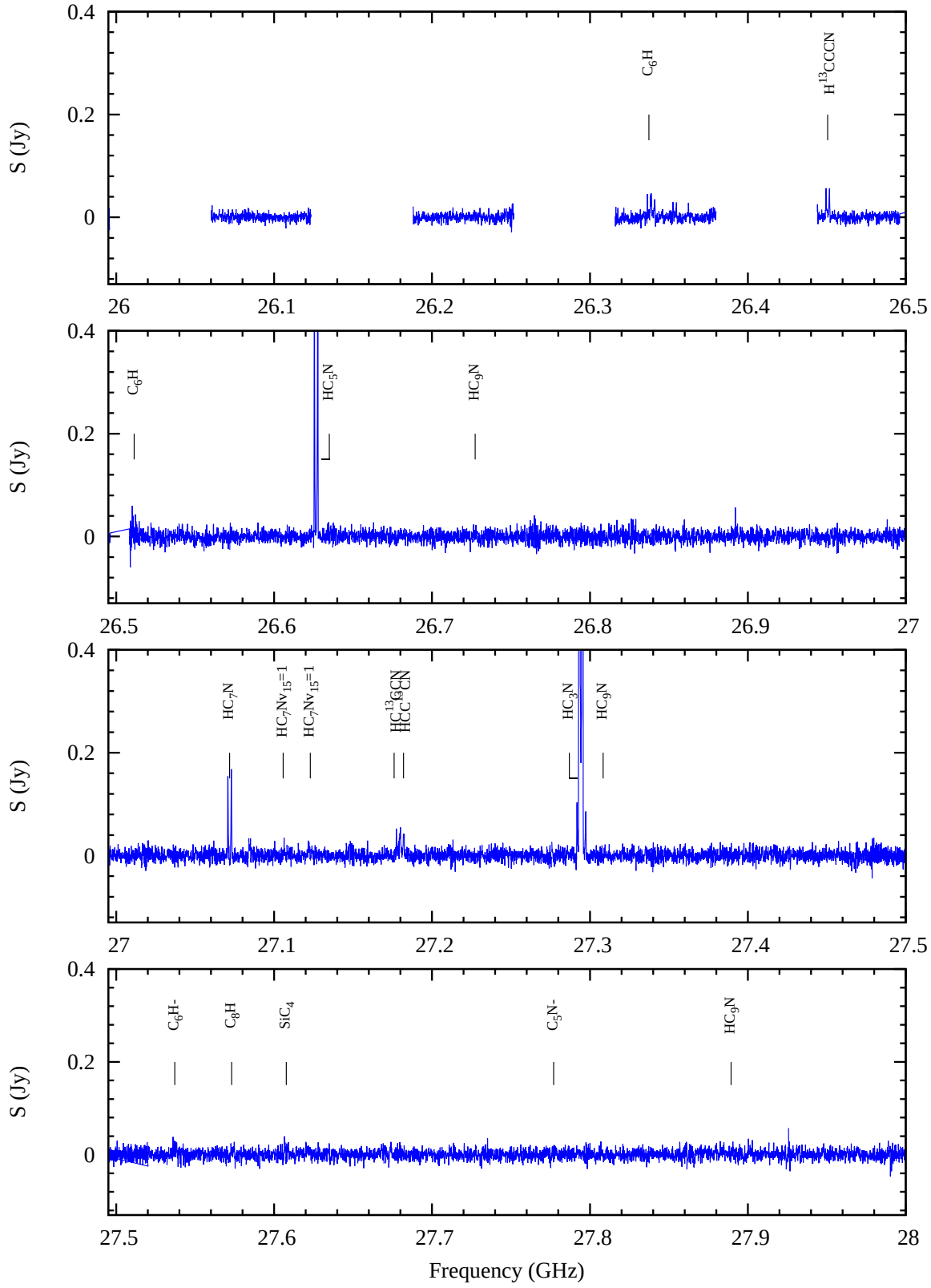

Figure A.5: Fig. A.1 cont'd.

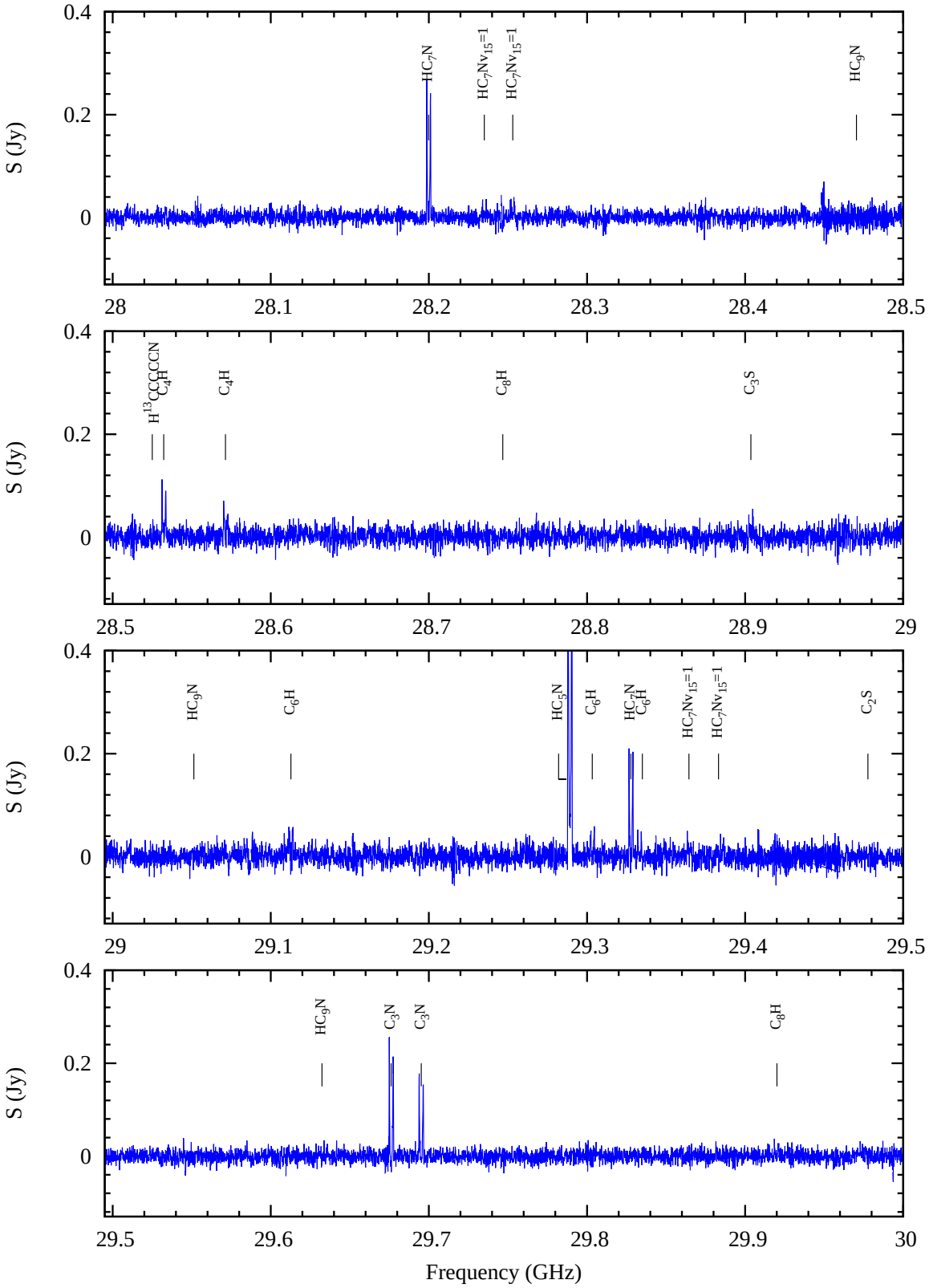

Figure A.6: Fig. A.1 cont'd.

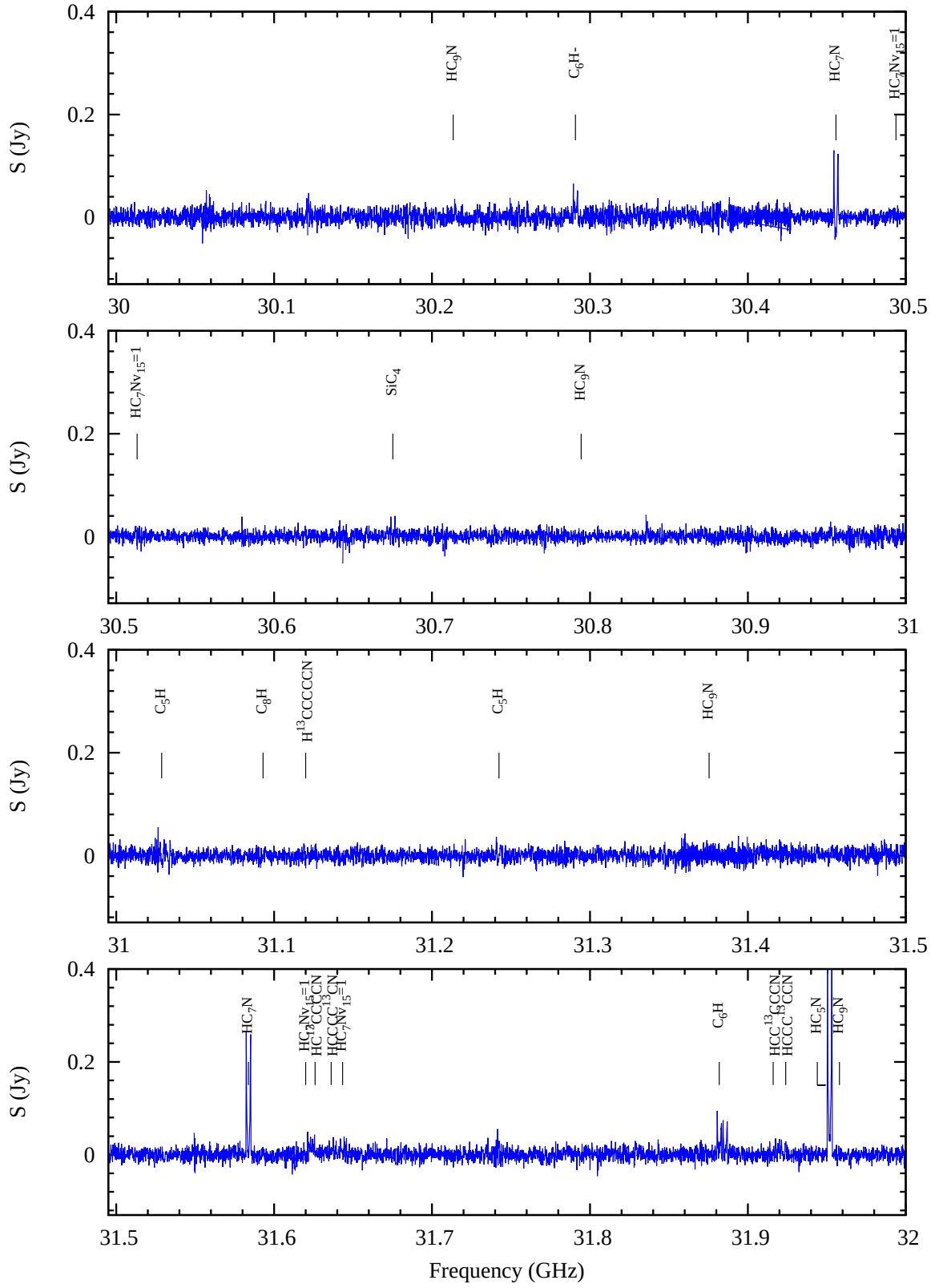

Figure A.7: Fig. A.1 cont'd.

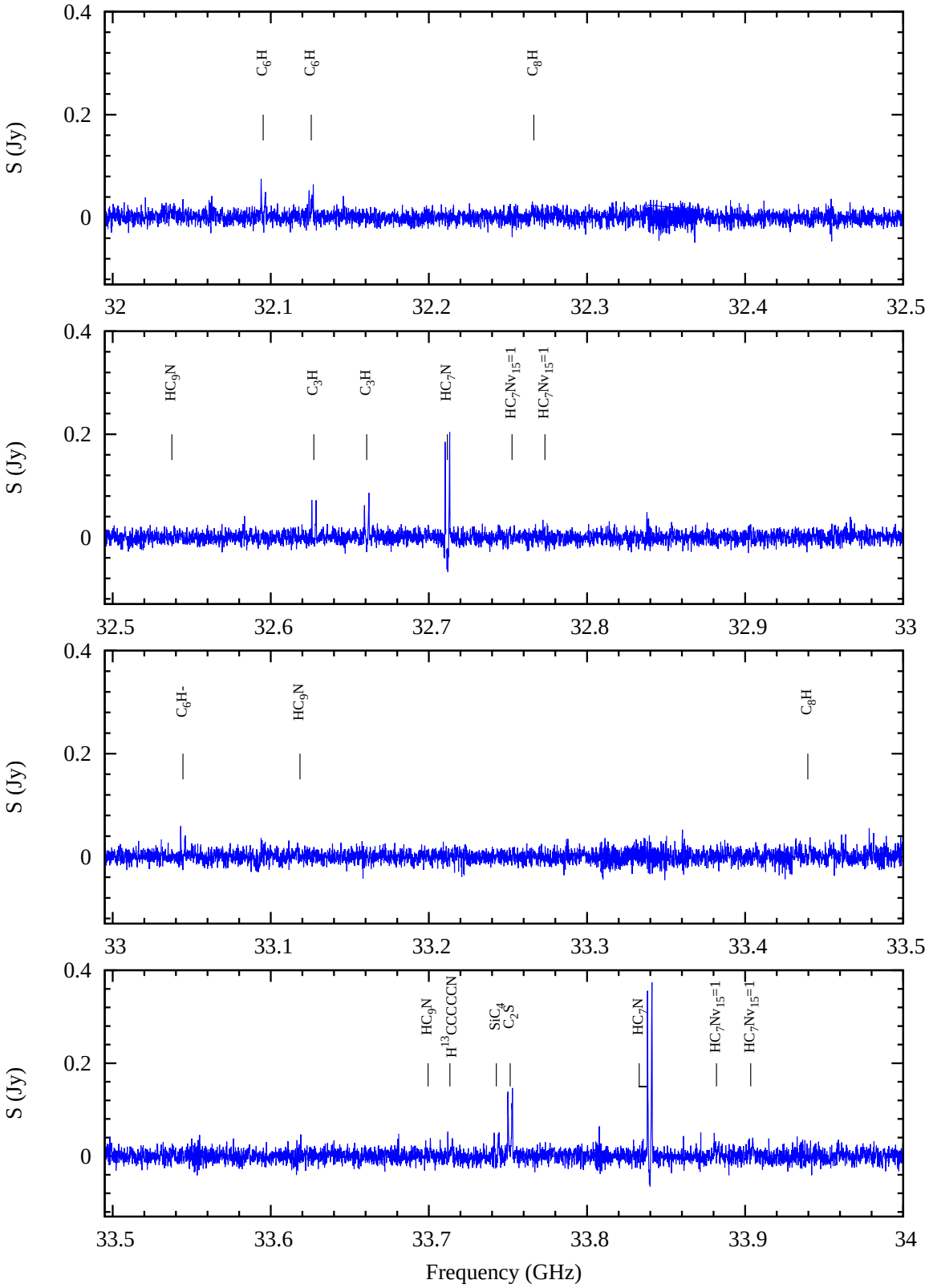

Figure A.8: Fig. A.1 cont'd.

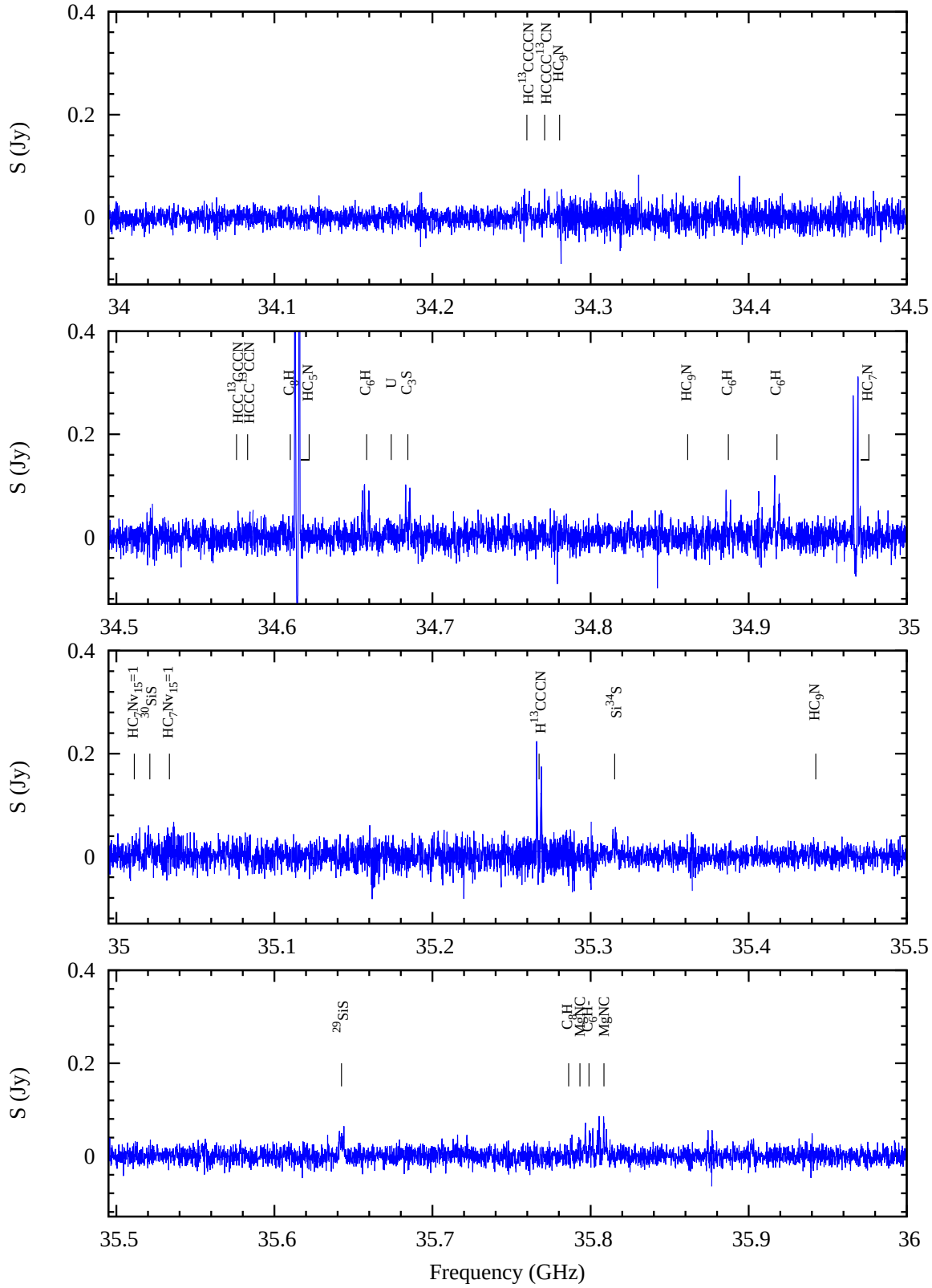

Figure A.9: Fig. A.1 cont'd.

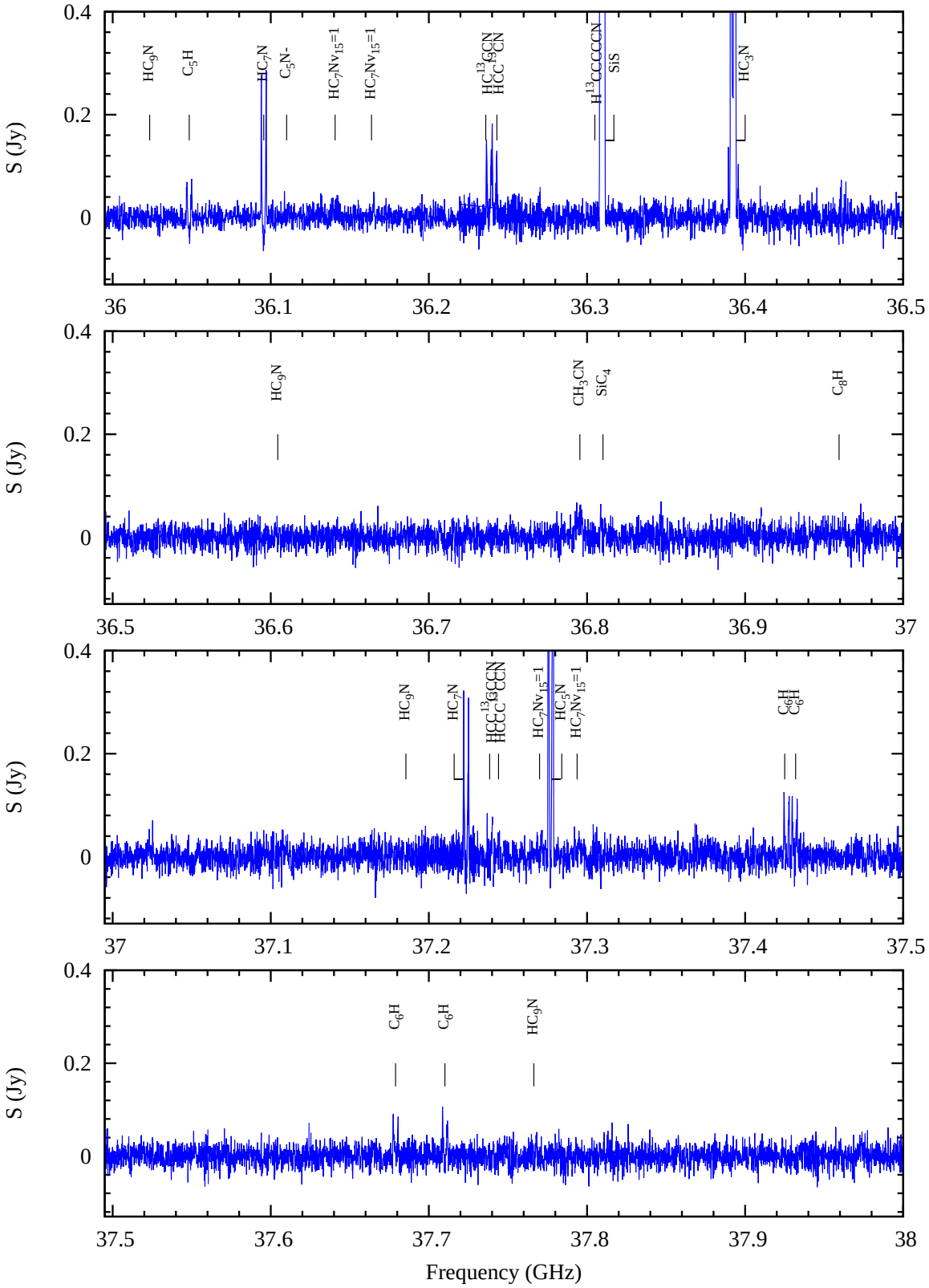

Figure A.10: Fig. A.1 cont'd.

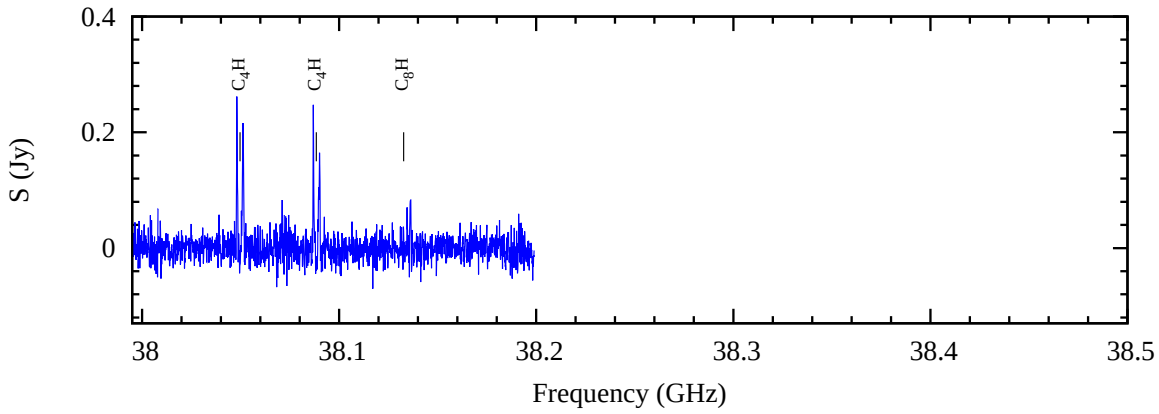

Figure A.11: Fig. A.1 cont'd.

Table A.1: List of identified spectral lines and their properties from the VLA survey of IRC+10216. The emission of those transitions for which no properties are given is weak and the detection is only tentative.

Frequency (GHz)	Species	Transition	$I_{\rm int}$ (Jy km s^{-1})	$I_{\rm int}$ (Jy beam^{-1} km s^{-1})	$I_{\rm int}$ (K km s^{-1})	σ (Jy beam^{-1})	σ (K)	$\theta_{\rm maj}$ (arcsec)	$\theta_{\rm min}$ (arcsec)	P.A. (°)	cell size
18.02061	C_6H	J=13/2-11/2,Ω=3/2,l=e									
18.02178	C_6H	J=13/2-11/2,Ω=3/2,l=f									
18.04797	HC_7N	J=16-15	0.22026	0.00874	1.31822	0.00099	0.14866	3.9806	6.2525	-3.168	0.9
18.07055	HC_7Nv_{15}=1	J=16-15,l=1e									
18.08206	HC_7Nv_{15}=1	J=16-15,l=1f									
18.15488	SiS	J=1-0	2.56465	0.08773	15.16550	0.00791	0.13676	4.1522	5.1646	-10.610	0.9
18.19623	HC_3N	J=2-1	3.07963	0.10494	18.12854	0.00064	0.11053	4.1441	5.1550	-10.597	0.9
18.63862	HC_5N	J=7-6									
19.01514	C_4H	N=2-1,J=5/2-3/2,F=3-2	0.12488	0.00388	0.67318	0.00046	0.07949	4.0908	4.7619	-17.165	0.9
19.05448	C_4H	N=2-1,J=3/2-1/2,F=2-1									
19.17596	HC_7N	J=17-16	0.38839	0.01126	2.05862	0.00045	0.08267	3.9411	4.6132	-16.566	0.9
19.19995	HC_7Nv_{15}=1	J=17-16,l=1e									
19.21218	HC_7Nv_{15}=1	J=17-16,l=1f									
19.78109	C_3N	N=2-1,J=5/2-3/2,F=7/2-5/2	0.20998	0.00620	1.04617	0.00052	0.08758	3.8423	4.8146	-27.362	0.9
19.80012	C_3N	N=2-1,J=3/2-1/2,F=5/2-3/2	0.11276	0.00332	0.56016	0.00053	0.08924	3.8382	4.8096	-27.358	0.9
20.30395	HC_7N	J=18-17	0.81408	0.02286	3.84863	0.00434	0.73026	3.7175	4.7356	-24.051	0.9
20.33613	HC_9N	J=35-34									
20.79291	C_6H	J=15/2-13/2,Ω=3/2,l=e	0.31106	0.00895	1.40197	0.00053	0.08315	4.0135	4.4921	-25.090	0.9
20.79447	C_6H	J=15/2-13/2,Ω=3/2,l=f	0.31110	0.00895	1.40218	0.00053	0.08312	4.0135	4.4921	-25.090	0.9
20.91716	HC_9N	J=36-35									
20.92735	C_6H	J=15/2-13/2,Ω=1/2,l=f									
20.95622	C_6H	J=15/2-13/2,Ω=1/2,l=e									
21.30126	HC_5N	J=8-7	1.73731	0.04618	7.46256	0.00046	0.07501	3.6515	4.5637	-28.220	0.9
21.43193	HC_7N	J=19-18	0.51603	0.01235	2.18958	0.00053	0.09390	3.5494	4.2265	19.783	0.9
21.45874	HC_7Nv_{15}=1	J=19-18,l=1e									
21.47241	HC_7Nv_{15}=1	J=19-18,l=1f									
21.49818	HC_9N	J=37-36									
21.70660	C_8H	J=37/2-35/2,Ω=3/2,F=19-18,l=e									
21.70678	C_8H	J=37/2-35/2,Ω=3/2,F=19-18,l=f									
22.02974	C_6H^-	J=8-7									
22.34403	C_2S	N=1-0,J=2-1	0.15133	0.00364	0.59073	0.00053	0.08662	3.5957	4.1992	18.347	0.9
22.55992	HC_7N	J=20-19	0.52083	0.01233	1.99455	0.00050	0.08091	3.5648	4.1619	18.454	0.9
22.58814	HC_7Nv_{15}=1	J=20-19,l=1e									
22.60252	HC_7Nv_{15}=1	J=20-19,l=1f									
23.12298	C_3S	J=4-3	0.26141	0.00584	0.95301	0.00051	0.08296	3.4884	4.0150	14.656	0.9
23.56518	C_6H	J=17/2-15/2,Ω=3/2,l=e	0.29828	0.00593	1.05524	0.00064	0.11456	3.1857	3.8792	-34.549	0.8
23.56720	C_6H	J=17/2-15/2,Ω=3/2,l=f	0.29868	0.00594	1.05665	0.00064	0.11457	3.1857	3.8792	-34.549	0.8
23.60023	SiC_2	1(0,1)-0(0,0)	0.59503	0.01180	2.09919	0.00061	0.10843	3.1818	3.8746	-34.550	0.8

Table A.1 continued.

Frequency (GHz)	Species	Transition	$I_{\rm int}$ (Jy km s^{-1})	$I_{\rm int}$ (Jy beam^{-1} km s^{-1})	$I_{\rm int}$ (K km s^{-1})	σ (Jy beam^{-1})	σ (K)	$\theta_{\rm maj}$ (arcsec)	$\theta_{\rm min}$ (arcsec)	P.A. (°)	cell size
23.69450	NH_3	1(1)-1(1)	0.42813	0.00842	1.49833	0.00065	0.11538	3.1693	3.8594	-34.554	0.8
23.71938	C_6H	J=17/2-15/2,Ω=1/2,l=f									
23.72263	NH_3	2(2)-2(2)	0.62988	0.01237	2.19939	0.00062	0.10940	3.1669	3.8565	-34.555	0.8
23.74855	C_6H	J=17/2-15/2,Ω=1/2,l=e									
23.87013	NH_3	3(3)-3(3)	0.43047	0.00835	1.48437	0.00061	0.10901	3.1476	3.8330	-34.561	0.8
23.87507	MgNC	N=2-1,J=5/2-3/2									
23.96390	HC_5N	J=9-8	2.62026	0.05046	8.96530	0.00061	0.10766	3.1358	3.8187	-34.565	0.8
24.13942	NH_3	4(4)-4(4)	0.14999	0.00285	0.50586	0.00066	0.11756	3.1144	3.7928	-34.571	0.8
24.40328	HC_9N	J=42-41									
24.53299	NH_3	5(5)-5(5)									
24.54023	SiC_4	J=8-7	0.09040	0.00166	0.29477	0.00059	0.10459	3.0658	3.7339	-34.588	0.8
24.78344	C_6H^-	J=9-8	0.11888	0.00215	0.38031	0.00063	0.11069	3.0370	3.6989	-34.598	0.8
24.81588	HC_7N	J=22-21	0.58272	0.01050	1.85918	0.00060	0.10569	3.0337	3.6949	-34.600	0.8
24.84692	HC_7Nv_{15}=1	J=22-21,l=1e									
24.86274	HC_7Nv_{15}=1	J=22-21,l=1f									
24.98430	HC_9N	J=43-42									
24.99130	SiC_2	J=8(2,6)-8(2,7)	0.17993	0.00339	0.56611	0.00056	0.09360	3.0366	3.8589	26.531	0.8
25.05603	NH_3	6(6)-6(6)	0.08399	0.00158	0.26286	0.00057	0.09518	3.0293	3.8500	26.555	0.8
25.56532	HC_9N	J=44-43									
25.91102	C_2S	N=2-1,J=2-1	0.70138	0.00692	1.21997	0.00078	0.13688	2.2119	2.7493	23.426	0.6
25.93341	$H^{13}CCCCCN$	J=10-9									
25.94385	HC_7N	J=23-22	0.77680	0.01453	2.26761	0.00061	0.09470	3.0251	3.8448	27.024	0.8
25.97631	HC_7Nv_{15}=1	J=23-22,l=1e									
25.99285	HC_7Nv_{15}=1	J=23-22,l=1f									
26.14634	HC_9N	J=45-44									
26.33741	C_6H	J=19/2-17/2,Ω=3/2,F=10-9,l=e									
26.33992	C_6H	J=19/2-17/2,Ω=3/2,F=10-9,l=f									
26.45059	$H^{13}CCCN$	J=3-2	0.35603	0.00784	0.99989	0.00076	0.09720	3.2097	4.2641	54.491	0.8
26.51138	C_6H	J=19/2-17/2,Ω=1/2,l=f	0.05015	0.00086	0.13882	0.00102	0.16319	2.8591	3.7752	-12.526	0.7
26.54089	C_6H	J=19/2-17/2,Ω=1/2,l=e	0.30466	0.00526	0.84519	0.00169	0.27167	2.8619	3.7791	-12.521	0.7
26.62650	HC_5N	J=10-9	3.11745	0.06353	8.57451	0.00114	0.15386	3.3606	3.7999	17.856	0.7
26.72735	HC_9N	J=46-45									
27.07181	HC_7N	J=24-23	0.77808	0.01290	2.07029	0.00101	0.16165	2.8058	3.7013	-12.617	0.7
27.10569	HC_7Nv_{15}=1	J=24-23,l=1e									
27.12295	HC_7Nv_{15}=1	J=24-23,l=1f									
27.17851	$HC^{13}CCN$	J=3-2	0.86592	0.01424	2.28566	0.00098	0.15706	2.7956	3.6872	-12.635	0.7
27.18112	$HCC^{13}CN$	J=3-2	0.86590	0.01424	2.28562	0.00098	0.15708	2.7956	3.6872	-12.635	0.7
27.29429	HC_3N	J=3-2	16.38456	0.26734	42.89051	0.00605	0.97029	2.7845	3.6718	-12.656	0.7
27.30836	HC_9N	J=47-46									
27.53713	C_6H^-	J=10-9									

Table A.1 continued.

Frequency (GHz)	Species	Transition	$I_{\rm int}$ (Jy km s^{-1})	$I_{\rm int}$ (Jy beam^{-1} km s^{-1})	$I_{\rm int}$ (K km s^{-1})	σ (Jy beam^{-1})	σ (K)	$\theta_{\rm maj}$ (arcsec)	$\theta_{\rm min}$ (arcsec)	P.A. (°)	cell size
27.57314	C_8H	J=47/2-45/2,Ω=3/2,F=24-23,l=e									
27.57344	C_8H	J=47/2-45/2,Ω=3/2,F=24-23,l=f									
27.60773	SiC_4	J=9-8									
27.77706	C_5N-	J=10-9									
27.88938	HC_9N	J=48-47									
28.19981	HC_7N	J=25-24	0.86079	0.01190	2.11072	0.00075	0.13273	2.6436	3.2769	22.826	0.7
28.23508	HC_7Nv_{15}=1	J=25-24,l=1e									
28.25305	HC_7Nv_{15}=1	J=25-24,l=1f									
28.47039	HC_9N	J=49-48									
28.52673	$H^{13}CCCCCN$	J=11-10									
28.53231	C_4H	N=3-2,J=7/2-5/2,F=3-2	0.31148	0.00460	0.74608	0.00115	0.18708	2.8909	3.2028	-4.917	0.7
28.57137	C_4H	N=3-2,J=5/2-3/2,F=3-2	0.24120	0.00355	0.57617	0.00143	0.23272	2.8859	3.1965	-4.742	0.7
28.74646	C_8H	J=49/2-47/2,Ω=3/2,F=24-23,l=e									
28.74678	C_8H	J=49/2-47/2,Ω=3/2,F=24-23,l=f									
28.90369	C_3S	J=5-4									
29.05140	HC_9N	J=50-49									
29.10966	C_6H	J=21/2-19/2,Ω=3/2,l=e									
29.11273	C_6H	J=21/2-19/2,Ω=3/2,l=f									
29.28915	HC_5N	J=11-10	3.60278	0.05025	8.18954	0.00102	0.16572	2.8126	3.1076	-2.479	0.7
29.30333	C_6H	J=21/2-19/2,Ω=1/2,l=f									
29.31122	$HC_3{}^{13}CC_3N$	J=26-25									
29.31380	$HC_4{}^{13}CC_2N$	J=26-25									
29.32777	HC_7N	J=26-25	0.76044	0.01058	1.72401	0.00101	0.16469	2.8089	3.1031	-2.377	0.7
29.33323	C_6H	J=21/2-19/2,Ω=1/2,l=e									
29.36446	HC_7Nv_{15}=1	J=26-25,l=1e									
29.38315	HC_7Nv_{15}=1	J=26-25,l=1f									
29.47770	C_2S	N=3-2,J=2-1									
29.63241	HC_9N	J=51-50									
29.67614	C_3N	N=3-2,J=7/2-5/2,F=5/2-3/2	0.53924	0.00927	1.21322	0.00118	0.15436	2.3712	4.4728	21.511	0.6
29.69513	C_3N	N=3-2,J=5/2-3/2,F=5/2-3/2	0.42600	0.00732	0.95726	0.00093	0.12191	2.3698	4.4714	21.509	0.6
29.91975	C_8H	J=51/2-49/2,Ω=3/2,F=25-24,l=e									
29.92010	C_8H	J=51/2-49/2,Ω=3/2,F=25-24,l=f									
30.21342	HC_9N	J=52-51									
30.29081	C_6H^-	J=11-10	0.28368	0.00431	0.60522	0.00013	0.01823	2.3931	3.9602	25.862	0.4
30.45575	HC_7N	J=27-26	0.61619	0.01155	1.31629	0.00118	0.13419	2.4243	4.7672	32.243	0.6
30.49384	HC_7Nv_{15}=1	J=27-26,l=1e									
30.51325	HC_7Nv_{15}=1	J=27-26,l=1f									
30.67522	SiC_4	J=10-9									
30.79443	HC_9N	J=53-52									
31.02881	C_5H	J=13/2-11/2,Ω=1/2,F=7-6,l=e									

Table A.1 continued.

Frequency (GHz)	Species	Transition	$I_{\rm int}$ (Jy km s^{-1})	$I_{\rm int}$ (Jy beam^{-1} km s^{-1})	$I_{\rm int}$ (K km s^{-1})	σ (Jy beam^{-1})	σ (K)	$\theta_{\rm maj}$ (arcsec)	$\theta_{\rm min}$ (arcsec)	P.A. (°)	cell size
31.03278	C_5H	J=13/2-11/2,Ω=1/2,F=7-6,l=f									
31.09304	C_8H	J=53/2-51/2,Ω=3/2,F=26-25,l=e									
31.09342	C_8H	J=53/2-51/2,Ω=3/2,F=26-25,l=f									
31.12004	$H^{13}CCCCCN$	J=12-11									
31.24220	C_5H	J=13/2-11/2,Ω=3/2,F=7-6,l=f									
31.24246	C_5H	J=13/2-11/2,Ω=3/2,F=7-6,l=e									
31.37544	HC_9N	J=54-53									
31.58370	HC_7N	J=28-27	1.59288	0.02853	3.16393	0.00112	0.12466	2.7330	4.0419	29.945	0.6
31.62320	HC_7Nv_{15}=1	J=28-27,l=1e									
31.62434	$HC^{13}CCCCN$	J=12-11									
31.63613	$HCCCC^{13}CN$	J=12-11									
31.64334	HC_7Nv_{15}=1	J=28-27,l=1f									
31.88186	C_6H	J=23/2-21/2,Ω=3/2,l=e									
31.88554	C_6H	J=23/2-21/2,Ω=3/2,l=f									
31.91870	$HCC^{13}CCCN$	J=12-11									
31.92257	$HCCC^{13}CCN$	J=12-11									
31.95177	HC_5N	J=12-11	7.00878	0.09970	13.60273	0.00163	0.22308	1.9310	4.5428	20.245	0.6
31.95644	HC_9N	J=55-54									
32.09524	C_6H	J=23/2-21/2,Ω=1/2,l=f									
32.12556	C_6H	J=23/2-21/2,Ω=1/2,l=e									
32.26634	C_8H	J=55/2-53/2,Ω=3/2,F=27-26,l=e									
32.26674	C_8H	J=55/2-53/2,Ω=3/2,F=27-26,l=f									
32.53745	HC_9N	J=56-55									
32.62730	C_3H	J=3/2-1/2,Ω=1/2,F=2-1,l=f	0.14085	0.00158	0.26211	0.00095	0.15765	2.2442	3.0805	-8.263	0.6
32.66065	C_3H	J=3/2-1/2,Ω=1/2,F=2-1,l=e	0.41997	0.00470	0.78001	0.00096	0.15963	2.2421	3.0776	-8.261	0.6
32.71168	HC_7N	J=29-28	0.58530	0.00653	1.08370	0.00132	0.21898	2.2387	3.0727	-8.258	0.6
32.75258	HC_7Nv_{15}=1	J=29-28,l=1e									
32.77343	HC_7Nv_{15}=1	J=29-28,l=1f									
33.04449	C_6H^-	J=12-11	0.49658	0.00538	0.89002	0.00022	0.03596	2.2185	3.0486	-8.605	0.4
33.11845	HC_9N	J=57-56									
33.43962	C_8H	J=57/2-55/2,Ω=3/2,F=28-27,l=e									
33.44006	C_8H	J=57/2-55/2,Ω=3/2,F=28-27,l=f									
33.69945	HC_9N	J=58-57									
33.71334	$H^{13}CCCCCN$	J=13-12									
33.74268	SiC_4	J=11-10									
33.75137	C_2S	N=2-1,J=3-2									
33.83962	HC_7N	J=30-29	1.36942	0.01344	2.36948	0.00088	0.15478	2.2066	2.7434	23.487	0.6
33.88195	HC_7Nv_{15}=1	J=30-29,l=1e									
33.90352	HC_7Nv_{15}=1	J=30-29,l=1f									
34.25967	$HC^{13}CCCCN$	J=13-12									

Table A.1 continued.

Frequency (GHz)	Species	Transition	I_{int} (Jy km s^{-1})	I_{int} (Jy beam^{-1} km s^{-1})	I_{int} (K km s^{-1})	σ (Jy beam^{-1})	σ (K)	θ_{maj} (arcsec)	θ_{min} (arcsec)	P.A. (°)	cell size
34.27245	$HCCCC^{13}CN$	J=13-12									
34.28045	HC_9N	J=59-58									
34.57855	$HCC^{13}CCCN$	J=13-12									
34.58275	$HCCC^{13}CCN$	J=13-12									
34.61291	C_8H	J=59/2-57/2,Ω=3/2,F=29-28,l=e									
34.61338	C_8H	J=59/2-57/2,Ω=3/2,F=29-28,l=f									
34.61439	HC_5N	J=13-12	4.95549	0.05018	8.19492	0.00143	0.23351	2.3787	2.6254	-1.519	0.6
34.65404	C_6H	J=25/2-23/2,Ω=3/2,l=e									
34.65838	C_6H	J=25/2-23/2,Ω=3/2,l=f									
34.67390	U	unidentified transition									
34.68437	C_3S	J=6-5									
34.86146	HC_9N	J=60-59									
34.88711	C_6H	J=25/2-23/2,Ω=1/2,l=f									
34.91788	C_6H	J=25/2-23/2,Ω=1/2,l=e									
34.96759	HC_7N	J=31-30	0.94972	0.00941	1.53900	0.00159	0.26069	2.3540	2.5961	-0.865	0.6
35.01132	HC_7Nv_{15}=1	J=31-30,l=1e									
35.02116	^{30}SiS	J=2-1									
35.03360	HC_7Nv_{15}=1	J=31-30,l=1f									
35.26740	$H^{13}CCCN$	J=4-3	0.88980	0.01206	1.41751	0.00138	0.16222	2.1188	3.9443	24.904	0.6
35.31528	$Si^{34}S$	J=2-1									
35.44245	HC_9N	J=61-60									
35.64246	^{29}SiS	J=2-1	0.59728	0.00747	0.93160	0.00116	0.14445	1.9422	3.9709	23.988	0.6
35.78619	C_8H	J=61/2-59/2,Ω=3/2,F=30-29,l=e									
35.78669	C_8H	J=61/2-59/2,Ω=3/2,F=30-29,l=f									
35.79331	MgNC	N=3-2,J=5/2									
35.79667	$Si^{33}S$	J=2-1									
35.79815	C_6H^-	J=13-12									
35.80853	MgNC	N=3-2,J=7/2-5/2									
36.02345	HC_9N	J=62-61									
36.04849	C_5H	J=15/2-13/2,Ω=3/2,F=8-7,l=f									
36.04884	C_5H	J=15/2-13/2,Ω=3/2,F=8-7,l=e									
36.09553	HC_7N	J=32-31									
36.11006	C_5N-	J=13-12									
36.14068	HC_7Nv_{15}=1	J=32-31,l=1e									
36.16368	HC_7Nv_{15}=1	J=32-31,l=1f									
36.23795	$HC^{13}CCN$	J=4-3	1.99727	0.02503	3.01329	0.00119	0.14330	1.9125	4.0409	23.784	0.6
36.24144	$HCC^{13}CN$	J=4-3	1.86556	0.02338	2.81458	0.00119	0.14279	1.9125	4.0409	23.784	0.6
36.30663	$H^{13}CCCCCN$	J=14-13									
36.30963	SiS	J=2-1	17.87958	0.17155	26.73769	0.00150	0.23384	1.9131	3.1083	43.385	0.5
36.39232	HC_3N	J=4-3	33.95259	0.32225	50.54335	0.00165	0.25817	1.8932	3.1070	42.818	0.5

Table A.1 continued.

Frequency (GHz)	Species	Transition	$I_{\rm int}$ (Jy km s^{-1})	$I_{\rm int}$ (Jy beam^{-1} km s^{-1})	$I_{\rm int}$ (K km s^{-1})	σ (Jy beam^{-1})	σ (K)	$\theta_{\rm maj}$ (arcsec)	$\theta_{\rm min}$ (arcsec)	P.A. (°)	cell size
36.60445	HC_9N	J=63-62									
36.79547	CH_3CN	2(0)-1(0)									
36.81013	SiC_4	J=12-11									
36.95946	C_8H	J=63/2-61/2,Ω=3/2,F=31-30,l=e									
36.96000	C_8H	J=63/2-61/2,Ω=3/2,F=31-30,l=f									
37.18544	HC_9N	J=64-63									
37.22349	HC_7N	J=33-32	1.44383	0.01469	2.05449	0.00234	0.32715	1.7938	3.5153	42.101	0.5
37.23839	$HCC^{13}CCCN$	J=14-13									
37.24292	$HCCC^{13}CCN$	J=14-13									
37.27699	HC_5N	J=14-13	13.35231	0.15084	18.94461	0.00184	0.23086	2.3224	3.0147	21.162	0.5
37.27004	HC_7Nv_{15}=1	J=33-32,l=1e									
37.29376	HC_7Nv_{15}=1	J=33-32,l=1f									
37.42619	C_6H	J=27/2-25/2,Ω=3/2,l=e									
37.43126	C_6H	J=27/2-25/2,Ω=3/2,l=f									
37.67894	C_6H	J=27/2-25/2,Ω=1/2,l=f									
37.71020	C_6H	J=27/2-25/2,Ω=1/2,l=e									
37.76644	HC_9N	J=65-64									
38.04969	C_4H	N=4-3,J=9/2-7/2,F=5-4	1.39536	0.01507	1.90016	0.00171	0.21545	2.2546	2.9681	21.470	0.5
38.08844	C_4H	N=4-3,J=7/2-5/2,F=4-3	0.91224	0.00997	1.23973	0.00174	0.21576	2.2902	2.9578	22.680	0.5
38.13274	C_8H	J=65/2-63/2,Ω=3/2,F=32-31,l=e									
38.13331	C_8H	J=65/2-63/2,Ω=3/2,F=32-31,l=f									

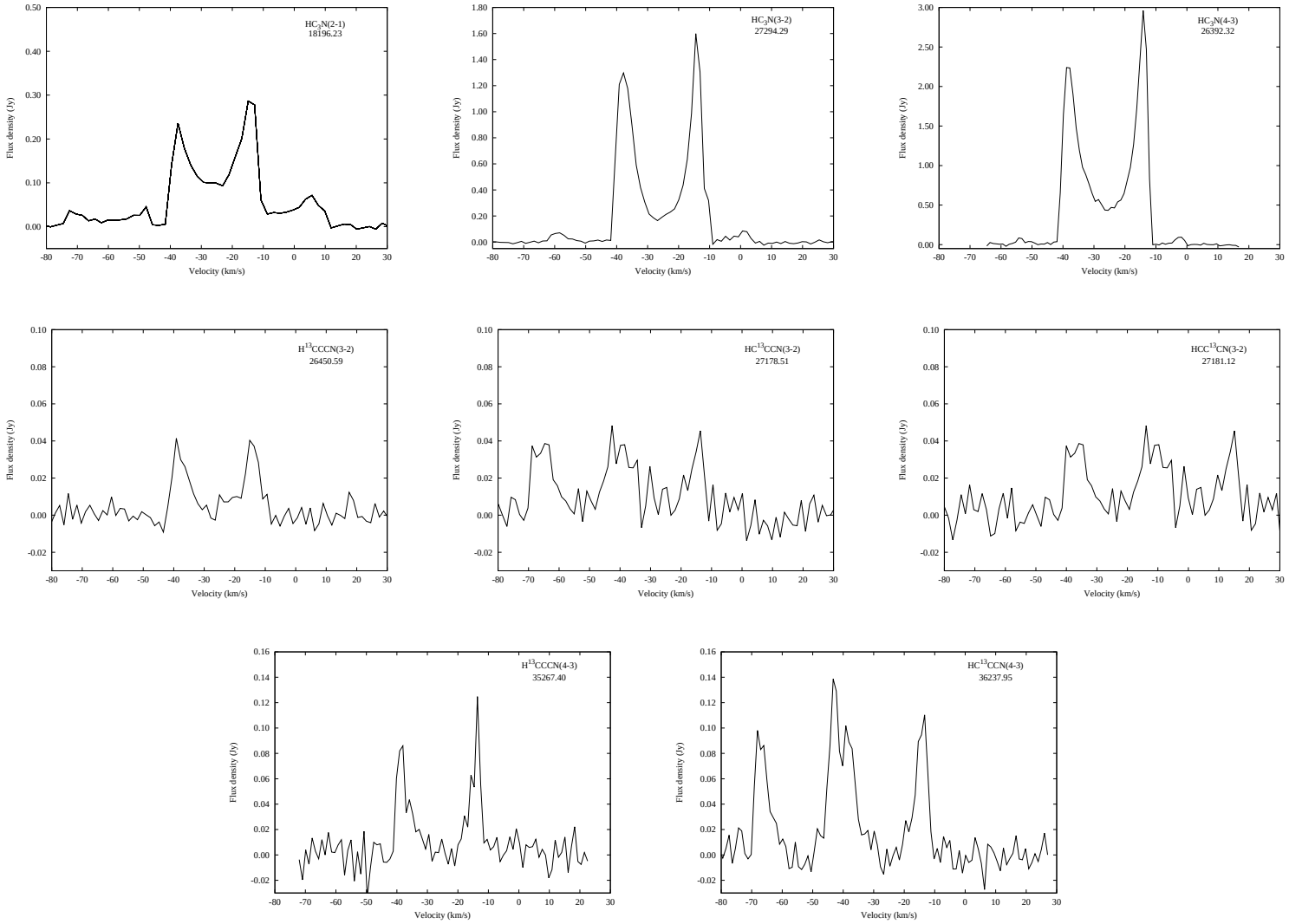

Figure A.12: Spectral line emission of HC_3N of IRC+10216 from the CLEANed images for an aperture region of 30 arcsec radius. The rest frequency of the transition in MHz is given on the top right.

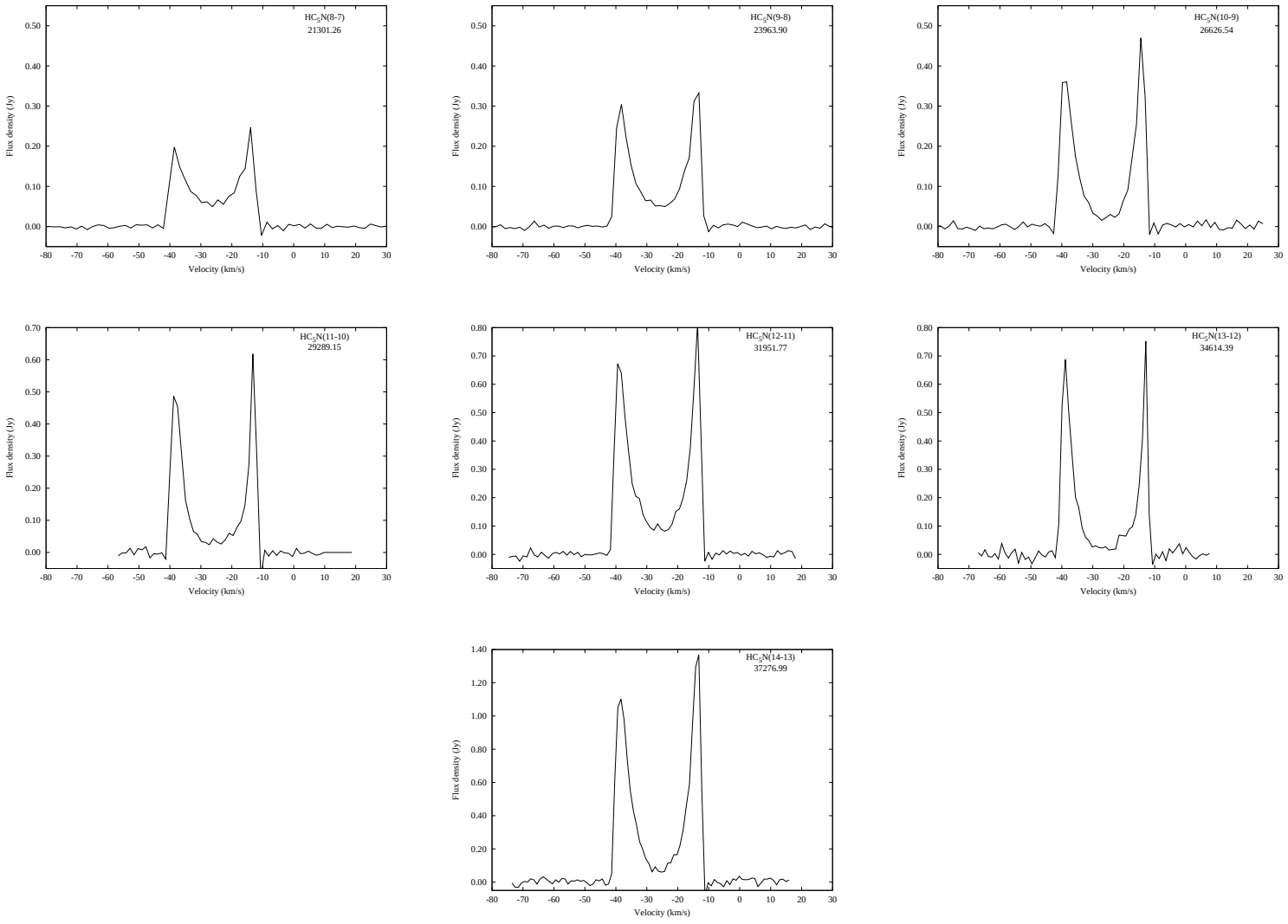

Figure A.13: Spectral line emission of HC_5N of IRC+10216 from the CLEANed images for an aperture region of 30 arcsec radius. The rest frequency of the transition in MHz is given on the top right.

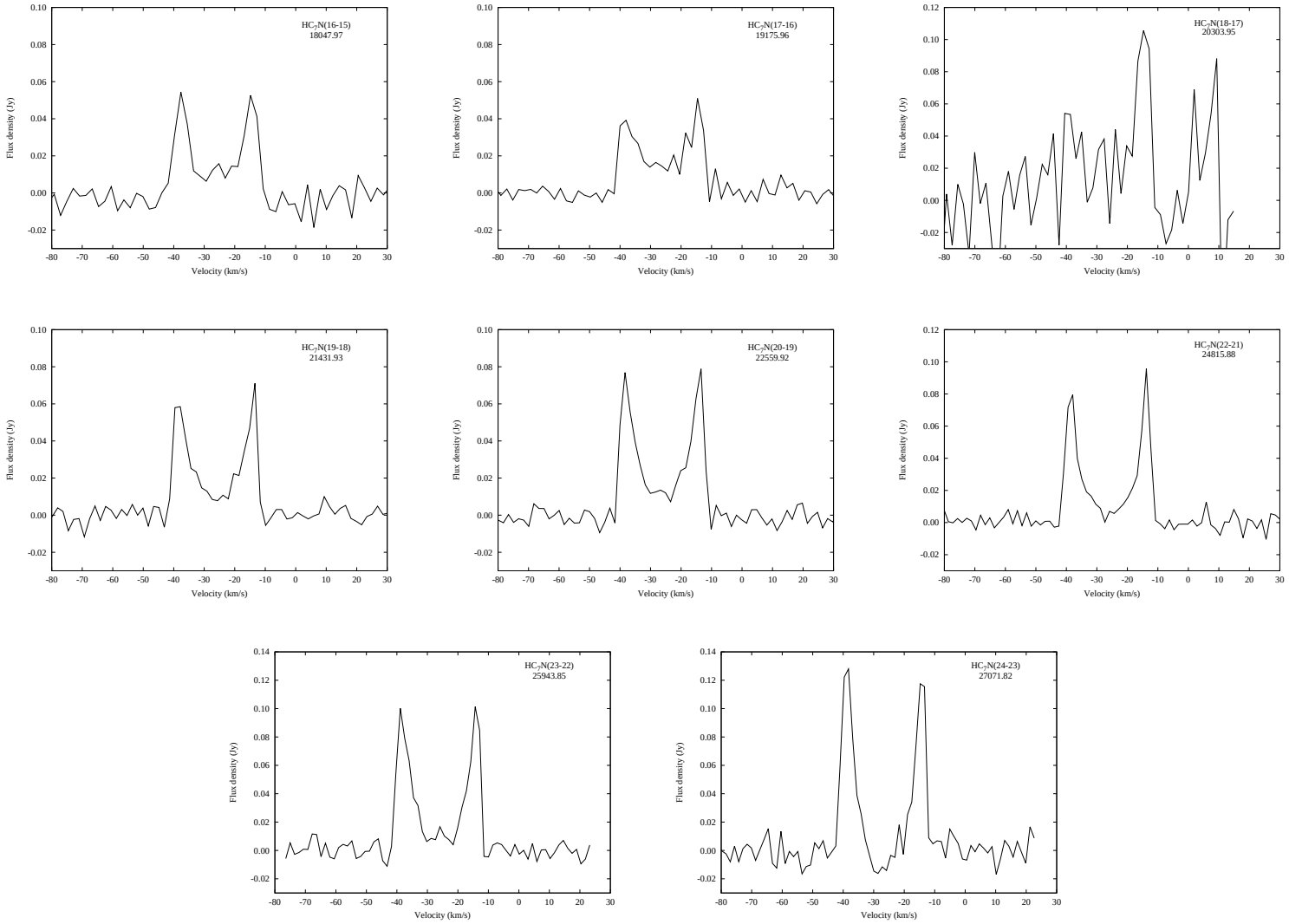

Figure A.14: Spectral line emission of HC_7N of IRC+10216 from the CLEANed images for an aperture region of 30 arcsec radius. The rest frequency of the transition in MHz is given on the top right.

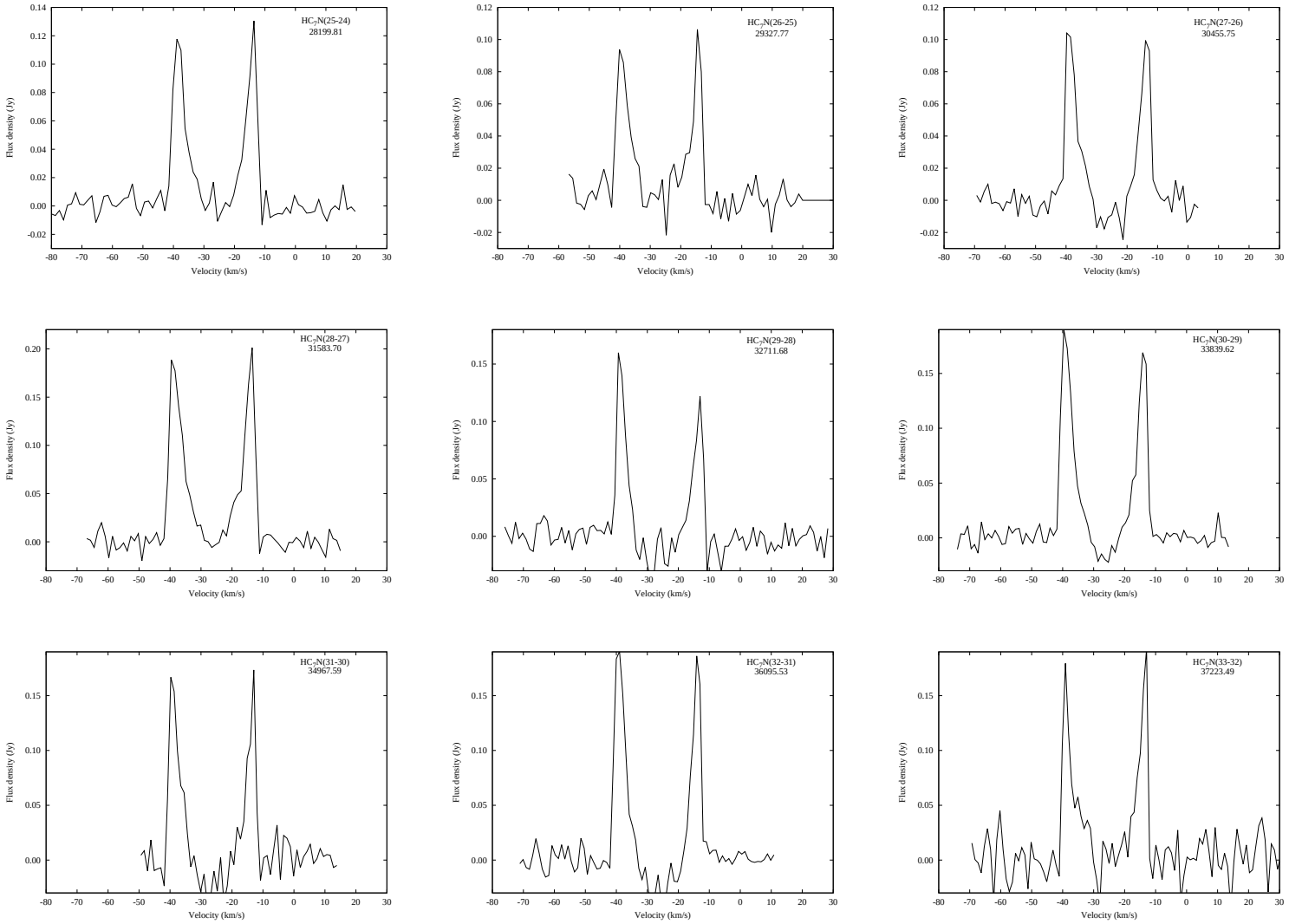

Figure A.15: Spectral line emission of HC_7N cont'd.

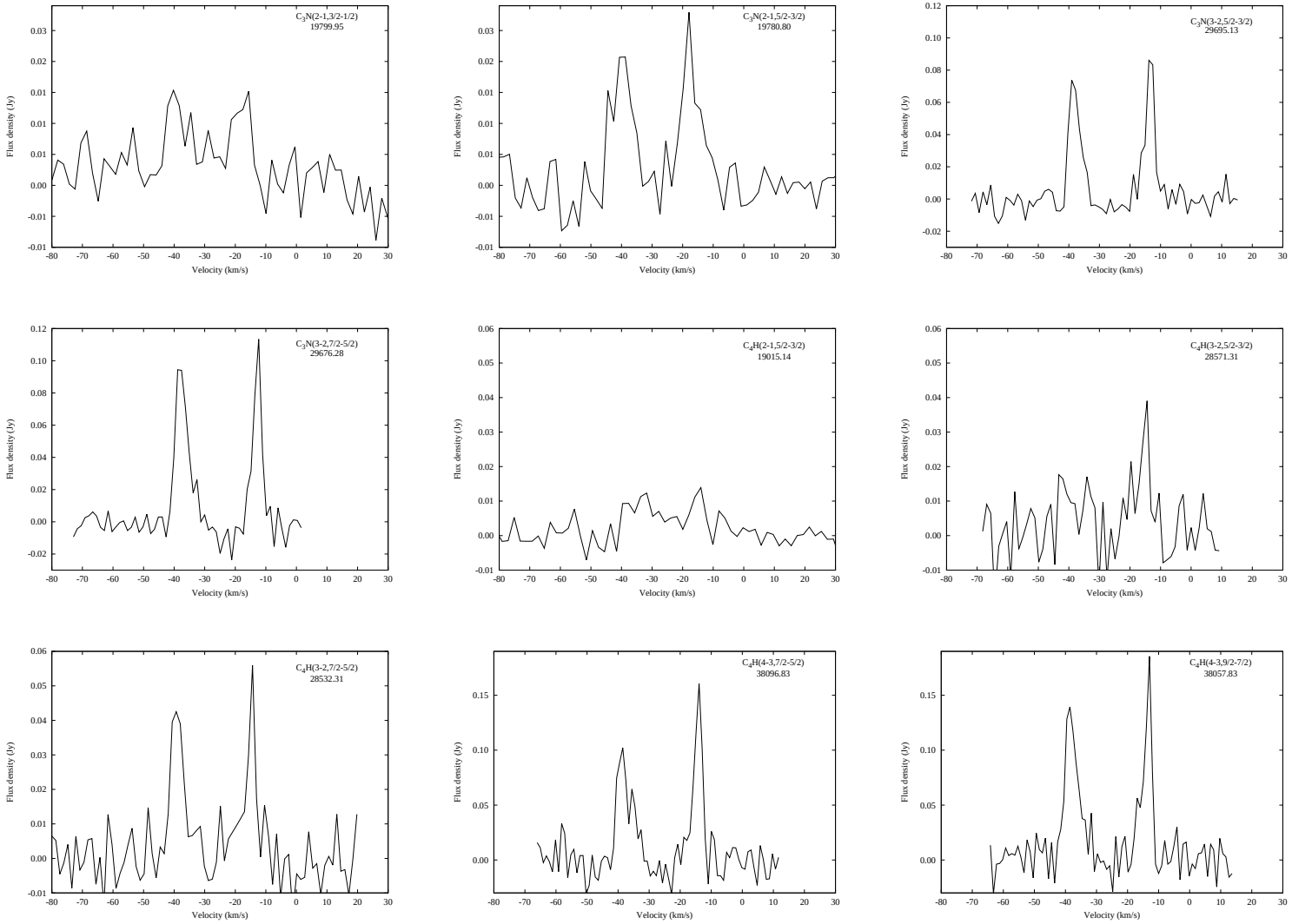

Figure A.16: Spectral line emission of C_3N and C_4H of IRC+10216 from the CLEANed images for an aperture region of 30 arcsec radius. The rest frequency of the transition in MHz is given on the top right.

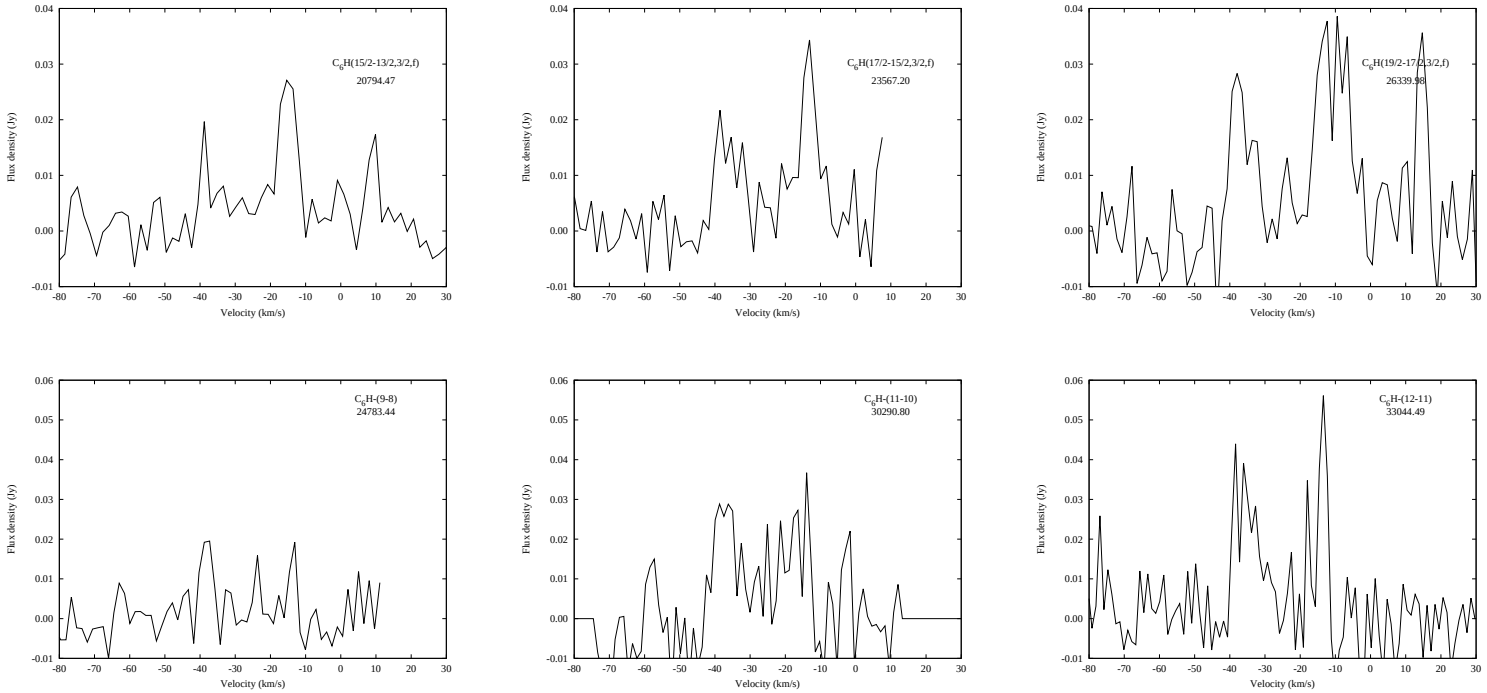

Figure A.17: Spectral line emission of C_6H and C_6H^- of IRC+10216 from the CLEANed images for an aperture region of 30 arcsec radius. The rest frequency of the transition in MHz is given on the top right.

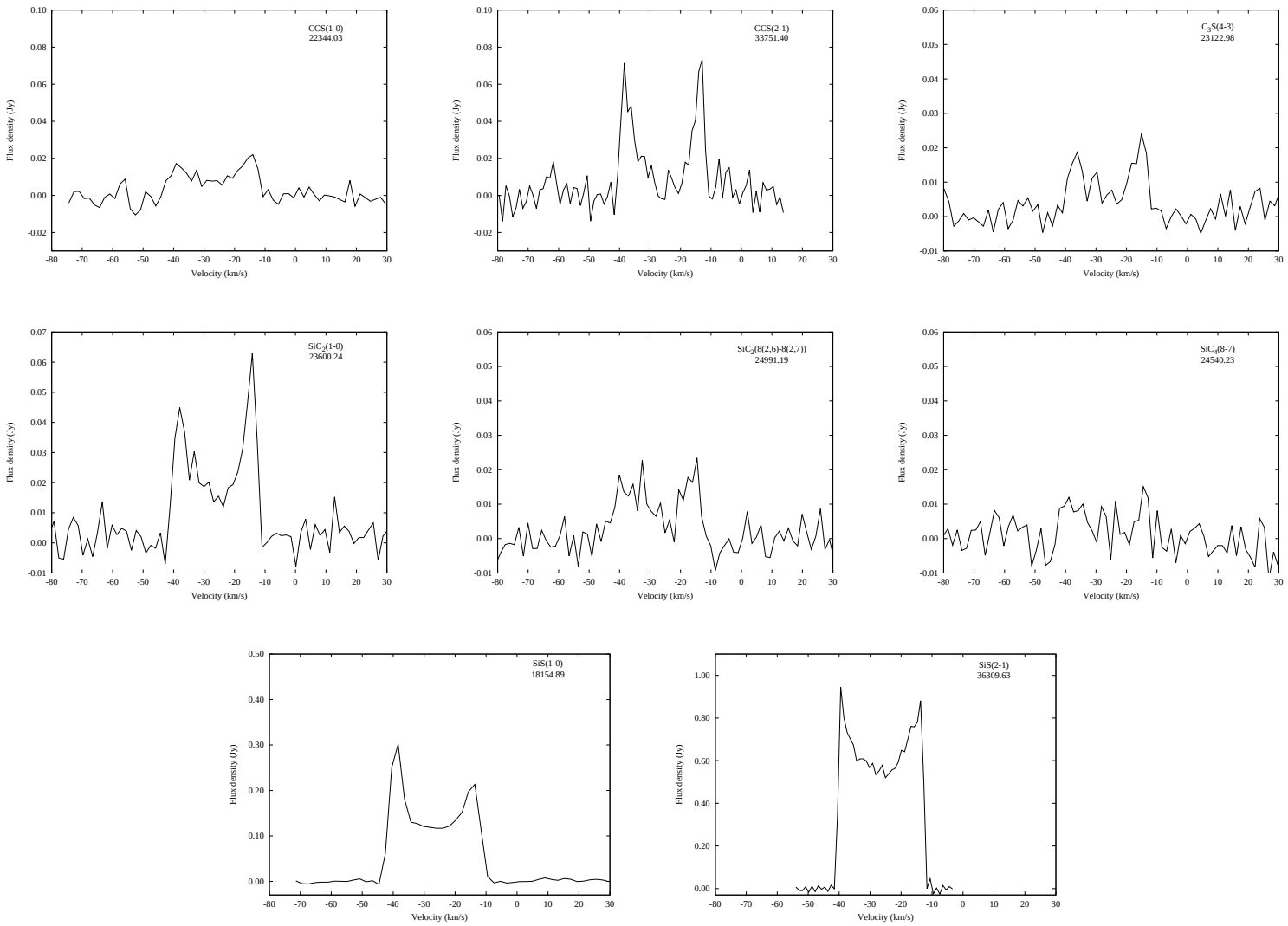

Figure A.18: Spectral line emission of CCS, C_3S, SiC_2, SiC_4, and SiS of IRC+10216 from the CLEANed images for an aperture region of 30 arcsec radius. The rest frequency of the transition in MHz is given on the top right.

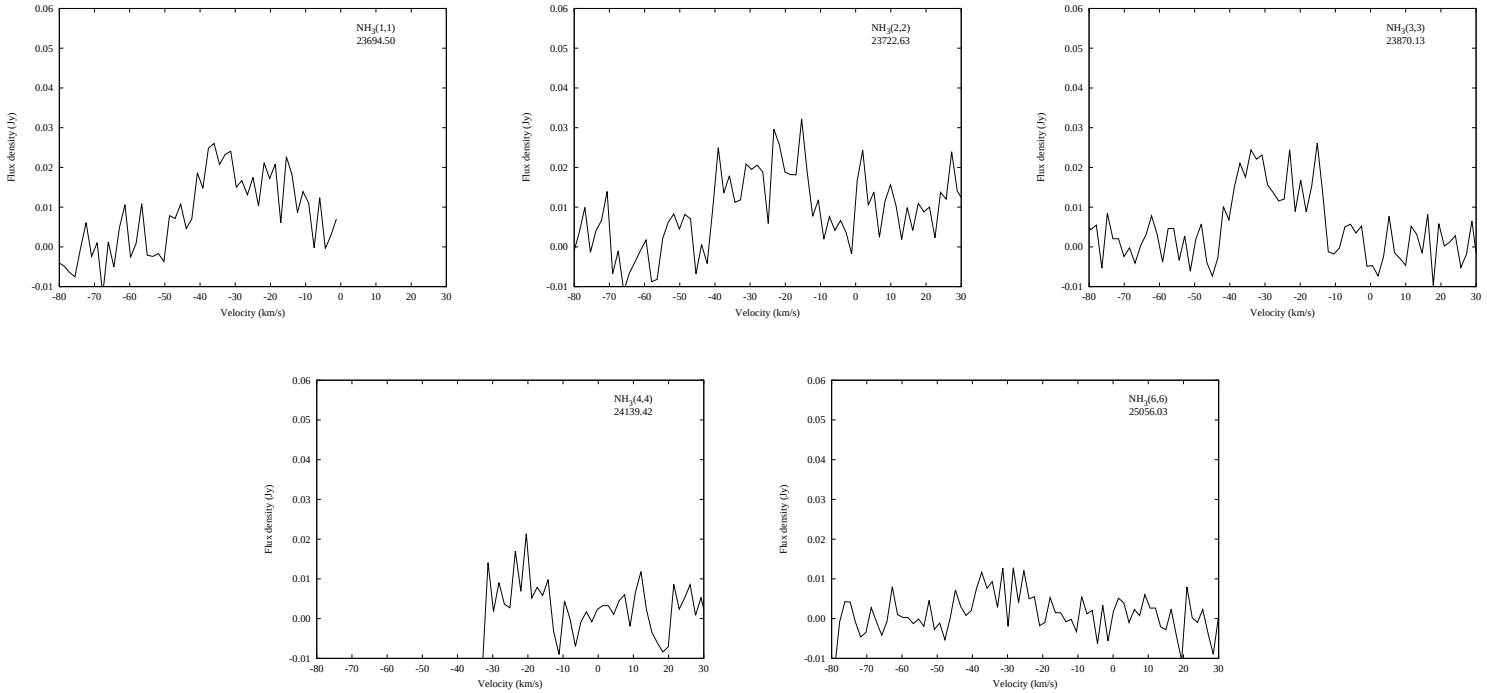

Figure A.19: Spectral line emission of NH_3 of IRC+10216 from the CLEANed images for an aperture region of 30 arcsec radius. The rest frequency of the transition in MHz is given on the top right.

APPENDIX **B**

Channel maps

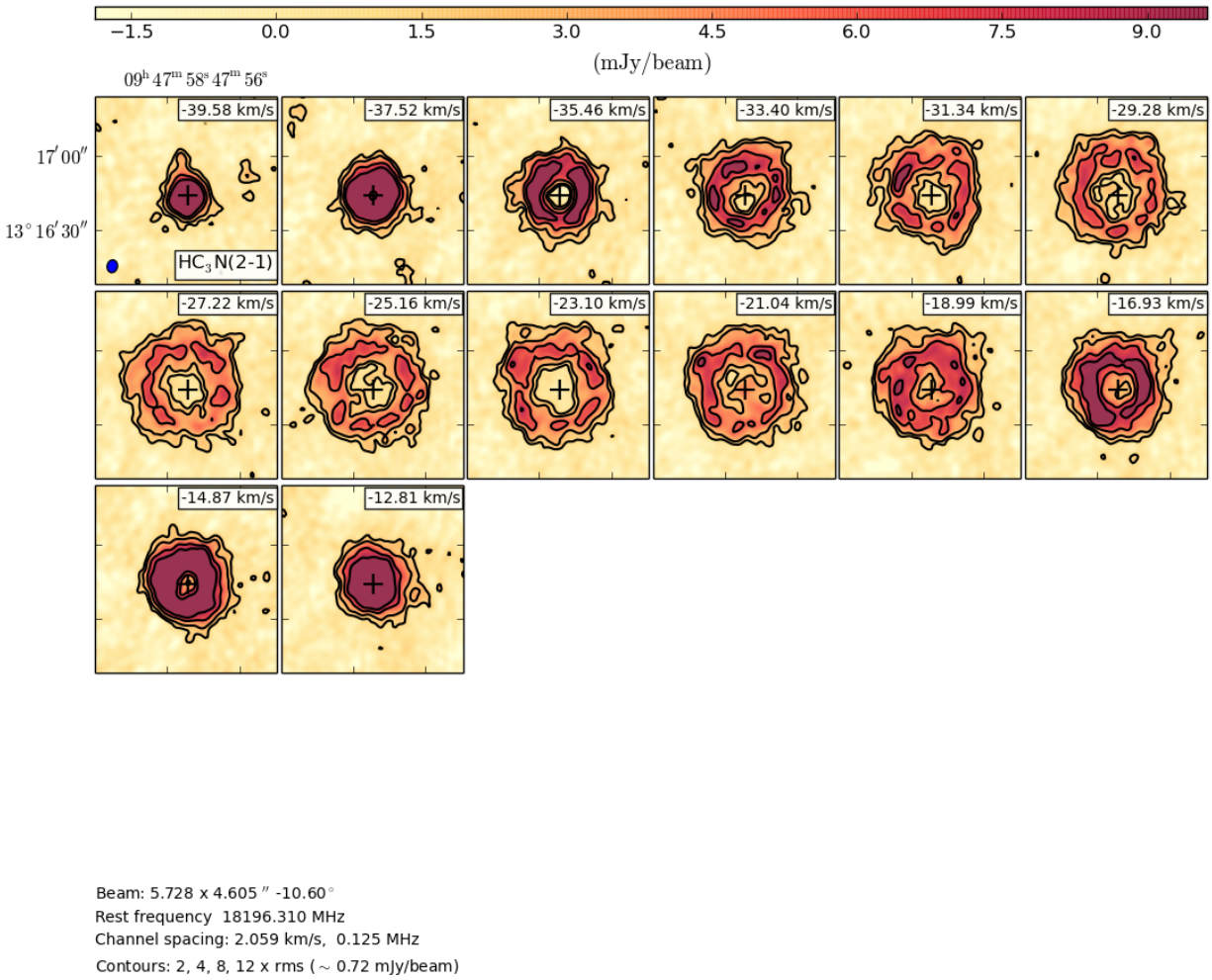

Figure B.1: Contours of molecular emission of HC_3N(2-1) around IRC+10216 for all velocity components in the data cube. The contour levels are 2, 4, 8, 12 $\times\,\sigma$(= 0.72 mJy beam^{-1}). The position of the radio continuum from the central star at $09^h47^m57.437^s$, $13°16'43.850''$ is marked with the +. The blue ellipse shows the synthesized beam of the datacube ($5.7 \times 4.6''$, $-10.6°$).

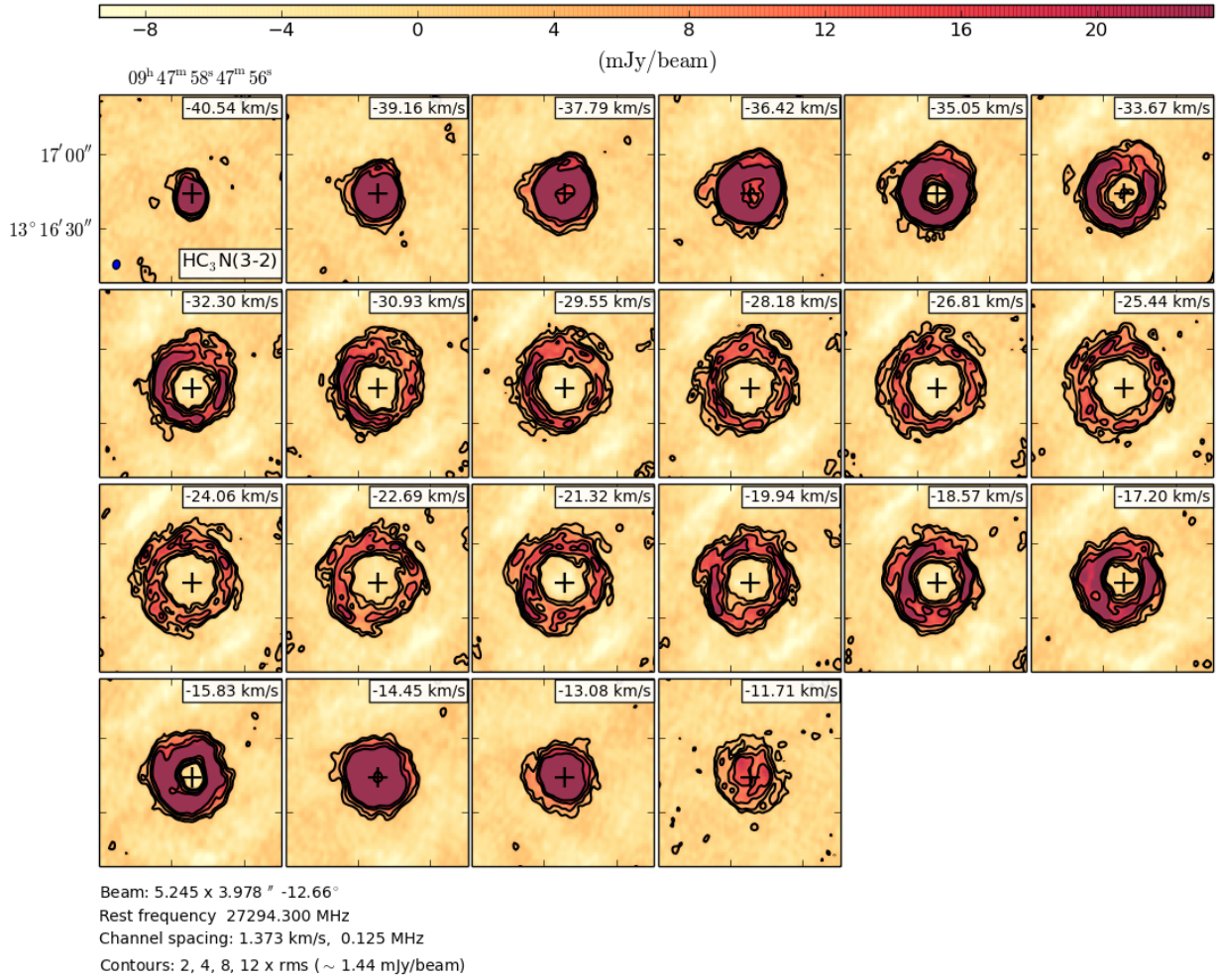

Figure B.2: As Fig. B.1, for HC_3N(3-2). The contour levels are 2, 4, 8, 12 $\times\sigma$(= 1.44 mJy beam^{-1}) and the synthesized beam is $5.2 \times 4.0''$, $-12.66°$.

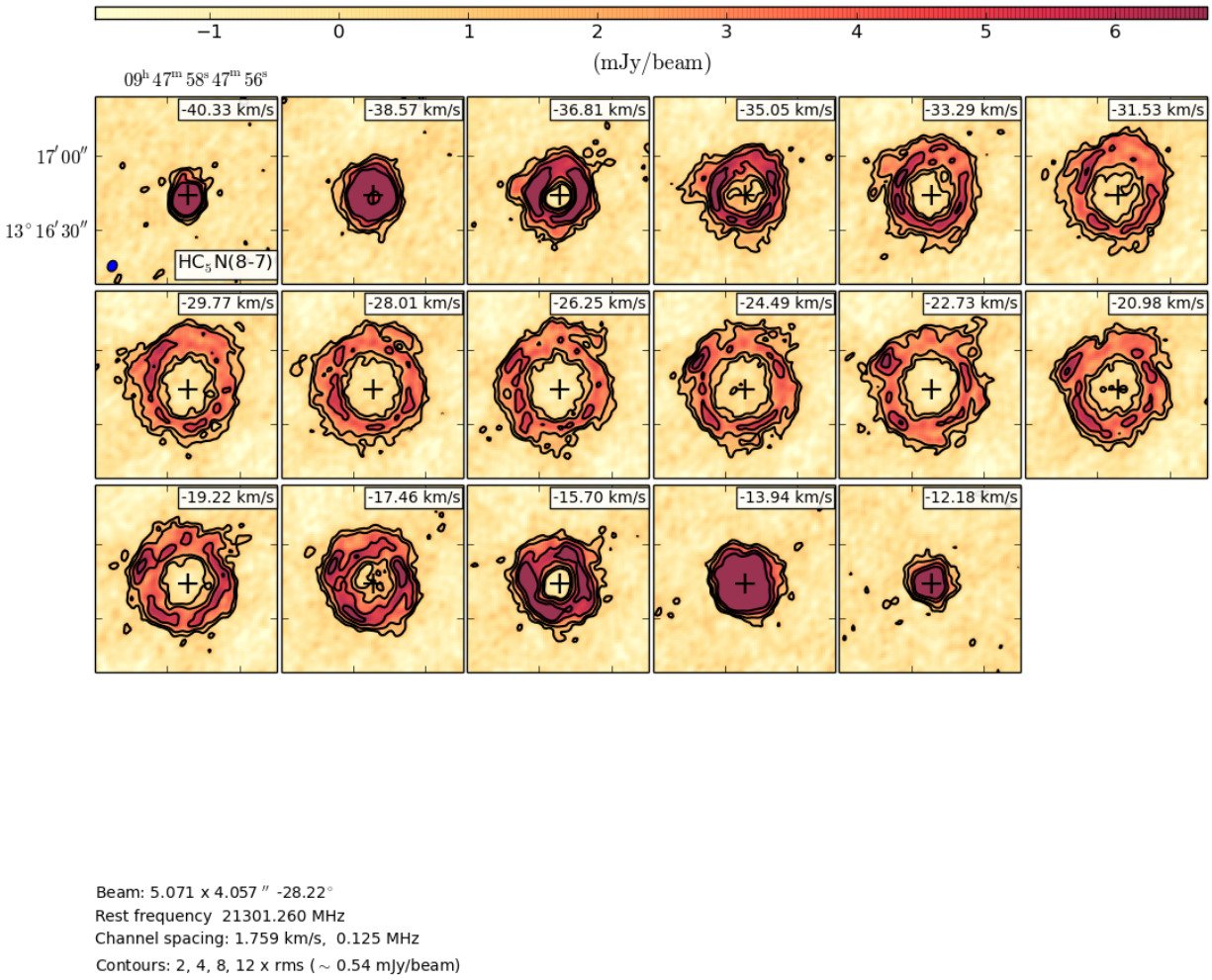

Figure B.3: As Fig. B.1, for HC_5N(8-7). The contour levels are 2, 4, 8, 12 $\times\sigma$(= 0.54 mJy beam^{-1}) and the synthesized beam is $5.1 \times 4.1''$, $-28.22°$.

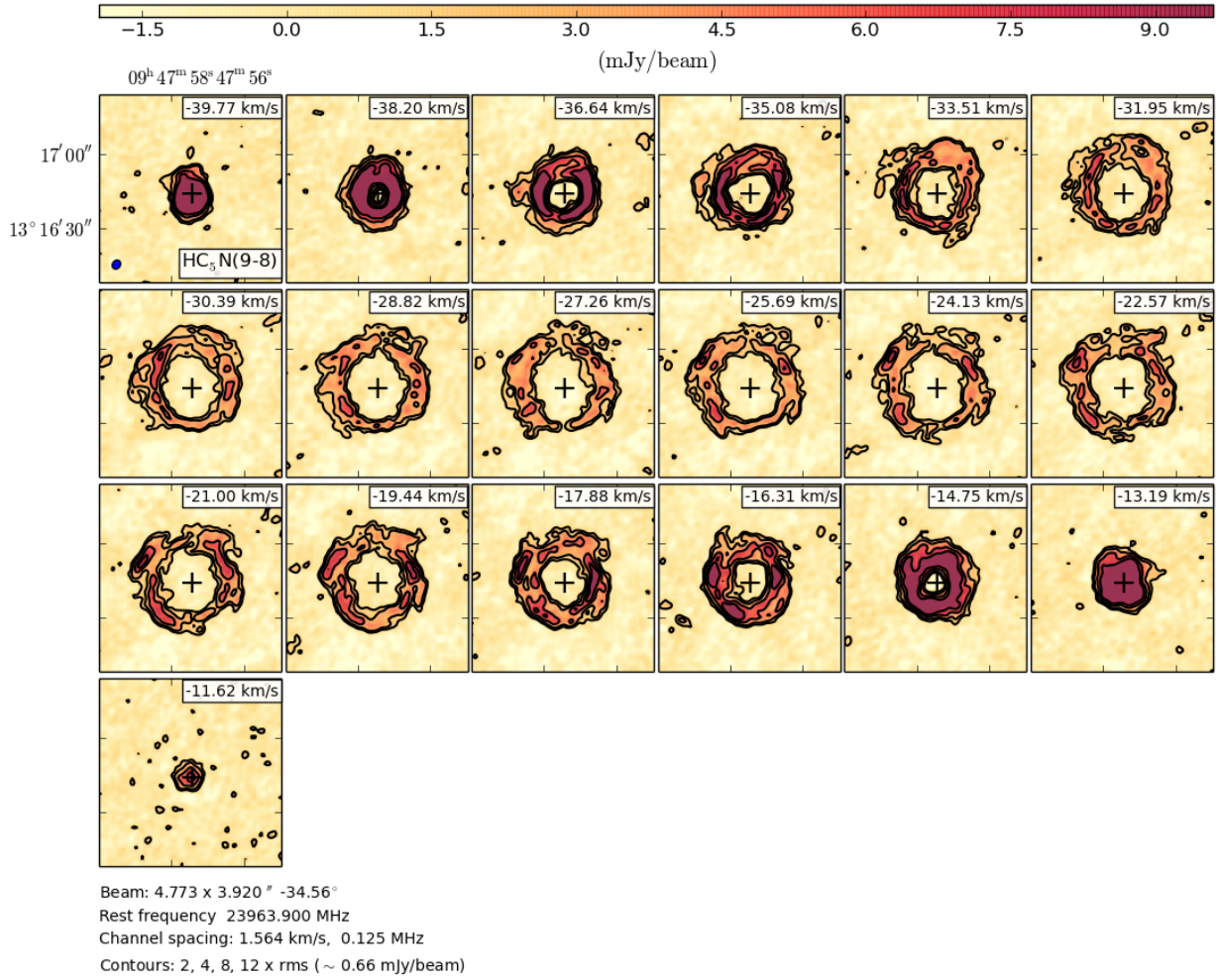

Figure B.4: As Fig. B.1, for HC_5N(9-8). The contour levels are 2, 4, 8, 12 $\times\sigma$(= 0.66 mJy beam^{-1}) and the synthesized beam is $4.8 \times 3.9''$, $-34.56°$.

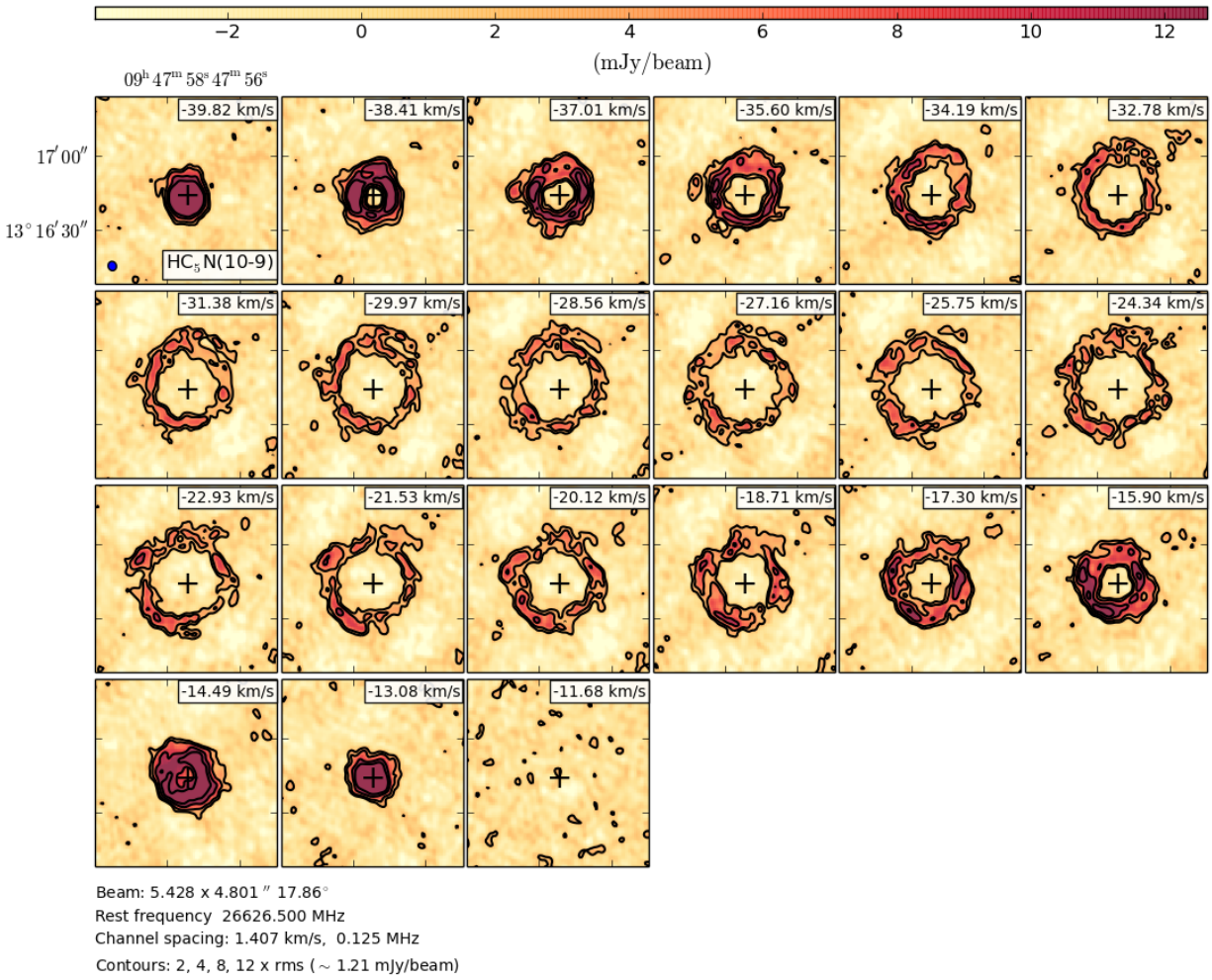

Figure B.5: As Fig. B.1, for HC_5N(10-9). The contour levels are 2, 4, 8, 12 $\times\sigma$(= 1.21 mJy beam^{-1}) and the synthesized beam is $5.4 \times 4.8''$, 17.86°.

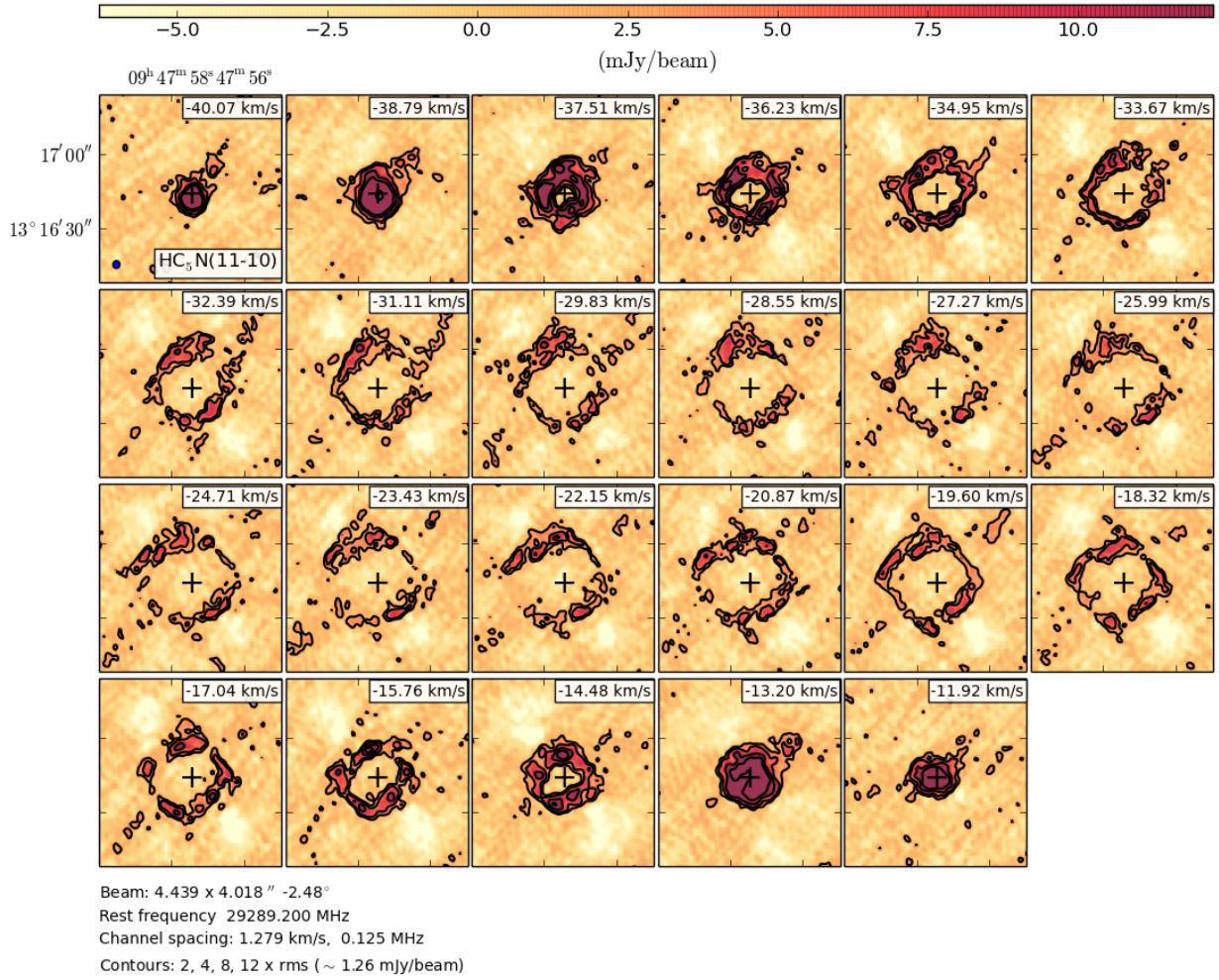

Figure B.6: As Fig. B.1, for HC_5N(11-10). The contour levels are 2, 4, 8, 12 $\times\sigma$(= 1.26 mJy beam^{-1}) and the synthesized beam is $4.4 \times 4.0''$, $-2.48°$.

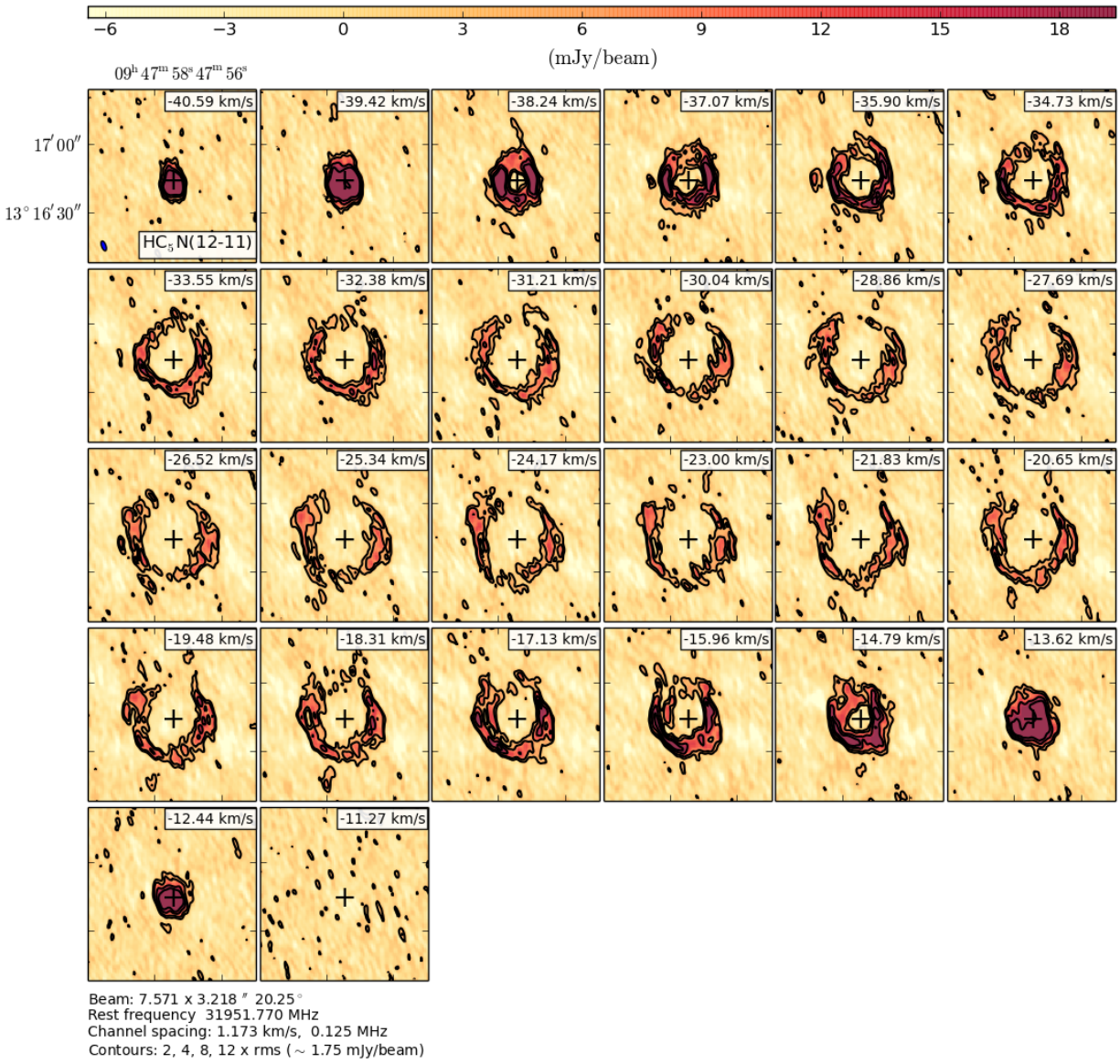

Figure B.7: As Fig. B.1, for HC_5N(12-11). The contour levels are 2, 4, 8, 12 $\times\sigma$(= 1.75 mJy beam^{-1}) and the synthesized beam is $7.6 \times 3.2''$, 20.25°.

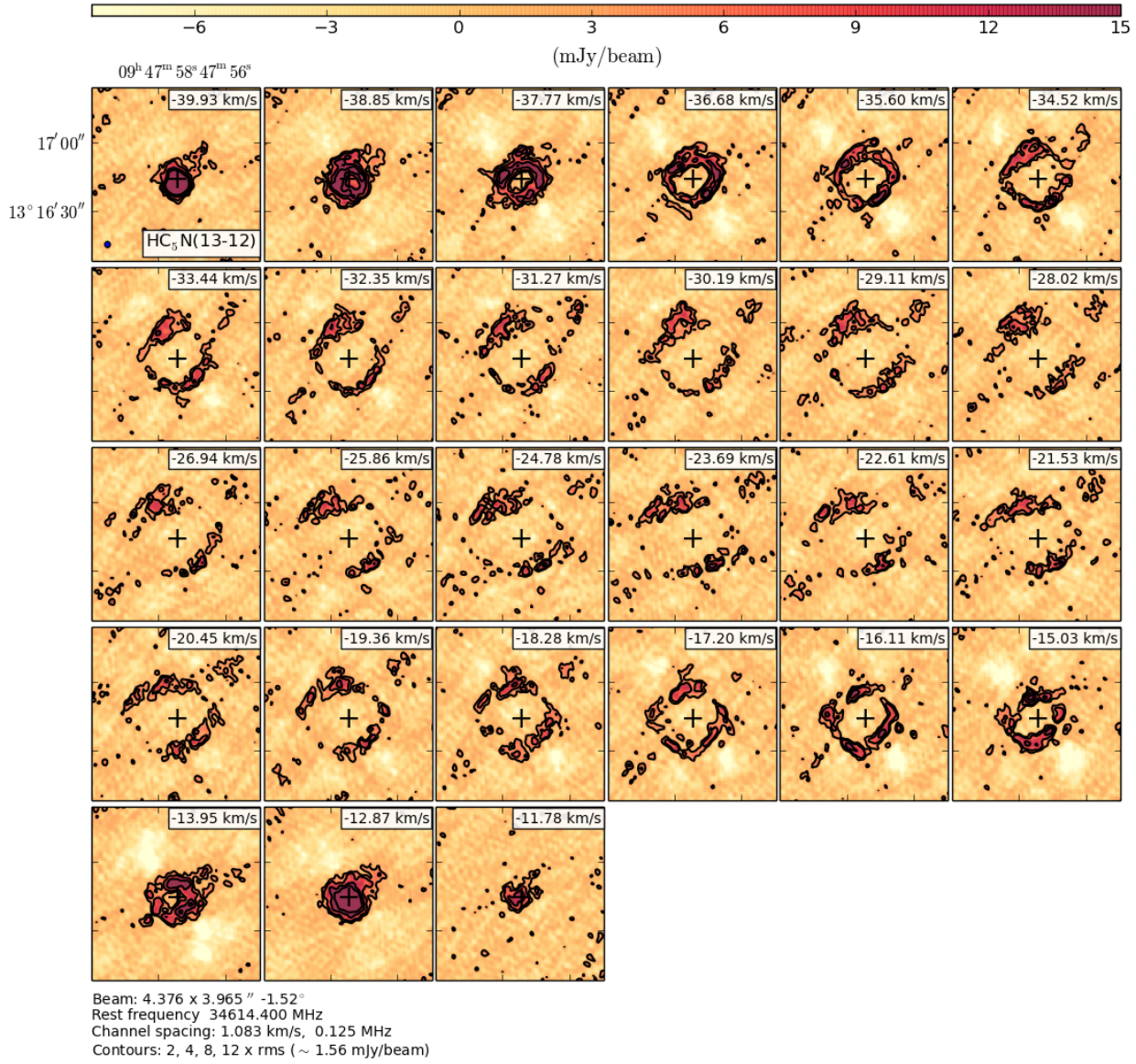

Figure B.8: As Fig. B.1, for HC_5N(13-12). The contour levels are 2, 4, 8, 12 $\times\sigma$(= 1.56 mJy beam^{-1}) and the synthesized beam is $4.4 \times 4.0''$, $-1.52°$.

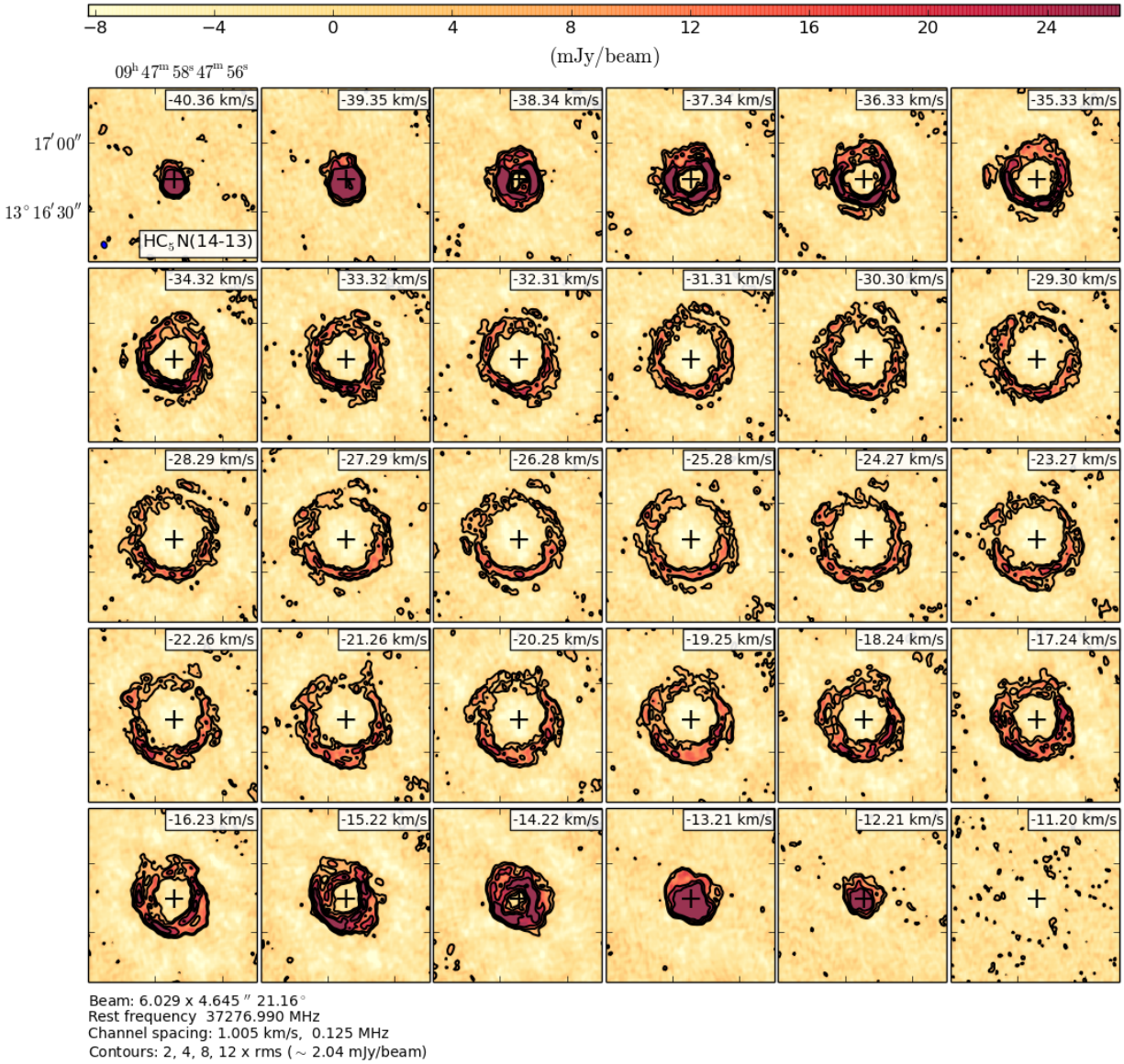

Figure B.9: As Fig. B.1, for HC_5N(14-13). The contour levels are 2, 4, 8, 12 $\times\sigma$(= 2.04 mJy beam^{-1}) and the synthesized beam is $6.0 \times 4.6''$, 21.16°.

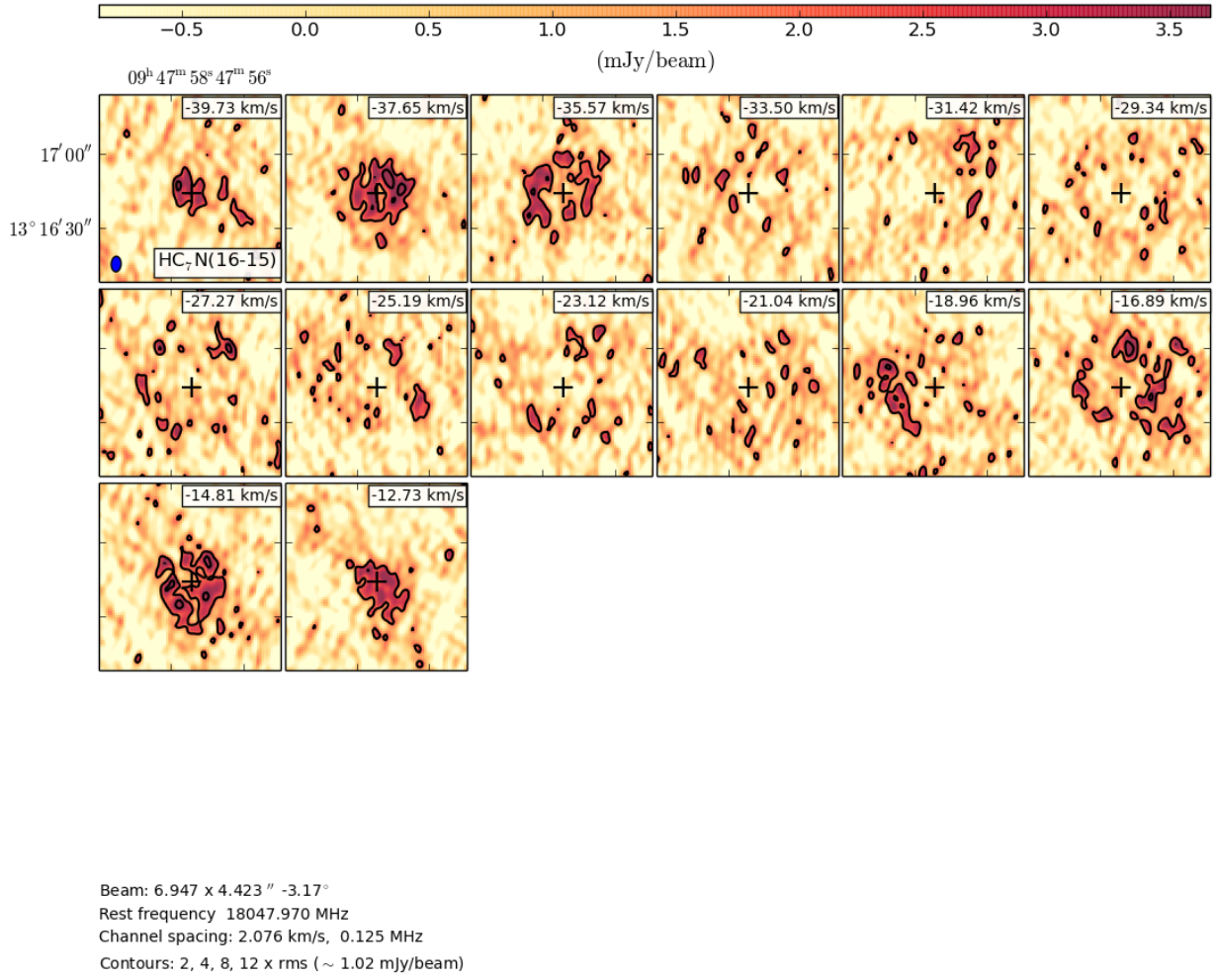

Figure B.10: As Fig. B.1, for HC_7N(16-15). The contour levels are 2, 4, 8, 12 $\times\sigma$(= 1.02 mJy beam^{-1}) and the synthesized beam is $7.0 \times 4.4''$, $-3.17°$.

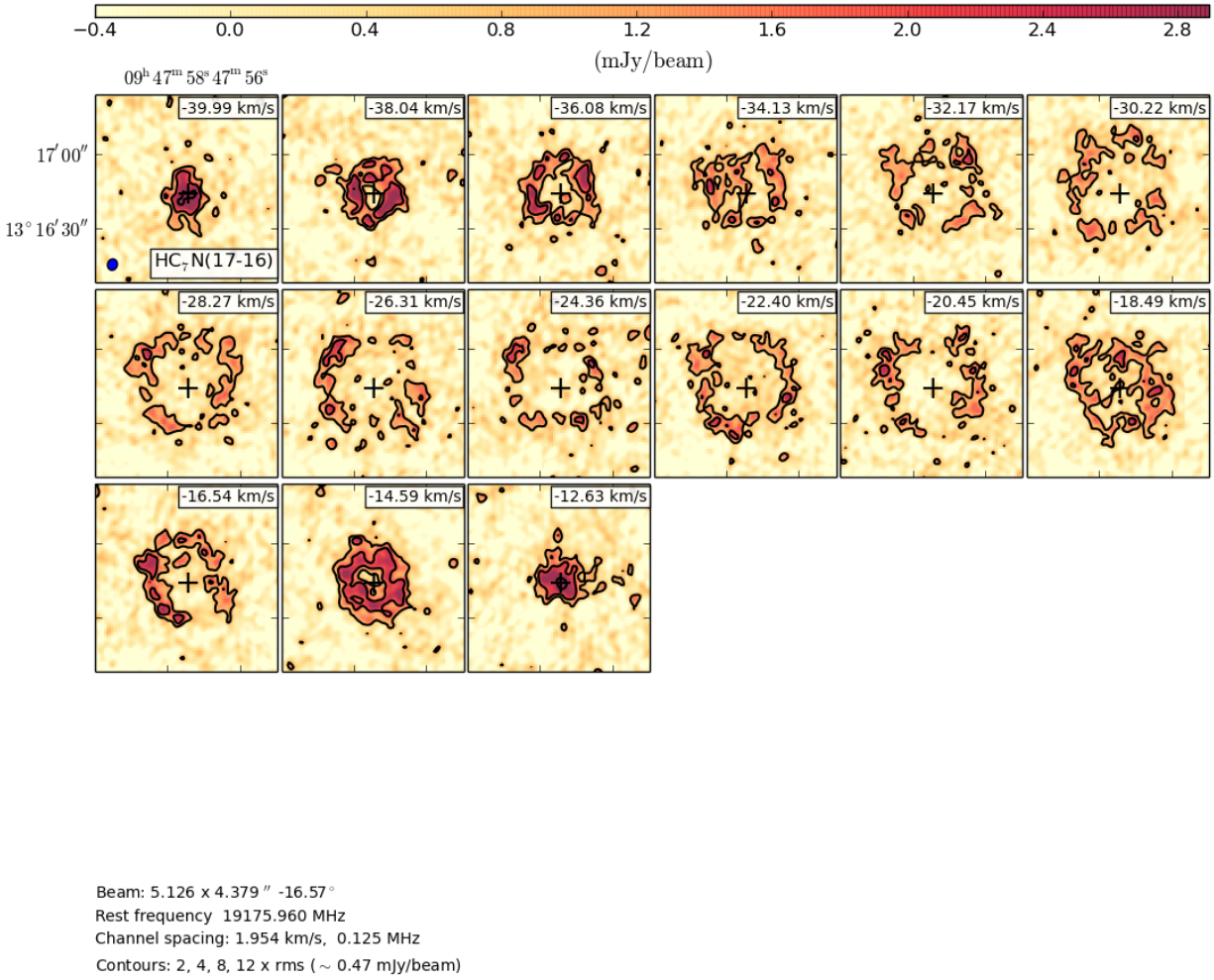

Figure B.11: As Fig. B.1, for HC_7N(17-16). The contour levels are 2, 4, 8, 12 $\times\sigma$(= 0.47 mJy beam^{-1}) and the synthesized beam is 5.1 $\times$ 4.4″, −16.57°.

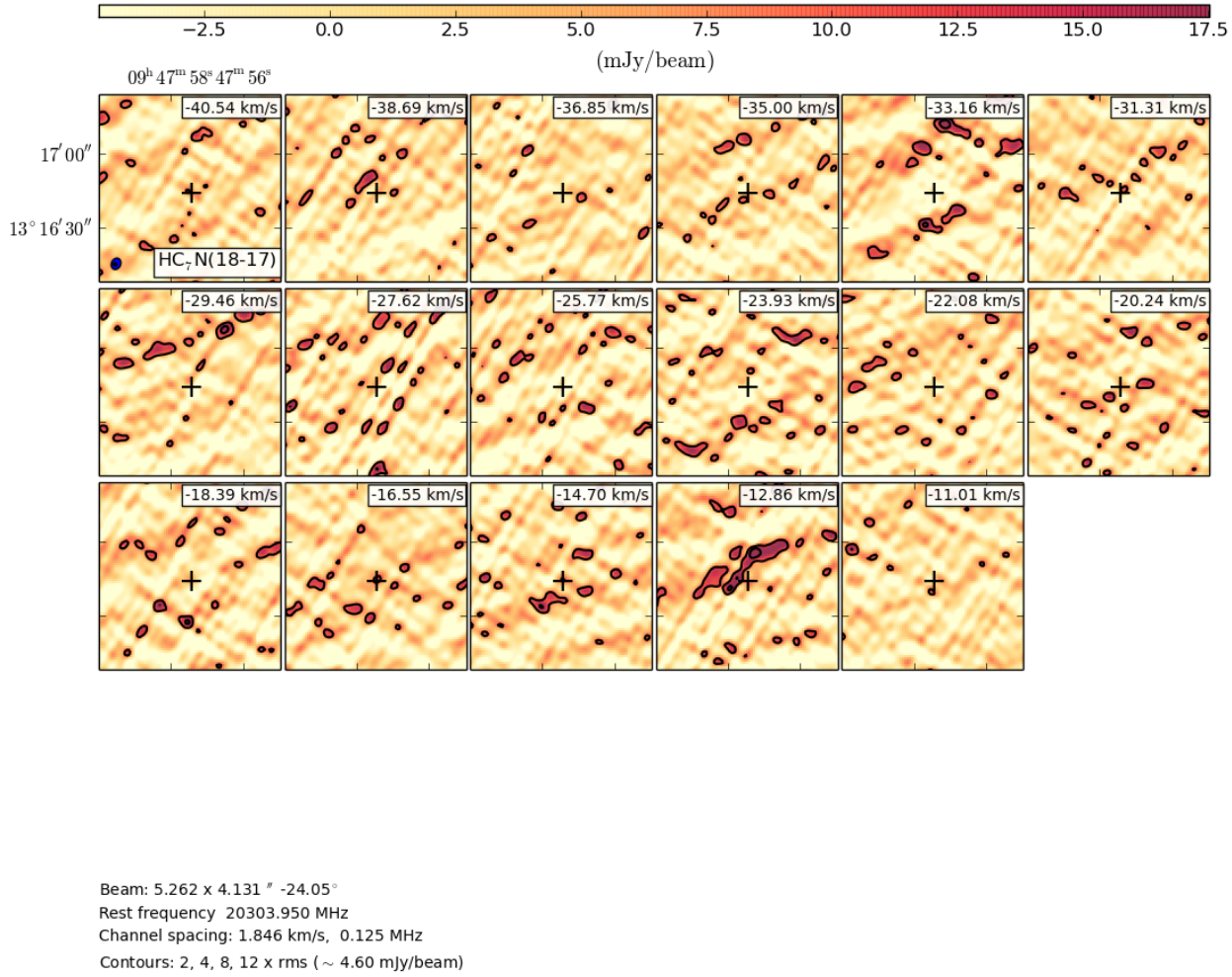

Figure B.12: As Fig. B.1, for HC_7N(18-17). The contour levels are 2, 4, 8, 12 $\times\sigma$(= 4.60 mJy beam^{-1}) and the synthesized beam is $5.3 \times 4.1''$, $-24.05°$.

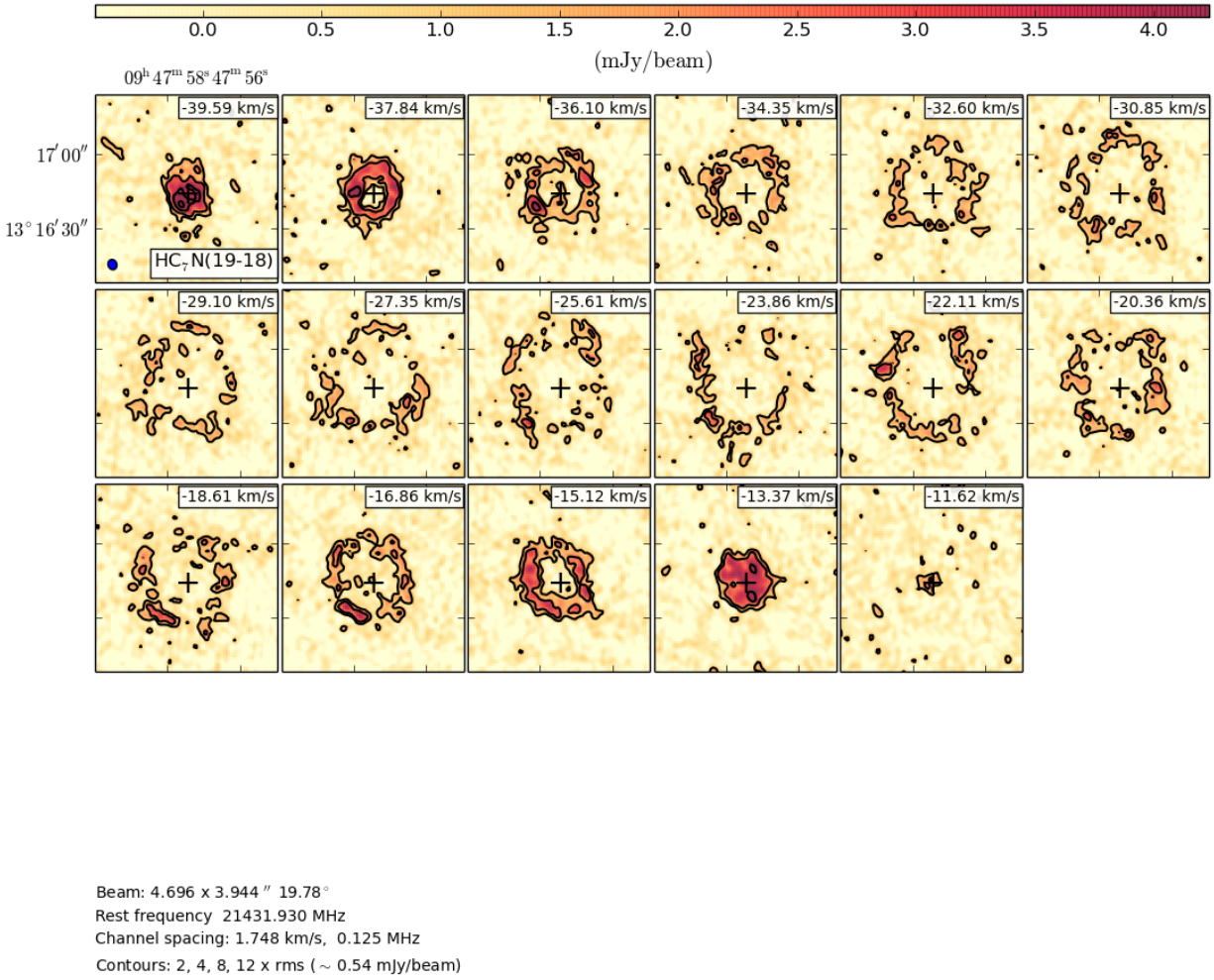

Figure B.13: As Fig. B.1, for HC_7N(19-18). The contour levels are 2, 4, 8, 12 $\times\sigma$(= 0.54 mJy beam^{-1}) and the synthesized beam is 4.7 $\times$ 3.9″, 19.78°.

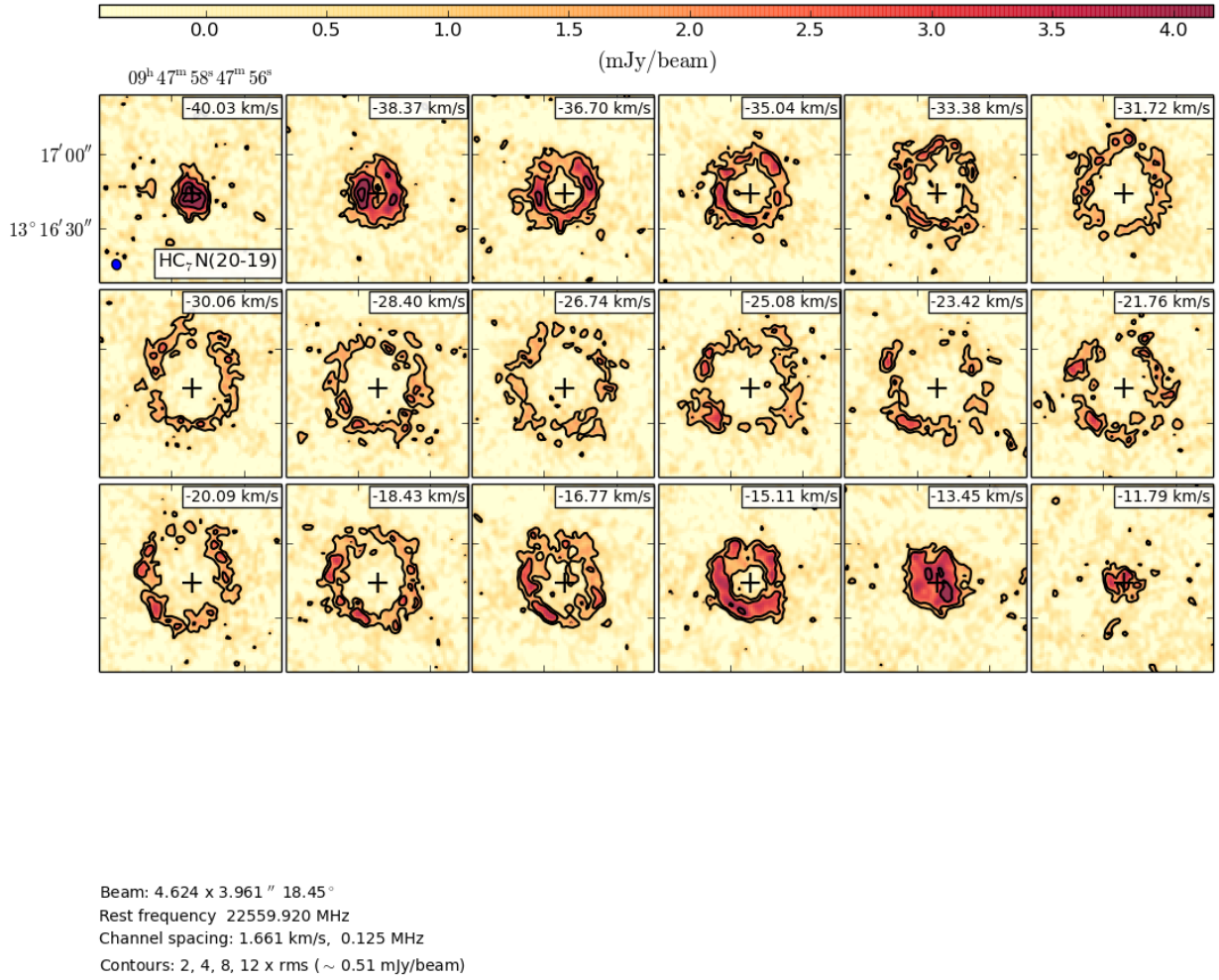

Figure B.14: As Fig. B.1, for HC_7N(20-19). The contour levels are 2, 4, 8, 12 $\times\sigma$(= 0.51 mJy beam^{-1}) and the synthesized beam is 4.6 $\times$ 4.0″, 18.45°.

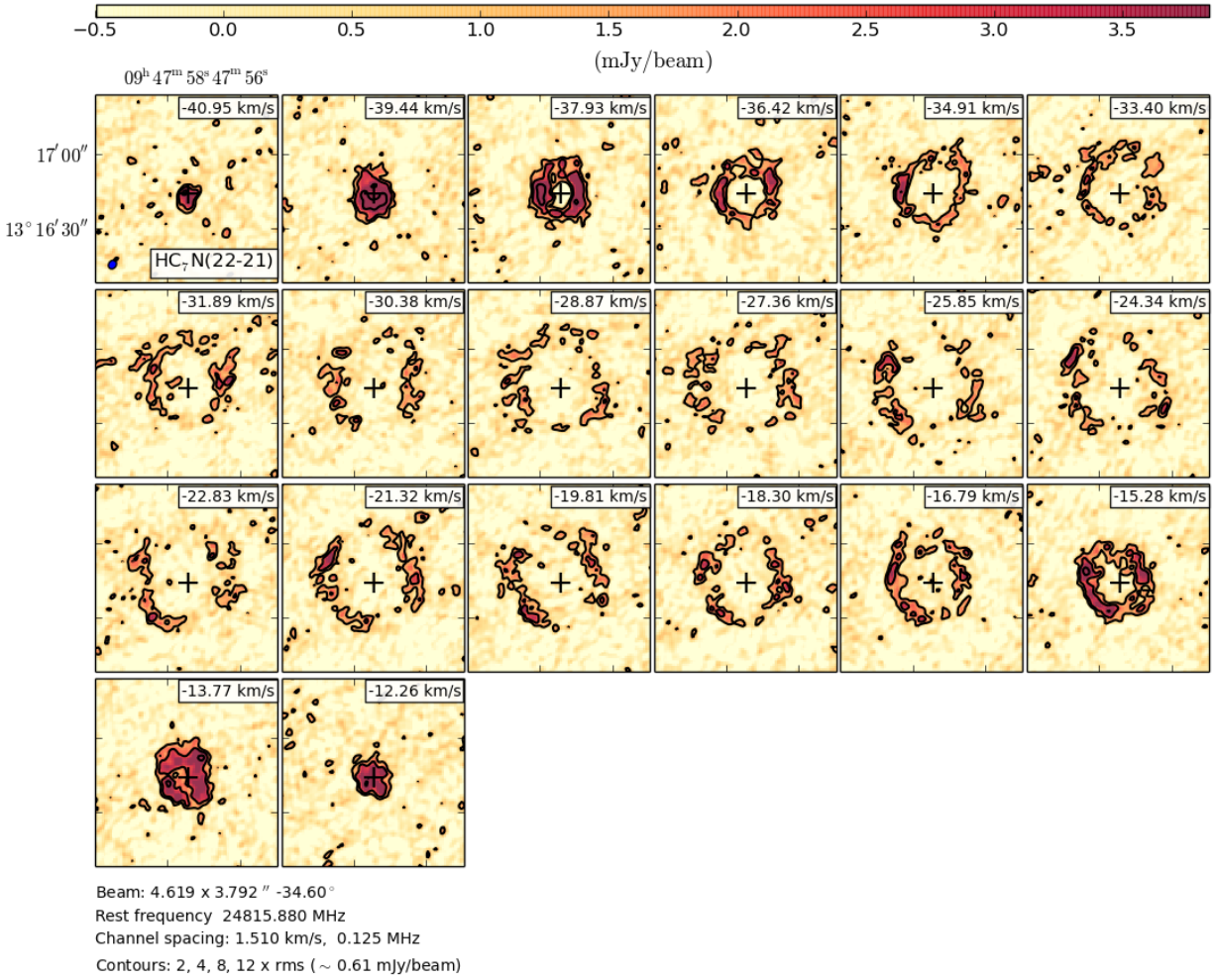

Figure B.15: As Fig. B.1, for HC_7N(22-21). The contour levels are 2, 4, 8, 12 $\times\sigma$(= 0.61 mJy beam^{-1}) and the synthesized beam is $4.6 \times 3.8''$, $-34.60°$.

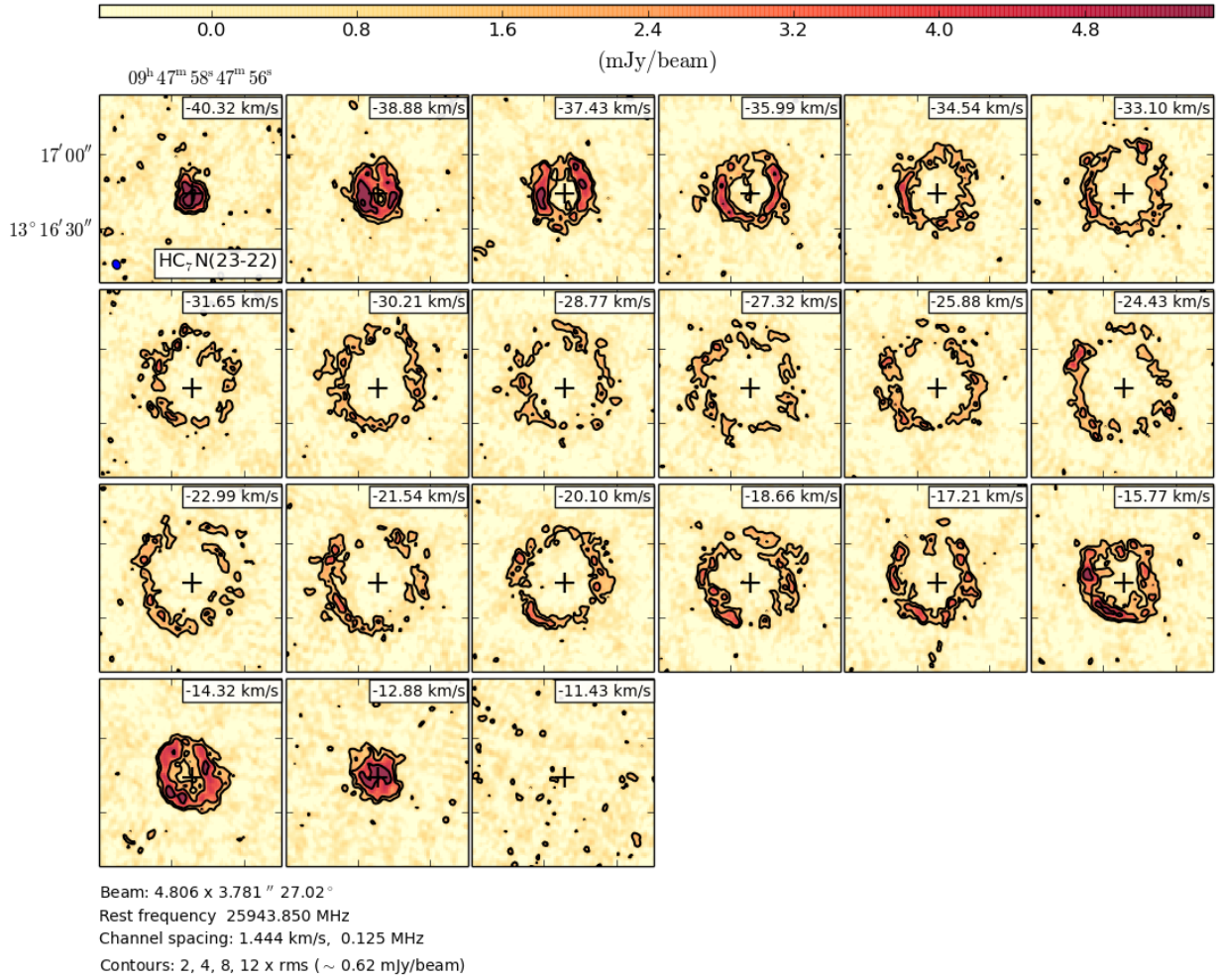

Figure B.16: As Fig. B.1, for HC_7N(23-22). The contour levels are 2, 4, 8, 12 $\times\sigma$(= 0.62 mJy beam^{-1}) and the synthesized beam is 4.8 $\times$ 3.8″, 27.02°.

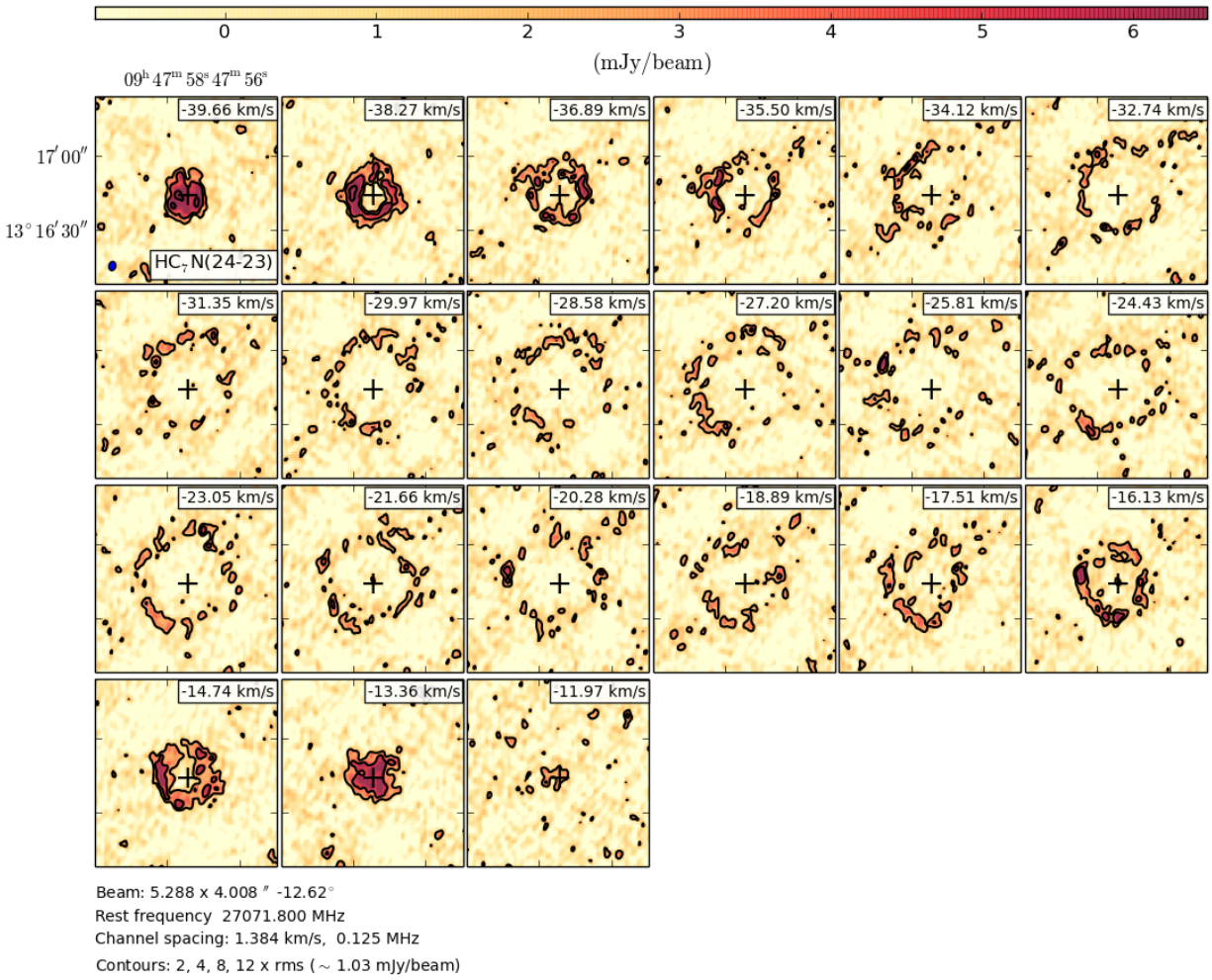

Figure B.17: As Fig. B.1, for HC_7N(24-23). The contour levels are 2, 4, 8, 12 $\times\sigma$(= 1.03 mJy beam^{-1}) and the synthesized beam is $5.3 \times 4.0''$, $-12.62°$.

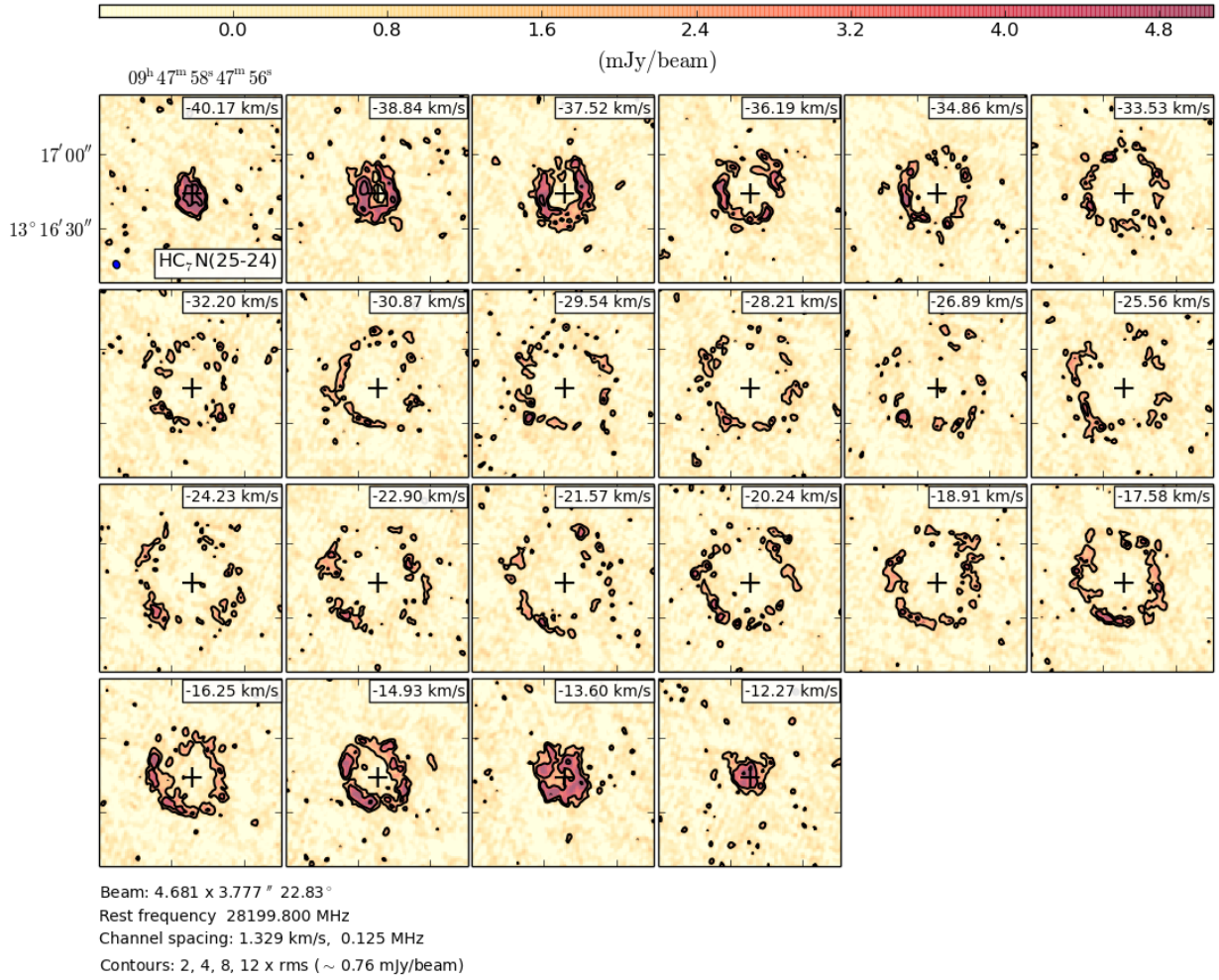

Figure B.18: As Fig. B.1, for HC_7N(25-24). The contour levels are 2, 4, 8, 12 $\times\sigma$(= 1.03 mJy beam^{-1}) and the synthesized beam is $5.3 \times 4.0''$, $-12.62°$.

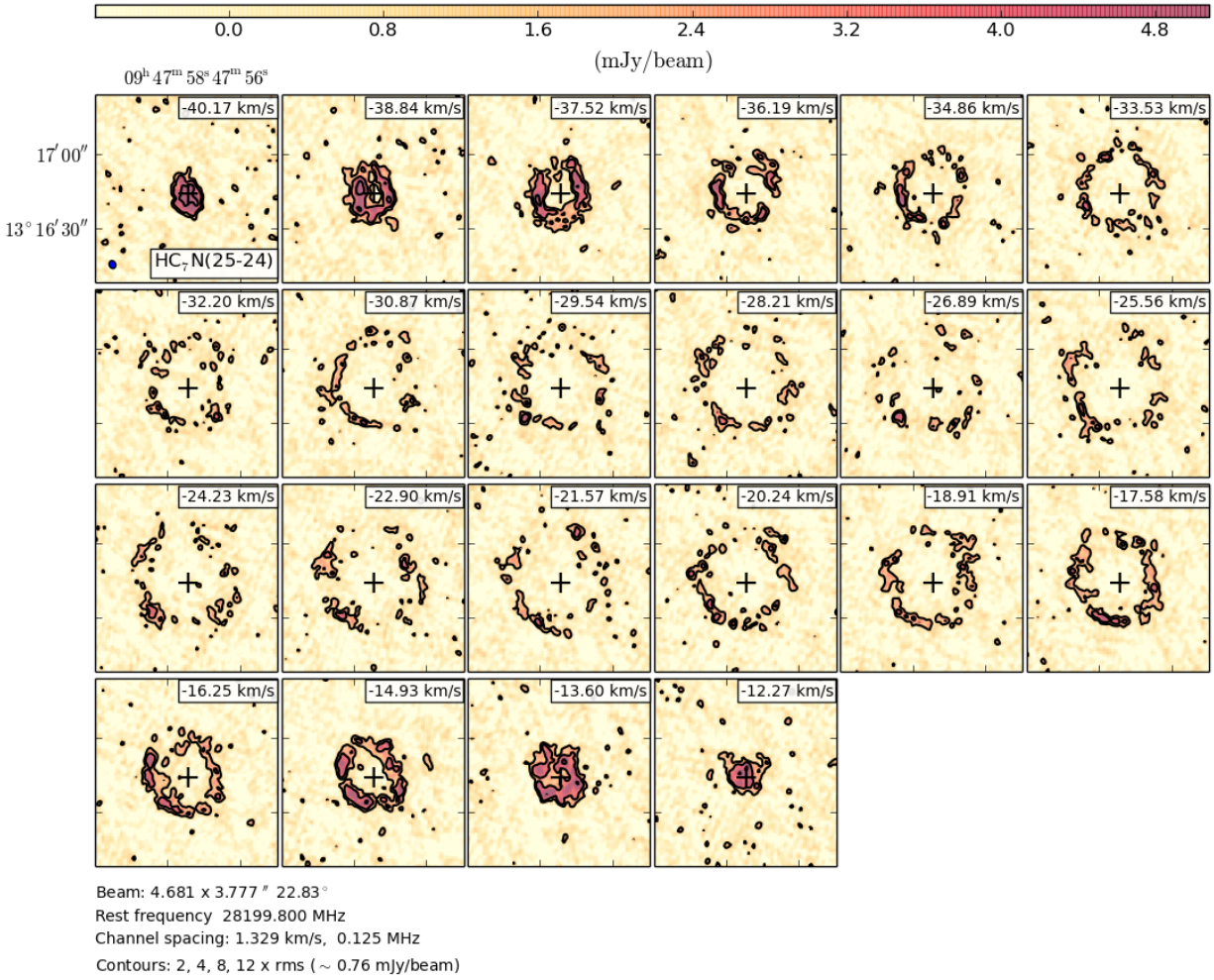

Figure B.19: As Fig. B.1, for HC_7N(26-25). The contour levels are 2, 4, 8, 12 $\times\sigma$(= 1.03 mJy beam^{-1}) and the synthesized beam is $5.3 \times 4.0''$, $-12.62°$.

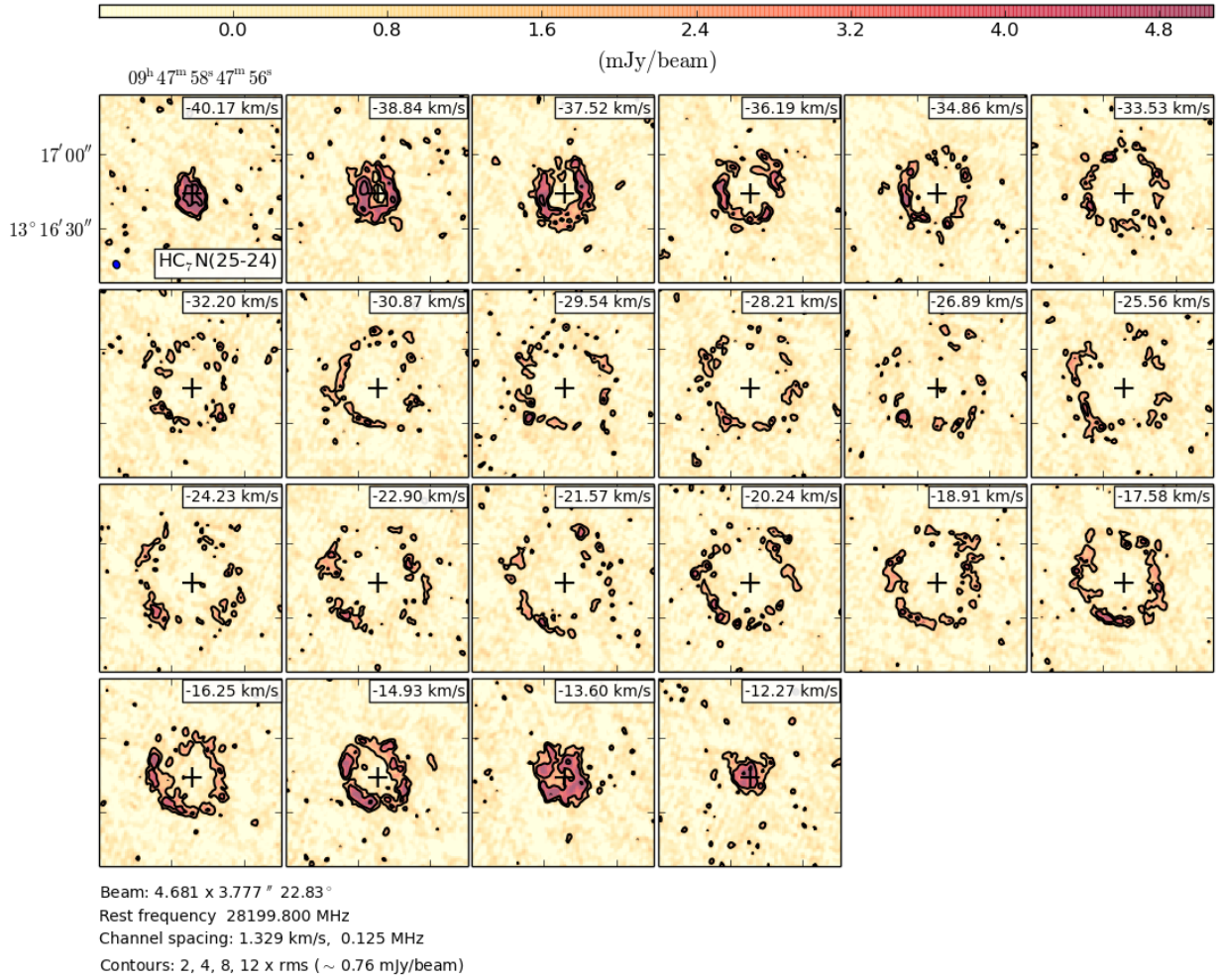

Figure B.20: As Fig. B.1, for HC_7N(27-26). The contour levels are 2, 4, 8, 12 $\times\sigma$(= 1.03 mJy beam^{-1}) and the synthesized beam is $5.3 \times 4.0''$, $-12.62°$.

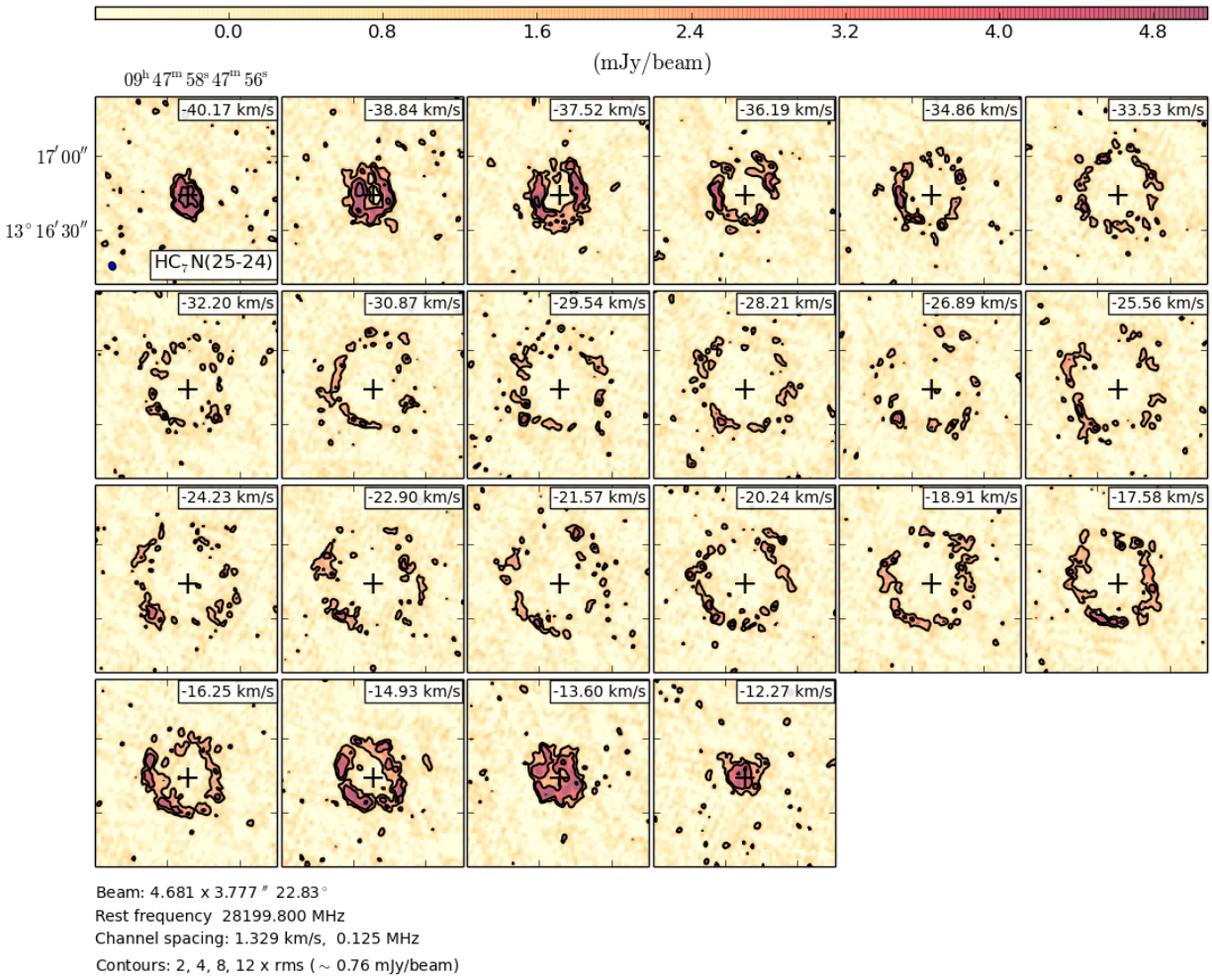

Figure B.21: As Fig. B.1, for HC_7N(28-27). The contour levels are 2, 4, 8, 12 $\times\sigma$(= 1.03 mJy beam^{-1}) and the synthesized beam is $5.3 \times 4.0''$, $-12.62°$.

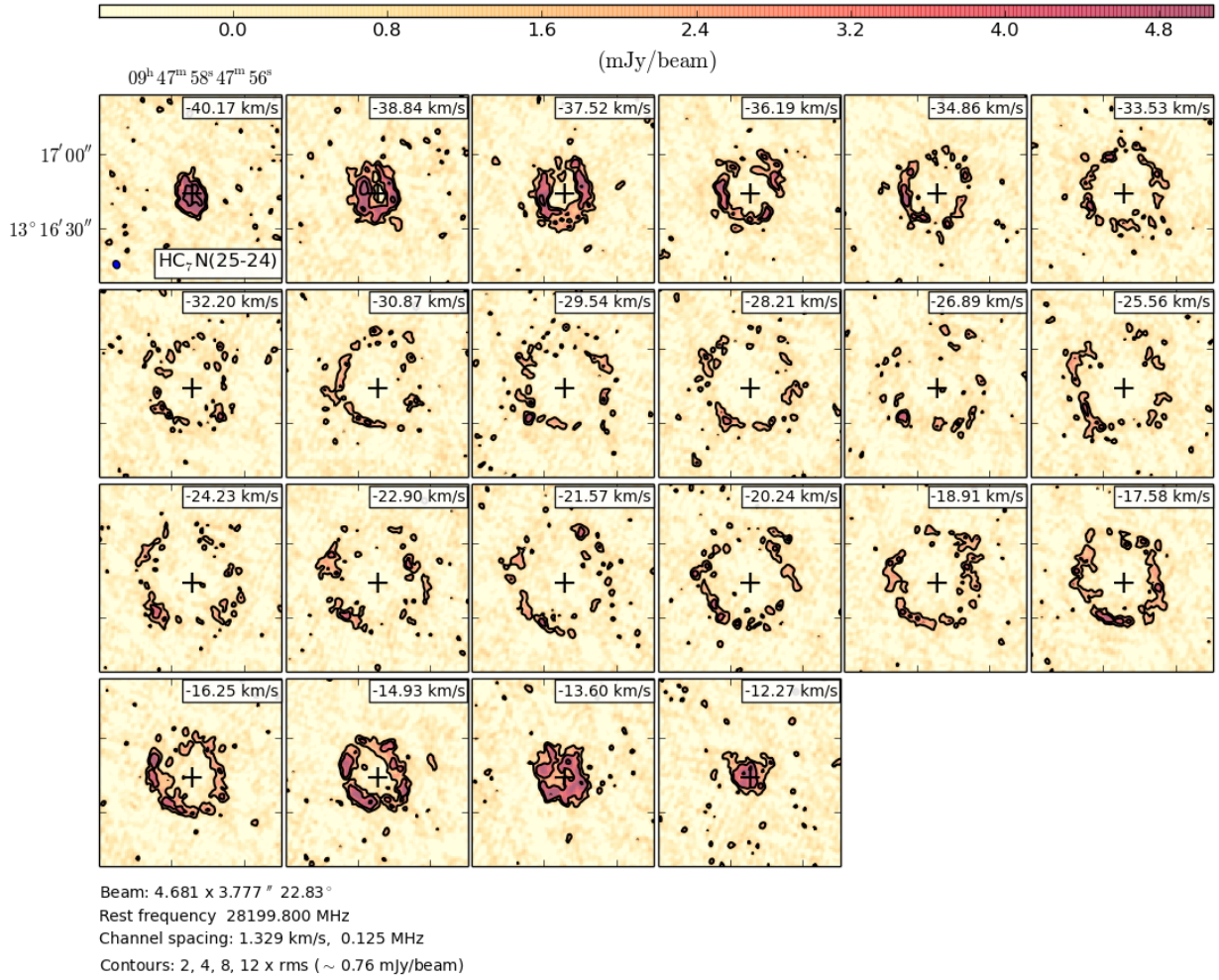

Figure B.22: As Fig. B.1, for HC_7N(29-28). The contour levels are 2, 4, 8, 12 $\times\sigma$(= 1.03 mJy beam^{-1}) and the synthesized beam is $5.3 \times 4.0''$, $-12.62°$.

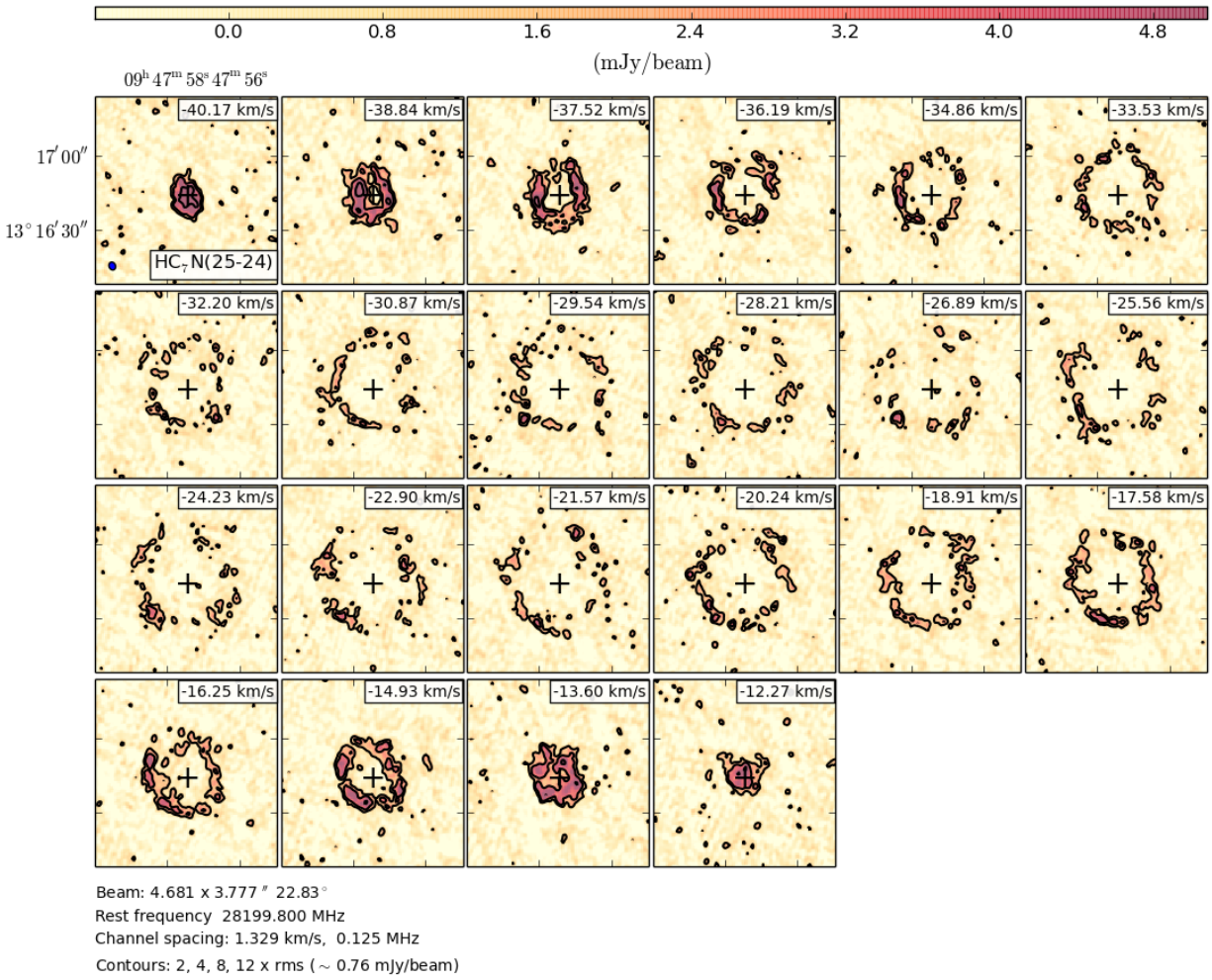

Figure B.23: As Fig. B.1, for HC_7N(30-29). The contour levels are 2, 4, 8, 12 $\times\sigma$(= 1.03 mJy beam^{-1}) and the synthesized beam is $5.3 \times 4.0''$, $-12.62°$.

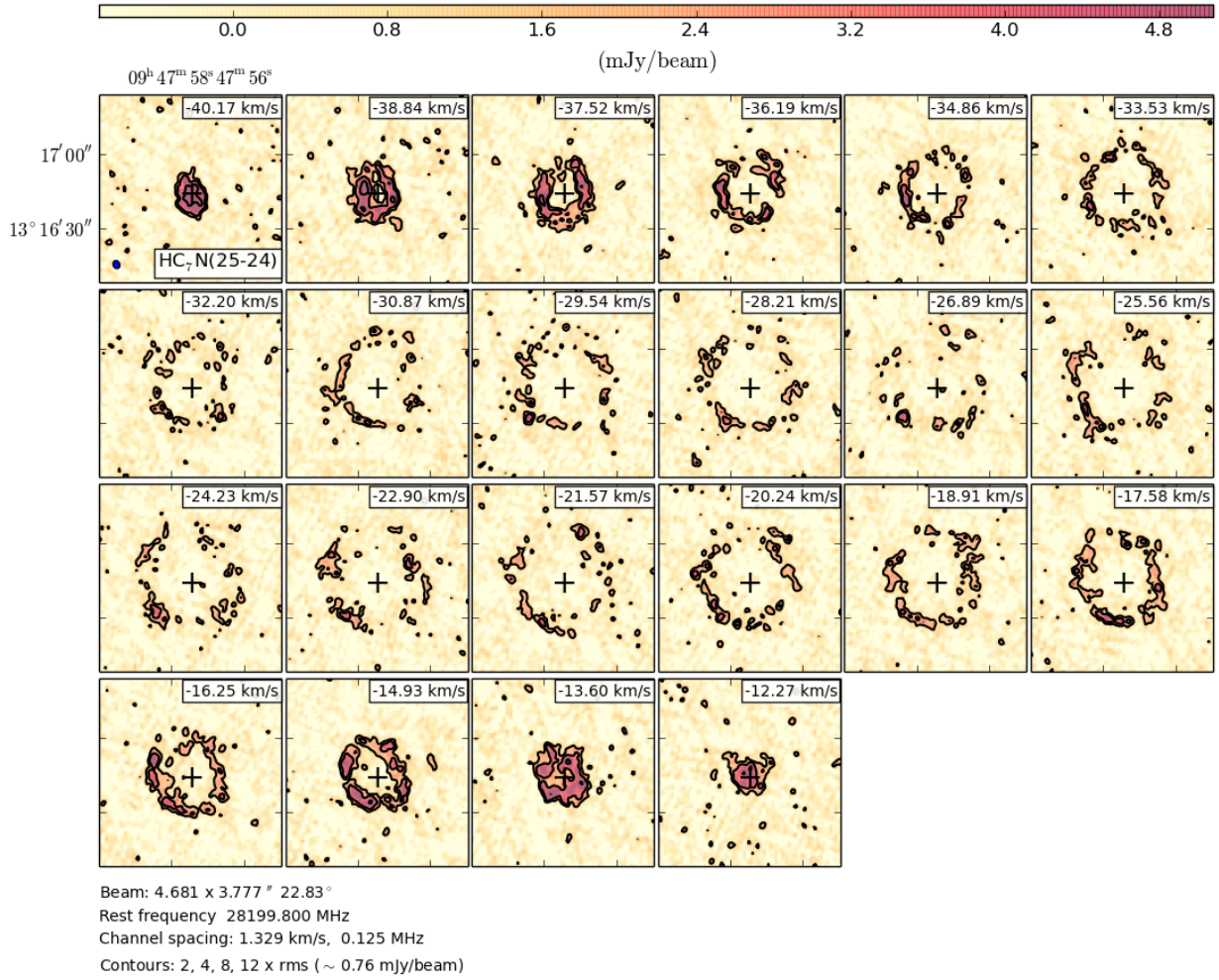

Figure B.24: As Fig. B.1, for HC_7N(31-30). The contour levels are 2, 4, 8, 12 $\times\sigma$(= 1.03 mJy beam^{-1}) and the synthesized beam is $5.3 \times 4.0''$, $-12.62°$.

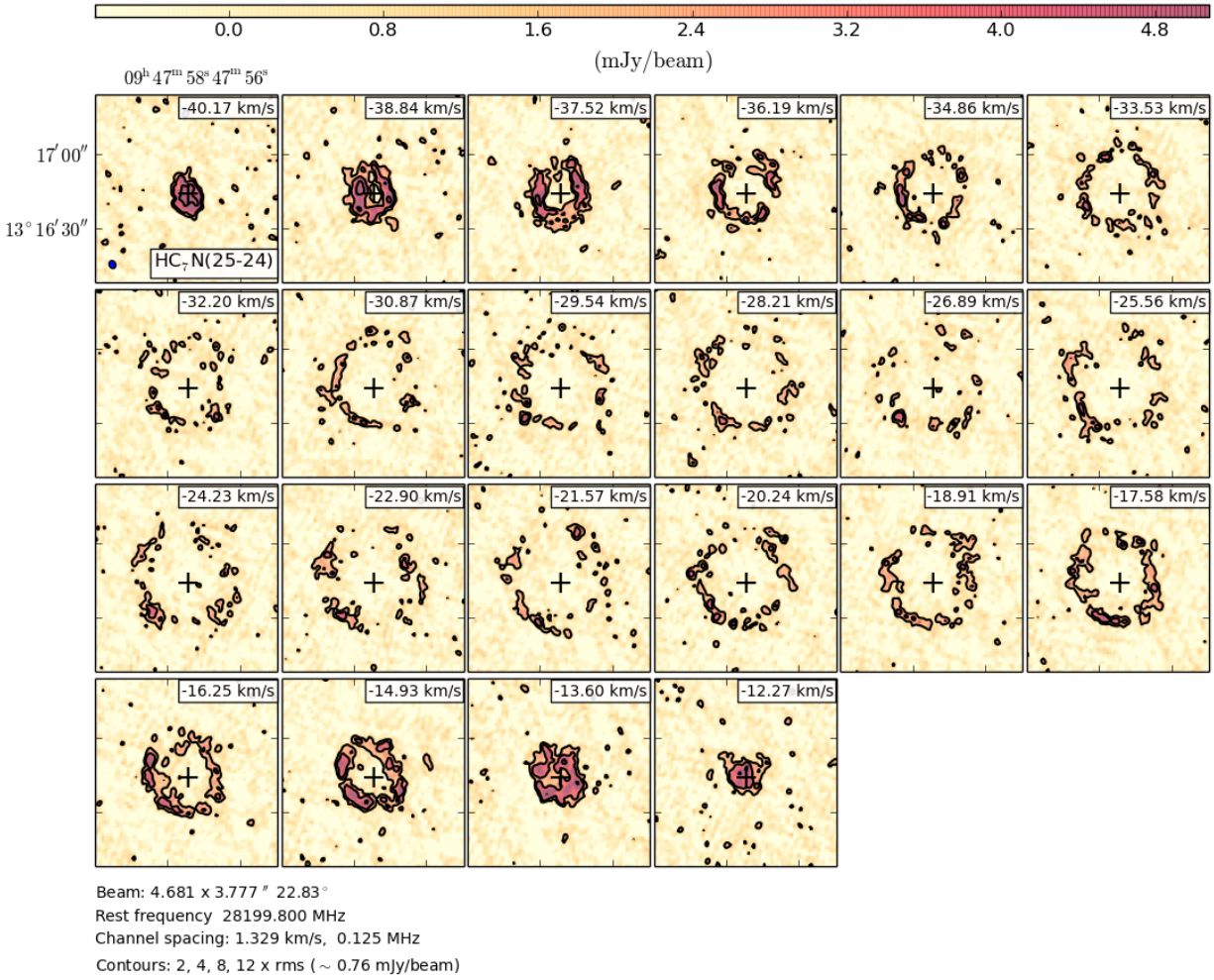

Figure B.25: As Fig. B.1, for HC_7N(32-31). The contour levels are 2, 4, 8, 12 $\times\sigma$(= 1.03 mJy beam^{-1}) and the synthesized beam is $5.3 \times 4.0''$, $-12.62°$.

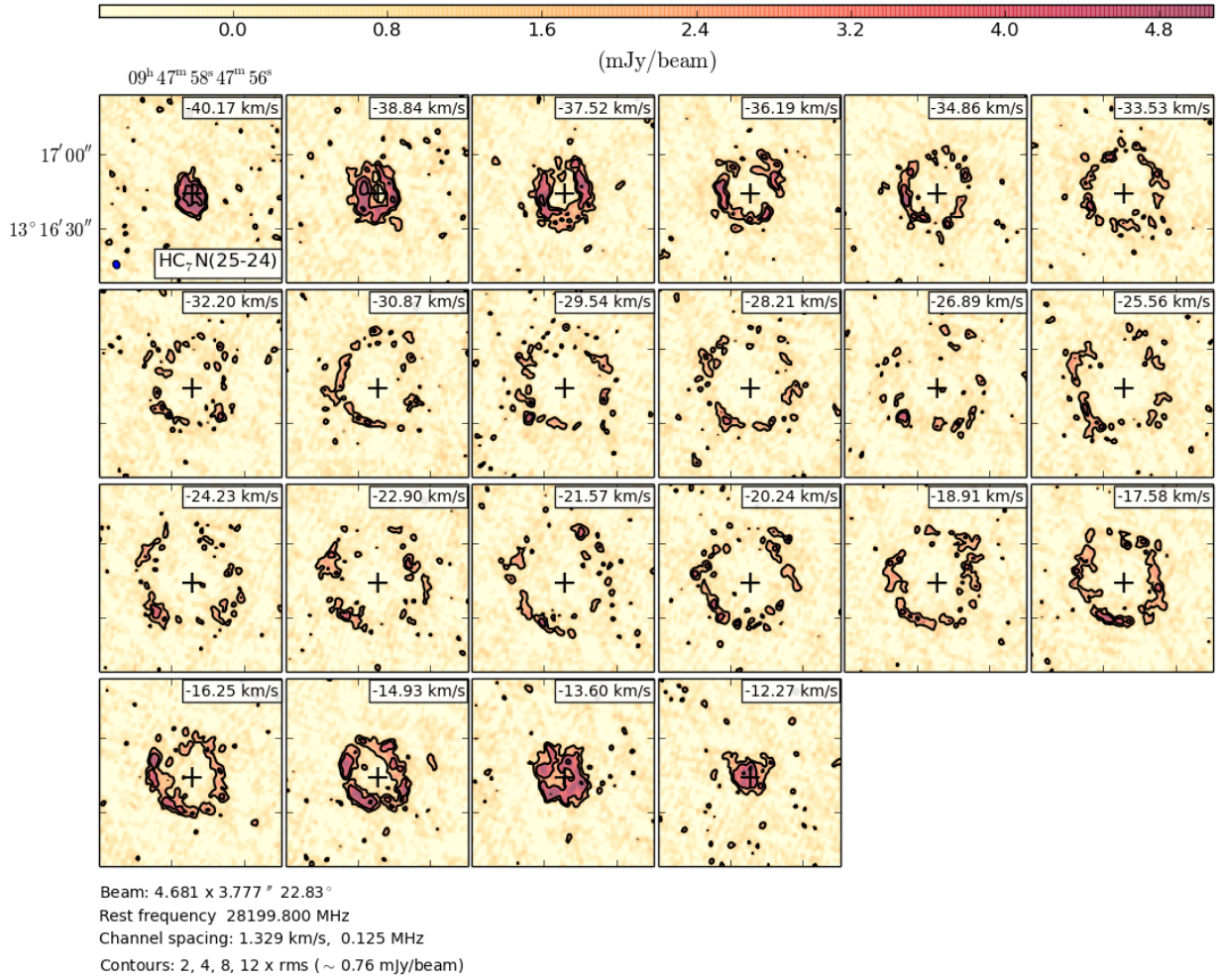

Figure B.26: As Fig. B.1, for HC_7N(33-32). The contour levels are 2, 4, 8, 12 $\times\sigma$(= 1.03 mJy beam^{-1}) and the synthesized beam is $5.3 \times 4.0''$, $-12.62°$.

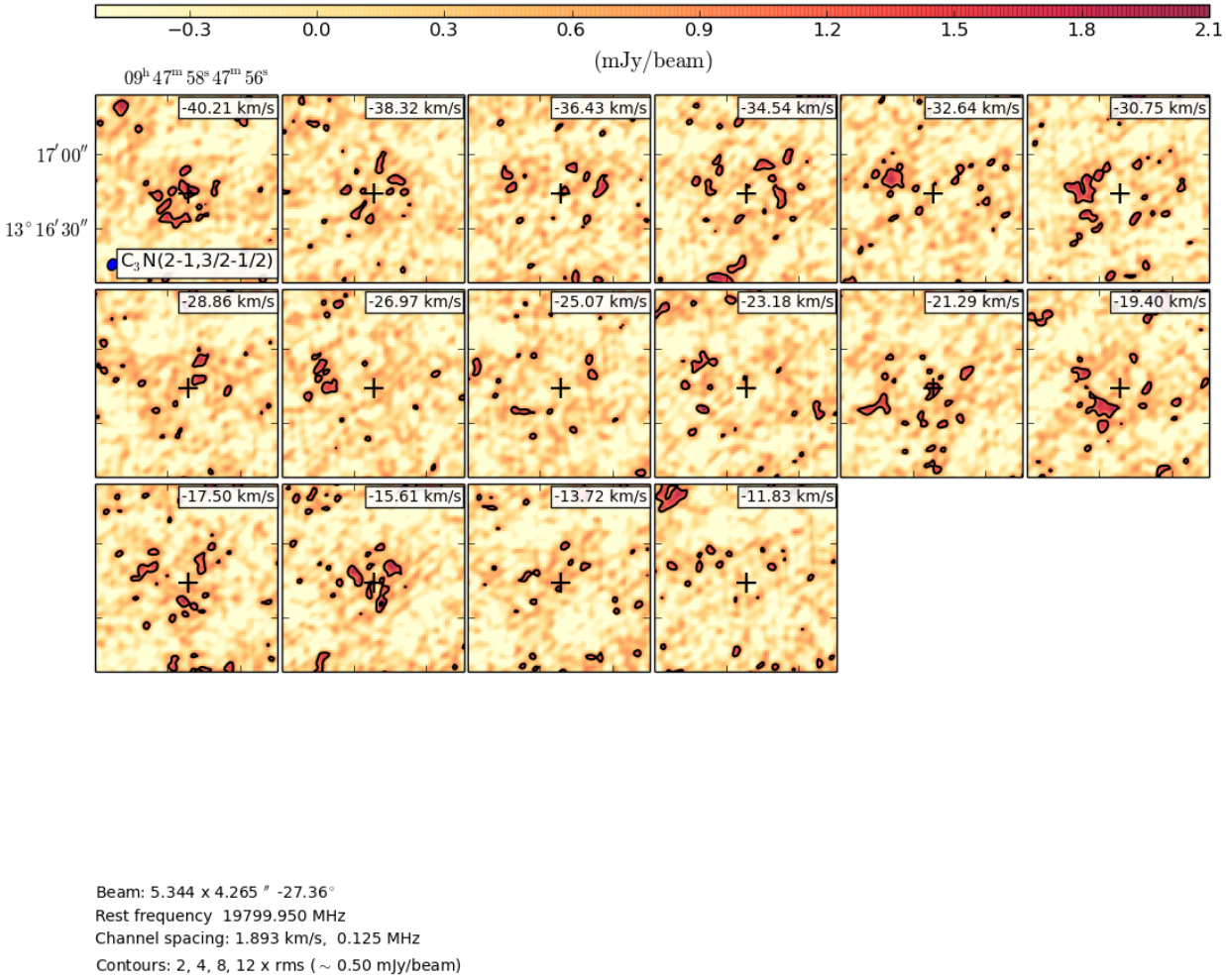

Figure B.27: As Fig. B.1, for C_3N(2-1,3/2-1/2). The contour levels are 2, 4, 8, 12 $\times\sigma$(= 0.50 mJy beam^{-1}) and the synthesized beam is $5.3 \times 4.3''$, $-27.36°$.

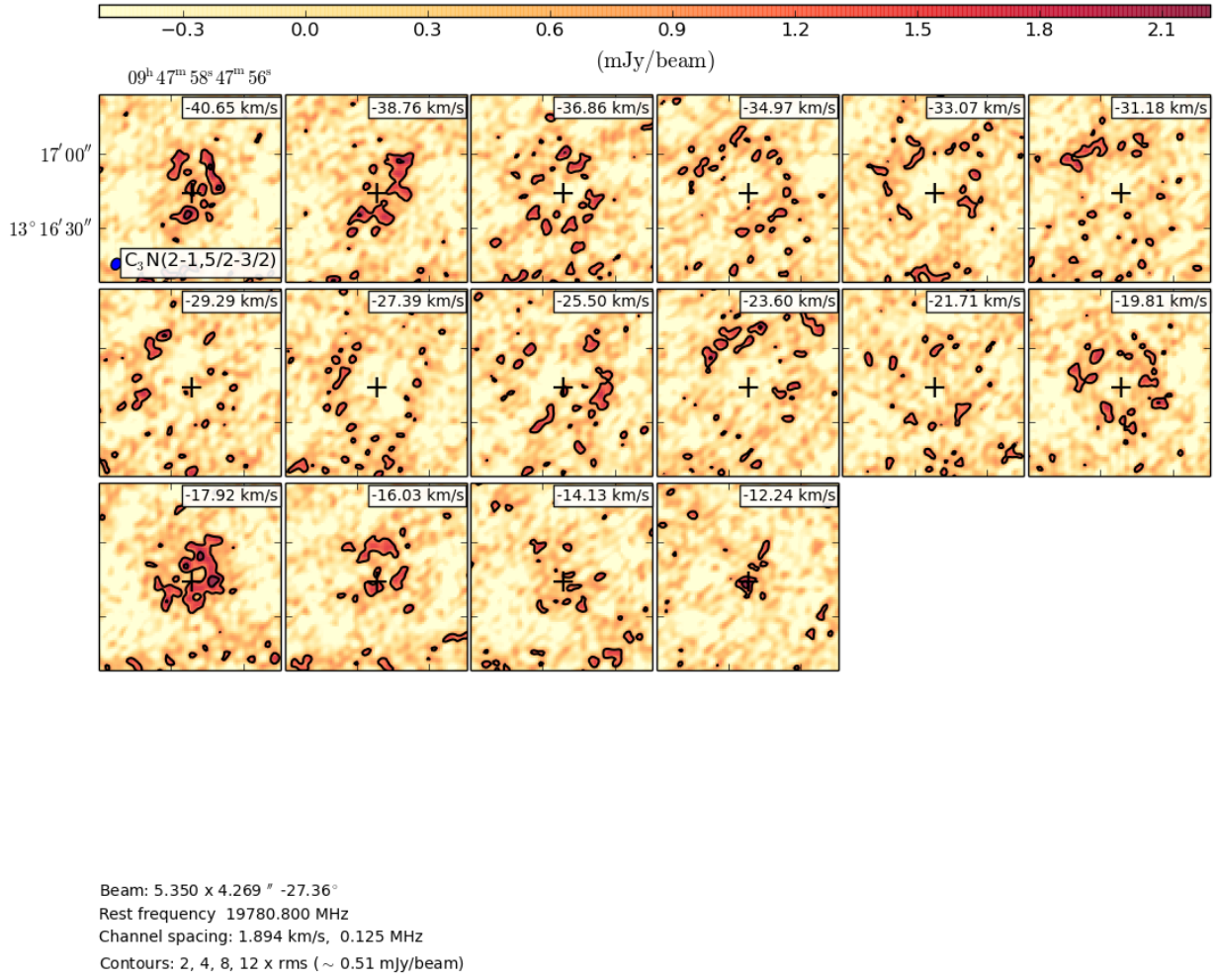

Figure B.28: As Fig. B.1, for C_3N(2-1,5/2-3/2). The contour levels are 2, 4, 8, 12 $\times\sigma$(= 0.51 mJy beam^{-1}) and the synthesized beam is $5.3 \times 4.3''$, $-27.36°$.

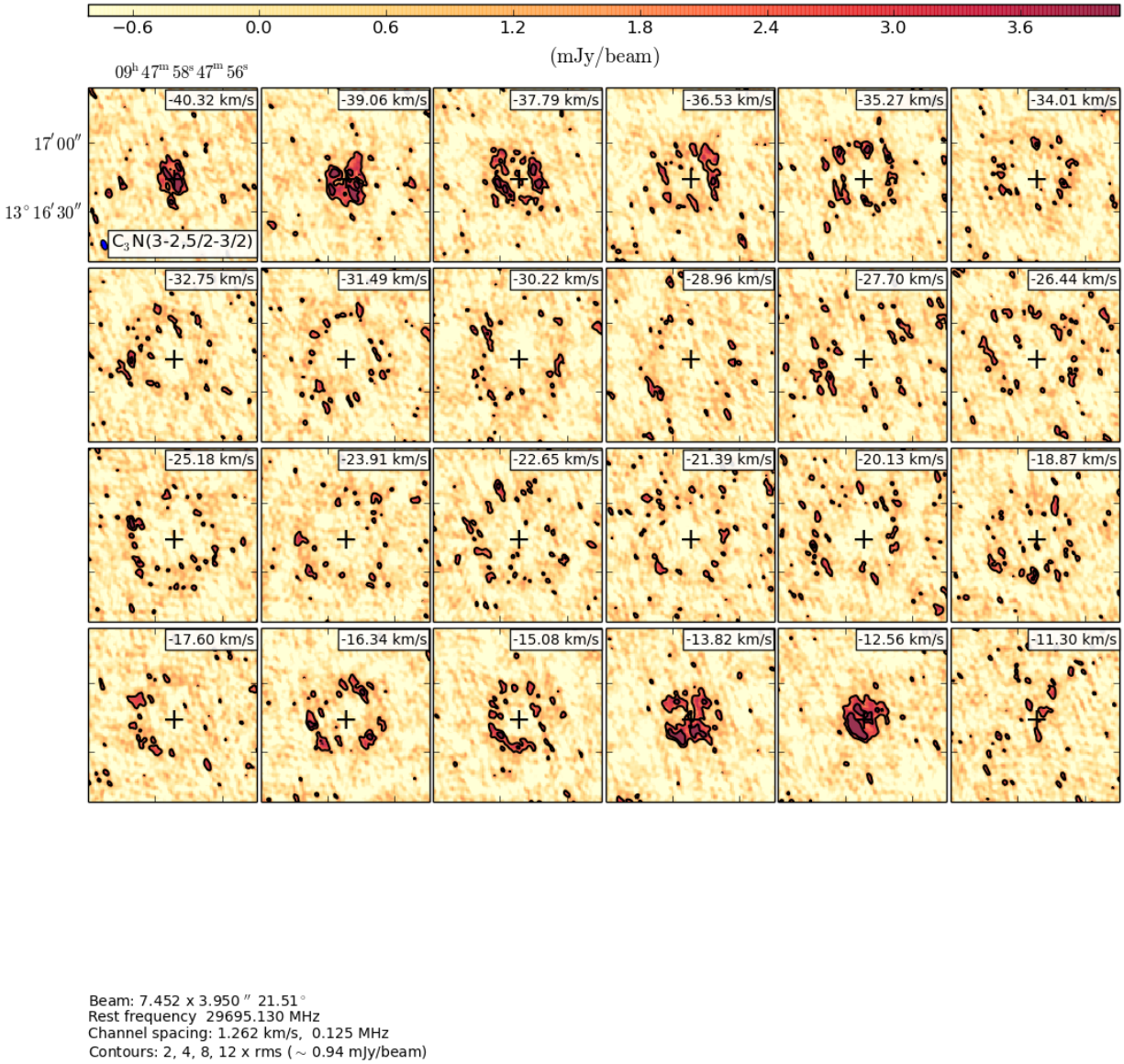

Figure B.29: As Fig. B.1, for C_3N(3-2,5/2-3/2). The contour levels are 2, 4, 8, 12 $\times\sigma$(= 0.94 mJy beam^{-1}) and the synthesized beam is $7.5 \times 4.0''$, 21.51°.

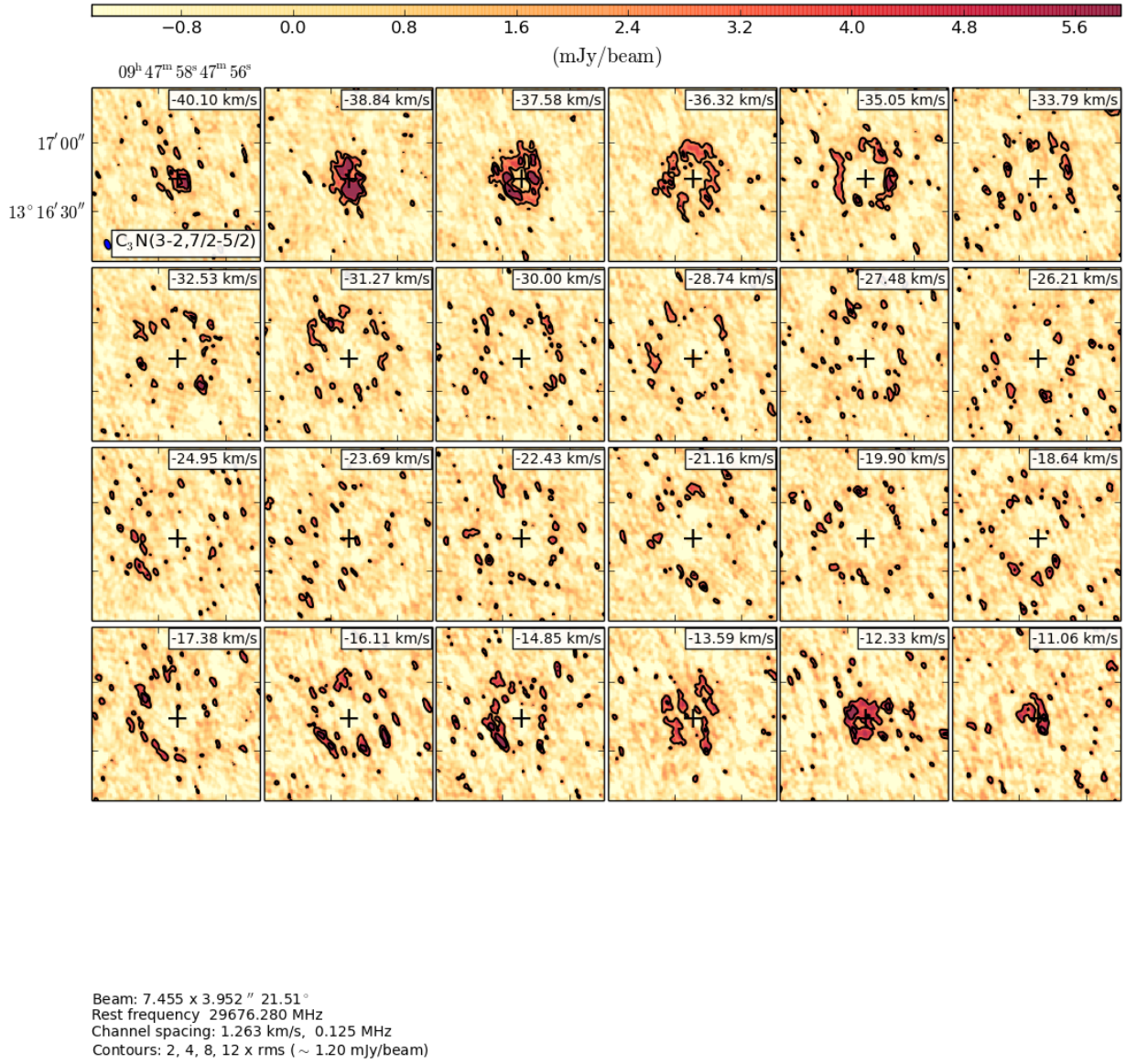

Figure B.30: As Fig. B.1, for C_3N(3-2,7/2-5/2). The contour levels are 2, 4, 8, 12 $\times\sigma$(= 1.20 mJy beam^{-1}) and the synthesized beam is $7.5 \times 4.0''$, 21.51°.

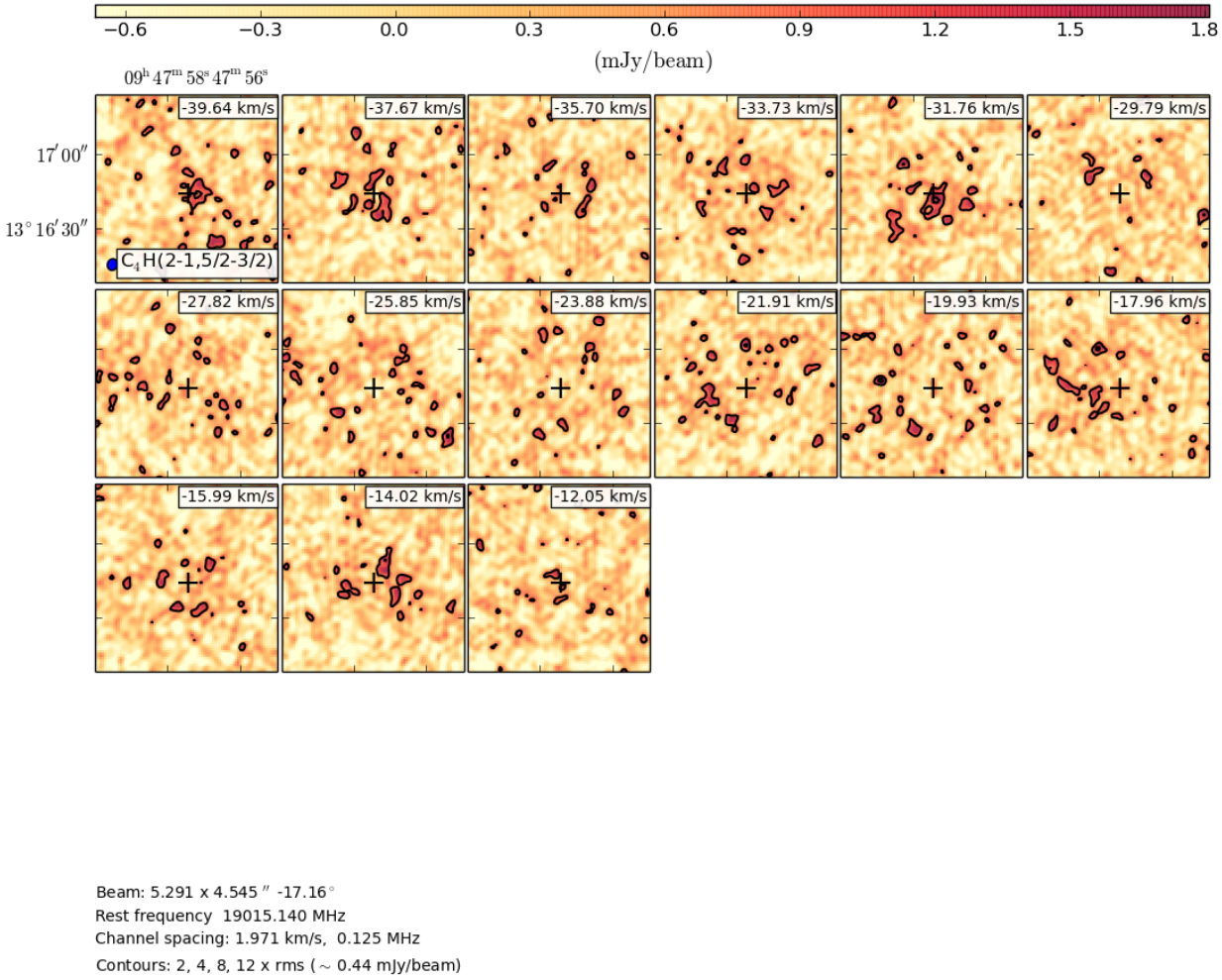

Figure B.31: As Fig. B.1, for C_4H(2-1,5/2-3/2). The contour levels are 2, 4, 8, 12 $\times\sigma$(= 0.44 mJy beam^{-1}) and the synthesized beam is $5.3 \times 4.5''$, $-17.16°$.

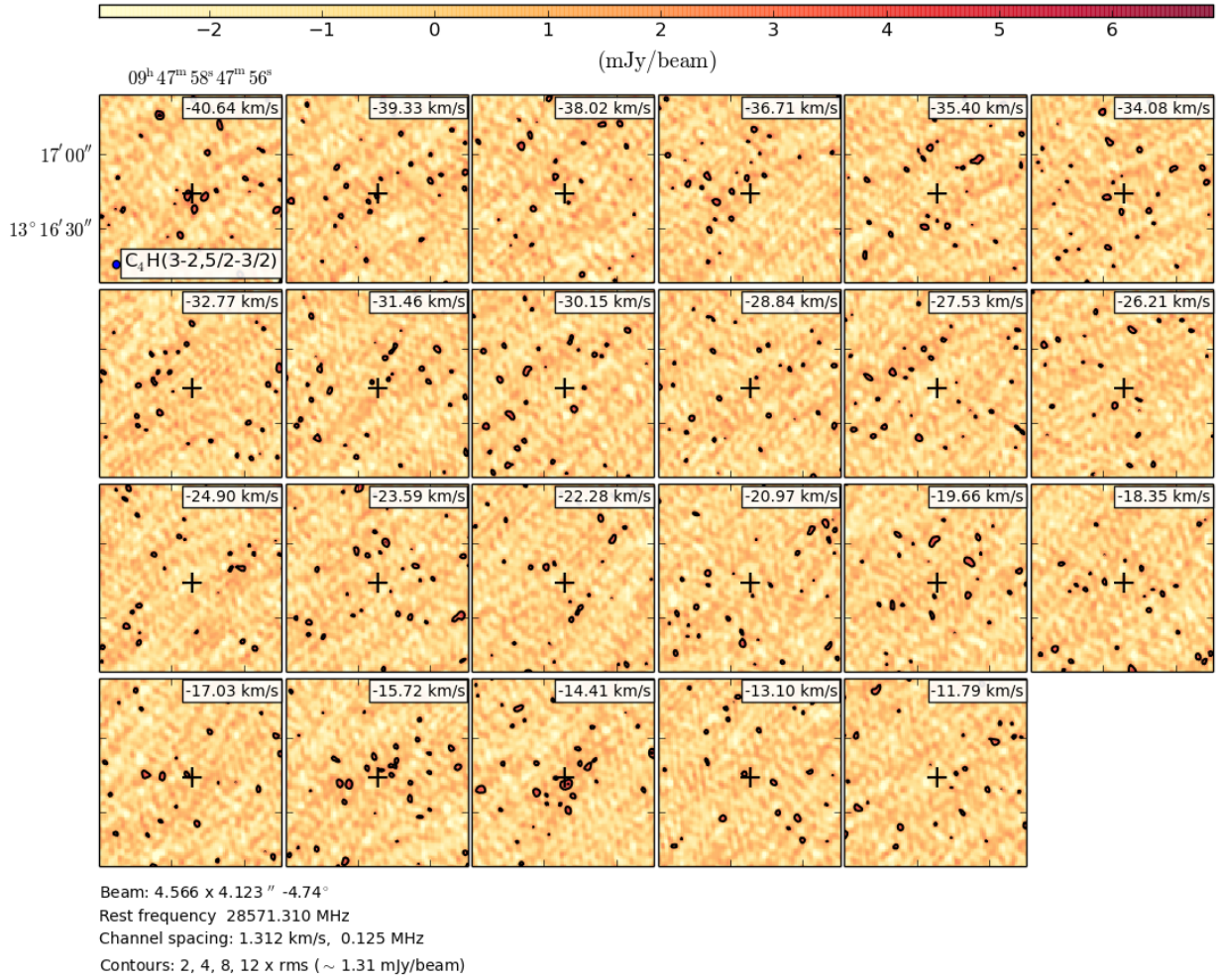

Figure B.32: As Fig. B.1, for C_4H(3-2,5/2-3/2). The contour levels are 2, 4, 8, 12 $\times\sigma$(= 1.31 mJy beam^{-1}) and the synthesized beam is $4.6 \times 4.1''$, $-4.74°$.

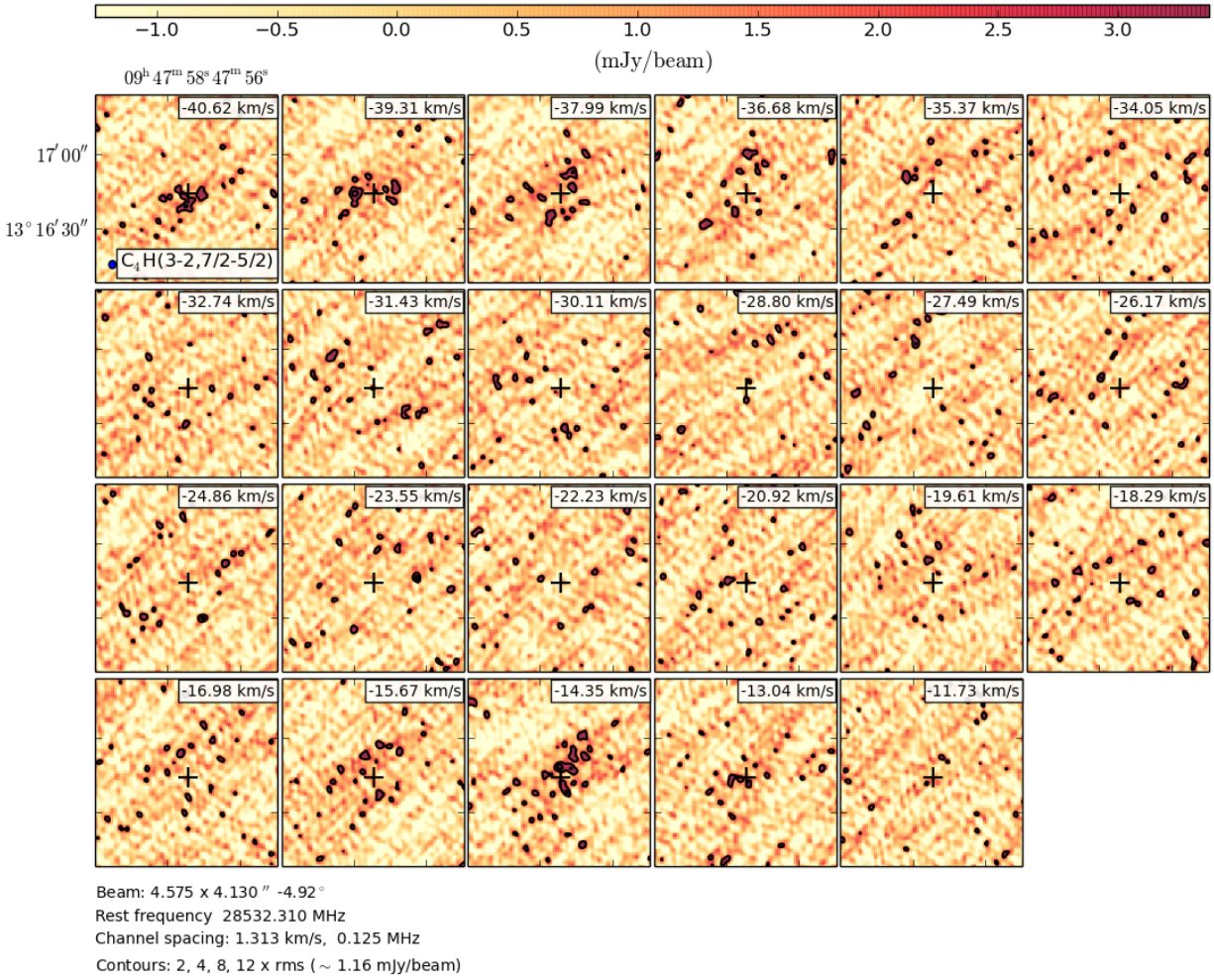

Figure B.33: As Fig. B.1, for C_4H(3-2,7/2-5/2). The contour levels are 2, 4, 8, 12 $\times\sigma$(= 1.16 mJy beam^{-1}) and the synthesized beam is $4.6 \times 4.1''$, $-4.92°$.

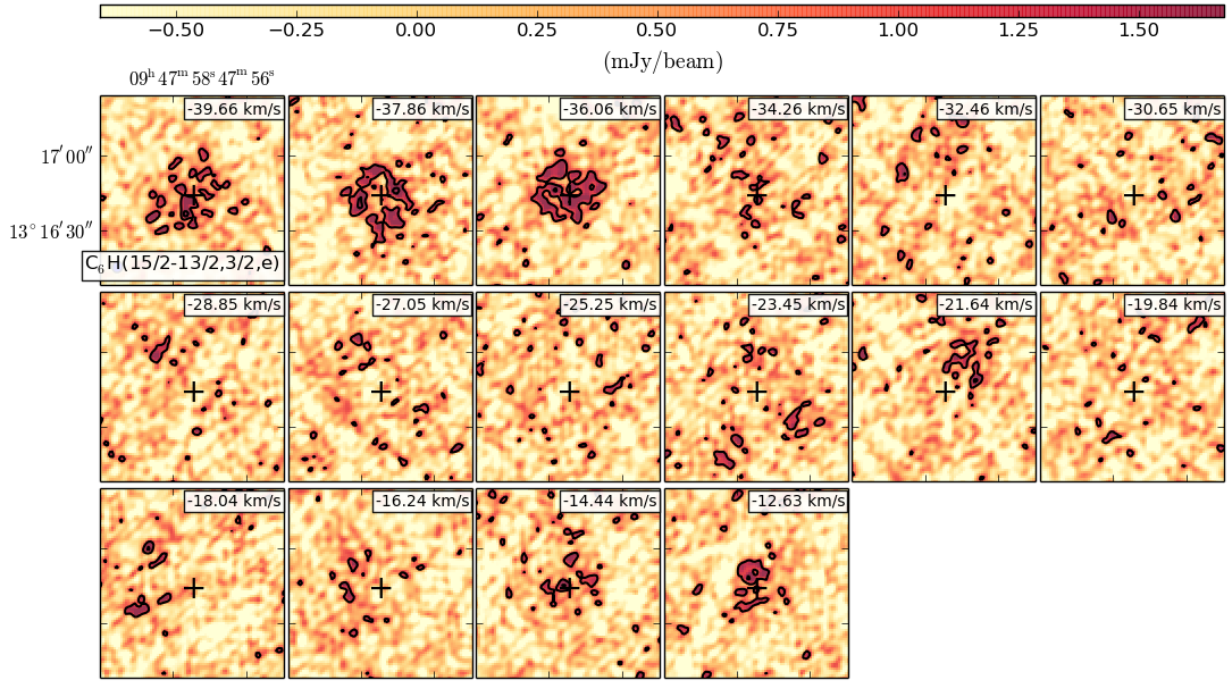

Figure B.34: As Fig. B.1, for C_6H(15/2-13/2,3-2,e). The contour levels are 2, 4, 8, 12 $\times\sigma$(= 0.54 mJy beam^{-1}) and the synthesized beam is $5.0 \times 4.5''$, $-25.09°$.

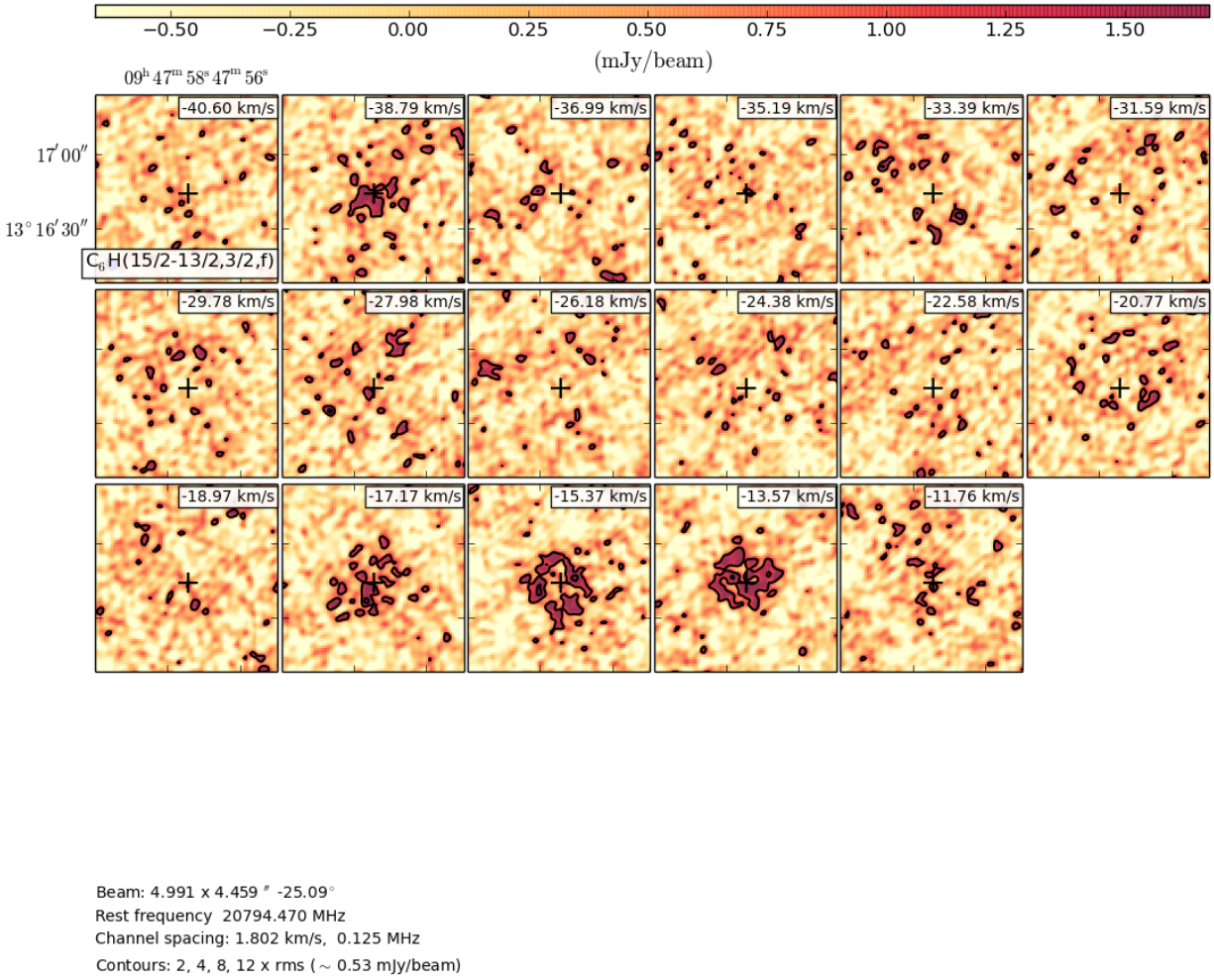

Figure B.35: As Fig. B.1, for C_6H(15/2-13/2,3-2,f). The contour levels are 2, 4, 8, 12 $\times\sigma$(= 0.53 mJy beam^{-1}) and the synthesized beam is $5.0 \times 4.5''$, $-25.09°$.

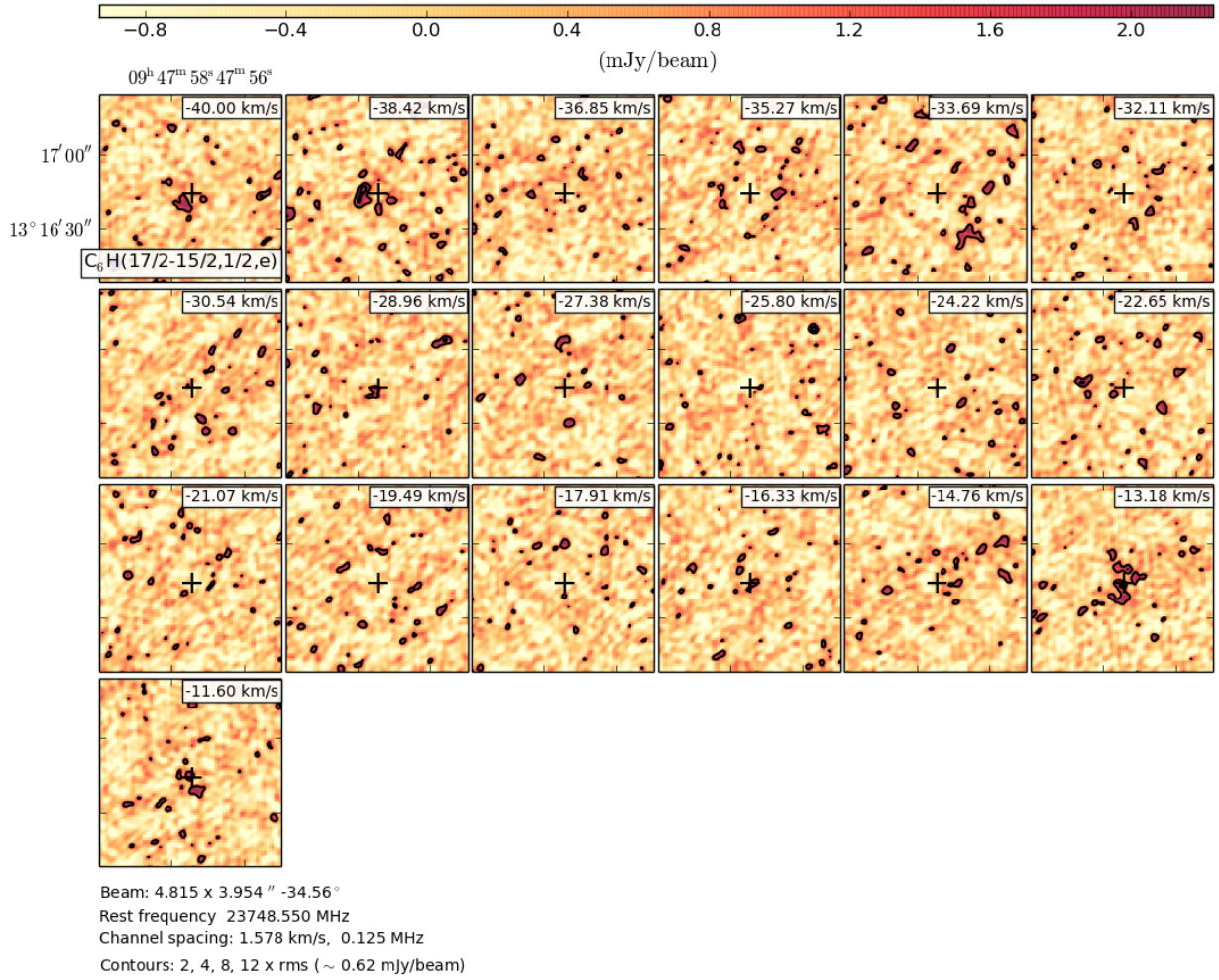

Figure B.36: As Fig. B.1, for $C_6H(17/2\text{-}15/2,1/2,e)$. The contour levels are 2, 4, 8, 12 $\times\sigma$(= 0.62 mJy beam^{-1}) and the synthesized beam is $4.8 \times 4.0''$, $-34.56°$.

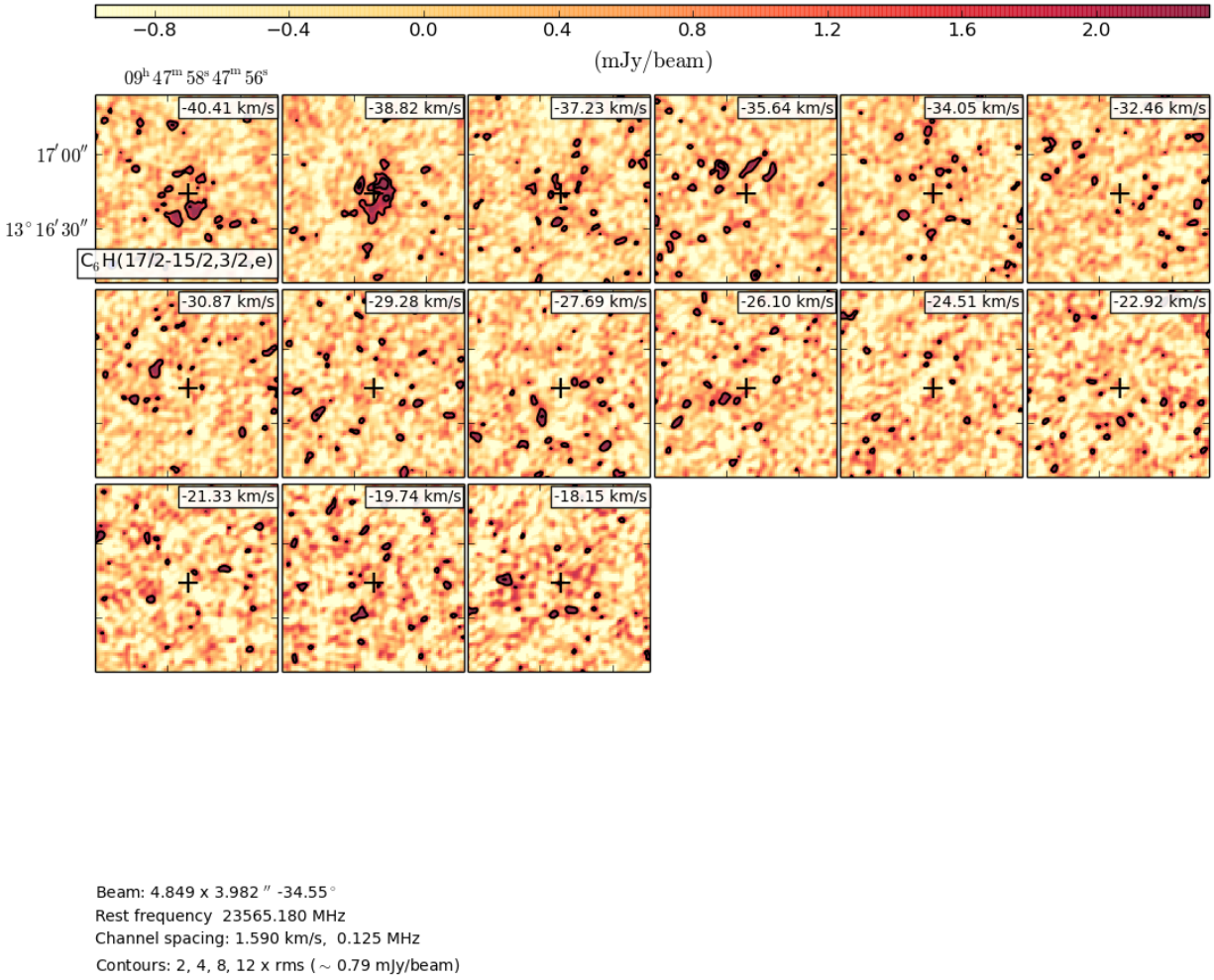

Figure B.37: As Fig. B.1, for C_6H(17/2-15/2,3/2,e). The contour levels are 2, 4, 8, 12 $\times\sigma$(= 0.79 mJy beam^{-1}) and the synthesized beam is $4.8 \times 4.0''$, $-34.55°$.

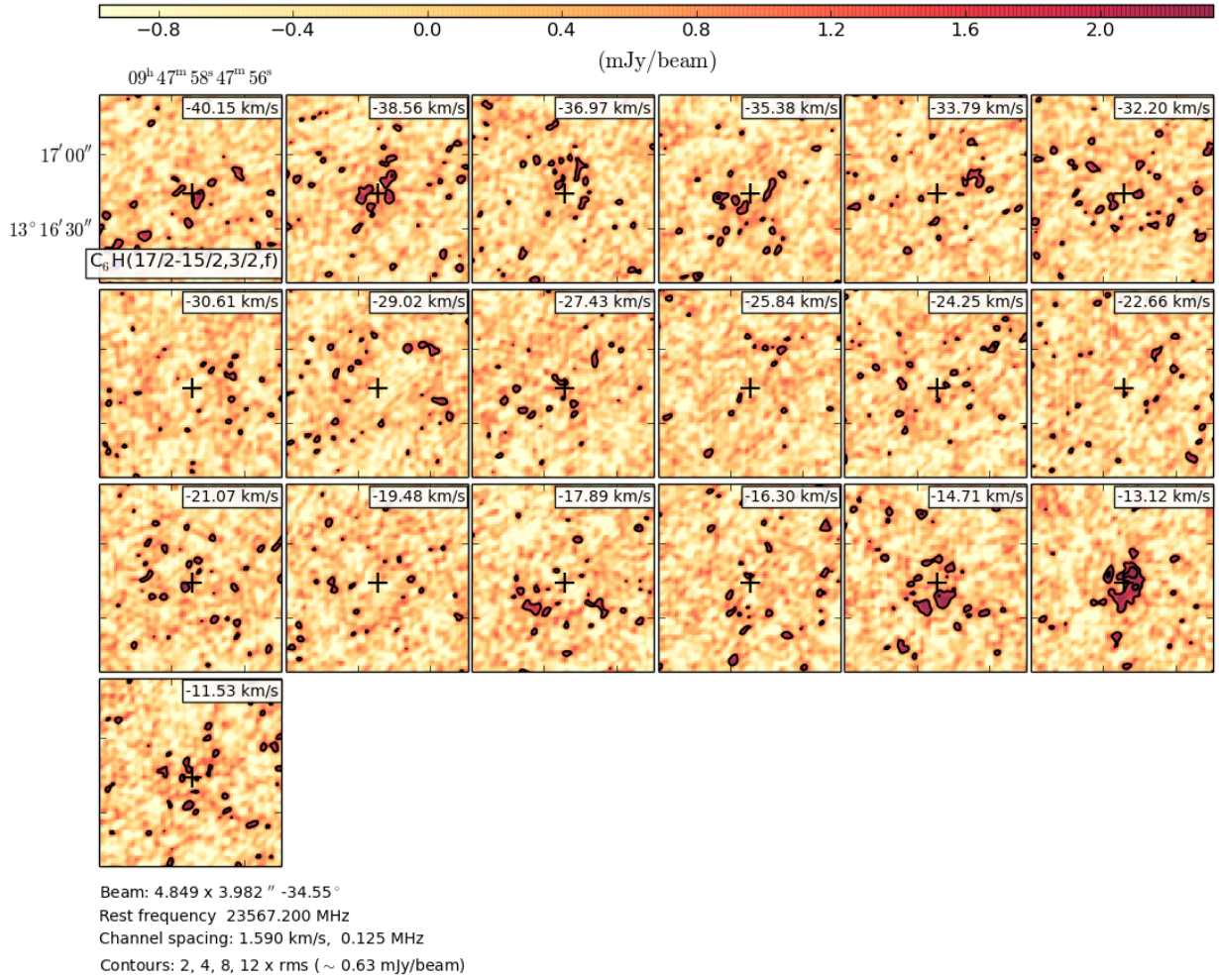

Figure B.38: As Fig. B.1, for $C_6H(17/2\text{-}15/2,3/2,f)$. The contour levels are 2, 4, 8, 12 $\times\sigma$(= 0.63 mJy beam^{-1}) and the synthesized beam is $4.8 \times 4.0''$, $-34.55°$.

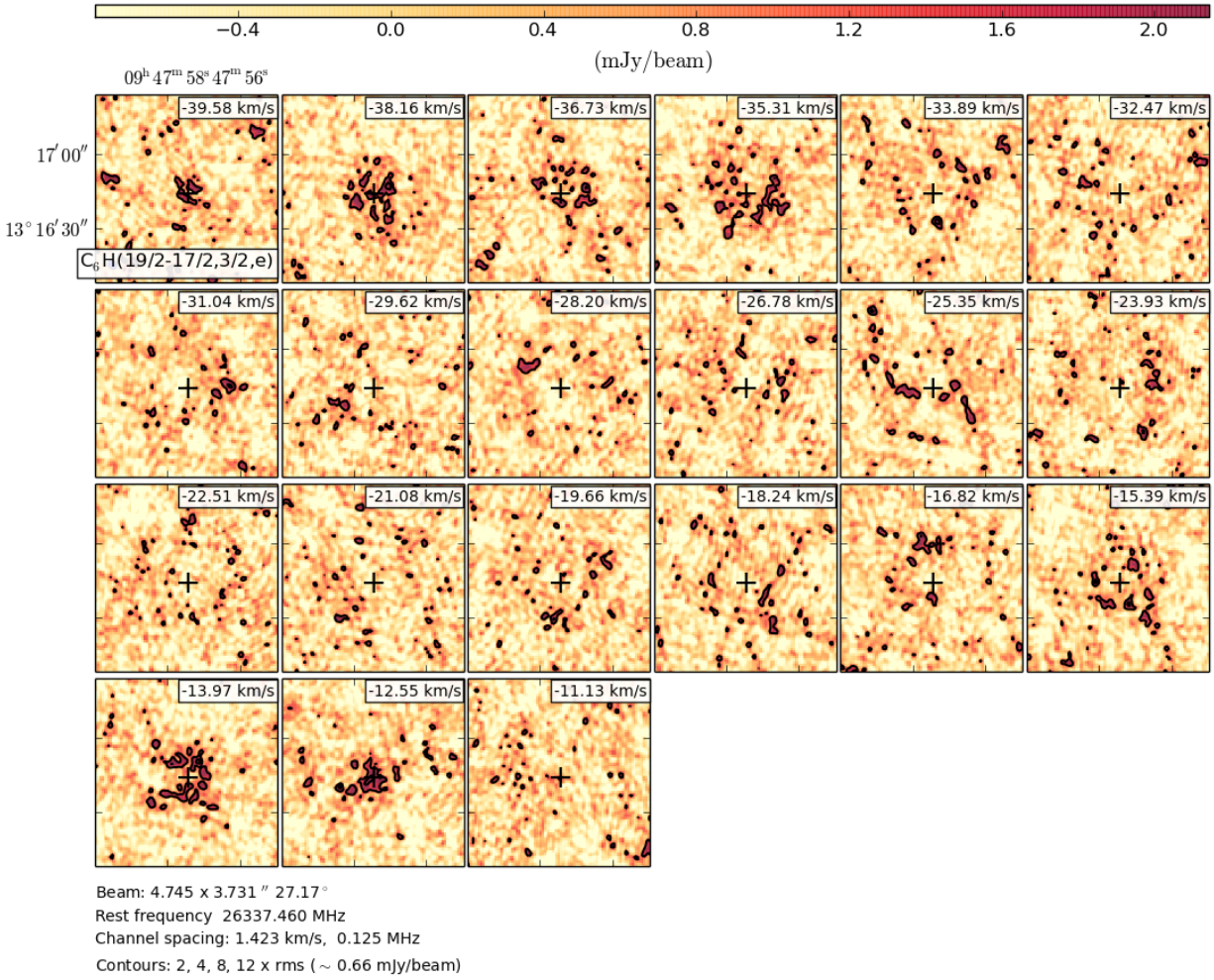

Figure B.39: As Fig. B.1, for $C_6H(19/2\text{-}17/2,3/2,e)$. The contour levels are 2, 4, 8, 12 $\times\sigma$(= 0.66 mJy beam^{-1}) and the synthesized beam is 4.7 $\times$ 3.7″, 27.17°.

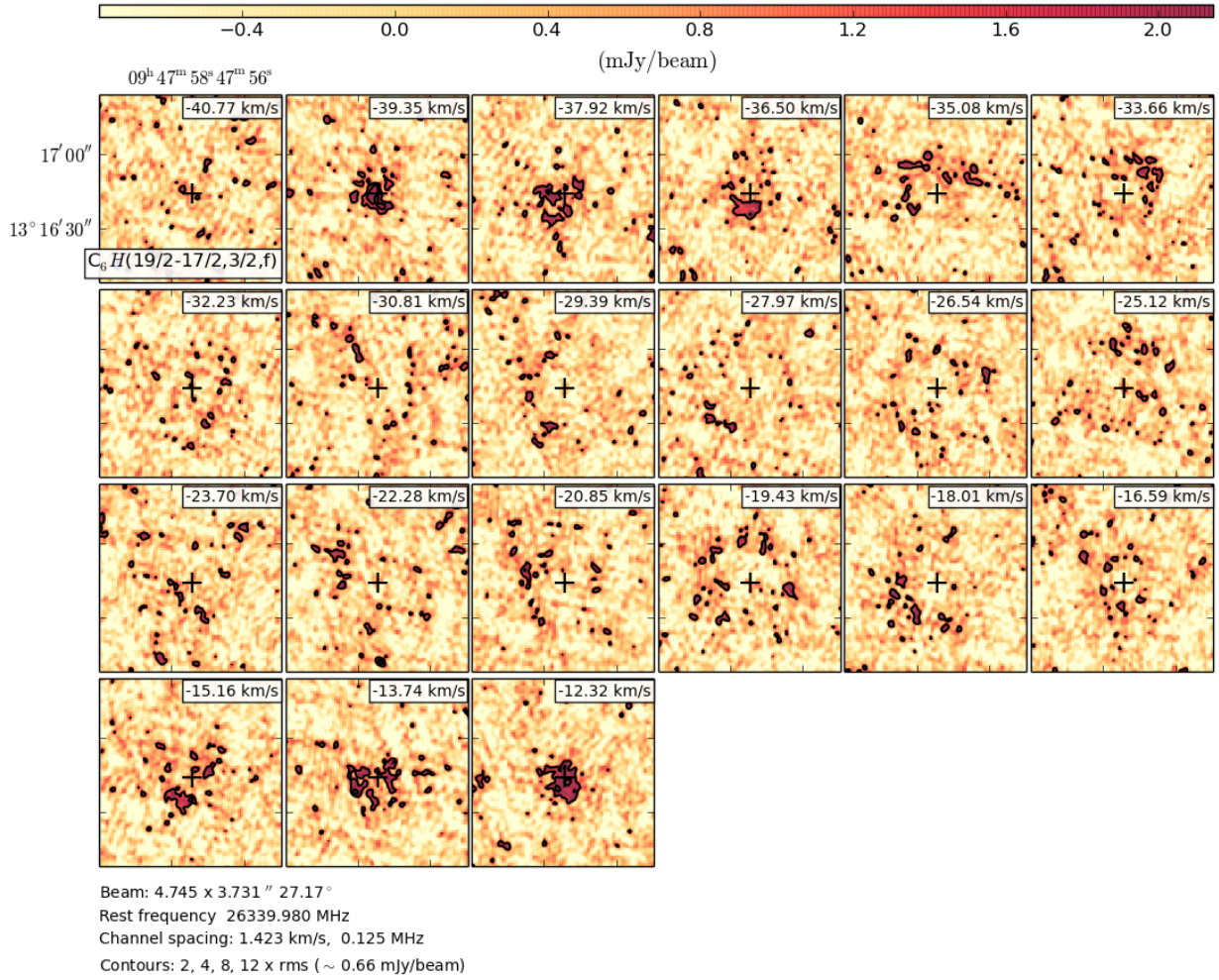

Figure B.40: As Fig. B.1, for C_6H(19/2-17/2,3/2,f). The contour levels are 2, 4, 8, 12 $\times\sigma$(= 0.66 mJy beam^{-1}) and the synthesized beam is $4.7 \times 3.7''$, 27.17°.

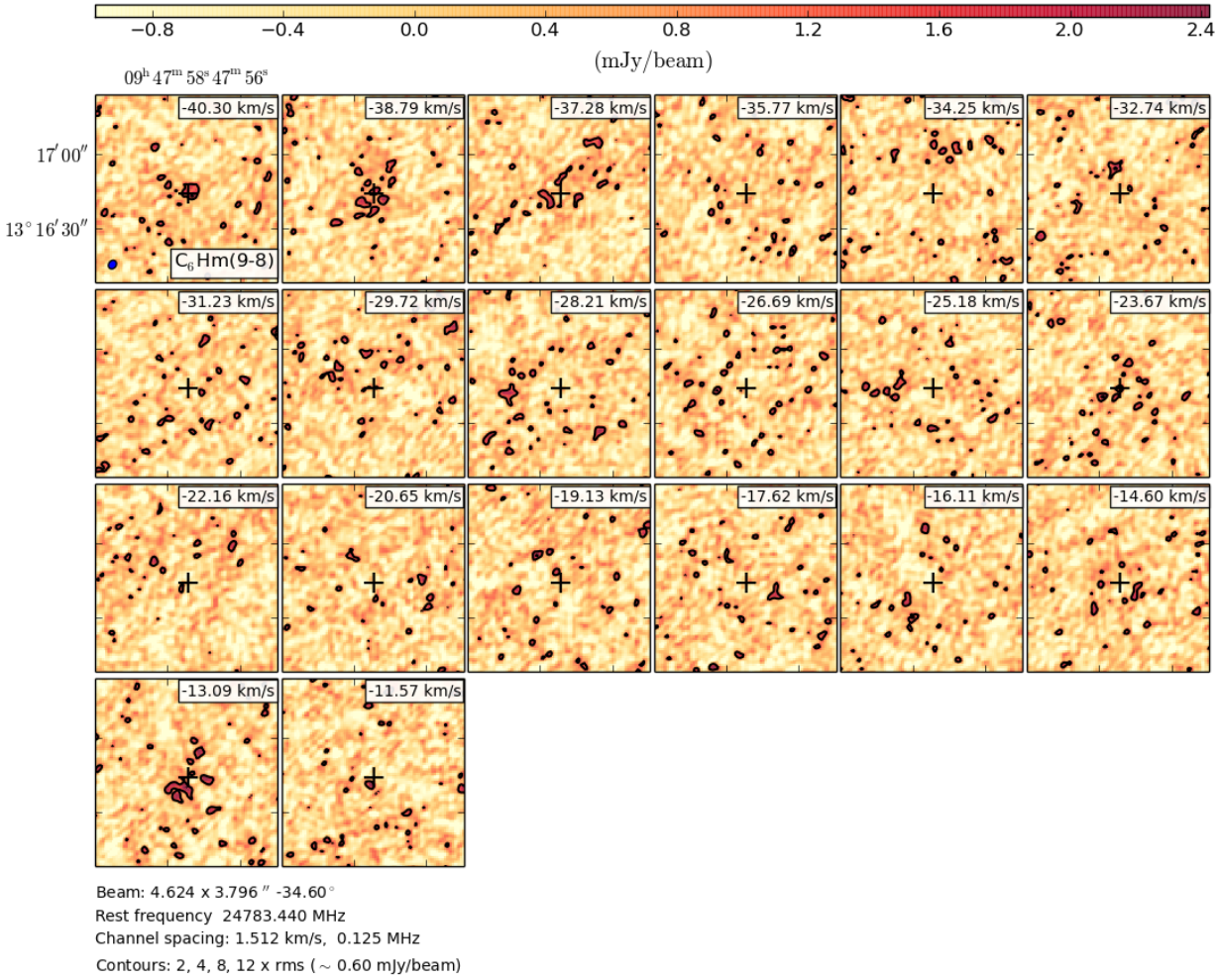

Figure B.41: As Fig. B.1, for C_6H^-(9-8). The contour levels are 2, 4, 8, 12 $\times\sigma$(= 0.60 mJy beam^{-1}) and the synthesized beam is $4.6 \times 3.8''$, $-34.60°$.

Figure B.42: As Fig. B.1, for C_6H^-(11-10). The contour levels are 2, 4, 8, 12 $\times\sigma$(= 0.91 mJy beam^{-1}) and the synthesized beam is $9.9 \times 6.0''$, 25.86°.

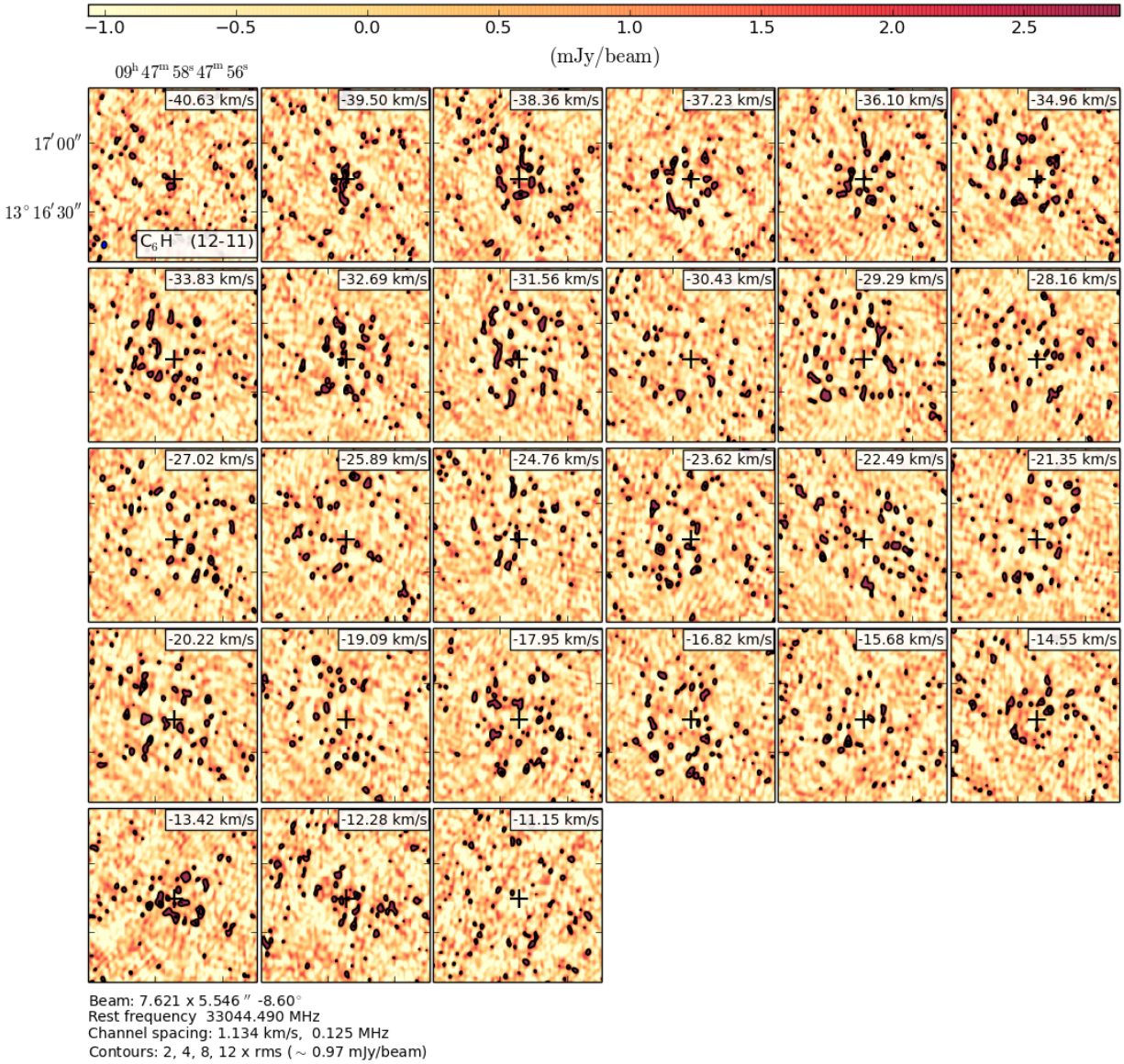

Figure B.43: As Fig. B.1, for C_6H^-(12-11). The contour levels are 2, 4, 8, 12 $\times\sigma$(= 0.97 mJy beam^{-1}) and the synthesized beam is $7.6 \times 5.5''$, $-8.60°$.

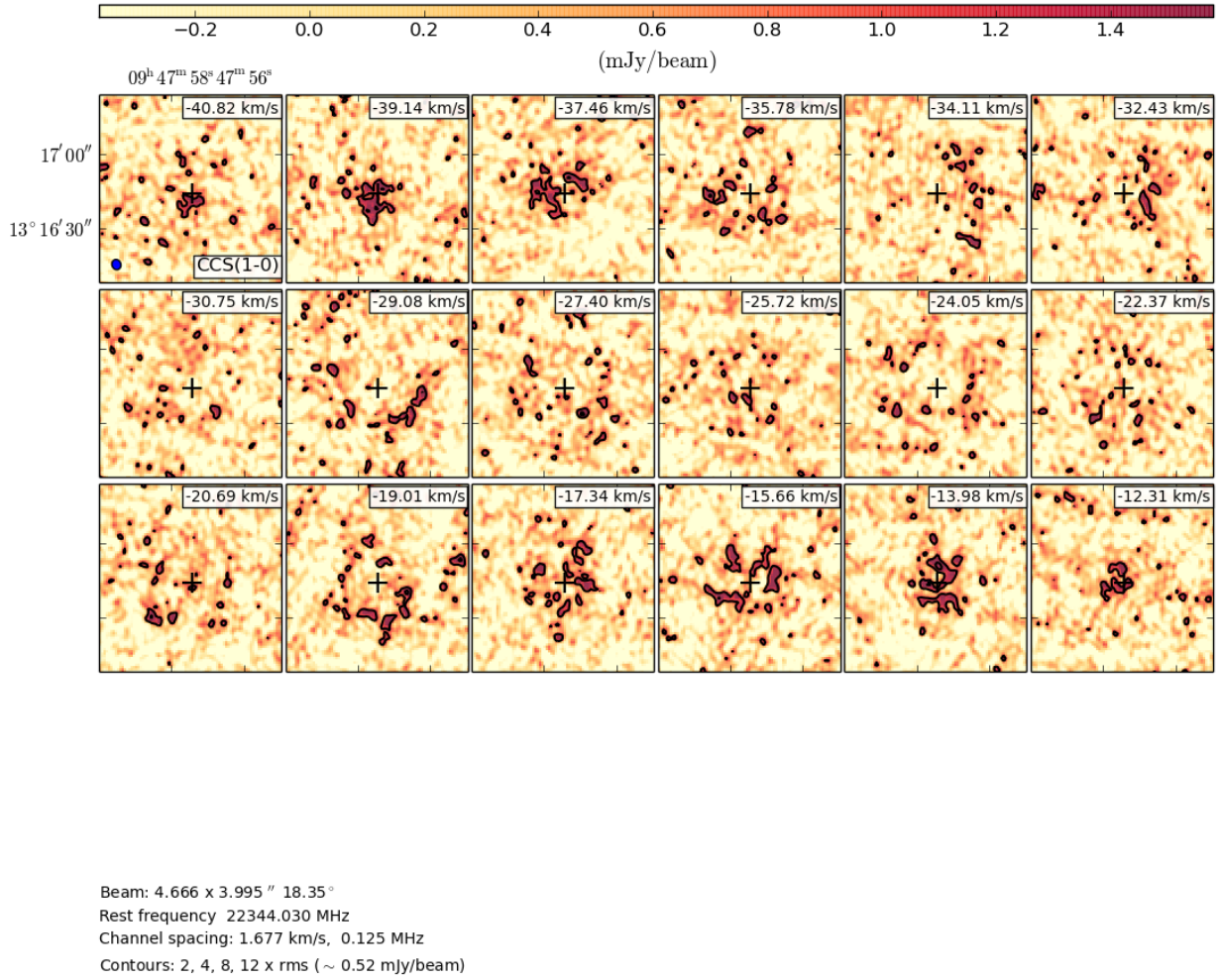

Figure B.44: As Fig. B.1, for C_2S(1-0). The contour levels are 2, 4, 8, 12 $\times\sigma$(= 0.52 mJy beam^{-1}) and the synthesized beam is $4.7 \times 4.0''$, 18.35°.

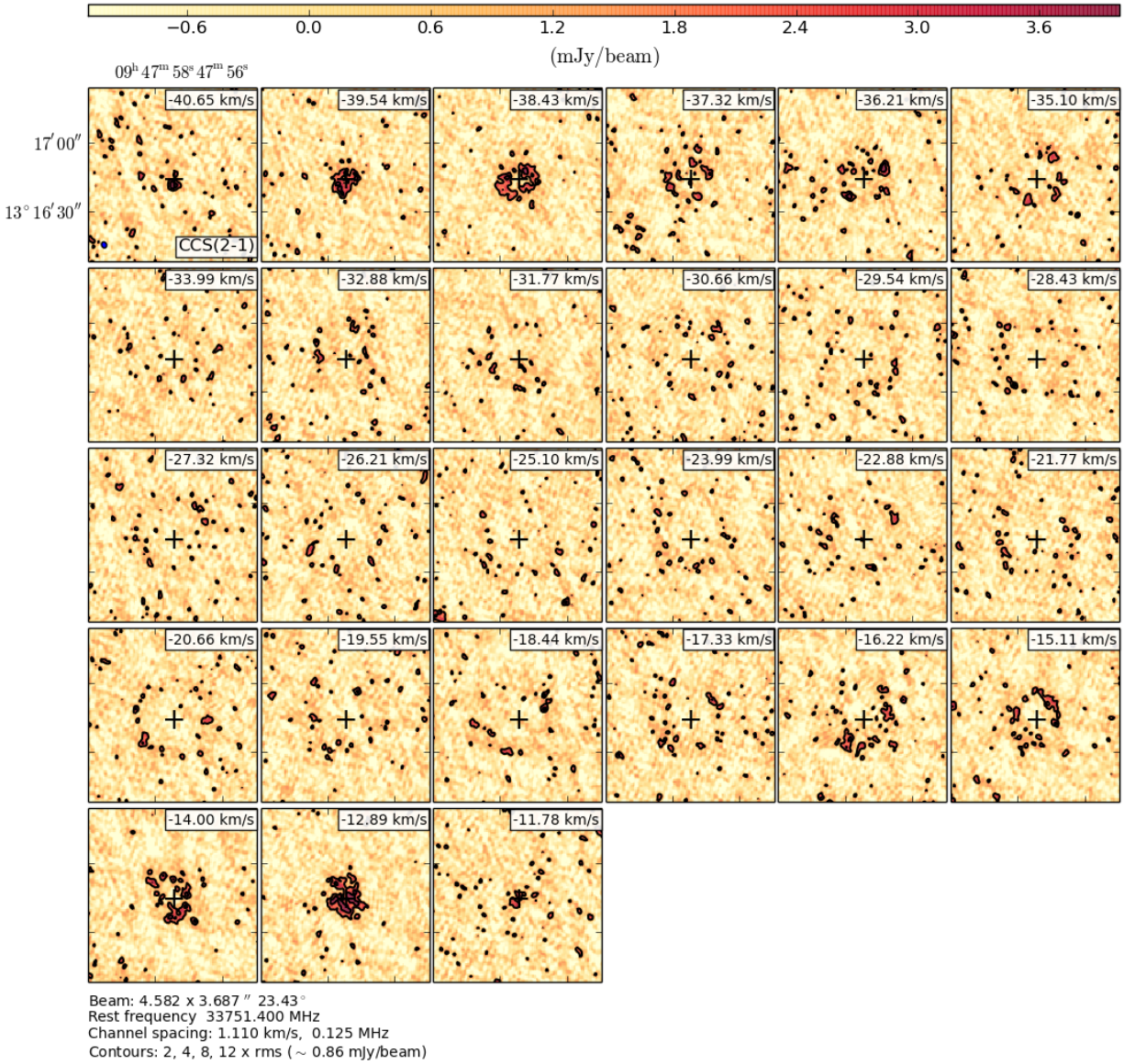

Figure B.45: As Fig. B.1, for C_2S(2-1). The contour levels are 2, 4, 8, 12 $\times\sigma$(= 0.86 mJy beam^{-1}) and the synthesized beam is $4.6 \times 3.7''$, 23.43°.

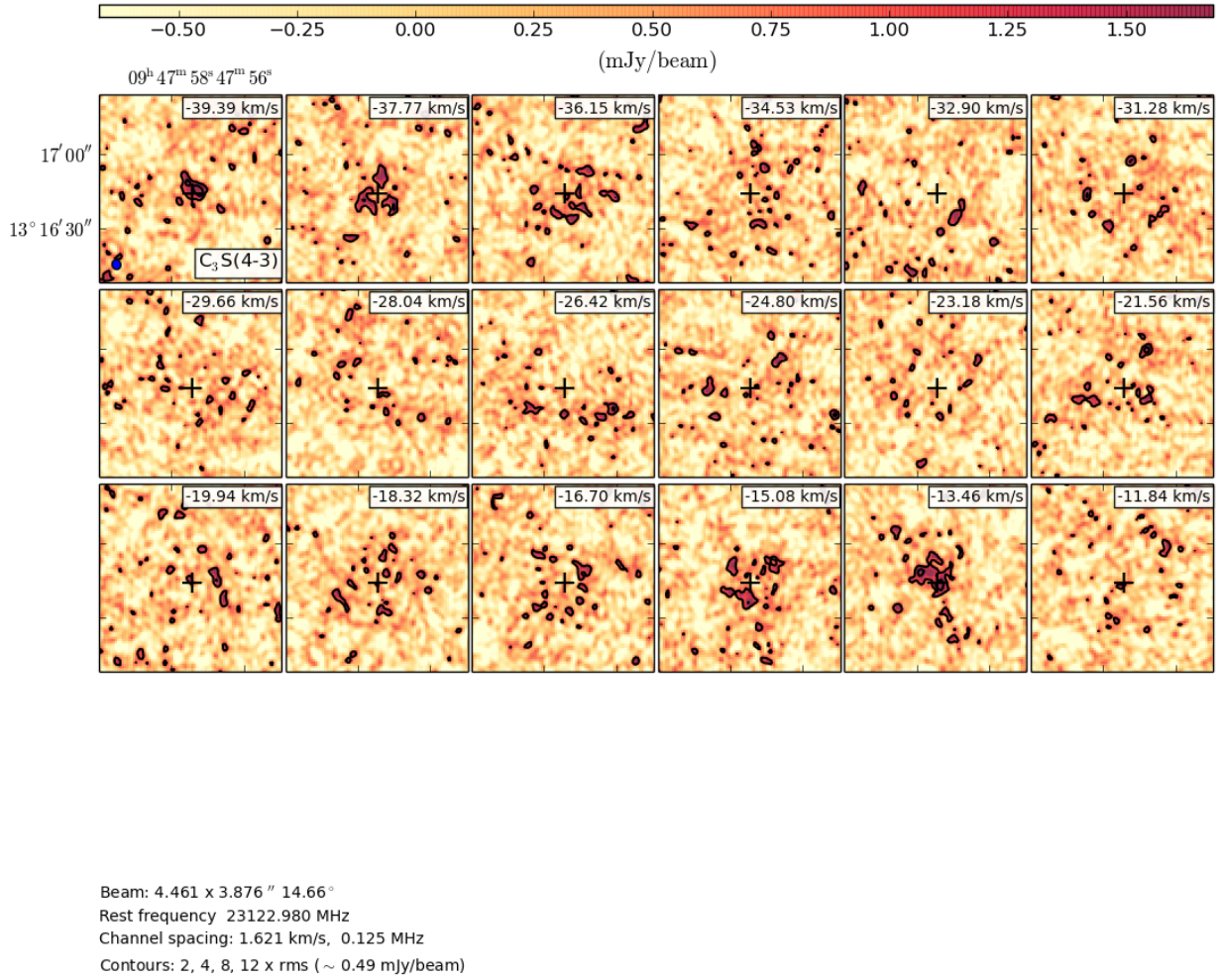

Figure B.46: As Fig. B.1, for C_3S(4-3). The contour levels are 2, 4, 8, 12 $\times\sigma$(= 0.49 mJy beam^{-1}) and the synthesized beam is $4.5 \times 3.9''$, 14.66°.

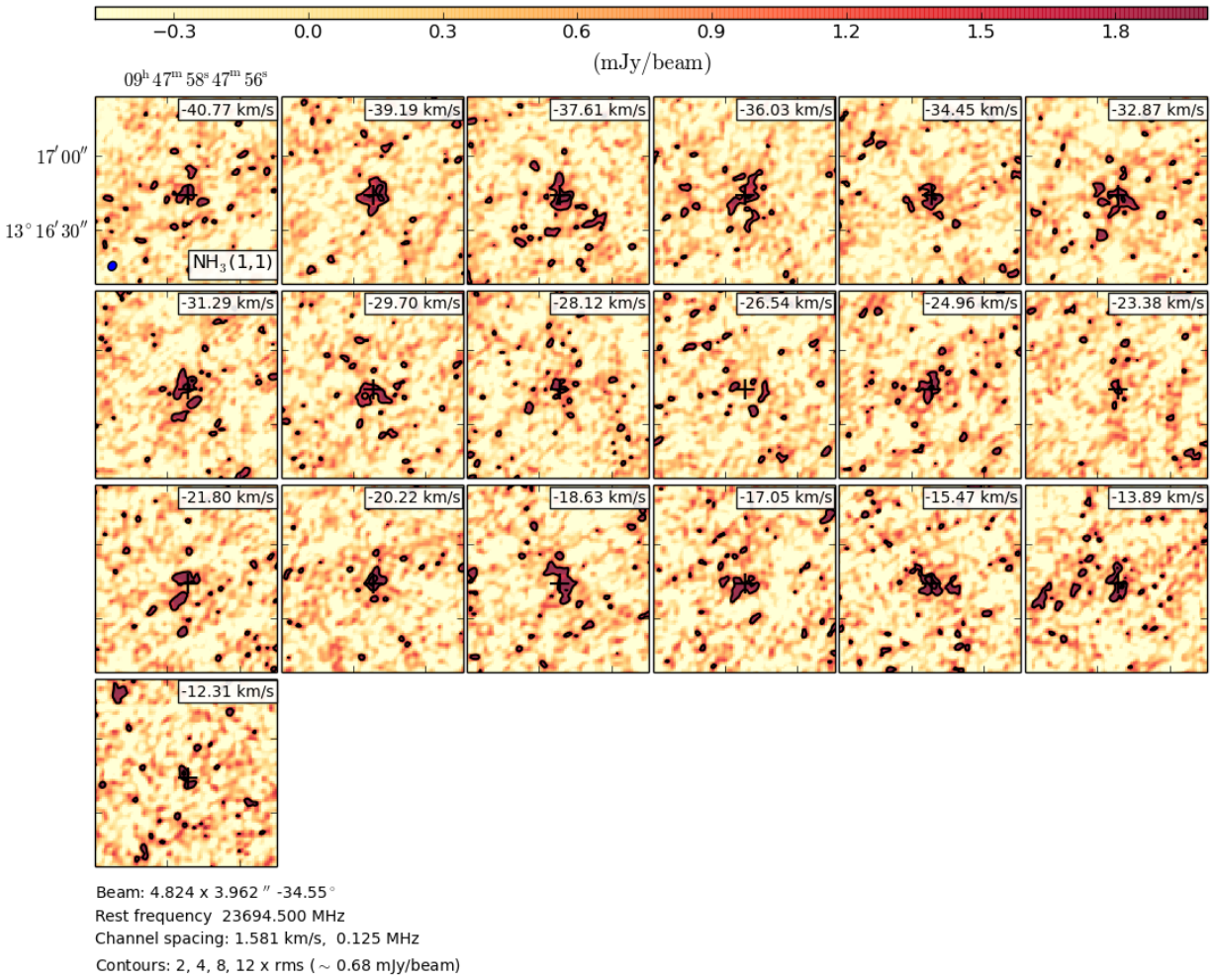

Figure B.47: As Fig. B.1, for NH_3(1,1). The contour levels are 2, 4, 8, 12 $\times\sigma$(= 0.68 mJy beam^{-1}) and the synthesized beam is $4.8 \times 4.0''$, $-34.55°$.

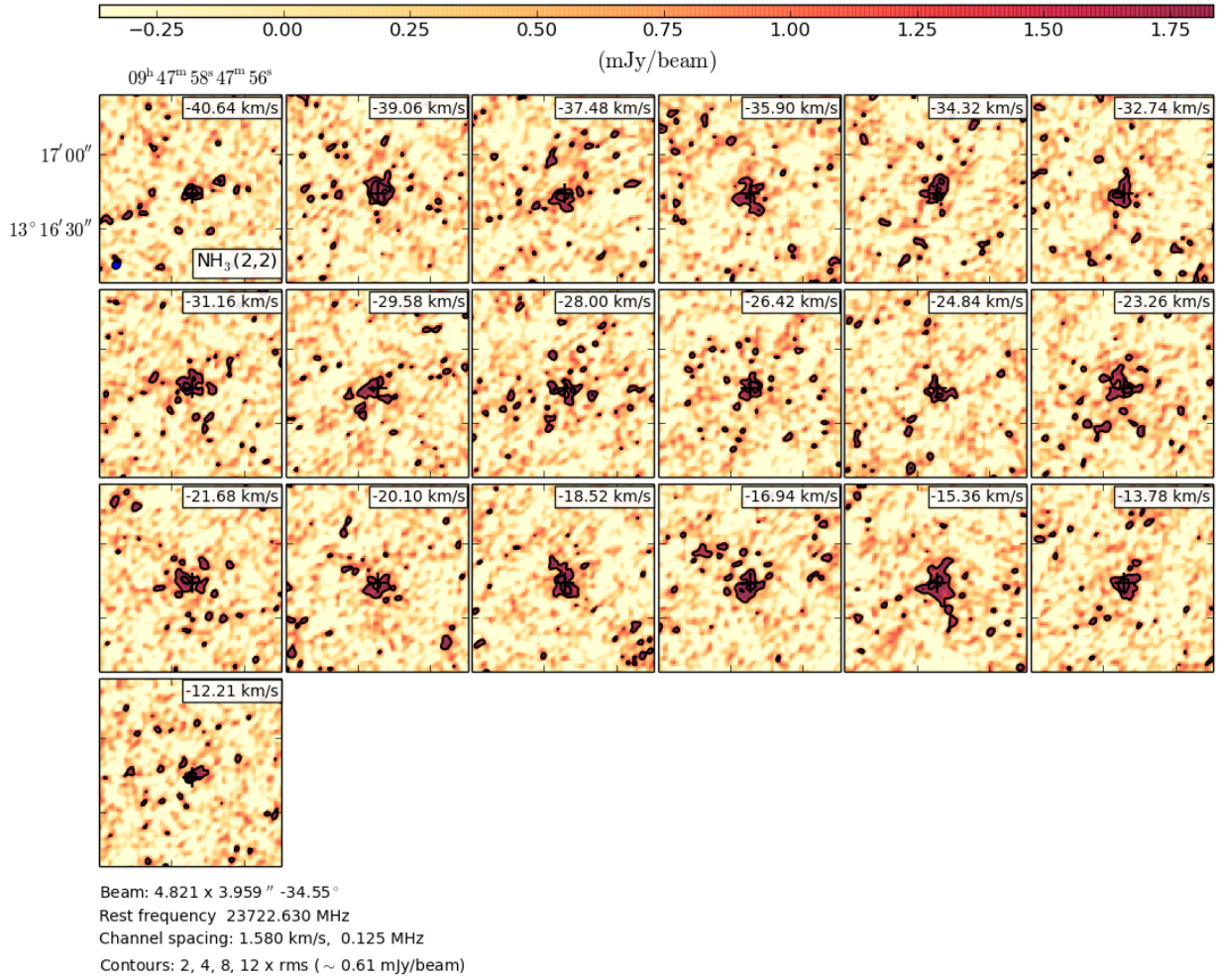

Figure B.48: As Fig. B.1, for $NH_3(2,2)$. The contour levels are 2, 4, 8, 12 $\times\sigma$(= 0.61 mJy beam^{-1}) and the synthesized beam is $4.8 \times 4.0''$, $-34.55°$.

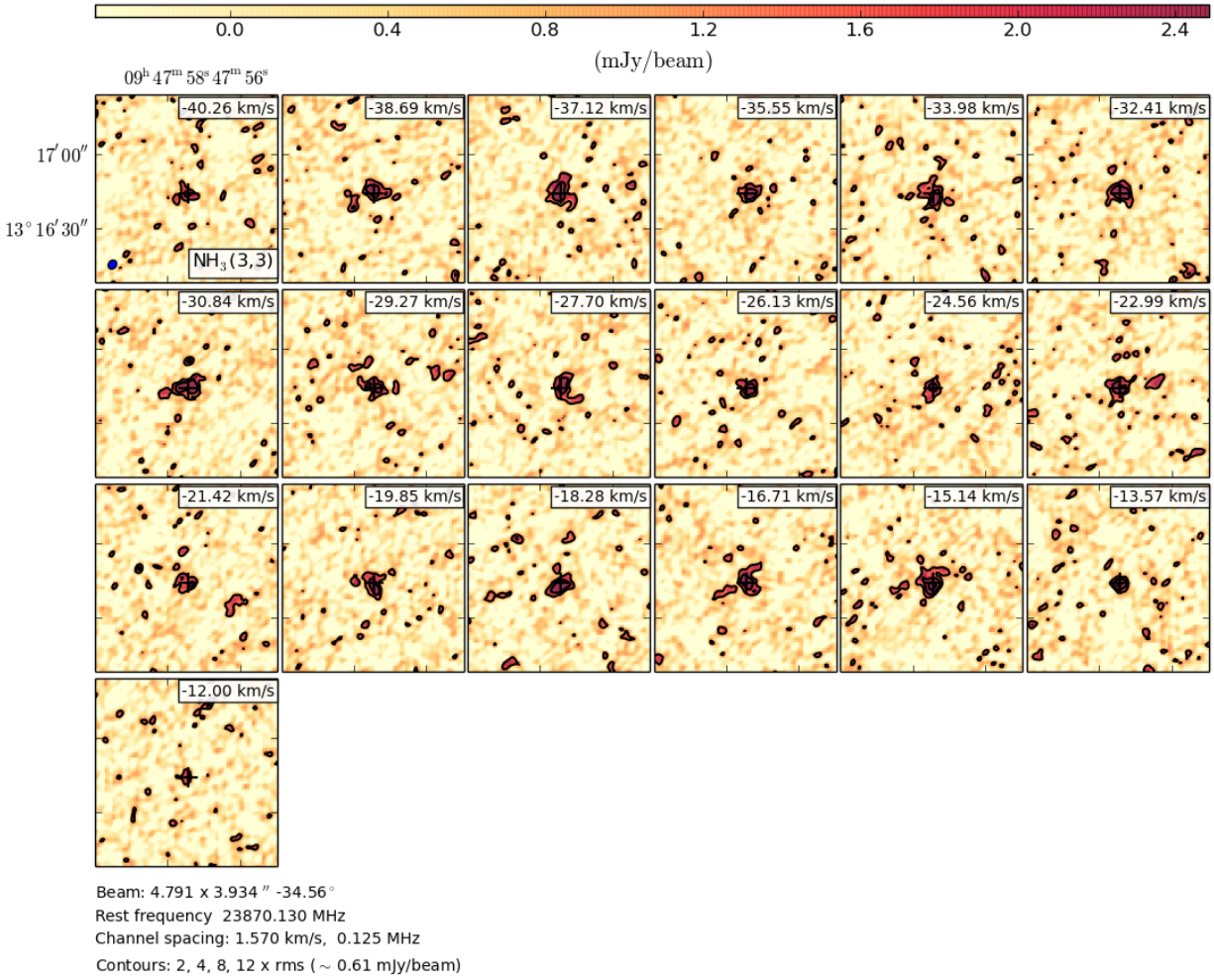

Figure B.49: As Fig. B.1, for NH_3(3,3). The contour levels are 2, 4, 8, 12 $\times\sigma$(= 0.61 mJy beam^{-1}) and the synthesized beam is $4.8 \times 4.0''$, $-34.55°$.

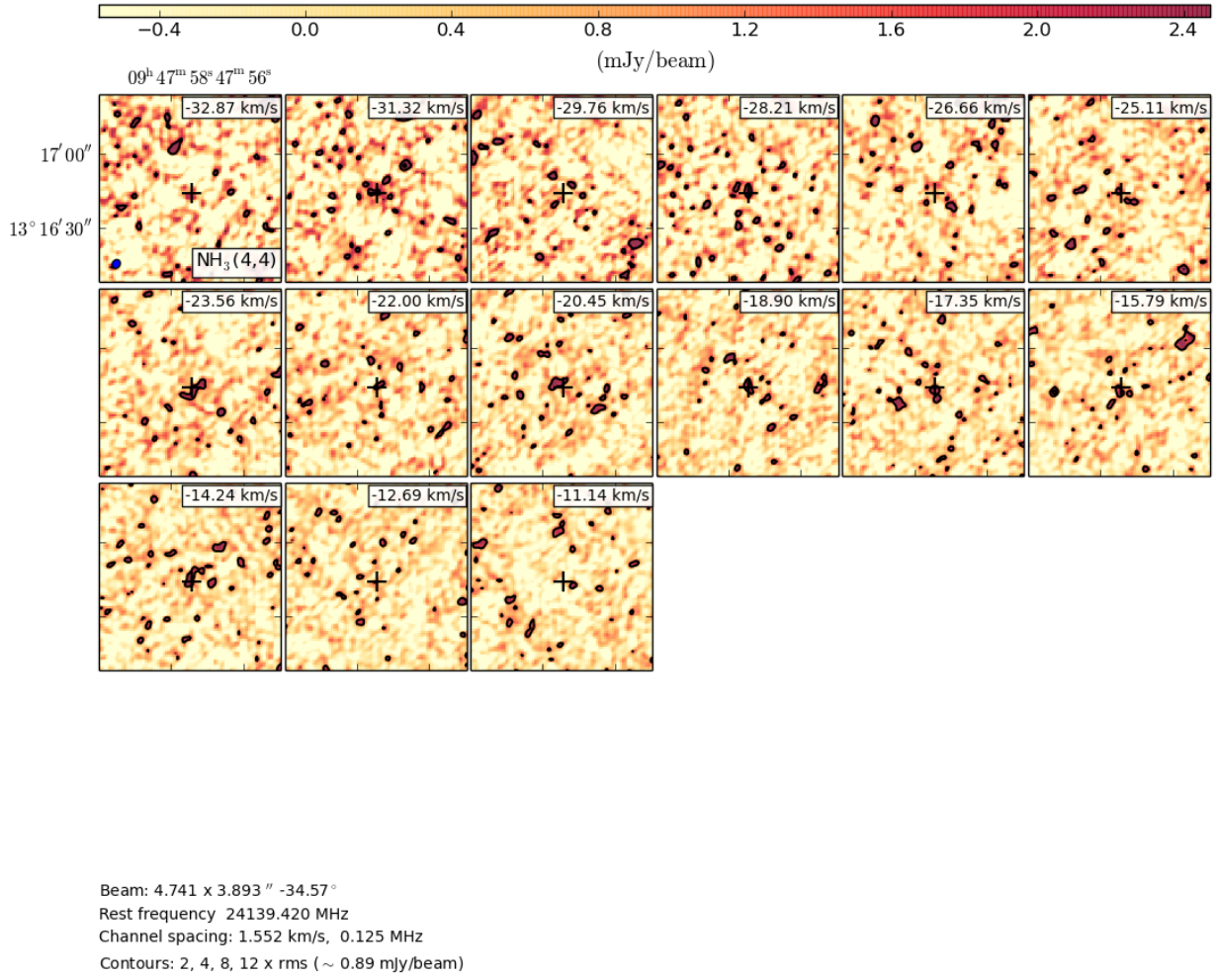

Figure B.50: As Fig. B.1, for NH_3(4,4). The contour levels are 2, 4, 8, 12 $\times\sigma$(= 0.89 mJy beam^{-1}) and the synthesized beam is $4.7 \times 3.9''$, $-34.57°$.

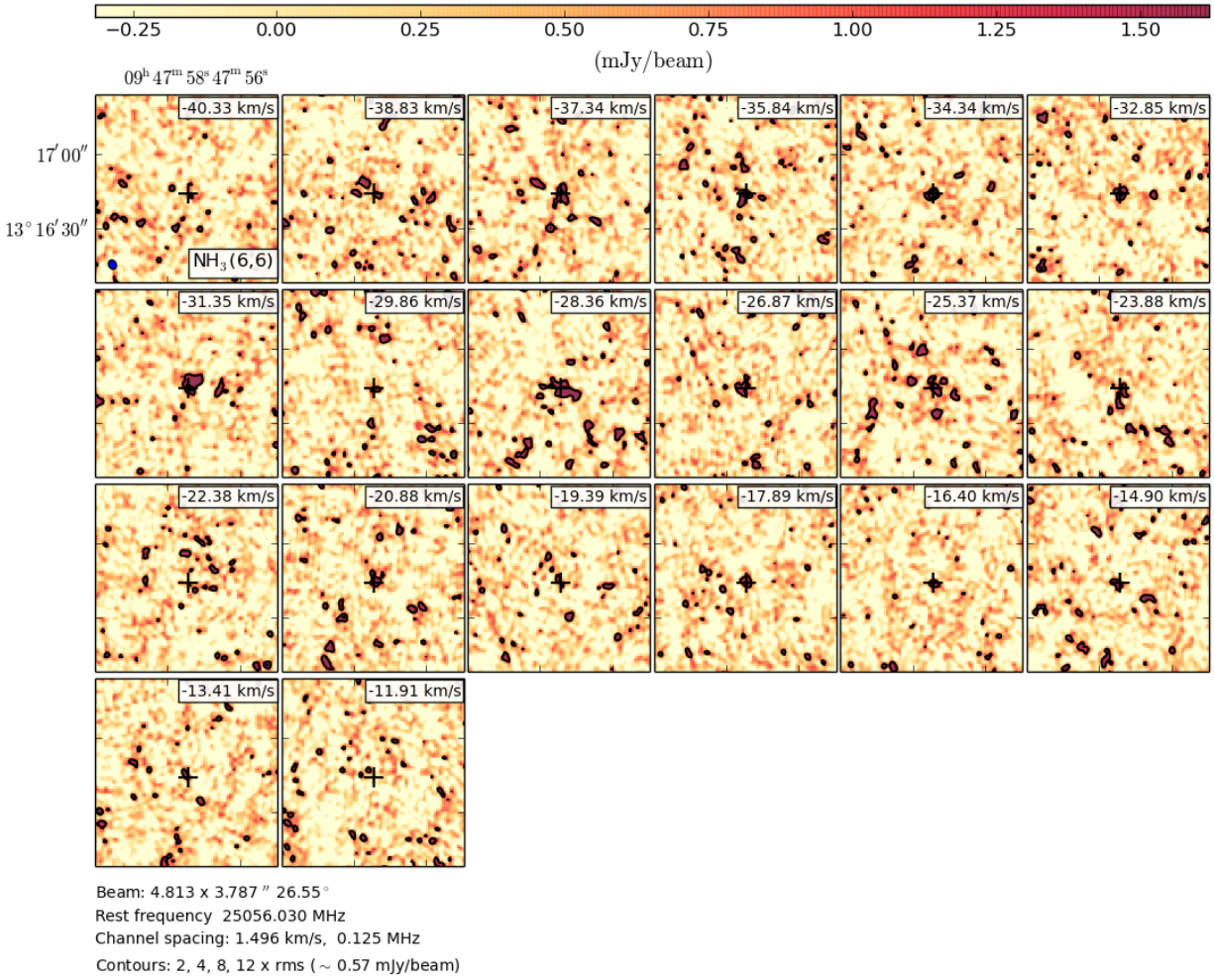

Figure B.51: As Fig. B.1, for NH_3(6,6). The contour levels are 2, 4, 8, 12 $\times\sigma$(= 0.57 mJy beam^{-1}) and the synthesized beam is $4.8 \times 3.8''$, 26.55°.

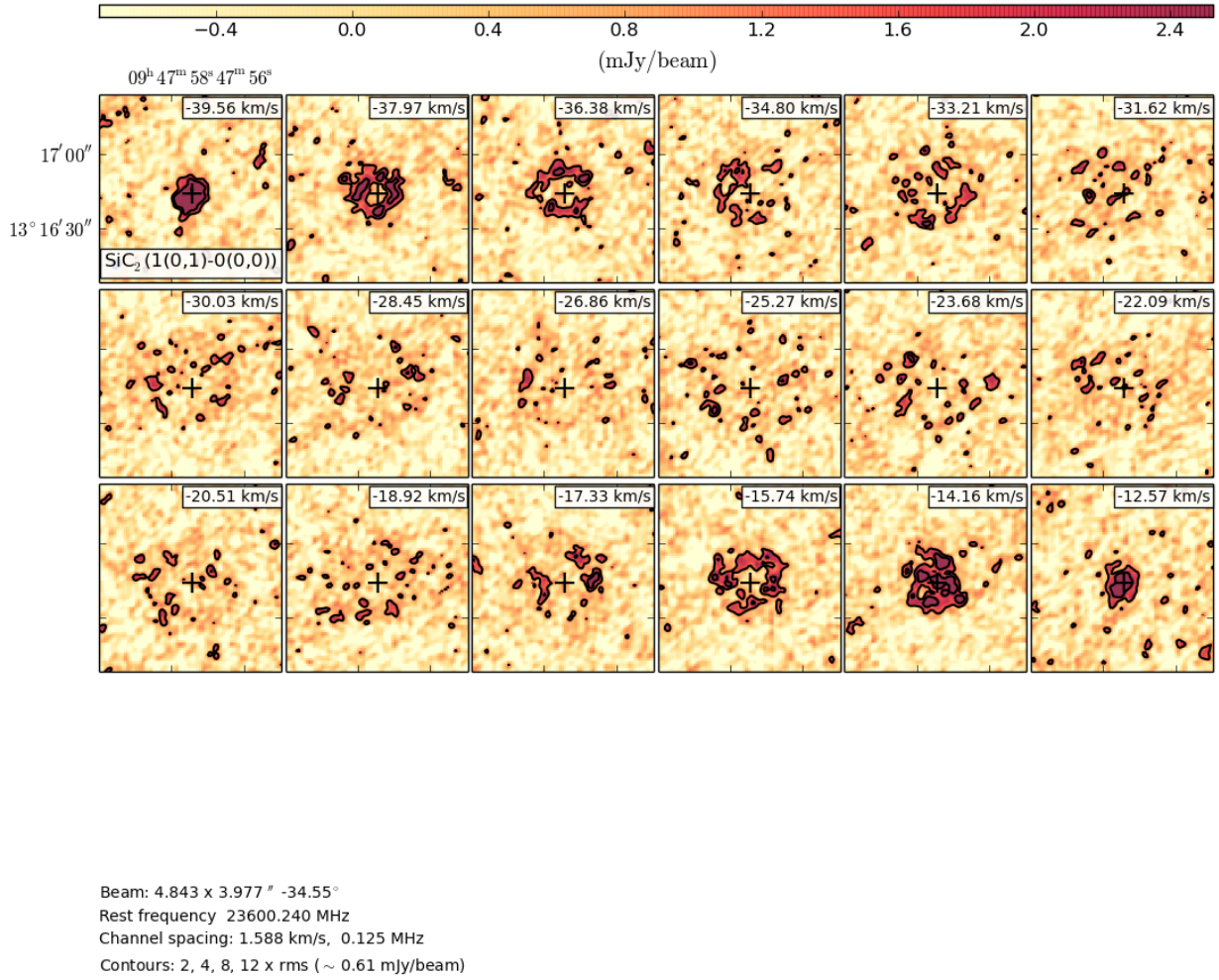

Figure B.52: As Fig. B.1, for SiC_2(1(0,1),0(0,0)). The contour levels are 2, 4, 8, 12 $\times\sigma$(= 0.61 mJy beam^{-1}) and the synthesized beam is $4.8 \times 4.0''$, $-34.55°$.

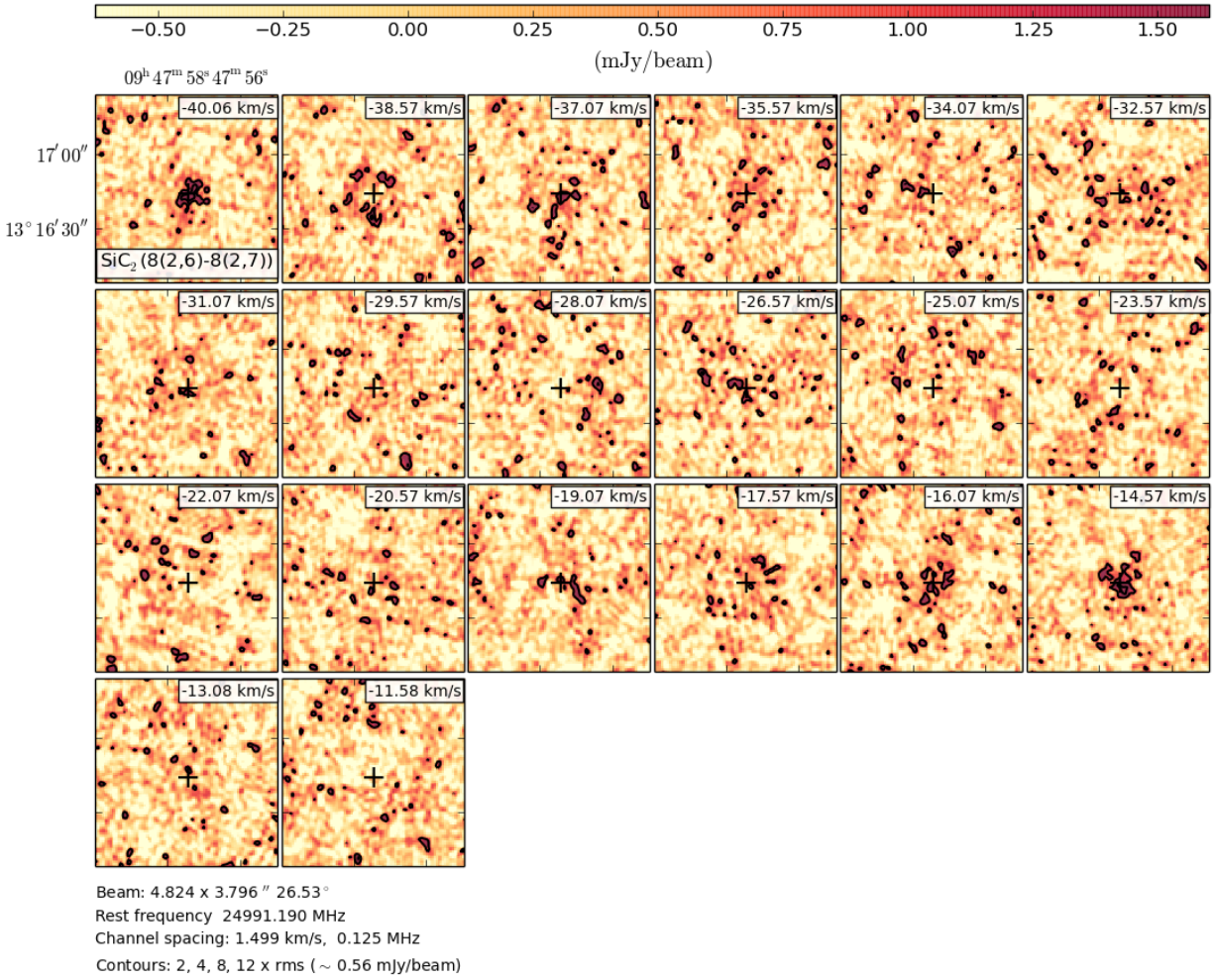

Figure B.53: As Fig. B.1, for SiC_2(8(2,6),8(2,7)). The contour levels are 2, 4, 8, 12 $\times\sigma$(= 0.56 mJy beam^{-1}) and the synthesized beam is $4.8 \times 3.8''$, 26.53°.

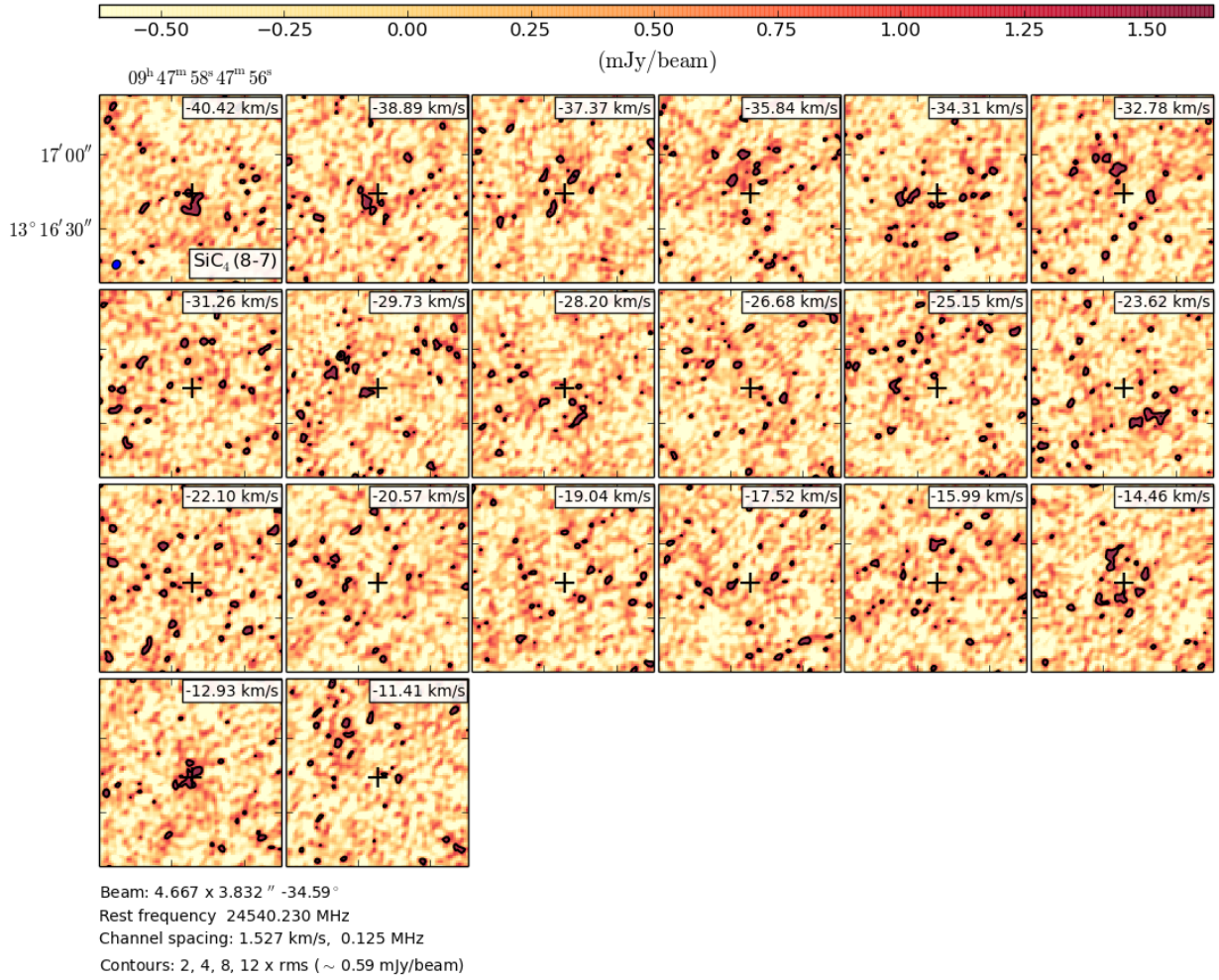

Figure B.54: As Fig. B.1, for SiC_4(8-7). The contour levels are 2, 4, 8, 12 $\times\sigma$(= 0.59 mJy beam^{-1}) and the synthesized beam is $4.7 \times 3.8''$, $-34.59°$.

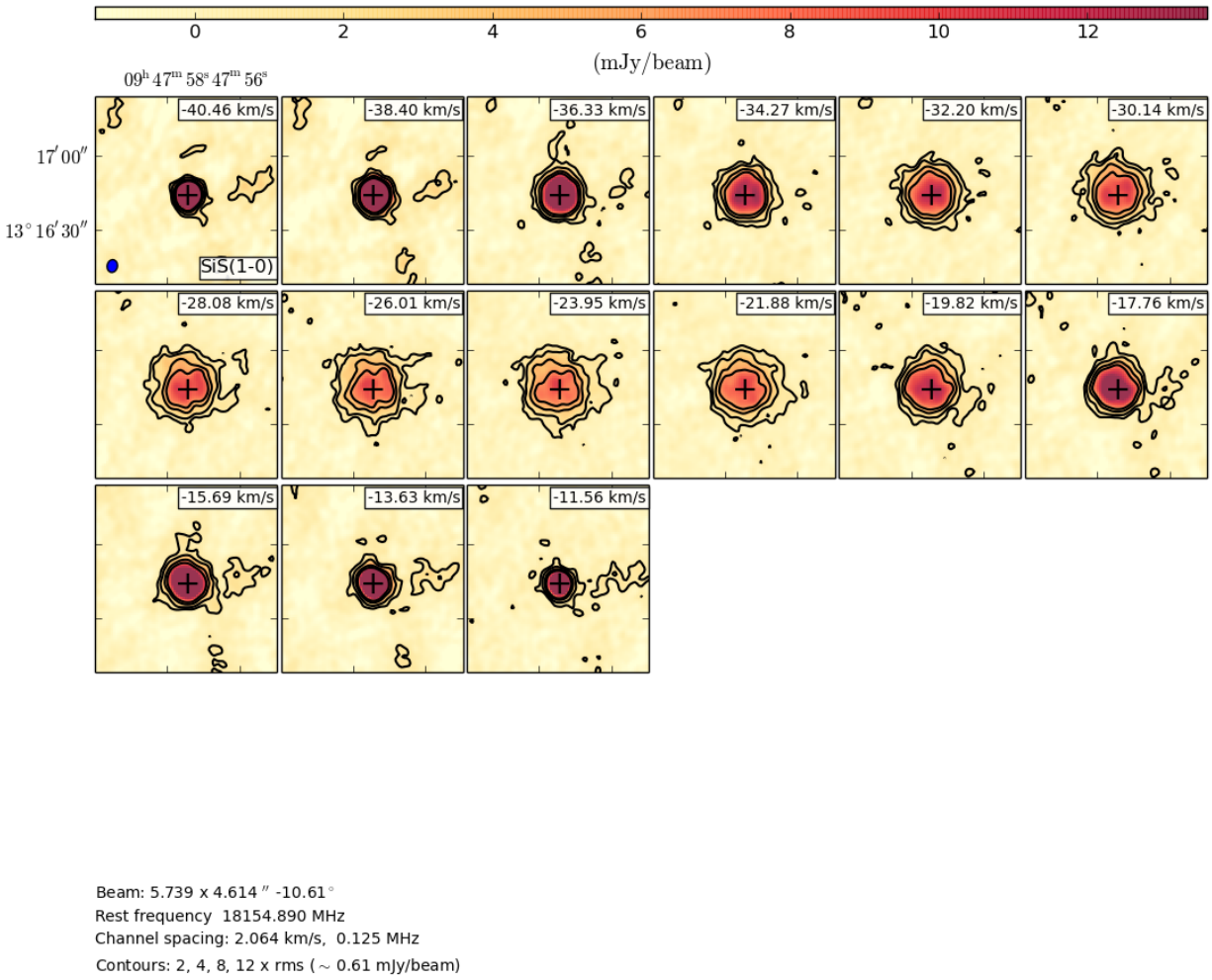

Figure B.55: As Fig. B.1, for SiS(1-0). The contour levels are 2, 4, 8, 12 $\times\sigma$(= 0.61 mJy beam^{-1}) and the synthesized beam is $5.7 \times 4.6''$, $-10.61°$.

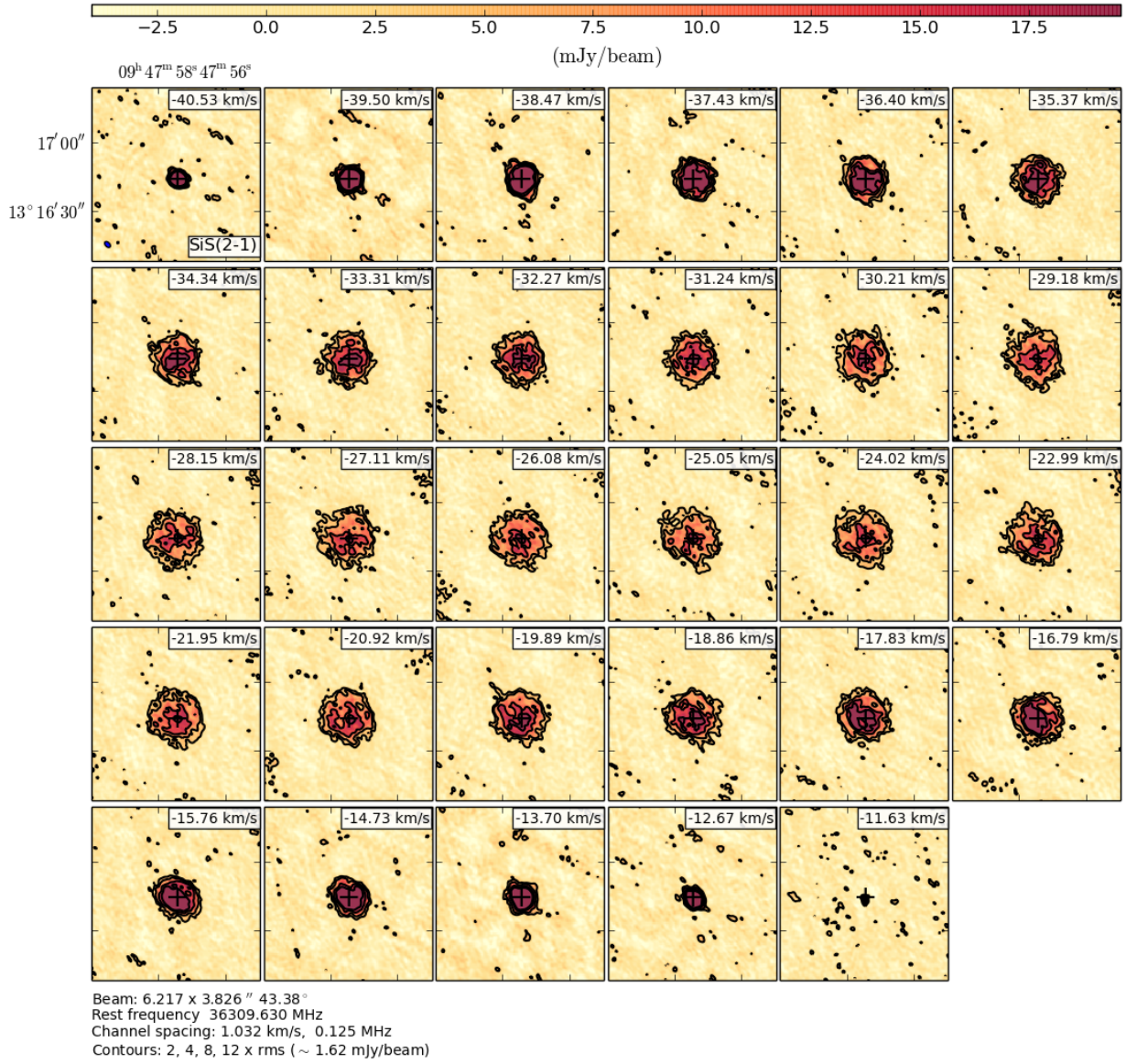

Figure B.56: As Fig. B.1, for SiS(2-1). The contour levels are 2, 4, 8, 12 $\times\sigma$(= 1.62 mJy beam^{-1}) and the synthesized beam is $6.2 \times 3.8''$, 43.38°.

APPENDIX C

Radial emission profiles and Gaussian fit results

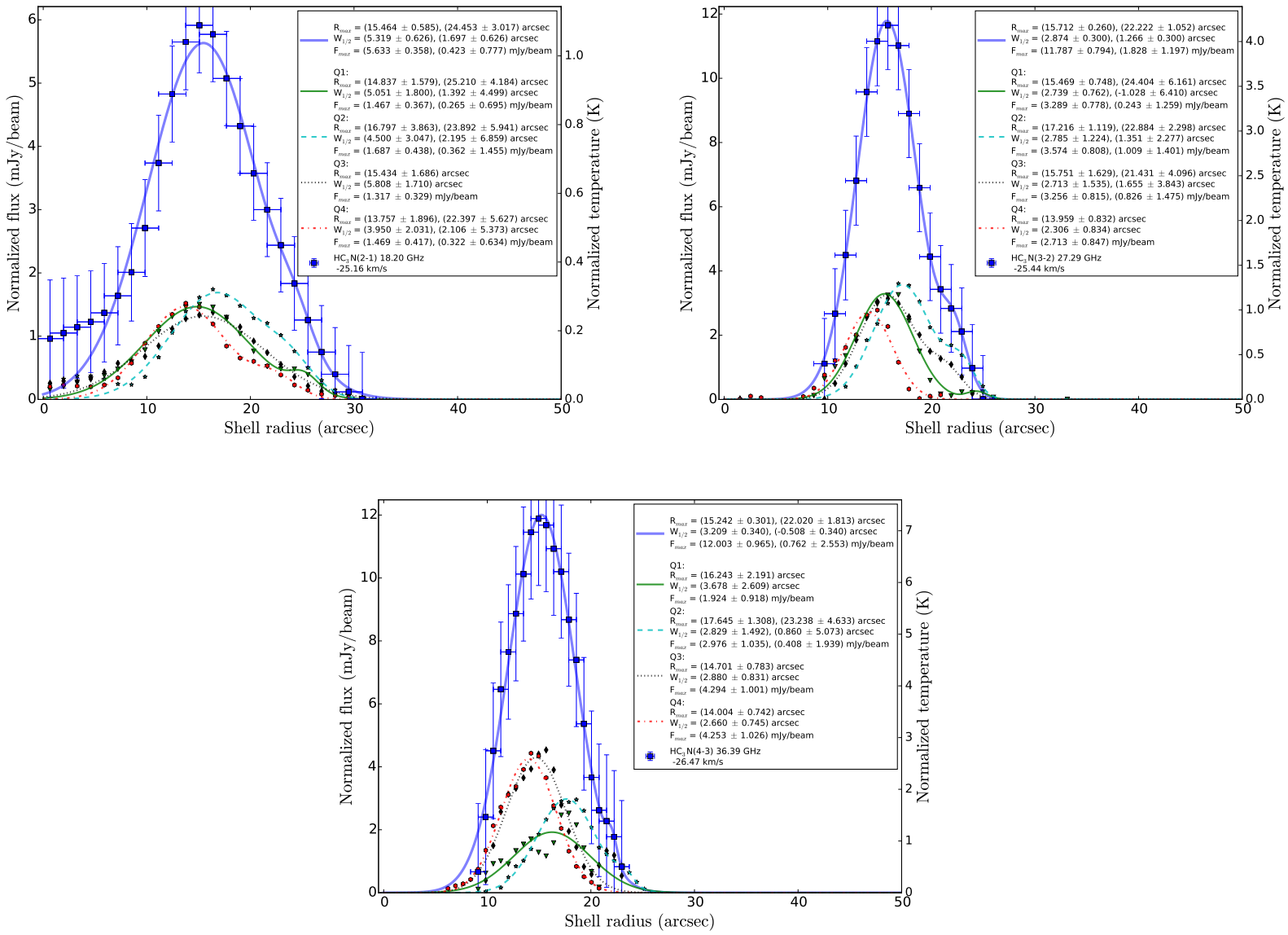

Figure C.1: Radial emission profiles of HC_3N for the channel closest to the systemic velocity (-26 km s^{-1}) for the four quarters (Q1, Q2, Q3, Q4) and their azimuthal sum (blue) and the according Gaussian fit results. The points are the data points and the lines are the fitted Gaussian functions with the parameters shell radius at maximum flux $R_{\max}$, half shell width $W_{1/2}$, and maximum flux $F_{\max}$.

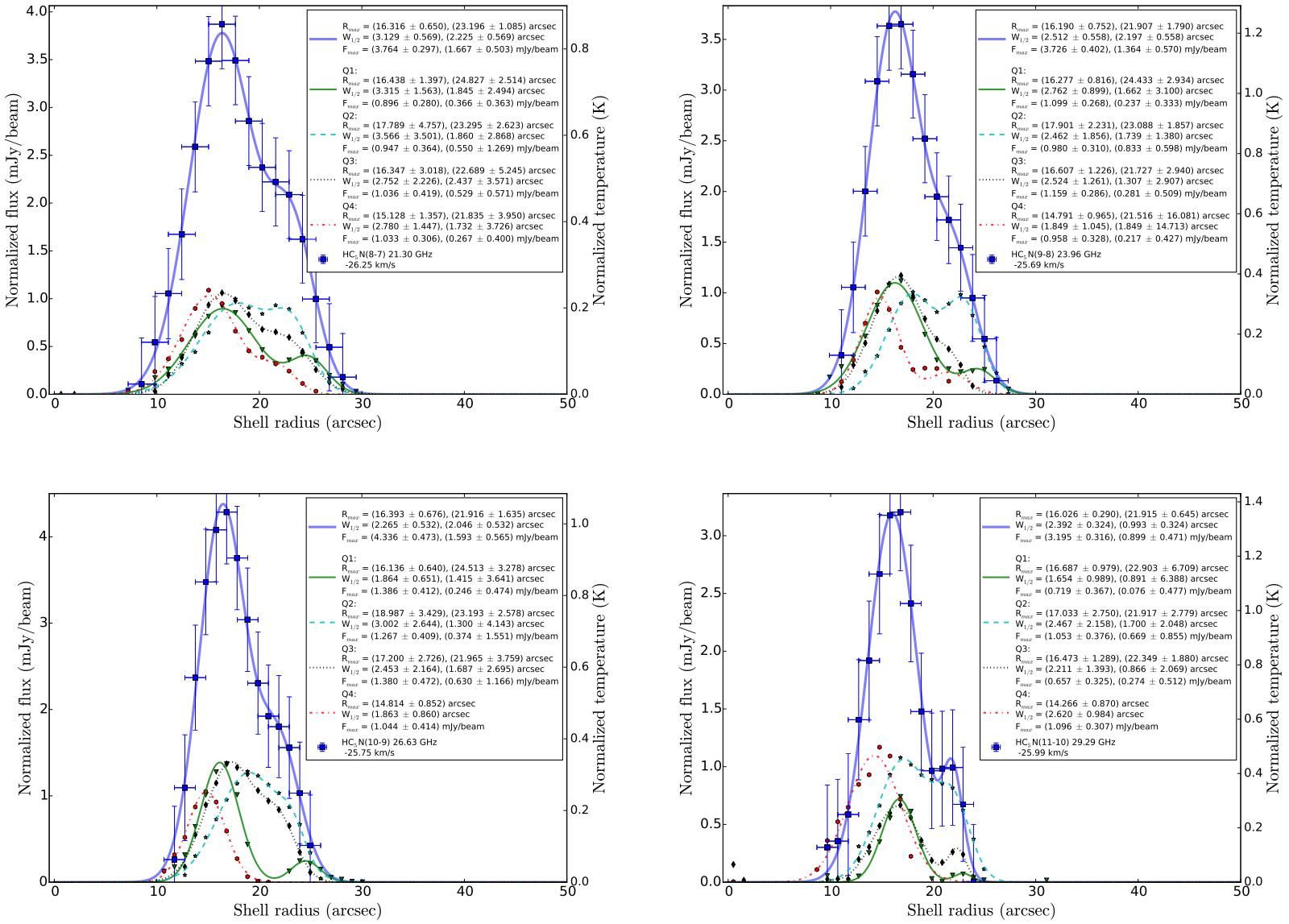

Figure C.2: Radial emission profiles of HC_5N for the channel closest to the systemic velocity (-26 km s^{-1}) for the four quarters (Q1, Q2, Q3, Q4) and their azimuthal sum (blue) and the according Gaussian fit results. The points are the data points and the lines are the fitted Gaussian functions with the parameters shell radius at maximum flux $R_{\max}$, half shell width $W_{1/2}$, and maximum flux $F_{\max}$.

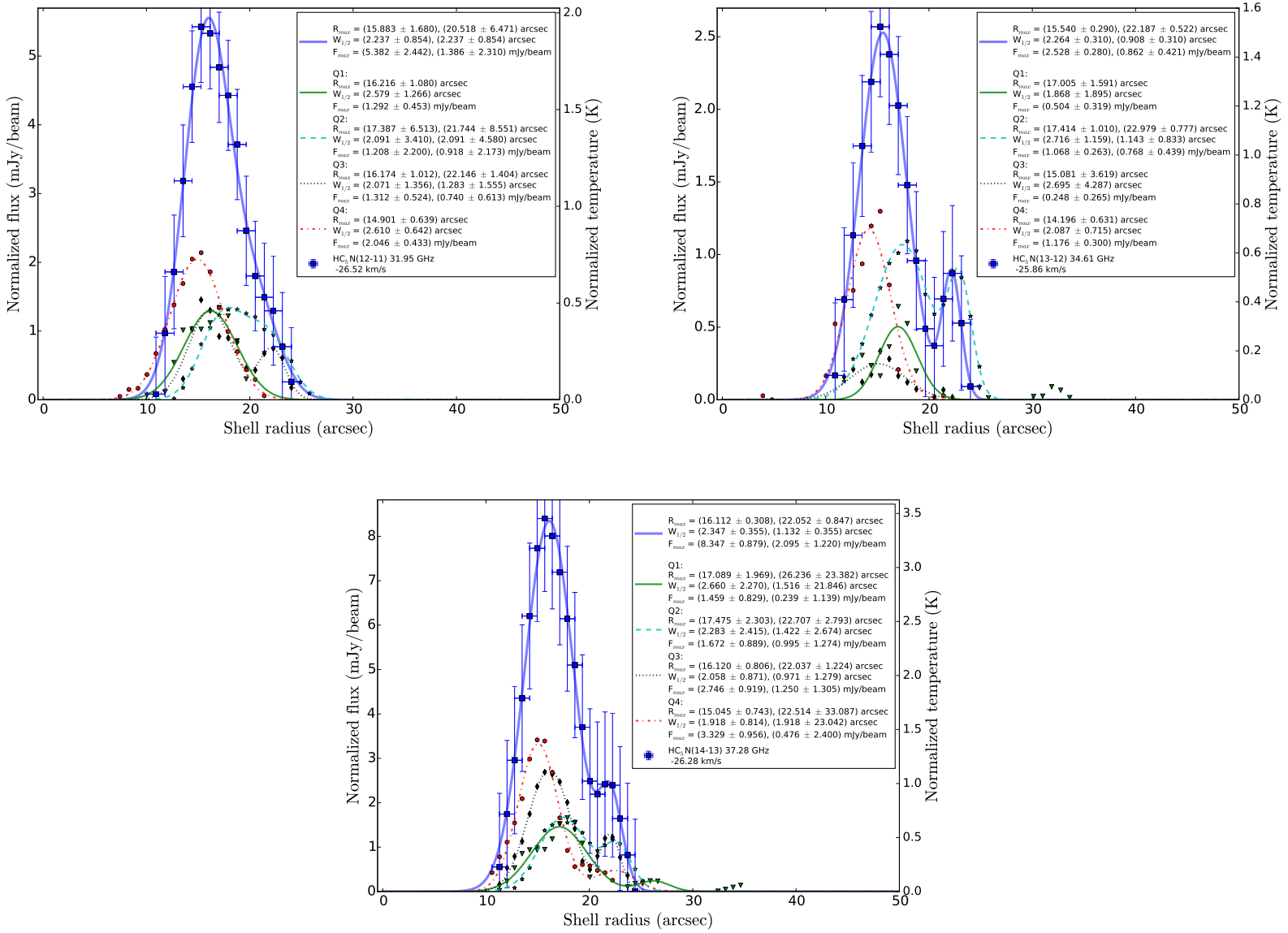

Figure C.3: Radial emission profiles of HC_5N and the Gaussian fit results cont'd.

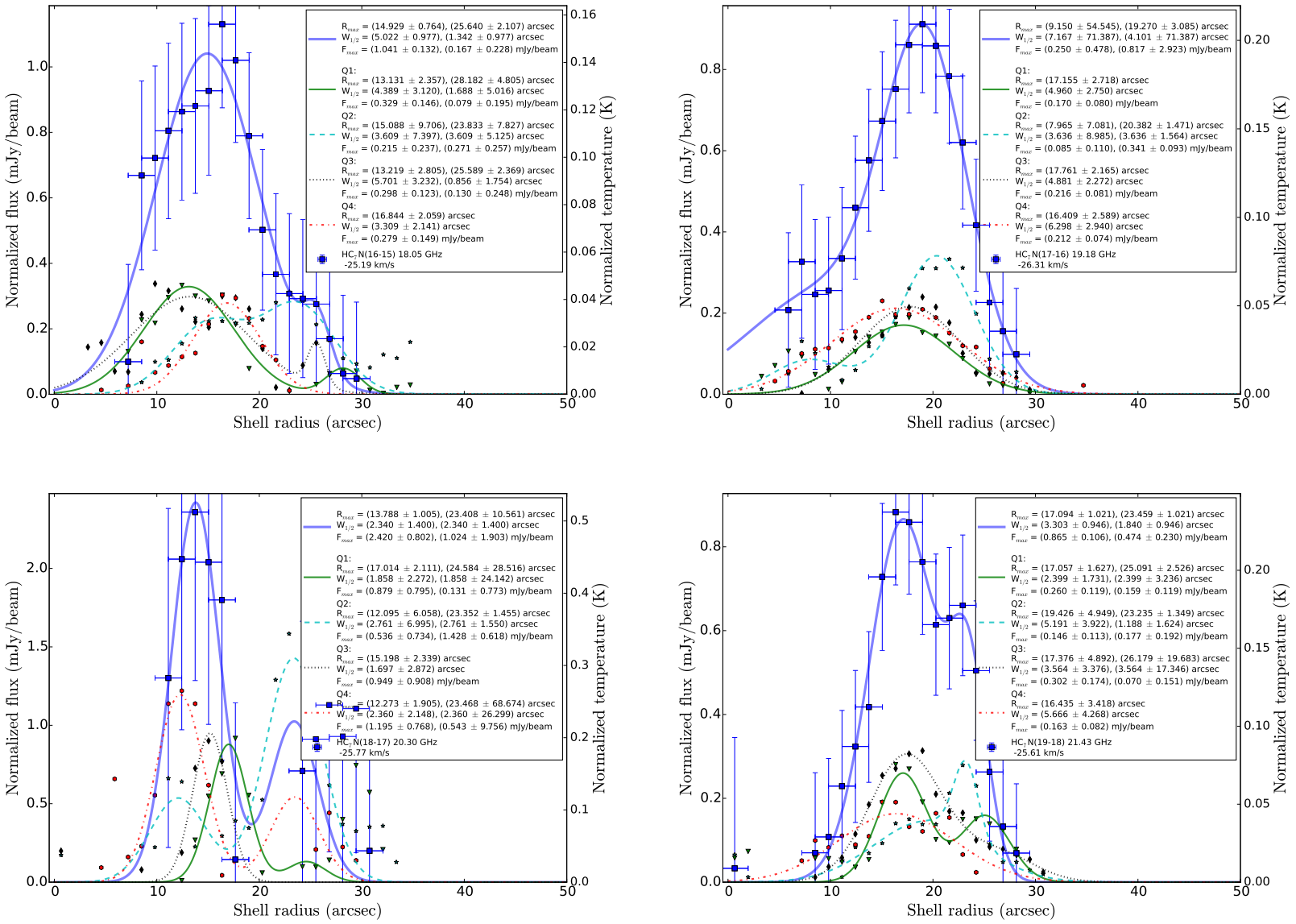

Figure C.4: Radial emission profiles of HC_7N for the channel closest to the systemic velocity (-26 km s^{-1}) for the four quarters (Q1, Q2, Q3, Q4) and their azimuthal sum (blue) and the according Gaussian fit results. The points are the data points and the lines are the fitted Gaussian functions with the parameters shell radius at maximum flux $R_{\max}$, half shell width $W_{1/2}$, and maximum flux $F_{\max}$.

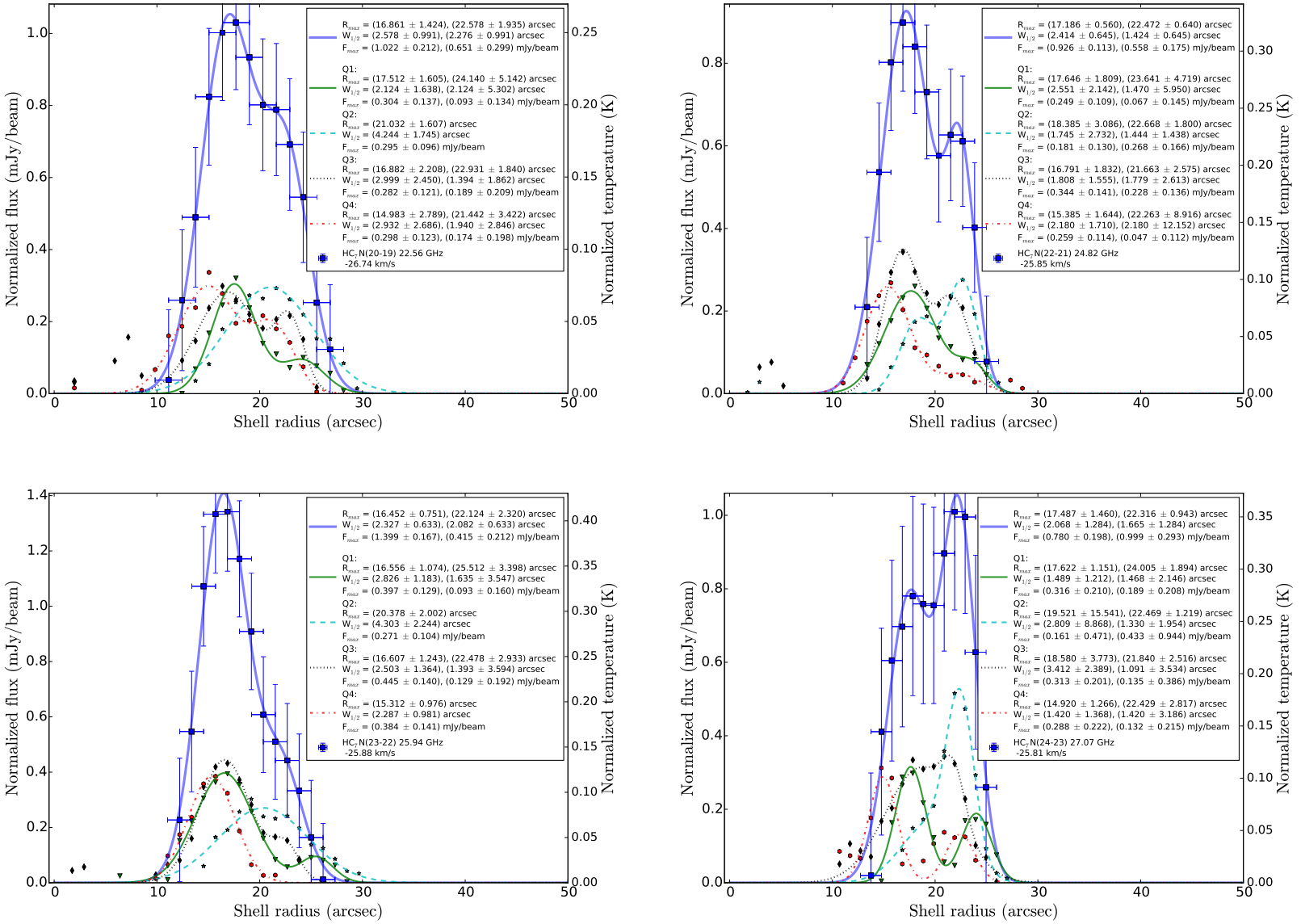

Figure C.5: Radial emission profiles of HC_7N and the Gaussian fit results cont'd.

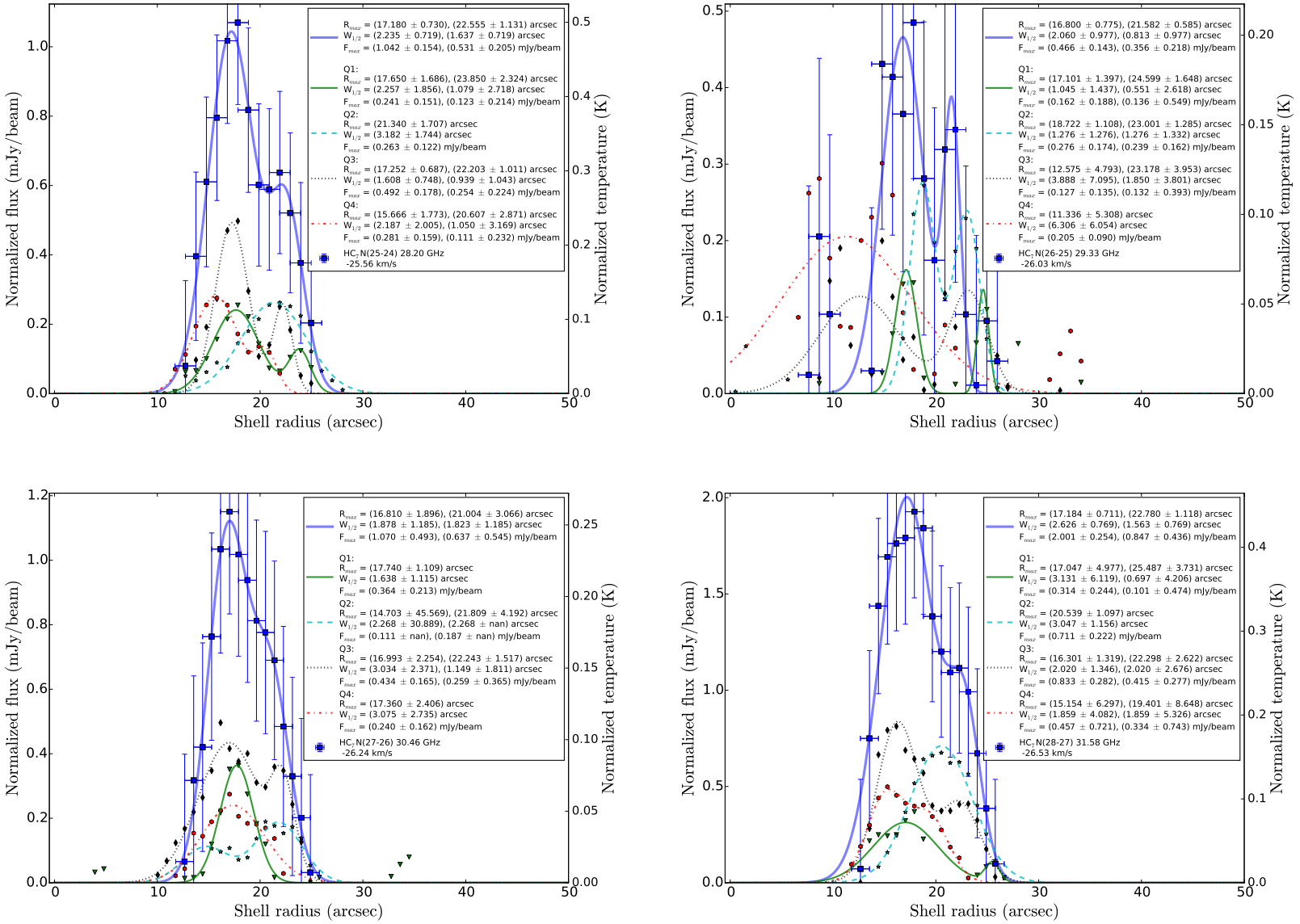

Figure C.6: Radial emission profiles of HC_7N and the Gaussian fit results cont'd.

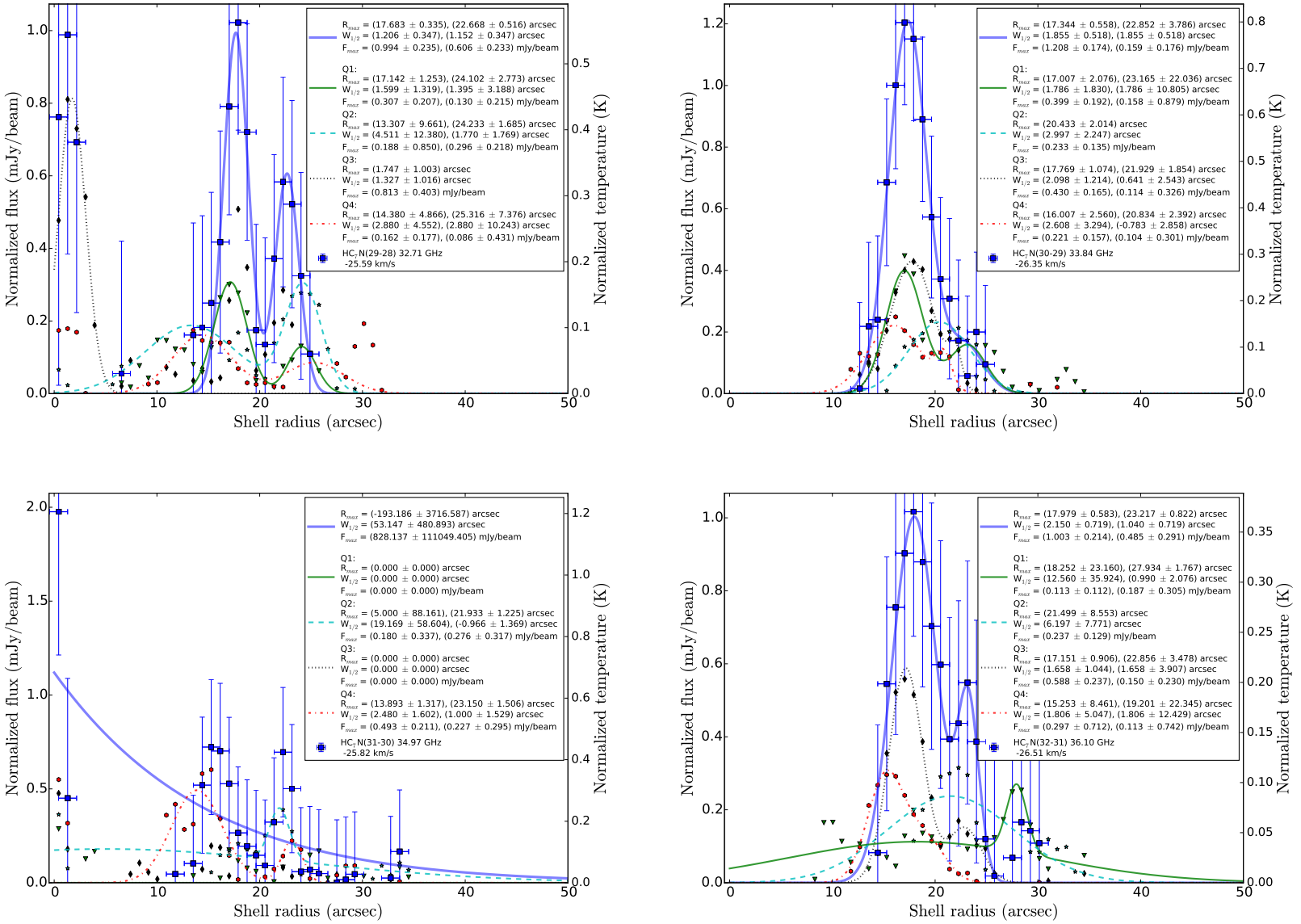

Figure C.7: Radial emission profiles of HC_7N and the Gaussian fit results cont'd.

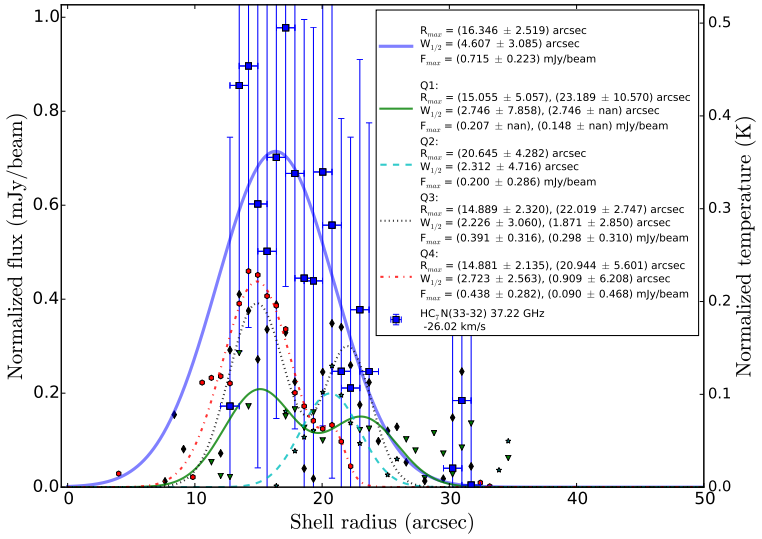

Figure C.8: Radial emission profiles of HC_7N and the Gaussian fit results cont'd.

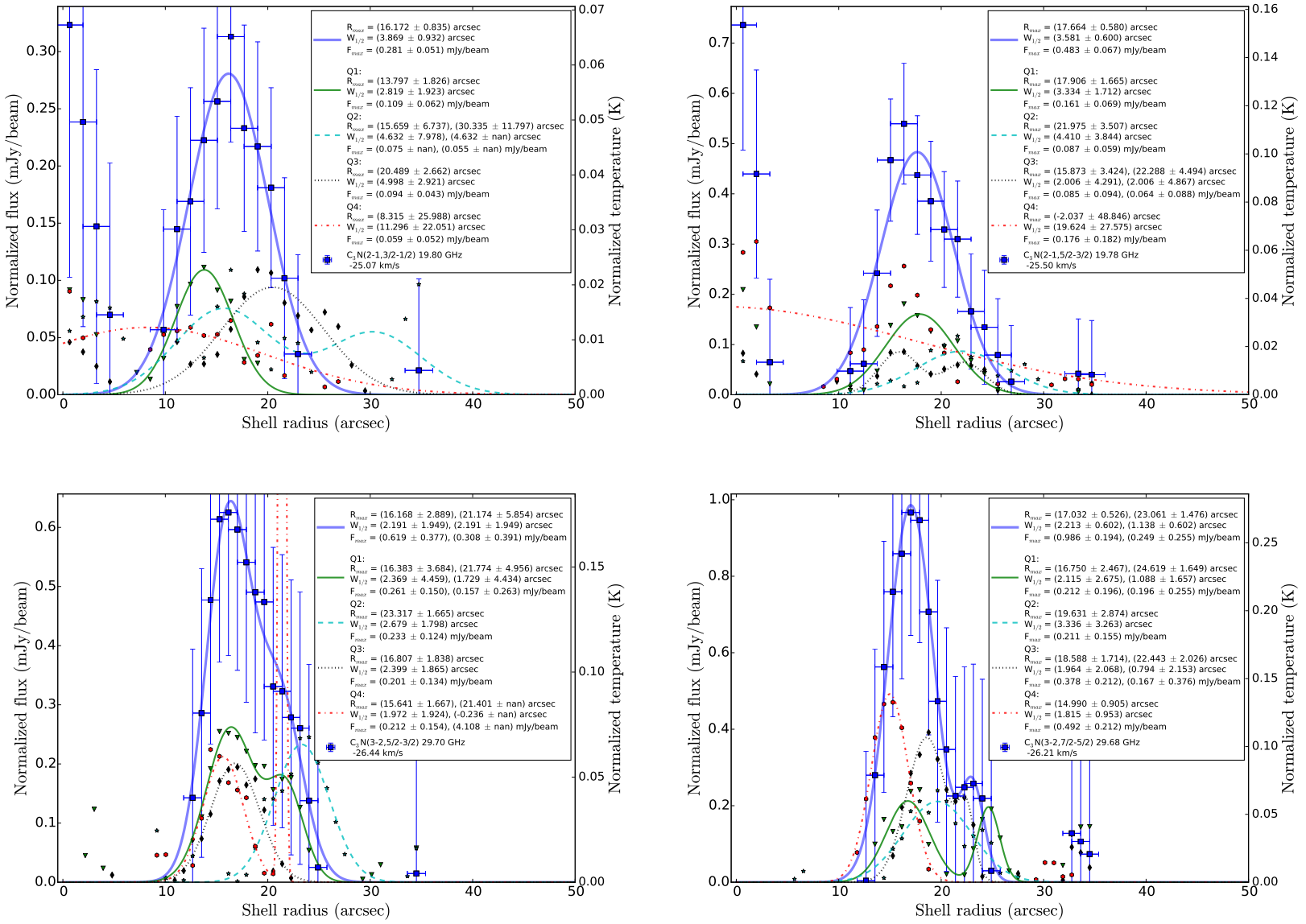

Figure C.9: Radial emission profiles of C_3N for the channel closest to the systemic velocity (-26 km s^{-1}) for the four quarters (Q1, Q2, Q3, Q4) and their azimuthal sum (blue) and the according Gaussian fit results. The points are the data points and the lines are the fitted Gaussian functions with the parameters shell radius at maximum flux $R_{\max}$, half shell width $W_{1/2}$, and maximum flux $F_{\max}$.

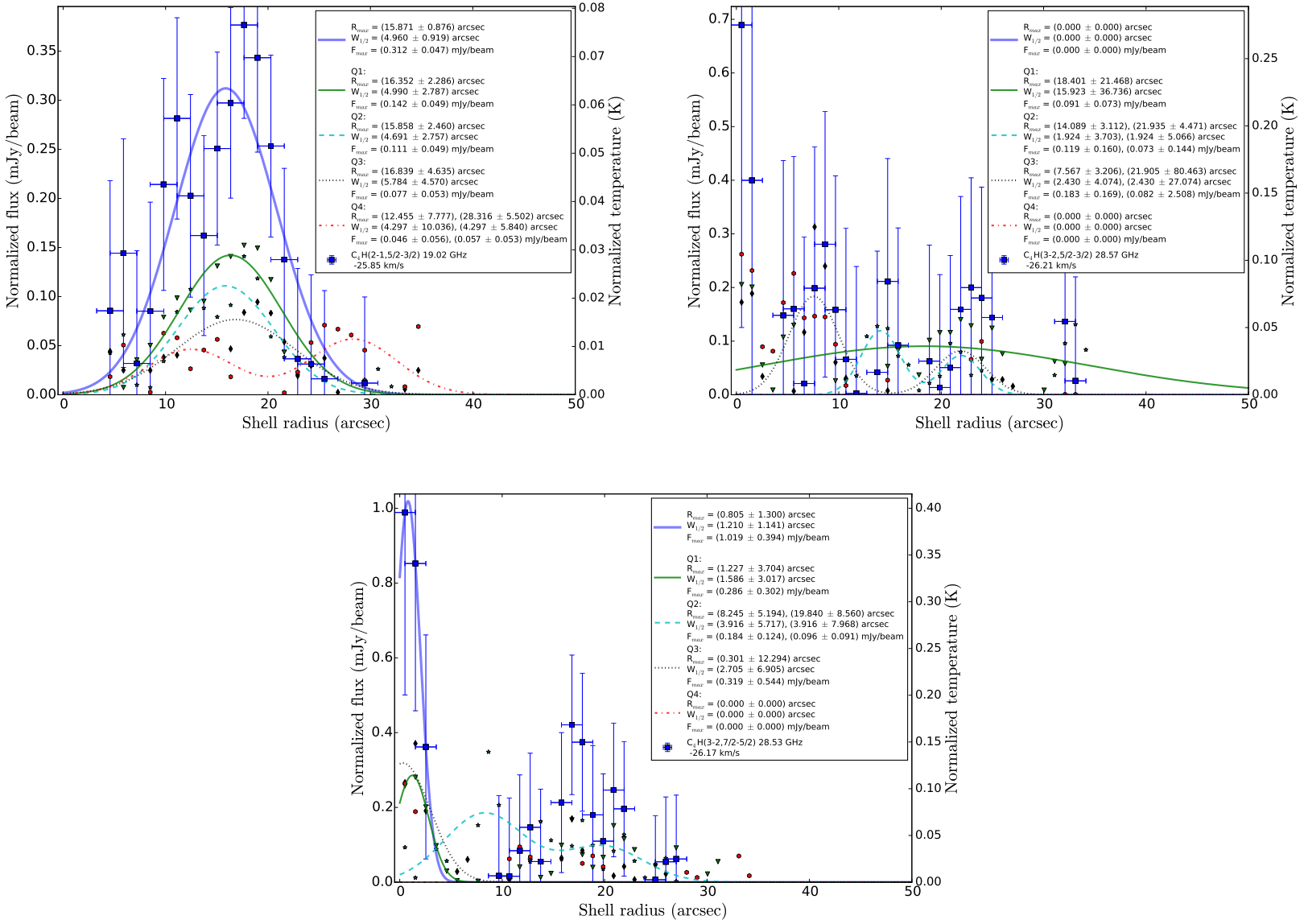

Figure C.10: Radial emission profiles of C_4H for the channel closest to the systemic velocity (−26 km s^{-1}) for the four quarters (Q1, Q2, Q3, Q4) and their azimuthal sum (blue) and the according Gaussian fit results. The points are the data points and the lines are the fitted Gaussian functions with the parameters shell radius at maximum flux $R_{\max}$, half shell width $W_{1/2}$, and maximum flux $F_{\max}$.

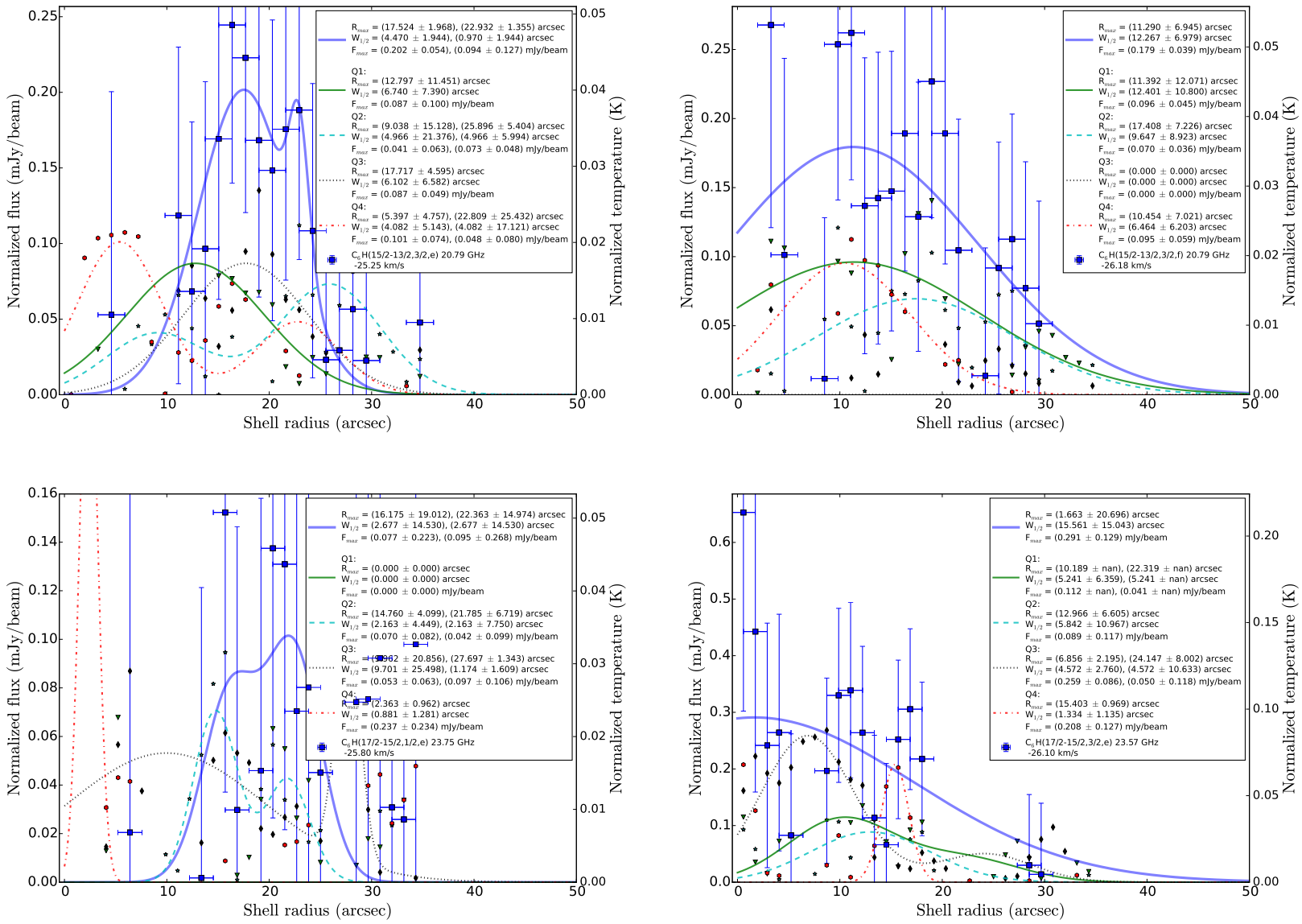

Figure C.11: Radial emission profiles of C_6H for the channel closest to the systemic velocity (-26 km s^{-1}) for the four quarters (Q1, Q2, Q3, Q4) and their azimuthal sum (blue) and the according Gaussian fit results. The points are the data points and the lines are the fitted Gaussian functions with the parameters shell radius at maximum flux $R_{\max}$, half shell width $W_{1/2}$, and maximum flux $F_{\max}$.

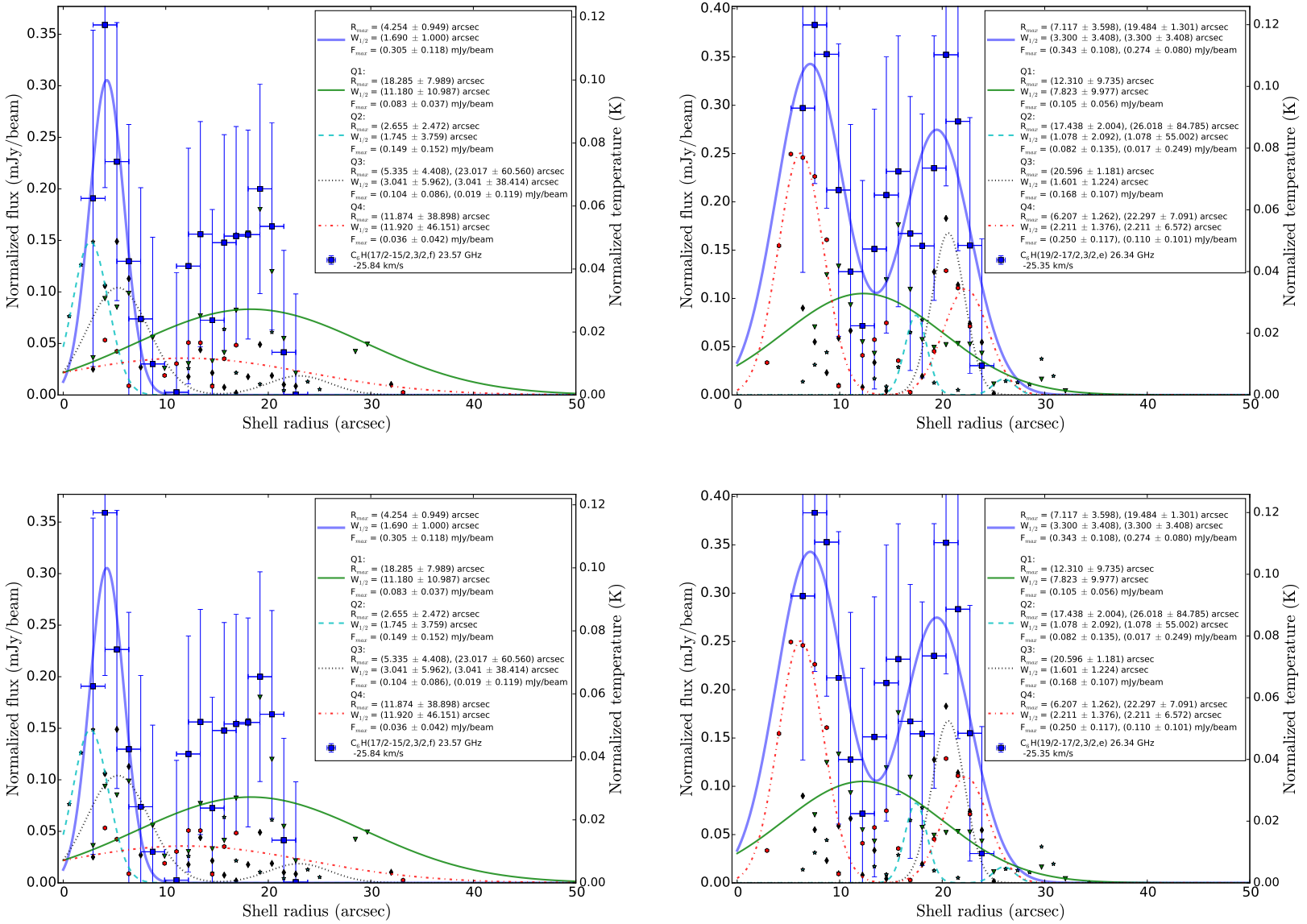

Figure C.12: Radial emission profiles of C_6H and the Gaussian fit results cont'd.

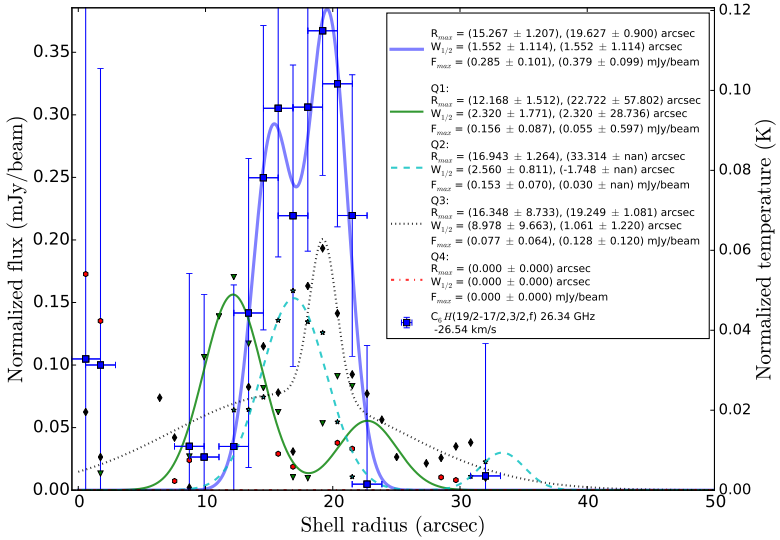

Figure C.13: Radial emission profiles of C_6H and the Gaussian fit results cont'd.

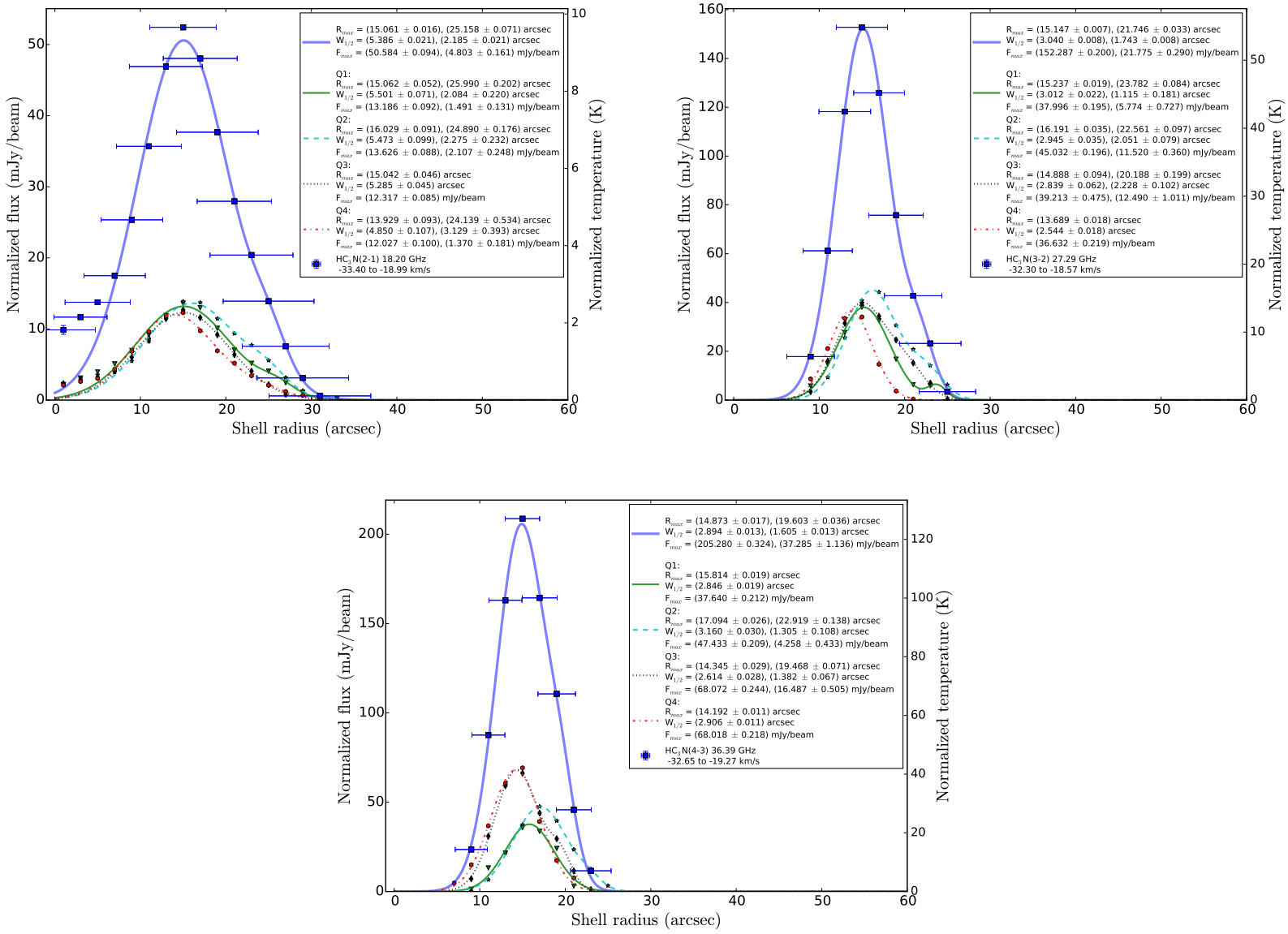

Figure C.14: Radial emission profiles of HC_3N for the velocity integrated flux of $\Delta v < 7.5$ km s^{-1} for the four quarters (Q1, Q2, Q3, Q4) and their azimuthal sum and the according Gaussian fit results. The points are the data points and the lines are the fitted Gaussian functions with the parameters shell radius at maximum flux $R_{\rm max}$, half shell width $W_{1/2}$, and maximum flux $F_{\rm max}$.

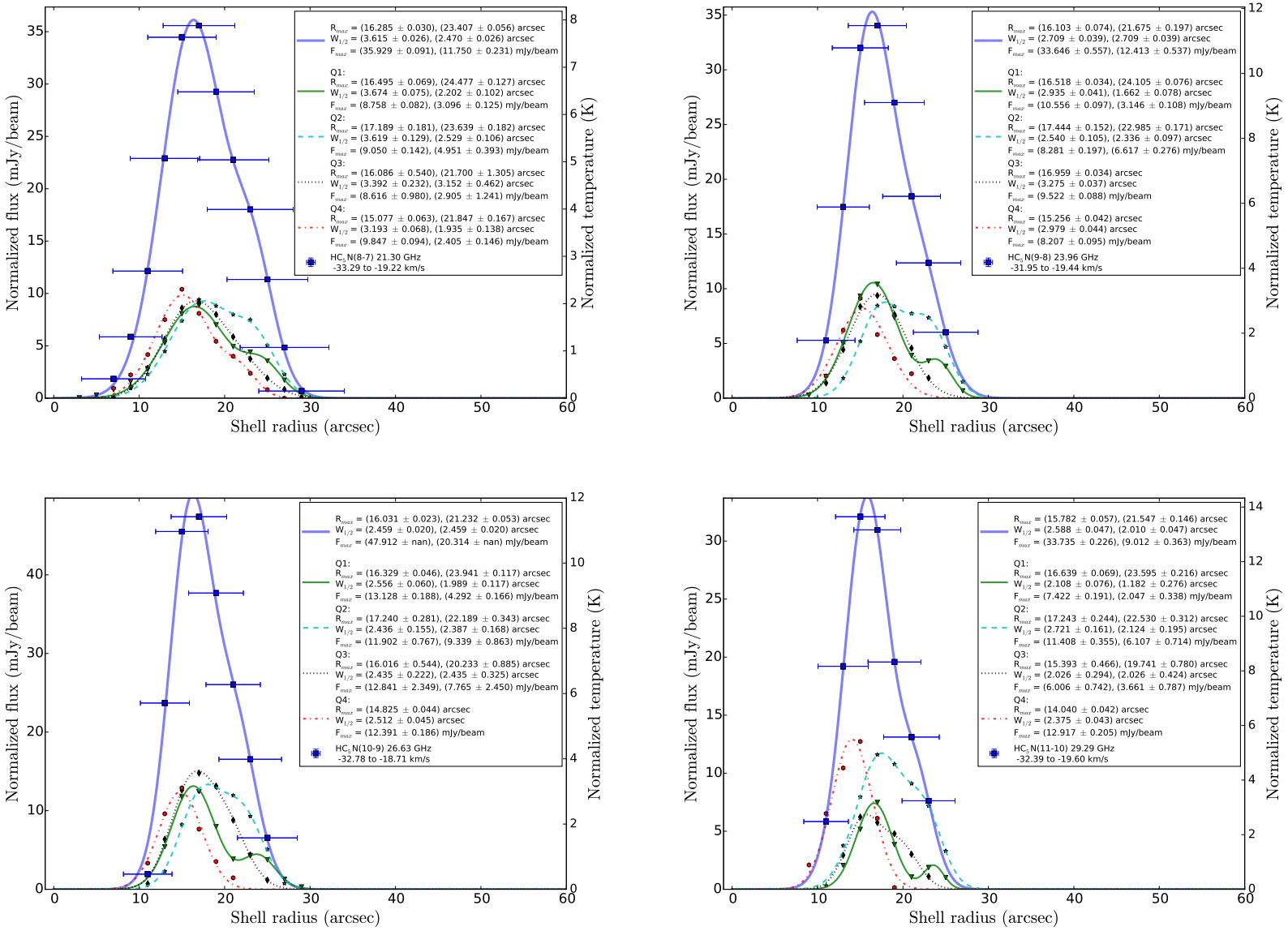

Figure C.15: Radial emission profiles of HC_5N for the velocity integrated flux of $\Delta v < 7.5$ km s^{-1} for the four quarters (Q1, Q2, Q3, Q4) and their azimuthal sum and the according Gaussian fit results. As Fig. C.14.

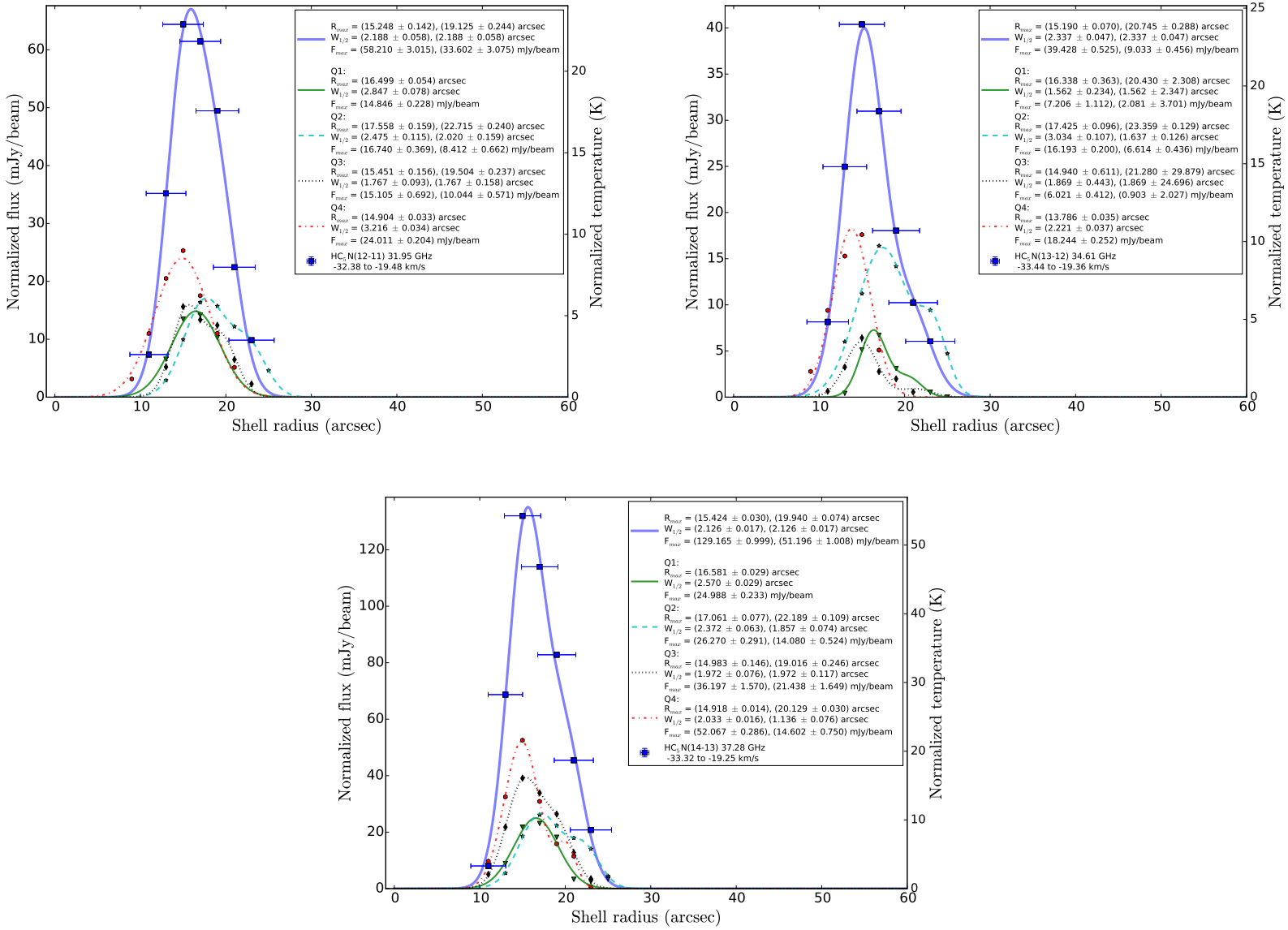

Figure C.16: Radial emission profiles of HC_5N for the velocity integrated flux for the four quarters and their azimuthal sum and the according Gaussian fit results cont'd.

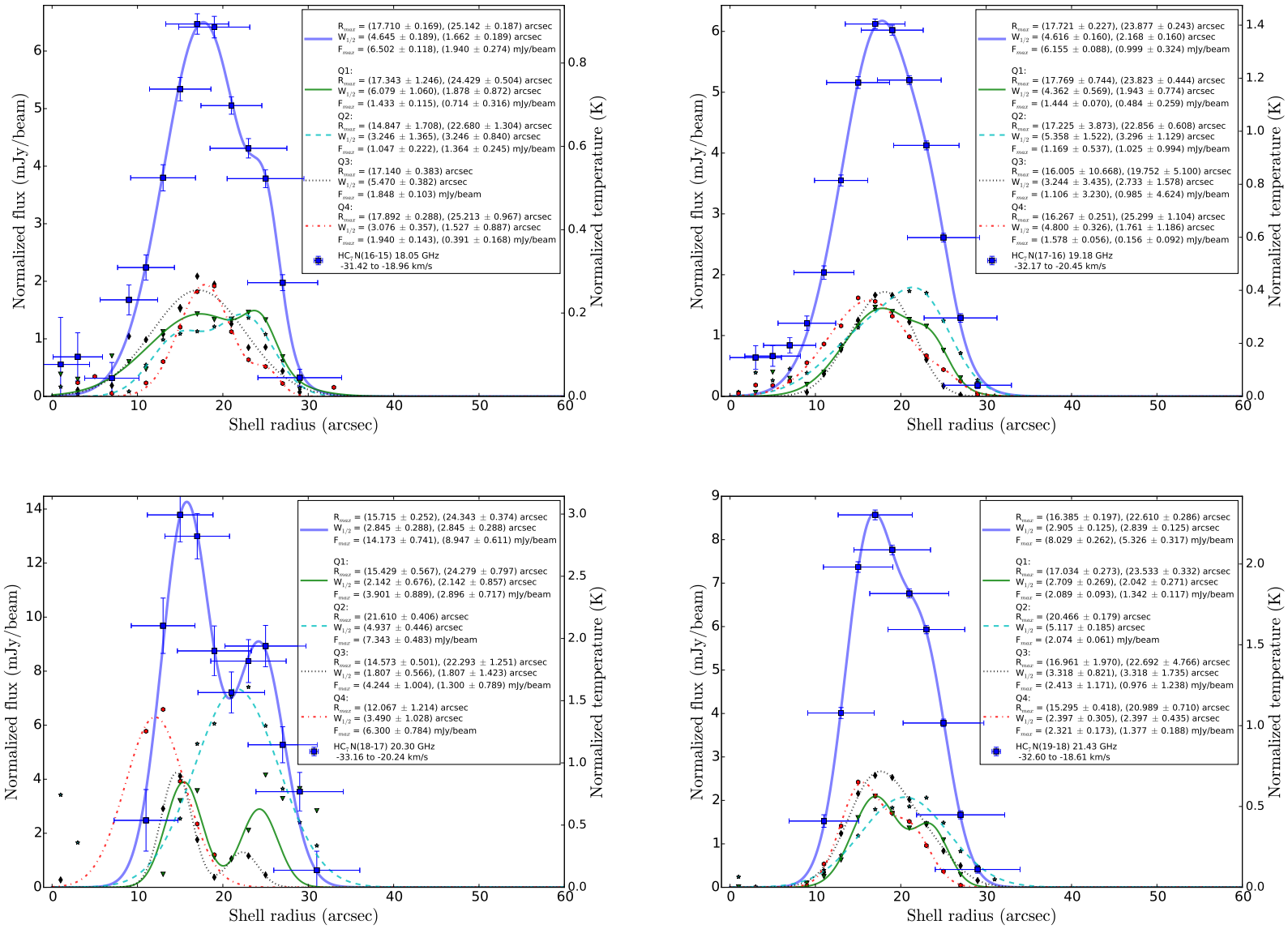

Figure C.17: Radial emission profiles of HC_7N for the velocity integrated flux of $\Delta v < 7.5$ km s^{-1} for the four quarters (Q1, Q2, Q3, Q4) and their azimuthal sum and the according Gaussian fit results. As Fig. C.14.

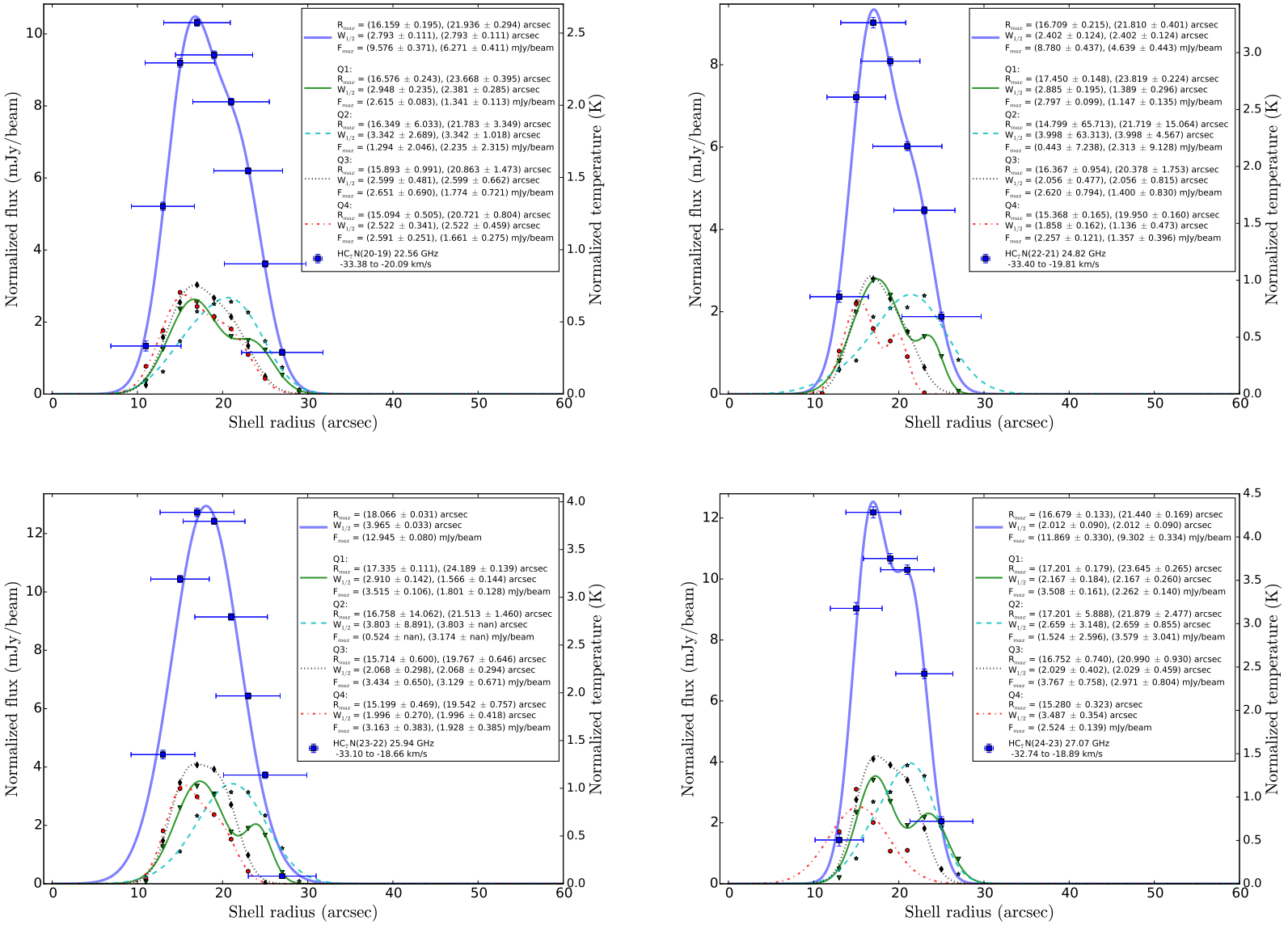

Figure C.18: Radial emission profiles of HC_7N for the velocity integrated flux for the four quarters and their azimuthal sum and the according Gaussian fit results cont'd.

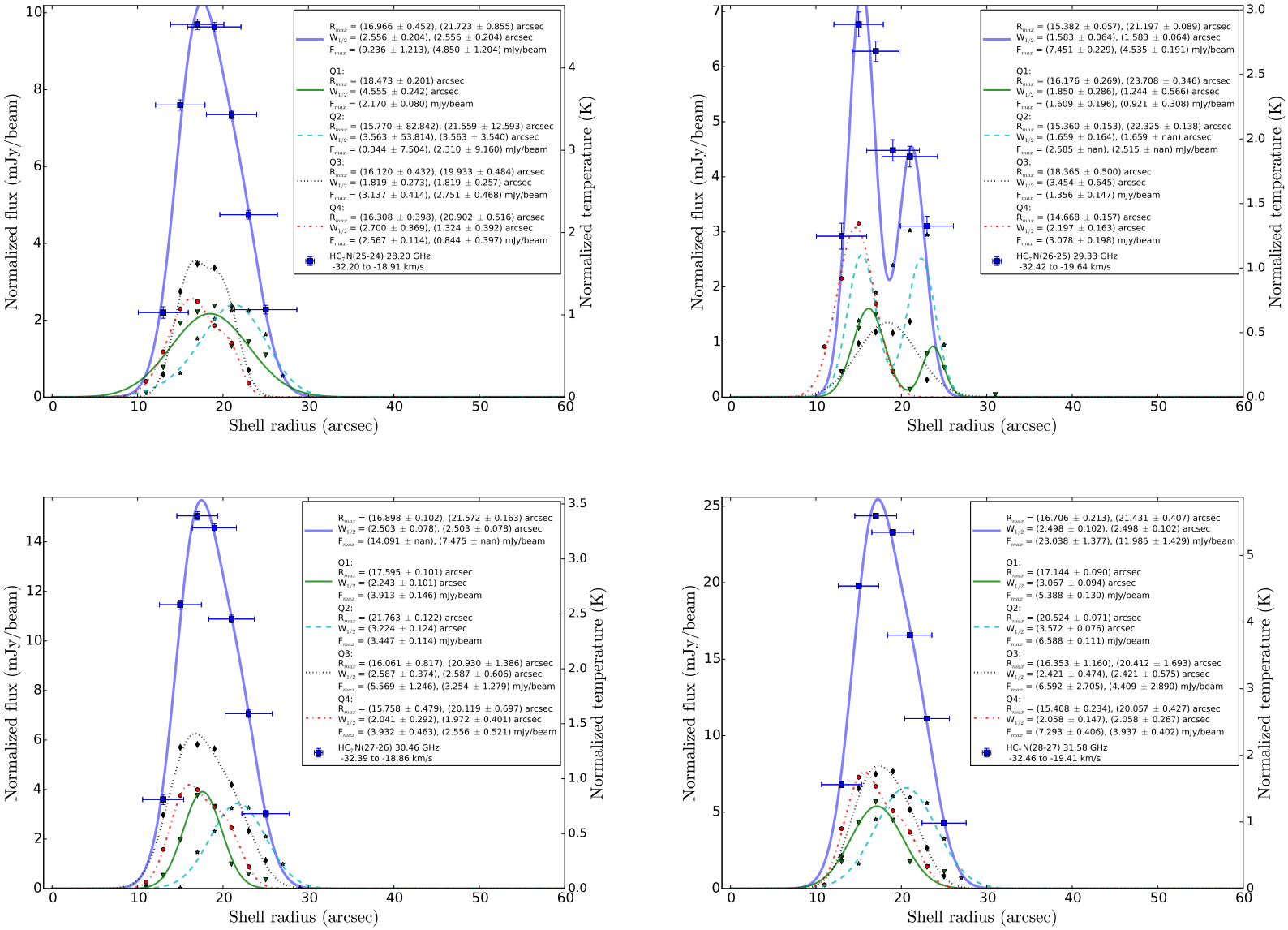

Figure C.19: Radial emission profiles of HC_7N for the velocity integrated flux for the four quarters and their azimuthal sum and the according Gaussian fit results cont'd.

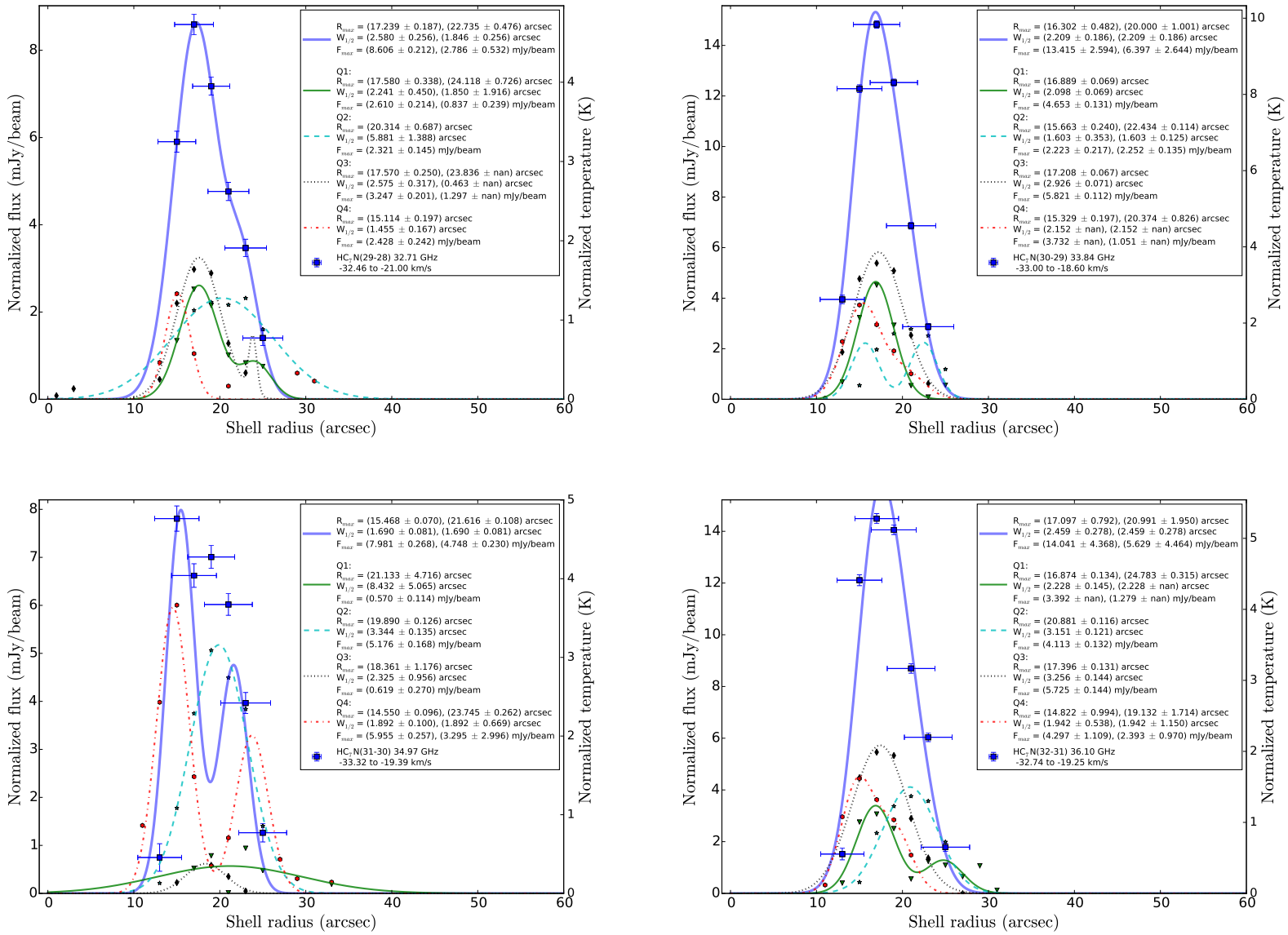

Figure C.20: Radial emission profiles of HC_7N for the velocity integrated flux for the four quarters and their azimuthal sum and the according Gaussian fit results cont'd.

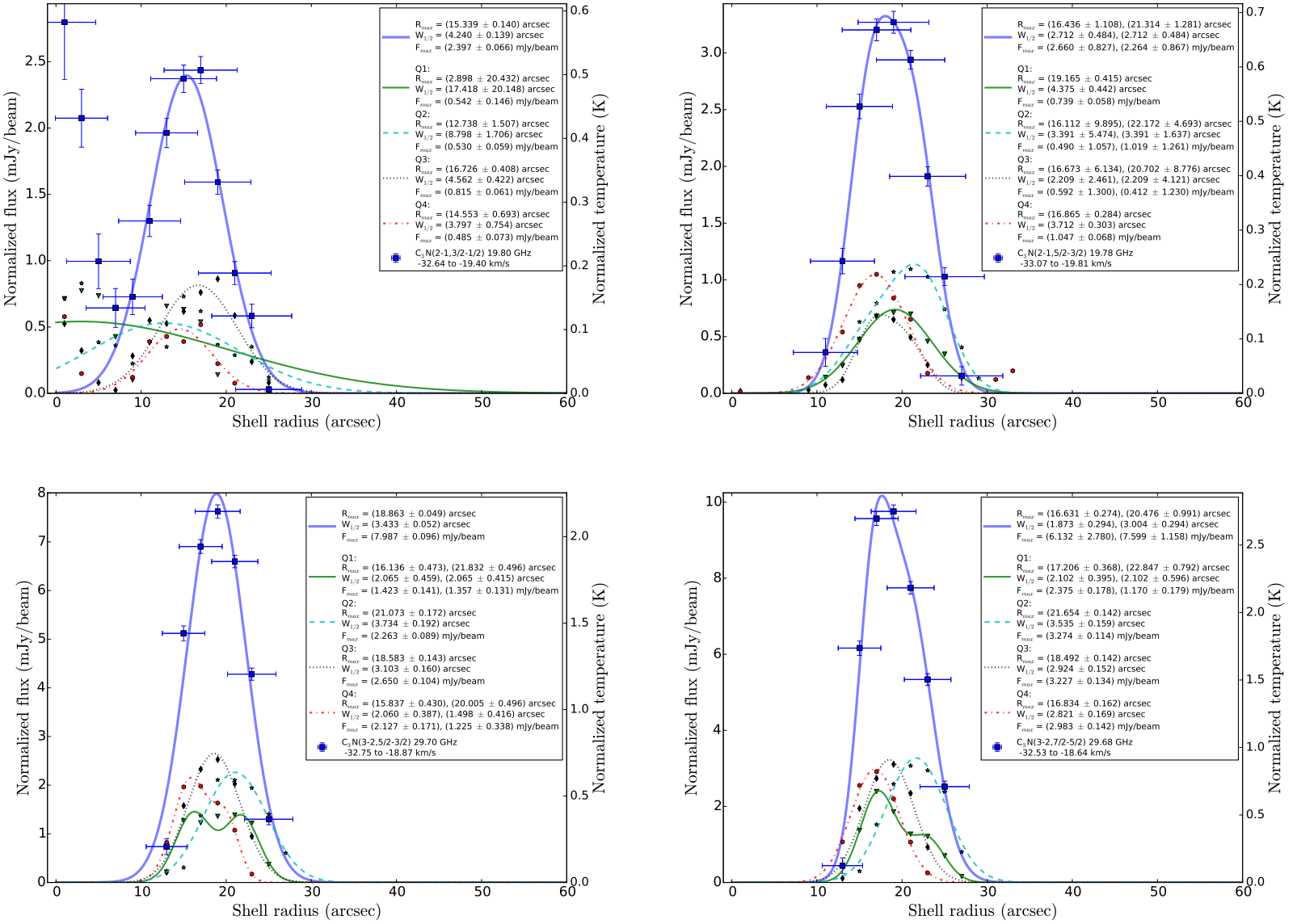

Figure C.21: Radial emission profiles of C_3N for the velocity integrated flux of $\Delta v < 7.5$ km s^{-1} for the four quarters (Q1, Q2, Q3, Q4) and their azimuthal sum and the according Gaussian fit results. As Fig. C.14.

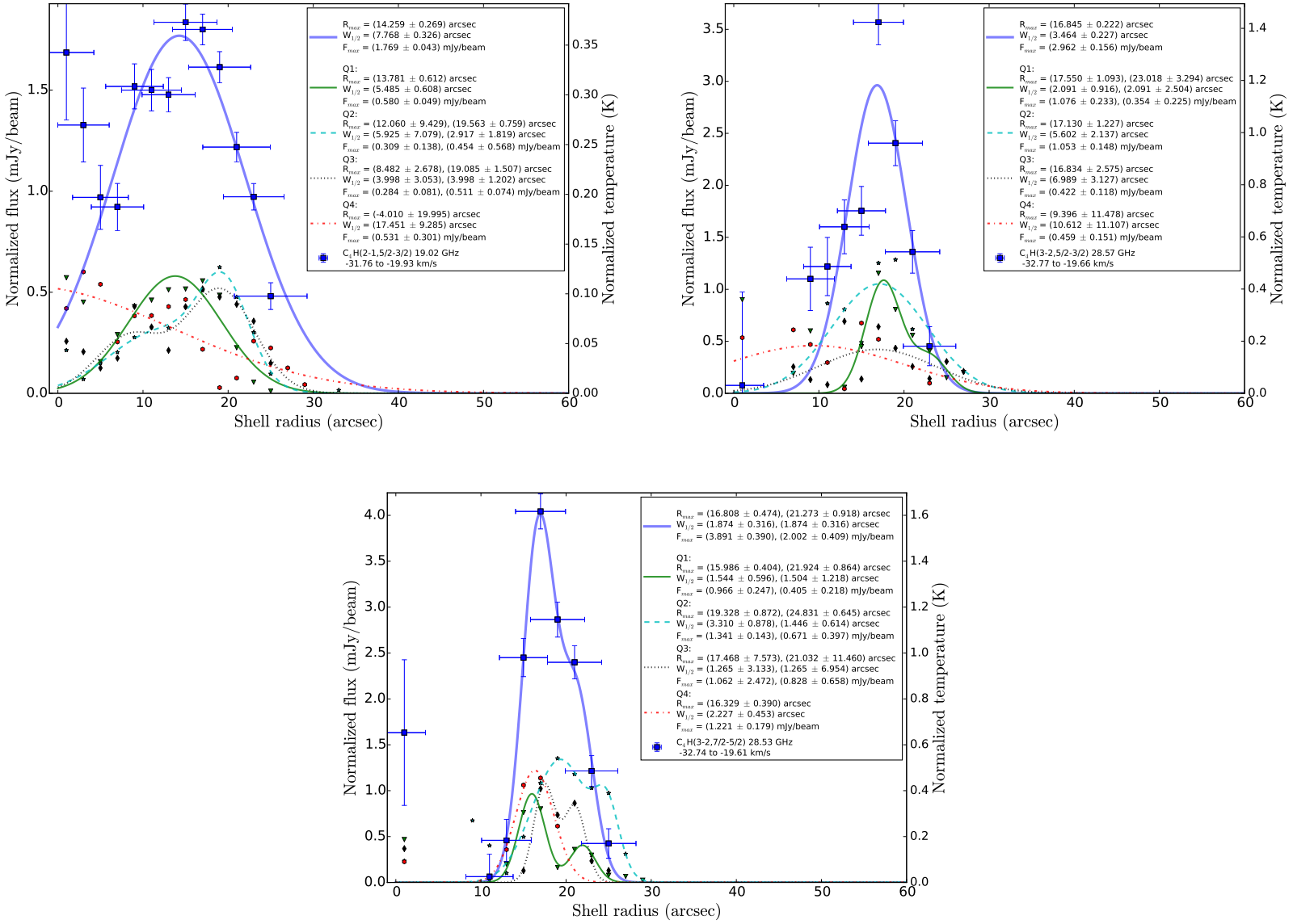

Figure C.22: Radial emission profiles of C_4H for the velocity integrated flux of $\Delta v < 7.5$ km s^{-1} for the four quarters (Q1, Q2, Q3, Q4) and their azimuthal sum and the according Gaussian fit results. As Fig. C.14.

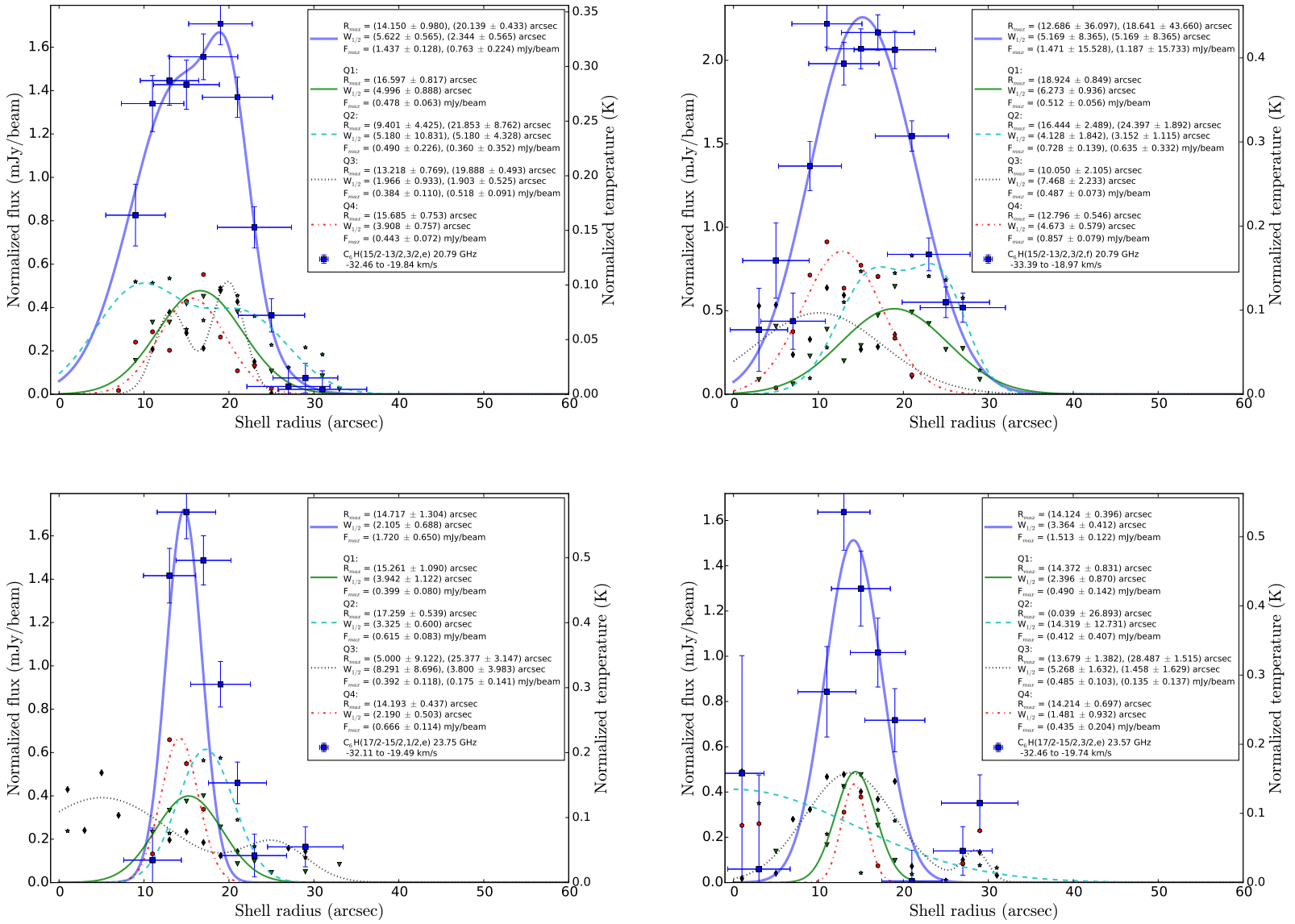

Figure C.23: Radial emission profiles of C_6H for the velocity integrated flux of $\Delta v < 7.5$ km s^{-1} for the four quarters (Q1, Q2, Q3, Q4) and their azimuthal sum and the according Gaussian fit results. As Fig. C.14.

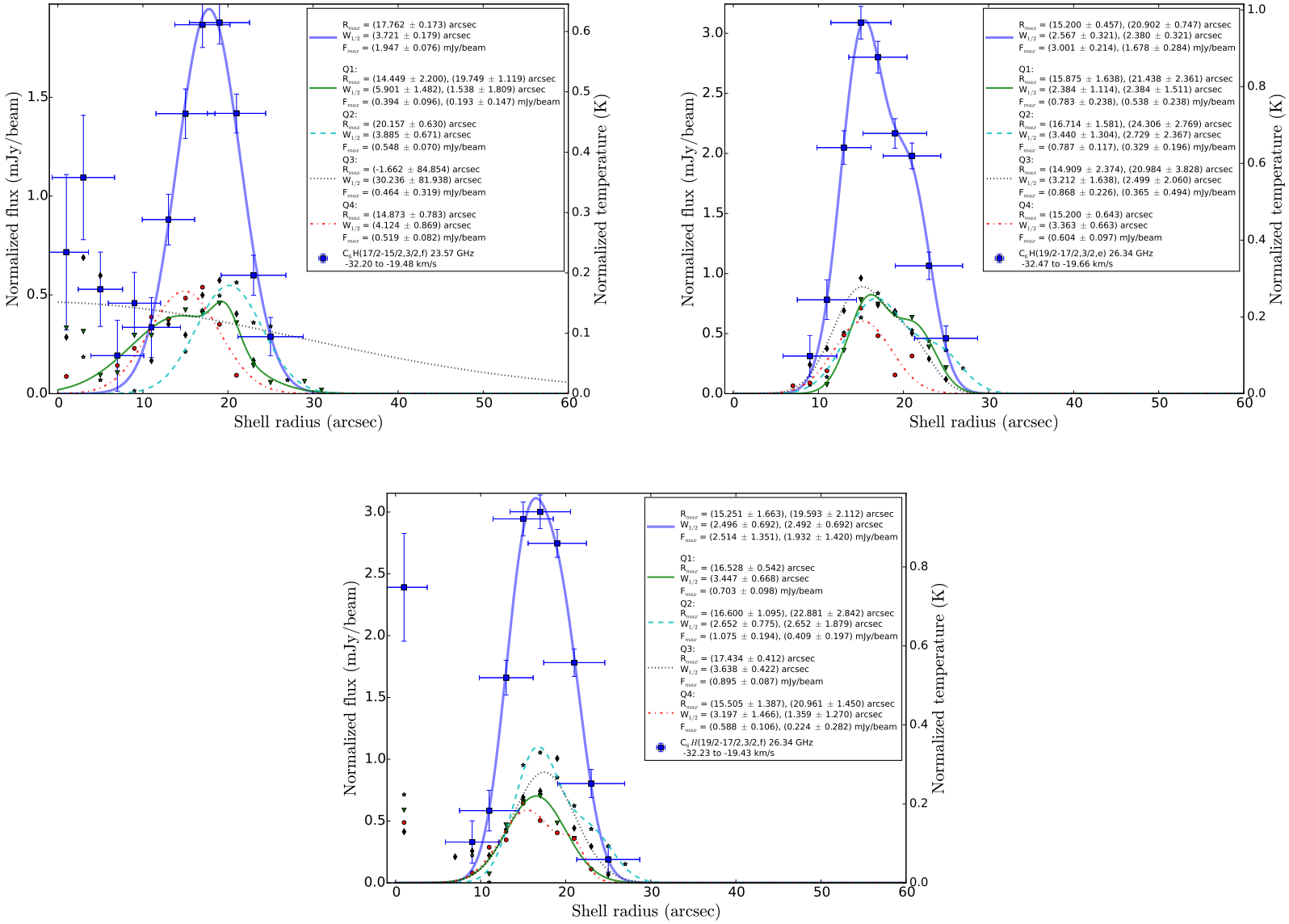

Figure C.24: Radial emission profiles of C_6H for the velocity integrated flux for the four quarters and their azimuthal sum and the according Gaussian fit results cont'd. As Fig. C.14.

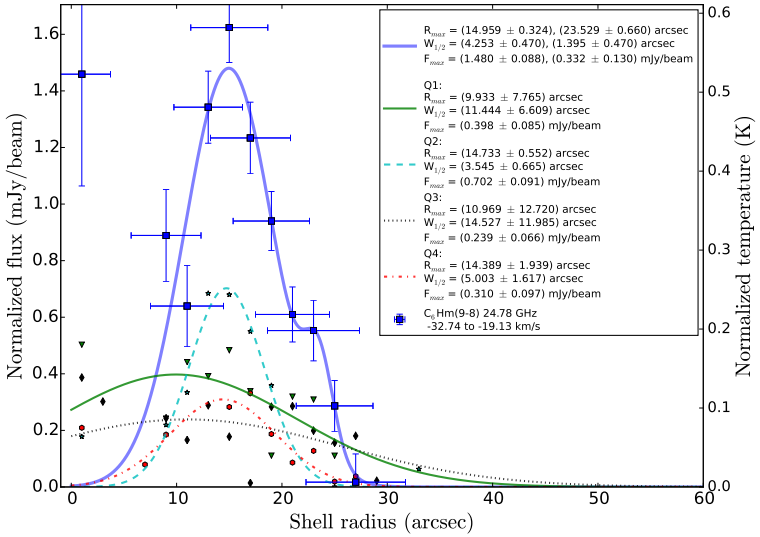

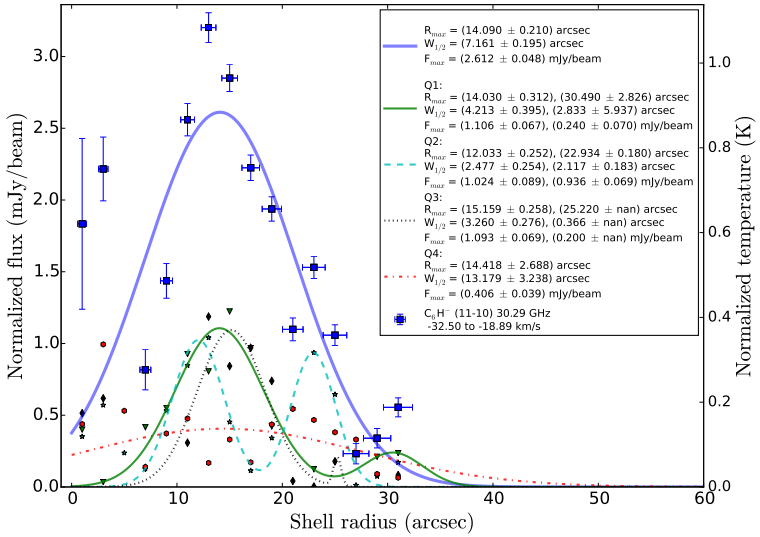

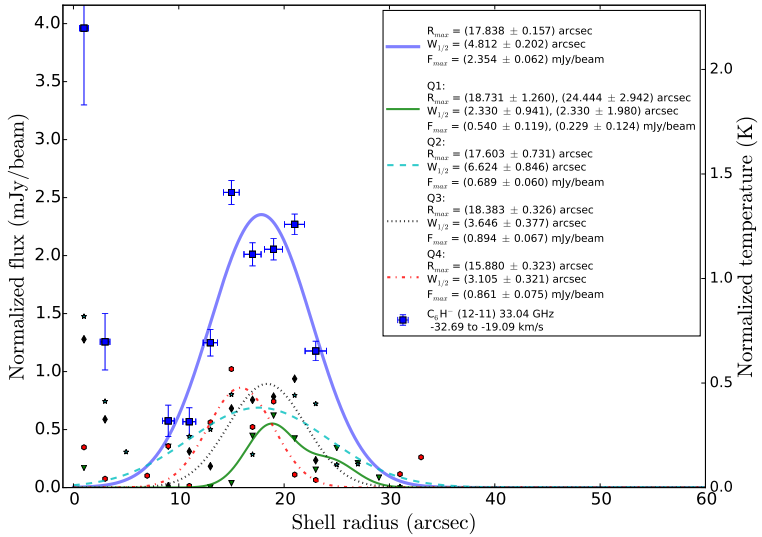

Figure C.25: Radial emission profiles of C_6H^- for the velocity integrated flux of $\Delta v < 7.5$ km s^{-1} for the four quarters (Q1, Q2, Q3, Q4) and their azimuthal sum and the according Gaussian fit results. As Fig. C.14.

Table C.1: List of Gaussian fit results from the radial emission profiles of each transition (restfrequency in GHz) of each channel (velocity in km s^{-1}) with $\Delta v < 7.5$ km s^{-1} for the azimuthal sum. The fit parameters are shell radius at maximum flux R_{max} (in arcsec), half shell width $W_{1/2}$ (in arcsec), and maximum flux F_{max} (in mJy $beam^{-1}$) for two components and their uncertainties determined from the least square fit routine.

Transition	Restfreq	Ch	v_{ch}	R_{max} 1	ΔR_{max} 1	$W_{1/2}$ 1	$\Delta W_{1/2}$ 1	F_{max} 1	ΔF_{max} 1	R_{max} 2	ΔR_{max} 2	$W_{1/2}$ 2	$\Delta W_{1/2}$ 2	F_{max} 2	ΔF_{max} 2
HC_3N(2-1)	18.20	79	-33.40	14.093	0.478	5.058	0.534	7.825	0.49	25.551	3.644	2.6	3.598	0.682	0.706
HC_3N(2-1)	18.20	80	-31.34	14.519	0.575	4.591	0.584	6.649	0.424	24.746	2.486	2.81	2.221	1.078	0.64
HC_3N(2-1)	18.20	81	-29.28	15.214	0.467	4.993	0.528	5.971	0.383	24.77	1.897	1.687	2.108	0.701	0.712
HC_3N(2-1)	18.20	82	-27.22	15.199	0.549	5.226	0.605	5.62	0.361	24.857	2.163	1.912	2.444	0.655	0.7
HC_3N(2-1)	18.20	83	-25.16	15.464	0.585	5.319	0.626	5.633	0.358	24.453	3.017	1.697	3.717	0.423	0.777
HC_3N(2-1)	18.20	84	-23.10	15.958	0.62	4.575	0.616	6.001	0.384	24.87	2.851	2.314	2.783	0.706	0.752
HC_3N(2-1)	18.20	85	-21.04	14.006	0.704	8.893	0.833	5.21	0.34	nan	nan	nan	nan	nan	nan
HC_3N(2-1)	18.20	86	-18.99	13.972	0.517	7.384	0.548	7.342	0.436	nan	nan	nan	nan	nan	nan
HC_3N(3-2)	27.29	85	-32.30	14.358	0.415	2.961	0.398	19.137	1.239	21.626	4.206	2.229	3.862	1.539	1.592
HC_3N(3-2)	27.29	86	-30.93	14.688	0.788	2.903	0.564	14.904	1.442	21.285	6.943	2.495	5.979	1.366	1.911
HC_3N(3-2)	27.29	87	-29.55	14.992	1.094	2.586	0.629	13.869	3.006	20.767	8.848	2.586	5.854	1.682	2.765
HC_3N(3-2)	27.29	88	-28.18	15.256	0.291	2.595	0.308	12.452	0.833	21.881	1.775	1.768	1.979	1.601	1.025
HC_3N(3-2)	27.29	89	-26.81	15.437	0.227	2.752	0.254	12.507	0.873	22.585	0.861	1.126	0.877	2.102	1.317
HC_3N(3-2)	27.29	90	-25.44	15.712	0.26	2.874	0.3	11.787	0.794	22.222	1.052	1.266	1.073	1.828	1.197
HC_3N(3-2)	27.29	91	-24.06	15.518	0.315	2.958	0.347	11.544	0.775	21.932	1.211	1.45	1.283	1.871	1.202
HC_3N(3-2)	27.29	92	-22.69	15.467	0.51	3.187	0.488	11.502	0.783	21.395	1.706	1.586	1.709	1.7	1.737
HC_3N(3-2)	27.29	93	-21.32	15.329	0.821	3.207	0.652	13.541	1.098	21.309	2.659	2.004	2.105	2.309	2.849
HC_3N(3-2)	27.29	94	-19.94	15.559	0.645	3.352	0.574	15.018	1.021	21.701	2.373	1.828	2.21	2.023	2.601
HC_3N(3-2)	27.29	95	-18.57	14.607	1.313	2.745	0.745	18.984	4.341	20.22	3.278	2.514	1.787	6.671	5.544
HC_3N(4-3)	36.39	31	-32.65	14.37	0.829	2.515	0.542	21.195	2.764	19.848	4.578	2.235	2.933	3.317	3.76
HC_3N(4-3)	36.39	32	-31.62	14.54	0.456	2.394	0.402	19.502	1.416	19.568	1.675	1.575	1.34	3.601	2.663
HC_3N(4-3)	36.39	33	-30.59	14.492	0.369	2.425	0.366	16.852	1.238	19.386	0.972	1.287	0.915	3.749	2.275
HC_3N(4-3)	36.39	34	-29.56	14.654	0.759	2.45	0.571	15.065	1.524	19.491	2.33	1.72	1.63	3.214	3.385
HC_3N(4-3)	36.39	35	-28.53	14.775	0.634	2.625	0.509	14.083	1.099	19.588	2.217	1.567	1.828	2.106	2.901
HC_3N(4-3)	36.39	36	-27.50	14.77	2.228	2.631	1.103	12.982	5.915	19.386	8.427	2.234	4.062	2.47	8.892
HC_3N(4-3)	36.39	37	-26.47	15.242	0.301	3.209	0.34	12.003	0.965	22.02	1.813	-0.508	2.144	0.762	2.553
HC_3N(4-3)	36.39	38	-25.44	15.186	0.303	3.296	0.323	12.045	0.957	nan	nan	nan	nan	nan	nan
HC_3N(4-3)	36.39	39	-24.41	15.284	0.311	3.43	0.336	12.303	0.963	nan	nan	nan	nan	nan	nan
HC_3N(4-3)	36.39	40	-23.38	15.597	0.304	3.388	0.319	12.464	0.971	nan	nan	nan	nan	nan	nan
HC_3N(4-3)	36.39	41	-22.35	15.512	0.272	3.283	0.28	14.175	1.019	nan	nan	nan	nan	nan	nan
HC_3N(4-3)	36.39	42	-21.32	15.753	0.257	3.229	0.26	15.149	1.045	nan	nan	nan	nan	nan	nan
HC_3N(4-3)	36.39	43	-20.30	15.76	0.261	3.338	0.266	16.62	1.126	nan	nan	nan	nan	nan	nan
HC_3N(4-3)	36.39	44	-19.27	15.843	0.259	3.488	0.264	18.529	1.192	nan	nan	nan	nan	nan	nan
HC_5N(8-7)	21.30	61	-33.29	15.547	0.603	3.369	0.525	5.163	0.367	23.668	1.904	2.743	1.522	1.391	0.489
HC_5N(8-7)	21.30	62	-31.53	16.239	0.532	3.935	0.542	4.136	0.287	24.381	1.374	2.098	1.301	0.97	0.493
HC_5N(8-7)	21.30	63	-29.77	16.178	0.843	3.432	0.676	3.946	0.328	23.338	1.789	2.469	1.292	1.316	0.649
HC_5N(8-7)	21.30	64	-28.01	16.474	0.604	3.37	0.548	4.015	0.288	23.57	1.352	2.135	1.198	1.174	0.522
HC_5N(8-7)	21.30	65	-26.25	16.316	0.65	3.129	0.569	3.764	0.297	23.196	1.085	2.225	0.851	1.667	0.503

Table C.1 continued.

Transition	Restfreq	Ch	v_{ch}	R_{max} 1	ΔR_{max} 1	$W_{1/2}$ 1	$\Delta W_{1/2}$ 1	F_{max} 1	ΔF_{max} 1	R_{max} 2	ΔR_{max} 2	$W_{1/2}$ 2	$\Delta W_{1/2}$ 2	F_{max} 2	ΔF_{max} 2
HC_5N(8-7)	21.30	66	-24.49	16.872	0.764	3.987	0.691	3.638	0.263	23.727	1.249	1.869	1.355	0.908	0.693
HC_5N(8-7)	21.30	67	-22.73	15.83	1.936	3.116	1.083	3.443	1.05	22.104	2.854	2.858	1.484	2.045	1.36
HC_5N(8-7)	21.30	68	-20.98	17.134	0.814	4.741	0.678	3.851	0.269	23.386	1.827	1.51	2.818	0.447	0.756
HC_5N(8-7)	21.30	69	-19.22	15.843	4.1	3.541	1.725	4.034	3.389	22.067	7.09	3.394	2.824	2.116	3.81
HC_5N(9-8)	23.96	51	-31.95	15.643	0.954	2.697	0.609	4.479	0.72	21.973	3.419	2.697	2.439	1.222	0.673
HC_5N(9-8)	23.96	52	-30.39	16.057	0.774	2.594	0.54	4.08	0.508	22.455	2.578	2.594	2.081	1.183	0.468
HC_5N(9-8)	23.96	53	-28.82	16.002	1.042	2.419	0.611	4.13	0.895	21.418	3.453	2.419	2.182	1.233	0.854
HC_5N(9-8)	23.96	54	-27.26	16.286	0.49	2.818	0.472	3.734	0.288	22.472	1.23	1.818	1.053	1.048	0.466
HC_5N(9-8)	23.96	55	-25.69	16.19	0.752	2.512	0.558	3.726	0.402	21.907	1.79	2.197	1.232	1.364	0.57
HC_5N(9-8)	23.96	56	-24.13	16.016	1.546	2.483	0.857	3.415	1.166	21.367	3.173	2.483	1.907	1.647	1.114
HC_5N(9-8)	23.96	57	-22.57	16.067	2.438	2.535	1.113	3.302	2.195	20.959	4.183	2.535	1.968	1.922	2.164
HC_5N(9-8)	23.96	58	-21.00	16.667	1.352	3.139	0.922	3.881	0.551	22.442	2.596	2.218	1.897	1.176	1.301
HC_5N(9-8)	23.96	59	-19.44	17.471	0.288	3.926	0.303	4.367	0.277	nan	nan	nan	nan	nan	nan
HC_5N(10-9)	26.63	38	-32.78	15.962	0.718	2.472	0.523	6.015	0.714	22.13	3.361	2.472	2.691	1.255	0.677
HC_5N(10-9)	26.63	39	-31.38	15.964	0.77	2.483	0.55	4.92	0.627	22.158	3.283	2.483	2.719	1.113	0.578
HC_5N(10-9)	26.63	40	-29.97	16.428	0.911	2.479	0.647	4.503	0.679	22.619	3.091	2.479	2.688	1.262	0.611
HC_5N(10-9)	26.63	41	-28.56	16.234	0.421	2.398	0.444	4.389	0.391	22.429	0.979	1.871	0.957	1.614	0.457
HC_5N(10-9)	26.63	42	-27.16	16.478	0.722	2.293	0.579	3.984	0.461	22.136	1.634	2.071	1.44	1.554	0.538
HC_5N(10-9)	26.63	43	-25.75	16.393	0.676	2.265	0.532	4.336	0.473	21.916	1.635	2.046	1.366	1.593	0.565
HC_5N(10-9)	26.63	44	-24.34	16.25	1.194	2.178	0.736	3.912	1.039	21.152	1.981	2.178	1.18	2.362	1.062
HC_5N(10-9)	26.63	45	-22.93	15.912	1.315	2.107	0.798	3.891	1.216	20.566	1.775	2.107	1.012	2.896	1.264
HC_5N(10-9)	26.63	46	-21.53	15.785	4.256	2.5	1.843	3.555	4.606	20.351	6.055	2.5	2.543	2.494	4.667
HC_5N(10-9)	26.63	47	-20.12	15.677	4.229	2.455	1.837	4.04	5.415	20.083	6.091	2.455	2.429	2.791	5.603
HC_5N(10-9)	26.63	48	-18.71	15.146	1.728	2.462	1.057	5.117	1.859	20.471	2.307	2.462	1.244	3.87	2.001
HC_5N(11-10)	29.29	19	-32.39	15.008	1.714	2.467	0.941	4.121	1.576	20.308	7.462	2.467	4.375	0.938	1.519
HC_5N(11-10)	29.29	20	-31.11	15.928	0.304	2.887	0.333	3.515	0.317	22.842	0.888	0.675	1.99	0.492	1.063
HC_5N(11-10)	29.29	21	-29.83	15.52	1.375	2.451	0.866	3.143	0.796	21.436	4.38	2.451	4.443	0.872	0.608
HC_5N(11-10)	29.29	22	-28.55	15.285	3.328	1.982	1.405	2.769	3.56	18.896	6.21	1.982	2.584	1.481	3.583
HC_5N(11-10)	29.29	23	-27.27	16.189	0.453	2.475	0.485	2.927	0.307	21.965	1.276	1.496	1.338	0.737	0.421
HC_5N(11-10)	29.29	24	-25.99	16.026	0.29	2.392	0.324	3.195	0.316	21.915	0.645	0.993	0.65	0.899	0.471
HC_5N(11-10)	29.29	25	-24.71	16.239	0.336	2.544	0.377	3.027	0.325	22.29	0.709	0.984	0.74	0.859	0.507
HC_5N(11-10)	29.29	26	-23.43	16.108	0.514	2.274	0.518	2.593	0.293	21.362	0.994	1.494	0.883	0.996	0.413
HC_5N(11-10)	29.29	27	-22.15	16.632	0.801	2.996	0.856	2.641	0.334	21.889	0.994	1.247	1.173	0.892	0.77
HC_5N(11-10)	29.29	28	-20.87	15.49	1.781	2.329	1	3.019	1.239	20.544	3.728	2.329	2.206	1.432	1.202
HC_5N(11-10)	29.29	29	-19.60	15.839	1.547	2.348	0.914	3.081	1.03	21.036	3.339	2.348	1.98	1.423	1.027
HC_5N(12-11)	31.95	36	-32.38	14.95	1.449	2.13	0.733	7.848	3.275	19.278	4.519	2.13	2.27	2.513	3.289
HC_5N(12-11)	31.95	37	-31.21	15.006	1.376	2.025	0.746	6.194	2.381	19.263	3.094	2.025	1.635	2.753	2.418
HC_5N(12-11)	31.95	38	-30.04	16.198	0.24	2.773	0.25	5.95	0.447	24.159	1.449	0.703	1.317	0.502	0.821
HC_5N(12-11)	31.95	39	-28.86	16.001	0.274	2.641	0.31	6.002	0.515	22.408	1.757	1.023	1.807	0.568	0.797
HC_5N(12-11)	31.95	40	-27.69	16.275	0.245	2.626	0.267	5.526	0.444	22.851	0.558	0.666	0.71	1.14	0.936
HC_5N(12-11)	31.95	41	-26.52	15.883	1.68	2.237	0.854	5.382	2.442	20.518	6.471	2.237	3.655	1.386	2.31
HC_5N(12-11)	31.95	42	-25.34	16.308	0.278	2.66	0.325	5.263	0.44	22.081	0.689	0.897	0.726	1.147	0.746

Table C.1 continued.

Transition	Restfreq	Ch	v_{ch}	R_{max} 1	ΔR_{max} 1	$W_{1/2}$ 1	$\Delta W_{1/2}$ 1	F_{max} 1	ΔF_{max} 1	R_{max} 2	ΔR_{max} 2	$W_{1/2}$ 2	$\Delta W_{1/2}$ 2	F_{max} 2	ΔF_{max} 2
HC_5N(12-11)	31.95	43	-24.17	16.659	0.277	2.877	0.285	5.125	0.426	nan	nan	nan	nan	nan	nan
HC_5N(12-11)	31.95	44	-23.00	17.069	0.291	3.081	0.3	4.974	0.407	nan	nan	nan	nan	nan	nan
HC_5N(12-11)	31.95	45	-21.83	16.927	0.322	3.405	0.34	4.986	0.408	nan	nan	nan	nan	nan	nan
HC_5N(12-11)	31.95	46	-20.65	15.071	1.303	1.912	0.75	5.037	1.792	19.237	1.487	1.912	0.835	4.41	1.819
HC_5N(12-11)	31.95	47	-19.48	16.976	0.276	3.212	0.29	6.847	0.507	nan	nan	nan	nan	nan	nan
HC_5N(13-12)	34.61	31	-33.44	14.849	1.197	2.682	0.834	4.392	0.775	21.999	9.425	2.682	21.41	0.39	0.496
HC_5N(13-12)	34.61	32	-32.35	15.259	0.257	2.34	0.264	3.902	0.371	22.922	nan	0.372	nan	2.565	nan
HC_5N(13-12)	34.61	33	-31.27	15.323	0.36	2.813	0.37	3.119	0.345	nan	nan	nan	nan	nan	nan
HC_5N(13-12)	34.61	34	-30.19	15.026	0.839	2.029	0.649	2.968	0.492	20.098	2.621	2.029	1.906	0.957	0.506
HC_5N(13-12)	34.61	35	-29.11	15.553	0.528	2.27	0.537	3.24	0.38	23.387	16.874	2.27	12.306	0.654	1.511
HC_5N(13-12)	34.61	36	-28.02	15.349	0.391	2.515	0.475	2.56	0.325	21.796	0.73	1.217	0.824	0.95	0.442
HC_5N(13-12)	34.61	37	-26.94	15.316	0.366	2.509	0.392	2.463	0.31	22.389	0.653	0.925	0.668	0.815	0.488
HC_5N(13-12)	34.61	38	-25.86	15.54	0.29	2.264	0.31	2.528	0.28	22.187	0.522	0.908	0.53	0.862	0.421
HC_5N(13-12)	34.61	39	-24.78	15.617	0.428	1.863	0.452	2.19	0.338	21.742	0.901	1.863	1.003	1.015	0.333
HC_5N(13-12)	34.61	40	-23.69	15.421	0.422	2.125	0.484	2.391	0.306	22.206	1.01	2.125	1.085	0.998	0.292
HC_5N(13-12)	34.61	41	-22.61	14.961	0.831	2.572	0.853	2.234	0.37	21.214	1.725	1.813	1.569	0.856	0.475
HC_5N(13-12)	34.61	42	-21.53	14.962	0.78	2.074	0.579	2.914	nan	19.158	2.345	2.074	nan	0.886	nan
HC_5N(13-12)	34.61	43	-20.45	15.878	0.378	3.14	0.403	2.768	0.283	nan	nan	nan	nan	nan	nan
HC_5N(13-12)	34.61	44	-19.36	16.232	0.369	2.86	0.426	3.222	0.336	23.307	2.299	1.216	2.94	0.416	0.511
HC_5N(14-13)	37.28	40	-33.32	15.129	0.483	2.254	0.4	13.38	1.162	21.137	2.503	2.254	2.215	2.531	1.136
HC_5N(14-13)	37.28	41	-32.31	15.197	0.475	2.324	0.439	11.279	0.991	21.791	2.483	2.324	2.919	2.001	0.977
HC_5N(14-13)	37.28	42	-31.31	14.844	1.322	1.904	0.729	9.618	3.685	18.894	3.059	1.904	1.643	4.159	3.745
HC_5N(14-13)	37.28	43	-30.30	14.761	0.6	1.697	0.44	9.561	1.398	19.01	1.284	1.697	0.93	4.469	1.403
HC_5N(14-13)	37.28	44	-29.30	16.003	0.284	2.74	0.295	8.594	0.771	nan	nan	nan	nan	nan	nan
HC_5N(14-13)	37.28	45	-28.29	15.512	0.793	2.045	0.599	8.575	1.348	20.644	2.76	2.045	2.062	2.465	1.351
HC_5N(14-13)	37.28	46	-27.29	15.725	0.849	2.074	0.594	8.312	1.432	20.78	2.777	2.074	2.033	2.515	1.393
HC_5N(14-13)	37.28	47	-26.28	16.112	0.308	2.347	0.355	8.347	0.879	22.052	0.847	1.132	0.863	2.095	1.22
HC_5N(14-13)	37.28	48	-25.28	15.988	0.546	2.027	0.472	8.209	0.878	21.061	1.487	1.756	1.238	2.686	1.069
HC_5N(14-13)	37.28	49	-24.27	16.459	1.821	2.501	1.039	8.488	3.009	22.715	7.083	2.501	17.202	1.441	1.834
HC_5N(14-13)	37.28	50	-23.27	15.263	2.471	2.001	1.257	6.885	5.315	19.285	3.661	2.001	1.802	4.649	5.404
HC_5N(14-13)	37.28	51	-22.26	15.386	2.194	2.044	1.11	7.374	4.863	19.543	3.14	2.044	1.594	5.147	4.855
HC_5N(14-13)	37.28	52	-21.26	15.772	1.108	2.113	0.745	8.729	1.681	20.124	1.6	1.744	0.962	4.747	2.893
HC_5N(14-13)	37.28	53	-20.25	15.643	2.427	2.106	1.207	8.288	6.108	19.821	3.753	2.106	1.777	5.358	6.264
HC_5N(14-13)	37.28	54	-19.25	15.357	2.476	2.205	1.212	8.617	6.338	19.68	3.516	2.205	1.627	6.064	6.518
HC_7N(16-15)	18.05	48	-31.42	17.444	14.165	3.653	7.453	0.457	1.073	25.337	11.549	3.653	11.252	0.481	0.826
HC_7N(16-15)	18.05	49	-29.34	17.398	0.789	2.831	0.904	1.073	0.159	24.002	1.125	1.804	1.175	0.547	0.216
HC_7N(16-15)	18.05	50	-27.27	14.28	14.771	5.456	6.548	0.586	0.864	19.726	1.081	2.881	3.079	0.807	1.81
HC_7N(16-15)	18.05	51	-25.19	14.929	0.764	5.022	0.977	1.041	0.132	25.64	2.107	1.342	2.245	0.167	0.228
HC_7N(16-15)	18.05	52	-23.12	15.756	3.225	3.032	2.087	0.981	0.521	22.422	6.448	3.032	3.775	0.494	0.554
HC_7N(16-15)	18.05	53	-21.04	17.977	1.704	10.757	2.266	0.72	0.09	nan	nan	nan	nan	nan	nan
HC_7N(16-15)	18.05	54	-18.96	18.439	0.843	6.458	0.874	1.248	0.138	nan	nan	nan	nan	nan	nan
HC_7N(17-16)	19.18	71	-32.17	17.066	1.216	4.768	1.139	0.918	0.09	25.493	3.2	2.323	3.374	0.151	0.228

Table C.1 continued.

Transition	Restfreq	Ch	v_{ch}	R_{max} 1	ΔR_{max} 1	$W_{1/2}$ 1	$\Delta W_{1/2}$ 1	F_{max} 1	ΔF_{max} 1	R_{max} 2	ΔR_{max} 2	$W_{1/2}$ 2	$\Delta W_{1/2}$ 2	F_{max} 2	ΔF_{max} 2
HC_7N(17-16)	19.18	72	-30.22	15.429	4.516	3.57	2.169	0.74	0.613	22.479	6.068	3.57	2.947	0.549	0.61
HC_7N(17-16)	19.18	73	-28.27	17.673	0.871	5.071	0.89	0.934	0.086	24.496	1.78	-1.129	2.28	0.128	0.224
HC_7N(17-16)	19.18	74	-26.31	9.15	54.545	7.167	71.387	0.25	0.478	19.27	3.085	4.101	4.747	0.817	2.923
HC_7N(17-16)	19.18	75	-24.36	16.459	1.333	3.082	1.017	0.779	0.117	23.348	2.06	2.554	1.441	0.414	0.184
HC_7N(17-16)	19.18	76	-22.40	5	9.688	11.159	17.388	0.413	0.085	18.985	0.792	3.652	1.65	0.826	0.472
HC_7N(17-16)	19.18	77	-20.45	17.584	36.068	3.625	9.274	0.602	7.972	22.194	37.387	3.625	8.998	0.57	8.08
HC_7N(18-17)	20.30	71	-33.16	16.17	0.717	2.221	0.864	4.522	1.009	22.147	2.291	1.565	2.255	1.183	1.107
HC_7N(18-17)	20.30	72	-31.31	0	0	0	0	0	0	nan	nan	nan	nan	nan	nan
HC_7N(18-17)	20.30	73	-29.46	12.651	16.912	10.886	14.224	1.453	0.435	19.225	1.085	1.28	1.377	1.127	0.966
HC_7N(18-17)	20.30	74	-27.62	7.603	37.791	18.463	34.351	0.695	0.404	nan	nan	nan	nan	nan	nan
HC_7N(18-17)	20.30	75	-25.77	13.788	1.005	2.34	1.4	2.42	0.802	23.408	10.561	2.34	5.77	1.024	1.903
HC_7N(18-17)	20.30	76	-23.93	16.627	0.496	2.533	0.535	4.117	0.686	24.858	2.044	1.144	2.117	0.612	0.943
HC_7N(18-17)	20.30	77	-22.08	13.453	2.701	3.875	4.101	1.011	0.545	22.75	0.677	2.01	0.672	2.705	0.654
HC_7N(18-17)	20.30	78	-20.24	0	0	0	0	0	0	nan	nan	nan	nan	nan	nan
HC_7N(19-18)	21.43	40	-32.60	16.082	0.679	3.294	0.684	1.176	0.119	23.469	1.236	2.089	1.109	0.457	0.175
HC_7N(19-18)	21.43	41	-30.85	16.145	1.479	2.49	1.056	0.904	0.228	22.081	1.911	2.49	1.233	0.707	0.241
HC_7N(19-18)	21.43	42	-29.10	16.378	0.8	2.65	0.722	0.934	0.118	23.056	1.306	2.255	1.085	0.505	0.141
HC_7N(19-18)	21.43	43	-27.35	16.262	1.486	2.639	1.05	0.956	0.228	22.597	2.634	2.639	1.763	0.541	0.235
HC_7N(19-18)	21.43	44	-25.61	17.094	1.021	3.303	0.946	0.865	0.106	23.459	1.021	1.84	0.907	0.474	0.23
HC_7N(19-18)	21.43	45	-23.86	16.553	1.793	2.83	1.365	0.864	0.233	23.175	3.162	2.83	1.932	0.506	0.266
HC_7N(19-18)	21.43	46	-22.11	18.445	1.653	3.65	1.284	1.004	0.139	24.965	1.976	2.233	1.542	0.424	0.397
HC_7N(19-18)	21.43	47	-20.36	5	48.334	18.387	37.364	0.26	0.112	18.993	0.76	3.681	1.088	0.87	0.221
HC_7N(19-18)	21.43	48	-18.61	19.35	0.506	4.952	0.524	1.105	0.097	nan	nan	nan	nan	nan	nan
HC_7N(20-19)	22.56	50	-33.38	15.499	1.85	3.081	1.107	1.36	0.408	22.366	3.622	3.081	2.182	0.691	0.406
HC_7N(20-19)	22.56	51	-31.72	16.207	1.957	2.742	1.149	1.227	0.45	22.212	3.548	2.742	2.024	0.676	0.458
HC_7N(20-19)	22.56	52	-30.06	16.254	0.539	2.557	0.534	1.202	nan	22.491	1.084	2.557	nan	0.639	nan
HC_7N(20-19)	22.56	53	-28.40	16.259	1.116	2.514	0.79	1.316	0.247	22.317	2.409	2.514	1.61	0.612	0.255
HC_7N(20-19)	22.56	54	-26.74	16.861	1.424	2.578	0.991	1.022	0.212	22.578	1.935	2.276	1.262	0.651	0.299
HC_7N(20-19)	22.56	55	-25.08	16.391	3.936	2.633	1.843	0.934	0.959	21.433	4.418	2.633	1.96	0.829	0.985
HC_7N(20-19)	22.56	56	-23.42	17.124	1.469	2.913	1.107	1.007	0.163	22.934	1.687	2.139	1.114	0.6	0.36
HC_7N(20-19)	22.56	57	-21.76	18.119	0.718	4.225	0.52	1.117	0.136	21.75	0.818	0.887	1.63	0.291	0.302
HC_7N(20-19)	22.56	58	-20.09	16.845	7.297	3.375	2.803	1.069	1.825	22.344	10.885	3.182	3.906	0.613	2.122
HC_7N(22-21)	24.82	49	-33.40	16.252	0.388	2.742	0.463	1.203	0.118	22.806	1.34	1.532	1.288	0.249	0.153
HC_7N(22-21)	24.82	50	-31.89	16.137	0.393	2.949	0.468	1.107	0.118	23.494	0.91	1.423	0.926	0.321	0.157
HC_7N(22-21)	24.82	51	-30.38	17.359	0.451	3.771	0.486	0.84	0.084	nan	nan	nan	nan	nan	nan
HC_7N(22-21)	24.82	52	-28.87	17.006	0.484	1.948	0.493	0.97	0.126	22.743	0.953	1.948	0.901	0.496	0.121
HC_7N(22-21)	24.82	53	-27.36	17.087	0.803	2.109	0.712	1.007	0.15	22.431	1.759	1.938	1.35	0.438	0.176
HC_7N(22-21)	24.82	54	-25.85	17.186	0.56	2.414	0.645	0.926	0.113	22.472	0.64	1.424	0.584	0.558	0.175
HC_7N(22-21)	24.82	55	-24.34	16.804	0.795	1.987	0.685	0.846	0.147	22.214	1.04	1.987	0.879	0.644	0.144
HC_7N(22-21)	24.82	56	-22.83	17.029	4.958	2.167	2.022	0.75	1.346	20.978	6.198	2.167	2.737	0.602	1.302
HC_7N(22-21)	24.82	57	-21.32	16.264	1.742	2.159	1.234	0.841	0.297	21.289	1.548	2.159	0.95	0.962	0.324
HC_7N(22-21)	24.82	58	-19.81	17.638	25.637	3.264	6.659	0.829	8.293	22.079	70.316	3.264	20.944	0.311	8.05

Table C.1 continued.

Transition	Restfreq	Ch	v_{ch}	R_{max} 1	ΔR_{max} 1	$W_{1/2}$ 1	$\Delta W_{1/2}$ 1	F_{max} 1	ΔF_{max} 1	R_{max} 2	ΔR_{max} 2	$W_{1/2}$ 2	$\Delta W_{1/2}$ 2	F_{max} 2	ΔF_{max} 2
HC_7N(23-22)	25.94	30	-33.10	16.148	0.696	2.557	0.593	1.697	0.178	22.606	1.91	2.363	1.49	0.582	0.206
HC_7N(23-22)	25.94	31	-31.65	16.848	0.409	3.187	0.481	1.204	0.125	24.312	0.875	1.269	0.897	0.336	0.187
HC_7N(23-22)	25.94	32	-30.21	16.89	0.492	3.301	0.627	1.212	0.137	24.336	1.291	1.477	1.313	0.29	0.198
HC_7N(23-22)	25.94	33	-28.77	16.135	2.616	2.301	1.394	0.96	0.624	20.974	3.812	2.301	2.058	0.657	0.619
HC_7N(23-22)	25.94	34	-27.32	17.172	1.825	2.85	1.588	0.992	0.186	22.904	2.694	2.157	1.74	0.486	0.47
HC_7N(23-22)	25.94	35	-25.88	16.452	0.751	2.327	0.633	1.399	0.167	22.124	2.32	2.082	1.748	0.415	0.212
HC_7N(23-22)	25.94	36	-24.43	17.62	2.277	2.467	1.485	1.013	0.343	22.19	2.351	1.896	1.375	0.643	0.727
HC_7N(23-22)	25.94	37	-22.99	17.595	6.516	2.914	2.632	1.027	1.879	22.805	23.066	2.914	10.273	0.29	1.812
HC_7N(23-22)	25.94	38	-21.54	18.99	1.823	3.175	1.307	1.298	0.218	24	3.629	1.799	3.756	0.228	0.729
HC_7N(23-22)	25.94	39	-20.10	18.354	0.716	3.012	0.701	1.409	0.139	23.7	0.896	1.402	0.964	0.493	0.337
HC_7N(23-22)	25.94	40	-18.66	16.104	13.499	3.116	5.08	0.95	3.831	21.126	11.455	3.116	3.792	1.102	3.991
HC_7N(24-23)	27.07	39	-32.74	16.647	0.673	2.106	0.646	1.463	0.205	22.516	2.286	2.106	2.128	0.43	0.2
HC_7N(24-23)	27.07	40	-31.35	16.396	0.793	1.961	0.729	1.152	0.211	21.859	0.865	1.961	0.739	1.064	0.206
HC_7N(24-23)	27.07	41	-29.97	16.633	1.777	2.021	1.487	1.293	0.465	21.433	3.084	2.021	2.006	0.785	0.538
HC_7N(24-23)	27.07	42	-28.58	17.189	2.27	2.374	1.556	1.131	0.379	21.77	2.66	1.849	1.506	0.678	0.799
HC_7N(24-23)	27.07	43	-27.20	16.737	0.635	1.862	0.672	1.127	0.201	22.229	0.811	1.862	0.765	0.898	0.194
HC_7N(24-23)	27.07	44	-25.81	17.487	1.46	2.068	1.284	0.78	0.198	22.316	0.943	1.665	0.757	0.999	0.293
HC_7N(24-23)	27.07	45	-24.43	16.333	1.546	2.064	1.106	1.068	0.34	21.233	2.469	2.064	1.587	0.677	0.363
HC_7N(24-23)	27.07	46	-23.05	17.323	2.866	1.887	1.554	1.124	0.998	21.211	2.925	1.887	1.467	1.104	1.041
HC_7N(24-23)	27.07	47	-21.66	10.532	4.332	12.882	4.833	1.002	0.177	nan	nan	nan	nan	nan	nan
HC_7N(24-23)	27.07	48	-20.28	16.605	1.627	2.002	1.187	1.041	0.35	21.498	1.76	2.002	1.209	0.967	0.361
HC_7N(24-23)	27.07	49	-18.89	14.807	7.788	2.551	4.721	0.802	1.599	19.719	6.104	2.551	2.506	1.042	1.888
HC_7N(25-24)	28.20	40	-32.20	15.71	1.121	1.99	0.742	1.121	0.286	20.32	2.831	1.99	1.754	0.446	0.297
HC_7N(25-24)	28.20	41	-30.87	16.672	0.878	2.436	0.798	1.032	0.153	23.412	2.883	2.436	3.103	0.296	0.147
HC_7N(25-24)	28.20	42	-29.54	17.046	2.075	2.465	1.328	0.997	0.411	22.535	5.915	2.465	3.554	0.351	0.427
HC_7N(25-24)	28.20	43	-28.21	17.231	0.81	2.185	0.822	1.068	0.153	22.296	1.541	1.651	1.227	0.461	0.238
HC_7N(25-24)	28.20	44	-26.89	16.968	0.455	3.101	0.466	0.778	0.098	nan	nan	nan	nan	nan	nan
HC_7N(25-24)	28.20	45	-25.56	17.18	0.73	2.235	0.719	1.042	0.154	22.555	1.131	1.637	1.062	0.531	0.205
HC_7N(25-24)	28.20	46	-24.23	16.856	11.127	2.479	4.939	0.713	2.663	21.093	13.509	2.479	4.757	0.579	2.884
HC_7N(25-24)	28.20	47	-22.90	15.667	4.907	2.424	2.725	0.641	0.777	20.583	4.142	2.424	2.001	0.763	0.835
HC_7N(25-24)	28.20	48	-21.57	19.958	0.471	3.172	0.494	0.944	0.122	nan	nan	nan	nan	nan	nan
HC_7N(25-24)	28.20	49	-20.24	17.633	18.58	2.791	5.584	0.911	6.841	21.694	32.979	2.791	10.159	0.515	6.8
HC_7N(25-24)	28.20	50	-18.91	16.621	14.189	2.542	5.262	0.596	3.059	20.77	8.1	2.542	2.772	1.034	3.142
HC_7N(26-25)	29.33	19	-32.42	16.113	1.884	2.302	1.62	0.856	0.273	21.817	2.99	2.302	2.181	0.557	0.296
HC_7N(26-25)	29.33	20	-31.14	14.913	0.676	1.729	0.734	0.551	0.183	23.1	0.673	1.729	0.738	0.509	0.171
HC_7N(26-25)	29.33	21	-29.87	15.475	0.572	2.381	0.669	0.713	0.144	22.205	0.983	1.296	1.126	0.299	0.18
HC_7N(26-25)	29.33	22	-28.59	16.56	0.683	2.488	0.892	0.637	0.14	22.378	0.883	1.065	0.909	0.302	0.199
HC_7N(26-25)	29.33	23	-27.31	16.859	0.84	1.879	0.945	0.518	0.16	21.638	0.652	1.153	0.635	0.507	0.196
HC_7N(26-25)	29.33	24	-26.03	16.8	0.775	2.06	0.977	0.466	0.143	21.582	0.585	0.813	0.63	0.356	0.218
HC_7N(26-25)	29.33	25	-24.75	16.589	1.275	1.832	1.322	0.553	0.202	20.812	1.203	1.166	1.081	0.429	0.283
HC_7N(26-25)	29.33	26	-23.48	15.921	0.693	2.692	0.841	0.755	0.149	21.418	0.651	-0.885	0.687	0.406	0.254
HC_7N(26-25)	29.33	27	-22.20	15.873	1.098	4.25	1.434	0.598	0.117	22.731	3.937	0.765	3.745	0.057	0.267

Table C.1 continued.

Transition	Restfreq	Ch	v_{ch}	R_{max} 1	ΔR_{max} 1	$W_{1/2}$ 1	$\Delta W_{1/2}$ 1	F_{max} 1	ΔF_{max} 1	R_{max} 2	ΔR_{max} 2	$W_{1/2}$ 2	$\Delta W_{1/2}$ 2	F_{max} 2	ΔF_{max} 2
HC_7N(26-25)	29.33	28	-20.92	15.986	1.058	2.128	1.026	0.814	0.176	22.043	1.751	2.128	2.073	0.456	0.168
HC_7N(26-25)	29.33	29	-19.64	15.425	1.445	2.729	1.457	0.899	0.193	21.571	1.953	1.934	1.552	0.511	0.312
HC_7N(27-26)	30.46	30	-32.39	15.253	0.665	2.259	0.771	1.228	0.186	21.896	1.158	2.259	1.14	0.726	0.177
HC_7N(27-26)	30.46	31	-31.16	14.892	3.311	2.165	2.153	1.167	0.889	19.628	3.455	2.165	1.869	1.138	0.991
HC_7N(27-26)	30.46	32	-29.93	16.276	1.966	2.078	1.443	1.385	0.561	21.174	2.935	2.078	1.927	0.944	0.599
HC_7N(27-26)	30.46	33	-28.70	16.957	1.911	2.469	1.308	1.595	0.548	22.758	7.856	2.469	5.817	0.38	0.524
HC_7N(27-26)	30.46	34	-27.47	16.5	1.033	1.724	0.734	1.556	0.393	20.699	2.337	1.724	1.597	0.69	0.4
HC_7N(27-26)	30.46	35	-26.24	16.81	1.896	1.878	1.185	1.07	0.493	21.004	3.066	1.823	1.848	0.637	0.545
HC_7N(27-26)	30.46	36	-25.01	16.55	1.09	1.921	0.871	1.242	0.279	21.429	1.215	1.838	0.927	1.073	0.303
HC_7N(27-26)	30.46	37	-23.78	16.6	17.689	2.594	5.587	0.94	6.949	20.421	26.656	2.594	7.894	0.616	7.07
HC_7N(27-26)	30.46	38	-22.55	19.26	0.466	2.986	0.47	1.331	0.18	nan	nan	nan	nan	nan	nan
HC_7N(27-26)	30.46	39	-21.32	19.575	1.152	2.998	1.066	1.5	0.223	23.538	0.977	0.883	1.55	0.42	0.686
HC_7N(27-26)	30.46	40	-20.09	18.169	0.427	2.206	0.457	1.87	0.22	23.893	1.05	1.569	0.991	0.63	0.257
HC_7N(27-26)	30.46	41	-18.86	17.763	0.619	2.803	0.699	1.711	0.257	24.416	1.62	1.521	1.748	0.455	0.349
HC_7N(28-27)	31.58	29	-32.46	16.042	1.576	2.637	1.126	2.646	0.713	22.065	4.755	2.637	2.821	0.901	0.798
HC_7N(28-27)	31.58	30	-31.27	16.431	1.131	2.397	0.877	2.419	0.462	22.282	2.912	2.397	2.05	0.956	0.486
HC_7N(28-27)	31.58	31	-30.08	16.558	1.605	2.428	1.011	2.423	0.774	22.044	5.062	2.428	3.274	0.763	0.762
HC_7N(28-27)	31.58	32	-28.90	16.176	1.825	2.407	1.248	1.793	0.606	21.777	2.715	2.407	1.758	1.212	0.626
HC_7N(28-27)	31.58	33	-27.71	16.337	1.11	2.121	0.875	2.073	0.391	21.287	1.897	1.924	1.301	1.117	0.532
HC_7N(28-27)	31.58	34	-26.53	17.184	0.711	2.626	0.769	2.001	0.254	22.78	1.118	1.563	1.002	0.847	0.436
HC_7N(28-27)	31.58	35	-25.34	17.445	0.746	2.57	0.8	1.931	0.283	23.109	1.816	1.546	1.704	0.546	0.439
HC_7N(28-27)	31.58	36	-24.15	17.07	5.803	2.187	2.585	1.767	3.523	21.137	10.178	2.187	4.743	1.006	3.462
HC_7N(28-27)	31.58	37	-22.97	17.284	22.195	2.706	5.872	1.601	16.711	20.906	48.217	2.706	13.201	0.743	16.589
HC_7N(28-27)	31.58	38	-21.78	18.165	0.48	3.528	0.606	2.196	0.244	24.768	2.333	0.717	2.882	0.175	0.543
HC_7N(28-27)	31.58	39	-20.59	18.557	0.34	3.085	0.366	2.67	0.251	nan	nan	nan	nan	nan	nan
HC_7N(28-27)	31.58	40	-19.41	18.513	0.392	3.598	0.4	2.482	0.234	nan	nan	nan	nan	nan	nan
HC_7N(29-28)	32.71	38	-32.46	15.507	0.464	1.913	0.52	1.351	0.217	21.826	3.386	1.913	4.526	0.177	0.215
HC_7N(29-28)	32.71	39	-31.31	17.804	1.269	4.274	1.678	0.674	0.15	24.497	1.816	-0.662	2.922	0.137	0.398
HC_7N(29-28)	32.71	40	-30.17	16.649	2.358	2.445	2.287	1.081	0.391	22.809	5.731	2.445	5.991	0.431	0.376
HC_7N(29-28)	32.71	41	-29.02	19.362	0.809	3.291	0.844	0.756	0.161	nan	nan	nan	nan	nan	nan
HC_7N(29-28)	32.71	42	-27.88	-40.413	354.401	35.112	117.051	2.013	15.036	nan	nan	nan	nan	nan	nan
HC_7N(29-28)	32.71	43	-26.73	17.002	0.587	2.524	0.661	0.925	0.18	23.996	0.624	0.619	0.501	0.41	0.308
HC_7N(29-28)	32.71	44	-25.59	17.683	0.335	1.206	0.347	0.994	0.235	22.668	0.516	1.152	0.541	0.606	0.233
HC_7N(29-28)	32.71	45	-24.44	18.59	0.623	1.707	0.727	0.828	0.195	24.058	1.431	1.707	1.597	0.356	0.186
HC_7N(29-28)	32.71	46	-23.29	17.065	0.775	1.667	0.85	1.007	0.287	21.295	1.025	1.139	0.952	0.616	0.344
HC_7N(29-28)	32.71	47	-22.15	9.782	3.544	9.742	3.205	0.953	0.269	nan	nan	nan	nan	nan	nan
HC_7N(29-28)	32.71	48	-21.00	17.027	2.622	5.488	3.034	0.566	0.192	19.647	1.098	0.586	1.906	0.271	0.578
HC_7N(30-29)	33.84	37	-33.00	16.332	0.446	3.031	0.508	1.203	0.144	nan	nan	nan	nan	nan	nan
HC_7N(30-29)	33.84	38	-31.89	16.205	1.617	1.952	0.981	1.252	0.532	20.464	3.822	1.952	2.145	0.532	0.557
HC_7N(30-29)	33.84	39	-30.78	16.708	0.387	2.484	0.433	1.097	0.148	23.829	1.017	0.951	1.236	0.293	0.237
HC_7N(30-29)	33.84	40	-29.68	15.575	1.11	1.724	0.796	1.151	0.311	19.758	2.148	1.724	1.446	0.599	0.322
HC_7N(30-29)	33.84	41	-28.57	16.558	0.452	2.232	0.543	0.954	0.161	23.062	0.81	1.343	0.866	0.41	0.193

Table C.1 continued.

Transition	Restfreq	Ch	v_{ch}	R_{max} 1	ΔR_{max} 1	$W_{1/2}$ 1	$\Delta W_{1/2}$ 1	F_{max} 1	ΔF_{max} 1	R_{max} 2	ΔR_{max} 2	$W_{1/2}$ 2	$\Delta W_{1/2}$ 2	F_{max} 2	ΔF_{max} 2
HC_7N(30-29)	33.84	42	-27.46	16.605	0.433	2.235	0.533	0.931	0.152	22.44	0.559	0.844	0.563	0.415	0.227
HC_7N(30-29)	33.84	43	-26.35	17.344	0.558	1.855	0.518	1.208	0.174	22.852	3.786	1.855	5.04	0.159	0.176
HC_7N(30-29)	33.84	44	-25.25	16.184	2.54	2.121	1.79	0.888	0.413	20.788	3.525	1.912	2.079	0.571	0.605
HC_7N(30-29)	33.84	45	-24.14	17.379	0.379	2.665	0.412	0.98	0.12	nan	nan	nan	nan	nan	nan
HC_7N(30-29)	33.84	46	-23.03	17.187	0.425	2.523	0.473	1.026	0.143	nan	nan	nan	nan	nan	nan
HC_7N(30-29)	33.84	47	-21.92	16.18	3.161	1.851	1.583	0.959	1.027	19.894	4.132	1.851	2.006	0.733	1.043
HC_7N(30-29)	33.84	48	-20.82	18.113	0.284	2.351	0.292	1.704	0.178	nan	nan	nan	nan	nan	nan
HC_7N(30-29)	33.84	49	-19.71	17.463	1.091	3.399	0.972	1.217	0.524	19.119	1.153	1.194	1.611	0.389	0.547
HC_7N(30-29)	33.84	50	-18.60	15.286	2.03	2.022	1.287	1.129	0.542	19.84	2.157	2.022	1.291	1.066	0.562
HC_7N(31-30)	34.97	15	-33.32	15.725	0.571	2.778	0.642	1.308	0.206	nan	nan	nan	nan	nan	nan
HC_7N(31-30)	34.97	16	-32.25	15.545	0.768	2.111	1.018	1.06	0.207	22.584	6.319	2.111	7.221	0.355	0.247
HC_7N(31-30)	34.97	17	-31.18	16.172	0.733	2.154	0.92	0.656	0.184	22.59	0.419	1.159	0.431	0.762	0.221
HC_7N(31-30)	34.97	18	-30.10	20.546	nan	7.15	24.732	0.221	nan	20.546	1.537	3.051	5.948	0.318	nan
HC_7N(31-30)	34.97	19	-29.03	0	0	0	0	0	0	nan	nan	nan	nan	nan	nan
HC_7N(31-30)	34.97	20	-27.96	19.704	1.283	3.635	1.726	0.605	0.175	nan	nan	nan	nan	nan	nan
HC_7N(31-30)	34.97	21	-26.89	16.229	0.928	1.661	1.246	0.597	0.261	22.234	1.378	1.661	1.468	0.379	0.237
HC_7N(31-30)	34.97	22	-25.82	-193.186	3716.587	53.147	480.893	828.137	111049.405	nan	nan	nan	nan	nan	nan
HC_7N(31-30)	34.97	23	-24.75	19.527	1.364	4.455	1.465	0.498	0.127	nan	nan	nan	nan	nan	nan
HC_7N(31-30)	34.97	24	-23.68	18.801	5.223	8.582	9.969	0.228	0.129	20.092	0.443	0.724	0.501	0.44	0.242
HC_7N(31-30)	34.97	25	-22.60	21.318	2.028	6.862	2.457	0.601	0.11	nan	nan	nan	nan	nan	nan
HC_7N(31-30)	34.97	26	-21.53	15.268	2.935	2.355	3.453	0.65	0.314	20.961	5.333	2.355	3.204	0.428	0.452
HC_7N(31-30)	34.97	27	-20.46	15.568	3.568	2.045	2.404	0.507	0.384	20.446	3.994	2.045	2.765	0.448	0.378
HC_7N(31-30)	34.97	28	-19.39	17.322	0.688	3.165	0.764	0.819	0.151	nan	nan	nan	nan	nan	nan
HC_7N(32-31)	36.10	37	-32.74	15.763	1.289	1.986	1.064	1.864	0.492	20.501	5.974	1.986	3.877	0.422	0.566
HC_7N(32-31)	36.10	38	-31.71	15.675	0.816	2.09	0.937	1.099	0.219	21.779	2.555	2.09	2.354	0.368	0.211
HC_7N(32-31)	36.10	39	-30.67	15.919	1.239	1.936	0.923	1.371	0.361	20.648	3.21	1.936	2.183	0.536	0.379
HC_7N(32-31)	36.10	40	-29.63	17.126	0.854	2.147	0.945	1.228	0.25	23.383	3.22	2.147	2.911	0.341	0.241
HC_7N(32-31)	36.10	41	-28.59	17.635	0.613	2.735	0.755	1.094	0.196	22.502	1.807	0.502	1.446	0.184	0.44
HC_7N(32-31)	36.10	42	-27.55	18	0.543	2.335	0.638	1.394	0.227	23.428	1.333	1.202	1.319	0.387	0.315
HC_7N(32-31)	36.10	43	-26.51	17.979	0.583	2.15	0.719	1.003	0.214	23.217	0.822	1.04	0.82	0.485	0.291
HC_7N(32-31)	36.10	44	-25.48	17.38	0.564	2.215	0.772	1.487	0.28	23.147	1.404	1.396	1.351	0.487	0.325
HC_7N(32-31)	36.10	45	-24.44	16.87	10.87	2.349	5.029	0.977	3.472	21.067	17.354	2.349	6.577	0.606	3.752
HC_7N(32-31)	36.10	46	-23.40	18.164	1.752	2.735	1.769	0.889	0.204	23.355	1.177	1.554	1.013	0.724	0.516
HC_7N(32-31)	36.10	47	-22.36	17.773	0.682	3.28	0.754	0.967	0.173	nan	nan	nan	nan	nan	nan
HC_7N(32-31)	36.10	48	-21.32	18.5	0.843	3.1	1.073	1.087	0.22	23.871	1.443	0.637	2.282	0.231	0.524
HC_7N(32-31)	36.10	49	-20.29	17.44	4.11	4.943	3.645	0.739	0.448	20.199	1.401	1.398	2.044	0.367	0.526
HC_7N(32-31)	36.10	50	-19.25	16.699	1.612	1.634	0.977	1.616	0.779	20.388	2.363	1.634	1.484	1.095	0.761
HC_7N(33-32)	37.22	36	-33.06	15.501	0.496	1.927	0.554	1.165	0.253	23.462	1.708	1.927	2.306	0.363	0.583
HC_7N(33-32)	37.22	37	-32.06	14.796	0.563	2.065	0.617	1.371	0.28	21.989	1.624	2.065	1.79	0.483	0.265
HC_7N(33-32)	37.22	38	-31.05	13.885	0.703	2.382	0.867	1.097	0.256	19.981	0.461	1.276	0.459	1.191	0.319
HC_7N(33-32)	37.22	39	-30.04	15.424	1.623	2.017	1.408	1.046	0.344	20.756	1.863	2.017	1.462	0.924	0.347
HC_7N(33-32)	37.22	40	-29.04	14.677	0.808	1.852	0.893	0.735	0.272	22.556	3.494	1.852	4.375	0.213	0.332

Table C.1 continued.

Transition	Restfreq	Ch	v_{ch}	R_{max} 1	ΔR_{max} 1	$W_{1/2}$ 1	$\Delta W_{1/2}$ 1	F_{max} 1	ΔF_{max} 1	R_{max} 2	ΔR_{max} 2	$W_{1/2}$ 2	$\Delta W_{1/2}$ 2	F_{max} 2	ΔF_{max} 2
HC_7N(33-32)	37.22	41	-28.03	16.118	3.125	2.609	3.275	1.027	0.487	22.368	11.453	2.609	7.235	0.319	0.646
HC_7N(33-32)	37.22	42	-27.02	14.867	1.189	1.966	1.178	0.856	0.25	20.482	1.254	1.966	1.103	0.823	0.24
HC_7N(33-32)	37.22	43	-26.02	16.346	2.519	4.607	3.085	0.715	0.223	nan	nan	nan	nan	nan	nan
HC_7N(33-32)	37.22	44	-25.01	15.515	1.423	1.92	2.042	0.846	0.36	22.202	1.368	1.92	1.433	0.665	0.317
HC_7N(33-32)	37.22	45	-24.00	17.342	1.399	4.631	1.616	0.647	0.167	nan	nan	nan	nan	nan	nan
HC_7N(33-32)	37.22	46	-23.00	15.278	0.649	1.17	0.706	0.869	0.403	19.847	0.565	1.17	0.595	0.973	0.387
HC_7N(33-32)	37.22	47	-21.99	15.44	4.059	2.464	4.897	0.493	0.256	20.135	0.979	1.466	0.842	1.178	0.79
HC_7N(33-32)	37.22	48	-20.98	14.664	2.424	2.184	3.94	0.5	0.272	20.965	1.526	2.184	1.434	0.93	0.265
HC_7N(33-32)	37.22	49	-19.98	14.261	1.483	1.994	1.282	1.063	0.341	19.708	2.405	1.994	2.076	0.649	0.333
HC_7N(33-32)	37.22	50	-18.97	18.402	0.427	2.024	0.451	1.507	0.276	nan	nan	nan	nan	nan	nan
C_3N(2-1,3/2-1/2)	19.80	58	-32.64	7.834	5.131	5.061	7.743	0.092	0.064	21.548	1.008	3.275	1.017	0.303	0.059
C_3N(2-1,3/2-1/2)	19.80	59	-30.75	14.101	0.575	3.506	0.666	0.544	0.076	nan	nan	nan	nan	nan	nan
C_3N(2-1,3/2-1/2)	19.80	60	-28.86	-215.91	9639.933	75.218	1603.226	26.843	5127.945	nan	nan	nan	nan	nan	nan
C_3N(2-1,3/2-1/2)	19.80	61	-26.97	0	0	0	0	0	0	nan	nan	nan	nan	nan	nan
C_3N(2-1,3/2-1/2)	19.80	62	-25.07	16.172	0.835	3.869	0.932	0.281	0.051	nan	nan	nan	nan	nan	nan
C_3N(2-1,3/2-1/2)	19.80	63	-23.18	0.844	2.739	1.554	2.126	0.357	0.19	nan	nan	nan	nan	nan	nan
C_3N(2-1,3/2-1/2)	19.80	64	-21.29	-1.085	4.518	3.596	2.017	1.542	0.961	nan	nan	nan	nan	nan	nan
C_3N(2-1,3/2-1/2)	19.80	65	-19.40	13.675	0.706	5.076	0.807	0.577	0.068	nan	nan	nan	nan	nan	nan
C_3N(2-1,5/2-3/2)	19.78	49	-33.07	17.937	4.778	2.793	2.532	0.393	0.399	23.664	6.339	2.793	3.19	0.296	0.411
C_3N(2-1,5/2-3/2)	19.78	50	-31.18	18.537	1.642	2.837	1.374	0.393	0.08	24.628	1.426	2.062	1.052	0.33	0.146
C_3N(2-1,5/2-3/2)	19.78	51	-29.29	3.311	0.602	-1.306	0.714	0.436	0.15	nan	nan	nan	nan	nan	nan
C_3N(2-1,5/2-3/2)	19.78	52	-27.39	15.977	1.68	2.115	1.749	0.419	0.126	21.306	1.926	2.115	1.296	0.406	0.155
C_3N(2-1,5/2-3/2)	19.78	53	-25.50	17.664	0.58	3.581	0.6	0.483	0.067	nan	nan	nan	nan	nan	nan
C_3N(2-1,5/2-3/2)	19.78	54	-23.60	20.213	0.568	3.361	0.582	0.508	0.074	nan	nan	nan	nan	nan	nan
C_3N(2-1,5/2-3/2)	19.78	55	-21.71	16.034	0.662	3.742	0.719	0.441	0.067	nan	nan	nan	nan	nan	nan
C_3N(2-1,5/2-3/2)	19.78	56	-19.81	12.077	1.74	2.757	1.356	0.663	0.17	18.716	2.046	2.757	1.357	0.575	0.186
C_3N(3-2,5/2-3/2)	29.70	31	-32.75	15.209	3.854	2.704	2.71	0.621	0.415	21.255	5.325	2.704	2.966	0.462	0.477
C_3N(3-2,5/2-3/2)	29.70	32	-31.49	18.599	0.666	3.123	0.712	0.746	0.135	nan	nan	nan	nan	nan	nan
C_3N(3-2,5/2-3/2)	29.70	33	-30.22	16.798	3.843	2.014	2.203	0.602	0.631	21.057	3.864	2.014	2.014	0.601	0.666
C_3N(3-2,5/2-3/2)	29.70	34	-28.96	8.682	13.189	4.055	19.089	0.136	1.15	20.069	0.986	2.574	0.833	0.652	0.127
C_3N(3-2,5/2-3/2)	29.70	35	-27.70	17.288	0.567	2.281	0.708	0.675	0.117	22.666	0.65	1.249	0.637	0.418	0.154
C_3N(3-2,5/2-3/2)	29.70	36	-26.44	16.168	2.889	2.191	1.949	0.619	0.377	21.174	5.854	2.191	3.715	0.308	0.391
C_3N(3-2,5/2-3/2)	29.70	37	-25.18	19.156	0.416	2.641	0.42	0.867	0.118	nan	nan	nan	nan	nan	nan
C_3N(3-2,5/2-3/2)	29.70	38	-23.91	18.159	2.395	2.718	1.92	0.607	0.145	21.754	0.542	1.127	1.068	0.476	0.593
C_3N(3-2,5/2-3/2)	29.70	39	-22.65	16.681	5.615	1.978	3.229	0.414	0.692	20.716	3.577	1.978	1.735	0.656	0.755
C_3N(3-2,5/2-3/2)	29.70	40	-21.39	15.817	2.781	1.997	2.929	0.612	0.364	20.425	5.014	1.997	2.782	0.396	0.517
C_3N(3-2,5/2-3/2)	29.70	41	-20.13	16.999	1.405	2.118	1.519	0.587	0.191	23.198	1.915	2.118	2.06	0.428	0.186
C_3N(3-2,5/2-3/2)	29.70	42	-18.87	18.917	0.747	3.634	0.811	0.902	0.11	23.587	5.597	0.702	5.676	0.037	0.285
C_3N(3-2,7/2-5/2)	29.68	32	-32.53	17.456	0.426	2.807	0.489	1.278	0.147	23.783	0.95	1.191	0.984	0.346	0.22
C_3N(3-2,7/2-5/2)	29.68	33	-31.27	16.8	6.401	2.64	3.112	0.973	1.64	21.824	9.402	2.64	4.181	0.662	1.707
C_3N(3-2,7/2-5/2)	29.68	34	-30.00	18.544	0.367	2.496	0.376	1.14	0.145	nan	nan	nan	nan	nan	nan
C_3N(3-2,7/2-5/2)	29.68	35	-28.74	-0.201	4.497	1.386	2.259	1.924	2.561	nan	nan	nan	nan	nan	nan

Table C.1 continued.

Transition	Restfreq	Ch	v_{ch}	R_{max} 1	ΔR_{max} 1	$W_{1/2}$ 1	$\Delta W_{1/2}$ 1	F_{max} 1	ΔF_{max} 1	R_{max} 2	ΔR_{max} 2	$W_{1/2}$ 2	$\Delta W_{1/2}$ 2	F_{max} 2	ΔF_{max} 2
C_3N(3-2,7/2-5/2)	29.68	36	-27.48	16.689	3.528	2.527	2.106	0.975	0.732	22.136	11.392	2.527	6.841	0.301	0.732
C_3N(3-2,7/2-5/2)	29.68	37	-26.21	17.032	0.526	2.213	0.602	0.986	0.194	23.061	1.476	1.138	1.558	0.249	0.255
C_3N(3-2,7/2-5/2)	29.68	38	-24.95	18.766	0.943	2.38	1.048	0.737	0.196	24.027	1.095	1.143	1.155	0.398	0.293
C_3N(3-2,7/2-5/2)	29.68	39	-23.69	4.076	9.991	13.047	7.647	0.643	0.17	nan	nan	nan	nan	nan	nan
C_3N(3-2,7/2-5/2)	29.68	40	-22.43	17.581	5.62	2.601	3.539	0.512	0.589	23.146	5.849	2.601	3.245	0.497	0.633
C_3N(3-2,7/2-5/2)	29.68	41	-21.16	19.702	0.845	3.749	1.018	0.868	0.154	nan	nan	nan	nan	nan	nan
C_3N(3-2,7/2-5/2)	29.68	42	-19.90	16.779	42.902	2.364	16.118	0.265	4.414	20.633	10.887	2.364	3.71	1.03	4.557
C_3N(3-2,7/2-5/2)	29.68	43	-18.64	20.742	0.76	3.583	0.83	0.943	0.172	nan	nan	nan	nan	nan	nan
C_4H(2-1,5/2-3/2)	19.02	37	-31.76	0	0	0	0	0	0	nan	nan	nan	nan	nan	nan
C_4H(2-1,5/2-3/2)	19.02	38	-29.79	11.775	0.918	4.578	1.095	0.317	0.053	23.446	nan	-0.734	nan	0.05	nan
C_4H(2-1,5/2-3/2)	19.02	39	-27.82	12.063	2.608	10.737	3.867	0.262	0.038	nan	nan	nan	nan	nan	nan
C_4H(2-1,5/2-3/2)	19.02	40	-25.85	15.871	0.876	4.96	0.919	0.312	0.047	nan	nan	nan	nan	nan	nan
C_4H(2-1,5/2-3/2)	19.02	41	-23.88	10.736	1.685	3.422	2.607	0.21	0.063	20.672	1.442	3.124	1.31	0.251	0.056
C_4H(2-1,5/2-3/2)	19.02	42	-21.91	13.178	1.935	9.28	2.233	0.262	0.038	nan	nan	nan	nan	nan	nan
C_4H(2-1,5/2-3/2)	19.02	43	-19.93	17.332	3.81	13.001	5.754	0.223	0.037	nan	nan	nan	nan	nan	nan
C_4H(3-2,5/2-3/2)	28.57	27	-32.77	16.597	1.045	3.978	1.076	0.527	0.118	nan	nan	nan	nan	nan	nan
C_4H(3-2,5/2-3/2)	28.57	28	-31.46	-6.923	127.299	24.026	75.288	0.302	0.623	nan	nan	nan	nan	nan	nan
C_4H(3-2,5/2-3/2)	28.57	29	-30.15	17.638	2.559	1.943	4.657	0.407	0.204	23.868	9.293	1.943	11.432	0.254	2.265
C_4H(3-2,5/2-3/2)	28.57	30	-28.84	0	0	0	0	0	0	nan	nan	nan	nan	nan	nan
C_4H(3-2,5/2-3/2)	28.57	31	-27.53	0	0	0	0	0	0	nan	nan	nan	nan	nan	nan
C_4H(3-2,5/2-3/2)	28.57	32	-26.21	0	0	0	0	0	0	nan	nan	nan	nan	nan	nan
C_4H(3-2,5/2-3/2)	28.57	33	-24.90	18.379	1.498	1.406	1.31	0.452	0.208	22.202	3.714	1.406	3.108	0.183	0.205
C_4H(3-2,5/2-3/2)	28.57	34	-23.59	15.783	3.465	2.361	3.185	0.394	0.209	21.947	8.674	2.361	7.826	0.175	0.224
C_4H(3-2,5/2-3/2)	28.57	35	-22.28	0	0	0	0	0	0	nan	nan	nan	nan	nan	nan
C_4H(3-2,5/2-3/2)	28.57	36	-20.97	0	0	0	0	0	0	nan	nan	nan	nan	nan	nan
C_4H(3-2,5/2-3/2)	28.57	37	-19.66	5	15.431	7.989	54.937	0.325	0.129	17.997	10.568	4.238	12.953	0.22	1.704
C_4H(3-2,7/2-5/2)	28.53	39	-32.74	0	0	0	0	0	0	nan	nan	nan	nan	nan	nan
C_4H(3-2,7/2-5/2)	28.53	40	-31.43	0	0	0	0	0	0	nan	nan	nan	nan	nan	nan
C_4H(3-2,7/2-5/2)	28.53	41	-30.11	20.014	1.634	4.394	1.775	0.281	0.084	nan	nan	nan	nan	nan	nan
C_4H(3-2,7/2-5/2)	28.53	42	-28.80	11.864	10.707	8.845	8.932	0.203	0.132	22.215	0.856	0.685	0.716	0.204	0.194
C_4H(3-2,7/2-5/2)	28.53	43	-27.49	17.259	4.291	2.089	4.316	0.279	0.182	24.413	24.334	2.089	9.544	0.293	2.019
C_4H(3-2,7/2-5/2)	28.53	44	-26.17	0.805	1.3	1.21	1.141	1.019	0.394	nan	nan	nan	nan	nan	nan
C_4H(3-2,7/2-5/2)	28.53	45	-24.86	16.049	0.616	1.272	0.633	0.395	0.162	21.513	0.797	1.272	0.825	0.288	0.155
C_4H(3-2,7/2-5/2)	28.53	46	-23.55	17.895	0.666	2.482	0.748	0.527	0.119	23.722	3.076	0.449	13.778	0.18	7.171
C_4H(3-2,7/2-5/2)	28.53	47	-22.23	16.635	0.527	1.402	0.606	0.662	0.19	22.762	42.991	1.402	17.579	0.326	5.483
C_4H(3-2,7/2-5/2)	28.53	48	-20.92	0	0	0	0	0	0	nan	nan	nan	nan	nan	nan
C_4H(3-2,7/2-5/2)	28.53	49	-19.61	16.044	2.368	7.11	4.096	0.413	0.093	nan	nan	nan	nan	nan	nan
C_6H(15/2-13/2,3/2,e)	20.79	100	-19.84	11.26	22.787	10.724	16.542	0.078	0.047	19.731	1.502	1.964	2.034	0.156	0.09
C_6H(15/2-13/2,3/2,e)	20.79	93	-32.46	16.129	41.419	3.574	20.98	0.128	1.157	22.393	23.629	3.574	8.182	0.222	1.326
C_6H(15/2-13/2,3/2,e)	20.79	94	-30.65	13.914	2.673	2.308	1.755	0.336	0.154	20.376	12.401	2.308	16.288	0.145	0.21
C_6H(15/2-13/2,3/2,e)	20.79	95	-28.85	7.266	11.287	5.41	26.468	0.215	0.228	20.646	77.456	5.41	38.751	0.041	0.304
C_6H(15/2-13/2,3/2,e)	20.79	96	-27.05	8.951	15.433	12.494	11.784	0.195	0.07	19.442	0.813	1.703	0.988	0.211	0.094

Table C.1 continued.

Transition	Restfreq	Ch	v_{ch}	R_{max} 1	ΔR_{max} 1	$W_{1/2}$ 1	$\Delta W_{1/2}$ 1	F_{max} 1	ΔF_{max} 1	R_{max} 2	ΔR_{max} 2	$W_{1/2}$ 2	$\Delta W_{1/2}$ 2	F_{max} 2	ΔF_{max} 2
C_6H(15/2-13/2,3/2,e)	20.79	97	-25.25	17.524	1.968	4.47	1.944	0.202	0.054	22.932	1.355	0.97	1.379	0.094	0.127
C_6H(15/2-13/2,3/2,e)	20.79	98	-23.45	16.04	1.009	5.965	1.068	0.367	0.052	nan	nan	nan	nan	nan	nan
C_6H(15/2-13/2,3/2,e)	20.79	99	-21.64	11.755	0.755	2.92	0.919	0.432	0.093	20.446	1.258	1.743	1.282	0.184	0.104
C_6H(15/2-13/2,3/2,f)	20.79	80	-33.39	15.577	0.941	4.606	1.266	0.4	0.066	25.579	2.184	1.432	2.883	0.089	0.109
C_6H(15/2-13/2,3/2,f)	20.79	81	-31.59	0	0	0	0	0	0	nan	nan	nan	nan	nan	nan
C_6H(15/2-13/2,3/2,f)	20.79	82	-29.78	14.803	0.906	4.931	1.034	0.4	0.061	nan	nan	nan	nan	nan	nan
C_6H(15/2-13/2,3/2,f)	20.79	83	-27.98	0	0	0	0	0	0	nan	nan	nan	nan	nan	nan
C_6H(15/2-13/2,3/2,f)	20.79	84	-26.18	11.29	6.945	12.267	6.979	0.179	0.039	nan	nan	nan	nan	nan	nan
C_6H(15/2-13/2,3/2,f)	20.79	85	-24.38	12.034	2.204	6.393	3.633	0.268	0.057	21.855	1.997	1.664	2.921	0.087	0.127
C_6H(15/2-13/2,3/2,f)	20.79	86	-22.58	10.667	4.22	8.185	3.861	0.18	0.048	19.687	1.193	-1.038	1.192	0.118	0.119
C_6H(15/2-13/2,3/2,f)	20.79	87	-20.77	12.619	0.78	3.638	0.979	0.472	0.08	26.021	2.693	3.618	3.261	0.139	0.07
C_6H(15/2-13/2,3/2,f)	20.79	88	-18.97	0	0	0	0	0	0	nan	nan	nan	nan	nan	nan
C_6H(17/2-15/2,1/2,e)	23.75	46	-32.11	14.472	0.679	3.348	0.731	0.48	0.081	nan	nan	nan	nan	nan	nan
C_6H(17/2-15/2,1/2,e)	23.75	47	-30.54	12.432	0.713	2.744	0.786	0.373	0.083	22.523	1.25	1.945	1.302	0.158	0.086
C_6H(17/2-15/2,1/2,e)	23.75	48	-28.96	-0.208	3.805	2.801	2.015	1.134	0.618	nan	nan	nan	nan	nan	nan
C_6H(17/2-15/2,1/2,e)	23.75	49	-27.38	4.749	14.875	17.377	11.276	0.265	0.072	nan	nan	nan	nan	nan	nan
C_6H(17/2-15/2,1/2,e)	23.75	50	-25.80	16.175	19.012	2.677	14.53	0.077	0.223	22.363	14.974	2.677	9.586	0.095	0.268
C_6H(17/2-15/2,1/2,e)	23.75	51	-24.22	18.996	8.964	10.706	10.276	0.074	0.038	nan	nan	nan	nan	nan	nan
C_6H(17/2-15/2,1/2,e)	23.75	52	-22.65	12.112	3.295	7.307	3.238	0.165	0.055	nan	nan	nan	nan	nan	nan
C_6H(17/2-15/2,1/2,e)	23.75	53	-21.07	10.632	3.048	4.396	3.984	0.146	0.071	26.073	1.977	3.414	2.517	0.146	0.066
C_6H(17/2-15/2,1/2,e)	23.75	54	-19.49	17.363	1.373	2.609	1.485	0.353	0.081	25.097	7.656	2.609	6.869	0.09	0.373
C_6H(17/2-15/2,3/2,e)	23.57	70	-32.46	13.511	0.459	1.431	0.469	0.398	0.112	nan	nan	nan	nan	nan	nan
C_6H(17/2-15/2,3/2,e)	23.57	71	-30.87	0	0	0	0	0	0	nan	nan	nan	nan	nan	nan
C_6H(17/2-15/2,3/2,e)	23.57	72	-29.28	9.202	9.145	9.98	6.954	0.195	0.066	nan	nan	nan	nan	nan	nan
C_6H(17/2-15/2,3/2,e)	23.57	73	-27.69	0	0	0	0	0	0	nan	nan	nan	nan	nan	nan
C_6H(17/2-15/2,3/2,e)	23.57	74	-26.10	1.663	20.696	15.561	15.043	0.291	0.129	nan	nan	nan	nan	nan	nan
C_6H(17/2-15/2,3/2,e)	23.57	75	-24.51	0.611	3.67	1.425	2.619	0.491	0.354	nan	nan	nan	nan	nan	nan
C_6H(17/2-15/2,3/2,e)	23.57	76	-22.92	11.868	5.957	3.1	4.948	0.21	0.131	21.145	16.641	3.1	19.72	0.175	0.244
C_6H(17/2-15/2,3/2,e)	23.57	77	-21.33	24.504	4.047	8.162	6.756	0.253	0.14	nan	nan	nan	nan	nan	nan
C_6H(17/2-15/2,3/2,e)	23.57	78	-19.74	-106.147	1333.313	36.115	205.235	47.115	2818.893	nan	nan	nan	nan	nan	nan
C_6H(17/2-15/2,3/2,f)	23.57	54	-32.20	5.716	0.617	2.126	0.636	0.52	0.117	22.16	1.224	2.126	1.337	0.182	0.09
C_6H(17/2-15/2,3/2,f)	23.57	55	-30.61	17.509	14.117	1.587	5.437	0.26	2.093	20.101	10.981	1.587	3.644	0.328	2.199
C_6H(17/2-15/2,3/2,f)	23.57	56	-29.02	7.577	10.462	4.876	13.629	0.182	0.642	21.739	7.074	4.876	5.141	0.168	0.087
C_6H(17/2-15/2,3/2,f)	23.57	57	-27.43	2.486	0.512	1.886	0.482	0.879	0.154	nan	nan	nan	nan	nan	nan
C_6H(17/2-15/2,3/2,f)	23.57	58	-25.84	4.254	0.949	1.69	1	0.305	0.118	nan	nan	nan	nan	nan	nan
C_6H(17/2-15/2,3/2,f)	23.57	59	-24.25	15.513	0.581	1.958	0.668	0.345	0.084	23.082	4.541	1.958	4.873	0.052	0.088
C_6H(17/2-15/2,3/2,f)	23.57	60	-22.66	-12.875	132.592	20.637	55.285	0.246	0.899	nan	nan	nan	nan	nan	nan
C_6H(17/2-15/2,3/2,f)	23.57	61	-21.07	0	0	0	0	0	0	nan	nan	nan	nan	nan	nan
C_6H(17/2-15/2,3/2,f)	23.57	62	-19.48	13.058	0.974	2.654	1.182	0.307	0.091	21.354	1.217	1.959	1.704	0.23	0.097
C_6H(19/2-17/2,3/2,e)	26.34	73	-32.47	15.89	1.504	4.179	1.811	0.333	0.069	21.631	2.569	-0.592	2.102	0.13	0.216
C_6H(19/2-17/2,3/2,e)	26.34	74	-31.04	14.661	24.647	3.741	9.888	0.377	2.096	21.438	59.782	3.741	33.729	0.152	1.876
C_6H(19/2-17/2,3/2,e)	26.34	75	-29.62	16.403	0.653	1.77	0.733	0.259	0.081	23.485	2.18	1.77	1.942	0.085	0.086

Table C.1 continued.

Transition	Restfreq	Ch	v_{ch}	R_{max} 1	ΔR_{max} 1	$W_{1/2}$ 1	$\Delta W_{1/2}$ 1	F_{max} 1	ΔF_{max} 1	R_{max} 2	ΔR_{max} 2	$W_{1/2}$ 2	$\Delta W_{1/2}$ 2	F_{max} 2	ΔF_{max} 2
C_6H(19/2-17/2,3/2,e)	26.34	76	-28.20	16.785	1.056	3.568	1.403	0.366	0.077	24.863	1.159	0.935	1.351	0.121	0.137
C_6H(19/2-17/2,3/2,e)	26.34	77	-26.78	13.816	2.267	6.666	2.819	0.297	0.067	nan	nan	nan	nan	nan	nan
C_6H(19/2-17/2,3/2,e)	26.34	78	-25.35	7.117	3.598	3.3	3.408	0.343	0.108	19.484	1.301	3.3	1.706	0.274	0.08
C_6H(19/2-17/2,3/2,e)	26.34	79	-23.93	17.261	3.799	3.835	3.492	0.356	0.089	22.234	3.057	1.534	6.784	0.07	0.414
C_6H(19/2-17/2,3/2,e)	26.34	80	-22.51	15.206	1.34	2.881	1.615	0.26	0.083	23.33	1.062	2.097	1.097	0.264	0.088
C_6H(19/2-17/2,3/2,e)	26.34	81	-21.08	15.008	2.861	3.322	2.676	0.185	0.071	24.251	5.8	3.322	5.176	0.089	0.066
C_6H(19/2-17/2,3/2,e)	26.34	82	-19.66	14.232	0.75	3.051	1.004	0.504	0.098	20.463	0.73	0.969	0.895	0.256	0.163
C_6H(19/2-17/2,3/2,f)	26.34	53	-32.23	14.545	1.812	7.164	2.129	0.274	0.054	nan	nan	nan	nan	nan	nan
C_6H(19/2-17/2,3/2,f)	26.34	54	-30.81	15.863	3.215	5.324	2.783	0.184	0.051	nan	nan	nan	nan	nan	nan
C_6H(19/2-17/2,3/2,f)	26.34	55	-29.39	15.247	0.764	2.138	0.824	0.441	0.096	21.952	1.317	2.138	1.385	0.249	0.09
C_6H(19/2-17/2,3/2,f)	26.34	56	-27.97	16.855	1.36	2.069	1.114	0.38	0.098	22.616	3.047	2.069	5.044	0.132	0.086
C_6H(19/2-17/2,3/2,f)	26.34	57	-26.54	15.267	1.207	1.552	1.114	0.285	0.101	19.627	0.9	1.552	0.788	0.379	0.099
C_6H(19/2-17/2,3/2,f)	26.34	58	-25.12	0	0	0	0	0	0	nan	nan	nan	nan	nan	nan
C_6H(19/2-17/2,3/2,f)	26.34	59	-23.70	5	8.947	9.076	35.095	0.238	0.073	18.76	5.374	3.839	18.547	0.082	0.668
C_6H(19/2-17/2,3/2,f)	26.34	60	-22.28	16.293	1.515	4.743	1.663	0.214	0.057	nan	nan	nan	nan	nan	nan
C_6H(19/2-17/2,3/2,f)	26.34	61	-20.85	15.998	0.752	3.476	0.819	0.387	0.071	nan	nan	nan	nan	nan	nan
C_6H(19/2-17/2,3/2,f)	26.34	62	-19.43	16.265	4.148	2.477	2.667	0.382	0.315	21.725	3.329	2.477	1.867	0.481	0.342

Table C.2: List of Gaussian fit results from the radial emission profiles of each transition (restfrequency in GHz) of each channel (velocity in km s^{-1}) with $\Delta v < 7.5$ km s^{-1} for quarter Q1. The fit parameters are shell radius at maximum flux R_{max} (in arcsec), half shell width $W_{1/2}$ (in arcsec), and maximum flux F_{max} (in mJy $beam^{-1}$) for two components and their uncertainties determined from the least square fit routine.

Transition	Restfreq	Ch	v_{ch}	R_{max} 1	ΔR_{max} 1	$W_{1/2}$ 1	$\Delta W_{1/2}$ 1	F_{max} 1	ΔF_{max} 1	R_{max} 2	ΔR_{max} 2	$W_{1/2}$ 2	$\Delta W_{1/2}$ 2	F_{max} 2	ΔF_{max} 2
HC_3N(2-1)	18.20	79	-33.40	15.243	1.615	5.961	1.637	1.847	0.431	nan	nan	nan	nan	nan	nan
HC_3N(2-1)	18.20	80	-31.34	15.437	1.601	5.922	1.621	1.546	0.36	nan	nan	nan	nan	nan	nan
HC_3N(2-1)	18.20	81	-29.28	15.412	1.873	5.488	2.13	1.448	0.364	25.336	5.879	1.373	6.773	0.191	0.756
HC_3N(2-1)	18.20	82	-27.22	15.062	1.655	5.364	1.903	1.492	0.355	25.715	9.608	1.55	10.492	0.122	0.666
HC_3N(2-1)	18.20	83	-25.16	14.837	1.579	5.051	1.8	1.467	0.367	25.21	4.184	1.392	4.499	0.265	0.695
HC_3N(2-1)	18.20	84	-23.10	15.263	1.389	4.462	1.577	1.623	0.389	25.676	4.766	1.956	4.861	0.3	0.576
HC_3N(2-1)	18.20	85	-21.04	14.536	2.19	7.915	2.361	1.496	0.35	nan	nan	nan	nan	nan	nan
HC_3N(2-1)	18.20	86	-18.99	13.384	2.082	7.896	2.252	1.941	0.425	nan	nan	nan	nan	nan	nan
HC_3N(3-2)	27.29	85	-32.30	14.577	4.984	3.094	3.113	3.779	2.762	22.005	21.569	3.094	19.961	0.797	2.207
HC_3N(3-2)	27.29	86	-30.93	14.986	1.311	3.753	1.552	2.949	0.856	23.738	4.316	1.31	4.828	0.52	1.42
HC_3N(3-2)	27.29	87	-29.55	15.353	1.075	3.07	1.15	2.873	0.869	23.81	2.783	1.041	2.815	0.641	1.448
HC_3N(3-2)	27.29	88	-28.18	15.354	0.897	2.89	0.959	2.904	0.777	23.552	2.793	1.158	2.963	0.593	1.204
HC_3N(3-2)	27.29	89	-26.81	15.281	0.802	2.663	0.823	3.319	0.866	23.837	3.393	1.086	3.429	0.496	1.331
HC_3N(3-2)	27.29	90	-25.44	15.469	0.748	2.739	0.762	3.289	0.778	24.404	6.161	-1.028	6.41	0.243	1.259
HC_3N(3-2)	27.29	91	-24.06	15.3	0.659	2.492	0.671	3.534	0.81	24.223	4.216	1.281	4.256	0.391	1.11
HC_3N(3-2)	27.29	92	-22.69	15.456	0.696	2.551	0.724	3.579	0.845	23.393	4.205	1.144	4.263	0.395	1.233
HC_3N(3-2)	27.29	93	-21.32	15.441	0.899	2.937	1	3.893	0.98	23.259	6.073	1.427	6.644	0.405	1.377
HC_3N(3-2)	27.29	94	-19.94	15.365	0.845	2.835	0.919	4.165	1.054	23.224	5.695	1.284	5.997	0.418	1.529
HC_3N(3-2)	27.29	95	-18.57	15.114	1.187	3.035	1.324	4.686	1.299	22.565	7.469	1.677	7.615	0.54	1.736
HC_3N(4-3)	36.39	31	-32.65	15.815	1.176	2.82	1.209	3.652	1.32	23.92	3.651	0.784	3.857	0.621	2.502
HC_3N(4-3)	36.39	32	-31.62	15.747	1.351	3.082	1.361	3.09	1.172	nan	nan	nan	nan	nan	nan
HC_3N(4-3)	36.39	33	-30.59	15.986	1.754	3.38	1.862	2.321	1.023	nan	nan	nan	nan	nan	nan
HC_3N(4-3)	36.39	34	-29.56	16.18	1.993	3.501	2.256	2.161	1.008	nan	nan	nan	nan	nan	nan
HC_3N(4-3)	36.39	35	-28.53	16.313	2.259	3.768	2.742	1.883	0.843	nan	nan	nan	nan	nan	nan
HC_3N(4-3)	36.39	36	-27.50	16.226	1.992	3.835	2.359	2.104	0.802	nan	nan	nan	nan	nan	nan
HC_3N(4-3)	36.39	37	-26.47	16.243	2.191	3.678	2.609	1.924	0.918	nan	nan	nan	nan	nan	nan
HC_3N(4-3)	36.39	38	-25.44	16.138	1.787	3.19	2.046	2.094	0.992	nan	nan	nan	nan	nan	nan
HC_3N(4-3)	36.39	39	-24.41	15.325	1.982	3.615	2.436	2.143	0.976	nan	nan	nan	nan	nan	nan
HC_3N(4-3)	36.39	40	-23.38	17.411	1.062	1.396	1.197	2.575	1.549	23.125	nan	0.661	nan	0	nan
HC_3N(4-3)	36.39	41	-22.35	15.53	1.126	2.423	1.139	2.931	1.18	23.044	9.427	0.58	8.59	0.176	2.285
HC_3N(4-3)	36.39	42	-21.32	15.842	0.875	2.161	0.883	3.636	1.276	22.786	6.504	0.556	5.467	0.261	2.321
HC_3N(4-3)	36.39	43	-20.30	15.67	1.136	2.609	1.149	3.368	1.271	nan	nan	nan	nan	nan	nan
HC_3N(4-3)	36.39	44	-19.27	15.702	2.59	2.218	2.106	4.203	1.695	20.309	11.166	1.55	8.303	0.675	3.365
HC_5N(8-7)	21.30	61	-33.29	16.974	3.437	5.409	2.966	0.952	0.284	23.598	5.487	1.414	7.776	0.161	0.75
HC_5N(8-7)	21.30	62	-31.53	17.18	2.819	5.65	2.436	0.903	0.238	24.27	4.688	1.408	6.36	0.162	0.59
HC_5N(8-7)	21.30	63	-29.77	17.406	2.949	4.066	2.799	0.869	0.266	24.911	3.379	2.005	3.376	0.368	0.599
HC_5N(8-7)	21.30	64	-28.01	16.662	1.417	3.48	1.587	0.954	0.281	24.727	2.756	1.665	2.768	0.322	0.406
HC_5N(8-7)	21.30	65	-26.25	16.438	1.397	3.315	1.563	0.896	0.28	24.827	2.514	1.845	2.494	0.366	0.363

Table C.2 continued.

Transition	Restfreq	Ch	v_{ch}	R_{max} 1	ΔR_{max} 1	$W_{1/2}$ 1	$\Delta W_{1/2}$ 1	F_{max} 1	ΔF_{max} 1	R_{max} 2	ΔR_{max} 2	$W_{1/2}$ 2	$\Delta W_{1/2}$ 2	F_{max} 2	ΔF_{max} 2
HC_5N(8-7)	21.30	66	-24.49	16.165	1.351	3.63	1.52	0.968	0.272	24.886	3.5	1.756	3.509	0.252	0.382
HC_5N(8-7)	21.30	67	-22.73	16.038	1.974	2.716	1.746	1.001	0.33	23.629	4.76	2.716	4.168	0.413	0.327
HC_5N(8-7)	21.30	68	-20.98	16.272	2.12	3.546	2.07	1.075	0.303	24.015	3.905	2.196	3.4	0.402	0.485
HC_5N(8-7)	21.30	69	-19.22	16.273	2.834	3.337	2.355	1.222	0.382	23.928	7.784	2.644	5.809	0.363	0.581
HC_5N(9-8)	23.96	51	-31.95	16.437	1.664	3.22	1.875	1.075	0.307	23.703	2.441	1.921	2.258	0.522	0.448
HC_5N(9-8)	23.96	52	-30.39	16.805	1.146	3.312	1.306	1.035	0.27	24.488	1.73	1.469	1.992	0.439	0.405
HC_5N(9-8)	23.96	53	-28.82	16.66	0.916	2.866	1.035	1.122	0.285	24.323	2.231	1.563	2.396	0.34	0.373
HC_5N(9-8)	23.96	54	-27.26	16.341	0.906	3.096	0.989	1.094	0.271	24.616	2.316	1.328	2.36	0.278	0.398
HC_5N(9-8)	23.96	55	-25.69	16.277	0.816	2.762	0.899	1.099	0.268	24.433	2.934	1.662	3.1	0.237	0.333
HC_5N(9-8)	23.96	56	-24.13	16.049	0.699	2.461	0.755	1.223	0.293	24.108	2.836	1.667	3.203	0.251	0.351
HC_5N(9-8)	23.96	57	-22.57	16.286	1.342	2.402	1.196	1.25	0.317	23.09	4.73	2.402	4.663	0.344	0.312
HC_5N(9-8)	23.96	58	-21.00	16.496	1.09	2.96	1.174	1.335	0.3	23.536	2.822	1.78	2.768	0.378	0.401
HC_5N(9-8)	23.96	59	-19.44	16.399	1.043	2.738	1.104	1.48	0.338	23.569	3.275	1.97	3.31	0.388	0.398
HC_5N(10-9)	26.63	38	-32.78	16.884	2.061	3.306	2.728	1.057	0.426	24.045	3.006	1.677	2.899	0.476	0.649
HC_5N(10-9)	26.63	39	-31.38	16.742	1.327	2.886	1.561	0.982	0.374	24.316	1.483	1.398	1.494	0.607	0.505
HC_5N(10-9)	26.63	40	-29.97	17.062	1.29	2.683	1.521	1.071	0.409	24.476	1.742	1.623	1.753	0.621	0.493
HC_5N(10-9)	26.63	41	-28.56	16.94	0.818	2.223	0.904	1.332	0.4	23.899	1.814	1.572	1.883	0.505	0.455
HC_5N(10-9)	26.63	42	-27.16	16.969	0.848	2.304	0.916	1.211	0.379	24.206	2.227	1.372	2.299	0.353	0.473
HC_5N(10-9)	26.63	43	-25.75	16.136	0.64	1.864	0.651	1.386	0.412	24.513	3.278	1.415	3.641	0.246	0.474
HC_5N(10-9)	26.63	44	-24.34	16.508	0.901	1.909	0.993	1.201	0.422	23.118	2.851	1.909	3.024	0.376	0.411
HC_5N(10-9)	26.63	45	-22.93	16.121	1.678	2.302	1.815	1.269	0.415	22.528	7.122	2.302	5.944	0.319	0.418
HC_5N(10-9)	26.63	46	-21.53	16.005	1.071	2.167	1.147	1.322	0.447	23.176	3.103	2.167	3.37	0.45	0.44
HC_5N(10-9)	26.63	47	-20.12	16.086	1.223	2.346	1.261	1.551	0.443	23.312	7.901	2.346	10.064	0.225	0.449
HC_5N(10-9)	26.63	48	-18.71	15.539	1.399	2.487	1.525	1.542	0.532	23.313	4.8	2.487	4.774	0.455	0.513
HC_5N(11-10)	29.29	19	-32.39	16.912	2.7	3.507	3.71	0.702	0.368	23.246	1.677	1.145	1.973	0.496	0.725
HC_5N(11-10)	29.29	20	-31.11	17.104	2.076	2.817	2.581	0.559	0.332	23.638	2.006	1.138	2.057	0.351	0.499
HC_5N(11-10)	29.29	21	-29.83	16.803	1.912	2.667	2.217	0.532	0.324	23.623	1.86	1.043	1.868	0.334	0.486
HC_5N(11-10)	29.29	22	-28.55	17.146	0.962	1.825	1.007	0.799	0.364	23.77	1.456	0.616	3.592	0.259	1.205
HC_5N(11-10)	29.29	23	-27.27	16.863	1.078	1.431	1.086	0.592	0.385	23.636	1.936	0.967	2.474	0.323	0.503
HC_5N(11-10)	29.29	24	-25.99	16.687	0.979	1.654	0.989	0.719	0.367	22.903	6.709	0.891	6.388	0.076	0.477
HC_5N(11-10)	29.29	25	-24.71	16.57	1.127	1.542	1.23	0.695	0.411	22.83	20.611	1.542	15.44	0.068	0.538
HC_5N(11-10)	29.29	26	-23.43	16.621	0.811	1.243	0.821	0.676	0.381	nan	nan	nan	nan	nan	nan
HC_5N(11-10)	29.29	27	-22.15	16.564	1.117	1.711	1.141	0.739	0.416	22.59	4.646	0.956	4.581	0.131	0.54
HC_5N(11-10)	29.29	28	-20.87	16.197	1.567	1.794	1.369	1.185	0.413	20.51	10.953	1.455	8.615	0.144	0.556
HC_5N(11-10)	29.29	29	-19.60	16.56	1.15	1.956	1.273	0.949	0.377	23.048	12.974	1.956	16.403	0.081	0.377
HC_5N(12-11)	31.95	36	-32.38	16.009	1.472	2.896	1.62	1.313	0.549	nan	nan	nan	nan	nan	nan
HC_5N(12-11)	31.95	37	-31.21	14.227	1.096	1.264	1.136	1.314	0.734	18.338	1.128	1.264	1.311	1.237	0.74
HC_5N(12-11)	31.95	38	-30.04	18.215	2.181	2.51	2.152	1.228	0.485	24.936	5.712	0.662	4.805	0.13	0.872
HC_5N(12-11)	31.95	39	-28.86	17.339	1.782	2.938	2.008	1.189	0.493	nan	nan	nan	nan	nan	nan
HC_5N(12-11)	31.95	40	-27.69	17.181	1.445	2.592	1.673	1.109	0.458	nan	nan	nan	nan	nan	nan
HC_5N(12-11)	31.95	41	-26.52	16.216	1.08	2.579	1.266	1.292	0.453	nan	nan	nan	nan	nan	nan
HC_5N(12-11)	31.95	42	-25.34	17.044	0.524	0.983	0.531	1.497	0.689	23	nan	0.492	0	0.898	nan

Table C.2 continued.

Transition	Restfreq	Ch	v_{ch}	R_{max} 1	ΔR_{max} 1	$W_{1/2}$ 1	$\Delta W_{1/2}$ 1	F_{max} 1	ΔF_{max} 1	R_{max} 2	ΔR_{max} 2	$W_{1/2}$ 2	$\Delta W_{1/2}$ 2	F_{max} 2	ΔF_{max} 2
HC_5N(12-11)	31.95	43	-24.17	16.122	0.949	2.038	0.989	1.262	0.51	nan	nan	nan	nan	nan	nan
HC_5N(12-11)	31.95	44	-23.00	16.182	0.765	1.831	0.804	1.469	0.533	nan	nan	nan	nan	nan	nan
HC_5N(12-11)	31.95	45	-21.83	15.778	2.965	2.035	2.061	1.504	0.91	21.166	10.05	2.035	11.953	0.462	1.819
HC_5N(12-11)	31.95	46	-20.65	15.892	1.333	2.08	1.409	1.79	0.552	22.183	23.06	2.08	37.31	0.092	0.566
HC_5N(12-11)	31.95	47	-19.48	16.122	0.867	2.315	0.889	1.835	0.595	nan	nan	nan	nan	nan	nan
HC_5N(13-12)	34.61	31	-33.44	16.524	2.578	2.174	2.465	0.756	0.453	23.26	10.068	2.174	16.985	0.173	0.48
HC_5N(13-12)	34.61	32	-32.35	16.115	2.144	2.885	2.426	0.594	0.343	23.436	2.774	0.741	3.242	0.195	0.678
HC_5N(13-12)	34.61	33	-31.27	16.265	3.171	2.996	4.643	0.494	0.375	23.378	2.89	0.971	3.167	0.235	0.611
HC_5N(13-12)	34.61	34	-30.19	16.766	2.616	2.665	3.21	0.371	0.305	24.804	14.52	1.263	13.773	0.112	0.422
HC_5N(13-12)	34.61	35	-29.11	17.381	1.418	1.524	1.464	0.558	0.45	24.423	3.996	0.749	4.342	0.14	0.632
HC_5N(13-12)	34.61	36	-28.02	16.292	4.689	2.705	7.965	0.296	0.338	25.326	41.775	2.705	30.536	0.059	0.475
HC_5N(13-12)	34.61	37	-26.94	17.365	1.292	1.26	1.315	0.481	0.426	25.25	nan	0.216	nan	0.078	nan
HC_5N(13-12)	34.61	38	-25.86	17.005	1.591	1.868	1.895	0.504	0.319	nan	nan	nan	nan	nan	nan
HC_5N(13-12)	34.61	39	-24.78	16.892	0.999	-0.748	1.046	0.463	0.545	29.074	54.747	-4.996	64.898	0.046	0.437
HC_5N(13-12)	34.61	40	-23.69	16.381	0.97	1.107	1.046	0.544	0.417	nan	nan	nan	nan	nan	nan
HC_5N(13-12)	34.61	41	-22.61	15.976	1.763	1.275	1.856	0.426	0.511	22.913	34.083	0.355	13.57	0.045	0.657
HC_5N(13-12)	34.61	42	-21.53	16.416	0.988	1.585	1.018	0.711	0.386	23.012	3.901	0.459	12.22	0.147	3.874
HC_5N(13-12)	34.61	43	-20.45	16.539	0.925	1.698	0.942	0.799	0.378	22.283	4.512	0.644	3.486	0.108	0.543
HC_5N(13-12)	34.61	44	-19.36	16.539	0.953	1.737	1.044	0.892	0.422	nan	nan	nan	nan	nan	nan
HC_5N(14-13)	37.28	40	-33.32	15.913	3.301	2.562	2.562	2.454	1.219	22.865	11.253	2.562	17.594	0.57	1.026
HC_5N(14-13)	37.28	41	-32.31	15.855	2.925	2.459	2.676	1.823	0.948	22.993	17.095	2.459	24.424	0.272	0.95
HC_5N(14-13)	37.28	42	-31.31	17.02	1.283	2.553	1.321	1.932	0.842	24.653	2.096	0.852	2.127	0.678	1.432
HC_5N(14-13)	37.28	43	-30.30	16.943	1.842	2.858	2.172	1.42	0.774	24.883	8.725	1.041	11.287	0.209	1.332
HC_5N(14-13)	37.28	44	-29.30	17.678	1.589	2.26	1.772	1.502	0.866	24.42	3.457	0.862	4.055	0.428	1.418
HC_5N(14-13)	37.28	45	-28.29	17.602	1.655	2.222	1.82	1.406	0.897	24.975	3.046	1.19	3.264	0.553	1.204
HC_5N(14-13)	37.28	46	-27.29	17.411	1.504	2.368	1.573	1.422	0.768	25.386	3.475	0.896	3.655	0.369	1.233
HC_5N(14-13)	37.28	47	-26.28	17.089	1.969	2.66	2.27	1.459	0.829	26.236	23.382	1.516	21.846	0.239	1.139
HC_5N(14-13)	37.28	48	-25.28	16.792	1.509	2.316	1.672	1.417	0.777	24.835	3.236	0.748	3.522	0.355	1.342
HC_5N(14-13)	37.28	49	-24.27	16.271	1.178	2.147	1.265	1.847	0.879	24.693	7.904	0.694	8.319	0.155	1.516
HC_5N(14-13)	37.28	50	-23.27	16.588	1.286	2.116	1.327	1.661	0.877	23.275	7.422	0.649	7.217	0.158	1.532
HC_5N(14-13)	37.28	51	-22.26	16.188	1.243	2.314	1.333	1.894	0.871	24.097	5.744	1.575	6.211	0.34	1.04
HC_5N(14-13)	37.28	52	-21.26	16.132	1.218	1.776	1.338	2.085	0.98	22.091	7.375	1.776	9.453	0.337	1
HC_5N(14-13)	37.28	53	-20.25	16.532	1.232	2.471	1.297	2.17	0.931	nan	nan	nan	nan	nan	nan
HC_5N(14-13)	37.28	54	-19.25	16.098	2.053	2.01	1.834	2.388	1.074	21.722	9.718	2.01	9.271	0.494	1.063
HC_7N(16-15)	18.05	48	-31.42	18.391	12.911	6.655	10.294	0.259	0.135	27.064	2.376	2.735	4.871	0.234	0.557
HC_7N(16-15)	18.05	49	-29.34	14.919	14.006	10.338	11.253	0.148	0.102	23.707	1.493	1.332	1.685	0.219	0.227
HC_7N(16-15)	18.05	50	-27.27	14.57	31.282	9.382	36.263	0.178	0.125	22.211	2.914	1.784	5.24	0.194	0.639
HC_7N(16-15)	18.05	51	-25.19	13.131	2.357	4.389	3.12	0.329	0.146	28.182	4.805	1.688	5.016	0.079	0.195
HC_7N(16-15)	18.05	52	-23.12	14.928	4.911	3.487	5.443	0.324	0.181	23.797	11.915	3.487	8.189	0.145	0.211
HC_7N(16-15)	18.05	53	-21.04	17.011	8.386	9.254	9.163	0.221	0.104	25.956	2.184	-1.454	3.017	0.171	0.265
HC_7N(16-15)	18.05	54	-18.96	7.881	670.79	70.448	3160.548	0.18	0.115	nan	nan	nan	nan	nan	nan
HC_7N(17-16)	19.18	71	-32.17	19.328	2.414	6.568	2.681	0.236	0.074	nan	nan	nan	nan	nan	nan

Table C.2 continued.

Transition	Restfreq	Ch	v_{ch}	R_{max} 1	ΔR_{max} 1	$W_{1/2}$ 1	$\Delta W_{1/2}$ 1	F_{max} 1	ΔF_{max} 1	R_{max} 2	ΔR_{max} 2	$W_{1/2}$ 2	$\Delta W_{1/2}$ 2	F_{max} 2	ΔF_{max} 2
HC_7N(17-16)	19.18	72	-30.22	16.596	7.844	6.214	6.298	0.146	0.085	23.176	2.182	1.64	3.259	0.128	0.21
HC_7N(17-16)	19.18	73	-28.27	16.861	19.649	5.788	7.888	0.197	0.447	22.456	7.501	3.168	14.095	0.089	0.773
HC_7N(17-16)	19.18	74	-26.31	17.155	2.718	4.96	2.75	0.17	0.08	nan	nan	nan	nan	nan	nan
HC_7N(17-16)	19.18	75	-24.36	16.198	1.019	1.927	1.104	0.28	0.114	23.08	2.612	1.927	2.777	0.106	0.11
HC_7N(17-16)	19.18	76	-22.40	18.878	3.739	3.495	2.907	0.267	0.113	23.114	10.631	1.057	20.206	0.021	0.302
HC_7N(17-16)	19.18	77	-20.45	19.104	3.349	4.896	2.752	0.228	0.095	23.932	4.904	1.112	7.285	0.044	0.199
HC_7N(18-17)	20.30	71	-33.16	16.712	2.304	1.514	2.359	0.87	1.146	nan	nan	nan	nan	nan	nan
HC_7N(18-17)	20.30	72	-31.31	0	0	0	0	0	0	nan	nan	nan	nan	nan	nan
HC_7N(18-17)	20.30	73	-29.46	14.466	8.359	3.28	9.283	0.379	0.558	24.412	7.118	3.28	7.191	0.438	0.5
HC_7N(18-17)	20.30	74	-27.62	10.989	2.76	3.358	3.848	0.953	0.613	24.884	5.369	3.358	5.627	0.661	0.498
HC_7N(18-17)	20.30	75	-25.77	17.014	2.111	1.858	2.272	0.879	0.795	24.584	28.516	1.858	24.142	0.131	0.773
HC_7N(18-17)	20.30	76	-23.93	12.034	9.691	7.648	16.478	0.731	0.778	26.097	1.634	1.352	2.182	0.847	1.157
HC_7N(18-17)	20.30	77	-22.08	16.568	3.745	2.138	4.676	0.488	0.643	24.064	2.181	2.138	2.305	0.783	0.581
HC_7N(18-17)	20.30	78	-20.24	18.963	17.047	16.366	35.698	0.571	0.444	nan	nan	nan	nan	nan	nan
HC_7N(19-18)	21.43	40	-32.60	18.149	3.498	7.546	4.596	0.241	0.082	nan	nan	nan	nan	nan	nan
HC_7N(19-18)	21.43	41	-30.85	16.981	5.37	2.587	4.73	0.171	0.131	22.749	3.597	1.924	2.708	0.197	0.218
HC_7N(19-18)	21.43	42	-29.10	17.54	1.626	1.935	1.764	0.187	0.132	23.789	2.114	1.245	2.669	0.121	0.166
HC_7N(19-18)	21.43	43	-27.35	17.636	4.234	2.176	3.77	0.199	0.153	23.502	6.311	2.056	7.376	0.117	0.156
HC_7N(19-18)	21.43	44	-25.61	17.057	1.627	2.399	1.731	0.26	0.119	25.091	2.526	2.399	3.236	0.159	0.119
HC_7N(19-18)	21.43	45	-23.86	15.968	3.84	2.737	4.467	0.135	0.116	24.474	5.408	2.737	5.319	0.097	0.108
HC_7N(19-18)	21.43	46	-22.11	16.94	3.035	2.514	2.64	0.27	0.143	23.837	4.209	2.514	3.532	0.194	0.141
HC_7N(19-18)	21.43	47	-20.36	17.028	1.809	2.654	1.922	0.318	0.13	23.86	2.661	1.878	2.471	0.177	0.153
HC_7N(19-18)	21.43	48	-18.61	17.87	1.745	4.782	1.765	0.317	0.099	nan	nan	nan	nan	nan	nan
HC_7N(20-19)	22.56	50	-33.38	18.196	4.487	5.537	3.974	0.239	0.114	24.126	3.033	1.179	4.482	0.1	0.262
HC_7N(20-19)	22.56	51	-31.72	15.704	4.638	2.564	3.453	0.297	0.219	22.053	5.434	2.564	3.823	0.254	0.225
HC_7N(20-19)	22.56	52	-30.06	17.067	3.351	2.939	3.101	0.306	0.132	23.594	4.134	2.121	3.146	0.188	0.224
HC_7N(20-19)	22.56	53	-28.40	16.411	2.279	2.889	2.337	0.319	0.136	24.063	4.559	2.306	4.131	0.14	0.152
HC_7N(20-19)	22.56	54	-26.74	17.512	1.605	2.124	1.638	0.304	0.137	24.14	5.142	2.124	5.302	0.093	0.134
HC_7N(20-19)	22.56	55	-25.08	16.091	2.364	3.253	2.893	0.273	0.124	24.248	2.618	2.181	2.404	0.202	0.148
HC_7N(20-19)	22.56	56	-23.42	17.908	2.817	2.771	3.461	0.23	0.127	24.141	3.776	1.689	3.384	0.126	0.188
HC_7N(20-19)	22.56	57	-21.76	16.015	1.222	2.243	1.347	0.367	0.147	22.633	2.357	1.696	2.391	0.164	0.16
HC_7N(20-19)	22.56	58	-20.09	16.219	1.334	3.257	1.52	0.4	0.129	26.158	2.857	2.384	3.347	0.157	0.142
HC_7N(22-21)	24.82	49	-33.40	17.857	3.742	3.092	3.288	0.254	0.11	23.761	2.979	1.785	2.761	0.172	0.255
HC_7N(22-21)	24.82	50	-31.89	15.349	8.92	2.919	5.204	0.306	0.522	21.453	13.442	2.919	6.883	0.204	0.562
HC_7N(22-21)	24.82	51	-30.38	16.553	2.092	3.016	2.724	0.21	0.101	23.386	1.568	1.541	1.556	0.187	0.14
HC_7N(22-21)	24.82	52	-28.87	16.803	2.23	3.438	2.555	0.185	0.096	24.711	2.177	1.338	2.34	0.111	0.147
HC_7N(22-21)	24.82	53	-27.36	17.434	1.23	2.497	1.417	0.33	0.127	23.961	3.956	1.389	3.934	0.076	0.159
HC_7N(22-21)	24.82	54	-25.85	17.646	1.809	2.551	2.142	0.249	0.109	23.641	4.719	1.47	5.95	0.067	0.145
HC_7N(22-21)	24.82	55	-24.34	16.989	1.389	1.829	1.487	0.287	0.141	22.844	6.45	1.829	6.751	0.061	0.135
HC_7N(22-21)	24.82	56	-22.83	17.192	2.029	2.51	2.608	0.252	0.12	23.074	2.929	1.509	3.699	0.125	0.16
HC_7N(22-21)	24.82	57	-21.32	16.996	2.983	2.226	2.131	0.384	0.215	22.49	5.187	2.226	3.831	0.219	0.209
HC_7N(22-21)	24.82	58	-19.81	16.945	1.546	2.516	1.447	0.403	0.114	23.852	4.564	2.329	4.363	0.127	0.118

Table C.2 continued.

Transition	Restfreq	Ch	v_{ch}	R_{max} 1	ΔR_{max} 1	$W_{1/2}$ 1	$\Delta W_{1/2}$ 1	F_{max} 1	ΔF_{max} 1	R_{max} 2	ΔR_{max} 2	$W_{1/2}$ 2	$\Delta W_{1/2}$ 2	F_{max} 2	ΔF_{max} 2
HC_7N(23-22)	25.94	30	-33.10	16.897	2.977	3.719	3.359	0.309	0.136	23.988	2.065	1.63	2.188	0.223	0.26
HC_7N(23-22)	25.94	31	-31.65	17.524	1.91	3.873	2.212	0.296	0.113	24.418	2.352	0.818	2.167	0.103	0.243
HC_7N(23-22)	25.94	32	-30.21	19.464	3.915	6.569	5.421	0.206	0.098	nan	nan	nan	nan	nan	nan
HC_7N(23-22)	25.94	33	-28.77	18.232	1.887	3.105	2.128	0.32	0.132	24.019	1.8	1.012	2.037	0.153	0.255
HC_7N(23-22)	25.94	34	-27.32	17.419	1.644	2.986	1.954	0.256	0.119	24.624	1.834	0.603	4.915	0.127	0.955
HC_7N(23-22)	25.94	35	-25.88	16.556	1.074	2.826	1.183	0.397	0.129	25.512	3.398	1.635	3.547	0.093	0.16
HC_7N(23-22)	25.94	36	-24.43	16.174	1.098	2.217	1.18	0.323	0.137	23.966	3.678	1.652	3.824	0.081	0.15
HC_7N(23-22)	25.94	37	-22.99	16.352	1.119	1.957	1.215	0.304	0.145	23.92	3.955	1.957	4.34	0.091	0.14
HC_7N(23-22)	25.94	38	-21.54	18.134	1.843	2.354	1.95	0.343	0.156	23.563	2.098	1.403	1.966	0.214	0.216
HC_7N(23-22)	25.94	39	-20.10	17.045	1.686	2.022	1.583	0.414	0.167	22.788	2.295	1.946	2.2	0.292	0.169
HC_7N(23-22)	25.94	40	-18.66	16.683	4.406	2.912	3.361	0.398	0.232	23.714	6.226	2.791	4.415	0.271	0.266
HC_7N(24-23)	27.07	39	-32.74	21.73	2.747	3.443	2.753	0.207	0.143	nan	nan	nan	nan	nan	nan
HC_7N(24-23)	27.07	40	-31.35	5	39.444	12.414	36.307	0.166	0.186	22.051	3.655	3.511	5.439	0.215	0.286
HC_7N(24-23)	27.07	41	-29.97	18.047	2.237	2.366	2.523	0.435	0.212	23.824	4.203	1.69	3.723	0.192	0.271
HC_7N(24-23)	27.07	42	-28.58	17.737	4.242	2.249	3.223	0.339	0.258	23.452	5.378	2.249	4.207	0.264	0.253
HC_7N(24-23)	27.07	43	-27.20	16.825	1.319	1.708	1.389	0.309	0.205	24.505	1.679	1.708	1.834	0.235	0.199
HC_7N(24-23)	27.07	44	-25.81	17.622	1.151	1.489	1.212	0.316	0.21	24.005	1.894	1.468	2.146	0.189	0.208
HC_7N(24-23)	27.07	45	-24.43	16.427	1.219	2.37	1.377	0.391	0.171	24.716	1.686	1.579	1.835	0.219	0.197
HC_7N(24-23)	27.07	46	-23.05	17.787	2.04	2.178	2.544	0.394	0.203	24.257	2.598	2.178	2.388	0.332	0.192
HC_7N(24-23)	27.07	47	-21.66	16.607	1.117	1.996	1.293	0.454	0.197	23.676	2.183	1.996	2.318	0.227	0.186
HC_7N(24-23)	27.07	48	-20.28	16.277	7.805	1.978	5.498	0.377	0.722	20.618	12.538	1.978	6.669	0.243	0.851
HC_7N(24-23)	27.07	49	-18.89	15.987	1.944	2.587	2.018	0.356	0.165	24.11	6.369	2.587	6.444	0.107	0.157
HC_7N(25-24)	28.20	40	-32.20	14.606	1.389	2.042	1.567	0.236	0.135	23.417	1.99	2.042	2.225	0.151	0.126
HC_7N(25-24)	28.20	41	-30.87	18.946	4.489	4.232	5.531	0.153	0.11	25.585	3.586	0.903	4.312	0.066	0.263
HC_7N(25-24)	28.20	42	-29.54	18.356	1.583	2.873	1.77	0.261	0.122	24.877	5.461	0.718	5.083	0.039	0.226
HC_7N(25-24)	28.20	43	-28.21	18.039	1.241	1.607	1.368	0.274	0.169	22.979	1.838	1.155	1.898	0.157	0.19
HC_7N(25-24)	28.20	44	-26.89	0	0	0	0	0	0	nan	nan	nan	nan	nan	nan
HC_7N(25-24)	28.20	45	-25.56	17.65	1.686	2.257	1.856	0.241	0.151	23.85	2.324	1.079	2.718	0.123	0.214
HC_7N(25-24)	28.20	46	-24.23	17.478	1.634	2.51	1.788	0.236	0.132	24.512	2.483	0.881	3.256	0.096	0.23
HC_7N(25-24)	28.20	47	-22.90	15.364	2.11	3.227	2.931	0.278	0.129	23.772	3.902	2.1	4.399	0.121	0.146
HC_7N(25-24)	28.20	48	-21.57	15.95	18.851	2.757	11.579	0.125	0.434	22.096	8.634	2.757	5.627	0.269	0.414
HC_7N(25-24)	28.20	49	-20.24	17.507	1.051	2.384	1.281	0.393	0.145	24.246	1.486	1.313	1.627	0.203	0.182
HC_7N(25-24)	28.20	50	-18.91	17.188	2.689	3.763	3.906	0.293	0.131	23.924	1.777	1.372	2.146	0.194	0.269
HC_7N(26-25)	29.33	19	-32.42	15.556	16.407	8.175	18.699	0.143	0.104	24.023	1.596	1.289	2.124	0.211	0.262
HC_7N(26-25)	29.33	20	-31.14	24.354	1.291	0.935	1.234	0.191	0.22	nan	nan	nan	nan	nan	nan
HC_7N(26-25)	29.33	21	-29.87	0	0	0	0	0	0	nan	nan	nan	nan	nan	nan
HC_7N(26-25)	29.33	22	-28.59	11.458	57.547	15.578	48.18	0.082	0.095	nan	nan	nan	nan	nan	nan
HC_7N(26-25)	29.33	23	-27.31	14.82	6.694	6.492	7.544	0.122	0.106	nan	nan	nan	nan	nan	nan
HC_7N(26-25)	29.33	24	-26.03	17.101	1.397	1.045	1.437	0.162	0.188	24.599	1.648	0.551	2.618	0.136	0.549
HC_7N(26-25)	29.33	25	-24.75	16.168	14.261	1.733	19.104	0.104	0.231	23.378	81.649	1.733	47.949	0.048	0.814
HC_7N(26-25)	29.33	26	-23.48	15.834	3.064	2.077	4.739	0.217	0.183	23.326	3.719	2.077	4.365	0.126	0.16
HC_7N(26-25)	29.33	27	-22.20	17.835	7.878	9.841	9.216	0.146	0.085	nan	nan	nan	nan	nan	nan

Table C.2 continued.

Transition	Restfreq	Ch	v_{ch}	R_{max} 1	ΔR_{max} 1	$W_{1/2}$ 1	$\Delta W_{1/2}$ 1	F_{max} 1	ΔF_{max} 1	R_{max} 2	ΔR_{max} 2	$W_{1/2}$ 2	$\Delta W_{1/2}$ 2	F_{max} 2	ΔF_{max} 2
HC_7N(26-25)	29.33	28	-20.92	16.55	1.103	1.472	1.211	0.314	0.2	23.425	2.469	1.472	2.531	0.128	0.186
HC_7N(26-25)	29.33	29	-19.64	14.64	3.261	2.23	3.971	0.311	0.215	21.149	7.962	2.23	6.224	0.156	0.365
HC_7N(27-26)	30.46	30	-32.39	19.968	1.78	-2.776	1.881	0.282	0.156	nan	nan	nan	nan	nan	nan
HC_7N(27-26)	30.46	31	-31.16	17.102	5.748	5.395	7.055	0.25	0.268	18.818	1.377	0.709	1.874	0.272	0.515
HC_7N(27-26)	30.46	32	-29.93	18.146	1.382	1.839	1.392	0.421	0.274	nan	nan	nan	nan	nan	nan
HC_7N(27-26)	30.46	33	-28.70	17.588	1.823	2.599	1.964	0.44	0.221	nan	nan	nan	nan	nan	nan
HC_7N(27-26)	30.46	34	-27.47	17.378	1.536	1.792	1.666	0.384	0.238	23.487	4.306	1.792	4.787	0.134	0.233
HC_7N(27-26)	30.46	35	-26.24	17.74	1.109	1.638	1.115	0.364	0.213	nan	nan	nan	nan	nan	nan
HC_7N(27-26)	30.46	36	-25.01	16.426	1.902	1.55	2.161	0.351	0.272	19.58	4.06	0.703	3.813	0.095	0.463
HC_7N(27-26)	30.46	37	-23.78	16.209	1.229	2.653	1.339	0.433	0.173	25.838	2.036	1.249	2.161	0.169	0.239
HC_7N(27-26)	30.46	38	-22.55	10.831	17.783	1.382	11.038	0.267	1.041	18.164	5.511	1.382	6.034	0.079	0.272
HC_7N(27-26)	30.46	39	-21.32	19.17	3.318	1.609	3.609	0.221	0.299	23.294	2.734	1.051	2.655	0.213	0.365
HC_7N(27-26)	30.46	40	-20.09	17.439	0.744	1.57	0.762	0.62	0.255	23.856	3.545	1.261	3.645	0.114	0.275
HC_7N(27-26)	30.46	41	-18.86	16.958	1.448	2.173	1.522	0.495	0.284	24.032	4.424	1.2	4.896	0.121	0.375
HC_7N(28-27)	31.58	29	-32.46	16.797	2.142	3.794	2.633	0.553	0.247	23.811	2.077	0.87	2.247	0.236	0.508
HC_7N(28-27)	31.58	30	-31.27	17.166	2.688	2.457	2.611	0.542	0.277	24.298	8.672	2.457	9.84	0.159	0.273
HC_7N(28-27)	31.58	31	-30.08	17.456	1.24	1.954	1.303	0.533	0.292	24.901	1.842	1.069	1.884	0.255	0.381
HC_7N(28-27)	31.58	32	-28.90	17.303	1.715	2.725	2.021	0.526	0.258	24.218	2.979	1.414	3.271	0.215	0.344
HC_7N(28-27)	31.58	33	-27.71	17.102	1.692	2.164	1.824	0.396	0.266	25.494	2.786	-0.949	2.942	0.152	0.388
HC_7N(28-27)	31.58	34	-26.53	17.047	4.977	3.131	6.119	0.314	0.244	25.487	3.731	0.697	4.206	0.101	0.474
HC_7N(28-27)	31.58	35	-25.34	16.912	1.587	2.071	1.74	0.519	0.307	25.016	15.962	2.071	19.916	0.084	0.323
HC_7N(28-27)	31.58	36	-24.15	16.731	1.475	1.723	1.581	0.423	0.314	24.096	5.36	0.633	4.691	0.071	0.469
HC_7N(28-27)	31.58	37	-22.97	16.907	1.352	2.199	1.444	0.527	0.232	24.461	10.709	2.199	14.25	0.066	0.377
HC_7N(28-27)	31.58	38	-21.78	14.917	2.801	2.441	2.948	0.477	0.287	21.838	6.218	2.193	6.712	0.198	0.298
HC_7N(28-27)	31.58	39	-20.59	16.473	2.328	1.637	1.804	0.872	0.499	20.571	6.686	1.637	4.826	0.307	0.516
HC_7N(28-27)	31.58	40	-19.41	16.973	26.417	2.903	11.578	0.48	2.69	21.71	24.349	2.454	11.405	0.351	3.881
HC_7N(29-28)	32.71	38	-32.46	-153.011	20792.649	67.926	4230.965	2.148	801.621	nan	nan	nan	nan	nan	nan
HC_7N(29-28)	32.71	39	-31.31	21.919	2.074	3.652	2.125	0.296	0.145	nan	nan	nan	nan	nan	nan
HC_7N(29-28)	32.71	40	-30.17	16.783	1.387	2.136	1.531	0.386	0.216	23.784	1.604	1.141	1.644	0.232	0.277
HC_7N(29-28)	32.71	41	-29.02	18.132	1.798	1.644	1.948	0.3	0.232	23.817	5.779	1.644	8.654	0.091	0.244
HC_7N(29-28)	32.71	42	-27.88	-3.047	143674.865	1.973	36135.199	2.901	206677.549	nan	nan	nan	nan	nan	nan
HC_7N(29-28)	32.71	43	-26.73	18.565	0.977	1.247	1	0.361	0.245	24.261	1.866	1.247	1.902	0.182	0.235
HC_7N(29-28)	32.71	44	-25.59	17.142	1.253	1.599	1.319	0.307	0.207	24.102	2.773	1.395	3.188	0.13	0.215
HC_7N(29-28)	32.71	45	-24.44	16.625	3.116	2.349	4.992	0.254	0.179	23.542	7.992	2.349	6.751	0.123	0.243
HC_7N(29-28)	32.71	46	-23.29	16.615	1.323	1.48	1.543	0.42	0.308	24.013	3.995	1.48	12.308	0.208	4.178
HC_7N(29-28)	32.71	47	-22.15	16.442	1.78	1.958	2.041	0.326	0.246	22.461	4.273	0.758	5.132	0.138	0.427
HC_7N(29-28)	32.71	48	-21.00	16.199	14.861	3.491	11.249	0.219	0.219	20.733	2.146	1.206	4.618	0.208	0.944
HC_7N(30-29)	33.84	37	-33.00	17.521	1.71	2.957	1.884	0.299	0.143	nan	nan	nan	nan	nan	nan
HC_7N(30-29)	33.84	38	-31.89	17.838	1.305	1.758	1.432	0.358	0.167	23.425	3.527	1.758	3.892	0.13	0.162
HC_7N(30-29)	33.84	39	-30.78	18.631	1.104	1.547	1.188	0.3	0.183	25.012	1.938	0.793	2.102	0.114	0.251
HC_7N(30-29)	33.84	40	-29.68	17.242	1.912	2.944	2.168	0.26	0.145	25.584	1.511	1.232	1.597	0.206	0.21
HC_7N(30-29)	33.84	41	-28.57	17.759	1.513	1.355	1.598	0.205	0.197	23.974	2.432	1.355	2.594	0.124	0.192

Table C.2 continued.

Transition	Restfreq	Ch	v_{ch}	R_{max} 1	ΔR_{max} 1	$W_{1/2}$ 1	$\Delta W_{1/2}$ 1	F_{max} 1	ΔF_{max} 1	R_{max} 2	ΔR_{max} 2	$W_{1/2}$ 2	$\Delta W_{1/2}$ 2	F_{max} 2	ΔF_{max} 2
HC_7N(30-29)	33.84	42	-27.46	17.181	1.285	1.93	1.333	0.269	0.155	27.643	9.462	1.93	18.209	0.049	0.515
HC_7N(30-29)	33.84	43	-26.35	17.007	2.076	1.786	1.83	0.399	0.192	23.165	22.036	1.786	10.805	0.158	0.879
HC_7N(30-29)	33.84	44	-25.25	15.625	1.965	2.496	2.16	0.273	0.182	27.063	12.843	2.496	11.572	0.047	0.198
HC_7N(30-29)	33.84	45	-24.14	16.189	1.424	1.845	1.56	0.338	0.149	23.038	35.831	1.845	16.65	0.051	0.61
HC_7N(30-29)	33.84	46	-23.03	16.993	0.861	1.574	0.89	0.373	0.177	nan	nan	nan	nan	nan	nan
HC_7N(30-29)	33.84	47	-21.92	16.583	1.059	1.822	1.186	0.403	0.189	23.31	5.173	1.822	5.693	0.081	0.183
HC_7N(30-29)	33.84	48	-20.82	16.22	5.653	1.516	2.867	0.555	1.301	19.247	12.615	1.516	6.003	0.249	1.344
HC_7N(30-29)	33.84	49	-19.71	16.989	0.971	2.543	0.975	0.51	0.169	nan	nan	nan	nan	nan	nan
HC_7N(30-29)	33.84	50	-18.60	16.016	1.463	2.19	1.496	0.54	0.193	23.226	24.684	2.19	33.762	0.055	0.203
HC_7N(31-30)	34.97	15	-33.32	11.203	46.937	5.325	34.707	0.168	0.997	26.436	47.18	5.325	45.675	0.105	0.428
HC_7N(31-30)	34.97	16	-32.25	1259.715	12510197.463	588.851	2977155.582	0.656	14551.986	nan	nan	nan	nan	nan	nan
HC_7N(31-30)	34.97	17	-31.18	10.16	5.099	4.268	5.279	0.223	0.359	22.431	0.858	0.911	0.881	0.308	0.251
HC_7N(31-30)	34.97	18	-30.10	23.17	17.205	7.084	18.395	0.104	0.123	nan	nan	nan	nan	nan	nan
HC_7N(31-30)	34.97	19	-29.03	-27.512	628.984	26.109	191.056	0.434	8.443	nan	nan	nan	nan	nan	nan
HC_7N(31-30)	34.97	20	-27.96	0	0	0	0	0	0	nan	nan	nan	nan	nan	nan
HC_7N(31-30)	34.97	21	-26.89	16.918	6.216	1.506	6.499	0.135	0.267	23.907	2.11	0.73	2.198	0.144	0.351
HC_7N(31-30)	34.97	22	-25.82	0	0	0	0	0	0	nan	nan	nan	nan	nan	nan
HC_7N(31-30)	34.97	23	-24.75	16.852	5.661	1.232	9.961	0.105	0.301	22.834	4.333	1.232	4.814	0.082	0.239
HC_7N(31-30)	34.97	24	-23.68	0	0	0	0	0	0	nan	nan	nan	nan	nan	nan
HC_7N(31-30)	34.97	25	-22.60	37.533	297.959	11.697	160.272	0.083	0.896	nan	nan	nan	nan	nan	nan
HC_7N(31-30)	34.97	26	-21.53	5.61	195.256	27.211	244.248	0.116	0.204	nan	nan	nan	nan	nan	nan
HC_7N(31-30)	34.97	27	-20.46	18.191	18.744	2.26	14.092	0.099	0.331	23.875	31.13	2.26	21.557	0.059	0.359
HC_7N(31-30)	34.97	28	-19.39	4.488	40.044	12.716	35.712	0.233	0.35	nan	nan	nan	nan	nan	nan
HC_7N(32-31)	36.10	37	-32.74	16.429	2.799	1.951	2.878	0.376	0.258	22.255	5.059	1.951	7.232	0.187	0.26
HC_7N(32-31)	36.10	38	-31.71	15.842	5.706	5.711	5.134	0.251	0.134	22.501	1.751	0.677	1.789	0.166	0.369
HC_7N(32-31)	36.10	39	-30.67	15.15	2.443	2.586	3.091	0.307	0.203	23.618	4.139	2.586	4.236	0.183	0.186
HC_7N(32-31)	36.10	40	-29.63	17.793	3.283	2.09	3.21	0.294	0.246	24.01	10.642	2.09	10.065	0.09	0.24
HC_7N(32-31)	36.10	41	-28.59	18.186	9.916	7.338	9.848	0.181	0.123	nan	nan	nan	nan	nan	nan
HC_7N(32-31)	36.10	42	-27.55	18.721	0.752	1.162	0.821	0.588	0.31	22.823	2.152	1.046	2.271	0.194	0.317
HC_7N(32-31)	36.10	43	-26.51	18.252	23.16	12.56	35.924	0.113	0.112	27.934	1.767	0.99	2.076	0.187	0.305
HC_7N(32-31)	36.10	44	-25.48	17.757	4.257	2.131	4.92	0.242	0.284	24.421	8.555	2.131	8.081	0.147	0.263
HC_7N(32-31)	36.10	45	-24.44	16.408	3.105	1.865	3.593	0.213	0.299	23.792	3.881	1.865	4.103	0.164	0.283
HC_7N(32-31)	36.10	46	-23.40	13.992	3.738	2.884	4.832	0.211	0.2	24.188	4.492	2.776	5.465	0.185	0.192
HC_7N(32-31)	36.10	47	-22.36	15.754	1.845	1.256	1.957	0.221	0.28	23.433	2.071	0.989	2.193	0.167	0.303
HC_7N(32-31)	36.10	48	-21.32	16.277	5.268	2.081	4.042	0.4	0.426	21.691	24.244	2.081	28.04	0.088	0.832
HC_7N(32-31)	36.10	49	-20.29	15.741	1.682	2	2.242	0.366	0.238	nan	nan	nan	nan	nan	nan
HC_7N(32-31)	36.10	50	-19.25	16.339	1.382	1.623	1.769	0.434	0.3	23.071	94.613	1.623	33.465	0.112	5.251
HC_7N(33-32)	37.22	36	-33.06	16.521	4.32	1.875	4.136	0.326	0.301	23.249	48.539	1.875	20.046	0.234	3.353
HC_7N(33-32)	37.22	37	-32.06	16.263	2.977	3.198	3.584	0.307	0.228	24.775	10.92	0.888	6.165	0.096	0.93
HC_7N(33-32)	37.22	38	-31.05	18.949	13.71	13.023	19.742	0.209	0.143	nan	nan	nan	nan	nan	nan
HC_7N(33-32)	37.22	39	-30.04	19.926	7.903	4.427	8.959	0.179	0.219	nan	nan	nan	nan	nan	nan
HC_7N(33-32)	37.22	40	-29.04	18.738	1.25	0.501	1.842	0.224	0.623	24.222	1.249	0.501	0.922	0.245	0.421

Table C.2 continued.

Transition	Restfreq	Ch	v_{ch}	R_{max} 1	ΔR_{max} 1	$W_{1/2}$ 1	$\Delta W_{1/2}$ 1	F_{max} 1	ΔF_{max} 1	R_{max} 2	ΔR_{max} 2	$W_{1/2}$ 2	$\Delta W_{1/2}$ 2	F_{max} 2	ΔF_{max} 2
HC_7N(33-32)	37.22	41	-28.03	24.501	6.678	-8.356	9.752	0.233	0.159	nan	nan	nan	nan	nan	nan
HC_7N(33-32)	37.22	42	-27.02	13.007	25.39	3.682	38.039	0.211	0.384	23.315	32.698	3.682	22.444	0.117	0.418
HC_7N(33-32)	37.22	43	-26.02	15.055	5.057	2.746	7.858	0.207	nan	23.189	10.57	2.746	nan	0.148	nan
HC_7N(33-32)	37.22	44	-25.01	0	0	0	0	0	0	nan	nan	nan	nan	nan	nan
HC_7N(33-32)	37.22	45	-24.00	8.823	1.071	1.13	1.197	0.516	0.377	nan	nan	nan	nan	nan	nan
HC_7N(33-32)	37.22	46	-23.00	11.032	11.992	5.784	12.6	0.228	0.658	25.398	1.07	0.706	1.153	0.37	0.495
HC_7N(33-32)	37.22	47	-21.99	0	0	0	0	0	0	nan	nan	nan	nan	nan	nan
HC_7N(33-32)	37.22	48	-20.98	23.637	6.494	5.07	8.41	0.207	0.212	nan	nan	nan	nan	nan	nan
HC_7N(33-32)	37.22	49	-19.98	13.983	12.207	6.312	18.88	0.184	0.243	29.1	8.69	2.374	7.911	0.116	0.309
HC_7N(33-32)	37.22	50	-18.97	0	0	0	0	0	0	nan	nan	nan	nan	nan	nan
C_3N(2-1,3/2-1/2)	19.80	58	-32.64	3.167	2.582	1.603	2.456	0.109	0.132	nan	nan	nan	nan	nan	nan
C_3N(2-1,3/2-1/2)	19.80	59	-30.75	6.759	24.875	5.734	41.033	0.055	nan	21.103	30.162	5.734	nan	0.035	nan
C_3N(2-1,3/2-1/2)	19.80	60	-28.86	4.62	10.736	9.742	8.569	0.186	0.065	nan	nan	nan	nan	nan	nan
C_3N(2-1,3/2-1/2)	19.80	61	-26.97	5	7.526	6.203	6.559	0.12	0.061	22.547	2.032	1.739	2.248	0.082	0.081
C_3N(2-1,3/2-1/2)	19.80	62	-25.07	13.797	1.826	2.819	1.923	0.109	0.062	nan	nan	nan	nan	nan	nan
C_3N(2-1,3/2-1/2)	19.80	63	-23.18	15.109	2.38	3.182	3.074	0.112	0.062	nan	nan	nan	nan	nan	nan
C_3N(2-1,3/2-1/2)	19.80	64	-21.29	0.545	8.394	3.133	5.114	0.31	0.286	nan	nan	nan	nan	nan	nan
C_3N(2-1,3/2-1/2)	19.80	65	-19.40	4.883	38.796	16.091	32.796	0.103	0.07	nan	nan	nan	nan	nan	nan
C_3N(2-1,5/2-3/2)	19.78	49	-33.07	16.485	20.055	2.499	19.652	0.115	0.714	22.811	14.229	2.499	7.517	0.124	0.347
C_3N(2-1,5/2-3/2)	19.78	50	-31.18	18.403	1.414	2.024	1.489	0.142	0.085	25.272	1.482	1.284	1.597	0.103	0.102
C_3N(2-1,5/2-3/2)	19.78	51	-29.29	0	0	0	0	0	0	nan	nan	nan	nan	nan	nan
C_3N(2-1,5/2-3/2)	19.78	52	-27.39	15.667	7.129	2.139	8.484	0.09	0.099	23.206	4.31	2.139	4.475	0.067	0.087
C_3N(2-1,5/2-3/2)	19.78	53	-25.50	17.906	1.665	3.334	1.712	0.161	0.069	nan	nan	nan	nan	nan	nan
C_3N(2-1,5/2-3/2)	19.78	54	-23.60	18.774	3.193	2.19	3.679	0.106	0.097	24.951	2.161	1.797	2.093	0.143	0.1
C_3N(2-1,5/2-3/2)	19.78	55	-21.71	7.471	6.78	6.013	12.85	0.094	0.122	21.018	3.316	2.414	4.027	0.085	0.097
C_3N(2-1,5/2-3/2)	19.78	56	-19.81	13.889	2.218	4.955	2.911	0.211	0.075	nan	nan	nan	nan	nan	nan
C_3N(3-2,5/2-3/2)	29.70	31	-32.75	13.831	4.068	2.363	5.943	0.162	0.169	21.213	4.547	2.363	5.74	0.147	0.158
C_3N(3-2,5/2-3/2)	29.70	32	-31.49	12.982	30.467	2.034	20.938	0.201	0.97	20.334	3.334	2.034	3.225	0.196	0.167
C_3N(3-2,5/2-3/2)	29.70	33	-30.22	20.676	16.018	4.462	20.03	0.07	0.146	23.245	4.433	0.665	4.283	0.053	0.306
C_3N(3-2,5/2-3/2)	29.70	34	-28.96	11.301	29.818	11.506	42.83	0.076	0.109	nan	nan	nan	nan	nan	nan
C_3N(3-2,5/2-3/2)	29.70	35	-27.70	16.115	1.561	1.576	1.691	0.157	0.135	22.891	0.986	1.442	1.009	0.222	0.131
C_3N(3-2,5/2-3/2)	29.70	36	-26.44	16.383	3.684	2.369	4.459	0.261	0.15	21.774	4.956	1.729	4.434	0.157	0.263
C_3N(3-2,5/2-3/2)	29.70	37	-25.18	18.187	1.725	1.419	1.886	0.175	0.166	22.961	2.381	1.251	2.673	0.117	0.172
C_3N(3-2,5/2-3/2)	29.70	38	-23.91	18.954	3.043	4.215	3.392	0.148	0.087	nan	nan	nan	nan	nan	nan
C_3N(3-2,5/2-3/2)	29.70	39	-22.65	14.826	2.169	1.799	2.25	0.127	0.13	22.406	1.895	1.799	1.963	0.137	0.123
C_3N(3-2,5/2-3/2)	29.70	40	-21.39	14.956	2.52	2.184	2.946	0.178	0.137	23.126	3.836	2.184	4.129	0.091	0.126
C_3N(3-2,5/2-3/2)	29.70	41	-20.13	17.299	1.714	1.423	1.909	0.233	0.227	22.551	3.482	1.423	3.729	0.113	0.219
C_3N(3-2,5/2-3/2)	29.70	42	-18.87	18.492	1.963	3.254	2.051	0.216	0.113	nan	nan	nan	nan	nan	nan
C_3N(3-2,7/2-5/2)	29.68	32	-32.53	17.381	2.229	2.88	2.46	0.304	0.146	22.772	0.914	1.077	1.025	0.346	0.275
C_3N(3-2,7/2-5/2)	29.68	33	-31.27	16.385	6.904	3.234	7.386	0.246	0.178	22.555	3.952	1.855	4.081	0.229	0.468
C_3N(3-2,7/2-5/2)	29.68	34	-30.00	17.84	1.122	2.984	1.163	0.412	0.134	nan	nan	nan	nan	nan	nan
C_3N(3-2,7/2-5/2)	29.68	35	-28.74	-156.209	18102.288	67.805	3641.187	3.194	1057.266	nan	nan	nan	nan	nan	nan

Table C.2 continued.

Transition	Restfreq	Ch	v_{ch}	R_{max} 1	ΔR_{max} 1	$W_{1/2}$ 1	$\Delta W_{1/2}$ 1	F_{max} 1	ΔF_{max} 1	R_{max} 2	ΔR_{max} 2	$W_{1/2}$ 2	$\Delta W_{1/2}$ 2	F_{max} 2	ΔF_{max} 2
C_3N(3-2,7/2-5/2)	29.68	36	-27.48	15.91	2.378	2.011	3.3	0.304	0.202	23.042	16.891	2.011	21.465	0.109	2.551
C_3N(3-2,7/2-5/2)	29.68	37	-26.21	16.75	2.467	2.115	2.675	0.212	0.196	24.619	1.649	1.088	1.657	0.196	0.255
C_3N(3-2,7/2-5/2)	29.68	38	-24.95	17.276	9.5	3.13	7.574	0.149	0.233	24.124	3.169	0.719	3.377	0.098	0.363
C_3N(3-2,7/2-5/2)	29.68	39	-23.69	7.025	10.731	6.995	11.231	0.347	0.54	nan	nan	nan	nan	nan	nan
C_3N(3-2,7/2-5/2)	29.68	40	-22.43	71.203	2301.878	39.409	887.59	0.281	10.538	nan	nan	nan	nan	nan	nan
C_3N(3-2,7/2-5/2)	29.68	41	-21.16	15.306	9.863	3.261	8.482	0.145	0.184	24.545	6.047	3.261	5.227	0.197	0.163
C_3N(3-2,7/2-5/2)	29.68	42	-19.90	18.032	2.359	2.456	2.749	0.294	0.194	nan	nan	nan	nan	nan	nan
C_3N(3-2,7/2-5/2)	29.68	43	-18.64	10.047	6.735	4.558	12.188	0.284	nan	24.919	8.022	4.558	nan	0.174	nan
C_4H(2-1,5/2-3/2)	19.02	37	-31.76	0	0	0	0	0	0	nan	nan	nan	nan	nan	nan
C_4H(2-1,5/2-3/2)	19.02	38	-29.79	12.807	3.547	6.04	3.875	0.108	0.044	nan	nan	nan	nan	nan	nan
C_4H(2-1,5/2-3/2)	19.02	39	-27.82	8.128	48.372	18.924	81.324	0.062	0.041	nan	nan	nan	nan	nan	nan
C_4H(2-1,5/2-3/2)	19.02	40	-25.85	16.352	2.286	4.99	2.787	0.142	0.049	nan	nan	nan	nan	nan	nan
C_4H(2-1,5/2-3/2)	19.02	41	-23.88	6.235	24.369	9.636	29.358	0.051	0.061	19.847	1.89	1.939	2.772	0.085	0.095
C_4H(2-1,5/2-3/2)	19.02	42	-21.91	-30.17	492.304	37.479	196.295	0.152	1.218	nan	nan	nan	nan	nan	nan
C_4H(2-1,5/2-3/2)	19.02	43	-19.93	14.931	5.587	6.427	5.3	0.074	0.047	nan	nan	nan	nan	nan	nan
C_4H(3-2,5/2-3/2)	28.57	27	-32.77	11.475	20.977	9.471	20.264	0.105	0.089	nan	nan	nan	nan	nan	nan
C_4H(3-2,5/2-3/2)	28.57	28	-31.46	14.818	10.095	12.208	12.948	0.153	0.071	nan	nan	nan	nan	nan	nan
C_4H(3-2,5/2-3/2)	28.57	29	-30.15	7.135	38.166	2.418	21.535	0.158	0.936	22.579	7.83	2.418	6.508	0.082	0.279
C_4H(3-2,5/2-3/2)	28.57	30	-28.84	0	0	0	0	0	0	nan	nan	nan	nan	nan	nan
C_4H(3-2,5/2-3/2)	28.57	31	-27.53	-0.022	23.18	1.295	13.634	0.47	2.852	nan	nan	nan	nan	nan	nan
C_4H(3-2,5/2-3/2)	28.57	32	-26.21	18.401	21.468	15.923	36.736	0.091	0.073	nan	nan	nan	nan	nan	nan
C_4H(3-2,5/2-3/2)	28.57	33	-24.90	17.137	2.944	1.753	3.316	0.133	0.175	21.884	1.884	1	2.131	0.154	0.222
C_4H(3-2,5/2-3/2)	28.57	34	-23.59	12.051	6.708	6.599	8.761	0.13	0.179	nan	nan	nan	nan	nan	nan
C_4H(3-2,5/2-3/2)	28.57	35	-22.28	0	0	0	0	0	0	nan	nan	nan	nan	nan	nan
C_4H(3-2,5/2-3/2)	28.57	36	-20.97	0	0	0	0	0	0	nan	nan	nan	nan	nan	nan
C_4H(3-2,5/2-3/2)	28.57	37	-19.66	14.368	11.408	9.226	15.778	0.1	0.088	27.754	2.573	0.785	2.221	0.086	0.229
C_4H(3-2,7/2-5/2)	28.53	39	-32.74	0	0	0	0	0	0	nan	nan	nan	nan	nan	nan
C_4H(3-2,7/2-5/2)	28.53	40	-31.43	15.054	3.365	1.698	4.173	0.116	0.196	23.512	4.834	1.698	6.58	0.075	0.274
C_4H(3-2,7/2-5/2)	28.53	41	-30.11	8.184	8.035	3.521	10.088	0.109	0.184	19.657	2.433	1.558	2.519	0.347	1.662
C_4H(3-2,7/2-5/2)	28.53	42	-28.80	24.281	6.71	6.462	9.423	0.099	0.08	nan	nan	nan	nan	nan	nan
C_4H(3-2,7/2-5/2)	28.53	43	-27.49	0	0	0	0	0	0	nan	nan	nan	nan	nan	nan
C_4H(3-2,7/2-5/2)	28.53	44	-26.17	1.227	3.704	1.586	3.017	0.286	0.302	nan	nan	nan	nan	nan	nan
C_4H(3-2,7/2-5/2)	28.53	45	-24.86	8.556	5.998	6.743	5.807	0.173	0.084	nan	nan	nan	nan	nan	nan
C_4H(3-2,7/2-5/2)	28.53	46	-23.55	17.16	0.945	2.135	0.969	0.329	0.125	24.481	4.378	-0.466	3.023	0.094	0.501
C_4H(3-2,7/2-5/2)	28.53	47	-22.23	0	0	0	0	0	0	nan	nan	nan	nan	nan	nan
C_4H(3-2,7/2-5/2)	28.53	48	-20.92	0	0	0	0	0	0	nan	nan	nan	nan	nan	nan
C_4H(3-2,7/2-5/2)	28.53	49	-19.61	16.593	0.836	1.395	0.87	0.335	0.177	22.534	1.012	1.027	1.058	0.225	0.193
C_6H(15/2-13/2,3/2,e)	20.79	100	-19.84	21.938	12.683	11.092	17.178	0.045	0.037	nan	nan	nan	nan	nan	nan
C_6H(15/2-13/2,3/2,e)	20.79	93	-32.46	24.372	9.892	8.783	13.891	0.056	0.045	nan	nan	nan	nan	nan	nan
C_6H(15/2-13/2,3/2,e)	20.79	94	-30.65	12.219	7.429	6.339	6.586	0.07	0.058	nan	nan	nan	nan	nan	nan
C_6H(15/2-13/2,3/2,e)	20.79	95	-28.85	32.543	67.636	8.714	55.745	0.027	0.061	nan	nan	nan	nan	nan	nan
C_6H(15/2-13/2,3/2,e)	20.79	96	-27.05	0	0	0	0	0	0	nan	nan	nan	nan	nan	nan

Table C.2 continued.

Transition	Restfreq	Ch	v_{ch}	R_{max} 1	ΔR_{max} 1	$W_{1/2}$ 1	$\Delta W_{1/2}$ 1	F_{max} 1	ΔF_{max} 1	R_{max} 2	ΔR_{max} 2	$W_{1/2}$ 2	$\Delta W_{1/2}$ 2	F_{max} 2	ΔF_{max} 2
C_6H(15/2-13/2,3/2,e)	20.79	97	-25.25	12.797	11.451	6.74	7.39	0.087	0.1	nan	nan	nan	nan	nan	nan
C_6H(15/2-13/2,3/2,e)	20.79	98	-23.45	11.686	7.103	8.804	9.938	0.093	0.05	nan	nan	nan	nan	nan	nan
C_6H(15/2-13/2,3/2,e)	20.79	99	-21.64	13.885	3.653	4.804	3.725	0.244	0.072	23.486	5.648	2.896	4.568	0.096	0.154
C_6H(15/2-13/2,3/2,f)	20.79	80	-33.39	5	47.022	7.948	52.565	0.051	0.09	20.419	2.621	1.645	3.784	0.078	0.137
C_6H(15/2-13/2,3/2,f)	20.79	81	-31.59	16.626	7.27	11.316	8.334	0.091	0.044	nan	nan	nan	nan	nan	nan
C_6H(15/2-13/2,3/2,f)	20.79	82	-29.78	10.989	4.512	6	6.146	0.117	0.062	22.974	1.997	1.176	2.361	0.077	0.121
C_6H(15/2-13/2,3/2,f)	20.79	83	-27.98	4.584	3.496	3.086	3.54	0.132	0.103	nan	nan	nan	nan	nan	nan
C_6H(15/2-13/2,3/2,f)	20.79	84	-26.18	11.392	12.071	12.401	10.8	0.096	0.045	nan	nan	nan	nan	nan	nan
C_6H(15/2-13/2,3/2,f)	20.79	85	-24.38	16.812	18.62	8.098	15.168	0.055	0.056	25.546	3.423	2.622	5.352	0.07	0.134
C_6H(15/2-13/2,3/2,f)	20.79	86	-22.58	10.023	75.254	21.232	96.372	0.058	0.052	nan	nan	nan	nan	nan	nan
C_6H(15/2-13/2,3/2,f)	20.79	87	-20.77	11.747	2.771	2.961	3.52	0.139	0.091	23.066	2.442	2.961	2.59	0.119	0.077
C_6H(15/2-13/2,3/2,f)	20.79	88	-18.97	0	0	0	0	0	0	nan	nan	nan	nan	nan	nan
C_6H(17/2-15/2,1/2,e)	23.75	46	-32.11	13.181	6.279	4.796	7.222	0.099	0.073	nan	nan	nan	nan	nan	nan
C_6H(17/2-15/2,1/2,e)	23.75	47	-30.54	13.419	7.43	3.395	6.062	0.138	0.117	21.752	20.155	3.395	12.737	0.054	0.194
C_6H(17/2-15/2,1/2,e)	23.75	48	-28.96	0	0	0	0	0	0	nan	nan	nan	nan	nan	nan
C_6H(17/2-15/2,1/2,e)	23.75	49	-27.38	5	9.614	5.357	13.011	0.088	0.078	20.543	7.126	3.772	6.047	0.069	0.084
C_6H(17/2-15/2,1/2,e)	23.75	50	-25.80	0	0	0	0	0	0	nan	nan	nan	nan	nan	nan
C_6H(17/2-15/2,1/2,e)	23.75	51	-24.22	5.13	11.986	3.419	11.312	0.088	0.212	17.759	36.643	3.419	43.063	0.032	0.079
C_6H(17/2-15/2,1/2,e)	23.75	52	-22.65	19.342	15.017	12.781	19.428	0.053	0.039	nan	nan	nan	nan	nan	nan
C_6H(17/2-15/2,1/2,e)	23.75	53	-21.07	9.442	1.948	2.131	2.102	0.132	0.098	22.517	2.518	2.131	2.827	0.108	0.085
C_6H(17/2-15/2,1/2,e)	23.75	54	-19.49	17.968	40.505	17.063	70.963	0.033	0.046	nan	nan	nan	nan	nan	nan
C_6H(17/2-15/2,3/2,e)	23.57	70	-32.46	14.371	1.599	1.167	2.009	0.125	0.132	nan	nan	nan	nan	nan	nan
C_6H(17/2-15/2,3/2,e)	23.57	71	-30.87	5.289	4.804	4.06	5.901	0.139	nan	25.059	6.44	4.06	nan	0.058	nan
C_6H(17/2-15/2,3/2,e)	23.57	72	-29.28	10.497	3.45	4.206	4.001	0.128	0.081	27.083	7.355	4.206	7.627	0.043	0.06
C_6H(17/2-15/2,3/2,e)	23.57	73	-27.69	-6.205	256.642	23.747	137.053	0.122	0.584	nan	nan	nan	nan	nan	nan
C_6H(17/2-15/2,3/2,e)	23.57	74	-26.10	10.189	nan	5.241	6.359	0.112	nan	22.319	nan	5.241	nan	0.041	nan
C_6H(17/2-15/2,3/2,e)	23.57	75	-24.51	22.083	15.025	11.795	23.839	0.074	0.099	nan	nan	nan	nan	nan	nan
C_6H(17/2-15/2,3/2,e)	23.57	76	-22.92	15.693	15.47	5.919	17.66	0.12	0.46	nan	nan	nan	nan	nan	nan
C_6H(17/2-15/2,3/2,e)	23.57	77	-21.33	6.015	2.661	2.694	2.351	0.239	0.148	nan	nan	nan	nan	nan	nan
C_6H(17/2-15/2,3/2,e)	23.57	78	-19.74	-8.859	164.537	18.751	76.132	0.206	0.913	nan	nan	nan	nan	nan	nan
C_6H(17/2-15/2,3/2,f)	23.57	54	-32.20	5.319	4.091	4.013	4.213	0.16	0.089	22.596	12.399	4.013	7.997	0.055	0.144
C_6H(17/2-15/2,3/2,f)	23.57	55	-30.61	10.41	12.351	9.089	10.198	0.126	0.062	nan	nan	nan	nan	nan	nan
C_6H(17/2-15/2,3/2,f)	23.57	56	-29.02	24.806	2.001	2.422	2.041	0.094	0.067	nan	nan	nan	nan	nan	nan
C_6H(17/2-15/2,3/2,f)	23.57	57	-27.43	0	0	0	0	0	0	nan	nan	nan	nan	nan	nan
C_6H(17/2-15/2,3/2,f)	23.57	58	-25.84	18.285	7.989	11.18	10.987	0.083	0.037	nan	nan	nan	nan	nan	nan
C_6H(17/2-15/2,3/2,f)	23.57	59	-24.25	0	0	0	0	0	0	nan	nan	nan	nan	nan	nan
C_6H(17/2-15/2,3/2,f)	23.57	60	-22.66	18.129	2.338	3.335	2.473	0.105	0.063	nan	nan	nan	nan	nan	nan
C_6H(17/2-15/2,3/2,f)	23.57	61	-21.07	0	0	0	0	0	0	nan	nan	nan	nan	nan	nan
C_6H(17/2-15/2,3/2,f)	23.57	62	-19.48	13.478	2.185	3.291	2.558	0.148	0.08	26.581	5.736	3.291	4.289	0.08	0.09
C_6H(19/2-17/2,3/2,e)	26.34	73	-32.47	24.958	98.952	22.667	169.273	0.036	0.055	nan	nan	nan	nan	nan	nan
C_6H(19/2-17/2,3/2,e)	26.34	74	-31.04	15.189	2.607	6.018	3.065	0.171	0.062	nan	nan	nan	nan	nan	nan
C_6H(19/2-17/2,3/2,e)	26.34	75	-29.62	0	0	0	0	0	0	nan	nan	nan	nan	nan	nan

Table C.2 continued.

Transition	Restfreq	Ch	v_{ch}	R_{max} 1	ΔR_{max} 1	$W_{1/2}$ 1	$\Delta W_{1/2}$ 1	F_{max} 1	ΔF_{max} 1	R_{max} 2	ΔR_{max} 2	$W_{1/2}$ 2	$\Delta W_{1/2}$ 2	F_{max} 2	ΔF_{max} 2
C_6H(19/2-17/2,3/2,e)	26.34	76	-28.20	16.312	2.417	3.659	2.456	0.123	0.07	nan	nan	nan	nan	nan	nan
C_6H(19/2-17/2,3/2,e)	26.34	77	-26.78	12.736	2.414	1.934	1.918	0.142	0.176	22.283	3.176	1.401	3.838	0.063	0.123
C_6H(19/2-17/2,3/2,e)	26.34	78	-25.35	12.31	9.735	7.823	9.977	0.105	0.056	nan	nan	nan	nan	nan	nan
C_6H(19/2-17/2,3/2,e)	26.34	79	-23.93	15.514	2.027	2.801	2.264	0.21	0.082	24.013	5.17	2.801	6.304	0.078	0.078
C_6H(19/2-17/2,3/2,e)	26.34	80	-22.51	0	0	0	0	0	0	nan	nan	nan	nan	nan	nan
C_6H(19/2-17/2,3/2,e)	26.34	81	-21.08	16.911	10.124	9.155	10.398	0.075	0.059	nan	nan	nan	nan	nan	nan
C_6H(19/2-17/2,3/2,e)	26.34	82	-19.66	14.922	3.421	2.299	3.373	0.13	0.103	21.741	3.467	2.299	3.296	0.126	0.097
C_6H(19/2-17/2,3/2,f)	26.34	53	-32.23	16.024	1.104	1.775	1.109	0.188	0.1	nan	nan	nan	nan	nan	nan
C_6H(19/2-17/2,3/2,f)	26.34	54	-30.81	0.104	62.025	15.456	35.444	0.106	0.198	nan	nan	nan	nan	nan	nan
C_6H(19/2-17/2,3/2,f)	26.34	55	-29.39	0	0	0	0	0	0	nan	nan	nan	nan	nan	nan
C_6H(19/2-17/2,3/2,f)	26.34	56	-27.97	16.333	0.758	1.094	0.788	0.189	0.115	nan	nan	nan	nan	nan	nan
C_6H(19/2-17/2,3/2,f)	26.34	57	-26.54	12.168	1.512	2.32	1.771	0.156	0.087	22.722	57.802	2.32	28.736	0.055	0.597
C_6H(19/2-17/2,3/2,f)	26.34	58	-25.12	5	60.777	15.692	57.645	0.079	0.077	20.014	1.11	-1.125	1.274	0.158	0.141
C_6H(19/2-17/2,3/2,f)	26.34	59	-23.70	0	0	0	0	0	0	nan	nan	nan	nan	nan	nan
C_6H(19/2-17/2,3/2,f)	26.34	60	-22.28	9.874	5.29	3.318	5.409	0.083	0.085	23.042	16.854	3.318	13.935	0.097	1.336
C_6H(19/2-17/2,3/2,f)	26.34	61	-20.85	7.139	21.544	7.1	14.804	0.084	0.159	nan	nan	nan	nan	nan	nan
C_6H(19/2-17/2,3/2,f)	26.34	62	-19.43	17.108	3.179	3.174	5.389	0.157	0.105	22.338	2.025	0.903	3.896	0.081	0.225

Table C.3: List of Gaussian fit results from the radial emission profiles of each transition (restfrequency in GHz) of each channel (velocity in km s^{-1}) with $\Delta v < 7.5$ km s^{-1} for quarter Q2. The fit parameters are shell radius at maximum flux R_{max} (in arcsec), half shell width $W_{1/2}$ (in arcsec), and maximum flux F_{max} (in mJy $beam^{-1}$) for two components and their uncertainties determined from the least square fit routine.

Transition	Restfreq	Ch	v_{ch}	R_{max} 1	ΔR_{max} 1	$W_{1/2}$ 1	$\Delta W_{1/2}$ 1	F_{max} 1	ΔF_{max} 1	R_{max} 2	ΔR_{max} 2	$W_{1/2}$ 2	$\Delta W_{1/2}$ 2	F_{max} 2	ΔF_{max} 2
HC_3N(2-1)	18.20	79	-33.40	14.049	1.596	5.789	1.857	2.122	0.459	27.547	16.317	2.435	17.951	0.129	0.693
HC_3N(2-1)	18.20	80	-31.34	15.057	1.666	4.566	1.804	1.914	0.427	25.241	4.687	2.458	4.488	0.454	0.627
HC_3N(2-1)	18.20	81	-29.28	16.322	3.154	5.397	2.721	1.616	0.37	23.917	8.72	1.862	13.155	0.159	1.064
HC_3N(2-1)	18.20	82	-27.22	16.684	2.745	5.63	2.462	1.47	0.341	24.26	5.538	1.584	7.893	0.21	0.884
HC_3N(2-1)	18.20	83	-25.16	16.797	3.863	4.5	3.047	1.687	0.438	23.892	5.941	2.195	6.859	0.362	1.455
HC_3N(2-1)	18.20	84	-23.10	16.205	10.099	4.177	5.263	1.527	1.799	23.459	16.681	3.397	7.903	0.619	3.075
HC_3N(2-1)	18.20	85	-21.04	5	51.138	13.611	30.464	0.611	0.431	19.087	2.724	4.428	3.932	1.32	1.193
HC_3N(2-1)	18.20	86	-18.99	14.967	2.694	6.854	2.954	1.945	0.464	25.562	6.912	1.749	8.897	0.261	1.077
HC_3N(3-2)	27.29	85	-32.30	15.232	0.977	3.213	1.08	5.677	1.193	23.707	12.888	2.065	14.512	0.339	1.473
HC_3N(3-2)	27.29	86	-30.93	15.25	10.523	2.934	4.205	4.323	12.604	20.48	50.005	2.934	21.162	0.912	12.327
HC_3N(3-2)	27.29	87	-29.55	16.461	0.74	3.171	0.756	4.172	0.842	nan	nan	nan	nan	nan	nan
HC_3N(3-2)	27.29	88	-28.18	16.037	2.539	2.509	1.818	3.571	1.222	21.163	5.56	1.924	3.661	1.185	2.374
HC_3N(3-2)	27.29	89	-26.81	16.662	1.173	2.671	1.232	3.691	0.892	22.611	2.458	1.547	2.281	1.212	1.337
HC_3N(3-2)	27.29	90	-25.44	17.216	1.119	2.785	1.224	3.574	0.808	22.884	2.298	1.351	2.277	1.009	1.401
HC_3N(3-2)	27.29	91	-24.06	16.99	1.304	2.812	1.383	3.568	0.801	22.648	2.189	1.479	2.145	1.236	1.496
HC_3N(3-2)	27.29	92	-22.69	16.711	2.185	2.961	1.912	3.456	0.862	22.678	4.388	1.918	3.747	1.077	1.888
HC_3N(3-2)	27.29	93	-21.32	16.468	1.292	2.632	1.298	4.113	1.034	22.856	2.719	1.845	2.486	1.55	1.348
HC_3N(3-2)	27.29	94	-19.94	16.358	1.359	2.924	1.352	4.649	1.051	22.848	2.692	1.818	2.431	1.647	1.621
HC_3N(3-2)	27.29	95	-18.57	15.767	2.09	2.831	1.678	5.519	1.528	22.636	5.701	2.496	4.36	1.812	1.937
HC_3N(4-3)	36.39	31	-32.65	15.504	8.615	2.951	4.047	4.483	8.769	21.273	60.256	2.951	28.693	0.641	8.712
HC_3N(4-3)	36.39	32	-31.62	15.574	4.709	2.585	2.878	4.366	3.166	20.593	17.055	2.102	9.593	0.891	5.545
HC_3N(4-3)	36.39	33	-30.59	16.372	2.352	2.956	2.166	3.597	1.129	21.663	7.565	1.444	7.736	0.509	2.757
HC_3N(4-3)	36.39	34	-29.56	16.686	3.303	2.858	2.714	3.21	1.207	21.632	6.223	1.524	5.934	0.744	3.463
HC_3N(4-3)	36.39	35	-28.53	17.182	1.65	2.874	1.727	2.977	0.941	22.102	3.662	0.986	4.428	0.535	2.064
HC_3N(4-3)	36.39	36	-27.50	17.695	1.432	3.048	1.518	2.944	0.876	22.55	3.79	0.747	4.703	0.399	2.017
HC_3N(4-3)	36.39	37	-26.47	17.645	1.308	2.829	1.492	2.976	1.035	23.238	4.633	0.86	5.073	0.408	1.939
HC_3N(4-3)	36.39	38	-25.44	17.801	1.178	3.08	1.191	2.929	0.971	nan	nan	nan	nan	nan	nan
HC_3N(4-3)	36.39	39	-24.41	17.98	1.56	3.113	1.595	3.005	1.004	22.495	12.061	-0.584	13.641	0.13	2.524
HC_3N(4-3)	36.39	40	-23.38	17.723	1.297	2.991	1.476	3.168	1.061	23.419	7.747	0.748	8.534	0.233	2.169
HC_3N(4-3)	36.39	41	-22.35	17.391	1.286	3.07	1.468	3.391	1.09	23.64	7.401	0.958	8.165	0.298	2.005
HC_3N(4-3)	36.39	42	-21.32	16.918	1.454	2.707	1.551	3.737	1.184	23.029	5.109	1.52	5.047	0.728	1.725
HC_3N(4-3)	36.39	43	-20.30	16.87	1.416	2.684	1.532	4.053	1.301	23.064	4.036	1.542	3.812	1.011	1.829
HC_3N(4-3)	36.39	44	-19.27	17.251	1.896	2.848	1.811	4.591	1.363	22.952	4.172	1.568	3.829	1.222	2.618
HC_5N(8-7)	21.30	61	-33.29	16.476	1.371	3.228	1.414	1.461	0.357	25.176	3.287	2.544	3.092	0.535	0.399
HC_5N(8-7)	21.30	62	-31.53	17.428	2.128	4.09	2.103	1.163	0.281	24.805	3.822	1.808	4.144	0.291	0.62
HC_5N(8-7)	21.30	63	-29.77	16.329	15.303	3.328	5.929	0.975	3.762	22.104	23.707	3.328	9.131	0.629	3.772
HC_5N(8-7)	21.30	64	-28.01	18.36	5.229	4.067	3.446	0.97	0.413	23.483	4.102	1.749	7.778	0.228	1.326
HC_5N(8-7)	21.30	65	-26.25	17.789	4.757	3.566	3.501	0.947	0.364	23.295	2.623	1.86	2.868	0.55	1.269

Table C.3 continued.

Transition	Restfreq	Ch	v_{ch}	R_{max} 1	ΔR_{max} 1	$W_{1/2}$ 1	$\Delta W_{1/2}$ 1	F_{max} 1	ΔF_{max} 1	R_{max} 2	ΔR_{max} 2	$W_{1/2}$ 2	$\Delta W_{1/2}$ 2	F_{max} 2	ΔF_{max} 2
HC_5N(8-7)	21.30	66	-24.49	18.534	4.559	4.13	3.139	0.933	0.349	23.807	2.029	1.698	3.603	0.43	1.096
HC_5N(8-7)	21.30	67	-22.73	17.468	5.034	3.288	3.59	0.9	0.435	23.398	3.487	2.183	2.417	0.715	1.151
HC_5N(8-7)	21.30	68	-20.98	18.271	3.169	5.248	2.152	0.872	0.31	23.358	2.047	1.481	2.748	0.406	0.626
HC_5N(8-7)	21.30	69	-19.22	15.929	7.769	3.223	4.357	0.923	1.195	22.876	7.03	3.223	3.875	1.019	1.207
HC_5N(9-8)	23.96	51	-31.95	17.715	1.126	3.238	1.256	1.218	0.299	25.289	2.456	1.615	2.719	0.373	0.427
HC_5N(9-8)	23.96	52	-30.39	17.145	6.418	2.637	3.258	1.027	1.54	22.481	9.684	2.637	4.776	0.68	1.564
HC_5N(9-8)	23.96	53	-28.82	16.974	5.509	2.256	2.924	0.994	1.421	21.64	7.452	2.256	3.788	0.736	1.456
HC_5N(9-8)	23.96	54	-27.26	17.372	3.689	2.526	2.657	0.873	0.43	22.514	3.141	1.927	2.04	0.742	0.85
HC_5N(9-8)	23.96	55	-25.69	17.901	2.231	2.462	1.856	0.98	0.31	23.088	1.857	1.739	1.38	0.833	0.598
HC_5N(9-8)	23.96	56	-24.13	17.959	2.346	2.449	2.047	0.86	0.308	23.253	1.8	1.713	1.391	0.811	0.548
HC_5N(9-8)	23.96	57	-22.57	17.561	3.343	2.304	2.557	0.868	0.484	23.032	3.163	2.191	2.115	0.888	0.589
HC_5N(9-8)	23.96	58	-21.00	17.739	3.079	2.923	2.785	0.803	0.311	23.554	1.726	1.79	1.418	0.872	0.674
HC_5N(9-8)	23.96	59	-19.44	17.441	3.668	2.334	2.533	0.902	0.606	23.091	2.976	2.334	2.025	1.111	0.61
HC_5N(10-9)	26.63	38	-32.78	17.449	0.859	2.759	0.963	1.893	0.437	25.191	3.461	1.869	3.703	0.385	0.511
HC_5N(10-9)	26.63	39	-31.38	17.153	12.316	2.861	5.24	1.244	4.069	22.455	25.099	2.861	11.571	0.611	3.937
HC_5N(10-9)	26.63	40	-29.97	17.676	13.198	2.432	5.564	1.16	4.959	22.013	21.385	2.432	8.411	0.712	5.101
HC_5N(10-9)	26.63	41	-28.56	17.053	33.259	2.604	13.047	0.641	7.217	21.391	25.529	2.604	8.891	0.824	7.518
HC_5N(10-9)	26.63	42	-27.16	17.892	13.991	2.495	7.497	0.823	2.306	22.132	9.921	2.045	4.41	0.763	4.056
HC_5N(10-9)	26.63	43	-25.75	18.987	3.429	3.002	2.644	1.267	0.409	23.193	2.578	1.3	4.143	0.374	1.551
HC_5N(10-9)	26.63	44	-24.34	17.387	6.351	2.223	3.983	0.889	1.265	22.314	5.528	2.223	3.306	1.026	1.301
HC_5N(10-9)	26.63	45	-22.93	16.962	30.221	2.808	12.935	0.703	6.271	21.796	21.675	2.808	7.898	0.969	6.642
HC_5N(10-9)	26.63	46	-21.53	17.587	3.788	2.259	2.602	1.185	0.737	22.505	4.292	1.945	2.792	0.878	1.096
HC_5N(10-9)	26.63	47	-20.12	16.829	20.522	2.795	10.279	0.741	3.736	22.168	16.251	2.795	7.207	0.937	3.942
HC_5N(10-9)	26.63	48	-18.71	16.782	3.822	2.296	2.666	1.39	0.992	22.272	4.343	2.296	2.877	1.231	1.022
HC_5N(11-10)	29.29	19	-32.39	16.271	0.819	2.942	0.822	1.5	0.361	nan	nan	nan	nan	nan	nan
HC_5N(11-10)	29.29	20	-31.11	17.029	0.822	2.874	0.938	1.423	0.321	23.583	3.441	1.119	3.582	0.201	0.504
HC_5N(11-10)	29.29	21	-29.83	15.663	4.611	2.386	3.011	0.973	0.771	20.75	3.908	2.15	2.248	1.009	1.089
HC_5N(11-10)	29.29	22	-28.55	18.711	0.93	3.528	0.95	1.132	0.258	nan	nan	nan	nan	nan	nan
HC_5N(11-10)	29.29	23	-27.27	17.895	3.178	3.101	2.045	1.138	0.43	21.653	2.145	1.295	3.956	0.329	1.242
HC_5N(11-10)	29.29	24	-25.99	17.033	2.75	2.467	2.158	1.053	0.376	21.917	2.779	1.7	2.048	0.669	0.855
HC_5N(11-10)	29.29	25	-24.71	17.608	1.132	2.343	1.21	1.17	0.338	22.804	1.022	1.262	0.997	0.857	0.503
HC_5N(11-10)	29.29	26	-23.43	17.929	2.488	2.305	1.947	0.929	0.34	22.943	2.362	1.754	1.944	0.72	0.58
HC_5N(11-10)	29.29	27	-22.15	17.878	2.6	1.976	1.895	1.055	0.562	22.747	2.769	1.935	1.997	0.968	0.589
HC_5N(11-10)	29.29	28	-20.87	20.385	1.066	3.617	1.143	1.068	0.272	nan	nan	nan	nan	nan	nan
HC_5N(11-10)	29.29	29	-19.60	16.408	3.892	2.537	3.573	0.771	0.447	22.938	3.011	2.537	2.51	1.019	0.463
HC_5N(12-11)	31.95	36	-32.38	17.193	3.564	2.545	2.313	1.953	1.211	23.297	25.875	2.545	20.951	0.257	1.063
HC_5N(12-11)	31.95	37	-31.21	16.78	14.641	2.356	5.87	1.337	6.748	20.951	23.16	2.356	9.319	0.845	6.739
HC_5N(12-11)	31.95	38	-30.04	16.875	2.682	2.133	1.705	1.954	1.129	21.837	6.444	2.133	4.236	0.808	1.104
HC_5N(12-11)	31.95	39	-28.86	17.065	1.879	2.279	1.783	1.56	0.555	22.229	2.258	1.571	1.906	0.972	0.85
HC_5N(12-11)	31.95	40	-27.69	18.25	2.339	2.846	2.264	1.398	0.44	23.139	2.647	1.31	2.934	0.499	1.18
HC_5N(12-11)	31.95	41	-26.52	17.387	6.513	2.091	3.41	1.208	2.2	21.744	8.551	2.091	4.58	0.918	2.173
HC_5N(12-11)	31.95	42	-25.34	18.109	3.756	2.7	3.019	1.215	0.51	22.896	2.553	1.601	2.094	0.87	1.514

Table C.3 continued.

Transition	Restfreq	Ch	v_{ch}	R_{max} 1	ΔR_{max} 1	$W_{1/2}$ 1	$\Delta W_{1/2}$ 1	F_{max} 1	ΔF_{max} 1	R_{max} 2	ΔR_{max} 2	$W_{1/2}$ 2	$\Delta W_{1/2}$ 2	F_{max} 2	ΔF_{max} 2
HC_5N(12-11)	31.95	43	-24.17	17.888	1.503	2.281	1.478	1.539	0.489	23.49	2.451	1.693	2.177	0.773	0.623
HC_5N(12-11)	31.95	44	-23.00	18.54	2.553	2.532	2.197	1.355	0.486	23.871	3.924	1.738	3.092	0.609	0.935
HC_5N(12-11)	31.95	45	-21.83	19.114	5.393	3.376	3.999	1.226	0.552	23.936	5.37	1.566	7.782	0.294	2.072
HC_5N(12-11)	31.95	46	-20.65	17.337	2.365	2.044	1.961	1.269	0.612	22.812	3.212	2.044	2.707	0.927	0.604
HC_5N(12-11)	31.95	47	-19.48	17.207	1.976	2.319	1.964	1.44	0.607	23.124	2.045	1.816	1.827	1.197	0.724
HC_5N(13-12)	34.61	31	-33.44	16.604	0.842	3.016	0.88	1.577	0.381	25.392	2.451	0.675	4.094	0.228	1.053
HC_5N(13-12)	34.61	32	-32.35	16.809	0.751	2.684	0.842	1.587	0.353	24.516	4.857	1.671	5.656	0.195	0.433
HC_5N(13-12)	34.61	33	-31.27	17.677	0.985	3.168	1.121	1.339	0.332	24.475	2.758	1.011	3.118	0.253	0.588
HC_5N(13-12)	34.61	34	-30.19	16.155	18.485	3.093	8.588	1.013	3.841	21.088	16.064	2.678	5.94	0.796	5.794
HC_5N(13-12)	34.61	35	-29.11	16.797	2.34	2.175	1.821	1.306	0.479	21.534	2.733	1.724	1.88	0.882	0.833
HC_5N(13-12)	34.61	36	-28.02	17.511	2.162	3.204	2.017	1.195	0.286	22.122	1.078	1.13	1.671	0.609	0.923
HC_5N(13-12)	34.61	37	-26.94	17.098	1.303	2.893	1.447	1.035	0.295	22.731	0.873	1.14	0.941	0.78	0.53
HC_5N(13-12)	34.61	38	-25.86	17.414	1.01	2.716	1.159	1.068	0.263	22.979	0.777	1.143	0.833	0.768	0.439
HC_5N(13-12)	34.61	39	-24.78	17.854	1.3	2.593	1.423	1.07	0.295	22.988	0.849	1.219	0.855	0.896	0.535
HC_5N(13-12)	34.61	40	-23.69	18.234	2.206	3.321	2.397	0.946	0.252	23.849	1.271	1.44	1.51	0.624	0.691
HC_5N(13-12)	34.61	41	-22.61	17.268	2.01	2.963	2.256	1.017	0.352	23.322	1.813	1.567	1.727	0.679	0.63
HC_5N(13-12)	34.61	42	-21.53	17.401	1.193	2.435	1.275	1.171	0.32	23.4	2.035	1.663	1.98	0.54	0.4
HC_5N(13-12)	34.61	43	-20.45	17.848	1.537	2.709	1.59	1.068	0.31	23.547	1.745	1.485	1.715	0.583	0.515
HC_5N(13-12)	34.61	44	-19.36	17.42	1.113	2.292	1.156	1.321	0.367	23.492	1.208	1.73	1.277	1.013	0.422
HC_5N(14-13)	37.28	40	-33.32	16.636	1.578	2.268	1.506	3.044	1.006	23.151	9.443	2.268	8.995	0.507	0.998
HC_5N(14-13)	37.28	41	-32.31	16.69	0.952	2.523	1.08	2.858	0.906	23.945	2.966	1.376	3.151	0.683	1.182
HC_5N(14-13)	37.28	42	-31.31	16.74	7.226	2.525	3.986	2.189	3.379	22.317	24.166	2.525	17.453	0.627	2.907
HC_5N(14-13)	37.28	43	-30.30	16.187	9.235	2.136	5.14	1.698	4.228	20.628	12.069	2.136	6.288	1.305	4.379
HC_5N(14-13)	37.28	44	-29.30	16.522	4.397	2.329	3.309	1.853	1.151	21.297	5.372	1.757	3.55	1.098	2.343
HC_5N(14-13)	37.28	45	-28.29	16.406	12.52	2.052	6.584	1.22	4.38	20.661	12.88	2.052	6.797	1.184	4.373
HC_5N(14-13)	37.28	46	-27.29	16.59	5.191	1.919	3.771	1.25	1.386	21.346	4.945	1.919	3.838	1.292	1.336
HC_5N(14-13)	37.28	47	-26.28	17.475	2.303	2.283	2.415	1.672	0.889	22.707	2.793	1.422	2.674	0.995	1.274
HC_5N(14-13)	37.28	48	-25.28	17.69	2.055	2.119	2.172	1.598	0.821	22.751	2.042	1.413	1.945	1.237	1.096
HC_5N(14-13)	37.28	49	-24.27	17.342	1.925	2.068	2.032	1.738	0.91	22.302	2.168	1.346	1.992	1.188	1.203
HC_5N(14-13)	37.28	50	-23.27	17.456	8.85	2.214	5.764	1.253	1.917	21.968	10.426	1.857	6.186	0.84	3.186
HC_5N(14-13)	37.28	51	-22.26	17.104	85.467	2.673	29.231	0.804	25.567	21.306	58.367	2.673	19.759	1.175	25.647
HC_5N(14-13)	37.28	52	-21.26	16.985	3.643	1.991	3.043	1.476	1.033	21.969	3.639	1.785	3.044	1.338	1.223
HC_5N(14-13)	37.28	53	-20.25	16.789	4.006	2.529	4.607	1.401	0.982	22.483	2.731	1.707	2.286	1.593	1.588
HC_5N(14-13)	37.28	54	-19.25	17.094	2.807	2.194	2.472	2.111	1.045	22.548	3.338	1.893	2.791	1.579	1.303
HC_7N(16-15)	18.05	48	-31.42	13.478	31.342	4.837	26.57	0.121	1.765	25.605	1.523	1.169	1.839	0.218	0.256
HC_7N(16-15)	18.05	49	-29.34	15.644	2.915	2.032	2.94	0.226	0.183	21.794	2.823	2.032	2.699	0.231	0.173
HC_7N(16-15)	18.05	50	-27.27	15.012	83.067	8.982	70.255	0.094	0.54	20.025	3.694	2.838	6.137	0.223	0.648
HC_7N(16-15)	18.05	51	-25.19	15.088	9.706	3.609	7.397	0.215	0.237	23.833	7.827	3.609	5.125	0.271	0.257
HC_7N(16-15)	18.05	52	-23.12	15.4	9.744	2.249	11.966	0.076	0.18	22.033	4.905	2.249	4.44	0.162	0.167
HC_7N(16-15)	18.05	53	-21.04	0.384	104.735	20.284	69.041	0.153	0.273	nan	nan	nan	nan	nan	nan
HC_7N(16-15)	18.05	54	-18.96	11.566	7.364	4.654	7.006	0.349	0.217	23.525	7.319	4.654	5.342	0.359	0.232
HC_7N(17-16)	19.18	71	-32.17	17.019	3.17	7.084	3.598	0.234	0.073	26.376	6.196	0.757	6.795	0.053	0.327

Table C.3 continued.

Transition	Restfreq	Ch	v_{ch}	R_{max} 1	ΔR_{max} 1	$W_{1/2}$ 1	$\Delta W_{1/2}$ 1	F_{max} 1	ΔF_{max} 1	R_{max} 2	ΔR_{max} 2	$W_{1/2}$ 2	$\Delta W_{1/2}$ 2	F_{max} 2	ΔF_{max} 2
HC_7N(17-16)	19.18	72	-30.22	18.516	2.256	7.064	2.402	0.251	0.069	nan	nan	nan	nan	nan	nan
HC_7N(17-16)	19.18	73	-28.27	5	31.888	9.461	79.159	0.083	0.099	21.217	2.345	3.858	3.857	0.275	0.389
HC_7N(17-16)	19.18	74	-26.31	7.965	7.081	3.636	8.985	0.085	0.11	20.382	1.471	3.636	1.564	0.341	0.093
HC_7N(17-16)	19.18	75	-24.36	20.802	1.878	5.159	1.953	0.216	0.068	nan	nan	nan	nan	nan	nan
HC_7N(17-16)	19.18	76	-22.40	11.584	8.359	9.25	11.291	0.152	0.072	23.01	1.465	1.992	2.151	0.215	0.182
HC_7N(17-16)	19.18	77	-20.45	16.717	41.865	3.532	20.078	0.136	1.207	23.079	22.439	3.532	8.49	0.251	1.327
HC_7N(18-17)	20.30	71	-33.16	21.779	2.404	5.837	3.026	1.777	0.594	nan	nan	nan	nan	nan	nan
HC_7N(18-17)	20.30	72	-31.31	5.043	18.689	11.7	12.914	0.914	0.494	nan	nan	nan	nan	nan	nan
HC_7N(18-17)	20.30	73	-29.46	2.472	1.664	1.615	1.874	1.691	1.322	nan	nan	nan	nan	nan	nan
HC_7N(18-17)	20.30	74	-27.62	1.986	9.155	4.039	7.345	1.302	0.97	nan	nan	nan	nan	nan	nan
HC_7N(18-17)	20.30	75	-25.77	12.095	6.058	2.761	6.995	0.536	0.734	23.352	1.455	2.761	1.55	1.428	0.618
HC_7N(18-17)	20.30	76	-23.93	6.083	3.289	3.219	4.516	1.044	0.818	19.646	2.569	3.219	3.321	1.054	0.632
HC_7N(18-17)	20.30	77	-22.08	16.475	1.894	2.615	1.899	1.408	0.566	24.331	4.422	2.615	4.175	0.589	0.527
HC_7N(18-17)	20.30	78	-20.24	23.856	57.993	21.422	97.79	0.495	0.317	nan	nan	nan	nan	nan	nan
HC_7N(19-18)	21.43	40	-32.60	17.335	2.627	4.229	3.116	0.27	0.107	24.812	3.424	1.339	4.241	0.084	0.214
HC_7N(19-18)	21.43	41	-30.85	5	48.881	13.622	38.978	0.106	0.107	21.836	3.133	3.724	4.517	0.185	0.193
HC_7N(19-18)	21.43	42	-29.10	16.892	3.105	6.908	3.762	0.241	0.074	27.286	3.536	1.366	4.453	0.066	0.171
HC_7N(19-18)	21.43	43	-27.35	18.161	18.739	12.668	48.596	0.08	0.25	19.891	3.809	3.031	6.211	0.123	0.247
HC_7N(19-18)	21.43	44	-25.61	19.426	4.949	5.191	3.922	0.146	0.113	23.235	1.349	1.188	1.624	0.177	0.192
HC_7N(19-18)	21.43	45	-23.86	16.483	4.315	3.176	5.99	0.142	nan	23.055	3.894	3.176	nan	0.199	nan
HC_7N(19-18)	21.43	46	-22.11	9.957	40.518	3.579	72.614	0.02	0.172	21.599	2.296	3.579	2.263	0.323	0.11
HC_7N(19-18)	21.43	47	-20.36	21.36	2.811	5.173	3.075	0.228	0.133	23.611	3.441	-0.786	2.66	0.091	0.229
HC_7N(19-18)	21.43	48	-18.61	22.302	2.024	4.808	2.045	0.266	0.097	nan	nan	nan	nan	nan	nan
HC_7N(20-19)	22.56	50	-33.38	17.638	1.701	4.138	2.018	0.426	0.127	26.119	4.364	1.555	4.652	0.088	0.211
HC_7N(20-19)	22.56	51	-31.72	17.488	6.931	2.886	4.132	0.356	0.439	23.782	14.523	2.886	8.068	0.17	0.458
HC_7N(20-19)	22.56	52	-30.06	16.826	49.477	3.433	18.15	0.176	2.32	22.44	34.47	3.433	11.863	0.249	2.372
HC_7N(20-19)	22.56	53	-28.40	18.936	1.665	3.576	1.738	0.296	0.119	nan	nan	nan	nan	nan	nan
HC_7N(20-19)	22.56	54	-26.74	21.032	1.607	4.244	1.745	0.295	0.096	nan	nan	nan	nan	nan	nan
HC_7N(20-19)	22.56	55	-25.08	17.588	67.054	2.271	21.179	0.139	4.306	21.03	30.042	2.271	9.523	0.309	4.302
HC_7N(20-19)	22.56	56	-23.42	16.189	3.044	2.462	3.198	0.179	0.128	23.34	1.895	2.223	1.814	0.272	0.13
HC_7N(20-19)	22.56	57	-21.76	17.272	10.789	2.357	6.316	0.181	0.42	22.501	6.293	2.357	3.804	0.308	0.412
HC_7N(20-19)	22.56	58	-20.09	17.841	6.73	2.304	5.105	0.183	0.216	23.595	3.291	2.304	2.409	0.374	0.219
HC_7N(22-21)	24.82	49	-33.40	16.934	1.128	2.571	1.159	0.435	0.115	24.937	3.103	2.562	3.124	0.154	0.11
HC_7N(22-21)	24.82	50	-31.89	18.194	1.183	2.232	1.282	0.36	0.13	24.918	1.515	1.912	1.52	0.259	0.132
HC_7N(22-21)	24.82	51	-30.38	15.593	32.545	5.814	13.572	0.124	0.453	21.363	4.21	3.274	7.833	0.157	0.806
HC_7N(22-21)	24.82	52	-28.87	21.334	1.588	4.129	1.96	0.274	0.087	nan	nan	nan	nan	nan	nan
HC_7N(22-21)	24.82	53	-27.36	16.397	71.12	3.498	52.918	0.151	2.19	23.122	61.402	3.498	26.817	0.19	2.614
HC_7N(22-21)	24.82	54	-25.85	18.385	3.086	1.745	2.732	0.181	0.13	22.668	1.8	1.444	1.438	0.268	0.166
HC_7N(22-21)	24.82	55	-24.34	17.054	2.103	1.822	2.264	0.167	0.14	23.251	1.013	1.822	1.07	0.341	0.134
HC_7N(22-21)	24.82	56	-22.83	21.172	1.884	3.861	2.127	0.223	0.089	nan	nan	nan	nan	nan	nan
HC_7N(22-21)	24.82	57	-21.32	15.475	27.001	2.376	48.998	0.024	0.144	22.731	1.822	2.376	1.666	0.378	0.131
HC_7N(22-21)	24.82	58	-19.81	22.159	6.787	4.021	5.025	0.164	0.559	23.902	3.548	1.934	5.173	0.133	0.554

Table C.3 continued.

Transition	Restfreq	Ch	v_{ch}	R_{max} 1	ΔR_{max} 1	$W_{1/2}$ 1	$\Delta W_{1/2}$ 1	F_{max} 1	ΔF_{max} 1	R_{max} 2	ΔR_{max} 2	$W_{1/2}$ 2	$\Delta W_{1/2}$ 2	F_{max} 2	ΔF_{max} 2
HC_7N(23-22)	25.94	30	-33.10	17.394	2.326	2.434	2.034	0.433	0.176	23.977	5.314	2.434	4.349	0.191	0.175
HC_7N(23-22)	25.94	31	-31.65	17.473	2.202	2.39	2.154	0.327	0.144	24.339	3.138	2.39	3.017	0.228	0.139
HC_7N(23-22)	25.94	32	-30.21	17.408	89.831	3.598	29.69	0.179	4.734	22.746	61.414	3.598	17.877	0.256	4.899
HC_7N(23-22)	25.94	33	-28.77	18.504	8.097	2.673	5.039	0.269	0.395	24.527	16.309	2.673	10.264	0.133	0.393
HC_7N(23-22)	25.94	34	-27.32	21.218	1.077	3.351	1.099	0.376	0.105	nan	nan	nan	nan	nan	nan
HC_7N(23-22)	25.94	35	-25.88	20.378	2.002	4.303	2.244	0.271	0.104	nan	nan	nan	nan	nan	nan
HC_7N(23-22)	25.94	36	-24.43	21.791	1.035	2.986	1.091	0.378	0.114	nan	nan	nan	nan	nan	nan
HC_7N(23-22)	25.94	37	-22.99	22.096	1.266	3.389	1.297	0.325	0.105	nan	nan	nan	nan	nan	nan
HC_7N(23-22)	25.94	38	-21.54	17.463	55.273	3.017	30.487	0.11	1.39	23.128	21.023	3.017	8.311	0.291	1.596
HC_7N(23-22)	25.94	39	-20.10	21.707	1.392	3.494	1.612	0.383	0.126	nan	nan	nan	nan	nan	nan
HC_7N(23-22)	25.94	40	-18.66	16.034	10.722	2.619	8.842	0.126	0.207	22.77	3.432	2.619	2.564	0.4	0.214
HC_7N(24-23)	27.07	39	-32.74	17.347	1.731	2.11	1.62	0.519	0.198	23.34	4.077	2.11	3.822	0.218	0.192
HC_7N(24-23)	27.07	40	-31.35	20.172	1.352	3.986	1.417	0.468	0.137	nan	nan	nan	nan	nan	nan
HC_7N(24-23)	27.07	41	-29.97	16.929	42.027	2.106	26.985	0.213	2.944	20.881	26.912	2.106	10.289	0.343	3.583
HC_7N(24-23)	27.07	42	-28.58	19.56	1.309	-2.751	1.381	0.41	0.167	nan	nan	nan	nan	nan	nan
HC_7N(24-23)	27.07	43	-27.20	16.226	2.262	1.97	2.949	0.258	0.201	22.576	1.389	1.97	1.413	0.432	0.185
HC_7N(24-23)	27.07	44	-25.81	19.521	15.541	2.809	8.868	0.161	0.471	22.469	1.219	1.33	1.954	0.433	0.944
HC_7N(24-23)	27.07	45	-24.43	17.419	2.238	1.561	2.414	0.192	0.206	22.921	1.391	1.561	1.66	0.3	0.205
HC_7N(24-23)	27.07	46	-23.05	20.877	1.247	2.869	1.354	0.449	0.168	nan	nan	nan	nan	nan	nan
HC_7N(24-23)	27.07	47	-21.66	0.866	4.691	1.846	3.464	0.476	0.408	nan	nan	nan	nan	nan	nan
HC_7N(24-23)	27.07	48	-20.28	15.091	3.457	2.208	4.851	0.227	0.416	22.912	1.718	2.208	1.812	0.38	0.202
HC_7N(24-23)	27.07	49	-18.89	16.646	2.199	2.196	2.645	0.259	nan	22.788	1.894	2.196	nan	0.342	nan
HC_7N(25-24)	28.20	40	-32.20	17.147	1.673	2.775	2.101	0.237	0.116	25.563	4.499	1.892	5.661	0.074	0.132
HC_7N(25-24)	28.20	41	-30.87	18.09	2.983	2.056	2.267	0.332	0.198	23.315	5.667	2.056	4.184	0.174	0.199
HC_7N(25-24)	28.20	42	-29.54	18.615	2.157	3.534	3.088	0.24	0.118	25.569	2.19	0.934	2.375	0.104	0.218
HC_7N(25-24)	28.20	43	-28.21	20.687	1.634	3.152	1.872	0.273	0.121	nan	nan	nan	nan	nan	nan
HC_7N(25-24)	28.20	44	-26.89	-5.848	653.952	3.079	145.608	2.214	525.54	nan	nan	nan	nan	nan	nan
HC_7N(25-24)	28.20	45	-25.56	21.34	1.707	3.182	1.744	0.263	0.122	nan	nan	nan	nan	nan	nan
HC_7N(25-24)	28.20	46	-24.23	18.932	25.315	1.798	14.039	0.072	0.558	22.771	7.381	1.798	3.989	0.248	0.567
HC_7N(25-24)	28.20	47	-22.90	17.967	20.149	3.705	17.023	0.155	0.203	23.339	3.102	1.931	4.142	0.233	0.957
HC_7N(25-24)	28.20	48	-21.57	15.163	3.274	1.78	3.877	0.12	0.174	22.907	1.625	1.78	1.688	0.204	0.159
HC_7N(25-24)	28.20	49	-20.24	21.847	1.635	3.632	1.784	0.285	0.111	nan	nan	nan	nan	nan	nan
HC_7N(25-24)	28.20	50	-18.91	19.08	45.294	2.094	20.913	0.097	1.503	23.017	14.44	2.094	6.435	0.302	1.529
HC_7N(26-25)	29.33	19	-32.42	19.606	1.513	4.288	1.652	0.417	0.123	nan	nan	nan	nan	nan	nan
HC_7N(26-25)	29.33	20	-31.14	10.723	25.272	8	53.868	0.092	0.151	21.28	1.859	2.343	3.868	0.253	0.477
HC_7N(26-25)	29.33	21	-29.87	15.559	1.749	1.736	2.104	0.201	0.169	22.233	1.253	1.736	1.462	0.264	0.157
HC_7N(26-25)	29.33	22	-28.59	17.694	3.054	4.412	3.843	0.263	0.104	22.797	1.71	0.69	4.064	0.102	0.316
HC_7N(26-25)	29.33	23	-27.31	15.596	1.839	1.596	2.195	0.188	0.178	22.175	0.901	1.596	0.975	0.34	0.163
HC_7N(26-25)	29.33	24	-26.03	18.722	1.108	1.276	1.276	0.276	0.174	23.001	1.285	1.276	1.332	0.239	0.162
HC_7N(26-25)	29.33	25	-24.75	20.05	13.59	3.125	8.804	0.265	0.358	24.277	10.395	1.623	15.202	0.07	1.239
HC_7N(26-25)	29.33	26	-23.48	18.341	1.572	1.407	1.464	0.354	0.196	22.401	1.931	1.407	1.752	0.286	0.191
HC_7N(26-25)	29.33	27	-22.20	12.476	28.965	11.2	63.467	0.092	0.094	21.836	1.226	1.22	1.919	0.241	0.316

Table C.3 continued.

Transition	Restfreq	Ch	v_{ch}	R_{max} 1	ΔR_{max} 1	$W_{1/2}$ 1	$\Delta W_{1/2}$ 1	F_{max} 1	ΔF_{max} 1	R_{max} 2	ΔR_{max} 2	$W_{1/2}$ 2	$\Delta W_{1/2}$ 2	F_{max} 2	ΔF_{max} 2
HC_7N(26-25)	29.33	28	-20.92	15.744	2.023	1.86	2.714	0.225	0.188	22.174	0.945	1.86	1.037	0.473	0.169
HC_7N(26-25)	29.33	29	-19.64	11.084	29.74	10.555	42.412	0.143	0.164	21.642	1.831	1.872	3.148	0.304	0.417
HC_7N(27-26)	30.46	30	-32.39	19.189	13.7	2.998	7.317	0.271	0.719	25.448	22.28	2.998	12.232	0.165	0.71
HC_7N(27-26)	30.46	31	-31.16	18.39	4.683	4.534	6.316	0.235	0.199	nan	nan	nan	nan	nan	nan
HC_7N(27-26)	30.46	32	-29.93	17.093	21.455	2.411	20.636	0.174	0.683	22.573	11.127	2.411	5.973	0.38	0.941
HC_7N(27-26)	30.46	33	-28.70	21.021	3.438	4.664	4.305	0.295	0.17	nan	nan	nan	nan	nan	nan
HC_7N(27-26)	30.46	34	-27.47	19.313	8.042	3.758	7.14	0.173	0.33	21.424	3.15	0.926	4.047	0.12	0.435
HC_7N(27-26)	30.46	35	-26.24	14.703	45.569	2.268	30.889	0.111	nan	21.809	4.192	2.268	nan	0.187	nan
HC_7N(27-26)	30.46	36	-25.01	18.402	21.557	1.987	13.426	0.143	0.799	22.697	6.385	1.987	3.408	0.488	0.873
HC_7N(27-26)	30.46	37	-23.78	14.925	13.652	1.792	11.635	0.103	0.234	22.707	1.681	1.792	1.777	0.253	0.201
HC_7N(27-26)	30.46	38	-22.55	0	0	0	0	0	0	nan	nan	nan	nan	nan	nan
HC_7N(27-26)	30.46	39	-21.32	21.642	1.985	2.835	2.01	0.356	0.216	nan	nan	nan	nan	nan	nan
HC_7N(27-26)	30.46	40	-20.09	23.848	2.603	4.276	3.003	0.297	0.155	nan	nan	nan	nan	nan	nan
HC_7N(27-26)	30.46	41	-18.86	24.537	3.63	3.161	4.132	0.248	0.234	nan	nan	nan	nan	nan	nan
HC_7N(28-27)	31.58	29	-32.46	17.83	4.387	2.355	3.055	0.683	0.546	23.456	9.824	2.355	6.522	0.307	0.561
HC_7N(28-27)	31.58	30	-31.27	17.428	5.177	2.153	4.099	0.571	0.568	22.548	6.83	2.153	4.424	0.45	0.639
HC_7N(28-27)	31.58	31	-30.08	17.376	7.237	2.195	4.686	0.555	0.915	22.174	9.332	2.195	5.061	0.438	1.016
HC_7N(28-27)	31.58	32	-28.90	20.457	1.775	3.304	1.801	0.475	0.221	nan	nan	nan	nan	nan	nan
HC_7N(28-27)	31.58	33	-27.71	18.239	10.355	2.201	4.825	0.588	1.897	22.47	15.809	2.201	7.136	0.384	1.927
HC_7N(28-27)	31.58	34	-26.53	20.539	1.097	3.047	1.156	0.711	0.222	nan	nan	nan	nan	nan	nan
HC_7N(28-27)	31.58	35	-25.34	18.567	2.926	1.796	2.476	0.577	0.382	23.328	3.788	1.796	3.145	0.446	0.381
HC_7N(28-27)	31.58	36	-24.15	20.713	1.508	-3.296	1.695	0.577	0.227	nan	nan	nan	nan	nan	nan
HC_7N(28-27)	31.58	37	-22.97	19.679	11.851	2.407	7.314	0.321	0.542	23.299	3.058	1.448	2.646	0.427	1.582
HC_7N(28-27)	31.58	38	-21.78	16.518	51.759	2.622	38.044	0.093	0.859	22.409	9.528	2.622	5.668	0.522	0.969
HC_7N(28-27)	31.58	39	-20.59	21.879	1.663	3.453	1.93	0.581	0.24	nan	nan	nan	nan	nan	nan
HC_7N(28-27)	31.58	40	-19.41	18.409	6.66	2.411	4.38	0.486	0.605	24.023	7.084	2.411	4.452	0.458	0.622
HC_7N(29-28)	32.71	38	-32.46	17.138	1.889	1.826	1.85	0.403	0.218	22.983	10.822	1.826	7.896	0.103	0.261
HC_7N(29-28)	32.71	39	-31.31	17.554	2.423	2.034	2.269	0.435	0.221	23.118	4.742	2.034	4.149	0.224	0.218
HC_7N(29-28)	32.71	40	-30.17	19.722	13.275	8.377	12.919	0.189	0.115	nan	nan	nan	nan	nan	nan
HC_7N(29-28)	32.71	41	-29.02	19.502	1.481	2.585	1.608	0.378	0.183	nan	nan	nan	nan	nan	nan
HC_7N(29-28)	32.71	42	-27.88	19.722	7.47	4.682	8.421	0.205	0.3	21.609	0.904	0.953	1.209	0.379	0.394
HC_7N(29-28)	32.71	43	-26.73	18.845	1.188	1.427	1.341	0.335	0.235	24.198	1.394	0.82	1.407	0.197	0.289
HC_7N(29-28)	32.71	44	-25.59	13.307	9.661	4.511	12.38	0.188	0.85	24.233	1.685	1.77	1.769	0.296	0.218
HC_7N(29-28)	32.71	45	-24.44	20.727	10.902	4.633	9.506	0.167	0.237	23.349	1.387	1.01	1.926	0.229	0.349
HC_7N(29-28)	32.71	46	-23.29	20.732	37.157	13.796	63.758	0.117	0.414	20.732	3.056	1.842	5.185	0.188	0.433
HC_7N(29-28)	32.71	47	-22.15	0	0	0	0	0	0	nan	nan	nan	nan	nan	nan
HC_7N(29-28)	32.71	48	-21.00	22.41	6.102	7.984	7.968	0.226	0.133	nan	nan	nan	nan	nan	nan
HC_7N(30-29)	33.84	37	-33.00	18.189	2.962	2.142	2.756	0.258	0.17	24.291	18.448	2.142	16.494	0.041	0.166
HC_7N(30-29)	33.84	38	-31.89	17.987	9.541	2.518	5.241	0.27	0.576	23.3	27.816	2.518	15.063	0.093	0.581
HC_7N(30-29)	33.84	39	-30.78	17.612	5.331	1.98	3.874	0.226	0.251	22.502	6.631	1.98	4.791	0.181	0.251
HC_7N(30-29)	33.84	40	-29.68	18.524	1.565	2.187	1.587	0.262	0.162	nan	nan	nan	nan	nan	nan
HC_7N(30-29)	33.84	41	-28.57	20.448	3.154	3.391	2.778	0.201	0.16	22.796	2.202	0.615	2.276	0.101	0.308

Table C.3 continued.

Transition	Restfreq	Ch	v_{ch}	R_{max} 1	ΔR_{max} 1	$W_{1/2}$ 1	$\Delta W_{1/2}$ 1	F_{max} 1	ΔF_{max} 1	R_{max} 2	ΔR_{max} 2	$W_{1/2}$ 2	$\Delta W_{1/2}$ 2	F_{max} 2	ΔF_{max} 2
HC_7N(30-29)	33.84	42	-27.46	18.448	6.68	1.695	6.133	0.146	0.222	22.751	5.574	1.695	3.961	0.185	0.248
HC_7N(30-29)	33.84	43	-26.35	20.433	2.014	2.997	2.247	0.233	0.135	nan	nan	nan	nan	nan	nan
HC_7N(30-29)	33.84	44	-25.25	20.038	14.475	2.975	9.997	0.173	0.256	23.186	2.378	0.991	5.161	0.153	0.907
HC_7N(30-29)	33.84	45	-24.14	20.442	7.411	4.464	7.176	0.094	0.128	23.169	1.336	0.844	1.559	0.157	0.23
HC_7N(30-29)	33.84	46	-23.03	17.782	36.358	2.205	22.481	0.099	0.736	21.982	16.834	1.892	9.088	0.165	1.198
HC_7N(30-29)	33.84	47	-21.92	21.77	2.161	2.647	2.353	0.218	0.153	nan	nan	nan	nan	nan	nan
HC_7N(30-29)	33.84	48	-20.82	18.464	4.083	1.702	4.23	0.25	0.239	23.074	4.99	1.702	4.398	0.214	0.245
HC_7N(30-29)	33.84	49	-19.71	15.102	2.041	1.309	2.296	0.221	0.248	22.921	1.282	1.309	1.296	0.269	0.229
HC_7N(30-29)	33.84	50	-18.60	15.735	19.833	2.37	27.091	0.067	0.219	21.956	4.267	2.37	3.021	0.38	0.274
HC_7N(31-30)	34.97	15	-33.32	17.402	0.926	3.117	0.996	0.751	0.188	nan	nan	nan	nan	nan	nan
HC_7N(31-30)	34.97	16	-32.25	12.621	8.757	7.531	10.346	0.242	0.154	20.537	1.052	1.473	1.426	0.394	0.307
HC_7N(31-30)	34.97	17	-31.18	19.712	1.028	3.316	1.17	0.537	0.139	nan	nan	nan	nan	nan	nan
HC_7N(31-30)	34.97	18	-30.10	20.425	1.325	3.318	1.48	0.423	0.141	nan	nan	nan	nan	nan	nan
HC_7N(31-30)	34.97	19	-29.03	4.561	28.982	17.839	23.937	0.362	0.233	nan	nan	nan	nan	nan	nan
HC_7N(31-30)	34.97	20	-27.96	16.62	8.826	6.024	7.343	0.198	0.191	20.521	1.503	1.209	1.909	0.279	0.339
HC_7N(31-30)	34.97	21	-26.89	16.988	1.952	1.978	2.152	0.293	0.227	23.203	1.573	1.534	1.627	0.316	0.243
HC_7N(31-30)	34.97	22	-25.82	5	88.161	19.169	58.604	0.18	0.337	21.933	1.225	-0.966	1.369	0.276	0.317
HC_7N(31-30)	34.97	23	-24.75	21.031	2.034	4.298	2.073	0.309	0.126	nan	nan	nan	nan	nan	nan
HC_7N(31-30)	34.97	24	-23.68	16.906	8.879	8.518	8.623	0.124	0.094	22.513	0.806	0.686	0.753	0.23	0.227
HC_7N(31-30)	34.97	25	-22.60	23.019	2.691	5.152	2.896	0.279	0.12	nan	nan	nan	nan	nan	nan
HC_7N(31-30)	34.97	26	-21.53	17.809	2.906	2.774	3.038	0.418	0.169	23.318	1.694	1.627	1.486	0.427	0.372
HC_7N(31-30)	34.97	27	-20.46	17.685	63.416	1.992	30.537	0.15	3.816	21.164	25.67	1.992	9.225	0.368	4.231
HC_7N(31-30)	34.97	28	-19.39	17.994	1.361	2.479	1.589	0.462	0.174	24.381	2.042	1.587	2.089	0.241	0.205
HC_7N(32-31)	36.10	37	-32.74	17.489	2.95	2.154	2.299	0.587	0.324	22.964	10.642	2.154	8.105	0.163	0.324
HC_7N(32-31)	36.10	38	-31.71	15.903	8.319	2.072	6.875	0.202	0.318	21.058	5.598	2.072	3.963	0.308	0.344
HC_7N(32-31)	36.10	39	-30.67	16.798	5.602	1.605	6.541	0.215	0.293	21.009	5.026	1.605	3.648	0.274	0.342
HC_7N(32-31)	36.10	40	-29.63	17.611	15.941	2.282	17.887	0.177	0.502	22.99	12.083	2.282	6.84	0.277	0.731
HC_7N(32-31)	36.10	41	-28.59	20.026	2.972	3.481	3.428	0.23	0.168	nan	nan	nan	nan	nan	nan
HC_7N(32-31)	36.10	42	-27.55	20.498	3.443	3.217	4.017	0.209	0.189	nan	nan	nan	nan	nan	nan
HC_7N(32-31)	36.10	43	-26.51	21.499	8.553	6.197	7.771	0.237	0.129	nan	nan	nan	nan	nan	nan
HC_7N(32-31)	36.10	44	-25.48	17.297	6.795	3.785	9.835	0.292	0.232	23.849	4.059	0.685	4.866	0.089	0.541
HC_7N(32-31)	36.10	45	-24.44	19.132	3.007	2.76	4.241	0.346	0.263	23.99	2.961	0.826	3.589	0.146	0.533
HC_7N(32-31)	36.10	46	-23.40	22.658	1.312	2.369	1.329	0.412	0.198	nan	nan	nan	nan	nan	nan
HC_7N(32-31)	36.10	47	-22.36	21.999	2.419	2.998	2.601	0.275	0.176	nan	nan	nan	nan	nan	nan
HC_7N(32-31)	36.10	48	-21.32	15.151	13.292	1.729	14.484	0.148	0.856	23.201	1.967	1.729	2.05	0.277	0.269
HC_7N(32-31)	36.10	49	-20.29	22.539	1.327	2.767	1.368	0.432	0.18	nan	nan	nan	nan	nan	nan
HC_7N(32-31)	36.10	50	-19.25	17.179	52.577	2.454	33.736	0.219	3.234	21.818	29.113	2.454	11.59	0.409	3.873
HC_7N(33-32)	37.22	36	-33.06	17.504	3.205	1.728	3.693	0.201	0.265	23.575	8.909	1.728	12.908	0.083	0.801
HC_7N(33-32)	37.22	37	-32.06	14.771	9.925	5.223	12.837	0.219	0.193	22.5	1.544	1.626	2.373	0.389	0.55
HC_7N(33-32)	37.22	38	-31.05	16.014	7.92	2.158	6.406	0.242	0.33	22.083	8.764	2.158	18.485	0.176	0.263
HC_7N(33-32)	37.22	39	-30.04	14.215	21.529	2.296	20.397	0.15	0.561	19.699	11.871	2.296	7.555	0.298	0.704
HC_7N(33-32)	37.22	40	-29.04	0	0	0	0	0	0	nan	nan	nan	nan	nan	nan

Table C.3 continued.

Transition	Restfreq	Ch	v_{ch}	R_{max} 1	ΔR_{max} 1	$W_{1/2}$ 1	$\Delta W_{1/2}$ 1	F_{max} 1	ΔF_{max} 1	R_{max} 2	ΔR_{max} 2	$W_{1/2}$ 2	$\Delta W_{1/2}$ 2	F_{max} 2	ΔF_{max} 2
HC_7N(33-32)	37.22	41	-28.03	17.669	2.978	1.783	3.515	0.308	0.304	23.69	9.036	1.783	13.307	0.152	1.939
HC_7N(33-32)	37.22	42	-27.02	20.277	2.861	2.802	2.456	0.343	0.337	21.908	2.297	0.655	3.001	0.138	0.483
HC_7N(33-32)	37.22	43	-26.02	20.645	4.282	2.312	4.716	0.2	0.286	nan	nan	nan	nan	nan	nan
HC_7N(33-32)	37.22	44	-25.01	22.02	2.045	-2.054	2.203	0.36	0.309	nan	nan	nan	nan	nan	nan
HC_7N(33-32)	37.22	45	-24.00	17.602	3.328	1.785	4.343	0.199	0.276	22.806	1.787	1.357	1.782	0.33	0.286
HC_7N(33-32)	37.22	46	-23.00	20.829	1.333	0.938	1.36	0.347	0.428	nan	nan	nan	nan	nan	nan
HC_7N(33-32)	37.22	47	-21.99	13.595	15.302	2.65	10.775	0.14	1	22.533	1.779	1.733	1.856	0.321	0.254
HC_7N(33-32)	37.22	48	-20.98	0	0	0	0	0	0	nan	nan	nan	nan	nan	nan
HC_7N(33-32)	37.22	49	-19.98	14.171	53.998	10.601	73.042	0.072	0.17	22.27	1.915	0.834	2.215	0.231	0.486
HC_7N(33-32)	37.22	50	-18.97	21.435	7.279	5.93	11.352	0.222	0.182	nan	nan	nan	nan	nan	nan
C_3N(2-1,3/2-1/2)	19.80	58	-32.64	20.108	2.556	7.16	2.979	0.14	0.04	nan	nan	nan	nan	nan	nan
C_3N(2-1,3/2-1/2)	19.80	59	-30.75	12.978	1.966	3.985	2.13	0.206	0.071	nan	nan	nan	nan	nan	nan
C_3N(2-1,3/2-1/2)	19.80	60	-28.86	4.707	26.015	12.262	25.723	0.11	0.065	nan	nan	nan	nan	nan	nan
C_3N(2-1,3/2-1/2)	19.80	61	-26.97	4.245	2.579	2.294	2.604	0.12	0.101	nan	nan	nan	nan	nan	nan
C_3N(2-1,3/2-1/2)	19.80	62	-25.07	15.659	6.737	4.632	7.978	0.075	nan	30.335	11.797	4.632	nan	0.055	nan
C_3N(2-1,3/2-1/2)	19.80	63	-23.18	2.4	1.785	1.749	1.701	0.188	0.13	nan	nan	nan	nan	nan	nan
C_3N(2-1,3/2-1/2)	19.80	64	-21.29	0	0	0	0	0	0	nan	nan	nan	nan	nan	nan
C_3N(2-1,3/2-1/2)	19.80	65	-19.40	13.447	6.976	10.44	12.29	0.128	0.063	nan	nan	nan	nan	nan	nan
C_3N(2-1,5/2-3/2)	19.78	49	-33.07	18.503	4.303	2.376	3.314	0.172	0.126	24.426	5.204	2.376	3.715	0.143	0.13
C_3N(2-1,5/2-3/2)	19.78	50	-31.18	15.789	42.888	3.566	38.408	0.06	0.398	23.255	15.044	3.566	6.856	0.192	0.539
C_3N(2-1,5/2-3/2)	19.78	51	-29.29	7.863	75.154	2.817	27.474	0.099	4.295	23.713	1.099	2.817	1.229	0.192	0.064
C_3N(2-1,5/2-3/2)	19.78	52	-27.39	15.476	2.471	2.485	2.897	0.198	0.091	22.476	3.743	2.485	3.304	0.14	0.089
C_3N(2-1,5/2-3/2)	19.78	53	-25.50	21.975	3.507	4.41	3.844	0.087	0.059	nan	nan	nan	nan	nan	nan
C_3N(2-1,5/2-3/2)	19.78	54	-23.60	20.332	1.631	3.801	1.667	0.189	0.07	nan	nan	nan	nan	nan	nan
C_3N(2-1,5/2-3/2)	19.78	55	-21.71	14.46	1.734	1.918	1.934	0.131	0.097	20.591	2.055	1.446	2.286	0.093	0.104
C_3N(2-1,5/2-3/2)	19.78	56	-19.81	17.691	2.171	5.383	2.561	0.198	0.067	nan	nan	nan	nan	nan	nan
C_3N(3-2,5/2-3/2)	29.70	31	-32.75	21.045	2.349	4.892	2.607	0.258	0.107	nan	nan	nan	nan	nan	nan
C_3N(3-2,5/2-3/2)	29.70	32	-31.49	19.329	1.608	2.44	1.713	0.271	0.152	nan	nan	nan	nan	nan	nan
C_3N(3-2,5/2-3/2)	29.70	33	-30.22	18.844	4.172	2.899	4.556	0.218	0.138	24.972	7	1.718	7.85	0.081	0.243
C_3N(3-2,5/2-3/2)	29.70	34	-28.96	18.164	1.834	2.066	2.03	0.22	0.12	22.671	2.866	1.061	2.859	0.089	0.181
C_3N(3-2,5/2-3/2)	29.70	35	-27.70	13.672	6.234	2.605	10.397	0.086	0.116	21.876	4.623	2.605	4.354	0.112	0.1
C_3N(3-2,5/2-3/2)	29.70	36	-26.44	23.317	1.665	2.679	1.798	0.233	0.124	nan	nan	nan	nan	nan	nan
C_3N(3-2,5/2-3/2)	29.70	37	-25.18	20.285	1.294	2.669	1.316	0.279	0.117	nan	nan	nan	nan	nan	nan
C_3N(3-2,5/2-3/2)	29.70	38	-23.91	20.755	1.815	2.932	2.205	0.201	0.106	nan	nan	nan	nan	nan	nan
C_3N(3-2,5/2-3/2)	29.70	39	-22.65	20.735	1.459	3.089	1.698	0.252	0.099	nan	nan	nan	nan	nan	nan
C_3N(3-2,5/2-3/2)	29.70	40	-21.39	18.937	9.878	5.581	8.198	0.146	0.119	23.195	2.32	1.148	2.871	0.107	0.211
C_3N(3-2,5/2-3/2)	29.70	41	-20.13	24.611	1.433	-2.056	1.435	0.294	0.178	nan	nan	nan	nan	nan	nan
C_3N(3-2,5/2-3/2)	29.70	42	-18.87	21.914	2.719	4.053	2.942	0.173	0.1	nan	nan	nan	nan	nan	nan
C_3N(3-2,7/2-5/2)	29.68	32	-32.53	20.82	1.923	4.262	1.994	0.288	0.112	nan	nan	nan	nan	nan	nan
C_3N(3-2,7/2-5/2)	29.68	33	-31.27	18.472	3.634	2.104	2.506	0.457	0.337	23.555	6.541	2.104	4.441	0.253	0.339
C_3N(3-2,7/2-5/2)	29.68	34	-30.00	21.161	2.629	4.41	3.048	0.226	0.112	nan	nan	nan	nan	nan	nan
C_3N(3-2,7/2-5/2)	29.68	35	-28.74	0	0	0	0	0	0	nan	nan	nan	nan	nan	nan

Table C.3 continued.

Transition	Restfreq	Ch	v_{ch}	R_{max} 1	ΔR_{max} 1	$W_{1/2}$ 1	$\Delta W_{1/2}$ 1	F_{max} 1	ΔF_{max} 1	R_{max} 2	ΔR_{max} 2	$W_{1/2}$ 2	$\Delta W_{1/2}$ 2	F_{max} 2	ΔF_{max} 2
C_3N(3-2,7/2-5/2)	29.68	36	-27.48	21.692	1.994	3.626	2.142	0.286	0.136	nan	nan	nan	nan	nan	nan
C_3N(3-2,7/2-5/2)	29.68	37	-26.21	19.631	2.874	3.336	3.263	0.211	0.155	nan	nan	nan	nan	nan	nan
C_3N(3-2,7/2-5/2)	29.68	38	-24.95	11.005	10.215	3.405	14.952	0.14	0.185	22.487	3.5	3.405	4.824	0.258	0.166
C_3N(3-2,7/2-5/2)	29.68	39	-23.69	16.932	2.096	2.425	2.251	0.308	0.154	23.547	3.391	1.945	3.377	0.166	0.166
C_3N(3-2,7/2-5/2)	29.68	40	-22.43	23.22	1.475	2.872	1.629	0.291	0.123	nan	nan	nan	nan	nan	nan
C_3N(3-2,7/2-5/2)	29.68	41	-21.16	21.331	2.578	3.916	2.886	0.274	0.146	nan	nan	nan	nan	nan	nan
C_3N(3-2,7/2-5/2)	29.68	42	-19.90	22.507	1.167	-2.419	1.239	0.438	0.182	nan	nan	nan	nan	nan	nan
C_3N(3-2,7/2-5/2)	29.68	43	-18.64	24.086	1.819	2.93	1.887	0.344	0.184	nan	nan	nan	nan	nan	nan
C_4H(2-1,5/2-3/2)	19.02	37	-31.76	0	0	0	0	0	0	nan	nan	nan	nan	nan	nan
C_4H(2-1,5/2-3/2)	19.02	38	-29.79	12.285	3.92	6.141	3.908	0.104	0.047	nan	nan	nan	nan	nan	nan
C_4H(2-1,5/2-3/2)	19.02	39	-27.82	10.806	19.759	6.154	16.604	0.072	0.095	25.334	35.869	6.154	24.213	0.04	0.107
C_4H(2-1,5/2-3/2)	19.02	40	-25.85	15.858	2.46	4.691	2.757	0.111	0.049	nan	nan	nan	nan	nan	nan
C_4H(2-1,5/2-3/2)	19.02	41	-23.88	8.925	4.786	2.638	7.306	0.073	0.079	21.621	1.625	2.638	1.775	0.111	0.059
C_4H(2-1,5/2-3/2)	19.02	42	-21.91	17.272	4.524	6.094	4.098	0.083	0.048	nan	nan	nan	nan	nan	nan
C_4H(2-1,5/2-3/2)	19.02	43	-19.93	20.629	2.102	3.776	2.158	0.109	0.052	nan	nan	nan	nan	nan	nan
C_4H(3-2,5/2-3/2)	28.57	27	-32.77	16.702	3.275	5.156	4.237	0.218	0.111	nan	nan	nan	nan	nan	nan
C_4H(3-2,5/2-3/2)	28.57	28	-31.46	3.777	0.968	0.8	0.813	0.348	0.337	nan	nan	nan	nan	nan	nan
C_4H(3-2,5/2-3/2)	28.57	29	-30.15	13.951	3.366	4.178	3.852	0.216	0.136	nan	nan	nan	nan	nan	nan
C_4H(3-2,5/2-3/2)	28.57	30	-28.84	1.254	6.85	1.699	6.833	0.213	0.365	nan	nan	nan	nan	nan	nan
C_4H(3-2,5/2-3/2)	28.57	31	-27.53	9.434	25.274	11.038	15.035	0.242	0.18	18.945	2.474	1.53	3.011	0.142	0.221
C_4H(3-2,5/2-3/2)	28.57	32	-26.21	14.089	3.112	1.924	3.703	0.119	0.16	21.935	4.471	1.924	5.066	0.073	0.144
C_4H(3-2,5/2-3/2)	28.57	33	-24.90	17.052	4.979	4.962	6.187	0.179	0.139	nan	nan	nan	nan	nan	nan
C_4H(3-2,5/2-3/2)	28.57	34	-23.59	-53.366	1744.477	41.857	532.997	0.451	15.244	nan	nan	nan	nan	nan	nan
C_4H(3-2,5/2-3/2)	28.57	35	-22.28	0	0	0	0	0	0	nan	nan	nan	nan	nan	nan
C_4H(3-2,5/2-3/2)	28.57	36	-20.97	-49.043	2014.587	25.825	448.581	1.162	101.182	nan	nan	nan	nan	nan	nan
C_4H(3-2,5/2-3/2)	28.57	37	-19.66	4.073	1.34	1.154	1.899	0.315	0.332	nan	nan	nan	nan	nan	nan
C_4H(3-2,7/2-5/2)	28.53	39	-32.74	0	0	0	0	0	0	nan	nan	nan	nan	nan	nan
C_4H(3-2,7/2-5/2)	28.53	40	-31.43	20.846	5.137	6.327	6.255	0.179	0.097	nan	nan	nan	nan	nan	nan
C_4H(3-2,7/2-5/2)	28.53	41	-30.11	24.197	5.716	7.227	6.697	0.138	0.067	nan	nan	nan	nan	nan	nan
C_4H(3-2,7/2-5/2)	28.53	42	-28.80	17.431	6.657	8.149	7.709	0.139	0.076	nan	nan	nan	nan	nan	nan
C_4H(3-2,7/2-5/2)	28.53	43	-27.49	17.315	3.544	2.236	3.98	0.184	0.137	23.726	15.603	2.236	13.682	0.041	0.133
C_4H(3-2,7/2-5/2)	28.53	44	-26.17	8.245	5.194	3.916	5.717	0.184	0.124	19.84	8.56	3.916	7.968	0.096	0.091
C_4H(3-2,7/2-5/2)	28.53	45	-24.86	2.293	2.445	1.932	2.401	0.312	0.232	nan	nan	nan	nan	nan	nan
C_4H(3-2,7/2-5/2)	28.53	46	-23.55	12.716	21.728	15.558	25.832	0.102	0.06	nan	nan	nan	nan	nan	nan
C_4H(3-2,7/2-5/2)	28.53	47	-22.23	9.817	8.152	4.909	10.148	0.141	0.181	23.791	2.999	2.095	3.332	0.127	0.146
C_4H(3-2,7/2-5/2)	28.53	48	-20.92	0	0	0	0	0	0	nan	nan	nan	nan	nan	nan
C_4H(3-2,7/2-5/2)	28.53	49	-19.61	10.459	1.703	2.925	1.869	0.278	0.136	22.404	4.373	2.925	4.683	0.103	0.124
C_6H(15/2-13/2,3/2,e)	20.79	100	-19.84	0	0	0	0	0	0	nan	nan	nan	nan	nan	nan
C_6H(15/2-13/2,3/2,e)	20.79	93	-32.46	20.847	3.199	6.345	3.432	0.116	0.05	nan	nan	nan	nan	nan	nan
C_6H(15/2-13/2,3/2,e)	20.79	94	-30.65	11.594	145.524	12.394	150.565	0.014	0.052	nan	nan	nan	nan	nan	nan
C_6H(15/2-13/2,3/2,e)	20.79	95	-28.85	10.117	3.471	3.725	3.962	0.11	0.063	21.685	3.431	3.725	3.548	0.105	0.053
C_6H(15/2-13/2,3/2,e)	20.79	96	-27.05	9.775	18.861	9.891	15.513	0.085	0.069	22.557	2.247	2.789	3.459	0.101	0.112

Table C.3 continued.

Transition	Restfreq	Ch	v_{ch}	R_{max} 1	ΔR_{max} 1	$W_{1/2}$ 1	$\Delta W_{1/2}$ 1	F_{max} 1	ΔF_{max} 1	R_{max} 2	ΔR_{max} 2	$W_{1/2}$ 2	$\Delta W_{1/2}$ 2	F_{max} 2	ΔF_{max} 2
C_6H(15/2-13/2,3/2,e)	20.79	97	-25.25	9.038	15.128	4.966	21.376	0.041	0.063	25.896	5.404	4.966	5.994	0.073	0.048
C_6H(15/2-13/2,3/2,e)	20.79	98	-23.45	11.245	7.26	8.269	7.398	0.11	0.052	nan	nan	nan	nan	nan	nan
C_6H(15/2-13/2,3/2,e)	20.79	99	-21.64	9.339	1.954	2.215	1.993	0.139	0.106	22.246	37.917	2.215	12.902	0.179	2.181
C_6H(15/2-13/2,3/2,f)	20.79	80	-33.39	15.192	2.113	2.958	2.24	0.173	0.077	24.429	2.532	2.958	2.472	0.141	0.07
C_6H(15/2-13/2,3/2,f)	20.79	81	-31.59	1.548	1.173	-0.823	2.045	0.209	0.439	nan	nan	nan	nan	nan	nan
C_6H(15/2-13/2,3/2,f)	20.79	82	-29.78	15.204	4.026	3.118	3.515	0.188	0.097	23.165	13.77	3.118	10.337	0.056	0.1
C_6H(15/2-13/2,3/2,f)	20.79	83	-27.98	17.124	1.986	3.348	2.298	0.171	0.078	25.75	3.498	1.858	3.495	0.07	0.096
C_6H(15/2-13/2,3/2,f)	20.79	84	-26.18	17.408	7.226	9.647	8.923	0.07	0.036	nan	nan	nan	nan	nan	nan
C_6H(15/2-13/2,3/2,f)	20.79	85	-24.38	13.416	1.905	2.473	2.28	0.17	0.082	21.065	3.727	2.473	3.583	0.089	0.073
C_6H(15/2-13/2,3/2,f)	20.79	86	-22.58	15.107	16.408	3.223	16.826	0.048	0.094	23.196	10.984	3.223	7.293	0.079	0.115
C_6H(15/2-13/2,3/2,f)	20.79	87	-20.77	15.59	6.18	2.404	5.678	0.077	0.094	22.402	4.129	2.404	3.672	0.115	0.089
C_6H(15/2-13/2,3/2,f)	20.79	88	-18.97	26.136	4.048	5.904	5.451	0.094	0.052	nan	nan	nan	nan	nan	nan
C_6H(17/2-15/2,1/2,e)	23.75	46	-32.11	15.984	3.687	3.753	4.593	0.096	0.078	24.49	2.225	0.978	2.762	0.068	0.146
C_6H(17/2-15/2,1/2,e)	23.75	47	-30.54	2.096	1.114	1.214	1.162	0.28	0.206	nan	nan	nan	nan	nan	nan
C_6H(17/2-15/2,1/2,e)	23.75	48	-28.96	2.29	56.665	18.835	44.657	0.129	0.133	nan	nan	nan	nan	nan	nan
C_6H(17/2-15/2,1/2,e)	23.75	49	-27.38	12.895	18.199	15.996	21.061	0.088	0.042	nan	nan	nan	nan	nan	nan
C_6H(17/2-15/2,1/2,e)	23.75	50	-25.80	14.76	4.099	2.163	4.449	0.07	0.082	21.785	6.719	2.163	7.75	0.042	0.099
C_6H(17/2-15/2,1/2,e)	23.75	51	-24.22	5	67.151	17.178	48.48	0.075	0.076	23.874	2.077	0.905	2.057	0.056	0.109
C_6H(17/2-15/2,1/2,e)	23.75	52	-22.65	4.011	44.653	18.224	39.056	0.099	0.07	nan	nan	nan	nan	nan	nan
C_6H(17/2-15/2,1/2,e)	23.75	53	-21.07	15.514	3.888	2.581	5.079	0.081	0.085	24.294	5.056	2.581	5.384	0.058	0.075
C_6H(17/2-15/2,1/2,e)	23.75	54	-19.49	16.751	2.225	1.97	2.298	0.159	0.09	22.783	12.099	1.97	13.129	0.052	0.104
C_6H(17/2-15/2,3/2,e)	23.57	70	-32.46	0	0	0	0	0	0	nan	nan	nan	nan	nan	nan
C_6H(17/2-15/2,3/2,e)	23.57	71	-30.87	15.998	1.017	2	1.165	0.252	0.108	24.136	13.744	2	15.353	0.022	0.207
C_6H(17/2-15/2,3/2,e)	23.57	72	-29.28	12.268	11.408	3.057	11.66	0.069	0.083	23.7	5.774	3.057	6.523	0.048	0.064
C_6H(17/2-15/2,3/2,e)	23.57	73	-27.69	15.541	3.068	1.684	3.277	0.072	0.112	24.479	4.005	1.684	5.212	1.594	37.841
C_6H(17/2-15/2,3/2,e)	23.57	74	-26.10	12.966	6.605	5.842	10.967	0.089	0.117	nan	nan	nan	nan	nan	nan
C_6H(17/2-15/2,3/2,e)	23.57	75	-24.51	5.249	9.286	5.598	9.045	0.133	0.177	nan	nan	nan	nan	nan	nan
C_6H(17/2-15/2,3/2,e)	23.57	76	-22.92	-2.576	110.359	20.698	69.269	0.123	0.245	nan	nan	nan	nan	nan	nan
C_6H(17/2-15/2,3/2,e)	23.57	77	-21.33	0	0	0	0	0	0	nan	nan	nan	nan	nan	nan
C_6H(17/2-15/2,3/2,e)	23.57	78	-19.74	7.217	1.188	1.656	1.221	0.288	nan	23.266	1.909	1.656	nan	0.137	nan
C_6H(17/2-15/2,3/2,f)	23.57	54	-32.20	19.777	2.421	2.822	2.5	0.106	0.078	nan	nan	nan	nan	nan	nan
C_6H(17/2-15/2,3/2,f)	23.57	55	-30.61	15.096	4.928	7.625	6.839	0.114	0.089	nan	nan	nan	nan	nan	nan
C_6H(17/2-15/2,3/2,f)	23.57	56	-29.02	15.447	3.528	6.342	3.773	0.115	0.047	nan	nan	nan	nan	nan	nan
C_6H(17/2-15/2,3/2,f)	23.57	57	-27.43	2.756	1.69	2.202	1.585	0.294	0.138	nan	nan	nan	nan	nan	nan
C_6H(17/2-15/2,3/2,f)	23.57	58	-25.84	2.655	2.472	1.745	3.759	0.149	0.152	nan	nan	nan	nan	nan	nan
C_6H(17/2-15/2,3/2,f)	23.57	59	-24.25	14.604	3.523	2.525	5.939	0.138	0.09	24.249	5.068	2.525	5.099	0.07	0.069
C_6H(17/2-15/2,3/2,f)	23.57	60	-22.66	24.099	5.084	4.839	4.499	0.079	0.064	nan	nan	nan	nan	nan	nan
C_6H(17/2-15/2,3/2,f)	23.57	61	-21.07	10.863	34.84	18.973	50.864	0.082	0.058	nan	nan	nan	nan	nan	nan
C_6H(17/2-15/2,3/2,f)	23.57	62	-19.48	25.944	58.963	20.081	95.972	0.044	0.045	nan	nan	nan	nan	nan	nan
C_6H(19/2-17/2,3/2,e)	26.34	73	-32.47	16.602	1.409	2.536	1.431	0.168	0.08	26.969	3.291	1.932	3.413	0.057	0.084
C_6H(19/2-17/2,3/2,e)	26.34	74	-31.04	15.254	6.164	2.41	8.637	0.054	0.102	23.117	2.575	1.927	2.672	0.1	0.097
C_6H(19/2-17/2,3/2,e)	26.34	75	-29.62	11.337	13.938	7.385	21.113	0.058	0.054	25.116	2.599	1.787	3.666	0.065	0.097

Table C.3 continued.

Transition	Restfreq	Ch	v_{ch}	R_{max} 1	ΔR_{max} 1	$W_{1/2}$ 1	$\Delta W_{1/2}$ 1	F_{max} 1	ΔF_{max} 1	R_{max} 2	ΔR_{max} 2	$W_{1/2}$ 2	$\Delta W_{1/2}$ 2	F_{max} 2	ΔF_{max} 2
C_6H(19/2-17/2,3/2,e)	26.34	76	-28.20	16.289	3.52	1.725	2.516	0.223	0.195	20.374	11.792	1.725	7.454	0.067	0.209
C_6H(19/2-17/2,3/2,e)	26.34	77	-26.78	16.877	4.574	7.073	5.2	0.121	0.057	nan	nan	nan	nan	nan	nan
C_6H(19/2-17/2,3/2,e)	26.34	78	-25.35	17.438	2.004	1.078	2.092	0.082	0.135	26.018	84.785	1.078	55.002	0.017	0.249
C_6H(19/2-17/2,3/2,e)	26.34	79	-23.93	20.248	3.451	3.546	3.716	0.102	0.069	nan	nan	nan	nan	nan	nan
C_6H(19/2-17/2,3/2,e)	26.34	80	-22.51	10.81	5.377	3.339	6.352	0.069	0.099	22.257	1.847	2.156	2.011	0.122	0.087
C_6H(19/2-17/2,3/2,e)	26.34	81	-21.08	14.64	14.723	5.892	16.984	0.059	0.056	26.996	5.666	1.156	7.823	0.028	0.115
C_6H(19/2-17/2,3/2,e)	26.34	82	-19.66	12.4	4.334	2.703	4.762	0.132	0.103	23.348	4.071	2.703	4.477	0.073	0.109
C_6H(19/2-17/2,3/2,f)	26.34	53	-32.23	0	0	0	0	0	0	nan	nan	nan	nan	nan	nan
C_6H(19/2-17/2,3/2,f)	26.34	54	-30.81	0	0	0	0	0	0	nan	nan	nan	nan	nan	nan
C_6H(19/2-17/2,3/2,f)	26.34	55	-29.39	15.163	1.514	2.226	1.609	0.209	0.094	22.38	3.678	2.226	3.84	0.083	0.088
C_6H(19/2-17/2,3/2,f)	26.34	56	-27.97	14.986	3.887	2.249	4.834	0.061	0.084	23.46	3.323	2.249	3.678	0.064	0.075
C_6H(19/2-17/2,3/2,f)	26.34	57	-26.54	16.943	1.264	2.56	0.811	0.153	0.07	33.314	nan	-1.748	nan	0.03	nan
C_6H(19/2-17/2,3/2,f)	26.34	58	-25.12	1.057	1.798	0.929	2.095	0.24	0.336	nan	nan	nan	nan	nan	nan
C_6H(19/2-17/2,3/2,f)	26.34	59	-23.70	0	0	0	0	0	0	nan	nan	nan	nan	nan	nan
C_6H(19/2-17/2,3/2,f)	26.34	60	-22.28	19.612	4.52	6.007	5.536	0.085	0.05	nan	nan	nan	nan	nan	nan
C_6H(19/2-17/2,3/2,f)	26.34	61	-20.85	15.569	4	8.883	4.315	0.15	0.046	nan	nan	nan	nan	nan	nan
C_6H(19/2-17/2,3/2,f)	26.34	62	-19.43	15.667	27.916	2.736	28.284	0.032	0.124	22.697	4.571	2.736	3.33	0.21	0.141

Table C.4: List of Gaussian fit results from the radial emission profiles of each transition (restfrequency in GHz) of each channel (velocity in km s^{-1}) with $\Delta v < 7.5$ km s^{-1} for quarter Q3. The fit parameters are shell radius at maximum flux R_{max} (in arcsec), half shell width $W_{1/2}$ (in arcsec), and maximum flux F_{max} (in mJy $beam^{-1}$) for two components and their uncertainties determined from the least square fit routine.

Transition	Restfreq	Ch	v_{ch}	R_{max} 1	ΔR_{max} 1	$W_{1/2}$ 1	$\Delta W_{1/2}$ 1	F_{max} 1	ΔF_{max} 1	R_{max} 2	ΔR_{max} 2	$W_{1/2}$ 2	$\Delta W_{1/2}$ 2	F_{max} 2	ΔF_{max} 2
HC_3N(2-1)	18.20	79	-33.40	14.092	1.263	3.979	1.421	2.145	0.547	23.303	9.465	1.52	9.685	0.17	0.864
HC_3N(2-1)	18.20	80	-31.34	13.704	1.44	4.325	1.598	1.566	0.434	25.186	8.706	1.992	9.022	0.174	0.614
HC_3N(2-1)	18.20	81	-29.28	14.974	1.434	4.315	1.627	1.573	0.409	23.858	6.963	1.299	7.481	0.161	0.747
HC_3N(2-1)	18.20	82	-27.22	14.753	1.913	4.963	2.146	1.391	0.369	23.502	4.612	1.353	5.449	0.236	0.764
HC_3N(2-1)	18.20	83	-25.16	15.434	1.686	5.808	1.71	1.317	0.329	nan	nan	nan	nan	nan	nan
HC_3N(2-1)	18.20	84	-23.10	16.581	1.357	4.672	1.374	1.452	0.365	nan	nan	nan	nan	nan	nan
HC_3N(2-1)	18.20	85	-21.04	5	23.1	11.631	18.356	0.852	0.381	17.666	2.415	3.369	3.446	1.13	1.039
HC_3N(2-1)	18.20	86	-18.99	14.403	1.902	6.655	1.997	1.861	0.458	nan	nan	nan	nan	nan	nan
HC_3N(3-2)	27.29	85	-32.30	14.215	0.785	2.699	0.859	5.241	1.287	22.92	6.334	1.791	6.607	0.531	1.534
HC_3N(3-2)	27.29	86	-30.93	14.831	0.813	2.495	0.891	4.458	1.027	22.614	7.768	2.121	9.47	0.425	1.117
HC_3N(3-2)	27.29	87	-29.55	14.964	0.873	2.342	0.918	4.207	0.997	22.282	7.206	2.142	9.743	0.467	1.077
HC_3N(3-2)	27.29	88	-28.18	15.287	1.083	2.183	0.993	3.859	0.913	21.587	6.195	2.183	6.19	0.657	0.909
HC_3N(3-2)	27.29	89	-26.81	15.617	0.84	2.738	0.947	3.46	0.878	22.477	2.118	1.133	2.326	0.882	1.34
HC_3N(3-2)	27.29	90	-25.44	15.751	1.629	2.713	1.535	3.256	0.815	21.431	4.096	1.655	3.843	0.826	1.475
HC_3N(3-2)	27.29	91	-24.06	14.101	9.184	2.448	4.327	2.263	5.648	18.931	10.317	2.448	5.174	2.01	5.479
HC_3N(3-2)	27.29	92	-22.69	16.566	1.02	3.9	1.086	3.04	0.687	nan	nan	nan	nan	nan	nan
HC_3N(3-2)	27.29	93	-21.32	16.36	1.057	4.169	1.134	3.698	0.812	nan	nan	nan	nan	nan	nan
HC_3N(3-2)	27.29	94	-19.94	17.058	0.985	3.769	1.034	3.989	0.902	nan	nan	nan	nan	nan	nan
HC_3N(3-2)	27.29	95	-18.57	13.695	3.665	2.441	2.373	4.665	3.219	19.32	4.427	2.441	2.74	3.88	3.311
HC_3N(4-3)	36.39	31	-32.65	13.851	0.551	2.132	0.595	7.621	1.539	21.905	19.467	2.132	25.245	0.303	1.637
HC_3N(4-3)	36.39	32	-31.62	14.138	0.472	1.828	0.489	6.93	1.536	22.323	17.899	1.828	18.782	0.333	1.597
HC_3N(4-3)	36.39	33	-30.59	14.106	0.447	1.888	0.466	6.732	1.363	22.421	17.256	1.888	18.071	0.326	1.418
HC_3N(4-3)	36.39	34	-29.56	14.377	0.483	1.903	0.513	6.363	1.342	22.049	7.128	1.903	8.901	0.546	1.412
HC_3N(4-3)	36.39	35	-28.53	14.443	0.463	1.994	0.499	6.118	1.105	21.975	7.252	1.994	9.339	0.562	1.175
HC_3N(4-3)	36.39	36	-27.50	14.551	0.469	2.131	0.506	5.522	1.04	21.862	2.883	1.418	3.476	0.905	1.308
HC_3N(4-3)	36.39	37	-26.47	14.701	0.783	2.88	0.831	4.294	1.001	nan	nan	nan	nan	nan	nan
HC_3N(4-3)	36.39	38	-25.44	14.446	2.134	2.778	1.823	4.19	1.205	22.885	35.564	2.778	42.084	0.593	1.88
HC_3N(4-3)	36.39	39	-24.41	14.967	0.992	3.551	1.093	3.985	0.953	nan	nan	nan	nan	nan	nan
HC_3N(4-3)	36.39	40	-23.38	15.574	1.171	3.833	1.302	3.541	0.929	nan	nan	nan	nan	nan	nan
HC_3N(4-3)	36.39	41	-22.35	15.759	1.045	3.838	1.168	4.206	0.966	nan	nan	nan	nan	nan	nan
HC_3N(4-3)	36.39	42	-21.32	16.075	1.058	3.922	1.182	4.282	0.976	nan	nan	nan	nan	nan	nan
HC_3N(4-3)	36.39	43	-20.30	15.983	0.916	3.652	1.002	5.131	1.099	nan	nan	nan	nan	nan	nan
HC_3N(4-3)	36.39	44	-19.27	15.9	0.974	3.875	1.069	5.436	1.156	nan	nan	nan	nan	nan	nan
HC_5N(8-7)	21.30	61	-33.29	15.459	0.904	3.257	0.915	1.449	0.349	nan	nan	nan	nan	nan	nan
HC_5N(8-7)	21.30	62	-31.53	15.769	1.84	3.017	1.781	1.081	0.324	23.617	8.994	2.458	8.007	0.194	0.374
HC_5N(8-7)	21.30	63	-29.77	15.564	2.133	2.879	1.939	1.042	0.32	22.47	6.239	2.231	5.316	0.292	0.432
HC_5N(8-7)	21.30	64	-28.01	15.984	3.364	2.835	2.245	1.146	0.56	22.473	9.12	2.673	5.911	0.395	0.657
HC_5N(8-7)	21.30	65	-26.25	16.347	3.018	2.752	2.226	1.036	0.419	22.689	5.245	2.437	3.571	0.529	0.571

Table C.4 continued.

Transition	Restfreq	Ch	v_{ch}	R_{max} 1	ΔR_{max} 1	$W_{1/2}$ 1	$\Delta W_{1/2}$ 1	F_{max} 1	ΔF_{max} 1	R_{max} 2	ΔR_{max} 2	$W_{1/2}$ 2	$\Delta W_{1/2}$ 2	F_{max} 2	ΔF_{max} 2
HC_5N(8-7)	21.30	66	-24.49	18.003	1.13	3.844	1.133	0.997	0.253	nan	nan	nan	nan	nan	nan
HC_5N(8-7)	21.30	67	-22.73	17.434	3.463	4.391	2.303	0.861	1.064	19.639	4.127	1.911	5.752	0.295	1.09
HC_5N(8-7)	21.30	68	-20.98	18.083	1.066	3.909	1.067	1.174	0.277	nan	nan	nan	nan	nan	nan
HC_5N(8-7)	21.30	69	-19.22	17.491	3.158	4.587	1.879	1.045	0.774	20.429	5.179	1.731	6.857	0.237	0.912
HC_5N(9-8)	23.96	51	-31.95	15.265	1.932	2.2	1.468	1.324	0.466	20.842	16.649	2.16	12.927	0.15	0.476
HC_5N(9-8)	23.96	52	-30.39	15.46	0.868	2.105	0.916	1.206	0.331	22.473	6.703	2.105	8.747	0.149	0.34
HC_5N(9-8)	23.96	53	-28.82	15.693	1.293	2.194	1.163	1.24	0.331	22.11	5.148	2.194	7.088	0.273	0.335
HC_5N(9-8)	23.96	54	-27.26	16.651	0.959	3.005	0.997	0.98	0.27	nan	nan	nan	nan	nan	nan
HC_5N(9-8)	23.96	55	-25.69	16.607	1.226	2.524	1.261	1.159	0.286	21.727	2.94	1.307	2.907	0.281	0.509
HC_5N(9-8)	23.96	56	-24.13	17.298	11.476	2.971	5.638	0.974	1.741	20.716	6.605	1.644	14.439	0.208	4.219
HC_5N(9-8)	23.96	57	-22.57	17.82	0.891	3.265	0.95	1.103	0.26	nan	nan	nan	nan	nan	nan
HC_5N(9-8)	23.96	58	-21.00	18.055	0.764	2.912	0.806	1.302	0.295	nan	nan	nan	nan	nan	nan
HC_5N(9-8)	23.96	59	-19.44	17.753	0.933	3.44	1.015	1.296	0.299	nan	nan	nan	nan	nan	nan
HC_5N(10-9)	26.63	38	-32.78	15.869	1.351	2.112	1.217	1.79	0.511	22.167	14.618	2.112	25.836	0.138	0.525
HC_5N(10-9)	26.63	39	-31.38	15.856	0.817	2.195	0.901	1.586	0.421	23.434	5.792	2.195	8.115	0.22	0.434
HC_5N(10-9)	26.63	40	-29.97	15.59	1.753	2.243	1.544	1.425	0.473	21.835	7.836	2.243	8.202	0.302	0.459
HC_5N(10-9)	26.63	41	-28.56	16.163	0.805	1.887	0.859	1.455	0.431	22.449	1.894	1.887	2.02	0.611	0.423
HC_5N(10-9)	26.63	42	-27.16	16.675	1.203	2.257	1.243	1.338	0.387	22.511	1.91	1.688	1.94	0.697	0.457
HC_5N(10-9)	26.63	43	-25.75	17.2	2.726	2.453	2.164	1.38	0.472	21.965	3.759	1.687	2.695	0.63	1.166
HC_5N(10-9)	26.63	44	-24.34	18.197	0.865	3.187	0.908	1.371	0.322	nan	nan	nan	nan	nan	nan
HC_5N(10-9)	26.63	45	-22.93	18.229	0.655	2.858	0.666	1.724	0.342	nan	nan	nan	nan	nan	nan
HC_5N(10-9)	26.63	46	-21.53	18.701	0.716	2.735	0.718	1.708	0.387	nan	nan	nan	nan	nan	nan
HC_5N(10-9)	26.63	47	-20.12	18.222	0.726	2.899	0.744	1.791	0.388	nan	nan	nan	nan	nan	nan
HC_5N(10-9)	26.63	48	-18.71	16.535	2.99	4.221	1.952	1.485	0.764	20.031	1.54	1.414	2.012	0.886	1.125
HC_5N(11-10)	29.29	19	-32.39	15.398	1.326	1.945	1.449	1.02	0.456	21.678	6.496	1.945	6.835	0.207	0.443
HC_5N(11-10)	29.29	20	-31.11	15.254	1.043	1.671	1.127	0.986	0.418	21.547	33.593	1.671	24.59	0.193	1
HC_5N(11-10)	29.29	21	-29.83	15.864	1.221	1.894	1.319	0.689	0.379	nan	nan	nan	nan	nan	nan
HC_5N(11-10)	29.29	22	-28.55	15.968	2.596	2.233	2.843	0.669	0.352	22.721	35.606	2.233	71.872	0.042	0.5
HC_5N(11-10)	29.29	23	-27.27	16.148	1.372	2.36	1.48	0.628	0.308	nan	nan	nan	nan	nan	nan
HC_5N(11-10)	29.29	24	-25.99	16.473	1.289	2.211	1.393	0.657	0.325	22.349	1.88	0.866	2.069	0.274	0.512
HC_5N(11-10)	29.29	25	-24.71	17.016	1.817	2.407	2.076	0.621	0.338	21.91	6.571	0.881	6.871	0.092	0.586
HC_5N(11-10)	29.29	26	-23.43	17.84	1.756	3.373	1.917	0.528	0.235	nan	nan	nan	nan	nan	nan
HC_5N(11-10)	29.29	27	-22.15	18.075	1.975	3.183	2.148	0.577	0.309	nan	nan	nan	nan	nan	nan
HC_5N(11-10)	29.29	28	-20.87	17.617	1.816	3.471	1.9	0.619	0.278	nan	nan	nan	nan	nan	nan
HC_5N(11-10)	29.29	29	-19.60	19.481	4.8	1.829	2.671	0.933	1.316	23.451	51.825	1.829	30.226	0.086	1.278
HC_5N(12-11)	31.95	36	-32.38	14.99	0.591	1.857	0.636	2.521	0.681	23.348	54.365	1.857	32.368	0.226	2.186
HC_5N(12-11)	31.95	37	-31.21	15.124	0.516	1.391	0.52	2.15	0.688	22.043	3.49	1.391	3.837	0.323	0.692
HC_5N(12-11)	31.95	38	-30.04	14.929	0.39	1.169	0.392	2.373	0.684	22.77	3.669	1.169	3.718	0.246	0.668
HC_5N(12-11)	31.95	39	-28.86	15.423	0.449	1.263	0.455	2.339	0.721	22.845	2.071	1.263	2.254	0.515	0.721
HC_5N(12-11)	31.95	40	-27.69	15.66	0.653	1.738	0.686	1.668	0.542	22.539	1.207	0.878	1.215	0.618	0.736
HC_5N(12-11)	31.95	41	-26.52	16.174	1.012	2.071	1.356	1.312	0.524	22.146	1.404	1.283	1.555	0.74	0.613
HC_5N(12-11)	31.95	42	-25.34	16.565	1.075	2.412	1.256	1.279	0.462	21.849	1.064	-0.788	1.181	0.689	0.799

Table C.4 continued.

Transition	Restfreq	Ch	v_{ch}	R_{max} 1	ΔR_{max} 1	$W_{1/2}$ 1	$\Delta W_{1/2}$ 1	F_{max} 1	ΔF_{max} 1	R_{max} 2	ΔR_{max} 2	$W_{1/2}$ 2	$\Delta W_{1/2}$ 2	F_{max} 2	ΔF_{max} 2
HC_5N(12-11)	31.95	43	-24.17	17.68	1.068	2.525	1.114	1.242	0.455	nan	nan	nan	nan	nan	nan
HC_5N(12-11)	31.95	44	-23.00	18.337	0.664	1.844	0.681	1.673	0.522	nan	nan	nan	nan	nan	nan
HC_5N(12-11)	31.95	45	-21.83	18.583	0.614	1.693	0.689	1.991	0.586	23.358	nan	0.493	nan	0	nan
HC_5N(12-11)	31.95	46	-20.65	18.355	0.693	2.278	0.708	1.9	0.501	nan	nan	nan	nan	nan	nan
HC_5N(12-11)	31.95	47	-19.48	18.526	0.638	2.016	0.666	2.322	0.636	nan	nan	nan	nan	nan	nan
HC_5N(13-12)	34.61	31	-33.44	14.386	1.156	2.042	1.267	1.003	0.476	nan	nan	nan	nan	nan	nan
HC_5N(13-12)	34.61	32	-32.35	15.047	0.75	1.133	0.747	0.927	0.529	nan	nan	nan	nan	nan	nan
HC_5N(13-12)	34.61	33	-31.27	14.962	0.68	0.928	0.732	0.951	0.608	nan	nan	nan	nan	nan	nan
HC_5N(13-12)	34.61	34	-30.19	15.226	0.849	0.973	0.997	0.754	0.506	nan	nan	nan	nan	nan	nan
HC_5N(13-12)	34.61	35	-29.11	15.416	0.651	0.852	0.684	0.923	0.61	nan	nan	nan	nan	nan	nan
HC_5N(13-12)	34.61	36	-28.02	15.236	2.355	1.681	2.223	0.358	0.376	nan	nan	nan	nan	nan	nan
HC_5N(13-12)	34.61	37	-26.94	15.071	3.309	2.623	4.01	0.294	0.315	nan	nan	nan	nan	nan	nan
HC_5N(13-12)	34.61	38	-25.86	15.081	3.619	2.695	4.287	0.248	0.265	nan	nan	nan	nan	nan	nan
HC_5N(13-12)	34.61	39	-24.78	15.088	7.078	4.145	8.404	0.166	0.236	nan	nan	nan	nan	nan	nan
HC_5N(13-12)	34.61	40	-23.69	15.331	5.62	3.28	9.904	0.234	0.286	21.344	nan	0.264	nan	1.045	nan
HC_5N(13-12)	34.61	41	-22.61	13.964	3.41	1.662	3.74	0.259	0.457	21.908	47.156	1.662	23.606	0.251	2.996
HC_5N(13-12)	34.61	42	-21.53	13.626	1.289	1.539	1.315	0.545	0.397	22.452	31.871	1.539	14.802	0.36	3.429
HC_5N(13-12)	34.61	43	-20.45	15.915	5.433	4.939	9.051	0.316	0.26	nan	nan	nan	nan	nan	nan
HC_5N(13-12)	34.61	44	-19.36	17.176	2.57	3.452	2.946	0.481	0.303	nan	nan	nan	nan	nan	nan
HC_5N(14-13)	37.28	40	-33.32	14.557	0.571	2.098	0.578	4.269	1.007	22.48	5.632	0.831	6.341	0.293	1.628
HC_5N(14-13)	37.28	41	-32.31	14.412	0.611	1.828	0.616	3.568	1.034	22.65	4.428	0.798	4.597	0.321	1.556
HC_5N(14-13)	37.28	42	-31.31	14.675	0.771	1.821	0.837	3.435	1.017	21.42	27.744	1.821	24.718	0.355	1.356
HC_5N(14-13)	37.28	43	-30.30	14.717	0.56	1.803	0.596	3.696	0.946	21.783	5.376	1.803	6.628	0.398	0.973
HC_5N(14-13)	37.28	44	-29.30	15.031	0.744	1.893	0.813	3.143	0.939	21.953	3.656	1.893	5.101	0.739	0.995
HC_5N(14-13)	37.28	45	-28.29	15.296	0.738	1.799	0.783	3.479	0.99	21.375	3.493	1.799	4.288	0.715	1.012
HC_5N(14-13)	37.28	46	-27.29	15.672	0.872	1.861	0.904	2.988	0.873	21.644	2.8	1.861	3.287	0.901	0.885
HC_5N(14-13)	37.28	47	-26.28	16.12	0.806	2.058	0.871	2.746	0.919	22.037	1.224	0.971	1.279	1.25	1.305
HC_5N(14-13)	37.28	48	-25.28	16.42	0.924	2.147	1.025	2.709	0.816	21.503	1.758	1.123	1.762	0.987	1.136
HC_5N(14-13)	37.28	49	-24.27	17.457	0.884	2.712	0.929	2.749	0.775	nan	nan	nan	nan	nan	nan
HC_5N(14-13)	37.28	50	-23.27	17.496	0.935	2.793	1.016	2.704	0.773	nan	nan	nan	nan	nan	nan
HC_5N(14-13)	37.28	51	-22.26	17.739	0.722	2.49	0.754	3.319	0.832	nan	nan	nan	nan	nan	nan
HC_5N(14-13)	37.28	52	-21.26	17.647	0.818	2.925	0.877	3.133	0.758	nan	nan	nan	nan	nan	nan
HC_5N(14-13)	37.28	53	-20.25	17.953	0.723	2.387	0.744	3.571	0.938	nan	nan	nan	nan	nan	nan
HC_5N(14-13)	37.28	54	-19.25	17.784	0.836	2.881	0.869	3.329	0.838	nan	nan	nan	nan	nan	nan
HC_7N(16-15)	18.05	48	-31.42	16.744	7.924	1.547	10.933	0.066	0.233	24.309	2.619	1.357	2.784	0.125	0.211
HC_7N(16-15)	18.05	49	-29.34	16.999	1.085	1.927	1.172	0.385	0.185	25.51	7.141	1.927	7.852	0.059	0.175
HC_7N(16-15)	18.05	50	-27.27	14.928	4.447	4.96	3.072	0.301	0.168	19.323	1.366	1.307	1.815	0.282	0.319
HC_7N(16-15)	18.05	51	-25.19	13.219	2.805	5.701	3.232	0.298	0.123	25.589	2.369	0.856	1.754	0.13	0.248
HC_7N(16-15)	18.05	52	-23.12	16.904	2.326	5.569	2.969	0.33	0.114	nan	nan	nan	nan	nan	nan
HC_7N(16-15)	18.05	53	-21.04	9.841	4.3	5.701	6.112	0.276	0.14	25.59	3.498	3.539	3.76	0.208	0.141
HC_7N(16-15)	18.05	54	-18.96	19.508	4.495	7.428	9.042	0.292	0.605	19.508	2.541	2.545	4.507	0.289	0.586
HC_7N(17-16)	19.18	71	-32.17	15.059	2.216	4.575	2.32	0.214	0.089	nan	nan	nan	nan	nan	nan

Table C.4 continued.

Transition	Restfreq	Ch	v_{ch}	R_{max} 1	ΔR_{max} 1	$W_{1/2}$ 1	$\Delta W_{1/2}$ 1	F_{max} 1	ΔF_{max} 1	R_{max} 2	ΔR_{max} 2	$W_{1/2}$ 2	$\Delta W_{1/2}$ 2	F_{max} 2	ΔF_{max} 2
HC_7N(17-16)	19.18	72	-30.22	19.01	1.651	3.746	1.729	0.245	0.093	nan	nan	nan	nan	nan	nan
HC_7N(17-16)	19.18	73	-28.27	16.85	1.325	2.856	1.503	0.31	0.115	23.527	3.747	1.118	3.871	0.066	0.176
HC_7N(17-16)	19.18	74	-26.31	17.761	2.165	4.881	2.272	0.216	0.081	nan	nan	nan	nan	nan	nan
HC_7N(17-16)	19.18	75	-24.36	16.741	5.697	3.502	3.743	0.185	0.126	20.796	2.617	1.353	4.412	0.091	0.323
HC_7N(17-16)	19.18	76	-22.40	18.113	1.237	3.653	1.346	0.351	0.101	nan	nan	nan	nan	nan	nan
HC_7N(17-16)	19.18	77	-20.45	18.692	3.672	3.033	2.374	0.209	0.3	20.517	3.177	1.194	3.736	0.096	0.344
HC_7N(18-17)	20.30	71	-33.16	15.508	2.049	1.414	2.155	0.965	1.22	22.66	5.245	1.207	7.323	0.351	1.393
HC_7N(18-17)	20.30	72	-31.31	14.246	98.169	10.631	66.864	0.195	1.11	nan	nan	nan	nan	nan	nan
HC_7N(18-17)	20.30	73	-29.46	10.95	4.14	3.604	3.317	0.826	0.786	22.402	3.054	1.41	3.121	0.406	0.756
HC_7N(18-17)	20.30	74	-27.62	1.418	5.742	2.04	5.248	1.207	1.372	nan	nan	nan	nan	nan	nan
HC_7N(18-17)	20.30	75	-25.77	15.198	2.339	1.697	2.872	0.949	0.908	nan	nan	nan	nan	nan	nan
HC_7N(18-17)	20.30	76	-23.93	15.243	2.391	1.854	2.754	1.014	0.829	21.103	5.487	1.854	5.644	0.442	0.766
HC_7N(18-17)	20.30	77	-22.08	5	48.676	4.554	50.743	0.241	1.832	23.11	1.755	1.759	1.998	0.779	0.662
HC_7N(18-17)	20.30	78	-20.24	7.171	12.776	6.495	19.189	0.926	0.642	25.038	28.677	6.495	49.174	0.369	0.568
HC_7N(19-18)	21.43	40	-32.60	15.234	1.8	2.363	1.818	0.352	0.14	22.18	4.776	2.363	4.459	0.133	0.134
HC_7N(19-18)	21.43	41	-30.85	15.682	8.162	2.286	4.895	0.241	0.437	20.724	7.963	2.286	4.813	0.246	0.437
HC_7N(19-18)	21.43	42	-29.10	15.448	2.351	2.465	2.361	0.224	0.119	22.918	3.499	2.465	3.529	0.147	0.114
HC_7N(19-18)	21.43	43	-27.35	16.287	1.271	2.292	1.351	0.376	0.138	23.746	3.225	2.292	3.415	0.145	0.133
HC_7N(19-18)	21.43	44	-25.61	17.376	4.892	3.564	3.376	0.302	0.174	26.179	19.683	3.564	17.346	0.07	0.151
HC_7N(19-18)	21.43	45	-23.86	17.915	7.757	3.063	4.315	0.335	0.489	24.242	29.698	3.063	14.705	0.088	0.521
HC_7N(19-18)	21.43	46	-22.11	18.448	1.358	3.395	1.548	0.364	0.117	25.734	3.056	0.961	4.627	0.075	0.245
HC_7N(19-18)	21.43	47	-20.36	5	91.953	17.483	74.644	0.094	0.099	18.731	1.468	2.351	1.776	0.271	0.159
HC_7N(19-18)	21.43	48	-18.61	20.078	1.44	4.44	1.448	0.363	0.101	nan	nan	nan	nan	nan	nan
HC_7N(20-19)	22.56	50	-33.38	15.237	1.63	2.82	1.619	0.505	0.15	22.915	7.295	2.403	7.295	0.1	0.162
HC_7N(20-19)	22.56	51	-31.72	15.857	8.033	2.431	4.602	0.288	0.501	21.125	13.557	2.431	7.552	0.17	0.511
HC_7N(20-19)	22.56	52	-30.06	15.891	2.15	2.524	2.563	0.369	0.144	23.115	9.081	2.524	9.353	0.09	0.14
HC_7N(20-19)	22.56	53	-28.40	16.299	1.06	2.291	1.277	0.427	0.156	22.903	2.112	1.529	2.156	0.176	0.178
HC_7N(20-19)	22.56	54	-26.74	16.882	2.208	2.999	2.45	0.282	0.121	22.931	1.84	1.394	1.862	0.189	0.209
HC_7N(20-19)	22.56	55	-25.08	16.912	14.921	2.529	6.53	0.316	1.417	21.498	22.842	2.529	9.158	0.205	1.471
HC_7N(20-19)	22.56	56	-23.42	17.877	1.053	3.341	1.102	0.396	0.108	nan	nan	nan	nan	nan	nan
HC_7N(20-19)	22.56	57	-21.76	18.847	1.105	3.165	1.12	0.393	0.119	nan	nan	nan	nan	nan	nan
HC_7N(20-19)	22.56	58	-20.09	15.493	16.467	5.021	8.205	0.161	0.284	20.105	1.307	2.079	2.402	0.389	0.556
HC_7N(22-21)	24.82	49	-33.40	15.127	0.924	1.991	0.988	0.333	0.134	nan	nan	nan	nan	nan	nan
HC_7N(22-21)	24.82	50	-31.89	15.543	0.966	1.829	1.015	0.317	0.144	22.919	nan	0.809	nan	0	nan
HC_7N(22-21)	24.82	51	-30.38	17.059	0.995	2.579	1.113	0.31	0.103	nan	nan	nan	nan	nan	nan
HC_7N(22-21)	24.82	52	-28.87	16.119	0.845	1.625	0.957	0.319	0.138	22.175	1.878	1.507	1.992	0.133	0.136
HC_7N(22-21)	24.82	53	-27.36	17.092	1.415	2.098	1.657	0.248	0.139	22.69	1.553	1.049	1.621	0.159	0.183
HC_7N(22-21)	24.82	54	-25.85	16.791	1.832	1.808	1.555	0.344	0.141	21.663	2.575	1.779	2.613	0.228	0.136
HC_7N(22-21)	24.82	55	-24.34	17.403	2.727	1.954	2.781	0.277	0.144	21.828	3.605	1.436	2.913	0.165	0.242
HC_7N(22-21)	24.82	56	-22.83	16.998	6.586	1.627	3.293	0.297	0.75	20.286	6.141	1.627	3.082	0.318	0.748
HC_7N(22-21)	24.82	57	-21.32	16.26	11.898	2.062	5.813	0.275	1.071	20.214	11.694	2.062	5.095	0.278	1.132
HC_7N(22-21)	24.82	58	-19.81	18.331	0.951	3.308	1.091	0.417	0.099	nan	nan	nan	nan	nan	nan

Table C.4 continued.

Transition	Restfreq	Ch	v_{ch}	R_{max} 1	ΔR_{max} 1	$W_{1/2}$ 1	$\Delta W_{1/2}$ 1	F_{max} 1	ΔF_{max} 1	R_{max} 2	ΔR_{max} 2	$W_{1/2}$ 2	$\Delta W_{1/2}$ 2	F_{max} 2	ΔF_{max} 2
HC_7N(23-22)	25.94	30	-33.10	15.569	0.744	2.239	0.802	0.601	0.169	21.376	1.458	0.695	7.301	0.139	1.331
HC_7N(23-22)	25.94	31	-31.65	14.785	1.046	2.185	1.224	0.444	0.154	19.943	1.531	1.094	1.551	0.206	0.21
HC_7N(23-22)	25.94	32	-30.21	15.881	0.965	2.644	1.015	0.462	0.144	nan	nan	nan	nan	nan	nan
HC_7N(23-22)	25.94	33	-28.77	15.862	2.915	2.295	2.376	0.358	0.174	22.674	14.542	2.295	24.048	0.094	0.163
HC_7N(23-22)	25.94	34	-27.32	16.526	1.558	1.994	1.603	0.304	0.141	22.719	2.813	1.994	2.933	0.166	0.137
HC_7N(23-22)	25.94	35	-25.88	16.607	1.243	2.503	1.364	0.445	0.14	22.478	2.933	1.393	3.594	0.129	0.192
HC_7N(23-22)	25.94	36	-24.43	18.986	0.903	2.786	0.943	0.425	0.119	nan	nan	nan	nan	nan	nan
HC_7N(23-22)	25.94	37	-22.99	17.257	33.585	2.219	12.334	0.32	3.498	19.942	12.687	1.712	6.067	0.297	5.732
HC_7N(23-22)	25.94	38	-21.54	19.349	0.731	2.313	0.733	0.549	0.15	nan	nan	nan	nan	nan	nan
HC_7N(23-22)	25.94	39	-20.10	18.799	0.826	2.493	0.864	0.512	0.147	nan	nan	nan	nan	nan	nan
HC_7N(23-22)	25.94	40	-18.66	18.147	0.897	3.154	0.91	0.593	0.146	nan	nan	nan	nan	nan	nan
HC_7N(24-23)	27.07	39	-32.74	16.298	0.754	1.419	0.817	0.515	0.237	23.007	5.04	1.419	5.096	0.072	0.221
HC_7N(24-23)	27.07	40	-31.35	16.078	1.207	1.636	1.443	0.405	0.227	21.718	2.531	1.636	2.762	0.192	0.213
HC_7N(24-23)	27.07	41	-29.97	16.699	3.601	2.287	2.962	0.494	0.308	22.374	12.532	2.287	8.586	0.147	0.338
HC_7N(24-23)	27.07	42	-28.58	16.659	2.608	2.288	2.439	0.423	0.204	22.871	4.662	2.288	3.798	0.242	0.206
HC_7N(24-23)	27.07	43	-27.20	17.505	3.876	1.823	2.435	0.456	0.455	21.683	4.596	1.823	2.832	0.384	0.46
HC_7N(24-23)	27.07	44	-25.81	18.58	3.773	3.412	2.389	0.313	0.201	21.84	2.516	1.091	3.534	0.135	0.386
HC_7N(24-23)	27.07	45	-24.43	18.092	14.553	1.922	6.322	0.391	1.816	21.041	12.09	1.576	4.964	0.282	2.88
HC_7N(24-23)	27.07	46	-23.05	18.688	0.974	2.645	1.066	0.557	0.178	nan	nan	nan	nan	nan	nan
HC_7N(24-23)	27.07	47	-21.66	14.733	15.15	3.669	12.143	0.223	0.237	20.183	2.014	1.919	2.448	0.445	0.999
HC_7N(24-23)	27.07	48	-20.28	17.621	8.188	2.211	5.241	0.318	0.566	22.568	12.9	2.211	7.419	0.204	0.605
HC_7N(24-23)	27.07	49	-18.89	13.723	26.89	5.748	18.014	0.145	0.201	19.757	1.351	2.045	2.844	0.412	0.694
HC_7N(25-24)	28.20	40	-32.20	16.265	1.838	2.054	1.677	0.45	0.146	23.057	80.185	2.054	50.335	0.102	1.553
HC_7N(25-24)	28.20	41	-30.87	15.612	0.592	1.476	0.636	0.52	0.181	22.876	3.396	1.476	3.434	0.085	0.17
HC_7N(25-24)	28.20	42	-29.54	15.771	4.258	2.404	3.805	0.38	0.275	21.441	11.608	2.404	6.975	0.151	0.346
HC_7N(25-24)	28.20	43	-28.21	15.783	3.381	1.461	2.417	0.433	0.451	19.106	9.248	1.461	5.337	0.163	0.516
HC_7N(25-24)	28.20	44	-26.89	16.641	1.183	2.593	1.337	0.285	0.111	22.952	2.27	0.836	2.095	0.082	0.177
HC_7N(25-24)	28.20	45	-25.56	17.252	0.687	1.608	0.748	0.492	0.178	22.203	1.011	0.939	1.043	0.254	0.224
HC_7N(25-24)	28.20	46	-24.23	18.409	0.911	2.566	0.989	0.423	0.13	nan	nan	nan	nan	nan	nan
HC_7N(25-24)	28.20	47	-22.90	18.655	0.948	2.388	0.971	0.388	0.134	nan	nan	nan	nan	nan	nan
HC_7N(25-24)	28.20	48	-21.57	19.399	0.856	2.113	0.899	0.425	0.15	nan	nan	nan	nan	nan	nan
HC_7N(25-24)	28.20	49	-20.24	19.104	0.585	-1.829	0.594	0.561	0.155	nan	nan	nan	nan	nan	nan
HC_7N(25-24)	28.20	50	-18.91	16.37	15.067	2.053	8.376	0.184	0.628	20.162	4.013	1.728	1.951	0.512	1.026
HC_7N(26-25)	29.33	19	-32.42	16.305	2.16	1.466	2.561	0.194	0.222	21.412	3.415	1.466	3.666	0.121	0.207
HC_7N(26-25)	29.33	20	-31.14	15.099	3.818	1.679	3.524	0.12	0.196	23.55	3.636	1.679	3.981	0.145	0.179
HC_7N(26-25)	29.33	21	-29.87	15.872	4.113	2.555	4.126	0.222	0.15	22.893	10.593	2.555	10.177	0.096	0.147
HC_7N(26-25)	29.33	22	-28.59	5	94.117	14.335	73.712	0.085	0.154	20.622	2.511	0.48	7.029	0.183	2.988
HC_7N(26-25)	29.33	23	-27.31	17.773	2.96	1.12	3.065	0.117	0.2	21.408	2.2	1.12	2.45	0.152	0.198
HC_7N(26-25)	29.33	24	-26.03	12.575	4.793	3.888	7.095	0.127	0.135	23.178	3.953	1.85	3.801	0.132	0.393
HC_7N(26-25)	29.33	25	-24.75	18.566	5.348	3.197	6.288	0.117	0.153	nan	nan	nan	nan	nan	nan
HC_7N(26-25)	29.33	26	-23.48	21.202	6.645	2.618	6.082	0.143	0.144	nan	nan	nan	nan	nan	nan
HC_7N(26-25)	29.33	27	-22.20	16.146	12.301	3.061	9	0.152	0.263	23.529	33.007	3.061	25.227	0.059	0.323

Table C.4 continued.

Transition	Restfreq	Ch	v_{ch}	R_{max} 1	ΔR_{max} 1	$W_{1/2}$ 1	$\Delta W_{1/2}$ 1	F_{max} 1	ΔF_{max} 1	R_{max} 2	ΔR_{max} 2	$W_{1/2}$ 2	$\Delta W_{1/2}$ 2	F_{max} 2	ΔF_{max} 2
HC_7N(26-25)	29.33	28	-20.92	19.42	1.38	-1.333	1.494	0.228	0.204	nan	nan	nan	nan	nan	nan
HC_7N(26-25)	29.33	29	-19.64	18.543	2.234	2.594	3.017	0.283	0.197	25.487	2.257	1.412	2.34	0.201	0.24
HC_7N(27-26)	30.46	30	-32.39	14.35	0.473	1.874	0.484	0.896	nan	22.297	3.634	1.874	nan	0.117	nan
HC_7N(27-26)	30.46	31	-31.16	14.615	3.365	2.07	2.857	0.489	0.325	20.074	4.797	2.07	3.741	0.347	0.331
HC_7N(27-26)	30.46	32	-29.93	15.038	1.224	2.011	1.334	0.701	0.272	21.484	2.921	2.011	3.215	0.289	0.265
HC_7N(27-26)	30.46	33	-28.70	15.715	1.183	2.011	1.298	0.667	0.253	22.211	3.302	2.011	3.826	0.233	0.249
HC_7N(27-26)	30.46	34	-27.47	16.213	1.637	2.412	1.615	0.654	0.212	23.136	15.97	2.412	15.132	0.067	0.206
HC_7N(27-26)	30.46	35	-26.24	16.993	2.254	3.034	2.371	0.434	0.165	22.243	1.517	1.149	1.811	0.259	0.365
HC_7N(27-26)	30.46	36	-25.01	17.624	2.61	4.091	2.211	0.438	0.191	21.091	1.722	0.826	2.126	0.2	0.396
HC_7N(27-26)	30.46	37	-23.78	18.195	1.149	3.602	1.294	0.541	0.148	nan	nan	nan	nan	nan	nan
HC_7N(27-26)	30.46	38	-22.55	18.596	0.77	2.739	0.924	0.839	0.198	24.885	2.426	0.877	2.53	0.143	0.333
HC_7N(27-26)	30.46	39	-21.32	19.051	1.755	2.584	1.754	0.757	0.239	24.156	3.366	1.358	3.18	0.222	0.462
HC_7N(27-26)	30.46	40	-20.09	18.531	1.259	3.146	1.459	0.575	0.186	24.632	1.84	0.632	2.066	0.173	0.417
HC_7N(27-26)	30.46	41	-18.86	17.743	1.047	2.592	1.118	0.744	0.26	24.976	3.017	0.825	3.322	0.14	0.455
HC_7N(28-27)	31.58	29	-32.46	15.508	0.825	1.924	0.921	0.941	0.336	22.962	3.965	1.924	4.216	0.19	0.323
HC_7N(28-27)	31.58	30	-31.27	15.471	1.609	2.339	1.729	0.785	0.283	22.406	6.929	2.339	6.846	0.185	0.274
HC_7N(28-27)	31.58	31	-30.08	15.742	2.245	2.214	1.956	0.726	0.307	21.829	5.661	2.214	5.655	0.276	0.297
HC_7N(28-27)	31.58	32	-28.90	15.92	1.705	2.072	2.005	0.614	0.296	22.241	2.267	2.072	2.193	0.481	0.281
HC_7N(28-27)	31.58	33	-27.71	15.62	0.886	1.847	0.974	0.747	0.291	21.73	1.708	1.466	1.882	0.343	0.317
HC_7N(28-27)	31.58	34	-26.53	16.301	1.319	2.02	1.346	0.833	0.282	22.298	2.622	2.02	2.676	0.415	0.277
HC_7N(28-27)	31.58	35	-25.34	17.496	1.994	2.302	2.269	0.498	0.297	22.783	3.901	1.165	3.933	0.17	0.424
HC_7N(28-27)	31.58	36	-24.15	18.649	1.001	2.764	1.112	0.794	0.249	nan	nan	nan	nan	nan	nan
HC_7N(28-27)	31.58	37	-22.97	18.427	0.613	2.295	0.634	0.964	0.223	nan	nan	nan	nan	nan	nan
HC_7N(28-27)	31.58	38	-21.78	18.415	0.663	2.29	0.696	1.141	0.286	25.311	2.253	0.965	2.33	0.215	0.427
HC_7N(28-27)	31.58	39	-20.59	18.831	0.59	2.069	0.589	1.215	0.299	nan	nan	nan	nan	nan	nan
HC_7N(28-27)	31.58	40	-19.41	16.194	40.423	7.631	59.501	0.18	0.764	18.993	1.241	1.801	1.929	0.743	0.831
HC_7N(29-28)	32.71	38	-32.46	15.394	0.676	2.007	0.738	0.735	0.211	25.005	10.914	2.007	24.467	0.071	2.13
HC_7N(29-28)	32.71	39	-31.31	12.834	4.736	3.893	7.825	0.228	0.175	22.195	10.939	1.738	6.676	0.116	0.654
HC_7N(29-28)	32.71	40	-30.17	17.384	1.645	2.961	1.847	0.441	0.185	nan	nan	nan	nan	nan	nan
HC_7N(29-28)	32.71	41	-29.02	12.934	42.797	6.838	42.235	0.164	0.323	22.843	3.505	2.768	8.511	0.227	1.111
HC_7N(29-28)	32.71	42	-27.88	10.962	4.9	6.936	4.775	0.408	0.337	nan	nan	nan	nan	nan	nan
HC_7N(29-28)	32.71	43	-26.73	17.102	1.317	1.851	1.462	0.345	0.208	nan	nan	nan	nan	nan	nan
HC_7N(29-28)	32.71	44	-25.59	1.747	1.003	1.327	1.016	0.813	0.403	nan	nan	nan	nan	nan	nan
HC_7N(29-28)	32.71	45	-24.44	18.429	0.786	1.521	0.788	0.446	0.2	nan	nan	nan	nan	nan	nan
HC_7N(29-28)	32.71	46	-23.29	18.134	4.524	1.843	5.704	0.33	0.318	23.022	18.159	1.843	13.8	0.099	0.387
HC_7N(29-28)	32.71	47	-22.15	18.796	1.157	1.617	1.158	0.412	0.255	nan	nan	nan	nan	nan	nan
HC_7N(29-28)	32.71	48	-21.00	18.97	0.57	1.293	0.598	0.749	0.284	nan	nan	nan	nan	nan	nan
HC_7N(30-29)	33.84	37	-33.00	14.777	1.359	1.863	1.401	0.49	0.187	18.978	5.102	1.131	5.158	0.09	0.272
HC_7N(30-29)	33.84	38	-31.89	15.618	0.494	1.554	0.494	0.638	0.175	nan	nan	nan	nan	nan	nan
HC_7N(30-29)	33.84	39	-30.78	15.644	0.435	1.246	0.436	0.674	0.203	23.467	2.476	0.789	2.673	0.094	0.249
HC_7N(30-29)	33.84	40	-29.68	15.097	0.637	1.526	0.668	0.555	0.199	21.848	2.878	1.526	3.24	0.122	0.196
HC_7N(30-29)	33.84	41	-28.57	15.622	0.811	2.225	0.918	0.509	0.159	22.963	2.29	1.331	2.717	0.144	0.2

Table C.4 continued.

Transition	Restfreq	Ch	v_{ch}	R_{max} 1	ΔR_{max} 1	$W_{1/2}$ 1	$\Delta W_{1/2}$ 1	F_{max} 1	ΔF_{max} 1	R_{max} 2	ΔR_{max} 2	$W_{1/2}$ 2	$\Delta W_{1/2}$ 2	F_{max} 2	ΔF_{max} 2
HC_7N(30-29)	33.84	42	-27.46	16.361	1.513	3.36	1.717	0.329	0.122	nan	nan	nan	nan	nan	nan
HC_7N(30-29)	33.84	43	-26.35	17.769	1.074	2.098	1.214	0.43	0.165	21.929	1.854	0.641	2.543	0.114	0.326
HC_7N(30-29)	33.84	44	-25.25	18.082	2.999	2.498	2.804	0.4	0.187	21.404	1.658	0.772	2.531	0.179	0.576
HC_7N(30-29)	33.84	45	-24.14	18.498	0.657	2.312	0.695	0.517	0.127	nan	nan	nan	nan	nan	nan
HC_7N(30-29)	33.84	46	-23.03	17.393	0.846	2.569	0.939	0.496	0.141	nan	nan	nan	nan	nan	nan
HC_7N(30-29)	33.84	47	-21.92	18.429	0.761	2.238	0.771	0.561	0.165	nan	nan	nan	nan	nan	nan
HC_7N(30-29)	33.84	48	-20.82	18.499	0.544	1.829	0.557	0.784	0.202	nan	nan	nan	nan	nan	nan
HC_7N(30-29)	33.84	49	-19.71	18.714	0.674	2.113	0.678	0.664	0.183	nan	nan	nan	nan	nan	nan
HC_7N(30-29)	33.84	50	-18.60	18.658	0.899	2.427	0.914	0.552	0.178	nan	nan	nan	nan	nan	nan
HC_7N(31-30)	34.97	15	-33.32	17.545	70.583	19.428	118.052	0.091	0.141	nan	nan	nan	nan	nan	nan
HC_7N(31-30)	34.97	16	-32.25	9.18	1.611	3.68	3.215	1.105	2.855	nan	nan	nan	nan	nan	nan
HC_7N(31-30)	34.97	17	-31.18	15.301	2.142	1.367	4.167	0.25	0.272	23.448	2.702	1.367	3.944	0.139	0.227
HC_7N(31-30)	34.97	18	-30.10	0	0	0	0	0	0	nan	nan	nan	nan	nan	nan
HC_7N(31-30)	34.97	19	-29.03	0	0	0	0	0	0	nan	nan	nan	nan	nan	nan
HC_7N(31-30)	34.97	20	-27.96	19.315	1.316	0.957	1.558	0.299	0.327	22.767	2.331	0.957	2.626	0.166	0.317
HC_7N(31-30)	34.97	21	-26.89	50.07	1402.237	12.091	402.102	0.241	23.538	nan	nan	nan	nan	nan	nan
HC_7N(31-30)	34.97	22	-25.82	0	0	0	0	0	0	nan	nan	nan	nan	nan	nan
HC_7N(31-30)	34.97	23	-24.75	25.65	45.026	9.109	100.698	0.047	0.297	nan	nan	nan	nan	nan	nan
HC_7N(31-30)	34.97	24	-23.68	5	42.143	7.876	47.596	0.075	0.243	20.132	0.811	0.763	1.059	0.26	0.281
HC_7N(31-30)	34.97	25	-22.60	19.348	7.911	4.414	9.062	0.183	0.143	nan	nan	nan	nan	nan	nan
HC_7N(31-30)	34.97	26	-21.53	15.288	88.899	13.507	90.303	0.054	0.171	nan	nan	nan	nan	nan	nan
HC_7N(31-30)	34.97	27	-20.46	8.316	261.5	11.234	201.696	0.088	0.487	nan	nan	nan	nan	nan	nan
HC_7N(31-30)	34.97	28	-19.39	19.407	41.402	12.48	48.653	0.082	0.143	nan	nan	nan	nan	nan	nan
HC_7N(32-31)	36.10	37	-32.74	15.449	0.618	1.566	0.635	0.821	0.28	nan	nan	nan	nan	nan	nan
HC_7N(32-31)	36.10	38	-31.71	15.46	0.936	1.17	1.16	0.445	nan	22.603	33.906	1.17	nan	0.151	nan
HC_7N(32-31)	36.10	39	-30.67	15.828	0.802	1.587	0.848	0.582	0.247	22.221	3.089	1.587	3.585	0.149	0.245
HC_7N(32-31)	36.10	40	-29.63	16.754	1.26	2.222	1.391	0.524	0.242	nan	nan	nan	nan	nan	nan
HC_7N(32-31)	36.10	41	-28.59	16.605	1.127	2.295	1.262	0.493	0.209	22.878	2.132	0.694	2.472	0.139	0.372
HC_7N(32-31)	36.10	42	-27.55	16.879	2.438	2.291	2.221	0.546	0.241	23.328	8.744	2.291	10.844	0.137	0.232
HC_7N(32-31)	36.10	43	-26.51	17.151	0.906	1.658	1.044	0.588	0.237	22.856	3.478	1.658	3.907	0.15	0.23
HC_7N(32-31)	36.10	44	-25.48	17.676	0.932	1.502	1.024	0.73	0.318	22.096	1.875	1.174	1.996	0.319	0.349
HC_7N(32-31)	36.10	45	-24.44	18.374	1.625	2.575	1.738	0.453	0.248	nan	nan	nan	nan	nan	nan
HC_7N(32-31)	36.10	46	-23.40	18.826	1.433	2.087	1.571	0.569	0.225	23.226	4.023	1.063	3.92	0.124	0.365
HC_7N(32-31)	36.10	47	-22.36	18.529	0.928	2.335	1.008	0.597	0.203	nan	nan	nan	nan	nan	nan
HC_7N(32-31)	36.10	48	-21.32	18.955	3.129	1.548	2.265	0.626	0.412	21.95	6.598	1.099	4.41	0.191	0.94
HC_7N(32-31)	36.10	49	-20.29	18.561	6.364	4.07	9.302	0.213	0.52	19.873	1.026	-1.128	1.487	0.428	0.539
HC_7N(32-31)	36.10	50	-19.25	18.805	1.461	2.746	1.808	0.516	0.228	nan	nan	nan	nan	nan	nan
HC_7N(33-32)	37.22	36	-33.06	14.339	1.844	2.048	2.222	0.39	0.258	22.666	6.284	2.048	4.068	0.242	0.463
HC_7N(33-32)	37.22	37	-32.06	14.657	0.981	1.271	1.098	0.541	0.361	23.345	3.018	1.271	3.02	0.159	0.328
HC_7N(33-32)	37.22	38	-31.05	14.141	1.47	1.925	1.599	0.506	0.272	20.555	1.619	1.925	1.692	0.447	0.256
HC_7N(33-32)	37.22	39	-30.04	14.892	1.483	1.947	1.939	0.532	0.317	21.955	1.967	1.947	2.241	0.375	0.292
HC_7N(33-32)	37.22	40	-29.04	14.481	0.734	1.428	0.733	0.683	0.302	nan	nan	nan	nan	nan	nan

Table C.4 continued.

Transition	Restfreq	Ch	v_{ch}	R_{max} 1	ΔR_{max} 1	$W_{1/2}$ 1	$\Delta W_{1/2}$ 1	F_{max} 1	ΔF_{max} 1	R_{max} 2	ΔR_{max} 2	$W_{1/2}$ 2	$\Delta W_{1/2}$ 2	F_{max} 2	ΔF_{max} 2
HC_7N(33-32)	37.22	41	-28.03	15.204	0.787	1.683	0.818	0.758	0.305	22.497	1.392	1.683	1.436	0.408	0.289
HC_7N(33-32)	37.22	42	-27.02	14.389	1.109	1.885	1.15	0.488	0.247	21.281	1.669	1.135	2.044	0.264	0.318
HC_7N(33-32)	37.22	43	-26.02	14.889	2.32	2.226	3.06	0.391	0.316	22.019	2.747	1.871	2.85	0.298	0.31
HC_7N(33-32)	37.22	44	-25.01	16.259	18.62	14.513	25.502	0.217	0.152	nan	nan	nan	nan	nan	nan
HC_7N(33-32)	37.22	45	-24.00	18.104	5.374	4.782	5.859	0.218	0.209	20.401	0.69	0.627	0.762	0.456	0.451
HC_7N(33-32)	37.22	46	-23.00	17.159	1.739	3.47	1.884	0.535	0.232	nan	nan	nan	nan	nan	nan
HC_7N(33-32)	37.22	47	-21.99	20.254	3.346	3.613	2.655	0.38	0.23	nan	nan	nan	nan	nan	nan
HC_7N(33-32)	37.22	48	-20.98	17.963	6.334	7.37	7.02	0.224	0.142	nan	nan	nan	nan	nan	nan
HC_7N(33-32)	37.22	49	-19.98	13.43	4.413	2.129	3.982	0.352	0.315	19.619	4.898	2.129	5.077	0.281	0.309
HC_7N(33-32)	37.22	50	-18.97	19.215	0.607	1.355	0.612	0.853	0.331	nan	nan	nan	nan	nan	nan
C_3N(2-1,3/2-1/2)	19.80	58	-32.64	7.11	3.163	3.308	4.012	0.102	0.078	19.144	0.785	0.638	16.517	0.127	4.36
C_3N(2-1,3/2-1/2)	19.80	59	-30.75	15.575	1.406	3.103	1.636	0.203	0.079	nan	nan	nan	nan	nan	nan
C_3N(2-1,3/2-1/2)	19.80	60	-28.86	0	0	0	0	0	0	nan	nan	nan	nan	nan	nan
C_3N(2-1,3/2-1/2)	19.80	61	-26.97	17.608	10.807	8.397	11.904	0.053	0.042	nan	nan	nan	nan	nan	nan
C_3N(2-1,3/2-1/2)	19.80	62	-25.07	20.489	2.662	4.998	2.921	0.094	0.043	nan	nan	nan	nan	nan	nan
C_3N(2-1,3/2-1/2)	19.80	63	-23.18	18.856	1.009	1.765	1.048	0.147	0.074	nan	nan	nan	nan	nan	nan
C_3N(2-1,3/2-1/2)	19.80	64	-21.29	0	0	0	0	0	0	nan	nan	nan	nan	nan	nan
C_3N(2-1,3/2-1/2)	19.80	65	-19.40	11.708	5.335	3.696	3.996	0.256	0.119	19.025	7.918	2.777	4.816	0.119	0.266
C_3N(2-1,5/2-3/2)	19.78	49	-33.07	16.547	1.819	1.898	2.078	0.126	0.102	24.765	4.977	1.878	6.193	0.05	0.099
C_3N(2-1,5/2-3/2)	19.78	50	-31.18	15.344	24.435	13.68	32.64	0.052	0.046	nan	nan	nan	nan	nan	nan
C_3N(2-1,5/2-3/2)	19.78	51	-29.29	-16.206	199.778	25.696	83.856	0.182	0.784	nan	nan	nan	nan	nan	nan
C_3N(2-1,5/2-3/2)	19.78	52	-27.39	18.421	7.764	3.452	3.602	0.11	0.253	20.812	4.729	1.547	6.661	0.059	0.306
C_3N(2-1,5/2-3/2)	19.78	53	-25.50	15.873	3.424	2.006	4.291	0.085	0.094	22.288	4.494	2.006	4.867	0.064	0.088
C_3N(2-1,5/2-3/2)	19.78	54	-23.60	19.518	3.508	2.808	4.142	0.088	0.086	nan	nan	nan	nan	nan	nan
C_3N(2-1,5/2-3/2)	19.78	55	-21.71	17.347	1.363	1.854	1.381	0.145	0.092	nan	nan	nan	nan	nan	nan
C_3N(2-1,5/2-3/2)	19.78	56	-19.81	12.837	2.011	3.186	2.453	0.183	nan	24.492	37.772	3.186	nan	0.043	nan
C_3N(3-2,5/2-3/2)	29.70	31	-32.75	15.94	1.705	2.041	1.914	0.247	0.17	23.846	3.407	2.041	4.362	0.126	0.169
C_3N(3-2,5/2-3/2)	29.70	32	-31.49	17.225	3.016	3.545	3.61	0.201	0.132	25.182	2.14	1.309	2.238	0.154	0.208
C_3N(3-2,5/2-3/2)	29.70	33	-30.22	16.543	8.833	3.373	9.207	0.194	0.16	20.966	2.536	1.369	4.757	0.14	0.616
C_3N(3-2,5/2-3/2)	29.70	34	-28.96	20.799	1.093	2.321	1.171	0.266	0.108	nan	nan	nan	nan	nan	nan
C_3N(3-2,5/2-3/2)	29.70	35	-27.70	17.606	2.018	1.695	1.5	0.367	0.175	21.985	4.351	1.695	4.06	0.16	0.158
C_3N(3-2,5/2-3/2)	29.70	36	-26.44	16.807	1.838	2.399	1.865	0.201	0.134	nan	nan	nan	nan	nan	nan
C_3N(3-2,5/2-3/2)	29.70	37	-25.18	19.156	1.573	2.726	1.738	0.244	0.12	nan	nan	nan	nan	nan	nan
C_3N(3-2,5/2-3/2)	29.70	38	-23.91	15.463	1.539	1.893	2.002	0.239	0.139	20.889	1.047	1.448	1.087	0.313	0.145
C_3N(3-2,5/2-3/2)	29.70	39	-22.65	19.414	3.89	6.283	3.023	0.218	0.081	nan	nan	nan	nan	nan	nan
C_3N(3-2,5/2-3/2)	29.70	40	-21.39	18.971	1.63	2.448	2.104	0.245	0.13	nan	nan	nan	nan	nan	nan
C_3N(3-2,5/2-3/2)	29.70	41	-20.13	16.773	5.006	1.913	5.776	0.122	0.198	22.781	4.055	1.913	4.257	0.152	0.19
C_3N(3-2,5/2-3/2)	29.70	42	-18.87	18.875	6.438	2.196	3.354	0.386	0.638	23.752	23.755	2.196	21.557	0.093	0.477
C_3N(3-2,7/2-5/2)	29.68	32	-32.53	16.898	1.353	1.861	1.632	0.345	0.182	23.623	7.894	1.861	7.378	0.092	0.175
C_3N(3-2,7/2-5/2)	29.68	33	-31.27	14.313	26.103	4.534	14.106	0.218	0.34	20.064	1.763	1.143	2.233	0.236	0.38
C_3N(3-2,7/2-5/2)	29.68	34	-30.00	18.835	1.597	1.859	1.641	0.226	0.168	nan	nan	nan	nan	nan	nan
C_3N(3-2,7/2-5/2)	29.68	35	-28.74	16.889	15.069	2.117	8.923	0.206	0.785	21.577	17.113	2.117	13.592	0.17	0.676

Table C.4 continued.

Transition	Restfreq	Ch	v_{ch}	R_{max} 1	ΔR_{max} 1	$W_{1/2}$ 1	$\Delta W_{1/2}$ 1	F_{max} 1	ΔF_{max} 1	R_{max} 2	ΔR_{max} 2	$W_{1/2}$ 2	$\Delta W_{1/2}$ 2	F_{max} 2	ΔF_{max} 2
C_3N(3-2,7/2-5/2)	29.68	36	-27.48	15.013	5.332	2.648	4.698	0.287	0.218	22.01	14.45	2.648	15.58	0.098	0.2
C_3N(3-2,7/2-5/2)	29.68	37	-26.21	18.588	1.714	1.964	2.068	0.378	0.212	22.443	2.026	0.794	2.153	0.167	0.376
C_3N(3-2,7/2-5/2)	29.68	38	-24.95	15.273	6.414	2.21	5.074	0.254	0.302	20.802	6.511	2.21	5.062	0.25	0.299
C_3N(3-2,7/2-5/2)	29.68	39	-23.69	0	0	0	0	0	0	nan	nan	nan	nan	nan	nan
C_3N(3-2,7/2-5/2)	29.68	40	-22.43	16.744	0.834	1.287	0.988	0.385	0.195	21.284	1.23	1.287	1.336	0.257	0.184
C_3N(3-2,7/2-5/2)	29.68	41	-21.16	18.599	1.518	2.438	1.61	0.343	0.184	nan	nan	nan	nan	nan	nan
C_3N(3-2,7/2-5/2)	29.68	42	-19.90	16.018	31.25	3.795	22.266	0.157	0.382	20.156	2.421	1.532	6.648	0.218	1.473
C_3N(3-2,7/2-5/2)	29.68	43	-18.64	19.245	1.96	3.042	3.663	0.381	0.791	19.357	2.54	1.016	4.379	0.167	0.771
C_4H(2-1,5/2-3/2)	19.02	37	-31.76	0	0	0	0	0	0	nan	nan	nan	nan	nan	nan
C_4H(2-1,5/2-3/2)	19.02	38	-29.79	0	0	0	0	0	0	nan	nan	nan	nan	nan	nan
C_4H(2-1,5/2-3/2)	19.02	39	-27.82	0	0	0	0	0	0	nan	nan	nan	nan	nan	nan
C_4H(2-1,5/2-3/2)	19.02	40	-25.85	16.839	4.635	5.784	4.57	0.077	0.053	nan	nan	nan	nan	nan	nan
C_4H(2-1,5/2-3/2)	19.02	41	-23.88	8.905	1.582	2.048	1.665	0.12	0.079	20.512	1.183	1.247	1.153	0.104	0.083
C_4H(2-1,5/2-3/2)	19.02	42	-21.91	15.565	1.174	3.445	1.324	0.206	0.059	24.149	2.529	1.311	2.56	0.055	0.087
C_4H(2-1,5/2-3/2)	19.02	43	-19.93	18.129	3.257	2.361	3.384	0.133	0.076	24.484	5.515	2.361	4.336	0.083	0.079
C_4H(3-2,5/2-3/2)	28.57	27	-32.77	-42.016	2256.151	54.322	1033.123	0.187	4.166	nan	nan	nan	nan	nan	nan
C_4H(3-2,5/2-3/2)	28.57	28	-31.46	7.728	4.256	3.217	4.804	0.176	0.15	21.674	7.078	3.217	7.93	0.072	0.155
C_4H(3-2,5/2-3/2)	28.57	29	-30.15	17.296	38.324	11.562	33.443	0.079	0.113	nan	nan	nan	nan	nan	nan
C_4H(3-2,5/2-3/2)	28.57	30	-28.84	12.544	5.756	6.834	5.453	0.171	0.11	nan	nan	nan	nan	nan	nan
C_4H(3-2,5/2-3/2)	28.57	31	-27.53	13.725	20.111	2.889	29.652	0.059	0.215	22.79	43.838	2.889	53.988	0.024	0.164
C_4H(3-2,5/2-3/2)	28.57	32	-26.21	7.567	3.206	2.43	4.074	0.183	0.169	21.905	80.463	2.43	27.074	0.082	2.508
C_4H(3-2,5/2-3/2)	28.57	33	-24.90	9.639	16.065	3.257	31.399	0.053	0.368	22.468	26.097	3.196	21.469	0.031	0.157
C_4H(3-2,5/2-3/2)	28.57	34	-23.59	-5.951	162.031	16.493	72.78	0.164	0.835	nan	nan	nan	nan	nan	nan
C_4H(3-2,5/2-3/2)	28.57	35	-22.28	0	0	0	0	0	0	nan	nan	nan	nan	nan	nan
C_4H(3-2,5/2-3/2)	28.57	36	-20.97	16.593	30.781	3.687	41.314	0.076	0.233	25.518	49.955	3.687	29.153	0.059	0.37
C_4H(3-2,5/2-3/2)	28.57	37	-19.66	5.305	42.771	14.842	31.836	0.17	0.14	nan	nan	nan	nan	nan	nan
C_4H(3-2,7/2-5/2)	28.53	39	-32.74	18.564	7.346	9.002	8.172	0.131	0.086	nan	nan	nan	nan	nan	nan
C_4H(3-2,7/2-5/2)	28.53	40	-31.43	0	0	0	0	0	0	nan	nan	nan	nan	nan	nan
C_4H(3-2,7/2-5/2)	28.53	41	-30.11	3.938	8.407	3.536	5.392	0.288	0.298	nan	nan	nan	nan	nan	nan
C_4H(3-2,7/2-5/2)	28.53	42	-28.80	0	0	0	0	0	0	nan	nan	nan	nan	nan	nan
C_4H(3-2,7/2-5/2)	28.53	43	-27.49	24.419	69.544	18.805	287.509	0.055	0.078	nan	nan	nan	nan	nan	nan
C_4H(3-2,7/2-5/2)	28.53	44	-26.17	0.301	12.294	2.705	6.905	0.319	0.544	nan	nan	nan	nan	nan	nan
C_4H(3-2,7/2-5/2)	28.53	45	-24.86	0	0	0	0	0	0	nan	nan	nan	nan	nan	nan
C_4H(3-2,7/2-5/2)	28.53	46	-23.55	19.117	1.673	1.936	1.701	0.172	0.129	nan	nan	nan	nan	nan	nan
C_4H(3-2,7/2-5/2)	28.53	47	-22.23	16.8	5.412	4.308	5.7	0.142	0.122	nan	nan	nan	nan	nan	nan
C_4H(3-2,7/2-5/2)	28.53	48	-20.92	21.228	2.331	2.295	2.348	0.169	0.148	nan	nan	nan	nan	nan	nan
C_4H(3-2,7/2-5/2)	28.53	49	-19.61	0	0	0	0	0	0	nan	nan	nan	nan	nan	nan
C_6H(15/2-13/2,3/2,e)	20.79	100	-19.84	15.493	5.828	6.696	4.246	0.106	0.084	nan	nan	nan	nan	nan	nan
C_6H(15/2-13/2,3/2,e)	20.79	93	-32.46	0	0	0	0	0	0	nan	nan	nan	nan	nan	nan
C_6H(15/2-13/2,3/2,e)	20.79	94	-30.65	12.569	1.242	3.094	1.454	0.203	0.066	19.306	0.764	0.728	3.666	0.125	0.54
C_6H(15/2-13/2,3/2,e)	20.79	95	-28.85	23.585	35.221	7.664	36.35	0.018	0.066	nan	nan	nan	nan	nan	nan
C_6H(15/2-13/2,3/2,e)	20.79	96	-27.05	17.602	1.275	2.476	1.35	0.156	0.069	nan	nan	nan	nan	nan	nan

Table C.4 continued.

Transition	Restfreq	Ch	v_{ch}	R_{max} 1	ΔR_{max} 1	$W_{1/2}$ 1	$\Delta W_{1/2}$ 1	F_{max} 1	ΔF_{max} 1	R_{max} 2	ΔR_{max} 2	$W_{1/2}$ 2	$\Delta W_{1/2}$ 2	F_{max} 2	ΔF_{max} 2
C_6H(15/2-13/2,3/2,e)	20.79	97	-25.25	17.717	4.595	6.102	6.582	0.087	0.049	nan	nan	nan	nan	nan	nan
C_6H(15/2-13/2,3/2,e)	20.79	98	-23.45	12.911	18.738	3.712	18.447	0.059	0.101	22.429	16.412	3.712	11.136	0.056	0.106
C_6H(15/2-13/2,3/2,e)	20.79	99	-21.64	8.841	5.176	3.64	6.065	0.074	0.087	23.934	11.415	3.64	14.191	0.04	0.077
C_6H(15/2-13/2,3/2,f)	20.79	80	-33.39	11.924	2.643	2.054	2.893	0.134	0.098	19.084	34.431	2.054	33.959	0.037	0.12
C_6H(15/2-13/2,3/2,f)	20.79	81	-31.59	4.896	100.019	20.082	86.775	0.067	0.08	nan	nan	nan	nan	nan	nan
C_6H(15/2-13/2,3/2,f)	20.79	82	-29.78	14.438	2.968	1.928	3.243	0.099	0.099	19.113	2.428	1.168	2.474	0.087	0.126
C_6H(15/2-13/2,3/2,f)	20.79	83	-27.98	3.021	1.372	2.323	1.316	0.349	0.132	nan	nan	nan	nan	nan	nan
C_6H(15/2-13/2,3/2,f)	20.79	84	-26.18	0	0	0	0	0	0	nan	nan	nan	nan	nan	nan
C_6H(15/2-13/2,3/2,f)	20.79	85	-24.38	6.395	3.982	4.196	5.074	0.146	0.076	22.014	14.271	4.196	11.712	0.074	0.099
C_6H(15/2-13/2,3/2,f)	20.79	86	-22.58	5.495	41.777	12.841	30.025	0.081	0.081	nan	nan	nan	nan	nan	nan
C_6H(15/2-13/2,3/2,f)	20.79	87	-20.77	9.109	4.158	5.383	5.07	0.134	0.072	26.998	3.519	1.372	3.78	0.05	0.111
C_6H(15/2-13/2,3/2,f)	20.79	88	-18.97	0.624	88.671	17.509	64.903	0.087	0.132	nan	nan	nan	nan	nan	nan
C_6H(17/2-15/2,1/2,e)	23.75	46	-32.11	12.755	9.823	4.136	9.377	0.083	0.085	24.463	25.898	4.136	27.065	0.037	0.235
C_6H(17/2-15/2,1/2,e)	23.75	47	-30.54	10.09	2.336	2.793	2.601	0.122	0.086	22.981	6.866	2.793	7.618	0.041	0.074
C_6H(17/2-15/2,1/2,e)	23.75	48	-28.96	-0.572	11.26	4.319	5.668	0.46	0.522	nan	nan	nan	nan	nan	nan
C_6H(17/2-15/2,1/2,e)	23.75	49	-27.38	10.035	116.338	25.786	142.601	0.05	0.049	nan	nan	nan	nan	nan	nan
C_6H(17/2-15/2,1/2,e)	23.75	50	-25.80	9.962	20.856	9.701	25.498	0.053	0.063	27.697	1.343	1.174	1.609	0.097	0.106
C_6H(17/2-15/2,1/2,e)	23.75	51	-24.22	20.056	2.229	1.09	2.355	0.058	0.104	nan	nan	nan	nan	nan	nan
C_6H(17/2-15/2,1/2,e)	23.75	52	-22.65	0	0	0	0	0	0	nan	nan	nan	nan	nan	nan
C_6H(17/2-15/2,1/2,e)	23.75	53	-21.07	5	6.203	3.304	4.552	0.184	0.109	22.906	3.068	1.766	3.032	0.081	0.211
C_6H(17/2-15/2,1/2,e)	23.75	54	-19.49	5	59.44	9.304	72.587	0.046	0.076	19.807	1.916	1.811	3.401	0.115	0.173
C_6H(17/2-15/2,3/2,e)	23.57	70	-32.46	9.583	23.763	5.381	35.084	0.067	0.124	22.939	33.657	5.381	22.852	0.064	0.183
C_6H(17/2-15/2,3/2,e)	23.57	71	-30.87	7.265	41.704	13.211	32.268	0.078	0.101	nan	nan	nan	nan	nan	nan
C_6H(17/2-15/2,3/2,e)	23.57	72	-29.28	5.618	3.73	3.577	3.576	0.147	0.089	23.629	3.639	3.577	5.501	0.079	0.161
C_6H(17/2-15/2,3/2,e)	23.57	73	-27.69	11.837	1.014	1.706	1.091	0.229	0.12	23.033	1.581	1.706	1.663	0.129	0.102
C_6H(17/2-15/2,3/2,e)	23.57	74	-26.10	6.856	2.195	4.572	2.76	0.259	0.086	24.147	8.002	4.572	10.633	0.05	0.118
C_6H(17/2-15/2,3/2,e)	23.57	75	-24.51	4.66	236.26	33.479	326.757	0.078	0.106	nan	nan	nan	nan	nan	nan
C_6H(17/2-15/2,3/2,e)	23.57	76	-22.92	14.905	10.792	4.737	14.273	0.066	0.085	nan	nan	nan	nan	nan	nan
C_6H(17/2-15/2,3/2,e)	23.57	77	-21.33	17.357	7.845	2.535	6.27	0.121	0.152	23.992	58.457	2.535	51.457	0.018	0.201
C_6H(17/2-15/2,3/2,e)	23.57	78	-19.74	12.809	3.859	3.741	5.164	0.138	0.113	22.081	42.17	1.411	50.813	0.027	3.059
C_6H(17/2-15/2,3/2,f)	23.57	54	-32.20	5.932	0.978	1.805	0.969	0.277	0.123	22.54	7.588	1.805	8.619	0.035	0.1
C_6H(17/2-15/2,3/2,f)	23.57	55	-30.61	17.741	1.911	1.281	1.961	0.124	0.108	21.429	2.342	1.16	2.149	0.097	0.108
C_6H(17/2-15/2,3/2,f)	23.57	56	-29.02	13.101	5.047	2.331	5.266	0.061	0.079	20.262	4.277	2.331	4.13	0.07	0.072
C_6H(17/2-15/2,3/2,f)	23.57	57	-27.43	3.025	1.883	2.006	2.461	0.22	0.153	nan	nan	nan	nan	nan	nan
C_6H(17/2-15/2,3/2,f)	23.57	58	-25.84	5.335	4.408	3.041	5.962	0.104	0.086	23.017	60.56	3.041	38.414	0.019	0.119
C_6H(17/2-15/2,3/2,f)	23.57	59	-24.25	14.696	5.591	1.884	3.98	0.123	0.151	19.323	6.256	1.884	5.179	0.105	0.138
C_6H(17/2-15/2,3/2,f)	23.57	60	-22.66	0	0	0	0	0	0	nan	nan	nan	nan	nan	nan
C_6H(17/2-15/2,3/2,f)	23.57	61	-21.07	0	0	0	0	0	0	nan	nan	nan	nan	nan	nan
C_6H(17/2-15/2,3/2,f)	23.57	62	-19.48	12.238	8.395	2.661	13.077	0.047	0.095	20.665	3.126	2.661	3.782	0.125	0.082
C_6H(19/2-17/2,3/2,e)	26.34	73	-32.47	9.019	21.656	10.225	15.044	0.081	0.063	19.91	2.869	-1.483	3.321	0.062	0.11
C_6H(19/2-17/2,3/2,e)	26.34	74	-31.04	19.045	3.81	5.121	4.232	0.099	0.063	nan	nan	nan	nan	nan	nan
C_6H(19/2-17/2,3/2,e)	26.34	75	-29.62	14.759	1.047	2.755	1.225	0.209	0.067	22.581	nan	0.492	nan	0.032	nan

Table C.4 continued.

Transition	Restfreq	Ch	v_{ch}	R_{max} 1	ΔR_{max} 1	$W_{1/2}$ 1	$\Delta W_{1/2}$ 1	F_{max} 1	ΔF_{max} 1	R_{max} 2	ΔR_{max} 2	$W_{1/2}$ 2	$\Delta W_{1/2}$ 2	F_{max} 2	ΔF_{max} 2
C_6H(19/2-17/2,3/2,e)	26.34	76	-28.20	15.052	2.548	1.475	2.841	0.081	0.114	23.273	2.67	1.475	2.685	0.065	0.102
C_6H(19/2-17/2,3/2,e)	26.34	77	-26.78	17.371	2.512	1.905	2.74	0.102	0.107	23.793	7.174	0.867	6.148	0.022	0.138
C_6H(19/2-17/2,3/2,e)	26.34	78	-25.35	20.596	1.181	1.601	1.224	0.168	0.107	nan	nan	nan	nan	nan	nan
C_6H(19/2-17/2,3/2,e)	26.34	79	-23.93	17.236	10.8	4.283	12.426	0.038	0.075	nan	nan	nan	nan	nan	nan
C_6H(19/2-17/2,3/2,e)	26.34	80	-22.51	0	0	0	0	0	0	nan	nan	nan	nan	nan	nan
C_6H(19/2-17/2,3/2,e)	26.34	81	-21.08	10.762	3.7	3.766	6.762	0.142	0.075	21.518	4.695	3.507	3.672	0.126	0.069
C_6H(19/2-17/2,3/2,e)	26.34	82	-19.66	15.299	1.664	2.801	1.681	0.179	0.091	nan	nan	nan	nan	nan	nan
C_6H(19/2-17/2,3/2,f)	26.34	53	-32.23	7.736	2.9	2.443	3.668	0.11	0.109	22.678	4.258	2.443	4.84	0.055	0.083
C_6H(19/2-17/2,3/2,f)	26.34	54	-30.81	5.302	4.058	0.585	2.965	0.076	0.313	nan	nan	nan	nan	nan	nan
C_6H(19/2-17/2,3/2,f)	26.34	55	-29.39	16.078	1.089	2.379	1.135	0.226	0.089	24.048	2.281	1.271	2.48	0.075	0.115
C_6H(19/2-17/2,3/2,f)	26.34	56	-27.97	18.344	1.817	3.673	1.989	0.146	0.062	nan	nan	nan	nan	nan	nan
C_6H(19/2-17/2,3/2,f)	26.34	57	-26.54	16.348	8.733	8.978	9.663	0.077	0.064	19.249	1.081	1.061	1.22	0.128	0.12
C_6H(19/2-17/2,3/2,f)	26.34	58	-25.12	16.039	2.302	3.604	2.371	0.141	0.077	nan	nan	nan	nan	nan	nan
C_6H(19/2-17/2,3/2,f)	26.34	59	-23.70	7.043	1.707	3.627	1.878	0.21	0.077	18.911	5.775	1.767	6.17	0.031	0.086
C_6H(19/2-17/2,3/2,f)	26.34	60	-22.28	17.742	2.539	3.278	3.309	0.118	0.071	26.04	2.907	0.681	2.128	0.052	0.125
C_6H(19/2-17/2,3/2,f)	26.34	61	-20.85	18.194	1.206	2.252	1.232	0.183	0.085	nan	nan	nan	nan	nan	nan
C_6H(19/2-17/2,3/2,f)	26.34	62	-19.43	18.87	3.645	5.565	4.372	0.129	0.069	nan	nan	nan	nan	nan	nan

Table C.5: List of Gaussian fit results from the radial emission profiles of each transition (restfrequency in GHz) of each channel (velocity in km s^{-1}) with $\Delta v < 7.5$ km s^{-1} for quarter Q4. The fit parameters are shell radius at maximum flux R_{max} (in arcsec), half shell width $W_{1/2}$ (in arcsec), and maximum flux F_{max} (in mJy $beam^{-1}$) for two components and their uncertainties determined from the least square fit routine.

Transition	Restfreq	Ch	v_{ch}	R_{max} 1	ΔR_{max} 1	$W_{1/2}$ 1	$\Delta W_{1/2}$ 1	F_{max} 1	ΔF_{max} 1	R_{max} 2	ΔR_{max} 2	$W_{1/2}$ 2	$\Delta W_{1/2}$ 2	F_{max} 2	ΔF_{max} 2
HC_3N(2-1)	18.20	79	-33.40	12.687	4.645	3.927	3.193	1.872	0.945	22.198	20.257	3.927	14.409	0.425	0.924
HC_3N(2-1)	18.20	80	-31.34	13.802	6.26	3.617	3.747	1.641	1.254	21.265	19.342	3.24	10.7	0.456	1.729
HC_3N(2-1)	18.20	81	-29.28	14.203	1.593	4.542	1.805	1.429	0.399	25.013	8.645	1.918	8.904	0.165	0.595
HC_3N(2-1)	18.20	82	-27.22	14.359	1.637	4.705	1.89	1.349	0.378	26.998	11.157	2.576	11.263	0.146	0.482
HC_3N(2-1)	18.20	83	-25.16	13.757	1.896	3.95	2.031	1.469	0.417	22.397	5.627	2.106	5.373	0.322	0.634
HC_3N(2-1)	18.20	84	-23.10	14.899	2.332	3.926	2.323	1.449	0.415	22.806	13.464	2.085	12.636	0.146	0.763
HC_3N(2-1)	18.20	85	-21.04	10.951	3.697	9.434	4.365	1.235	0.338	nan	nan	nan	nan	nan	nan
HC_3N(2-1)	18.20	86	-18.99	12.617	2.814	7.535	2.901	1.668	0.439	21.49	9.849	-1.028	9.039	0.149	1.165
HC_3N(3-2)	27.29	85	-32.30	13.472	0.842	2.711	0.917	4.846	1.287	22.636	nan	0.864	nan	0	nan
HC_3N(3-2)	27.29	86	-30.93	13.649	0.866	2.611	0.895	3.438	0.989	nan	nan	nan	nan	nan	nan
HC_3N(3-2)	27.29	87	-29.55	13.96	0.819	2.325	0.832	3.236	0.987	nan	nan	nan	nan	nan	nan
HC_3N(3-2)	27.29	88	-28.18	13.805	0.904	2.45	0.964	2.651	0.847	nan	nan	nan	nan	nan	nan
HC_3N(3-2)	27.29	89	-26.81	13.98	0.89	2.327	0.945	2.842	0.939	nan	nan	nan	nan	nan	nan
HC_3N(3-2)	27.29	90	-25.44	13.959	0.832	2.306	0.834	2.713	0.847	nan	nan	nan	nan	nan	nan
HC_3N(3-2)	27.29	91	-24.06	13.672	0.874	2.427	0.917	2.67	0.831	nan	nan	nan	nan	nan	nan
HC_3N(3-2)	27.29	92	-22.69	13.257	0.906	2.563	0.909	2.746	0.839	nan	nan	nan	nan	nan	nan
HC_3N(3-2)	27.29	93	-21.32	13.553	0.931	2.551	0.943	3.249	1.027	nan	nan	nan	nan	nan	nan
HC_3N(3-2)	27.29	94	-19.94	13.624	0.908	2.863	0.911	3.751	1.029	nan	nan	nan	nan	nan	nan
HC_3N(3-2)	27.29	95	-18.57	14.116	2.153	2.599	1.774	4.839	1.542	22.182	44.621	2.599	46.192	0.711	2.993
HC_3N(4-3)	36.39	31	-32.65	14.17	0.854	2.919	0.951	6.303	1.342	21.454	9.672	1.573	11.475	0.404	1.83
HC_3N(4-3)	36.39	32	-31.62	14.338	0.687	2.885	0.688	5.887	1.212	nan	nan	nan	nan	nan	nan
HC_3N(4-3)	36.39	33	-30.59	14.206	0.682	2.723	0.709	5.252	1.137	21.073	12.97	0.577	11.357	0.131	2.31
HC_3N(4-3)	36.39	34	-29.56	14.257	0.777	2.852	0.782	4.591	1.083	nan	nan	nan	nan	nan	nan
HC_3N(4-3)	36.39	35	-28.53	14.132	0.667	2.879	0.669	4.519	0.905	nan	nan	nan	nan	nan	nan
HC_3N(4-3)	36.39	36	-27.50	14.306	0.662	2.671	0.666	4.253	0.912	nan	nan	nan	nan	nan	nan
HC_3N(4-3)	36.39	37	-26.47	14.004	0.742	2.66	0.745	4.253	1.026	nan	nan	nan	nan	nan	nan
HC_3N(4-3)	36.39	38	-25.44	14.008	0.679	2.504	0.68	4.599	1.08	nan	nan	nan	nan	nan	nan
HC_3N(4-3)	36.39	39	-24.41	14.188	0.71	2.542	0.711	4.535	1.097	nan	nan	nan	nan	nan	nan
HC_3N(4-3)	36.39	40	-23.38	14.205	0.735	2.666	0.789	4.688	1.105	20.714	2.359	0.745	2.499	0.762	2.067
HC_3N(4-3)	36.39	41	-22.35	14.152	0.658	2.426	0.707	5.197	1.202	20.561	2.385	0.906	2.458	0.875	1.926
HC_3N(4-3)	36.39	42	-21.32	14.283	0.748	2.858	0.75	4.902	1.11	nan	nan	nan	nan	nan	nan
HC_3N(4-3)	36.39	43	-20.30	14.198	1.021	2.859	1.13	5.275	1.268	20.125	2.365	1.188	2.483	1.283	2.12
HC_3N(4-3)	36.39	44	-19.27	14.111	1.211	2.914	1.241	6.136	1.353	20.141	5.008	1.513	4.84	0.893	2.308
HC_5N(8-7)	21.30	61	-33.29	14.552	1.712	2.891	1.597	1.442	0.383	21.727	5.276	2.288	4.503	0.397	0.48
HC_5N(8-7)	21.30	62	-31.53	15.324	1.503	3.803	1.681	1.076	0.294	23.821	13.87	1.804	13.962	0.074	0.438
HC_5N(8-7)	21.30	63	-29.77	15.345	1.337	3.294	1.512	1.033	0.299	22.543	5.452	1.434	5.546	0.153	0.463
HC_5N(8-7)	21.30	64	-28.01	15.493	1.608	2.987	1.63	1.081	0.303	22.209	7.272	1.824	6.66	0.168	0.448
HC_5N(8-7)	21.30	65	-26.25	15.128	1.357	2.78	1.447	1.033	0.306	21.835	3.95	1.732	3.726	0.267	0.4

Table C.5 continued.

Transition	Restfreq	Ch	v_{ch}	R_{max} 1	ΔR_{max} 1	$W_{1/2}$ 1	$\Delta W_{1/2}$ 1	F_{max} 1_{max} 1	ΔF_{max} 1	R_{max} 2	ΔR_{max} 2	$W_{1/2}$ 2	$\Delta W_{1/2}$ 2	F_{max} 2	ΔF_{max} 2
HC_5N(8-7)	21.30	66	-24.49	15.096	1.574	3.263	1.687	1.004	0.289	22.055	3.211	1.642	3.145	0.305	0.457
HC_5N(8-7)	21.30	67	-22.73	14.703	1.768	2.826	1.73	1.046	0.316	21.41	2.966	1.988	2.556	0.49	0.428
HC_5N(8-7)	21.30	68	-20.98	14.938	1.663	3.546	1.817	1.058	0.308	21.802	3.367	1.412	3.622	0.265	0.56
HC_5N(8-7)	21.30	69	-19.22	15.581	3.501	3.621	2.835	1.226	0.372	21.051	3.804	1.598	5.137	0.324	1.237
HC_5N(9-8)	23.96	51	-31.95	14.826	1.059	2.569	1.156	1.261	nan	22.626	20.413	2.569	nan	0.163	nan
HC_5N(9-8)	23.96	52	-30.39	15.516	0.846	2.459	0.85	1.015	0.302	nan	nan	nan	nan	nan	nan
HC_5N(9-8)	23.96	53	-28.82	15.244	0.857	2.49	0.876	1.001	0.298	nan	nan	nan	nan	nan	nan
HC_5N(9-8)	23.96	54	-27.26	14.81	0.947	2.137	1.067	0.996	0.332	20.435	3.381	1.222	4.116	0.212	0.434
HC_5N(9-8)	23.96	55	-25.69	14.791	0.965	1.849	1.045	0.958	0.328	21.516	16.081	1.849	14.713	0.217	0.427
HC_5N(9-8)	23.96	56	-24.13	15.024	1.09	2.163	1.214	0.963	0.317	22.82	13.7	2.163	12.697	0.281	0.418
HC_5N(9-8)	23.96	57	-22.57	15.487	1.277	3.3	1.391	0.789	0.262	nan	nan	nan	nan	nan	nan
HC_5N(9-8)	23.96	58	-21.00	14.715	0.944	2.023	1.062	1.06	0.365	20.316	2.365	1.354	2.383	0.348	0.427
HC_5N(9-8)	23.96	59	-19.44	14.427	1.337	2.273	1.371	1.179	0.375	19.721	2.091	1.442	1.895	0.558	0.52
HC_5N(10-9)	26.63	38	-32.78	14.826	1.016	2.245	1.067	1.762	0.482	22.958	69.528	2.245	50.762	0.162	1.424
HC_5N(10-9)	26.63	39	-31.38	14.886	0.771	2.179	0.798	1.362	0.418	22.715	nan	0.669	-0	0	nan
HC_5N(10-9)	26.63	40	-29.97	15.514	0.982	2.232	0.994	1.129	0.431	nan	nan	nan	nan	nan	nan
HC_5N(10-9)	26.63	41	-28.56	14.398	0.816	2.202	0.873	1.264	0.403	nan	nan	nan	nan	nan	nan
HC_5N(10-9)	26.63	42	-27.16	14.842	0.954	2.016	0.976	0.981	0.403	nan	nan	nan	nan	nan	nan
HC_5N(10-9)	26.63	43	-25.75	14.814	0.852	1.863	0.86	1.044	0.414	nan	nan	nan	nan	nan	nan
HC_5N(10-9)	26.63	44	-24.34	14.955	1.365	2.129	1.375	1.149	0.402	22.367	34.11	2.129	27.574	0.232	0.978
HC_5N(10-9)	26.63	45	-22.93	14.587	0.909	1.701	0.918	0.97	0.45	nan	nan	nan	nan	nan	nan
HC_5N(10-9)	26.63	46	-21.53	14.531	1.018	2.075	1.15	1.159	0.468	19.785	5.21	0.921	5.251	0.151	0.67
HC_5N(10-9)	26.63	47	-20.12	14.813	7.641	2.781	4.945	1.168	1.39	22.237	58.304	2.781	84.325	0.255	1.888
HC_5N(10-9)	26.63	48	-18.71	14.18	1.854	1.877	1.61	1.51	0.653	19.354	3.037	1.877	2.659	0.915	0.644
HC_5N(11-10)	29.29	19	-32.39	13.508	0.804	2.444	0.816	1.418	0.403	nan	nan	nan	nan	nan	nan
HC_5N(11-10)	29.29	20	-31.11	14.201	0.958	2.637	0.994	1.053	0.33	nan	nan	nan	nan	nan	nan
HC_5N(11-10)	29.29	21	-29.83	14.073	0.878	2.62	0.953	1.125	0.325	nan	nan	nan	nan	nan	nan
HC_5N(11-10)	29.29	22	-28.55	14.335	0.743	2.218	0.783	1.161	0.336	nan	nan	nan	nan	nan	nan
HC_5N(11-10)	29.29	23	-27.27	14.386	0.84	2.315	0.863	0.984	0.31	22.251	nan	0.103	nan	0.798	nan
HC_5N(11-10)	29.29	24	-25.99	14.266	0.87	2.62	0.984	1.096	0.307	nan	nan	nan	nan	nan	nan
HC_5N(11-10)	29.29	25	-24.71	14.376	0.897	2.519	0.987	1.087	0.328	nan	nan	nan	nan	nan	nan
HC_5N(11-10)	29.29	26	-23.43	14.394	0.685	2.177	0.711	1.085	0.295	nan	nan	nan	nan	nan	nan
HC_5N(11-10)	29.29	27	-22.15	13.935	0.98	2.575	0.986	1.045	0.343	nan	nan	nan	nan	nan	nan
HC_5N(11-10)	29.29	28	-20.87	13.912	0.839	2.704	0.911	1.231	0.326	22.219	nan	0.328	nan	1.807	nan
HC_5N(11-10)	29.29	29	-19.60	14.369	0.607	2.287	0.617	1.503	0.344	nan	nan	nan	nan	nan	nan
HC_5N(12-11)	31.95	36	-32.38	14.31	2.396	2.404	1.612	2.977	1.08	19.247	8.51	1.961	5.179	0.648	1.885
HC_5N(12-11)	31.95	37	-31.21	14.954	0.724	3.128	0.742	2.306	0.462	nan	nan	nan	nan	nan	nan
HC_5N(12-11)	31.95	38	-30.04	14.825	0.816	3.021	0.891	1.894	0.437	23.28	nan	0.743	nan	0	nan
HC_5N(12-11)	31.95	39	-28.86	14.422	0.8	2.931	0.883	2.078	0.488	23.042	nan	0.777	nan	0	nan
HC_5N(12-11)	31.95	40	-27.69	15.07	0.684	2.798	0.704	2.011	0.426	nan	nan	nan	nan	nan	nan
HC_5N(12-11)	31.95	41	-26.52	14.901	0.639	2.61	0.642	2.046	0.433	nan	nan	nan	nan	nan	nan
HC_5N(12-11)	31.95	42	-25.34	14.944	0.718	2.691	0.73	1.828	0.421	nan	nan	nan	nan	nan	nan

Table C.5 continued.

Transition	Restfreq	Ch	v_{ch}	R_{max} 1	ΔR_{max} 1	$W_{1/2}$ 1	$\Delta W_{1/2}$ 1	F_{max} 1_{max} 1	ΔF_{max} 1	R_{max} 2	ΔR_{max} 2	$W_{1/2}$ 2	$\Delta W_{1/2}$ 2	F_{max} 2	ΔF_{max} 2
HC_5N(12-11)	31.95	43	-24.17	14.595	0.82	2.459	0.928	1.958	0.482	20.121	1.503	1.061	1.66	0.656	0.739
HC_5N(12-11)	31.95	44	-23.00	14.297	0.872	2.585	0.999	1.878	0.467	20.204	1.248	1.179	1.261	0.835	0.685
HC_5N(12-11)	31.95	45	-21.83	13.815	0.839	2.723	1.003	2.003	0.481	20.051	1.311	1.146	1.349	0.789	0.721
HC_5N(12-11)	31.95	46	-20.65	14.26	0.977	2.641	1.068	2.118	0.492	19.873	1.235	1.255	1.271	1.006	0.78
HC_5N(12-11)	31.95	47	-19.48	14.644	1.449	2.661	1.38	2.527	0.581	19.841	2.031	1.439	2.031	0.987	1.187
HC_5N(13-12)	34.61	31	-33.44	13.208	0.614	2.229	0.664	1.919	0.455	24.121	nan	0.97	nan	5.528	nan
HC_5N(13-12)	34.61	32	-32.35	13.923	0.578	1.876	0.611	1.583	0.422	nan	nan	nan	nan	nan	nan
HC_5N(13-12)	34.61	33	-31.27	13.397	0.759	2.431	0.82	1.414	0.38	nan	nan	nan	nan	nan	nan
HC_5N(13-12)	34.61	34	-30.19	13.898	0.734	2.297	0.783	1.162	0.32	nan	nan	nan	nan	nan	nan
HC_5N(13-12)	34.61	35	-29.11	14.74	2.491	3.217	2.168	1.522	0.357	23.315	nan	1.525	nan	0	nan
HC_5N(13-12)	34.61	36	-28.02	13.972	0.742	2.198	0.81	1.183	0.339	nan	nan	nan	nan	nan	nan
HC_5N(13-12)	34.61	37	-26.94	14.166	0.73	2.055	0.803	1.158	0.348	nan	nan	nan	nan	nan	nan
HC_5N(13-12)	34.61	38	-25.86	14.196	0.631	2.087	0.715	1.176	0.3	nan	nan	nan	nan	nan	nan
HC_5N(13-12)	34.61	39	-24.78	13.876	0.892	2.594	1.036	1.091	0.299	22.522	4.267	1.923	3.307	0.36	0.915
HC_5N(13-12)	34.61	40	-23.69	13.988	0.541	2.002	0.592	1.35	0.315	20.926	1.406	1.152	1.598	0.43	0.407
HC_5N(13-12)	34.61	41	-22.61	13.251	1.188	2.993	1.378	1.094	0.347	nan	nan	nan	nan	nan	nan
HC_5N(13-12)	34.61	42	-21.53	13.993	0.64	2.256	0.719	1.418	0.337	nan	nan	nan	nan	nan	nan
HC_5N(13-12)	34.61	43	-20.45	13.61	0.757	2.716	0.811	1.289	0.309	nan	nan	nan	nan	nan	nan
HC_5N(13-12)	34.61	44	-19.36	13.984	0.753	2.059	0.858	1.366	0.4	19.193	5.747	0.979	6.768	0.124	0.563
HC_5N(14-13)	37.28	40	-33.32	14.555	0.926	2.127	0.898	4.5	1.021	20.953	4.168	2.127	4.755	0.953	1.031
HC_5N(14-13)	37.28	41	-32.31	14.688	1.199	2.037	1.047	4.029	1.052	20.388	4.568	2.037	4.357	1.031	1.038
HC_5N(14-13)	37.28	42	-31.31	14.949	1.145	2.216	1.115	3.483	0.921	22.04	15.044	2.216	24.017	0.331	0.988
HC_5N(14-13)	37.28	43	-30.30	14.861	0.736	2.376	0.745	3.038	0.815	nan	nan	nan	nan	nan	nan
HC_5N(14-13)	37.28	44	-29.30	15.176	0.657	2.018	0.737	3.521	0.923	19.819	4.797	0.749	4.901	0.284	1.489
HC_5N(14-13)	37.28	45	-28.29	15.011	0.651	2.012	0.66	3.3	0.925	nan	nan	nan	nan	nan	nan
HC_5N(14-13)	37.28	46	-27.29	15.258	0.742	2.001	0.789	3.454	0.847	22.715	55.04	2.001	38.179	0.315	2.639
HC_5N(14-13)	37.28	47	-26.28	15.045	0.743	1.918	0.814	3.329	0.956	22.514	33.087	1.918	23.042	0.476	2.4
HC_5N(14-13)	37.28	48	-25.28	15.019	0.551	1.774	0.594	3.438	0.881	22.578	14.053	1.774	8.976	0.952	2.348
HC_5N(14-13)	37.28	49	-24.27	15.147	0.7	1.882	0.785	3.338	0.95	22.543	13.947	1.882	10.191	0.933	1.906
HC_5N(14-13)	37.28	50	-23.27	14.869	0.724	2.024	0.805	3.536	0.917	22.484	11.245	2.024	9.729	0.884	1.258
HC_5N(14-13)	37.28	51	-22.26	14.933	0.682	1.925	0.744	3.574	0.961	22.557	15.485	1.925	10.557	1.034	2.468
HC_5N(14-13)	37.28	52	-21.26	15.248	1.756	2.291	1.446	3.4	1.001	21.931	8.194	2.291	15.252	0.743	0.922
HC_5N(14-13)	37.28	53	-20.25	15.239	4.208	2.607	2.68	3.247	2.235	22.06	16.669	2.607	37.625	0.615	1.404
HC_5N(14-13)	37.28	54	-19.25	15.006	2.244	2.459	1.701	3.609	1.238	22	9.645	2.459	17.859	0.883	1.039
HC_7N(16-15)	18.05	48	-31.42	17.921	1.008	1.989	1.01	0.411	0.179	nan	nan	nan	nan	nan	nan
HC_7N(16-15)	18.05	49	-29.34	18.917	1.474	3.294	1.524	0.358	0.138	nan	nan	nan	nan	nan	nan
HC_7N(16-15)	18.05	50	-27.27	8.034	24.626	15.455	25.646	0.189	0.094	nan	nan	nan	nan	nan	nan
HC_7N(16-15)	18.05	51	-25.19	16.844	2.059	3.309	2.141	0.279	0.149	nan	nan	nan	nan	nan	nan
HC_7N(16-15)	18.05	52	-23.12	15.507	6.602	3.165	5.873	0.277	0.221	23.391	24.926	3.165	18.213	0.076	0.244
HC_7N(16-15)	18.05	53	-21.04	21.866	6.647	11.632	8.953	0.208	0.086	nan	nan	nan	nan	nan	nan
HC_7N(16-15)	18.05	54	-18.96	-6.317	137.976	20.993	71.624	0.286	0.823	nan	nan	nan	nan	nan	nan
HC_7N(17-16)	19.18	71	-32.17	17.372	2.248	3.183	2.417	0.267	0.109	22.963	5.91	0.876	11.746	0.044	0.313

Table C.5 continued.

Transition	Restfreq	Ch	v_{ch}	R_{max} 1	ΔR_{max} 1	$W_{1/2}$ 1	$\Delta W_{1/2}$ 1	F_{max} 1_{max} 1	ΔF_{max} 1	R_{max} 2	ΔR_{max} 2	$W_{1/2}$ 2	$\Delta W_{1/2}$ 2	F_{max} 2	ΔF_{max} 2
HC_7N(17-16)	19.18	72	-30.22	14.682	3.128	3.315	2.881	0.285	0.113	23.632	12.995	3.315	10.64	0.07	0.113
HC_7N(17-16)	19.18	73	-28.27	15.459	3.386	4.513	3.591	0.239	0.094	24.357	24.979	2.195	24.69	0.018	0.171
HC_7N(17-16)	19.18	74	-26.31	16.409	2.589	6.298	2.94	0.212	0.074	nan	nan	nan	nan	nan	nan
HC_7N(17-16)	19.18	75	-24.36	15.87	2.969	2.991	2.777	0.217	0.096	24.162	7.02	2.86	7.154	0.085	0.096
HC_7N(17-16)	19.18	76	-22.40	14.309	3.014	7.308	3.519	0.219	0.075	nan	nan	nan	nan	nan	nan
HC_7N(17-16)	19.18	77	-20.45	14.863	7.303	9.816	6.848	0.142	0.088	20.745	2.142	1.853	2.56	0.134	0.147
HC_7N(18-17)	20.30	71	-33.16	14.059	1.336	2.737	1.471	2.137	0.895	nan	nan	nan	nan	nan	nan
HC_7N(18-17)	20.30	72	-31.31	21.51	1.667	2.661	1.679	1.103	0.597	nan	nan	nan	nan	nan	nan
HC_7N(18-17)	20.30	73	-29.46	12.301	4.264	2.227	4.593	0.74	0.701	19.811	16.478	2.227	15.197	0.777	1.326
HC_7N(18-17)	20.30	74	-27.62	10.372	2.788	3.267	2.376	1.19	0.932	nan	nan	nan	nan	nan	nan
HC_7N(18-17)	20.30	75	-25.77	12.273	1.905	2.36	2.148	1.195	0.768	23.468	68.674	2.36	26.299	0.543	9.756
HC_7N(18-17)	20.30	76	-23.93	15.736	1.12	2.601	1.305	1.929	0.702	23.714	nan	0.942	nan	0	nan
HC_7N(18-17)	20.30	77	-22.08	11.887	2.356	1.352	2.522	0.574	0.841	21.635	1.097	1.223	1.176	0.998	0.786
HC_7N(18-17)	20.30	78	-20.24	8.548	1.154	1.838	1.178	1.728	0.94	nan	nan	nan	nan	nan	nan
HC_7N(19-18)	21.43	40	-32.60	16.01	1.354	2.611	1.526	0.352	0.134	22.488	4.337	1.445	4.208	0.079	0.17
HC_7N(19-18)	21.43	41	-30.85	15.975	2.373	2.42	2.109	0.344	0.141	22.476	9.156	2.42	7.341	0.09	0.141
HC_7N(19-18)	21.43	42	-29.10	16.218	3.318	2.34	3.006	0.28	0.141	21.831	6.567	2.048	4.723	0.13	0.199
HC_7N(19-18)	21.43	43	-27.35	14.988	1.995	2.199	1.927	0.341	0.147	21.238	3.21	2.199	2.816	0.215	0.143
HC_7N(19-18)	21.43	44	-25.61	16.435	3.418	5.666	4.268	0.163	0.082	nan	nan	nan	nan	nan	nan
HC_7N(19-18)	21.43	45	-23.86	15.586	2.914	2.264	2.407	0.284	0.15	21.507	7.63	2.264	5.86	0.109	0.151
HC_7N(19-18)	21.43	46	-22.11	16.575	4.222	3.987	6.014	0.185	0.119	25.568	5.307	2.31	5.186	0.107	0.169
HC_7N(19-18)	21.43	47	-20.36	8.545	73.425	7.704	75.996	0.112	0.221	18.537	3.483	3.67	11.03	0.224	1.419
HC_7N(19-18)	21.43	48	-18.61	14.418	4.678	2.354	3.723	0.236	0.19	20.459	5.132	2.354	3.889	0.215	0.19
HC_7N(20-19)	22.56	50	-33.38	15.135	3.128	2.539	2.625	0.337	0.177	21.935	4.799	2.539	3.893	0.219	0.174
HC_7N(20-19)	22.56	51	-31.72	15.612	5.973	2.69	3.878	0.336	0.346	21.747	18.651	2.69	11.223	0.108	0.364
HC_7N(20-19)	22.56	52	-30.06	15.892	7.707	2.481	4.118	0.328	0.576	21.15	42.53	2.481	24.154	0.059	0.558
HC_7N(20-19)	22.56	53	-28.40	15.67	1.397	2.433	1.668	0.371	nan	21.75	3.671	2.433	nan	0.183	nan
HC_7N(20-19)	22.56	54	-26.74	14.983	2.789	2.932	2.686	0.298	0.123	21.442	3.422	1.94	2.846	0.174	0.198
HC_7N(20-19)	22.56	55	-25.08	15.341	10.764	2.39	5.469	0.246	0.672	20.216	12.521	2.39	6.281	0.211	0.677
HC_7N(20-19)	22.56	56	-23.42	15.746	6.721	2.584	4.673	0.225	0.255	21.811	7.506	2.584	4.781	0.203	0.268
HC_7N(20-19)	22.56	57	-21.76	14.961	4.481	2.965	4.324	0.271	0.139	20.756	2.922	1.834	2.274	0.25	0.344
HC_7N(20-19)	22.56	58	-20.09	16.623	1.614	4.217	1.724	0.336	0.111	nan	nan	nan	nan	nan	nan
HC_7N(22-21)	24.82	49	-33.40	15.421	2.481	2.592	2.265	0.288	0.125	23.232	23.051	2.592	17.598	0.093	0.337
HC_7N(22-21)	24.82	50	-31.89	14.854	1.321	2.27	1.576	0.279	0.136	nan	nan	nan	nan	nan	nan
HC_7N(22-21)	24.82	51	-30.38	15.641	2.213	3.296	2.918	0.177	0.097	nan	nan	nan	nan	nan	nan
HC_7N(22-21)	24.82	52	-28.87	16.716	0.897	1.973	0.938	0.314	0.123	nan	nan	nan	nan	nan	nan
HC_7N(22-21)	24.82	53	-27.36	15.95	4.924	1.604	3.599	0.214	0.273	19.826	10.309	1.604	7.004	0.103	0.284
HC_7N(22-21)	24.82	54	-25.85	15.385	1.644	2.18	1.71	0.259	0.114	22.263	8.916	2.18	12.152	0.047	0.112
HC_7N(22-21)	24.82	55	-24.34	14.943	1.479	1.587	1.675	0.215	0.154	20.531	1.455	1.587	1.543	0.214	0.147
HC_7N(22-21)	24.82	56	-22.83	15.511	2.622	4.372	3.212	0.177	0.089	nan	nan	nan	nan	nan	nan
HC_7N(22-21)	24.82	57	-21.32	15.003	1.362	1.436	1.481	0.233	0.172	20.088	1.343	1.41	1.455	0.229	0.168
HC_7N(22-21)	24.82	58	-19.81	14.456	1.487	1.227	1.574	0.157	0.164	20.126	1.199	1.082	1.287	0.18	0.165

Table C.5 continued.

Transition	Restfreq	Ch	v_{ch}	R_{max} 1	ΔR_{max} 1	$W_{1/2}$ 1	$\Delta W_{1/2}$ 1	F_{max} 1_{max} 1	ΔF_{max} 1	R_{max} 2	ΔR_{max} 2	$W_{1/2}$ 2	$\Delta W_{1/2}$ 2	F_{max} 2	ΔF_{max} 2
HC_7N(23-22)	25.94	30	-33.10	15.865	5.836	2.629	3.601	0.428	0.476	21.639	22.776	2.629	12.645	0.11	0.507
HC_7N(23-22)	25.94	31	-31.65	16.29	1.729	2.659	2.058	0.264	0.138	nan	nan	nan	nan	nan	nan
HC_7N(23-22)	25.94	32	-30.21	16.012	1.247	2.469	1.302	0.342	0.149	nan	nan	nan	nan	nan	nan
HC_7N(23-22)	25.94	33	-28.77	15.626	1.733	2.11	1.951	0.261	0.161	20.864	1.619	1.104	1.578	0.198	0.213
HC_7N(23-22)	25.94	34	-27.32	15.898	11.801	2.222	5.315	0.294	1.101	20.144	39.986	2.222	18.675	0.086	1.084
HC_7N(23-22)	25.94	35	-25.88	15.312	0.976	2.287	0.981	0.384	0.141	nan	nan	nan	nan	nan	nan
HC_7N(23-22)	25.94	36	-24.43	15.603	2.858	1.764	2.487	0.247	0.169	20.382	3.107	1.764	2.583	0.227	0.168
HC_7N(23-22)	25.94	37	-22.99	15.033	2.113	2.244	2.151	0.297	0.139	20.025	2.453	1.391	2.153	0.179	0.211
HC_7N(23-22)	25.94	38	-21.54	17.058	2.132	4.089	2.58	0.28	0.121	nan	nan	nan	nan	nan	nan
HC_7N(23-22)	25.94	39	-20.10	14.888	3.571	1.944	2.843	0.368	0.27	19.666	7.052	1.944	4.834	0.191	0.292
HC_7N(23-22)	25.94	40	-18.66	14.84	8.301	2.266	5.276	0.233	0.395	20.067	5.918	2.266	3.701	0.326	0.4
HC_7N(24-23)	27.07	39	-32.74	15.095	4.266	1.671	2.727	0.46	0.468	18.591	6.621	1.449	3.948	0.245	0.698
HC_7N(24-23)	27.07	40	-31.35	16.026	2.417	2.077	3.054	0.215	0.207	21.843	1.376	0.886	1.589	0.22	0.297
HC_7N(24-23)	27.07	41	-29.97	15.38	1.6	1.396	1.781	0.273	0.274	nan	nan	nan	nan	nan	nan
HC_7N(24-23)	27.07	42	-28.58	13.975	10.591	3.451	8.908	0.175	0.172	nan	nan	nan	nan	nan	nan
HC_7N(24-23)	27.07	43	-27.20	15.352	1.944	1.346	2.184	0.196	0.239	nan	nan	nan	nan	nan	nan
HC_7N(24-23)	27.07	44	-25.81	14.92	1.266	1.42	1.368	0.288	0.222	22.429	2.817	1.42	3.186	0.132	0.215
HC_7N(24-23)	27.07	45	-24.43	15.204	0.999	1.543	1.082	0.377	0.213	nan	nan	nan	nan	nan	nan
HC_7N(24-23)	27.07	46	-23.05	14.234	1.936	2.076	2.255	0.285	0.212	20.832	1.072	0.773	1.964	0.292	0.44
HC_7N(24-23)	27.07	47	-21.66	15.227	0.894	1.577	0.914	0.443	0.219	nan	nan	nan	nan	nan	nan
HC_7N(24-23)	27.07	48	-20.28	15.359	1.969	2.573	2.637	0.365	0.211	20.917	4.812	1.071	5.109	0.088	0.323
HC_7N(24-23)	27.07	49	-18.89	14.389	8.992	10.538	13.417	0.249	0.111	nan	nan	nan	nan	nan	nan
HC_7N(25-24)	28.20	40	-32.20	15.947	2.052	4.414	2.651	0.245	0.095	nan	nan	nan	nan	nan	nan
HC_7N(25-24)	28.20	41	-30.87	15.834	10.498	1.653	4.943	0.299	1.153	19.604	31.65	1.653	64.004	0.06	0.648
HC_7N(25-24)	28.20	42	-29.54	16.723	2.661	1.896	2.657	0.185	0.149	22.529	9.813	1.896	9.697	0.049	0.145
HC_7N(25-24)	28.20	43	-28.21	16.091	2.517	1.855	2.017	0.336	0.187	20.996	6.227	1.855	5.245	0.133	0.182
HC_7N(25-24)	28.20	44	-26.89	16.215	1.407	3.598	1.606	0.283	0.095	nan	nan	nan	nan	nan	nan
HC_7N(25-24)	28.20	45	-25.56	15.666	1.773	2.187	2.005	0.281	0.159	20.607	2.871	1.05	3.169	0.111	0.232
HC_7N(25-24)	28.20	46	-24.23	15.804	2.177	1.875	2.148	0.266	0.155	20.874	2.396	1.623	2.13	0.222	0.167
HC_7N(25-24)	28.20	47	-22.90	16.374	3.916	2.216	4.671	0.161	0.152	20.898	1.895	1.145	1.803	0.2	0.269
HC_7N(25-24)	28.20	48	-21.57	16.248	1.971	1.427	2.142	0.178	0.186	21.245	2.061	1.427	2.186	0.168	0.18
HC_7N(25-24)	28.20	49	-20.24	15.534	7.149	2.969	7.027	0.237	0.157	21.203	9.86	1.935	7.839	0.102	0.492
HC_7N(25-24)	28.20	50	-18.91	17.571	1.753	3.803	1.988	0.305	0.118	nan	nan	nan	nan	nan	nan
HC_7N(26-25)	29.33	19	-32.42	15.595	1.226	1.741	1.269	0.323	0.198	nan	nan	nan	nan	nan	nan
HC_7N(26-25)	29.33	20	-31.14	14.177	1.067	1.994	1.067	0.366	0.168	23.394	5.277	0.879	5.116	0.046	0.23
HC_7N(26-25)	29.33	21	-29.87	13.504	2.504	3.731	3.054	0.236	0.121	nan	nan	nan	nan	nan	nan
HC_7N(26-25)	29.33	22	-28.59	16.8	1.448	1.863	1.624	0.237	0.154	nan	nan	nan	nan	nan	nan
HC_7N(26-25)	29.33	23	-27.31	-10.028	212.556	19.135	95.679	0.226	1.274	nan	nan	nan	nan	nan	nan
HC_7N(26-25)	29.33	24	-26.03	11.336	5.308	6.306	6.054	0.205	0.09	nan	nan	nan	nan	nan	nan
HC_7N(26-25)	29.33	25	-24.75	15.141	3.086	2.858	3.519	0.192	0.165	nan	nan	nan	nan	nan	nan
HC_7N(26-25)	29.33	26	-23.48	14.617	0.97	2.601	1.021	0.457	0.147	nan	nan	nan	nan	nan	nan
HC_7N(26-25)	29.33	27	-22.20	2.02	1.392	1.621	1.392	0.556	0.304	nan	nan	nan	nan	nan	nan

Table C.5 continued.

Transition	Restfreq	Ch	v_{ch}	R_{max} 1	ΔR_{max} 1	$W_{1/2}$ 1	$\Delta W_{1/2}$ 1	F_{max} 1_{max} 1	ΔF_{max} 1	R_{max} 2	ΔR_{max} 2	$W_{1/2}$ 2	$\Delta W_{1/2}$ 2	F_{max} 2	ΔF_{max} 2
HC_7N(26-25)	29.33	28	-20.92	14.237	1.205	2.445	1.237	0.368	0.156	nan	nan	nan	nan	nan	nan
HC_7N(26-25)	29.33	29	-19.64	14.142	1.443	2.438	1.44	0.382	0.194	nan	nan	nan	nan	nan	nan
HC_7N(27-26)	30.46	30	-32.39	15.315	1.99	2.335	2.563	0.265	0.186	22.001	2.971	1.375	3.029	0.132	0.217
HC_7N(27-26)	30.46	31	-31.16	16.733	1.435	2.247	1.44	0.47	0.26	nan	nan	nan	nan	nan	nan
HC_7N(27-26)	30.46	32	-29.93	16.703	2.561	2.912	4.159	0.393	0.255	22.323	2.898	0.778	3.177	0.138	0.471
HC_7N(27-26)	30.46	33	-28.70	16.865	1.905	3.362	2.089	0.398	0.195	nan	nan	nan	nan	nan	nan
HC_7N(27-26)	30.46	34	-27.47	16.304	8.165	2.19	5.37	0.38	0.609	21.95	16.713	2.19	41.253	0.122	0.373
HC_7N(27-26)	30.46	35	-26.24	17.36	2.406	3.075	2.735	0.24	0.162	nan	nan	nan	nan	nan	nan
HC_7N(27-26)	30.46	36	-25.01	15.764	1.566	2.008	1.72	0.427	0.233	21.71	2.49	1.623	2.5	0.241	0.245
HC_7N(27-26)	30.46	37	-23.78	15.959	1.883	1.214	2.03	0.242	0.256	19.948	1.883	1.214	1.962	0.241	0.248
HC_7N(27-26)	30.46	38	-22.55	16.366	3.876	2.801	3.642	0.284	0.194	20.255	1.684	0.783	2.207	0.197	0.499
HC_7N(27-26)	30.46	39	-21.32	14.694	3.818	2.532	4.235	0.342	0.25	20.81	3.655	1.837	3.151	0.296	0.329
HC_7N(27-26)	30.46	40	-20.09	17.756	1.163	2.939	1.213	0.545	0.187	nan	nan	nan	nan	nan	nan
HC_7N(27-26)	30.46	41	-18.86	17.805	1.77	3.565	1.841	0.513	0.22	nan	nan	nan	nan	nan	nan
HC_7N(28-27)	31.58	29	-32.46	15.437	3.411	2.082	2.346	0.848	0.593	20.459	8.674	2.082	6.311	0.329	0.573
HC_7N(28-27)	31.58	30	-31.27	15.878	5.804	2.345	4.123	0.691	0.78	21.255	18.293	2.345	11.995	0.222	0.818
HC_7N(28-27)	31.58	31	-30.08	15.109	4.261	1.842	2.515	0.805	0.942	19.204	8.473	1.842	5.242	0.402	0.917
HC_7N(28-27)	31.58	32	-28.90	15.938	1.728	3.475	1.929	0.551	0.226	nan	nan	nan	nan	nan	nan
HC_7N(28-27)	31.58	33	-27.71	15.947	1.55	2.237	1.685	0.64	0.269	21.165	2.223	1.309	2.218	0.317	0.368
HC_7N(28-27)	31.58	34	-26.53	15.154	6.297	1.859	4.082	0.457	0.721	19.401	8.648	1.859	5.326	0.334	0.743
HC_7N(28-27)	31.58	35	-25.34	15.145	3.923	2.056	2.912	0.595	0.456	20.378	7.741	2.056	6.948	0.287	0.416
HC_7N(28-27)	31.58	36	-24.15	15.954	3.278	2.17	2.71	0.578	0.31	20.691	5.457	1.594	4.385	0.256	0.533
HC_7N(28-27)	31.58	37	-22.97	15.436	2.008	1.839	1.872	0.49	0.26	20.731	3.041	1.839	2.82	0.321	0.255
HC_7N(28-27)	31.58	38	-21.78	15.381	2.975	1.838	2.551	0.672	0.385	19.794	3.843	1.601	3.028	0.462	0.52
HC_7N(28-27)	31.58	39	-20.59	15.742	5.099	1.999	3.198	0.606	0.718	20.372	7.925	1.999	5.225	0.386	0.696
HC_7N(28-27)	31.58	40	-19.41	16.283	1.424	3.728	1.515	0.713	0.235	nan	nan	nan	nan	nan	nan
HC_7N(29-28)	32.71	38	-32.46	14.45	2.278	1.576	2.747	0.242	0.253	24.545	16.907	1.576	13.705	0.104	3.184
HC_7N(29-28)	32.71	39	-31.31	14.45	2.278	1.576	2.747	0.242	0.253	24.545	16.907	1.576	13.705	0.104	3.184
HC_7N(29-28)	32.71	40	-30.17	15.054	2.421	1.605	2.62	0.193	0.251	22.017	3.734	1.071	3.957	0.097	0.291
HC_7N(29-28)	32.71	41	-29.02	13.229	29.723	2.903	25.533	0.104	0.26	nan	nan	nan	nan	nan	nan
HC_7N(29-28)	32.71	42	-27.88	0	0	0	0	0	0	nan	nan	nan	nan	nan	nan
HC_7N(29-28)	32.71	43	-26.73	15.209	1.27	1.901	1.417	0.418	0.21	24.19	5.27	1.901	7.797	0.109	0.833
HC_7N(29-28)	32.71	44	-25.59	14.38	4.866	2.88	4.552	0.162	0.177	25.316	7.376	2.88	10.243	0.086	0.431
HC_7N(29-28)	32.71	45	-24.44	13.488	2.734	2.023	2.729	0.223	0.191	22.593	5.195	2.023	6.721	0.095	0.428
HC_7N(29-28)	32.71	46	-23.29	14.893	2.677	2.408	4.205	0.36	0.257	22.911	13.439	2.408	13.345	0.096	0.251
HC_7N(29-28)	32.71	47	-22.15	12.867	5.578	6.403	4.514	0.363	0.258	nan	nan	nan	nan	nan	nan
HC_7N(29-28)	32.71	48	-21.00	17.322	6.584	3.363	6.135	0.172	0.357	nan	nan	nan	nan	nan	nan
HC_7N(30-29)	33.84	37	-33.00	14.948	1.467	2.756	1.874	0.413	0.16	20.704	2.834	1.113	3.067	0.12	0.256
HC_7N(30-29)	33.84	38	-31.89	15.68	1.544	1.883	1.76	0.294	0.166	20.292	1.408	1.083	1.377	0.236	0.215
HC_7N(30-29)	33.84	39	-30.78	15.674	2.681	2.547	2.626	0.267	0.147	23.656	54.607	2.547	46.022	0.03	0.221
HC_7N(30-29)	33.84	40	-29.68	15.947	1.521	2.335	1.708	0.312	0.164	nan	nan	nan	nan	nan	nan
HC_7N(30-29)	33.84	41	-28.57	15.102	1.525	2.034	1.632	0.257	0.164	nan	nan	nan	nan	nan	nan

Table C.5 continued.

Transition	Restfreq	Ch	v_{ch}	R_{max} 1	ΔR_{max} 1	$W_{1/2}$ 1	$\Delta W_{1/2}$ 1	F_{max} 1_{max} 1	ΔF_{max} 1	R_{max} 2	ΔR_{max} 2	$W_{1/2}$ 2	$\Delta W_{1/2}$ 2	F_{max} 2	ΔF_{max} 2
HC_7N(30-29)	33.84	42	-27.46	15.435	1.004	1.519	1.032	0.308	0.176	23.516	62.688	1.519	53.628	0.038	0.399
HC_7N(30-29)	33.84	43	-26.35	16.007	2.56	2.608	3.294	0.221	0.157	20.834	2.392	-0.783	2.858	0.104	0.301
HC_7N(30-29)	33.84	44	-25.25	15.4	2.096	2.306	2.442	0.259	0.194	20.582	2.803	0.765	2.979	0.108	0.326
HC_7N(30-29)	33.84	45	-24.14	15.988	14.26	2.881	8.656	0.186	0.438	22.769	60.52	2.881	31.038	0.062	0.333
HC_7N(30-29)	33.84	46	-23.03	14.483	2.147	2.249	2.206	0.183	0.15	nan	nan	nan	nan	nan	nan
HC_7N(30-29)	33.84	47	-21.92	15.56	1.555	2.38	1.626	0.292	0.164	nan	nan	nan	nan	nan	nan
HC_7N(30-29)	33.84	48	-20.82	15.809	6.316	2.459	5.312	0.228	0.193	20.048	3.108	1.281	3.054	0.197	0.555
HC_7N(30-29)	33.84	49	-19.71	15.093	5.959	1.927	4.033	0.347	0.374	19.016	6.888	1.522	5.151	0.214	0.665
HC_7N(30-29)	33.84	50	-18.60	14.9	5.132	3.012	4.801	0.354	0.215	23.25	89.943	3.012	56.443	0.044	0.654
HC_7N(31-30)	34.97	15	-33.32	14.517	0.78	1.549	0.85	0.633	0.277	nan	nan	nan	nan	nan	nan
HC_7N(31-30)	34.97	16	-32.25	14.257	1.163	2.267	1.437	0.537	0.204	nan	nan	nan	nan	nan	nan
HC_7N(31-30)	34.97	17	-31.18	15.93	8.276	2.235	6.439	0.194	0.23	24.298	68.844	2.235	23.788	0.377	7.966
HC_7N(31-30)	34.97	18	-30.10	14.557	1.996	2.59	2.559	0.328	0.175	24.328	2.878	2.59	2.943	0.224	0.254
HC_7N(31-30)	34.97	19	-29.03	13.414	2.766	3.905	3.792	0.32	0.143	26.496	1.475	0.586	1.27	0.148	0.282
HC_7N(31-30)	34.97	20	-27.96	16.705	1.949	2.256	1.978	0.279	0.209	nan	nan	nan	nan	nan	nan
HC_7N(31-30)	34.97	21	-26.89	15.116	2.027	2.47	2.161	0.401	0.205	23.366	5.388	2.47	5.085	0.205	0.468
HC_7N(31-30)	34.97	22	-25.82	13.893	1.317	2.48	1.602	0.493	0.211	23.15	1.506	1	1.529	0.227	0.295
HC_7N(31-30)	34.97	23	-24.75	14.176	0.957	1.872	1.064	0.471	0.206	20.786	0.653	1.043	0.667	0.473	0.256
HC_7N(31-30)	34.97	24	-23.68	14.614	1.267	2.296	1.372	0.361	0.138	22.499	2.695	2.296	2.757	0.205	0.247
HC_7N(31-30)	34.97	25	-22.60	15.526	1.508	2.446	1.726	0.444	0.186	23.573	2.485	2.446	2.931	0.259	0.177
HC_7N(31-30)	34.97	26	-21.53	14.383	0.763	1.549	0.877	0.541	0.225	nan	nan	nan	nan	nan	nan
HC_7N(31-30)	34.97	27	-20.46	14.085	0.873	2.399	0.964	0.613	0.192	25.492	7.315	2.399	4.026	0.254	1.088
HC_7N(31-30)	34.97	28	-19.39	13.455	1.884	2.756	2.76	0.417	0.179	22.696	8.078	2.756	8.068	0.166	0.552
HC_7N(32-31)	36.10	37	-32.74	14.403	1.409	1.823	1.577	0.405	0.268	22.541	33.016	1.823	21.037	0.118	0.636
HC_7N(32-31)	36.10	38	-31.71	15.705	2.976	3.11	3.797	0.236	0.184	nan	nan	nan	nan	nan	nan
HC_7N(32-31)	36.10	39	-30.67	16.458	1.705	2.715	2.208	0.385	0.201	nan	nan	nan	nan	nan	nan
HC_7N(32-31)	36.10	40	-29.63	15.252	2.43	2.669	2.735	0.289	0.224	nan	nan	nan	nan	nan	nan
HC_7N(32-31)	36.10	41	-28.59	17.279	2.63	2.799	2.871	0.231	0.187	nan	nan	nan	nan	nan	nan
HC_7N(32-31)	36.10	42	-27.55	16.605	1.692	2.485	1.71	0.357	0.21	nan	nan	nan	nan	nan	nan
HC_7N(32-31)	36.10	43	-26.51	15.253	8.461	1.806	5.047	0.297	0.712	19.201	22.345	1.806	12.429	0.113	0.742
HC_7N(32-31)	36.10	44	-25.48	14.331	1.925	2.315	2.488	0.447	0.273	20.746	2.914	1.621	2.911	0.252	0.299
HC_7N(32-31)	36.10	45	-24.44	14.497	3.615	2.165	3.85	0.358	0.283	20.174	5.707	1.811	5.273	0.206	0.321
HC_7N(32-31)	36.10	46	-23.40	15.924	3.356	1.881	3.046	0.304	0.244	21.216	7.973	1.881	7.561	0.125	0.239
HC_7N(32-31)	36.10	47	-22.36	14.752	1.568	3.351	1.657	0.429	0.172	nan	nan	nan	nan	nan	nan
HC_7N(32-31)	36.10	48	-21.32	15.655	4.94	2.192	4.606	0.272	0.256	20.529	4.037	1.501	3.269	0.245	0.412
HC_7N(32-31)	36.10	49	-20.29	14.742	4.616	2.394	4.318	0.258	0.212	22.413	49.245	2.394	50.4	0.075	0.374
HC_7N(32-31)	36.10	50	-19.25	16.687	1.343	2.912	1.411	0.533	0.213	nan	nan	nan	nan	nan	nan
HC_7N(33-32)	37.22	36	-33.06	14.32	1.597	4.39	1.67	0.546	0.168	26.889	2.642	1.138	2.656	0.147	0.291
HC_7N(33-32)	37.22	37	-32.06	13.848	1.81	2.656	1.855	0.419	0.246	nan	nan	nan	nan	nan	nan
HC_7N(33-32)	37.22	38	-31.05	11.13	4.527	4.122	4.45	0.368	0.204	15.623	5.1	-0.805	6.729	0.077	0.505
HC_7N(33-32)	37.22	39	-30.04	16.051	1.485	2.271	1.655	0.507	0.281	22.072	3.107	0.955	3.519	0.158	0.416
HC_7N(33-32)	37.22	40	-29.04	14.804	1.868	2.403	2.049	0.389	0.239	24.351	8.944	1.819	10.661	0.083	0.788

Table C.5 continued.

Transition	Restfreq	Ch	v_{ch}	R_{max} 1	ΔR_{max} 1	$W_{1/2}$ 1	$\Delta W_{1/2}$ 1	F_{max} 1_{max} 1	ΔF_{max} 1	R_{max} 2	ΔR_{max} 2	$W_{1/2}$ 2	$\Delta W_{1/2}$ 2	F_{max} 2	ΔF_{max} 2
HC_7N(33-32)	37.22	41	-28.03	15.056	1.58	1.036	1.587	0.291	0.385	nan	nan	nan	nan	nan	nan
HC_7N(33-32)	37.22	42	-27.02	15.98	3.537	3.946	3.693	0.358	0.175	20.403	1.431	0.494	2.883	0.175	0.578
HC_7N(33-32)	37.22	43	-26.02	14.881	2.135	2.723	2.563	0.438	0.282	20.944	5.601	0.909	6.208	0.09	0.468
HC_7N(33-32)	37.22	44	-25.01	15.109	1.703	2.17	1.877	0.531	0.314	23.007	6.744	2.17	9.21	0.137	0.318
HC_7N(33-32)	37.22	45	-24.00	14.081	1.788	3.196	1.988	0.427	0.204	21.832	2.863	-0.629	3.082	0.112	0.429
HC_7N(33-32)	37.22	46	-23.00	12.982	5.649	4.66	9.867	0.308	0.244	24.626	31.906	2.294	36.237	0.04	0.668
HC_7N(33-32)	37.22	47	-21.99	17.395	2.843	3.215	2.15	0.519	0.244	20.224	1.578	0.753	2.182	0.236	0.538
HC_7N(33-32)	37.22	48	-20.98	15.792	2.637	1.903	2.88	0.409	0.278	20.907	2.176	1.669	1.866	0.476	0.298
HC_7N(33-32)	37.22	49	-19.98	14.309	6.076	2.828	6.05	0.471	0.367	21.582	15.326	2.828	10.182	0.23	0.392
HC_7N(33-32)	37.22	50	-18.97	15.635	1.865	3.631	2.325	0.52	0.221	nan	nan	nan	nan	nan	nan
C_3N(2-1,3/2-1/2)	19.80	58	-32.64	23.314	3.632	4.57	3.98	0.086	0.049	nan	nan	nan	nan	nan	nan
C_3N(2-1,3/2-1/2)	19.80	59	-30.75	13.373	2.403	2.859	2.642	0.116	0.083	nan	nan	nan	nan	nan	nan
C_3N(2-1,3/2-1/2)	19.80	60	-28.86	17.306	7.703	5.121	7.282	0.062	0.089	nan	nan	nan	nan	nan	nan
C_3N(2-1,3/2-1/2)	19.80	61	-26.97	-3.555	49.075	9.984	20.916	0.191	0.489	nan	nan	nan	nan	nan	nan
C_3N(2-1,3/2-1/2)	19.80	62	-25.07	8.315	25.988	11.296	22.051	0.059	0.052	nan	nan	nan	nan	nan	nan
C_3N(2-1,3/2-1/2)	19.80	63	-23.18	0	0	0	0	0	0	nan	nan	nan	nan	nan	nan
C_3N(2-1,3/2-1/2)	19.80	64	-21.29	0	0	0	0	0	0	nan	nan	nan	nan	nan	nan
C_3N(2-1,3/2-1/2)	19.80	65	-19.40	13.167	4.855	3.613	4.335	0.163	0.086	24.053	16.23	3.613	16.727	0.075	0.455
C_3N(2-1,5/2-3/2)	19.78	49	-33.07	16.009	6.551	3.118	5.602	0.124	0.086	21.547	4.386	1.679	5.016	0.081	0.232
C_3N(2-1,5/2-3/2)	19.78	50	-31.18	10.524	2.338	2.777	2.507	0.115	0.081	23.359	2.423	2.777	2.699	0.095	0.071
C_3N(2-1,5/2-3/2)	19.78	51	-29.29	15.221	11.899	1.649	8.385	0.132	3.011	17.949	90.571	-2.295	35.808	0.065	1.669
C_3N(2-1,5/2-3/2)	19.78	52	-27.39	16.337	2.351	1.329	2.535	0.096	0.116	20.527	1.871	1.221	1.864	0.116	0.115
C_3N(2-1,5/2-3/2)	19.78	53	-25.50	-2.037	48.846	19.624	27.575	0.176	0.182	nan	nan	nan	nan	nan	nan
C_3N(2-1,5/2-3/2)	19.78	54	-23.60	21.647	6.474	8.904	7.972	0.098	0.059	nan	nan	nan	nan	nan	nan
C_3N(2-1,5/2-3/2)	19.78	55	-21.71	15.096	1.428	3.235	1.492	0.189	0.072	nan	nan	nan	nan	nan	nan
C_3N(2-1,5/2-3/2)	19.78	56	-19.81	11.842	8.041	3.738	6.922	0.149	0.1	19.607	4.948	2.719	3.636	0.17	0.217
C_3N(3-2,5/2-3/2)	29.70	31	-32.75	14.935	3.428	3.626	4.128	0.173	0.132	nan	nan	nan	nan	nan	nan
C_3N(3-2,5/2-3/2)	29.70	32	-31.49	17.019	2.789	3.019	2.983	0.174	0.138	nan	nan	nan	nan	nan	nan
C_3N(3-2,5/2-3/2)	29.70	33	-30.22	16.074	6.882	1.929	4.573	0.228	0.348	20.572	7.38	1.878	5.389	0.201	0.353
C_3N(3-2,5/2-3/2)	29.70	34	-28.96	19.806	2.573	3.831	2.837	0.148	0.085	nan	nan	nan	nan	nan	nan
C_3N(3-2,5/2-3/2)	29.70	35	-27.70	16.919	1.659	1.834	1.742	0.156	0.123	nan	nan	nan	nan	nan	nan
C_3N(3-2,5/2-3/2)	29.70	36	-26.44	15.641	1.667	1.972	1.924	0.212	0.154	21.401	nan	-0.236	nan	4.108	nan
C_3N(3-2,5/2-3/2)	29.70	37	-25.18	17.261	2.29	3.818	2.631	0.207	0.103	nan	nan	nan	nan	nan	nan
C_3N(3-2,5/2-3/2)	29.70	38	-23.91	16.946	14.111	2.509	12.748	0.131	0.333	22.591	43.785	2.509	23.246	0.047	0.447
C_3N(3-2,5/2-3/2)	29.70	39	-22.65	16.55	3.364	1.621	3.337	0.144	0.142	21.153	2.457	1.621	2.182	0.201	0.138
C_3N(3-2,5/2-3/2)	29.70	40	-21.39	15.606	1.169	1.729	1.198	0.253	0.147	nan	nan	nan	nan	nan	nan
C_3N(3-2,5/2-3/2)	29.70	41	-20.13	16.559	2.455	3.192	2.701	0.23	0.152	nan	nan	nan	nan	nan	nan
C_3N(3-2,5/2-3/2)	29.70	42	-18.87	15.855	2.269	2.676	3.271	0.267	0.141	21.897	3.363	1.533	3.169	0.132	0.201
C_3N(3-2,7/2-5/2)	29.68	32	-32.53	16.359	1.272	3.262	1.481	0.415	0.137	nan	nan	nan	nan	nan	nan
C_3N(3-2,7/2-5/2)	29.68	33	-31.27	15.576	1.818	2.262	2.106	0.323	0.198	23.517	7.723	2.262	8.673	0.074	0.189
C_3N(3-2,7/2-5/2)	29.68	34	-30.00	18.198	1.37	2.276	1.431	0.295	0.153	nan	nan	nan	nan	nan	nan
C_3N(3-2,7/2-5/2)	29.68	35	-28.74	15.901	0.922	1.602	0.944	0.369	0.185	nan	nan	nan	nan	nan	nan

Table C.5 continued.

Transition	Restfreq	Ch	v_{ch}	R_{max} 1	ΔR_{max} 1	$W_{1/2}$ 1	$\Delta W_{1/2}$ 1	F_{max} 1_{max} 1	ΔF_{max} 1	R_{max} 2	ΔR_{max} 2	$W_{1/2}$ 2	$\Delta W_{1/2}$ 2	F_{max} 2	ΔF_{max} 2
C_3N(3-2,7/2-5/2)	29.68	36	-27.48	17.31	1.23	2.288	1.254	0.372	0.173	nan	nan	nan	nan	nan	nan
C_3N(3-2,7/2-5/2)	29.68	37	-26.21	14.99	0.905	1.815	0.953	0.492	0.212	nan	nan	nan	nan	nan	nan
C_3N(3-2,7/2-5/2)	29.68	38	-24.95	18.01	3.183	2.536	3.9	0.202	0.195	nan	nan	nan	nan	nan	nan
C_3N(3-2,7/2-5/2)	29.68	39	-23.69	14.702	1.737	1.755	2.086	0.246	0.186	21.367	14.391	1.755	14.044	0.056	0.788
C_3N(3-2,7/2-5/2)	29.68	40	-22.43	17.19	1.699	1.817	1.926	0.25	0.165	21.414	4.128	0.88	5.531	0.068	0.239
C_3N(3-2,7/2-5/2)	29.68	41	-21.16	16.683	8.558	1.809	8.509	0.121	0.241	21.565	4.962	1.809	4.033	0.216	0.245
C_3N(3-2,7/2-5/2)	29.68	42	-19.90	11.922	11.176	2.247	8.716	0.1	0.492	20.493	1.69	2.247	1.837	0.326	0.192
C_3N(3-2,7/2-5/2)	29.68	43	-18.64	16.634	6.817	2.186	4.747	0.332	0.438	21.934	22.609	2.186	18.225	0.096	0.403
C_4H(2-1,5/2-3/2)	19.02	37	-31.76	0	0	0	0	0	0	nan	nan	nan	nan	nan	nan
C_4H(2-1,5/2-3/2)	19.02	38	-29.79	8.73	2.93	3.722	3.367	0.098	0.062	24.26	12.512	3.722	15.041	0.022	0.062
C_4H(2-1,5/2-3/2)	19.02	39	-27.82	14.384	4.676	5.718	5.087	0.095	0.044	21.518	1.636	1.119	2.061	0.072	0.109
C_4H(2-1,5/2-3/2)	19.02	40	-25.85	12.455	7.777	4.297	10.036	0.046	0.056	28.316	5.502	4.297	5.84	0.057	0.053
C_4H(2-1,5/2-3/2)	19.02	41	-23.88	14.488	2.646	2.781	3.453	0.108	0.067	23.918	7.91	2.781	7.31	0.065	0.06
C_4H(2-1,5/2-3/2)	19.02	42	-21.91	0	0	0	0	0	0	nan	nan	nan	nan	nan	nan
C_4H(2-1,5/2-3/2)	19.02	43	-19.93	0	0	0	0	0	0	nan	nan	nan	nan	nan	nan
C_4H(3-2,5/2-3/2)	28.57	27	-32.77	15.229	3.024	1.607	3.564	0.136	0.198	23.543	9.956	1.607	16.526	0.05	0.372
C_4H(3-2,5/2-3/2)	28.57	28	-31.46	2.02	1.5	1.209	1.606	0.386	0.371	nan	nan	nan	nan	nan	nan
C_4H(3-2,5/2-3/2)	28.57	29	-30.15	7.214	7.199	5.311	9.683	0.259	0.212	23.879	6.234	2.612	6.599	0.122	0.304
C_4H(3-2,5/2-3/2)	28.57	30	-28.84	12.156	9.093	6.657	12.189	0.113	0.134	nan	nan	nan	nan	nan	nan
C_4H(3-2,5/2-3/2)	28.57	31	-27.53	13.963	11.727	7.149	11.697	0.108	0.13	nan	nan	nan	nan	nan	nan
C_4H(3-2,5/2-3/2)	28.57	32	-26.21	0	0	0	0	0	0	nan	nan	nan	nan	nan	nan
C_4H(3-2,5/2-3/2)	28.57	33	-24.90	19.046	2.909	2.135	3.191	0.134	0.154	25.142	2.68	1.048	3.217	0.107	0.212
C_4H(3-2,5/2-3/2)	28.57	34	-23.59	10.084	18.959	6.255	26.564	0.072	0.182	19.56	1.705	0.686	3.79	0.104	0.357
C_4H(3-2,5/2-3/2)	28.57	35	-22.28	-1.985	132.242	21.846	82.548	0.158	0.358	nan	nan	nan	nan	nan	nan
C_4H(3-2,5/2-3/2)	28.57	36	-20.97	10.963	37.644	15.972	49.517	0.089	0.073	nan	nan	nan	nan	nan	nan
C_4H(3-2,5/2-3/2)	28.57	37	-19.66	15.226	2.384	2.626	2.801	0.225	0.146	24.441	nan	0.895	nan	0.026	nan
C_4H(3-2,7/2-5/2)	28.53	39	-32.74	0	0	0	0	0	0	nan	nan	nan	nan	nan	nan
C_4H(3-2,7/2-5/2)	28.53	40	-31.43	15.796	1.452	2.433	1.815	0.323	0.163	22.588	2.742	1.115	3.251	0.113	0.22
C_4H(3-2,7/2-5/2)	28.53	41	-30.11	19.735	1.656	2.855	1.696	0.206	0.103	nan	nan	nan	nan	nan	nan
C_4H(3-2,7/2-5/2)	28.53	42	-28.80	16.167	1.834	1.107	2.119	0.129	0.171	nan	nan	nan	nan	nan	nan
C_4H(3-2,7/2-5/2)	28.53	43	-27.49	9.819	22.67	6.653	49.091	0.126	0.15	28.033	70.677	6.653	66.938	0.068	0.227
C_4H(3-2,7/2-5/2)	28.53	44	-26.17	0	0	0	0	0	0	nan	nan	nan	nan	nan	nan
C_4H(3-2,7/2-5/2)	28.53	45	-24.86	15.818	1.411	1.281	1.626	0.206	0.17	nan	nan	nan	nan	nan	nan
C_4H(3-2,7/2-5/2)	28.53	46	-23.55	0	0	0	0	0	0	nan	nan	nan	nan	nan	nan
C_4H(3-2,7/2-5/2)	28.53	47	-22.23	15.089	6.616	5.776	9.826	0.154	0.115	24.218	nan	0.942	nan	0	nan
C_4H(3-2,7/2-5/2)	28.53	48	-20.92	19.57	12.003	8.629	12.869	0.09	0.084	nan	nan	nan	nan	nan	nan
C_4H(3-2,7/2-5/2)	28.53	49	-19.61	15.946	3.252	2.261	3.422	0.112	0.14	nan	nan	nan	nan	nan	nan
C_6H(15/2-13/2,3/2,e)	20.79	100	-19.84	15.344	1.031	1.436	1.035	0.141	0.089	nan	nan	nan	nan	nan	nan
C_6H(15/2-13/2,3/2,e)	20.79	93	-32.46	15.84	16.227	2.397	27.573	0.046	0.092	22.913	8.498	2.397	6.599	0.07	0.094
C_6H(15/2-13/2,3/2,e)	20.79	94	-30.65	12.819	5.473	5.394	6.759	0.066	0.065	nan	nan	nan	nan	nan	nan
C_6H(15/2-13/2,3/2,e)	20.79	95	-28.85	8.624	0.831	1.374	0.944	0.215	0.11	nan	nan	nan	nan	nan	nan
C_6H(15/2-13/2,3/2,e)	20.79	96	-27.05	5	60.736	13.23	41.295	0.073	0.104	22.985	1.429	1.114	1.516	0.09	0.102

Table C.5 continued.

Transition	Restfreq	Ch	v_{ch}	R_{max} 1	ΔR_{max} 1	$W_{1/2}$ 1	$\Delta W_{1/2}$ 1	F_{max} 1_{max} 1	ΔF_{max} 1	R_{max} 2	ΔR_{max} 2	$W_{1/2}$ 2	$\Delta W_{1/2}$ 2	F_{max} 2	ΔF_{max} 2
C_6H(15/2-13/2,3/2,e)	20.79	97	-25.25	5.397	4.757	4.082	5.143	0.101	0.074	22.809	25.432	4.082	17.121	0.048	0.08
C_6H(15/2-13/2,3/2,e)	20.79	98	-23.45	17.296	3.237	7.248	3.428	0.127	0.047	nan	nan	nan	nan	nan	nan
C_6H(15/2-13/2,3/2,e)	20.79	99	-21.64	11.465	1.915	1.176	2.059	0.104	0.139	nan	nan	nan	nan	nan	nan
C_6H(15/2-13/2,3/2,f)	20.79	80	-33.39	16.295	1.053	2.536	1.124	0.228	0.082	23.629	2.442	1.067	1.922	0.066	0.104
C_6H(15/2-13/2,3/2,f)	20.79	81	-31.59	10.015	11.937	8.787	15.955	0.068	0.059	nan	nan	nan	nan	nan	nan
C_6H(15/2-13/2,3/2,f)	20.79	82	-29.78	10.058	4.633	3.253	6.172	0.091	0.084	21.9	11.269	3.253	11.865	0.027	0.068
C_6H(15/2-13/2,3/2,f)	20.79	83	-27.98	-3.84	125.871	19.103	66.688	0.095	0.254	nan	nan	nan	nan	nan	nan
C_6H(15/2-13/2,3/2,f)	20.79	84	-26.18	10.454	7.021	6.464	6.203	0.095	0.059	nan	nan	nan	nan	nan	nan
C_6H(15/2-13/2,3/2,f)	20.79	85	-24.38	9.366	1.473	1.386	1.517	0.123	0.114	nan	nan	nan	nan	nan	nan
C_6H(15/2-13/2,3/2,f)	20.79	86	-22.58	7.343	5.203	4.529	8.759	0.134	nan	20.122	11.792	4.529	nan	0.09	nan
C_6H(15/2-13/2,3/2,f)	20.79	87	-20.77	13.732	2.429	4.146	3.406	0.18	0.078	nan	nan	nan	nan	nan	nan
C_6H(15/2-13/2,3/2,f)	20.79	88	-18.97	11.137	2.717	5.798	3.207	0.162	0.06	nan	nan	nan	nan	nan	nan
C_6H(17/2-15/2,1/2,e)	23.75	46	-32.11	14.125	1.096	2.342	1.129	0.237	0.097	21.924	2.004	0.679	4.719	0.088	0.546
C_6H(17/2-15/2,1/2,e)	23.75	47	-30.54	13.141	1.752	2.728	1.907	0.151	0.082	23.811	1.602	1.529	1.726	0.107	0.097
C_6H(17/2-15/2,1/2,e)	23.75	48	-28.96	1.676	4.148	2.232	3.758	0.214	0.171	nan	nan	nan	nan	nan	nan
C_6H(17/2-15/2,1/2,e)	23.75	49	-27.38	13.723	1.258	1.268	1.295	0.133	0.114	nan	nan	nan	nan	nan	nan
C_6H(17/2-15/2,1/2,e)	23.75	50	-25.80	2.363	0.962	0.881	1.281	0.237	0.234	nan	nan	nan	nan	nan	nan
C_6H(17/2-15/2,1/2,e)	23.75	51	-24.22	15.283	8.205	9.827	8.431	0.081	0.038	nan	nan	nan	nan	nan	nan
C_6H(17/2-15/2,1/2,e)	23.75	52	-22.65	0	0	0	0	0	0	nan	nan	nan	nan	nan	nan
C_6H(17/2-15/2,1/2,e)	23.75	53	-21.07	6.718	15.926	3.267	10.853	0.106	0.15	25.603	7.889	3.267	9.936	0.056	0.137
C_6H(17/2-15/2,1/2,e)	23.75	54	-19.49	15.465	2.189	3.19	2.498	0.122	0.071	28.736	2.744	1.775	3.009	0.065	0.084
C_6H(17/2-15/2,3/2,e)	23.57	70	-32.46	11.587	1.508	2.185	1.607	0.16	0.094	nan	nan	nan	nan	nan	nan
C_6H(17/2-15/2,3/2,e)	23.57	71	-30.87	-95.489	5342.007	30.182	769.803	26.24	8041.206	nan	nan	nan	nan	nan	nan
C_6H(17/2-15/2,3/2,e)	23.57	72	-29.28	0	0	0	0	0	0	nan	nan	nan	nan	nan	nan
C_6H(17/2-15/2,3/2,e)	23.57	73	-27.69	52.727	484.72	17.902	152.168	0.234	4.918	nan	nan	nan	nan	nan	nan
C_6H(17/2-15/2,3/2,e)	23.57	74	-26.10	15.403	0.969	1.334	1.135	0.208	0.127	nan	nan	nan	nan	nan	nan
C_6H(17/2-15/2,3/2,e)	23.57	75	-24.51	0	0	0	0	0	0	nan	nan	nan	nan	nan	nan
C_6H(17/2-15/2,3/2,e)	23.57	76	-22.92	11.575	3.17	2.531	3.653	0.12	0.116	22.067	6.548	2.531	5.548	0.059	0.127
C_6H(17/2-15/2,3/2,e)	23.57	77	-21.33	16.193	10.422	2.059	13.107	0.037	0.13	nan	nan	nan	nan	nan	nan
C_6H(17/2-15/2,3/2,e)	23.57	78	-19.74	0	0	0	0	0	0	nan	nan	nan	nan	nan	nan
C_6H(17/2-15/2,3/2,f)	23.57	54	-32.20	17.403	1.357	1.821	1.358	0.153	0.098	24.49	1.468	0.753	3.824	0.075	0.309
C_6H(17/2-15/2,3/2,f)	23.57	55	-30.61	15.723	9.592	6.067	9.581	0.064	0.061	20.421	1.748	0.958	1.963	0.08	0.137
C_6H(17/2-15/2,3/2,f)	23.57	56	-29.02	15.178	4.248	2.755	4.348	0.052	0.069	23.905	2.582	0.82	4.095	0.041	0.148
C_6H(17/2-15/2,3/2,f)	23.57	57	-27.43	5.627	5.014	5.671	5.03	0.167	0.074	nan	nan	nan	nan	nan	nan
C_6H(17/2-15/2,3/2,f)	23.57	58	-25.84	11.874	38.898	11.92	46.151	0.036	0.042	nan	nan	nan	nan	nan	nan
C_6H(17/2-15/2,3/2,f)	23.57	59	-24.25	3.635	15.451	7.767	10.086	0.124	0.074	nan	nan	nan	nan	nan	nan
C_6H(17/2-15/2,3/2,f)	23.57	60	-22.66	2.075	0.972	1.059	1.347	0.281	0.234	nan	nan	nan	nan	nan	nan
C_6H(17/2-15/2,3/2,f)	23.57	61	-21.07	18.667	3.155	3.787	3.141	0.119	0.079	nan	nan	nan	nan	nan	nan
C_6H(17/2-15/2,3/2,f)	23.57	62	-19.48	13.871	3.166	4.021	3.476	0.127	0.071	nan	nan	nan	nan	nan	nan
C_6H(19/2-17/2,3/2,e)	26.34	73	-32.47	14.063	1.941	2.312	2.247	0.126	0.091	21.542	1.452	0.888	1.136	0.099	0.117
C_6H(19/2-17/2,3/2,e)	26.34	74	-31.04	12.813	1.867	2.903	1.959	0.16	0.089	nan	nan	nan	nan	nan	nan
C_6H(19/2-17/2,3/2,e)	26.34	75	-29.62	-290.313	44994.792	97.621	7175.429	5.773	4131.934	nan	nan	nan	nan	nan	nan

Table C.5 continued.

Transition	Restfreq	Ch	v_{ch}	R_{max} 1	ΔR_{max} 1	$W_{1/2}$ 1	$\Delta W_{1/2}$ 1	F_{max} 1_{max} 1	ΔF_{max} 1	R_{max} 2	ΔR_{max} 2	$W_{1/2}$ 2	$\Delta W_{1/2}$ 2	F_{max} 2	ΔF_{max} 2
C_6H(19/2-17/2,3/2,e)	26.34	76	-28.20	1.758	4.382	1.166	4.444	0.08	0.231	nan	nan	nan	nan	nan	nan
C_6H(19/2-17/2,3/2,e)	26.34	77	-26.78	-5.91	189.97	15.097	84.296	0.165	1.112	nan	nan	nan	nan	nan	nan
C_6H(19/2-17/2,3/2,e)	26.34	78	-25.35	6.207	1.262	2.211	1.376	0.25	0.117	22.297	7.091	2.211	6.572	0.11	0.101
C_6H(19/2-17/2,3/2,e)	26.34	79	-23.93	17.094	12.871	1.624	6.643	0.1	0.478	20.426	14.371	1.624	7.247	0.09	0.483
C_6H(19/2-17/2,3/2,e)	26.34	80	-22.51	14.507	1.241	1.921	1.337	0.186	0.1	22.034	4.487	1.921	5.353	0.049	0.095
C_6H(19/2-17/2,3/2,e)	26.34	81	-21.08	0	0	0	0	0	0	nan	nan	nan	nan	nan	nan
C_6H(19/2-17/2,3/2,e)	26.34	82	-19.66	12.597	4.646	3.11	5.501	0.122	0.095	21.946	14.318	3.11	13.456	0.046	0.126
C_6H(19/2-17/2,3/2,f)	26.34	53	-32.23	13.875	3.563	3.328	3.527	0.18	0.084	22.96	13.517	3.328	11.607	0.048	0.08
C_6H(19/2-17/2,3/2,f)	26.34	54	-30.81	15.734	1.353	2.068	1.461	0.144	0.079	24.278	5.129	2.068	6.016	0.042	0.073
C_6H(19/2-17/2,3/2,f)	26.34	55	-29.39	5	58.618	5.927	83.241	0.04	0.445	22.49	3.448	2.523	3.524	0.092	0.095
C_6H(19/2-17/2,3/2,f)	26.34	56	-27.97	11.386	15.564	8.261	18.679	0.055	0.068	nan	nan	nan	nan	nan	nan
C_6H(19/2-17/2,3/2,f)	26.34	57	-26.54	0	0	0	0	0	0	nan	nan	nan	nan	nan	nan
C_6H(19/2-17/2,3/2,f)	26.34	58	-25.12	1.722	25.456	10.035	15.335	0.149	0.139	nan	nan	nan	nan	nan	nan
C_6H(19/2-17/2,3/2,f)	26.34	59	-23.70	12.244	3.832	5.728	5.042	0.104	0.056	nan	nan	nan	nan	nan	nan
C_6H(19/2-17/2,3/2,f)	26.34	60	-22.28	13.359	14.562	5.425	14.472	0.043	0.062	20.77	2.088	-0.697	2.434	0.072	0.165
C_6H(19/2-17/2,3/2,f)	26.34	61	-20.85	0	0	0	0	0	0	nan	nan	nan	nan	nan	nan
C_6H(19/2-17/2,3/2,f)	26.34	62	-19.43	-23.895	501.828	31.542	205.262	0.18	1.692	nan	nan	nan	nan	nan	nan

Table C.6: List of Gaussian fit results from the radial emission profiles of each transition (restfrequency in GHz) of velocity integrated flux with $\Delta v < 7.5$ km s^{-1} for the azimuthal sum. The fit parameters are shell radius at maximum flux $R_{\rm max}$ (in arcsec), half shell width $W_{1/2}$ (in arcsec), and maximum flux $F_{\rm max}$ (in mJy beam^{-1}) for two components and their uncertainties determined from the least square fit routine.

Transition	Restfreq	$R_{\rm max}$ 1	$\Delta R_{\rm max}$ 1	$W_{1/2}$ 1	$\Delta W_{1/2}$ 1	$F_{\rm max}$ 1	$\Delta F_{\rm max}$ 1	$R_{\rm max}$ 2	$\Delta R_{\rm max}$ 2	$W_{1/2}$ 2	$\Delta W_{1/2}$ 2	$F_{\rm max}$ 2	$\Delta F_{\rm max}$ 2
HC_3N(2-1)	18.19631	15.061	0.016	5.386	0.021	50.584	0.094	25.158	0.071	2.185	0.078	4.803	0.161
HC_3N(3-2)	27.2943	15.147	0.007	3.04	0.008	152.287	0.2	21.746	0.033	1.743	0.03	21.775	0.29
HC_3N(4-3)	36.39232	14.873	0.017	2.894	0.013	205.28	0.324	19.603	0.036	1.605	0.036	37.285	1.136
HC_5N(8-7)	21.30126	16.285	0.03	3.615	0.026	35.929	0.091	23.407	0.056	2.47	0.037	11.75	0.231
HC_5N(9-8)	23.9639	16.103	0.074	2.709	0.039	33.646	0.557	21.675	0.197	2.709	0.11	12.413	0.537
HC_5N(10-9)	26.6265	16.031	0.023	2.459	0.02	47.912	nan	21.232	0.053	2.459	nan	20.314	nan
HC_5N(11-10)	29.2892	15.782	0.057	2.588	0.047	33.735	0.226	21.547	0.146	2.01	0.162	9.012	0.363
HC_5N(12-11)	31.95177	15.248	0.142	2.188	0.058	58.21	3.015	19.125	0.244	2.188	0.095	33.602	3.075
HC_5N(13-12)	34.61440	15.190	0.070	2.337	0.047	39.428	0.525	20.745	0.288	2.337	0.239	9.033	0.456
HC_5N(14-13)	37.27699	15.424	0.03	2.126	0.017	129.165	0.999	19.94	0.074	2.126	0.041	51.196	1.008
HC_7N(16-15)	18.04797	17.71	0.169	4.645	0.189	6.502	0.118	25.142	0.187	1.662	0.233	1.94	0.274
HC_7N(17-16)	19.17596	17.721	0.227	4.616	0.16	6.155	0.088	23.877	0.243	2.168	0.45	0.999	0.324
HC_7N(18-17)	20.30395	15.715	0.252	2.845	0.288	14.173	0.741	24.343	0.374	2.845	0.346	8.947	0.611
HC_7N(19-18)	21.43193	16.385	0.197	2.905	0.125	8.029	0.262	22.61	0.286	2.839	0.148	5.326	0.317
HC_7N(20-19)	22.55992	16.159	0.195	2.793	0.111	9.576	0.371	21.936	0.294	2.793	0.145	6.271	0.411
HC_7N(22-21)	24.81588	16.709	0.215	2.402	0.124	8.78	0.437	21.81	0.401	2.402	0.23	4.639	0.443
HC_7N(23-22)	25.94385	18.066	0.031	3.965	0.033	12.945	0.08	nan	nan	nan	nan	nan	nan
HC_7N(24-23)	27.0718	16.679	0.133	2.012	0.09	11.869	0.33	21.44	0.169	2.012	0.108	9.302	0.334
HC_7N(25-24)	28.1998	16.966	0.452	2.556	0.204	9.236	1.213	21.723	0.855	2.556	0.392	4.85	1.204
HC_7N(26-25)	29.3277	15.382	0.057	1.583	0.064	7.451	0.229	21.197	0.089	1.583	0.089	4.535	0.191
HC_7N(27-26)	30.45575	16.898	0.102	2.503	0.078	14.091	nan	21.572	0.163	2.503	nan	7.475	nan
HC_7N(28-27)	31.5837	16.706	0.213	2.498	0.102	23.038	1.377	21.431	0.407	2.498	0.179	11.985	1.429
HC_7N(29-28)	32.7117	17.239	0.187	2.58	0.256	8.606	0.212	22.735	0.476	1.846	0.316	2.786	0.532
HC_7N(30-29)	33.8396	16.302	0.482	2.209	0.186	13.415	2.594	20	1.001	2.209	0.37	6.397	2.644
HC_7N(31-30)	34.9676	15.468	0.07	1.69	0.081	7.981	0.268	21.616	0.108	1.69	0.114	4.748	0.23
HC_7N(32-31)	36.0955	17.097	0.792	2.459	0.278	14.041	4.368	20.991	1.95	2.459	0.641	5.629	4.464
HC_7N(33-32)	37.2235	15.379	0.08	1.701	0.075	12.977	0.345	20.229	0.091	1.701	0.083	10.833	0.319
C_3N(2-1,3/2-1/2)	19.79995	15.339	0.14	4.24	0.139	2.397	0.066	nan	nan	nan	nan	nan	nan
C_3N(2-1,5/2-3/2)	19.7808	16.436	1.108	2.712	0.484	2.66	0.827	21.314	1.281	2.712	0.503	2.264	0.867
C_3N(3-2,5/2-3/2)	29.69513	18.863	0.049	3.433	0.052	7.987	0.096	nan	nan	nan	nan	nan	nan
C_3N(3-2,7/2-5/2)	29.67628	16.631	0.274	1.873	0.294	6.132	2.78	20.476	0.991	3.004	0.503	7.599	1.158
C_4H(2-1,5/2-3/2)	19.01514	14.259	0.269	7.768	0.326	1.769	0.043	nan	nan	nan	nan	nan	nan
C_4H(3-2,5/2-3/2)	28.57131	16.845	0.222	3.464	0.227	2.962	0.156	nan	nan	nan	nan	nan	nan
C_4H(3-2,7/2-5/2)	28.53231	16.808	0.474	1.874	0.316	3.891	0.39	21.273	0.918	1.874	0.575	2.002	0.409
C_6H(15/2-13/2,3/2,e)	20.79291	14.15	0.98	5.622	0.565	1.437	0.128	20.139	0.433	2.344	0.599	0.763	0.224
C_6H(15/2-13/2,3/2,f)	20.79447	12.686	36.097	5.169	8.365	1.471	15.528	18.641	43.66	5.169	9.342	1.187	15.733
C_6H(17/2-15/2,1/2,e)	23.74855	14.717	1.304	2.105	0.688	1.72	0.65	18.927	3.113	2.105	1.43	0.714	0.701
C_6H(17/2-15/2,3/2,e)	23.56518	14.124	0.396	3.364	0.412	1.513	0.122	nan	nan	nan	nan	nan	nan

Table C.6 continued.

Transition	Restfreq	R_{max} 1	ΔR_{max} 1	$W_{1/2}$ 1	$\Delta W_{1/2}$ 1	F_{max} 1	ΔF_{max} 1	R_{max} 2	ΔR_{max} 2	$W_{1/2}$ 2	$\Delta W_{1/2}$ 2	F_{max} 2	ΔF_{max} 2
C_6H(17/2-15/2,3/2,f)	23.5672	17.762	0.173	3.721	0.179	1.947	0.076	nan	nan	nan	nan	nan	nan
C_6H(19/2-17/2,3/2,e)	26.33746	15.2	0.457	2.567	0.321	3.001	0.214	20.902	0.747	2.38	0.436	1.678	0.284
C_6H(19/2-17/2,3/2,f)	26.33998	15.251	1.663	2.496	0.692	2.514	1.351	19.593	2.112	2.492	0.781	1.932	1.42
C_6H^-(9-8)	24.78344	14.959	0.324	4.253	0.47	1.48	0.088	23.529	0.66	1.395	0.786	0.332	0.13
C_6H^-(11-10)	30.2908	14.09	0.21	7.161	0.195	2.612	0.048	nan	nan	nan	nan	nan	nan
C_6H^-(12-11)	33.04449	17.838	0.157	4.812	0.202	2.354	0.062	nan	nan	nan	nan	nan	nan

Table C.7: List of Gaussian fit results from the radial emission profiles of each transition (restfrequency in GHz) of velocity integrated flux with $\Delta v < 7.5$ km s^{-1} for quarter Q1. The fit parameters are shell radius at maximum flux $R_{\rm max}$ (in arcsec), half shell width $W_{1/2}$ (in arcsec), and maximum flux $F_{\rm max}$ (in mJy beam^{-1}) for two components and their uncertainties determined from the least square fit routine.

Transition	Restfreq	R_{max} 1	ΔR_{max} 1	$W_{1/2}$ 1	$\Delta W_{1/2}$ 1	F_{max} 1	ΔF_{max} 1	R_{max} 2	ΔR_{max} 2	$W_{1/2}$ 2	$\Delta W_{1/2}$ 2	F_{max} 2	ΔF_{max} 2
HC_3N(2-1)	18.19631	15.062	0.052	5.501	0.071	13.186	0.092	25.99	0.202	2.084	0.22	1.491	0.131
HC_3N(3-2)	27.2943	15.237	0.019	3.012	0.022	37.996	0.195	23.782	0.084	1.115	0.181	5.774	0.727
HC_3N(4-3)	36.39232	15.814	0.019	2.846	0.019	37.64	0.212	nan	nan	nan	nan	nan	nan
HC_5N(9-8)	21.30126	16.495	0.069	3.674	0.075	8.758	0.082	24.477	0.127	2.202	0.102	3.096	0.125
HC_5N(9-8)	23.9639	16.518	0.034	2.935	0.041	10.556	0.097	24.105	0.076	1.662	0.078	3.146	0.108
HC_5N(10-9)	26.6265	16.329	0.046	2.556	0.06	13.128	0.188	23.941	0.117	1.989	0.117	4.292	0.166
HC_5N(11-10)	29.2892	16.639	0.069	2.108	0.076	7.422	0.191	23.595	0.216	1.182	0.276	2.047	0.338
HC_5N(12-11)	31.95177	16.499	0.054	2.847	0.078	14.846	0.228	nan	nan	nan	nan	nan	nan
HC_5N(13-12)	34.61440	16.338	0.363	1.562	0.234	7.206	1.112	20.430	2.308	1.562	2.347	2.081	3.701
HC_5N(14-13)	37.27699	16.581	0.029	2.57	0.029	24.988	0.233	nan	nan	nan	nan	nan	nan
HC_7N(16-15)	18.04797	17.343	1.246	6.079	1.06	1.433	0.115	24.429	0.504	1.878	0.872	0.714	0.316
HC_7N(17-16)	19.17596	17.769	0.744	4.362	0.569	1.444	0.07	23.823	0.444	1.943	0.774	0.484	0.259
HC_7N(18-17)	20.30395	15.429	0.567	2.142	0.676	3.901	0.889	24.279	0.797	2.142	0.857	2.896	0.717
HC_7N(19-18)	21.43193	17.034	0.273	2.709	0.269	2.089	0.093	23.533	0.332	2.042	0.271	1.342	0.117
HC_7N(20-19)	22.55992	16.576	0.243	2.948	0.235	2.615	0.083	23.668	0.395	2.381	0.285	1.341	0.113
HC_7N(22-21)	24.81588	17.45	0.148	2.885	0.195	2.797	0.099	23.819	0.224	1.389	0.296	1.147	0.135
HC_7N(23-22)	25.94385	17.335	0.111	2.91	0.142	3.515	0.106	24.189	0.139	1.566	0.144	1.801	0.128
HC_7N(24-23)	27.0718	17.201	0.179	2.167	0.184	3.508	0.161	23.645	0.265	2.167	0.26	2.262	0.14
HC_7N(25-24)	28.1998	18.473	0.201	4.555	0.242	2.17	0.08	nan	nan	nan	nan	nan	nan
HC_7N(26-25)	29.3277	16.176	0.269	1.85	0.286	1.609	0.196	23.708	0.346	1.244	0.566	0.921	0.308
HC_7N(27-26)	30.45575	17.595	0.101	2.243	0.101	3.913	0.146	nan	nan	nan	nan	nan	nan
HC_7N(28-27)	31.5837	17.144	0.09	3.067	0.094	5.388	0.13	nan	nan	nan	nan	nan	nan
HC_7N(29-28)	32.7117	17.58	0.338	2.241	0.45	2.61	0.214	24.118	0.726	1.85	1.916	0.837	0.239
HC_7N(30-29)	33.8396	16.889	0.069	2.098	0.069	4.653	0.131	nan	nan	nan	nan	nan	nan
HC_7N(31-30)	34.9676	21.133	4.716	8.432	5.065	0.57	0.114	nan	nan	nan	nan	nan	nan
HC_7N(32-31)	36.0955	16.874	0.134	2.228	0.145	3.392	nan	24.783	0.315	2.228	nan	1.279	nan
HC_7N(33-32)	37.2235	19.429	1.846	0.767	1.231	2.231	4.122	nan	nan	nan	nan	nan	nan
C_3N(2-1,3/2-1/2)	19.79995	2.898	20.432	17.418	20.148	0.542	0.146	nan	nan	nan	nan	nan	nan
C_3N(2-1,5/2-3/2)	19.7808	19.165	0.415	4.375	0.442	0.739	0.058	nan	nan	nan	nan	nan	nan
C_3N(3-2,5/2-3/2)	29.69513	16.136	0.473	2.065	0.459	1.423	0.141	21.832	0.496	2.065	0.415	1.357	0.131
C_3N(3-2,7/2-5/2)	29.67628	17.206	0.368	2.102	0.395	2.375	0.178	22.847	0.792	2.102	0.596	1.17	0.179
C_4H(2-1,5/2-3/2)	19.01514	13.781	0.612	5.485	0.608	0.58	0.049	nan	nan	nan	nan	nan	nan
C_4H(3-2,5/2-3/2)	28.57131	17.55	1.093	2.091	0.916	1.076	0.233	23.018	3.294	2.091	2.504	0.354	0.225
C_4H(3-2,7/2-5/2)	28.53231	15.986	0.404	1.544	0.596	0.966	0.247	21.924	0.864	1.504	1.218	0.405	0.218
C_6H(15/2-13/2,3/2,e)	20.79291	16.597	0.817	4.996	0.888	0.478	0.063	nan	nan	nan	nan	nan	nan
C_6H(15/2-13/2,3/2,f)	20.79447	18.924	0.849	6.273	0.936	0.512	0.056	nan	nan	nan	nan	nan	nan
C_6H(17/2-15/2,1/2,e)	23.74855	15.261	1.09	3.942	1.122	0.399	0.08	nan	nan	nan	nan	nan	nan
C_6H(17/2-15/2,3/2,e)	23.56518	14.372	0.831	2.396	0.87	0.49	0.142	nan	nan	nan	nan	nan	nan
C_6H(17/2-15/2,3/2,f)	23.5672	14.449	2.2	5.901	1.482	0.394	0.096	19.749	1.119	1.538	1.809	0.193	0.147
C_6H(19/2-17/2,3/2,e)	26.33746	15.875	1.638	2.384	1.114	0.783	0.238	21.438	2.361	2.384	1.511	0.538	0.238

Table C.7 continued.

Transition	Restfreq	R_{max} 1	ΔR_{max} 1	$W_{1/2}$ 1	$\Delta W_{1/2}$ 1	F_{max} 1	ΔF_{max} 1	R_{max} 2	ΔR_{max} 2	$W_{1/2}$ 2	$\Delta W_{1/2}$ 2	F_{max} 2	ΔF_{max} 2
C_6H(19/2-17/2,3/2,f)	26.33998	16.528	0.542	3.447	0.668	0.703	0.098	nan	nan	nan	nan	nan	nan
C_6H^-(9-8)	24.78344	9.933	7.765	11.444	6.609	0.398	0.085	nan	nan	nan	nan	nan	nan
C_6H^-(11-10)	30.2908	14.03	0.312	4.213	0.395	1.106	0.067	30.49	2.826	2.833	5.937	0.24	0.07
C_6H^-(12-11)	33.04449	18.731	1.26	2.33	0.941	0.54	0.119	24.444	2.942	2.33	1.98	0.229	0.124

Table C.8: List of Gaussian fit results from the radial emission profiles of each transition (restfrequency in GHz) of velocity integrated flux with $\Delta v < 7.5$ km s^{-1} for quarter Q2. The fit parameters are shell radius at maximum flux $R_{\rm max}$ (in arcsec), half shell width $W_{1/2}$ (in arcsec), and maximum flux $F_{\rm max}$ (in mJy beam^{-1}) for two components and their uncertainties determined from the least square fit routine.

Transition	Restfreq	R_{max} 1	ΔR_{max} 1	$W_{1/2}$ 1	$\Delta W_{1/2}$ 1	F_{max} 1	ΔF_{max} 1	R_{max} 2	ΔR_{max} 2	$W_{1/2}$ 2	$\Delta W_{1/2}$ 2	F_{max} 2	ΔF_{max} 2
HC_3N(2-1)	18.19631	16.029	0.091	5.473	0.099	13.626	0.088	24.89	0.176	2.275	0.232	2.107	0.248
HC_3N(3-2)	27.2943	16.191	0.035	2.945	0.035	45.032	0.196	22.561	0.097	2.051	0.079	11.52	0.36
HC_3N(4-3)	36.39232	17.094	0.026	3.16	0.03	47.433	0.209	22.919	0.138	1.305	0.108	4.258	0.433
HC_5N(8-7)	21.30126	17.189	0.181	3.619	0.129	9.05	0.142	23.639	0.182	2.529	0.106	4.951	0.393
HC_5N(9-8)	23.9639	17.444	0.152	2.54	0.105	8.281	0.197	22.985	0.171	2.336	0.097	6.617	0.276
HC_5N(10-9)	26.6265	17.24	0.281	2.436	0.155	11.902	0.767	22.189	0.343	2.387	0.168	9.339	0.863
HC_5N(11-10)	29.2892	17.243	0.244	2.721	0.161	11.408	0.355	22.53	0.312	2.124	0.195	6.107	0.714
HC_5N(12-11)	31.95177	17.558	0.159	2.475	0.115	16.74	0.369	22.715	0.24	2.02	0.159	8.412	0.662
HC_5N(13-12)	34.61440	17.425	0.096	3.034	0.107	16.193	0.200	23.359	0.129	1.637	0.126	6.614	0.436
HC_5N(14-13)	37.27699	17.061	0.077	2.372	0.063	26.27	0.291	22.189	0.109	1.857	0.074	14.08	0.524
HC_7N(16-15)	18.04797	14.847	1.708	3.246	1.365	1.047	0.222	22.68	1.304	3.246	0.84	1.364	0.245
HC_7N(17-16)	19.17596	17.225	3.873	5.358	1.522	1.169	0.537	22.856	0.608	3.296	1.129	1.025	0.994
HC_7N(18-17)	20.30395	21.61	0.406	4.937	0.446	7.343	0.483	nan	nan	nan	nan	nan	nan
HC_7N(19-18)	21.43193	20.466	0.179	5.117	0.185	2.074	0.061	nan	nan	nan	nan	nan	nan
HC_7N(20-19)	22.55992	16.349	6.033	3.342	2.689	1.294	2.046	21.783	3.349	3.342	1.018	2.235	2.315
HC_7N(22-21)	24.81588	14.799	65.713	3.998	63.313	0.443	7.238	21.719	15.064	3.998	4.567	2.313	9.128
HC_7N(23-22)	25.94385	16.758	14.062	3.803	8.891	0.524	nan	21.513	1.46	3.803	nan	3.174	nan
HC_7N(24-23)	27.0718	17.201	5.888	2.659	3.148	1.524	2.596	21.879	2.477	2.659	0.855	3.579	3.041
HC_7N(25-24)	28.1998	15.77	82.842	3.563	53.814	0.344	7.504	21.559	12.593	3.563	3.54	2.31	9.16
HC_7N(26-25)	29.3277	15.36	0.153	1.659	0.164	2.585	nan	22.325	0.138	1.659	nan	2.515	nan
HC_7N(27-26)	30.45575	21.763	0.122	3.224	0.124	3.447	0.114	nan	nan	nan	nan	nan	nan
HC_7N(28-27)	31.5837	20.524	0.071	3.572	0.076	6.588	0.111	nan	nan	nan	nan	nan	nan
HC_7N(29-28)	32.7117	20.314	0.687	5.881	1.388	2.321	0.145	nan	nan	nan	nan	nan	nan
HC_7N(30-29)	33.8396	15.663	0.24	1.603	0.353	2.223	0.217	22.434	0.114	1.603	0.125	2.252	0.135
HC_7N(31-30)	34.9676	19.89	0.126	3.344	0.135	5.176	0.168	nan	nan	nan	nan	nan	nan
HC_7N(32-31)	36.0955	20.881	0.116	3.151	0.121	4.113	0.132	nan	nan	nan	nan	nan	nan
HC_7N(33-32)	37.2235	15.842	0.407	1.609	0.762	2.136	0.482	22.186	0.247	1.609	0.324	2.428	0.304
C_3N(2-1,3/2-1/2)	19.79995	12.738	1.507	8.798	1.706	0.53	0.059	nan	nan	nan	nan	nan	nan
C_3N(2-1,5/2-3/2)	19.7808	16.112	9.895	3.391	5.474	0.49	1.057	22.172	4.693	3.391	1.637	1.019	1.261
C_3N(3-2,5/2-3/2)	29.69513	21.073	0.172	3.734	0.192	2.263	0.089	nan	nan	nan	nan	nan	nan
C_3N(3-2,7/2-5/2)	29.67628	21.654	0.142	3.535	0.159	3.274	0.114	nan	nan	nan	nan	nan	nan
C_4H(2-1,5/2-3/2)	19.01514	12.06	9.429	5.925	7.079	0.309	0.138	19.563	0.759	2.917	1.819	0.454	0.568
C_4H(3-2,5/2-3/2)	28.57131	17.13	1.227	5.602	2.137	1.053	0.148	nan	nan	nan	nan	nan	nan
C_4H(3-2,7/2-5/2)	28.53231	19.328	0.872	3.31	0.878	1.341	0.143	24.831	0.645	1.446	0.614	0.671	0.397
C_6H(15/2-13/2,3/2,e)	20.79291	9.401	4.425	5.18	10.831	0.49	0.226	21.853	8.762	5.18	4.328	0.36	0.352
C_6H(15/2-13/2,3/2,f)	20.79447	16.444	2.489	4.128	1.842	0.728	0.139	24.397	1.892	3.152	1.115	0.635	0.332
C_6H(17/2-15/2,1/2,e)	23.74855	17.259	0.539	3.325	0.6	0.615	0.083	nan	nan	nan	nan	nan	nan
C_6H(17/2-15/2,3/2,e)	23.56518	0.039	26.893	14.319	12.731	0.412	0.407	nan	nan	nan	nan	nan	nan
C_6H(17/2-15/2,3/2,f)	23.5672	20.157	0.63	3.885	0.671	0.548	0.07	nan	nan	nan	nan	nan	nan
C_6H(19/2-17/2,3/2,e)	26.33746	16.714	1.581	3.44	1.304	0.787	0.117	24.306	2.769	2.729	2.367	0.329	0.196

Table C.8 continued.

Transition	Restfreq	R_{max} 1	ΔR_{max} 1	$W_{1/2}$ 1	$\Delta W_{1/2}$ 1	F_{max} 1	ΔF_{max} 1	R_{max} 2	ΔR_{max} 2	$W_{1/2}$ 2	$\Delta W_{1/2}$ 2	F_{max} 2	ΔF_{max} 2
C_6H(19/2-17/2,3/2,f)	26.33998	16.6	1.095	2.652	0.775	1.075	0.194	22.881	2.842	2.652	1.879	0.409	0.197
C_6H^-(9-8)	24.78344	14.733	0.552	3.545	0.665	0.702	0.091	nan	nan	nan	nan	nan	nan
C_6H^-(11-10)	30.2908	12.033	0.252	2.477	0.254	1.024	0.089	22.934	0.18	2.117	0.183	0.936	0.069
C_6H^-(12-11)	33.04449	17.603	0.731	6.624	0.846	0.689	0.06	nan	nan	nan	nan	nan	nan

Table C.9: List of Gaussian fit results from the radial emission profiles of each transition (restfrequency in GHz) of velocity integrated flux with $\Delta v < 7.5$ km s^{-1} for quarter Q3. The fit parameters are shell radius at maximum flux $R_{\rm max}$ (in arcsec), half shell width $W_{1/2}$ (in arcsec), and maximum flux $F_{\rm max}$ (in mJy beam^{-1}) for two components and their uncertainties determined from the least square fit routine.

Transition	Restfreq	R_{max} 1	ΔR_{max} 1	$W_{1/2}$ 1	$\Delta W_{1/2}$ 1	F_{max} 1	ΔF_{max} 1	R_{max} 2	ΔR_{max} 2	$W_{1/2}$ 2	$\Delta W_{1/2}$ 2	F_{max} 2	ΔF_{max} 2
HC_3N(2-1)	18.19631	15.042	0.046	5.285	0.045	12.317	0.085	nan	nan	nan	nan	nan	nan
HC_3N(3-2)	27.2943	14.888	0.094	2.839	0.062	39.213	0.475	20.188	0.199	2.228	0.102	12.49	1.011
HC_3N(4-3)	36.39232	14.345	0.029	2.614	0.028	68.072	0.244	19.468	0.071	1.382	0.067	16.487	0.505
HC_5N(8-7)	21.30126	16.086	0.54	3.392	0.232	8.616	0.98	21.7	1.305	3.152	0.462	2.905	1.241
HC_5N(9-8)	23.9639	16.959	0.034	3.275	0.037	9.522	0.088	nan	nan	nan	nan	nan	nan
HC_5N(10-9)	26.6265	16.016	0.544	2.435	0.222	12.841	2.349	20.233	0.885	2.435	0.325	7.765	2.45
HC_5N(11-10)	29.2892	15.393	0.466	2.026	0.294	6.006	0.742	19.741	0.78	2.026	0.424	3.661	0.787
HC_5N(12-11)	31.95177	15.451	0.156	1.767	0.093	15.105	0.692	19.504	0.237	1.767	0.158	10.044	0.571
HC_5N(13-12)	34.61440	14.940	0.611	1.869	0.443	6.021	0.412	21.280	29.879	1.869	24.696	0.903	2.027
HC_5N(14-13)	37.27699	14.983	0.146	1.972	0.076	36.197	1.57	19.016	0.246	1.972	0.117	21.438	1.649
HC_7N(16-15)	18.04797	17.14	0.383	5.47	0.382	1.848	0.103	nan	nan	nan	nan	nan	nan
HC_7N(17-16)	19.17596	16.005	10.668	3.244	3.435	1.106	3.23	19.752	5.1	2.733	1.578	0.985	4.624
HC_7N(18-17)	20.30395	14.573	0.501	1.807	0.566	4.244	1.004	22.293	1.251	1.807	1.423	1.3	0.789
HC_7N(19-18)	21.43193	16.961	1.97	3.318	0.821	2.413	1.171	22.692	4.766	3.318	1.735	0.976	1.238
HC_7N(20-19)	22.55992	15.893	0.991	2.599	0.481	2.651	0.69	20.863	1.473	2.599	0.662	1.774	0.721
HC_7N(22-21)	24.81588	16.367	0.954	2.056	0.477	2.62	0.794	20.378	1.753	2.056	0.815	1.4	0.83
HC_7N(23-22)	25.94385	15.714	0.6	2.068	0.298	3.434	0.65	19.767	0.646	2.068	0.294	3.129	0.671
HC_7N(24-23)	27.0718	16.752	0.74	2.029	0.402	3.767	0.758	20.99	0.93	2.029	0.459	2.971	0.804
HC_7N(25-24)	28.1998	16.12	0.432	1.819	0.273	3.137	0.414	19.933	0.484	1.819	0.257	2.751	0.468
HC_7N(26-25)	29.3277	18.365	0.5	3.454	0.645	1.356	0.147	nan	nan	nan	nan	nan	nan
HC_7N(27-26)	30.45575	16.061	0.817	2.587	0.374	5.569	1.246	20.93	1.386	2.587	0.606	3.254	1.279
HC_7N(28-27)	31.5837	16.353	1.16	2.421	0.474	6.592	2.705	20.412	1.693	2.421	0.575	4.409	2.89
HC_7N(29-28)	32.7117	17.57	0.25	2.575	0.317	3.247	0.201	23.836	nan	0.463	nan	1.297	nan
HC_7N(30-29)	33.8396	17.208	0.067	2.926	0.071	5.821	0.112	nan	nan	nan	nan	nan	nan
HC_7N(31-30)	34.9676	18.361	1.176	2.325	0.956	0.619	0.27	nan	nan	nan	nan	nan	nan
HC_7N(32-31)	36.0955	17.396	0.131	3.256	0.144	5.725	0.144	nan	nan	nan	nan	nan	nan
HC_7N(33-32)	37.2235	15.086	0.119	1.623	0.114	5.993	0.328	21.053	0.186	1.623	0.183	3.361	0.291
C_3N(2-1,3/2-1/2)	19.79995	16.726	0.408	4.562	0.422	0.815	0.061	nan	nan	nan	nan	nan	nan
C_3N(2-1,5/2-3/2)	19.7808	16.673	6.134	2.209	2.461	0.592	1.3	20.702	8.776	2.209	4.121	0.412	1.23
C_3N(3-2,5/2-3/2)	29.69513	18.583	0.143	3.103	0.16	2.65	0.104	nan	nan	nan	nan	nan	nan
C_3N(3-2,7/2-5/2)	29.67628	18.492	0.142	2.924	0.152	3.227	0.134	nan	nan	nan	nan	nan	nan
C_4H(2-1,5/2-3/2)	19.01514	8.482	2.678	3.998	3.053	0.284	0.081	19.085	1.507	3.998	1.202	0.511	0.074
C_4H(3-2,5/2-3/2)	28.57131	16.834	2.575	6.989	3.127	0.422	0.118	nan	nan	nan	nan	nan	nan
C_4H(3-2,7/2-5/2)	28.53231	17.468	7.573	1.265	3.133	1.062	2.472	21.032	11.46	1.265	6.954	0.828	0.658
C_6H(15/2-13/2,3/2,e)	20.79291	13.218	0.769	1.966	0.933	0.384	0.11	19.888	0.493	1.903	0.525	0.518	0.091
C_6H(15/2-13/2,3/2,f)	20.79447	10.05	2.105	7.468	2.233	0.487	0.073	nan	nan	nan	nan	nan	nan
C_6H(17/2-15/2,1/2,e)	23.74855	5	9.122	8.291	8.696	0.392	0.118	25.377	3.147	3.8	3.983	0.175	0.141
C_6H(17/2-15/2,3/2,e)	23.56518	13.679	1.382	5.268	1.632	0.485	0.103	28.487	1.515	1.458	1.629	0.135	0.137
C_6H(17/2-15/2,3/2,f)	23.5672	-1.662	84.854	30.236	81.938	0.464	0.319	nan	nan	nan	nan	nan	nan
C_6H(19/2-17/2,3/2,e)	26.33746	14.909	2.374	3.212	1.638	0.868	0.226	20.984	3.828	2.499	2.06	0.365	0.494

Table C.9 continued.

Transition	Restfreq	R_{max} 1	ΔR_{max} 1	$W_{1/2}$ 1	$\Delta W_{1/2}$ 1	F_{max} 1	ΔF_{max} 1	R_{max} 2	ΔR_{max} 2	$W_{1/2}$ 2	$\Delta W_{1/2}$ 2	F_{max} 2	ΔF_{max} 2
C_6H(19/2-17/2,3/2,f)	26.33998	17.434	0.412	3.638	0.422	0.895	0.087	nan	nan	nan	nan	nan	nan
C_6H^-(9-8)	24.78344	10.969	12.72	14.527	11.985	0.239	0.066	nan	nan	nan	nan	nan	nan
C_6H^-(11-10)	30.2908	15.159	0.258	3.26	0.276	1.093	0.069	25.22	nan	0.366	nan	0.2	nan
C_6H^-(12-11)	33.04449	18.383	0.326	3.646	0.377	0.894	0.067	nan	nan	nan	nan	nan	nan

Table C.10: List of Gaussian fit results from the radial emission profiles of each transition (restfrequency in GHz) of velocity integrated flux with $\Delta v < 7.5$ km s^{-1} for quarter Q4. The fit parameters are shell radius at maximum flux $R_{\rm max}$ (in arcsec), half shell width $W_{1/2}$ (in arcsec), and maximum flux $F_{\rm max}$ (in mJy beam^{-1}) for two components and their uncertainties determined from the least square fit routine.

Transition	Restfreq	R_{max} 1	ΔR_{max} 1	$W_{1/2}$ 1	$\Delta W_{1/2}$ 1	F_{max} 1	ΔF_{max} 1	R_{max} 2	ΔR_{max} 2	$W_{1/2}$ 2	$\Delta W_{1/2}$ 2	F_{max} 2	ΔF_{max} 2
HC_3N(2-1)	18.19631	13.929	0.093	4.85	0.107	12.027	0.1	24.139	0.534	3.129	0.393	1.37	0.181
HC_3N(3-2)	27.2943	13.689	0.018	2.544	0.018	36.632	0.219	nan	nan	nan	nan	nan	nan
HC_3N(4-3)	36.39232	14.192	0.011	2.906	0.011	68.018	0.218	nan	nan	nan	nan	nan	nan
HC_5N(8-7)	21.30126	15.077	0.063	3.193	0.068	9.847	0.094	21.847	0.167	1.935	0.138	2.405	0.146
HC_5N(9-8)	23.9639	15.256	0.042	2.979	0.044	8.207	0.095	nan	nan	nan	nan	nan	nan
HC_5N(10-9)	26.6265	14.825	0.044	2.512	0.045	12.391	0.186	nan	nan	nan	nan	nan	nan
HC_5N(11-10)	29.2892	14.04	0.042	2.375	0.043	12.917	0.205	nan	nan	nan	nan	nan	nan
HC_5N(12-11)	31.95177	14.904	0.033	3.216	0.034	24.011	0.204	nan	nan	nan	nan	nan	nan
HC_5N(13-12)	34.61440	13.786	0.035	2.221	0.037	18.244	0.252	nan	nan	nan	nan	nan	nan
HC_5N(14-13)	37.27699	14.918	0.014	2.033	0.016	52.067	0.286	20.129	0.03	1.136	0.076	14.602	0.75
HC_7N(16-15)	18.04797	17.892	0.288	3.076	0.357	1.94	0.143	25.213	0.967	1.527	0.887	0.391	0.168
HC_7N(17-16)	19.17596	16.267	0.251	4.8	0.326	1.578	0.056	25.299	1.104	1.761	1.186	0.156	0.092
HC_7N(18-17)	20.30395	12.067	1.214	3.49	1.028	6.3	0.784	nan	nan	nan	nan	nan	nan
HC_7N(19-18)	21.43193	15.295	0.418	2.397	0.305	2.321	0.173	20.989	0.71	2.397	0.435	1.377	0.188
HC_7N(20-19)	22.55992	15.094	0.505	2.522	0.341	2.591	0.251	20.721	0.804	2.522	0.459	1.661	0.275
HC_7N(22-21)	24.81588	15.368	0.165	1.858	0.162	2.257	0.121	19.95	0.16	1.136	0.473	1.357	0.396
HC_7N(23-22)	25.94385	15.199	0.469	1.996	0.27	3.163	0.383	19.542	0.757	1.996	0.418	1.928	0.385
HC_7N(24-23)	27.0718	15.28	0.323	3.487	0.354	2.524	0.139	nan	nan	nan	nan	nan	nan
HC_7N(25-24)	28.1998	16.308	0.398	2.7	0.369	2.567	0.114	20.902	0.516	1.324	0.392	0.844	0.397
HC_7N(26-25)	29.3277	14.668	0.157	2.197	0.163	3.078	0.198	nan	nan	nan	nan	nan	nan
HC_7N(27-26)	30.45575	15.758	0.479	2.041	0.292	3.932	0.463	20.119	0.697	1.972	0.401	2.556	0.521
HC_7N(28-27)	31.5837	15.408	0.234	2.058	0.147	7.293	0.406	20.057	0.427	2.058	0.267	3.937	0.402
HC_7N(29-28)	32.7117	15.114	0.197	1.455	0.167	2.428	0.242	nan	nan	nan	nan	nan	nan
HC_7N(30-29)	33.8396	15.329	0.197	2.152	nan	3.732	nan	20.374	0.826	2.152	nan	1.051	nan
HC_7N(31-30)	34.9676	14.55	0.096	1.892	0.1	5.955	0.257	23.745	0.262	1.892	0.669	3.295	2.996
HC_7N(32-31)	36.0955	14.822	0.994	1.942	0.538	4.297	1.109	19.132	1.714	1.942	1.15	2.393	0.97
HC_7N(33-32)	37.2235	15.347	0.178	3.413	0.178	5.602	0.235	nan	nan	nan	nan	nan	nan
C_3N(2-1,3/2-1/2)	19.79995	14.553	0.693	3.797	0.754	0.485	0.073	nan	nan	nan	nan	nan	nan
C_3N(2-1,5/2-3/2)	19.7808	16.865	0.284	3.712	0.303	1.047	0.068	nan	nan	nan	nan	nan	nan
C_3N(3-2,5/2-3/2)	29.69513	15.837	0.43	2.06	0.387	2.127	0.171	20.005	0.496	1.498	0.416	1.225	0.338
C_3N(3-2,7/2-5/2)	29.67628	16.834	0.162	2.821	0.169	2.983	0.142	nan	nan	nan	nan	nan	nan
C_4H(2-1,5/2-3/2)	19.01514	-4.01	19.995	17.451	9.285	0.531	0.301	nan	nan	nan	nan	nan	nan
C_4H(3-2,5/2-3/2)	28.57131	9.396	11.478	10.612	11.107	0.459	0.151	nan	nan	nan	nan	nan	nan
C_4H(3-2,7/2-5/2)	28.53231	16.329	0.39	2.227	0.453	1.221	0.179	nan	nan	nan	nan	nan	nan
C_6H(15/2-13/2,3/2,e)	20.79291	15.685	0.753	3.908	0.757	0.443	0.072	nan	nan	nan	nan	nan	nan
C_6H(15/2-13/2,3/2,f)	20.79447	12.796	0.546	4.673	0.579	0.857	0.079	nan	nan	nan	nan	nan	nan
C_6H(17/2-15/2,1/2,e)	23.74855	14.193	0.437	2.19	0.503	0.666	0.114	nan	nan	nan	nan	nan	nan
C_6H(17/2-15/2,3/2,e)	23.56518	14.214	0.697	1.481	0.932	0.435	0.204	nan	nan	nan	nan	nan	nan
C_6H(17/2-15/2,3/2,f)	23.5672	14.873	0.783	4.124	0.869	0.519	0.082	nan	nan	nan	nan	nan	nan
C_6H(19/2-17/2,3/2,e)	26.33746	15.2	0.643	3.363	0.663	0.604	0.097	nan	nan	nan	nan	nan	nan

Table C.10 continued.

Transition	Restfreq	R_{max} 1	ΔR_{max} 1	$W_{1/2}$ 1	$\Delta W_{1/2}$ 1	F_{max} 1	ΔF_{max} 1	R_{max} 2	ΔR_{max} 2	$W_{1/2}$ 2	$\Delta W_{1/2}$ 2	F_{max} 2	ΔF_{max} 2
C_6H(19/2-17/2,3/2,f)	26.33998	15.505	1.387	3.197	1.466	0.588	0.106	20.961	1.45	1.359	1.27	0.224	0.282
C_6H^-(9-8)	24.78344	14.389	1.939	5.003	1.617	0.31	0.097	nan	nan	nan	nan	nan	nan
C_6H^-(11-10)	30.2908	14.418	2.688	13.179	3.238	0.406	0.039	nan	nan	nan	nan	nan	nan
C_6H^-(12-11)	33.04449	15.88	0.323	3.105	0.321	0.861	0.075	nan	nan	nan	nan	nan	nan

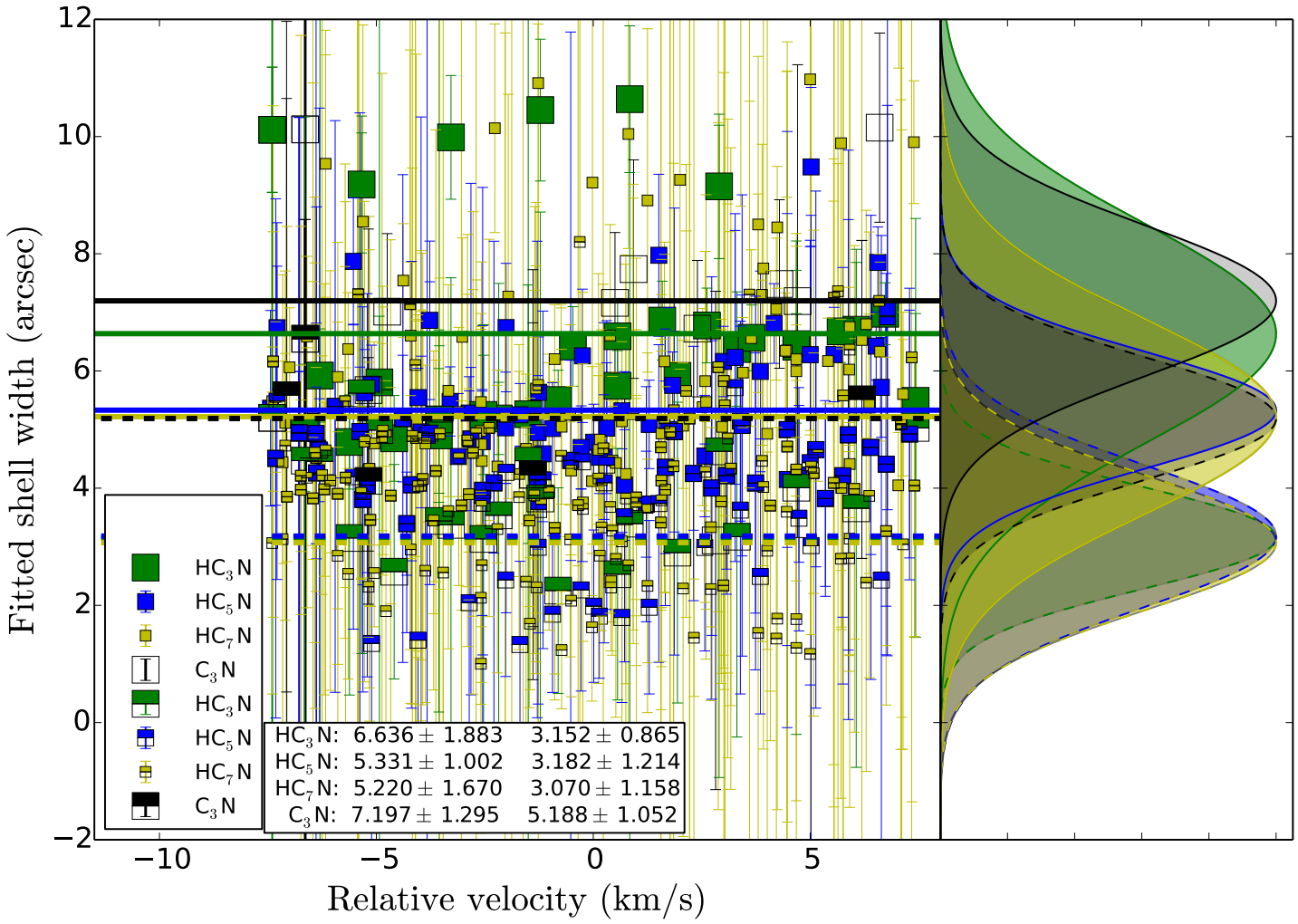

Figure C.26: Resulting shell width from the Gaussian fits to the radial profiles of each molecular transition of HC_3N (green), HC_5N (blue), HC_7N (yellow), and C_3N (black) for each channel, hence as a function of velocity (zero means the position of the star), for the azimuthal sum for two shell components. The error bars are the uncertainties from the fitting routine resulting from the flux uncertainties in the original data cube. The lines and the values in the text box are the weighted averages of each molecule for two shell components (after Eq. 4.27). These averages are visualized in the histograms on the side. The peak amplitude is arbitrarily set to the same value for each molecule, the width gives the uncertainty of the weighted average (after Eq. 4.29).

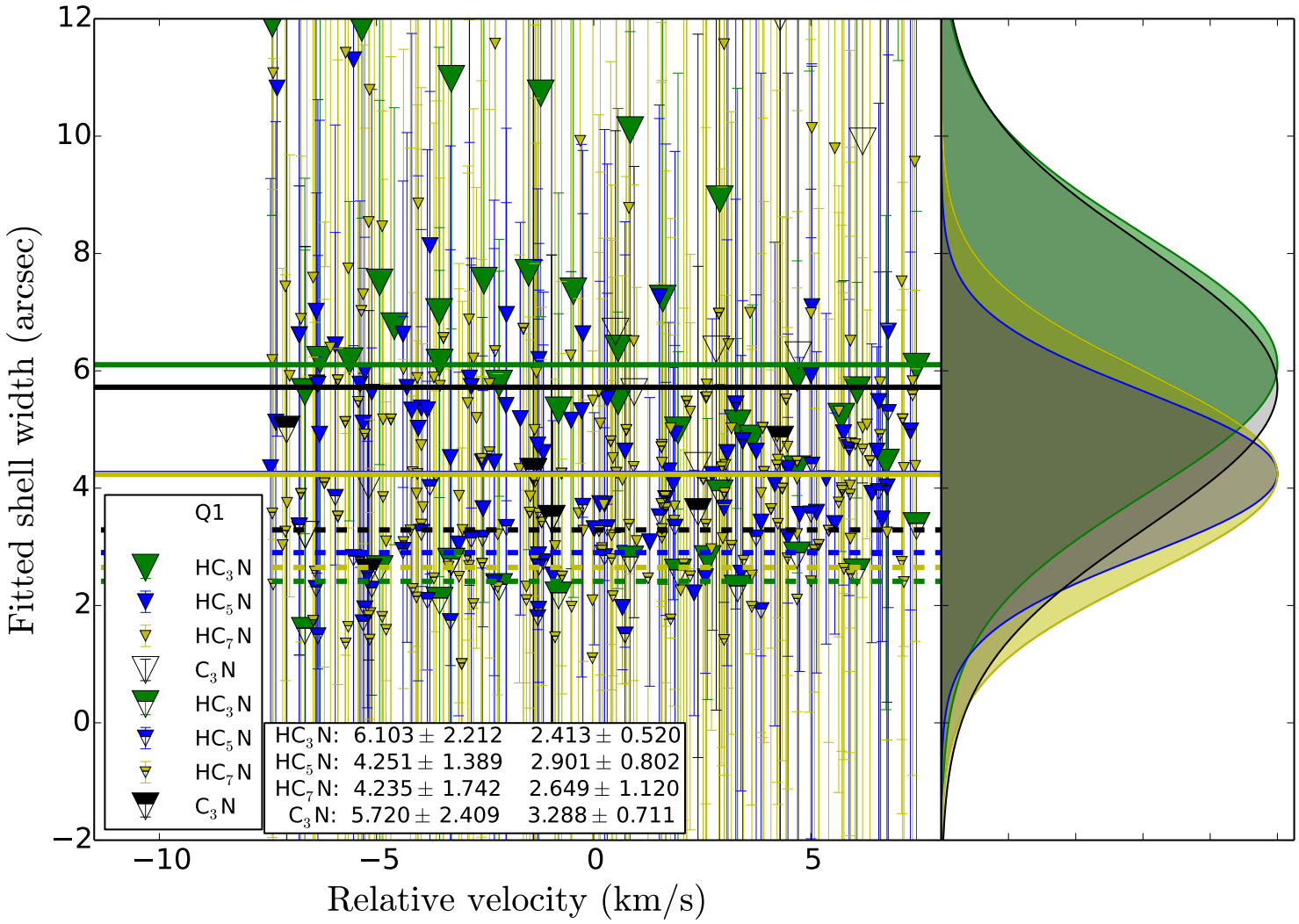

Figure C.27: As Fig. C.26 for quarter Q1.

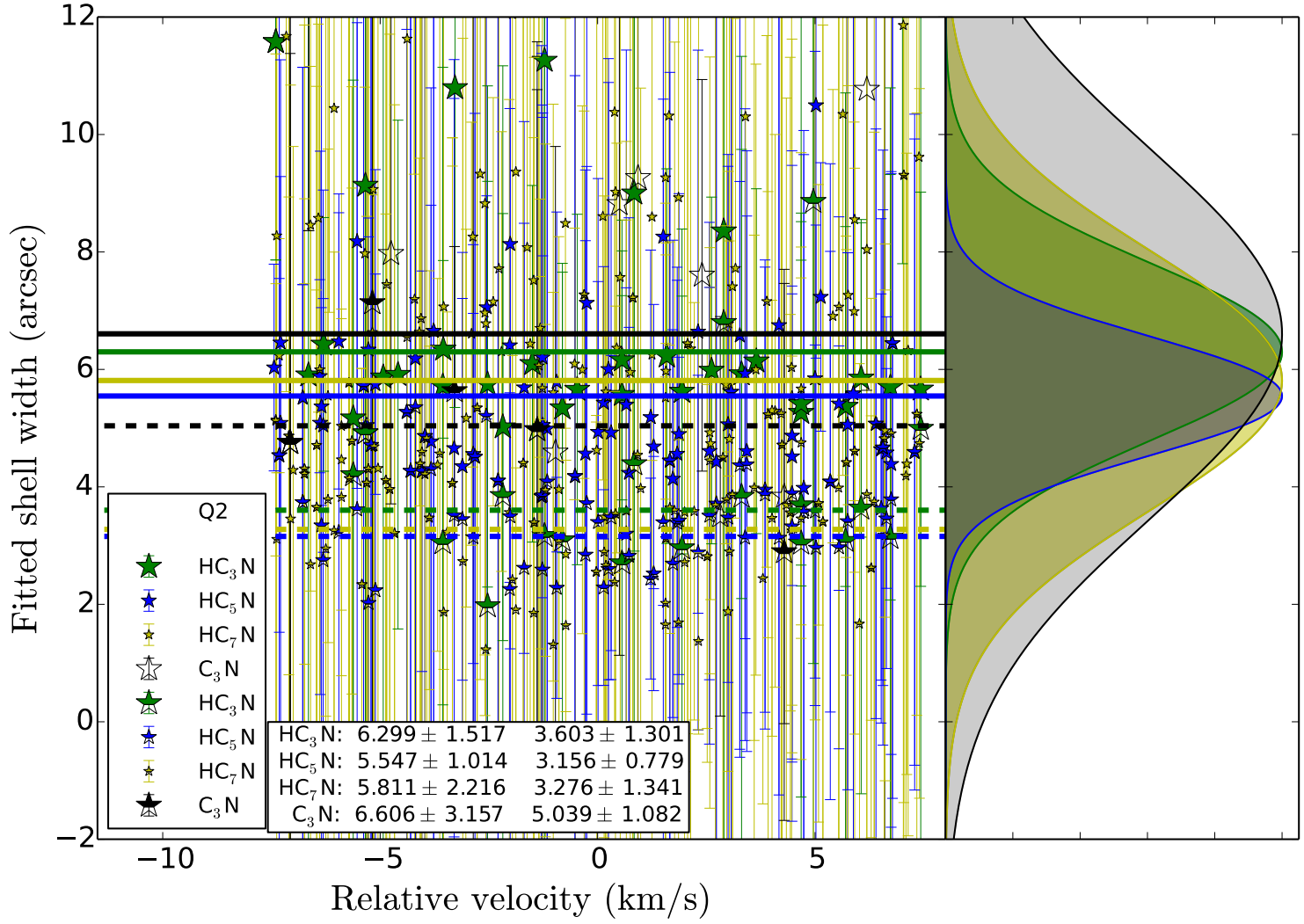

Figure C.28: As Fig. C.26 for quarter Q2.

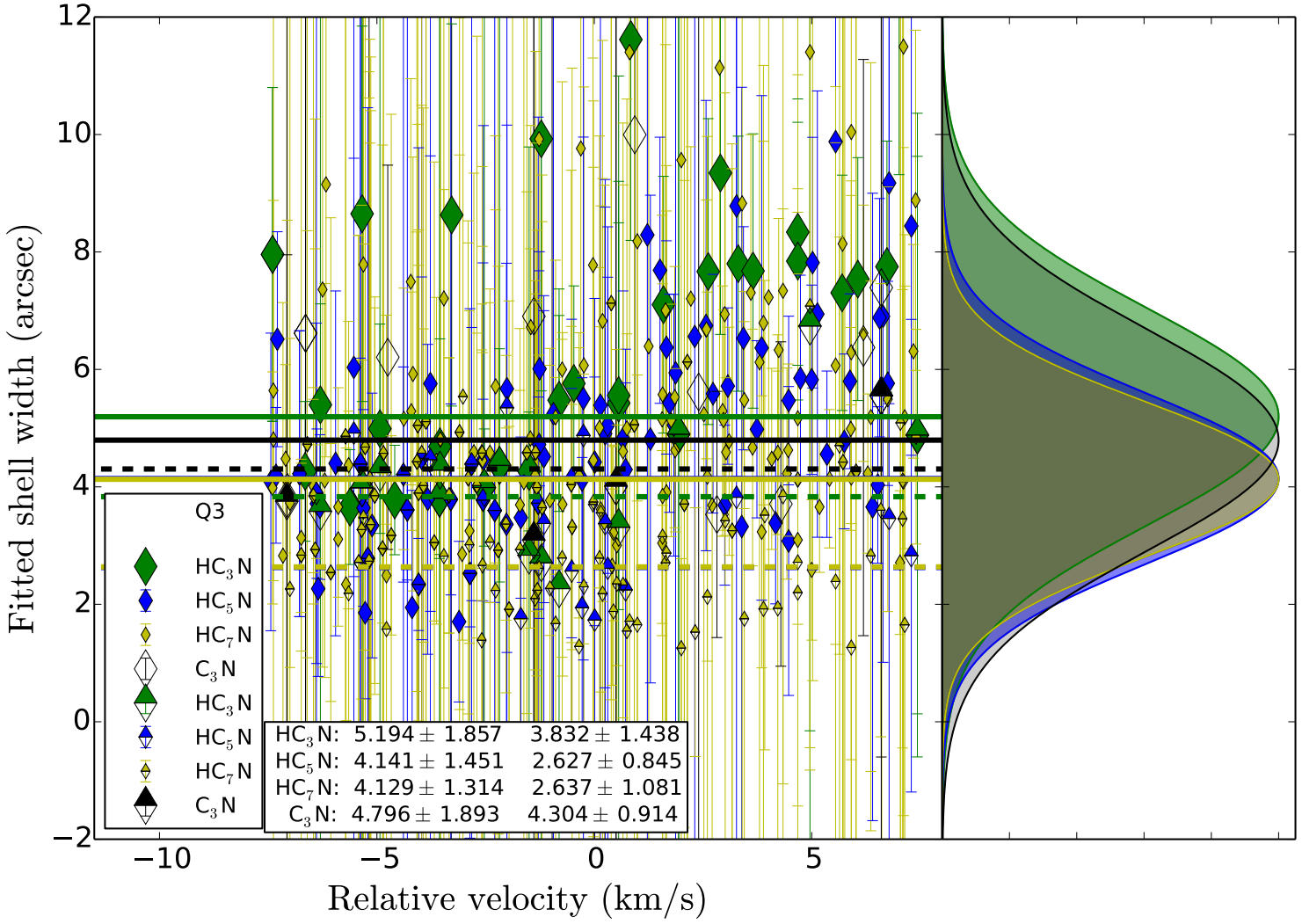

Figure C.29: As Fig. C.26 for quarter Q3.

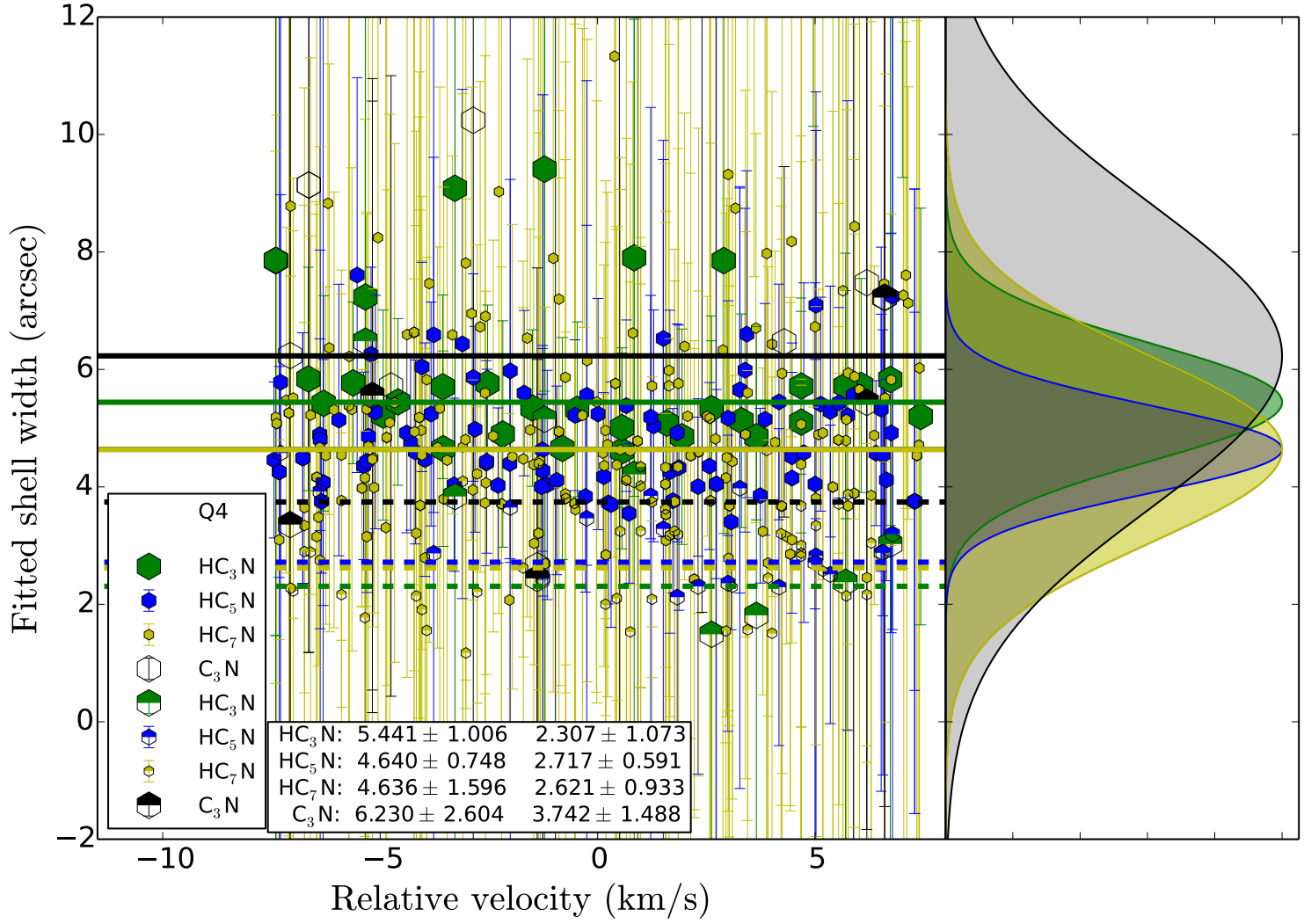

Figure C.30: As Fig. C.26 for quarter Q4.

References

Abell, G. O. & Goldreich, P. (1966). *PASP* 78, 232.
Aerts, C., Christensen-Dalsgaard, J., & Kurtz, D. W. (2010).
Agúndez, M. et al. (2008). *A&A* 479, 493–501.
Agúndez, M., Cernicharo, J., & Guélin, M. (2010). *ApJL* 724, L133–L136.
Agúndez, M. et al. (2012). *A&A* 543, A48.
Agúndez, M. et al. (2015). *ApJ* 814, 143.
Anderson, J. K. & Ziurys, L. M. (2014). *ApJL* 795, L1.
Aurière, M. et al. (2010). *A&A* 516, L2.
Balick, B. & Frank, A. (2002). *ARA&A* 40, 439–486.
Becklin, E. E. et al. (1969). *ApJL* 158, L133.
Belloche, A., Garrod, R. T., Müller, H. S. P., & Menten, K. M. (2014). *Science* 345, 1584–1587.
– (2015). In: *Revolution in Astronomy with ALMA: The Third Year*. Ed. by D. Iono, K. Tatematsu, A. Wootten, & L. Testi. Vol. 499. Astronomical Society of the Pacific Conference Series, 181.
Bell, M. B. et al. (1997). *ApJL* 483, L61–L64.
Bethe, H. A. (1939). *Physical Review* 55, 434–456.
Bieging, J. H. & Tafalla, M. (1993). *AJ* 105, 576–594.
Blackman, E. G. et al. (2001). *Nature* 409, 485–487.
Braun, R. & Walterbos, R. A. M. (1985). *A&A* 143, 307–312.
Briggs, D. (1995). PhD thesis. New Mexico Institute of Mining and Technology.
Brown, J. M. & Millar, T. J. (2003). *MNRAS* 339, 1041–1047.
Burbidge, E. M., Burbidge, G. R., Fowler, W. A., & Hoyle, F. (1957). *Reviews of Modern Physics* 29, 547–650.
Busso, M., Gallino, R., & Wasserburg, G. J. (1999). *ARA&A* 37, 239–309.
Cami, J., Bernard-Salas, J., Peeters, E., & Malek, S. E. (2010). *Science* 329, 1180.
Cernicharo, J., Guélin, M., & Kahane, C. (2000). *A&AS* 142, 181–215.
Cernicharo, J., Guélin, M., & Pardo, J. R. (2004). *ApJL* 615, L145–L148.
Cernicharo, J. et al. (2007). *A&A* 467, L37–L40.
Cernicharo, J. et al. (2010). *A&A* 521, L8.
Cernicharo, J. et al. (2011). *A&A* 529, L3.
Cernicharo, J. et al. (2013). *ApJL* 778, L25.
Cernicharo, J., Marcelino, N., Agúndez, M., & Guélin, M. (2015). *A&A* 575, A91.
Cernicharo, J. et al. (1996). *A&A* 315, L201–L204.
Chapman, J. F. et al. (2009). *MNRAS* 394, 221–230.
Cherchneff, I. & Glassgold, A. E. (1993). *ApJL* 419, L41.
Cherchneff, I., Glassgold, A. E., & Mamon, G. A. (1993). *ApJ* 410, 188–201.
Cherchneff, I. (2012). *A&A* 545, A12.

Claussen, M. J. et al. (2011). *ApJL* 739, L5.
Clayton, D. D. (1968).
Clark, B. G. (1980). *A&A* 89, 377.
Cohen, M. (1979). *MNRAS* 186, 837–852.
Condon, J. J. & Ransom, S. M. (2016). NRAO.
Cordiner, M. A. & Millar, T. J. (2009). *ApJ* 697, 68–78.
Cornwell, T. J. (2008). *IEEE Journal of Selected Topics in Signal Processing* 2, 793–801.
Cox, N. L. J. et al. (2012). *A&A* 537, A35.
Crosas, M. & Menten, K. M. (1997). *ApJ* 483, 913–924.
Crowther, P. A. (2007). *ARA&A* 45, 177–219.
De Beck, E. et al. (2012). *A&A* 539, A108.
De Marco, O. (2009). *PASP* 121, 316–342.
Decin, L. et al. (2010). *Nature* 467, 64–67.
Decin, L. et al. (2011). *A&A* 534, A1.
Decin, L. et al. (2015). *A&A* 574, A5.
Dinh-V-Trung & Lim, J. (2008). *ApJ* 678, 303–308.
Dinh-V.-Trung & Lim, J. (2009). *ApJ* 701, 292–297.
Duley, W. W. & Williams, D. A. (1984).
Eldridge, J. J. & Tout, C. A. (2004). *MmSAI* 75, 694.
Ewen, H. I. & Purcell, E. M. (1951). *Nature* 168, 356.
Fong, D., Meixner, M., & Shah, R. Y. (2003). *ApJL* 582, L39–L42.
Fonfría, J. P., Cernicharo, J., Richter, M. J., & Lacy, J. H. (2008). *ApJ* 673, 445–469.
Freytag, B. & Höfner, S. (2008). *A&A* 483, 571–583.
Gail, H.-P. & Sedlmayr, E. (2014).
– (1999). *A&A* 347, 594–616.
García-Segura, G., López, J. A., & Franco, J. (2001). *ApJ* 560, 928–933.
Girart, J. M., Patel, N., Vlemmings, W. H. T., & Rao, R. (2012). *ApJL* 751, L20.
Glassgold, A. E. (1996). *ARA&A* 34, 241–278.
Gong, Y. et al. (2015). *A&A* 574, A56.
Green, S. & Chapman, S. (1978). *ApJS* 37, 169–194.
Groenewegen, M. A. T. et al. (2012). *A&A* 543, L8.
Groenewegen, M. A. T. & Whitelock, P. A. (1996). *MNRAS* 281, 1347–1351.
Guelin, M. et al. (1995). *A&A* 297, 183–196.
Guélin, M., Neininger, N., Lucas, R., & Cernicharo, J. (1999). In: *The Physics and Chemistry of the Interstellar Medium*. Ed. by V. Ossenkopf, J. Stutzki, & G. Winnewisser, 326.
Guélin, M. (1994). In: *The Structure and Content of Molecular Clouds*. Ed. by T. L. Wilson & K. J. Johnston. Vol. 439. Lecture Notes in Physics, Berlin Springer Verlag, 260.
Habing, H. J. & Olofsson, H., eds. (2003).
Hall, P. D., Tout, C. A., Izzard, R. G., & Keller, D. (2013). *MNRAS* 435, 2048–2059.
Hamann, W.-R., Gräfener, G., & Liermann, A. (2006). *A&A* 457, 1015–1031.
Hayashi, C. (1961). *PASJ* 13.
He, J. H. et al. (2008). *ApJS* 177, 275–325.
Herbig, G. H. & Zappala, R. R. (1970). *ApJL* 162, L15.
Hertzsprung, E. (1913). *Astronomische Nachrichten* 195, 449.
Högbom, J. A. (1974). *A&AS* 15, 417.
Homan, W. et al. (2015). *A&A* 579, A118.
Howe, D. A. & Millar, T. J. (1990). *MNRAS* 244, 444–449.

Huggins, P. J., Mauron, N., & Wirth, E. A. (2009). *MNRAS* 396, 1805–1814.
Iben Jr., I. & Renzini, A. (1983). *ARA&A* 21, 271–342.
Izzard, R. G., Tout, C. A., Karakas, A. I., & Pols, O. R. (2004). *MNRAS* 350, 407–426.
Izzard, R. G. & Poelarends, A. J. T. (2006). *MmSAI* 77, 840.
Izzard, R. G. et al. (2006). *A&A* 460, 565–572.
Izzard, R. G., Glebbeek, E., Stancliffe, R. J., & Pols, O. R. (2009). *A&A* 508, 1359–1374.
Izzard, R. G. & Keller, D. (2015). In: *Why Galaxies Care about AGB Stars III: A Closer Look in Space and Time*. Ed. by F. Kerschbaum, R. F. Wing, & J. Hron. Vol. 497. Astronomical Society of the Pacific Conference Series, 161.
Jewell, P. R. & Snyder, L. E. (1984). *ApJ* 278, 176–185.
Justtanont, K., Skinner, C. J., & Tielens, A. G. G. M. (1994). *ApJ* 435, 852–863.
Kahane, C. et al. (2000). *A&A* 357, 669–676.
Karakas, A. & Lattanzio, J. (2007). *PASA* 24, 103–117.
Kawaguchi, K., Kasai, Y., Ishikawa, S.-I., & Kaifu, N. (1995). *PASJ* 47, 853–876.
Keller, D., Menten, K. M., Kamiński, T., & Claussen, M. J. (2015). In: *Why Galaxies Care about AGB Stars III: A Closer Look in Space and Time*. Ed. by F. Kerschbaum, R. F. Wing, & J. Hron. Vol. 497. Astronomical Society of the Pacific Conference Series, 123.
Kervella, P. et al. (2016). *A&A* 585, A28.
Kim, H. & Taam, R. E. (2012). *ApJL* 759, L22.
Kim, H., Hsieh, I.-T., Liu, S.-Y., & Taam, R. E. (2013). *ApJ* 776, 86.
Kim, H., Lee, H.-G., Mauron, N., & Chu, Y.-H. (2015a). *ApJL* 804, L10.
Kim, H. et al. (2015b). *ApJ* 814, 61.
Klein, U. (2006). University of Bonn.
Komatsu, E. et al. (2011). *ApJS* 192, 18.
Kroupa, P., Tout, C. A., & Gilmore, G. (1993). *MNRAS* 262, 545–587.
Kukarkin, B. V. et al. (1971). In: *General Catalogue of Variable Stars, 3rd ed. (1971)*.
Langer, N. (2009). University of Bonn.
Lattanzio, J. & Karakas, A. (2016). *ArXiv e-prints*.
Le Bertre, T., Magain, P., & Remy, M. (1989). *The Messenger* 55, 25–28.
Le Bertre, T. (1988). *A&A* 203, 85–98.
– (1992). *A&AS* 94, 377–398.
Leão, I. C. et al. (2006). *A&A* 455, 187–194.
Li, X. et al. (2014). *A&A* 568, A111.
Lindqvist, M., Schöier, F. L., Lucas, R., & Olofsson, H. (2000). *A&A* 361, 1036–1057.
Lodders, K. & Fegley Jr., B. (1999). In: *Asymptotic Giant Branch Stars*. Ed. by T. Le Bertre, A. Lebre, & C. Waelkens. Vol. 191. IAU Symposium, 279.
Lombaert, R. et al. (2016). *A&A* 588, A124.
Lucas, R. et al. (1995). *Ap&SS* 224, 293–296.
Lucas, R. & Guélin, M. (1999). In: *Asymptotic Giant Branch Stars*. Ed. by T. Le Bertre, A. Lebre, & C. Waelkens. Vol. 191. IAU Symposium, 305.
Maercker, M. et al. (2016). *A&A* 586, A5.
Maercker, M. (2009). PhD thesis. University of Stockholm.
Mangum, J. G. & Shirley, Y. L. (2015). *PASP* 127, 266–298.
Mastrodemos, N. & Morris, M. (1999). *ApJ* 523, 357–380.
Mauron, N. & Huggins, P. J. (2000). *A&A* 359, 707–715.
– (2006). *A&A* 452, 257–268.
Mauron, N., Huggins, P. J., & Cheung, C.-L. (2013). *A&A* 551, A110.

Mauron, N. & Huggins, P. J. (1999). *A&A* 349, 203–208.
Men'shchikov, A. B. et al. (2001). *A&A* 368, 497–526.
Menten, K. M. et al. (2006). *A&A* 453, 301–307.
Menten, K. M., Reid, M. J., Kamiński, T., & Claussen, M. J. (2012). *A&A* 543, A73.
Mestel, L. & Ruderman, M. A. (1967). *MNRAS* 136, 27.
Millar, T. J., Herbst, E., & Bettens, R. P. A. (2000). *MNRAS* 316, 195–203.
Millar, T. J. et al. (2007). *ApJL* 662, L87–L90.
Millar, T. J. & Herbst, E. (1994). *A&A* 288.
Millar, T. J. (2016). *Journal of Physics Conference Series* 728.5, 052001.
Miszalski, B. et al. (2009). *A&A* 496, 813–825.
Mohamed, S. & Podsiadlowski, P. (2012). *Baltic Astronomy* 21, 88–96.
Montargès, M. et al. (2016). *A&A* 588, A130.
Morris, M. et al. (2006). In: *Planetary Nebulae in our Galaxy and Beyond*. Ed. by M. J. Barlow & R. H. Méndez. Vol. 234. IAU Symposium, 469–470.
Morris, K. & Momjian, E. (2012). *VLA Expansion Project Memoranda* 154.
Morris, M., Zuckerman, B., Palmer, P., & Turner, B. E. (1971). *ApJL* 170, L109.
Morris, M. et al. (1975). *ApJL* 199, L47–L51.
Morris, M. (1975). *ApJ* 197, 603–610.
Müller, H. S. P., Thorwirth, S., Roth, D. A., & Winnewisser, G. (2001). *A&A* 370, L49–L52.
Müller, H. S. P., Schlöder, F., Stutzki, J., & Winnewisser, G. (2005). *Journal of Molecular Structure* 742, 215–227.
Neufeld, D. A. et al. (2011a). *ApJL* 727, L28.
Neufeld, D. A. et al. (2011b). *ApJL* 727, L29.
Neugebauer, G. & Leighton, R. B. (1969).
Nittler, L. R. (2008). In: *Organic Matter in Space*. Ed. by S. Kwok & S. Sanford. Vol. 251. IAU Symposium, 343–344.
Ohnaka, K. et al. (2011). *A&A* 529, A163.
Ohnaka, K. et al. (2013). *A&A* 555, A24.
Ohnaka, K., Weigelt, G., & Hofmann, K.-H. (2016). *A&A* 589, A91.
Olofsson, H. et al. (2000). *A&A* 353, 583–597.
Paczyński, B. (1971). *ActaA* 21, 417.
Parker, Q. A. et al. (2015). In: *American Astronomical Society Meeting Abstracts*. Vol. 225. American Astronomical Society Meeting Abstracts, 108.06.
Patel, N. A. et al. (2011). *ApJS* 193, 17.
Pickett, H. M. et al. (1998). *JQSRT* 60, 883–890.
Planck Collaboration et al. (2014). *A&A* 571, A16.
Pols, O. R. (2009).
Quintana-Lacaci, G. et al. (2016). *ApJ* 818, 192.
Reber, G. (1940). *ApJ* 91, 621–624.
– (1944). *ApJ* 100, 279.
Reimers, D. (1975). *Memoires of the Societe Royale des Sciences de Liege* 8, 369–382.
Sahai, R. & Chronopoulos, C. K. (2010). *ApJL* 711, L53–L56.
Schmidt, G. D., Hines, D. C., & Swift, S. (2002). *ApJ* 576, 429–444.
Schöier, F. L., van der Tak, F. F. S., van Dishoeck, E. F., & Black, J. H. (2005). *A&A* 432, 369–379.
Schwarzschild, M. & Härm, R. (1965). *ApJ* 142, 855.
Schwab, F. R. (1984). *AJ* 89, 1076–1081.
Siess, L. (2006). *A&A* 448, 717–729.

Simis, Y. J. W., Icke, V., & Dominik, C. (2001). *A&A* 371, 205–221.
Skrutskie, M. F. et al. (2006). *AJ* 131, 1163–1183.
Smolders, K., Acke, B., Verhoelst, T., & al., et (2010). *A&A* 514, L1.
Soker, N. & Clayton, G. C. (1999). *MNRAS* 307, 993–1000.
Soker, N. (2000). *ApJ* 540, 436–441.
– (2002a). *MNRAS* 336, 826–830.
– (2002b). *ApJ* 570, 369–372.
– (2006). *PASP* 118, 260–269.
Solomon, P., Jefferts, K. B., Penzias, A. A., & Wilson, R. W. (1971). *ApJL* 163, L53.
Stanghellini, L. (2009). In: *The Magellanic System: Stars, Gas, and Galaxies*. Ed. by J. T. Van Loon & J. M. Oliveira. Vol. 256. IAU Symposium, 421–430.
Steffen, M. & Schönberner, D. (2000). *A&A* 357, 180–196.
Stewart, P. N. et al. (2016). *MNRAS* 455, 3102–3109.
Taylor, G. B., Carilli, C. L., & Perley, R. A., eds. (1999). Vol. 180. Astronomical Society of the Pacific Conference Series.
Tenenbaum, E. D. et al. (2010). *ApJS* 190, 348–417.
Tielens, A. G. G. M. (2005).
Tsuji, T., Ohnaka, K., Aoki, W., & Yamamura, I. (1997). *A&A* 320, L1–L4.
Tsuji, T. (1964). *Annals of the Tokyo Astronomical Observatory* 9.
Tucker, K. D., Kutner, M. L., & Thaddeus, P. (1974). *ApJL* 193, L115–L119.
Vassiliadis, E. & Wood, P. R. (1993). *ApJ* 413, 641–657.
– (1994). *ApJS* 92, 125–144.
Villaver, E., García-Segura, G., & Manchado, A. (2002). *ApJ* 571, 880–900.
Vlemmings, W. H. T., van Langevelde, H. J., & Diamond, P. J. (2005). *A&A* 434, 1029–1038.
Weinreb, S., Barrett, A. H., Meeks, M. L., & Henry, J. C. (1963). *Nature* 200, 829–831.
Wilson, T. L., Rohlfs, K., & Hüttemeister, S. (2013).
Wilson, R. W., Solomon, P. M., Penzias, A. A., & Jefferts, K. B. (1971). *ApJL* 169, L35.
Wilson, W. J., Schwartz, P. R., & Epstein, E. E. (1973). *ApJ* 183, 871–881.
Winget, D. E. et al. (1987). *ApJL* 315, L77–L81.
Winters, J. M., Dominik, C., & Sedlmayr, E. (1994). *A&A* 288, 255–272.
Wittkowski, M. et al. (2016). *A&A* 587, A12.
Woitke, P. (2006). *A&A* 452, 537–549.
Woods, P. M., Schöier, F. L., Nyman, L.-Å., & Olofsson, H. (2003). *A&A* 402, 617–634.

List of Figures

List of Tables

Acknowledgements

The long journey comes to an end, and yet it feels like time passed by very quickly. I am glad to have been accompanied by many great and interesting people along the way, whom I would like to thank here.

First of all, I thank Karl Menten for the opportunity to work in his working group. Thank you for your generous support for my travels to workshops, meetings, and conferences to expand my knowledge, present my project and connect with colleagues. Thank you for the chance to perform observations with the APEX telescope in Chile and the Effelsberg telescope. I admire your excitement for science, your continuos flow of new ideas, and your effort to push the boundaries of the possible.

I am thanking Norbert Langer for agreeing to be my second examiner and his kind support. You are a constant in my academic path from the Bachelor thesis, the Master thesis and now the PhD thesis.

I am also thanking my third and fourth examiners, Stephan Schlemmer and Diana Imhof, for their interest in my work and the straightforward communication.

Furthermore, I am thankful to the International Max Planck Research School for Astronomy & Astrophysics (IMPRS) and the Bonn-Cologne Graduate School for Physics and Astronomy (BCGS) for their guidance, supporting lectures and seminars, community and their financial support.

A very big thank you goes to Leen Decin and Alex de Koter. Your support and guidance helped so much to shape my dissertation and I am deeply grateful that you included me into your team in which I feel very welcome. Without you and our regular meetings in Leuven, my PhD time would have been a lot harder.

Thank you, Tomek, for your interest, your support, and your time for proof-reading. Thank you for teaching me several tricks regarding data reduction and interpretation and how to observe with APEX. We had good times at the telescope. Thank you for including me into your projects.

I would like to thank Friedrich Wyrowski for his support and constructive thoughts. Whenever you were available, you had open ears for my questions and valuable ideas. With your sharp mind and your understanding you were of great help to me.

I am thanking Mark Claussen for providing the VLA data for my dissertation. Thank you for the opportunity to work on this. You gave a warm welcome and great support during my time in Socorro. Also thank you to the rest of the NRAO colleagues who made my time in Socorro special.

Thank you, Andreas, for answering countless question about the VLA data, helping me to understand the data, its calibration and imaging. You were very important in going through the hard-work of data reduction.

Thank you, Helmut, for your interest in my work, for your help with the Effelsberg proposal, and for attending several meetings.

Thank you to the colleagues, operators, and staff at APEX who made my time in Chile during three observation runs very comfortable, interesting, exciting, and enjoyable. I learned so much from all of you, not just regarding astronomy.

A huge thank you to Shahram, for your enormous help and guidance in understanding the interferometric data. You were essential on my path to extract meaningful information from the data. I am very thankful that you provided me with a helpful start and support for my exploration of the Python world.

Thank you, Benjamin, for the guidance, your help and explanations for the Effelsberg proposal and observations. I have great appreciation for your time performing the data reduction.

Thank you so much, Tobias, for your enormous amount of time for proof-reading my thesis in detail and improving it significantly with so many great tips and thoughts.

Of course, thanks a lot to the rest of our group from the AIfA, for making my time in Bonn – free time and working time – very great and fun: Verena, Kathi, Nadya, Lars, Daniel, Fabian, Daniel, Henrik. A special wholehearted thank you to Verena, you are always there with the right supporting encouraging words and actions. Also, thank you, Steffi, for your unshakable support and kindness.

I thank my lovely colleagues, Carsten and Denise, for great conversations at countless coffee or tea breaks, after-work drinks and, of course, at APEX. You always have an open ear for me during hard and also good times.

Thanks to all colleagues in the sub-mm group, the office mates I had during my time at the MPIfR, and everyone who I haven't mentioned yet, you are not forgotten, all of you made the working hours more pleasant.

Also many thanks to the wonderful smart funny colleagues in Leuven, especially my new office mates Marie and Ward. You enable an easy transition and start for me at the IvS. I'm looking forward to a great time full of science.

I thank all my other friends and my family, who always believed in me, for their steady support. A wholehearted big thank you goes to my dad and to my partner. Without you I could not have reached this accomplishment. Thank you for your endless support, belief in me, and encouragement. You are my anchors.